

Proceedings of the
14th International Conference on
Condensed Matter Nuclear Science
and the
14th International Conference on
Cold Fusion (ICCF-14)

10-15 August 2008
Washington DC

Volume 1

General Editors:

David J. Nagel and Michael E. Melich

Theory Editors:

Rodney W. Johnson and Scott R. Chubb

Copy Editor:

Jed Rothwell

ISBN: 978-0-578-06694-3

Rights to the papers herein are reserved by their
respective authors

Printing was done by the
Marriott Library of the University of Utah

Copies of these proceedings can be purchased on a DVD
for \$20 from:

New Energy Foundation, Inc.
P.O. Box 2816
Concord, NH 03302-2816

<http://www.infinite-energy.com>
Phone: 603-485-4700

Preface

This Preface has five main sections:

Background. The development of the field, which was originally called “cold fusion” and is now known by various other names, is discussed here.

Terminology - What name do you give this discovery? A review is given of the diversity of terms and motivations for their use to describe the field.

The International Conferences on Cold Fusion – A statistical history. This conference series has been the primary venue for exchange of scientific information in the field. Locations, dates, and the numbers of attendees, countries represented, papers, and authors, are tabulated along with other data and comments.

Strategies for ICCF-14 and These Proceedings. A deliberate strategy was developed to set the location and the agenda for ICCF-14. This section gives an overview of the main parts of the conference, and provides the motivations for why they were scheduled as they were. It also explains the character of introductions written specifically for each section of these proceedings in order to make them intelligible to a wider audience.

Summary of the Field. Presents an overall summary of the field, organized by what is not known and what is known.

Background

Truly unexpected experimental results, which seem beyond explanation by well-developed physical theory, became increasingly rare at the end of the twentieth century. After World War II, physical scientists sought, with significant success, to work out the implications of electromagnetism, relativity, nuclear and elementary particle processes, and even superconductivity, all within the context of the various flavors of quantum mechanics.

The last time such confidence had existed in natural science was around 1870. By 1870 the crisis of Newtonian mechanics was seemingly resolved with the theoretical prediction of a new planet, its orbit and mass, and the subsequent observation of Neptune. The integration of electricity and magnetism by Maxwell in the 1860s set the foundation for all subsequent thinking about this class of effects. This confidence began eroding in the mid-1870s. The experimentally driven revolutions of the last twenty-five years of the nineteenth century, notably “x-rays”, “radioactivity”, and “charged corpuscles” (electrons), delivered to the twentieth century science a wealth of change that seemed mostly under control by the 1980’s.

Thus, two unexpected announcements in the late 1980’s, high temperature superconductivity and “cold fusion”, echoed the disruptive experiments of the end of the nineteenth century. Bednorz and Mueller discovered high temperature superconductors in 1986 and were awarded the Nobel Prize in Physics in 1987. In 1989, it was reported that the metal palladium, when densely loaded with hydrogen, particularly the mass two isotope deuterium, produced so much heat that known chemistry could not explain the observed energy. This immediately led to speculation that nuclear processes had to be responsible for the anomalous heat production, a

potentially even more amazing discovery. These discoveries share a common property: they occur in complex solids operating under conditions not normally found in nature. They are so-called many-body systems, whose complexities are legendary. An unusually readable and scientifically superb account of superconductivity is available from Herbert Frohlich "The Theory of the Superconductive State", Reports on Progress in Physics, Volume XXIV(1961).

The discoverers of what they called "cold fusion", Martin Fleischman and Stanley Pons, set off a scientific firestorm by speculating that chemical systems can control nuclear processes. Their 26 April 1989 testimony before the Committee on Science, Space, and Technology of the US House of Representatives included a speculation that, if deuterium was indeed the fuel in their experiments, then they had measured a process that produced at least eight times as much energy as was required to operate the "reactor", which would burn that fuel. This claim was incredible to those who had labored intensely for 40 years trying to build machines that would burn deuterium by simulating the conditions found in the sun. But, they had yet to demonstrate they could produce enough energy to sustain operation of their "hot fusion" reactors. The experiments had even not reached "break-even." Even more incredible to those versed in nuclear physics was the absence of harmful levels of ionizing radiation or neutrons. Furthermore, the Fleischmann-Pons experiment seemed simple and cheap, which it was in terms of equipment, but not in terms of the physical processes involved.

In retrospect, the Fleischmann-Pons Effect (FPE) experiments, which showed that the chemically impossible amounts of energy generated by deuterated palladium, were anything but simple. They involved the complexities found in materials science, nuclear physics, electrochemistry, and other disciplines, plus the analytical challenge of trace element detection and quantification. The majority judgment made in the Department of Energy's November 1989 Report of its Cold Fusion Panel, part of the Energy Research Advisory Board, asserted that the large quantity of measured heat was an experimental artifact. The Panel's report is a marvel of bureaucratic civility and correctness. It delivered with finesse a door-closing end to further serious consideration by the general science community. The tension between the panel members and the co-chairman, Prof. John Huizenga, is captured in the line from the Executive Summary: "The Panel also concludes that some observations attributed to cold fusion are not yet invalidated." But, true to the threat that a new mouth to feed would be added to the nuclear and particle physics research table, the following was produced: "The Panel recommends against the establishment of special programs or research centers to develop cold fusion. However, there remain unresolved issues, which may have interesting implications. The Panel is, therefore, sympathetic toward modest support for carefully focused and cooperative experiments within the present funding system." To our knowledge, all LENR proposals from non-DOE laboratories have been rejected for funding by the DOE. Interestingly, Prof Huizenga promoted his provocatively entitled assessment of the matter in his 1993 book *Cold Fusion: The Scientific Fiasco of the Century*. Professor Huizenga had been Chairman of the National Academy of Science Committee on Nuclear and Radio Chemistry that was in place in the late 1980s. His unyielding vigor in lobbying colleagues on the committee for the narrow interests of his field of specialty was noteworthy. He attended ICCF-4 in 1993, but found no compelling evidence in what was presented there. As late as 1999, in an interview during press conference

on the tenth anniversary of the FPE, Huizenga was holding to his position: “It’s as dead as ever.”

Most of the essential elements of the DOE Panel critique of the FPE heat discovery have been extensively examined and addressed in the literature, particularly as to the presence of an effect. However, there does not exist at this time a “simple” experiment with a clear theoretical explanation, which comes with the two-body scattering models that have been the bread and butter of the nuclear physics world. There are strong experimental indications that some nuclear processes are modulated by the environments inside solids. Notably, the enhancement of fusion cross-sections in metals and compounds containing deuterium has been measured in diverse experiments.

Despite the very limited amount of work done on the FPE compared to the complexity of the problem, research has been supported by the US Department of Defense, government funding agencies in Japan, Russia, Italy, France, and China, and a number of private investors and closely held corporations. Because some of the investigations do not require large capital investments there is a hardy band of researchers who have independently added important understanding about the FPE. This demonstrates that the industrial science model of post WWII in physics is not the only approach to science. Just as the chemists and biologists have joined forces to dominate late twentieth century science, the FPE offers the opportunity for important results to be obtained by individuals and small groups.

Terminology – What name do you give this discovery?

The field of this conference has been called cold fusion since Fleischmann and Pons speculated that their heat production could only be explained by non-chemical processes, that their fuel was deuterium, and that it wasn’t “hot fusion.” The term cold fusion was already in use to describe muon-catalyzed fusion, an understood physical mechanism in which fusion of two deuterons occurs at relatively high rates in the presence of muons. In 1989, the term “cold” for the new and mysterious effect, was meant to contrast deuteron fusion at room temperature with known fusion processes in plasmas, which have temperatures of millions of degrees K.

As time passed during the 1990s, processes other than fusion of two deuterons were reported. These transmutation reactions involved and produced isotopes of nuclei with moderate and high atomic weights, and not only two light nuclei undergoing fusion. Because of this, and to emphasize their viewpoints, some researchers in the field sought other names for the effect announced by Fleischmann and Pons. A tabular summary with the various names applied to “cold fusion” follows, plus our comments on the strengths and weaknesses of the various names.

Table 1. Names given to the study of “cold fusion” since 1989

Terminology	Comments
Cold Fusion	Original and recognized name, but incomplete
Low Energy Nuclear Reactions	Low is a relative term and unclear
Lattice Enabled Nuclear Reactions	Clear and specific, but very new and little known
Lattice Assisted Nuclear Reactions	Also accurate, but little used
Chemically Assisted Nuclear Reactions	Many chemists like this
Cold Fusion Nuclear Reactions	Little used
Cold Nuclear Transmutations	A Russian favorite
New Hydrogen Energy	A major Japanese program
Metal Deuterium Energy	A current program in Japan
SANER	<u>S</u> Afe <u>N</u> uclear <u>E</u> nergy <u>R</u> elease
Fleischmann-Pons Effect	Clear and encompassing

Table 1 shows most of the titles given to the study of “cold fusion” over the 20 years since its announcement. The field is now widely considered to be part of “Condensed Matter Nuclear Science.”

None of these names has gained universal acceptance. In the minds of some workers in the field, they suffer from various shortcomings. For example, "cold" and "low" are relative terms without precise meanings. The variety, and indeed confusion, over terminology is also promoted by the lack of a clear understanding of the basic mechanism (or mechanisms) active in this field. The overall terminology situation was not aided by the foundation of a software company called Cold Fusion, which often shows up in internet searches.

In 2002, a new and broader name was introduced, namely “Condensed Matter Nuclear Science” (CMNS). “Condensed matter” is a term that has been employed by the American Physical Society for a few decades to embrace both solids and liquids. CMNS was meant to focus on the science of nuclear effects in systems involving solids (always) and liquids (often). It is an appropriate description for the current and continuing science of the field, but it will fail to embrace anticipated engineering work based on that science. The International Society for Condensed Matter Nuclear Science was founded in the U.K. in 2003 (www.iscmns.org). It is the primary intellectual scientific society for the field.

At present, given all the problems with the name of the field, many people are simply and clearly referring to the mechanism(s) active in the experiments that followed from the 1989 announcement as the "Fleischmann-Pons Effect" (FPE). That effect is the production of heat and other products in a metallic system under unusual circumstances of very high densities of hydrogen or deuterium. It is interesting to remember that, in the Fleischman-Pons patent application, light water and nickel, as well as other hydrided metals, were included in their claims. Although much of the focus has been on deuterium and palladium, there are credible Italian papers reporting heat being produced from light water and nickel.

Input Processes: Loading a Solid	Output (Measurements)			
	Excess Heat	Nuclear Products	Prompt Radiation	Low Energy Emissions
Liquids: Electrochemical				
Gases: Thermodynamic				
Plasmas: Kinetic				
Beams: Kinetic				

Figure 1. The means of loading protons or deuterons into lattices, and the types of measurements made to prove the existence and determine the properties of LENR.

It is known experimentally that the amount of heat produced per reaction can be over 1000 times the energy released by any known chemical reaction. The power densities (measured in watts per cubic centimeter of the metal) occasionally exceed those in fission nuclear power systems. Associated with this heat in many experiments is the production of helium-4 at levels that account for the heat, if each atom of helium is associated with about 24 million electron volts of energy. Small amounts of tritium, the mass-three isotope of hydrogen, plus other nuclei, energetic particles and photons, and low energy quanta, such as infrared radiation, have been reported for many experiments. Figure 1 shows one way to organize the four means of loading hydrogen isotopes into lattices and the four classes of measurements just mentioned. This arrangement served as the organizing principle for the conference and, hence, for these proceedings.

History of the International Conferences on Cold Fusion

While this sequence of conferences has been the major venue for presentation of results on the FPE effect, its continuation and evolution are subject to much current discussion. The characteristics of past conferences provide a basis for that consideration. The rest of this section presents some statistics on the ICCF and discusses trends over the almost 20-year history of the series. The conferences have generally rotated across three continents, North America, Europe and Asia. The next table is a summary of the dates, locations and the numbers of attendees, papers in the proceedings and authors of those papers. It is based on the proceedings of each conference and other materials, which we have acquired from our attendance at each of the ICCFs.

The number of attendees can be estimated in different ways, all of which have problems. The first method is from the lists published by conference organizers. These commonly contain more names than people who actually attended the conference, so they tend to give high numbers. The second way to estimate the number of attendees is from the official conference photo. The photos usually had some people missing, though they included administrative personnel. Hence, the numbers from the photos are generally low. The last count of attendees is the number given in the proceedings. The reported and published numbers are commonly rounded off. For example, ICCF-2 was said to have >200 attendees. Numbers from the provided lists, from counting faces in conference photos and from the proceedings are given in Table 2. The large discrepancies in the numbers of people attending ICCF-3 and -13 are indicative of the problem of accurately counting attendees. It is likely that the numbers published in the proceedings are most accurate. It must be noted that, in general, not all of the attendees were present for the entire conference.

Table 2. Summary of the dates, locations, attendees, papers and authors for the ICCF conferences

General Information			Attendees				Proceedings	
	Date	Location	List	Photo	Proceedings	Countries	Papers	Authors
1	1990	Salt Lake City UT USA	296		>200		35	90
2	1991	Lake Como Italy			>200		57	294
3	1992	Nagoya Japan	324	223	346	18	102	320
4	1993	Lahaina, Maui, HI USA			242	12	65	164
5	1995	Monte Carlo Monaco	207		228	15	76	91
6	1996	Lake Toya Hokaido Japan	175		179	17	110	288
7	1998	Vancouver BC Canada	218		206	21	*89	
8	2000	Lerici La Spezia Italy	145		145	18	68	176
9	2002	Beijing China	113	111	113	17	87	193
10	2003	Cambridge MA USA	135	98	>150		93	170
11	2004	Marseilles France			170	20	74	164
12	2005	Yokohama Japan		58			63	158
13	2007	Sochi Russia	75	52			93	
14	2008	Washington DC	180			15	97	

*The ICCF-7 Proceedings have 76 papers presented at the conference, plus 13 additional papers, which were not presented.

The number of papers can be obtained more confidently by simply counting the papers in the proceedings. But not all of the presented papers or posters result in proceeding publications. Similarly, papers that were not presented at the conference are sometimes inserted into proceedings. The author index in the proceedings gives the numbers of people with their names on the published papers. These were counted and tabulated

Given the incompleteness and uncertainty of the number of attendees, it is difficult to be very specific about attendance trends. But the general picture is evident. For the first seven meetings during 1990-1998, attendance was somewhat in excess of 200. ICCF-3 and ICCF-6, both in Japan, were the exceptions in this period. For ICCF 8 through 11, attendance was usually closer to 150. For ICCF-12 and 13, the attendance dropped significantly to well below 100. ICCF-14 had 180 attendees from 15 countries.

The numbers of countries from which attendees came for the ICCFs are shown in the table. Here again, it is not possible to draw any detailed conclusions. However, the overall picture is clear from the numbers given in the proceedings. Generally, 10 to 20 countries were represented at the conferences, and the larger delegations are usually from about six countries. There has been a significant number of attendees from the host country or continent. For example, at ICCF-3, held in Nagoya, 229 of the 346 attendees were from Japan.

The numbers of papers in the proceedings of the ICCF series varies between 35 and 110, with no strong trends over the years. The total for the first 12 conferences is 920 papers, an average of 77 published papers per conference. The total number of papers in the ICCF proceedings probably represents around one-third of the papers on the FPE since 1989. In addition to drawing most of the key scientists in the community, these conferences provide in their proceedings a primary repository of information in the field. There will probably be a need to reprint the proceedings from the earlier ICCFs as the number of scientists in the field increases. However, many of the papers presented at ICCF and published in their proceedings are available on the internet at LENR-CANR.org.

The total number of authors listed for ICCF-1 through ICCF-12, excepting ICCF-7 for which an author index is not available, is 2108. This gives an average of 192 authors for those 11 conferences. The total number over the years necessarily includes double counting of individuals who attended more than one of the ICCFs. It would be laborious to determine accurately how many individual scientists contributed to the papers in the proceedings. But, the number is at least several hundred.

There are significant factors and trends that cannot be gotten from the data in Table 2. The number of reporters present at each conference is not generally recorded. However, from attending these conferences, we know what the general level of press interest has been over the years. Initially, there was great and evident press presence, especially at ICCF-1 and -2. The number of general reporters in attendance declined to few or none throughout the following several conferences, which continued in the most recent conferences. Some researchers welcomed this absence of external scrutiny, which permitted work on the FPE to proceed without distractions from the press. We feel that this field, like any field of science, must be able to communicate its activities and results both to the broader scientific community and to the public generally. When the field is recognized and accepted as a subject for legitimate scientific inquiry, and public funds are made available to researchers in the field, then such communications will become necessary and routine.

Strategies for ICCF-14 and These Proceedings

As noted already, the ICCF series of conferences is on a three-continent rotation. Hence, it was appropriate to hold ICCF-14 in North America. We volunteered to organize ICCF-14 in Washington DC, a few minutes' walk from the national capitol and close to the regional Metro system, with two hopes in mind. One desire was to attract staffers from the nearby offices of Senators and Congressmen. The other was to make it easy for program managers from US government funding agencies to attend, especially those with responsibilities for science, energy and the environment. Such agencies include the US Departments of Energy and

Defense, the National Science Foundation and the Environmental Protection Agency. We also hoped that having the conference in the heart of the US capitol would attract mainstream press coverage. None of these possibilities materialized. However, the CBS TV show 60 Minutes did videotape part of the conference and a report on the field, not the conference, was broadcast in April 2009. The limited number of new local attendees was likely due to the conference being scheduled in August, when many people are on vacation. The ICCFs have uniformly been held in high quality settings that encouraged intense exchanges of ideas. Holding a conference in a capital city is generally expensive and ICCF-14 timing was chosen to reduce the hotel room rates, which were about half of what they are during other times of the year.

Regarding the agenda, conference organizers can be either reactive or proactive in their approach to obtaining papers for presentation. In the reactive mode, they form the agenda from the papers that have been offered in response to a Call for Papers. However, for most conferences, the organizers also invite presentations from important workers in the field that will be of broad interest to the attendees. These invitations are honorific, and they insure that the best work is highlighted.

We felt that some topics in the field needed up-to-date technical reviews at the conference. Hence, we commissioned a few reviews from key workers, in addition to inviting several luminaries in the field to give papers. The commissioned reviews were on:

1. Calorimeter design and performance for measurement of excess power and energy in the FPE experiments.
2. The experimental evidence of excess heat, the Fleischmann-Pons Effect.
3. Experiments using gas loading to produce excess heat.
4. Scattering of deuterons on deuterons within a metallic environment to assess the “screening” at energies below the coulomb barrier.

It is hoped that the commissioned papers will form the basis of later papers in a mainstream review journal, such as the Reviews of Modern Physics. These papers are identified in the introductions to the sections in which they are found in these proceedings.

The architecture of the agenda was chosen for a few purposes. One such goal was to provide during the first two days of the conference a broad overview of the field. The very important work on heat and materials was scheduled on the opening day. This was done to insure that people who could attend only one or two days of the conference would be able to get a sense of the breadth and quality of what has been done and found in the field. This strategy proved to be very successful.

Several people in the field, who have made major contributions to its development, are well past retirement age. It was felt that the chances to publicly honor such pioneers would likely be few. Hence, we scheduled two sessions on the second day to honor Professor Yoshiaki Arata from Osaka University in Japan and Dr. Stanislaw Szpak from the SPAWAR Systems Center in San Diego. The session for Professor Arata began with an overview of his work on cold fusion, and ended with a presentation by Professor Arata on his most recent and very provocative results. That session was organized by Dr. Talbot Chubb, who gave the overview.

The session for Dr. Szpak, who could not attend, consisted of an overview of the work he and his colleagues have done and published since the inception of the field. It was organized by Frank Gordon and presented by him and a few colleagues of Dr. Szpak's. We hope that future ICCFs will also include sessions recognizing key pioneers in the field.

The second day also included sessions on three very important topics: gas loading, particle measurements, and challenges facing the field. In the evening, the annual public session of the International Society for Condensed Matter Nuclear Science (ISCMNS) was held. It was organized and chaired by William Collis, the organizer and Chief Executive of the Society.

There are four classes of measurements done on FPE experiments: heat, nuclear ash, energetic particles, and low-energy phenomena, as already noted. The measurements of nuclear reaction products have tended to fall into two main classes, namely the detection of light products, such as tritium and helium, and the measurement of elements of moderate or heavy mass. The second type of research goes under the banner of transmutations, and is of widespread interest and major importance in the field. Hence, the opening session on the third day was on transmutations. However, there was too little time in that session to cover all the work in the sub-field. Hence, Professor George Miley from the University of Illinois organized a workshop on transmutations on Friday afternoon immediately after the conference. Approximately 50 scientists attended, which is a measure of the interest in transmutations.

Most of the third day was designed to serve workers in the field, both technically and for recreation. There was a session during which leading workers from several countries presented histories of work on the FPE in their countries during the almost two decades since the inception of the field. Presentations were made on work in China, France, India, Italy, Japan and Russia. This session was a major step forward in a separate project to produce and publish country histories for activities and results in the field. Some already exist in either English or the language of the country. Translations to English are in progress, with the goal of publishing a matched set of books, one for each country, in the near future.

The afternoon of the third day was devoted to the traditional conference outing. Most of the attendees participated in a visit to the Udvar-Hazy Center of the Smithsonian Air and Space Museum about an hour's drive from the conference hotel. The conference banquet was held after the tour on the third day. In addition to the meal and musical entertainment, the evening included the presentation of the Preparata Medal to Dr. Irving Dardik. The medal was prepared by William Collis on behalf of the ISCMNS. Dr. Michael McKubre gave introductory remarks, prior of the presentation to Dr. Dardik and his remarks. Several members of the Dardik family and other friends attended the dinner and award ceremony.

The fourth day of the conference included two sessions on modeling and theories that covered a very broad range of ideas. Theoretical ideas had the most papers at the conference. There were also full sessions on ion beam experimental results, on optical experiments and another partial session on materials. That Thursday included the last of three poster sessions, the other two being late on Monday and Tuesday of the conference.

The conference concluded with a half day of presentations. Several significant experimental papers, which did not fit well in the earlier sessions, were given in the first session. That was

followed by the concluding session, which included Dr. Thomas Passell's conference summary, followed by two panel discussions. The first dialogue was on Experimental Design and the second was on Realizing the Promise.

During this conference, the accumulated evidence was reviewed to show that the FPE is not an experimental artifact. The feedback from attendees indicated that ICCF-14 was a successful scientific conference. The 97 papers scheduled for oral or poster presentation included some very important new results. The information given at the conference and published in these proceedings adds significantly to the large and increasingly compelling evidence for the ability to trigger nuclear reactions, which give millions of electron volts of energy, with chemical energies on the scale of electron volts. This new and exciting scientific field is sufficient in itself. However, the possibility of clean and safe distributed nuclear power sources based on the FPE makes understanding, controlling and optimizing low energy nuclear reactions even more interesting and urgent.

This ICCF was the Fourteenth to present research results that have been developed and published by hundreds of investigators world-wide. The DOE has conducted within its national laboratories important experiments on the production of tritium in non-conventional FPE inspired configurations. The US Patent Office (PTO), as a matter of policy since the 1989 DOE Report, has rejected all devices that assume the existence of the FPE, citing the popular press accounts that say it does not exist. Clearly, the DOE and the PTO are now only occasional followers, and not leaders, of the limited understanding of the FPE. (Note added in proof: the World Intellectual Property Organization published a "cold fusion" patent on 15 October 2009.)

These proceedings depart from past documentation of the ICCF. As with the earlier volumes, the papers are binned into sections by topic. However, we seek to make the proceedings useful to a wider audience than the attendees and people already familiar with the field. Hence, we provide an introduction to each of the sections. Those introductions have two parts. The first is a technical overview of the subject of the sections. For example, the introduction to the section on calorimeters defines the various types of calorimeters discussed in the following detailed papers given at the conference. The second part of the introductory material for each section briefly cites or summarizes each of the papers in the section. It is hoped that both aspects of the section introductions will make these proceedings more useful, especially to students, who are needed to advance the field in the coming years.

Summary of the Field

The experiments in many countries over 20 years have given the field a very strong database. Part of that key data was presented at this conference. The experience to date has revealed both problems and progress. We begin with a "high level" summary of the current technical and other problems. Then, issues that have been resolved are summarized.

Unresolved Technical Issues

- Most fundamentally, the mechanisms at the heart of the production of heat by LENR are not understood, despite about two-dozen theories.

- Unknown material properties apparently play a key role in producing the FPE.
- The characteristics of the nanometer-scale locations at which LENR occur are unknown.
- Reproducibility of LENR is still below 100% in almost all experiments.
- While significant factors are known for triggering the FPE, the controllability of experiments to date is unsatisfactory.
- The net power levels from experiments to date are only on the order of 10 watts, well below what is needed for most applications or profitable commercialization.
- Continuous power production from the past experiments rarely exceeds one month.

Unresolved Support Issues

- Adequate government funding is not available for research on the FPE using modern tools, such as synchrotron radiation and atomic-force microscopes.
- Major journals and science magazines still refuse to publish papers from the field because it is still haunted by an early and poor reputation.
- The US Patent and Trademark Office generally has not approved patents on LENR based devices and processes, which deters investments by venture capitalists.

The last three problems are all due to the scientific community, which alone can legitimize the study of LENR, continuing to ignore the field for a variety of reasons. Negative statements by some prominent ex-scientists exacerbate the inattention problem. Because the study of LENR is still only a science and not yet a technology, products based on nuclear reactions at ordinary temperatures may take one or two decades to appear. However, predictions of this sort are notoriously dependent upon the cumulative man-hours devoted to studying these complex systems and the “luck” that investigators have in these largely Edisonian searches.

Resolved Issues

The above problems notwithstanding, major progress has been made on the characteristics of the FPE in the past two decades. Based on many measurements by credentialed scientists with good equipment, proper calibrations, adequate controls, and good signal-to-noise ratios, we now know that:

- It is possible to initiate nuclear reactions, each of which gives energies of about one million electron volts, by using chemical energies on the order of one electron volt.
- High temperatures are not needed to produce LENR, greatly simplifying the experimental study of the phenomenon and its potential applications.
- There are four approaches to FPE experiments, namely the use of liquids, gases, plasmas and beams to load hydrogen isotopes into certain solids, notably Palladium.
- Four types of measurements, heat that cannot be explained by chemistry, nuclear reaction (transmutation) products, low intensities of energetic particles and some low-energy phenomena, all point to the occurrence of nuclear reactions.
- Power gains in excess of ten have been observed in a few experiments
- Power densities exceeding those within nuclear fission fuel rods by 100 times have been measured.
- Values of generated energy (in electron volts per atom of the metal catalyst) in excess of 20,000 have been observed in FPE experiments.

- **The experiments do not emit dangerous radiation during their operation.**
- **No significant radioactive waste has been observed after FPE experiments.**
- **LENR do not produce greenhouse gases.**

Concluding Thoughts

As a result of the empirical knowledge now in hand, it is not unreasonable to imagine safe and green sources of nuclear power for homes, free of carbon emissions, which also will relieve stress on the power grid, because they might be small and distributed. LENR could be the basis for portable nuclear power sources, maybe even batteries. The production of clean drinking water by desalination or by purification of polluted river waters is one of the many, and perhaps the most attractive potential applications of LENR. The world health implications of clean water would be momentous. Those of us who work on the Fleischmann-Pons Effect find it an exciting and challenging field of research with remarkable practical potential. As a scientific effect, it is already historic. It remains to be seen if it will turn out to be a “game changing” practical source of energy. The field is indeed EXCITING NEW SCIENCE and it offers POTENTIAL CLEAN ENERGY.

Table of Contents

VOLUME 1

<i>Preface</i>	<i>i</i>
<i>Table of Contents</i>	<i>xiii</i>
<i>Calorimetry</i>	<i>1</i>
Twenty Year Review of Isoperibolic Calorimetric Measurements of the Fleischmann-Pons Effect.....	6
M. H. Miles and M. Fleischmann	
The Method and Results Using Seebeck Calorimetry.....	11
Edmund Storms	
Construction of a Seebeck Envelope Calorimeter and Reproducibility of Excess Heat	26
Wu-Shou Zhang, John Dash and Zhong-Liang Zhang	
Mass Flow Calorimetry	32
Michael C. H. McKubre and Francis Tanzella	
MOAC – A High Accuracy Calorimeter for Cold Fusion Studies.....	47
Scott R. Little, George A. Luce, Marissa E. Little	
Constant Heat Flow Calorimeter	53
T. V. Lautzenhiser, D. W. Phelps and M. Eisner	
A Simple Calorimetric Method to Avoid Artifacts in a Controversial Field: The Ice Calorimeter	60
Jacques Dufour, Xavier Dufour, Denis Murat and Jacques Foos	
<i>Heat Measurements</i>	<i>67</i>
The Enabling Criteria of Electrochemical Heat: Beyond Reasonable Doubt.....	71
Dennis Cravens and Dennis Letts	
Ultrasonically-Excited Electrolysis Experiments at Energetics Technologies	106
I. Dardik, T. Zilov, H. Branover, A. El-Boher, E. Greenspan, B. Khachaturov, V. Krakov, S. Lesin, A. Shapiro and M. Tsirlin	
Excess Power Gain using High Impedance and Codepositional LANR Devices Monitored by Calorimetry, Heat Flow, and Paired Stirling Engines.....	123
Mitchell Swartz	
Anomalous Heat Generation during Hydrogenation of Carbon (Phenanthrene)	147
Tadahiko Mizuno and Shigemi Sawada	

Electric and Heat Measurements in High Voltage Electrolysis Cell Experiments.....	169
A. B. Karabut and E. A. Karabut	

Nuclear Reaction Products **176**

Trace Analysis of Elements in a Palladium Matrix.....	180
David A. Kidwell	

Investigation of Nuclear Transmutation Using Multilayered CaO/X/Pd Samples Under Deuterium Permeation	195
T. Yamaguchi, Y. Sasaki, T. Nohmi, A. Taniike, Y. Furuyama, A. Kitamura and A. Takahashi	

Influence of Deuterium Gas Permeation on Surface Elemental Change of ⁸⁸Sr Ion-Implanted Pd and Pd/CaO Multi-layer System.....	203
T. Hioki, J. Gao, N. Takahashi, S. Hibi, A. Murase, T. Motohiro and J. Kasagi	

Summary of the Transmutation Workshop Held in Association with ICCF-14	212
George H. Miley	

Energetic Particle Measurements **217**

Charged Particle Emission during Electron Beam Excitation of Deuterium Subsystem in Pd and Ti- Deuteride Targets.....	220
Andrei Lipson, Ivan Chernov, Alexei Roussetski, Yuri Chardantsev, Boris Lyakhov, Eugeny Saunin and Michael Melich	

Reproducible Evidence for the Generation of a Nuclear Reaction During Electrolysis.....	250
R. A. Oriani	

Detection of Radiation Emitted from LENR.....	263
Edmund Storms and Brian Scanlan	

Partial Replication of Storms/Scanlan Glow Discharge Radiation.....	288
Rick Cantwell and Matt McConnell	

New Results of Charged Particles Released From Deuterium-Loaded Metal at Low Temperature.....	299
Songsheng Jiang, Jinghuai Li, Ming He, Shaoyong Wu, Jianqing Wang, Hongtao Zhang, Shunhe Yao, Yonggang Zhao and Chen Wang	

Development of New Detector System for Charged Particle Emission	310
Yu Toriyabe and Jirohta Kasagi	

Ion Beam Experiments **316**

Screening Potential for Nuclear Reactions in Condensed Matter.....	318
J. Kasagi	

Photon Measurements **326**

- Excess Heat Triggering by 532 nm Laser in a D/Pd Gas-Loading System** 328
J. Tian, L. H. Jin, B. J. Shen, Z. K. Weng and X. Lu
- Stimulation of Optical Phonons in Deuterated Palladium**..... 333
Dennis Letts and Peter Hagelstein
- Observation of Optical Phonon in Palladium Hydrides Using Raman Spectroscopy..** 338
Ken-ichi Tsuchiya, Aya Watanabe, Masao Ozaki and Shigeru Sasabe
- Non-Thermal Near-IR Emission from High Impedance and Codeposition LANR Devices** 343
Mitchell Swartz, Gayle Verner and Alan Weinberg
- Research into Spectra of X-ray Emission from Solid Cathode Medium During and After High Current Glow Discharge Operation** 362
A. B. Karabut and E. A. Karabut

Gas Loading **368**

- Cold Fusion by Gas Loading: A Review**..... 370
Jean-Paul Biberian
- Deuteron Electromigration in Thin Pd Wires Coated With Nano-Particles: Evidence for Ultra-Fast Deuterium Loading and Anomalous, Large Thermal Effects** 385
Francesco Celani, P. Marini, V. Di Stefano, A. Spallone, M. Nakamura, E. Purchi, O. M. Calamai, V. Andreassi, E. Righi, G. Trenta, A. Marmigi, G. Cappuccio, D. Hampai, F. Todarello, U. Mastromatteo, A. Mancini, F. Falcioni, M. Marchesini, P. Di Biagio, U. Martini, P. G. Sona, F. Fontana, L. Gamberale and D. Garbelli
- Basic Research on Condensed Matter Nuclear Reaction Using Pd Powders Charged With High Density Deuterium**..... 400
T. Nohmi, Y. Sasaki, T. Yamaguchi, A. Taniike, A. Kitamura, A. Takahashi, R. Seto and Y. Fujita

VOLUME 2

Cavitation Experiments **409**

- Bubble Driven Fusion**..... 411
Roger Stringham
- Investigation of Radiation Effects at Bubble Cavitation in Running Liquid**..... 418
Alla A. Kornilova, Vladimir I. Vysotskii, Nickolai N. Sysoev and Andrey V. Desyatov

Materials

425

- Material Science on Pd-D System to Study the Occurrence of Excess Power 429**
V. Violante, F. Sarto, E. Castagna, M. Sansovini, S. Lecci, D. L. Knies, K. S. Grabowski,
and G. K. Hubler
- Electrode Surface Morphology Characterization by Atomic Force Microscopy 437**
F. Sarto, E. Castagna, M. Sansovini, S. Lecci, V. Violante, D. L. Knies, K. S. Grabowski,
and G. K. Hubler
- Metallurgical Characterization of Pd Electrodes Employed in Calorimetric
Experiments Under Electrochemical Deuterium Loading 444**
E. Castagna, M. Sansovini, S. Lecci, A. Rufoloni, F. Sarto, V. Violante, D. L. Knies,
K. S. Grabowski, and G. K. Hubler, M. McKubre and F. Tanzella
- Condensed Matter “Cluster” Reactions in LENRs 451**
George H. Miley, Heinz Hora and Xiaoling Yang
- The Phusor®-type LANR Cathode is a Metamaterial Creating Deuteron Flux for
Excess Power Gain..... 458**
Mitchell Swartz and Gayle Verner

Theory Papers

475

- The Possible Mechanism of Creation of Light Magnetic Monopoles in Strong Magnetic
Field of a Laboratory System 484**
V. Adamenko and V. I. Vysotskii
- Heavy Electrons in Nano-Structure Clusters of Disordered Solids 490**
Dimitar Alexandrov
- Empirical System Identification (ESID) and Optimal Control of Lattice-Assisted
Nuclear Reactors..... 497**
Robert W. Bass and Mitchell Swartz
- Can Established Physical Principles Explain Solid-State Fusion?..... 503**
Ben R. Breed
- Resonant Electromagnetic-Dynamics Explains the Fleischmann-Pons Effect 521**
Scott R. Chubb
- Interface Model of Cold Fusion..... 534**
Talbot A. Chubb
- Toward an Explanation of Transmutation Products on Palladium Cathodes 540**
Norman D. Cook
- An Experimental Device to Test the YPCP (“Yukawa Pico Chemistry And Physics”)
Model: Implications for the CF-LENR Field..... 546**
Jacques Dufour, Xavier Dufour, Denis Murat and Jacques Foos

Investigation of Deuteron-Deuteron Cold Fusion in a Cavity	553
Cheng-ming Fou	
“The Coulomb Barrier not Static in QED” A correction to the Theory by Preparata on the Phenomenon of Cold Fusion and Theoretical Hypothesis.....	556
Fulvio Frisone	
Quantum Fusion Hypothesis	573
Robert E. Godes	
Excitation Transfer and Energy Exchange Processes for Modeling The Fleischmann-Pons Excess Heat Effect	579
Peter L Hagelstein and Irfan U Chaudhary	
Input to Theory from Experiment in the Fleischmann-Pons Effect	586
Peter L. Hagelstein, Michael Melich and Rodney Johnson	
A Theoretical Formulation for Problems in Condensed Matter Nuclear Science.....	596
Peter Hagelstein, Irfan Chaudhary, Michael Melich and Rodney Johnson	
Theory of Low-Energy Deuterium Fusion in Micro/Nano-Scale Metal Grains and Particles	604
Yeong E. Kim	
Complexity in the Cold Fusion Phenomenon.....	613
Hideo Kozima	
Nuclear Transmutations in Polyethylene (XLPE) Films and Water Tree Generation in Them	618
Hideo Kozima and Hiroshi Date	
Exploring a Self-Sustaining Heater without Strong Nuclear Radiation.....	623
Xing Z. Li, Bin Liu, Qing M. Wei, Shu X. Zheng and Dong X. Cao	
A Model for Enhanced Fusion Reaction in a Solid Matrix of Metal Deuterides.....	633
K. P. Sinha and A. Meulenberg	
Optimal Operating Point Manifolds in Active, Loaded Palladium Linked to Three Distinct Physical Regions	639
Mitchell Swartz	
Analysis and Confirmation of the “Superwave-as-Transitory–OOP-Peak” Hypothesis	653
Mitchell R. Swartz and Lawrence P.G. Forsley	
Dynamic Mechanism of TSC Condensation Motion	663
Akito Takahashi	

<i>Challenges and Summary</i>	670
The Importance of Replication.....	673
Michael C. H. McKubre	
Electrical Breakeven from LANR Phusor Device Systems: Relative Limitations of Thermal Loss in Feedback Loop	689
Mitchell Swartz	
Self-Polarisation of Fusion Diodes: From Excess Energy to Energy	696
Fabrice David and John Giles	
Weight of Evidence for the Fleischmann-Pons Effect	704
Rodney Johnson and Michael Melich	
Nuclear or Not Nuclear: How to Decide?	723
Ludwik Kowalski	
Open Source Science Applied to CMNS Research: A Paradigm for Enhancing Cold Fusion Prospects and the Public Interest	729
Thomas W. Grimshaw	
ICCF-14 Summary	737
Thomas O. Passell	
<i>Honoring Pioneers</i>	742
In Honor of Yoshiaki Arata	743
Talbot A. Chubb	
Establishment of the “Solid Fusion” Reactor	752
Yoshiaki Arata and Y-C Zhang	
LENR Research using Co-Deposition	766
S. Szpak, P. A. Mosier-Boss, F. Gordon, J. Dea, M. Miles, J. Khim and L. Forsley	
SPAWAR Systems Center-Pacific Pd:D Co-Deposition Research: Overview of Refereed LENR Publications	772
S. Szpak, P. A. Mosier-Boss, F. Gordon, J. Dea, J. Khim and L. Forsley	
Preparata Prize Acceptance Speech.....	778
I. Dardik	
<i>Cold Fusion Country History Project</i>	780
Xing Z. Li, Jean-Paul Biberian, Jacques Dufour, M. Srinivasan, F. Scaramuzzi, J. Kasagi, Y. Iwamura, Andrei Lipson, Ivan Chernov and Yu. N. Bazhutov	
<i>Acknowledgements</i>	789
<i>Author Index</i>	792

Introduction to Calorimetry

The production of power and heat energy is the first, most studied, and some would say, the most important, activity for the experimental study of LENR. It requires that the energy source be within a calorimeter, which gives the power flowing into and out of the vessel containing the source, and hence, the net power and energy. Because of their importance to the study of LENR, calorimeters were featured during ICCF-14. It is noted in passing there has been some calorimetry done in experiments involving gas, plasma and beam loading of materials with hydrogen isotopes. However, most LENR calorimetry has been done with electrochemical loading, and that is our focus. This section provides some basic information on calorimeters and introduces the papers on the following pages.

In most LENR experiments, the ultimate goal is to measure net power (output minus input) as a function of time. Integration of the net power-time curve gives the net energy produced. In one type of calorimeter based on melting ice, the net energy is obtained directly without having power as an intermediate value. The ice calorimeter is a so-called “first principles” calorimeter since the heat of formation of ice is well established and does not depend upon calibration of the device, just accurate weight and volume measurements.

A calorimeter is, most fundamentally, a measurement instrument. Like most measuring devices, it requires a calibration curve, which relates the value that is wanted to the signal provided by the instrument. This curve is sometimes called an “instrument function.” Calibration curves almost always have three regions, (a) a lowest signal value due to some kind of noise, (b) a range of usefulness (the dynamic range) and (c) a region where the output no longer increases or saturates for some reason. In the case of LENR experiments, the power at any time is what is needed from a calorimeter. The noise largely determines the minimum value of power that can be reliably measured. The signals from LENR calorimeters are generally voltages, but can also electrical currents or weights.

Like all sensors and measuring instruments, some fundamental mechanisms are behind the operation of LENR calorimeters. There are two primary mechanisms of interest here. The first is the heating of some material, commonly a liquid electrolyte, in which the energy source is immersed. The relevant equation is $(\Delta H/\Delta t) = M C_p (\Delta T/\Delta t)$, where H is the heat energy, M the mass of the material heated, C_p the heat capacity, ΔT temperature rise of the material and t is time. This equation shows that, when M and C_p are known, measurement of $(\Delta T/\Delta t)$ will give the thermal power $(\Delta H/\Delta t)$ produced at some time. The second mechanism is thermal conductivity through some barrier to the escape of heat from the region of the source. It is governed by the equation, $(\Delta H/\Delta t) = KA(\Delta T/\Delta x)$, through area A in the x direction, where K is the thermal conductivity. Some LENR calorimeters work on the basis of heating of a material and others by heat conductivity. They will be noted below.

In general, the production and flow of heat in thermal science is closely analogous to the motion of electrons or photons. In all three cases, there are sources, intermediate objects and sinks. In electronics, a source of electrons (such as a battery) sends current to active or passive devices (for example, transistors and resistors) and ultimately to ground. In optics, sources

(such as light emitting diodes) send photons through optical devices (notably, lenses) to absorbers. For LENR power measurements, the source of interest is the region in which the nuclear reactions occur and produce energy, the intermediate objects are thermal barriers and the sink is ultimately the surrounding environment. In electronics and optics, there are usually sources of currents or light that compete with the process of interest. This is also true of thermal measurements, including calorimetry for measuring the effects of LENR.

All three types of heat transfer are relevant: conductive, convective and radiative. There can be desirable and undesirable additions or losses of heat to and from the cell in a calorimeter, as summarized in the following table. It is assumed that the cell is at a higher temperature than its surroundings, that is, heat flows from the cell into nearby matter.

	Addition of Energy	Loss of Energy
Wanted	LENR Calibration Heater	Conduction via the Desired Path
Unwanted	Chemical Reactions Electrochemical Reactions Warm makeup electrolyte	Conduction by Other Paths IR Radiation Gas Escape or PV Work

Several types of calorimeters have been used in LENR experiments. Isoperibolic calorimeters were used by Fleischmann and Pons, and many other researchers. They have constant temperatures in their surrounding regions (termed “jackets”) in contrast to isothermal calorimeters, for which an auxiliary system maintains the heat-producing cell at a constant temperature over time. There are different configurations for isoperibolic calorimeters. In one, the temperature difference between the cell and jacket is measured. This arrangement sometimes suffers from problems with the non-uniform distribution of temperatures within the cell, and spatial differences between a cathode producing LENR and a nearby calibration heater. In another configuration, there is a second wall between the jacket immediately around the cell and the surroundings. In this case, the temperature difference is measured between the two regions outside of the cell. It is insensitive to temperature variations within the cell due to any cause. Both of these configurations have temperature measurements made at a few specific locations within the liquids of the cell, the jacket region or the outer water bath. Thermistors or thermocouples are commonly used for the temperature determinations.

Another variation of the isoperibolic calorimeter is termed the Seebeck calorimeter. In this case, many thermocouples are used to measure the temperature drop due to heat conductivity between the inside and outside of a thermal barrier containing the cell. This arrangement is also insensitive to details of the temperature distributions within the cell and, because the voltage-producing thermocouples are connected in series, larger signals can be obtained. Recent widespread availability of Peltier devices has made them a popular choice to replace the thermocouples in Seebeck calorimeters.

Another type of calorimeter is described as “mass flow.” Here, a liquid, commonly water at a known temperature flows into the vicinity of the cell, acquiring heat and increasing in temperature. Measurement of the output temperature, that is, the temperature increase, and the

flow rate, gotten by weighing, gives the measure of power production. The “heat flow” calorimeter, like the ice calorimeter, is a “first principles” device.

The above types of calorimeters have been the main instruments used in LENR heat-production experiments. However, other calorimeter types have also been employed. One of them is called a “heat flow” instrument. There are essentially four constant temperature regions in this kind of calorimeter. They include the following, from the outside to the interior cell. The outer region is a constant temperature bath. The second is a metal heat sink maintained at a constant temperature with a feedback system. It is connected to a region surrounding the cell by another metal piece that serves as a heat leak from the third region to the metal plate (and contains the electrical leads). The third region contains the fourth, the electrolytic cell. The cell and surrounding region are maintained at a constant temperature by an electrical heater driven by a current. Hence, the output signal from this type of calorimeter is the current, that is, the power that must be supplied to maintain the interior temperature. If heat is produced in this isothermal calorimeter, less current is needed. The principle behind this instrument is widely applied in engineering: feedback is used to keep a system near its unchanged condition, with the feedback signal being the output. It permits very sensitive measurements over a wide dynamic range.

The last kind of LENR calorimeter is also very different from the isoperibolic, Seebeck and mass flow instruments that have been most widely used. It is an “ice calorimeter.” Heat produced in an electrochemical cell is coupled into a surrounding ice and water mixture, melting some of the ice. The approximately 9% decrease in volume when ice melts is transferred to a container of liquid mercury. The difference in that volume is obtained by weighing the mercury volume change. The denser mercury permits more precise weight determinations.

A tabular summary of main features of the different types of LENR calorimeters follows.

	Isoperibolic			Mass Flow	Heat Flow	Ice
	Single Wall	Double Wall	Seebeck			
Principle Mechanism	Heat Conductivity	Heat Conductivity	Heat Conductivity	Heat Capacity	Heat Conductivity	Heat Capacity
Hotter Region	Cell electrolyte	Cell jacket	Inside of Barrier	Cell jacket	Metal Plate	Cell
Colder Region	Cell jacket	Outer bath	Outside of barrier	Flowing fluid	Cell and jacket	Ice-water
Measured	Power	Power	Power	Power	Power	Energy
Sensors	Temperature	Temperature	Temperature	Temperature & weight	Temperature	Weight
Signals	Voltage	Voltage	Voltage	Voltage	Voltage	Voltage

As noted, thermal sensors can be thermocouples, thermistors or Peltier devices. The voltage signals can be obtained in either analog or digital form, although acquisition, storage and manipulations of digital data are most common nowadays.

The characteristics, advantages and disadvantages of the different types of calorimeters vary widely. And, their design, construction, and operation also can be quite different even for one type of calorimeter. The same is true of their performance features. The features of the calibration curve for any calorimeter embodiment are central to the choice and use of a calorimeter for a specific experiment. They include the noise floor (for the combination of a calorimeter and its associated electronics), the sensitivity (the minimum power levels that can be measured adequately), the responsivity (slope of the calibration curve), and the dynamic range (in power or energy). Accuracy and precision are important for calorimeters, as for most measurement systems. The temporal response and the stability are other crucial parameters. The temperature range over which a calorimeter works is often important. Redundant measurements, ease of use, low cost and safety are other considerations. Cell size is an important consideration, which influences many of the performance and other characteristics.

In his presentation at ICCF-14, Storms gave the requirements for accurate calorimetry and sources of errors in measurements. The requirements for accuracy are constant temperatures for the ambient and reference media, controllable and constant applied power, stable measurement equipment, redundant measurements (with associated calibrations), and measurement of gas loss or gain. Errors in calorimetry, especially at low power (or heat) levels, can arise from inaccurate calibration curves, changes in ambient temperatures, variations in thermal conductivity, unknown recombination, electrical and other noise, and bubble action.

The papers in this section are arranged in the order discussed above. Miles and Fleischman presented details on the use of isoperibolic calorimeters in their invited review. Storms gave the invited paper on Seebeck calorimeters, and Zhang, Dash and Zhang provided a contributed paper on their new Seebeck instrument. McKubre and Tanzella, who have done over 100,000 hours of mass flow calorimetry, were invited to describe that kind of instrument. Little, Luce and Little described their version of a mass flow calorimeter. The heat flow calorimeter was presented in an invited paper by Lautzenhiser, Phelps and Eisner. Finally, the ice calorimeter was described in the invited paper by Dufour, Dufour, Murat and Foos.

This collection of review and recent papers on LENR calorimeters represents one of the best resources for study of these challenging and crucial instruments. If a person wants a primer on calorimeters for LENR, the 2004 paper by Storms is recommended. It is entitled "Calorimetry 101 for Cold Fusion: Methods, Problems and Errors," and is available under Storms in the library at LENR-CANR.org (<http://lenr-canr.org/acrobat/StormsEcalorimetr.pdf>).

The overall situation on LENR calorimeters is now quite clear. Several types of calorimeters, and many variations of some of them, have been developed, calibrated and employed in hundreds of experiments. It has been demonstrated by calibrations, test measurements and live cell measurements, that many of the calorimeters used for LENR experiments can reliably measure powers of 100 mW and greater. Some have achieved sensitivities near 1 mW. The power levels from LENR experiments have often exceeded 1 W and sometimes tens of watts. Hence, there is no longer a question of having adequate signal-to-noise ratios. Some critics still assert that LENR experimenters are incapable of measuring input powers (energies) properly. However, that is not a problem, although better documentation of input power checks is desirable. In short, advances in calorimetry can be expected. However, if there were no further

improvements, the calorimeters now available to the field would suffice. These include both “homemade” and commercial instruments.

There is also a class of calorimeter that uses identical devices but places the active experiment in one and a “blank” experiment in the other. The difference in output is attributed to the experiment and the noise from the environment can be cancelled by subtraction of the blank from the experimental chambers. These differential devices can be made to do high precision and stable heat measurements over wide dynamic ranges and for modest cost. It is expected that such instruments will be used increasingly in the study of LENR.

Twenty Year Review of Isoperibolic Calorimetric Measurements of the Fleischmann-Pons Effect

M. H. Miles¹ and M. Fleischmann²

¹ *The Dixie Foundation, Dixie State College, St. George, UT 84770*

² *Bury Lodge, Duck Street, Tisbury, Salisbury, Wiltshire, SP36LJ, U.K.*

Introduction: Why Choose a Dewar Isoperibolic Calorimeter?

The Dewar type of isoperibolic calorimeters developed by Fleischmann and Pons provides a wide dynamic range for both the cell temperature and cell input power. The experimental temperature range can be as great as the liquid range of the electrolyte system (3.82°C to 101.42°C for pure D₂O). For typical D₂O+0.1 M LiOD electrolytes, the temperature range used is typically from 20°C dictated by the bath temperature up to the boiling point of the electrolyte. The maximum cell input power will vary with the size of the cell, but input powers up to 10 W are possible before the cell contents are driven to boiling temperatures.

The ability provided by the Dewar type cells for directly observing processes inside the cell is a very important advantage. This is especially important for co-deposition and cell boil-off experiments. Other calorimetric systems generally do not provide for visual observations inside the cell.

The relatively low cost of the Dewar type cells is another important factor for the selection of this isoperibolic system. This makes possible the simultaneous use of multiple cells involving different experiments in a single water bath of sufficient size for handling the total heat output. The major cost is simply the construction of glass Dewar cells with a high vacuum between the inner and outer glass surfaces. The top portion (about 30%) needs to be silvered to minimize the effect of the decreasing electrolyte level caused by the electrolysis of D₂O to produce D₂ and O₂ gases. Larger cells will obviously exhibit smaller changes in the electrolyte level during electrolysis.

Another important positive feature of these Dewar cells, as well as other open systems, is that they are self-purifying. Ordinary H₂O will act as a poison to the Fleischmann-Pons effect (FPE) in D₂O+0.1 M LiOD electrolytes. Because H is preferentially electrolyzed versus D at the cathode, any H₂O contamination will be gradually removed during electrolysis. In closed systems, the initial H₂O contamination will remain trapped throughout the experiment. Not to be overlooked is the inherent safety of an open system that allows the deuterium and oxygen gases to escape as fast as they are generated.

The main heat transfer pathway for Dewar isoperibolic cells is via electromagnetic radiation (mostly infrared radiation). The radiative heat transfer coefficient, therefore, can be estimated by using the Stefan-Boltzmann constant and the experimental surface area of the inner, unsilvered portion of the glass surface of the Dewar cell. This provides a useful guide to the integrity of the Dewar vacuum and the extent of minimization of heat transfer pathways via conduction. Because of the predominate heat transfer by electromagnetic radiation, this Dewar

cell system has no memory effect. For example, gas bubbles or stagnant layers that form on the inner cell wall will exert no effect on the radiative heat transfer coefficient. Any media in the cell will suffice that maintains the temperature of the inner cell wall.

The Fleischmann-Pons Dewar System

The Fleischmann-Pons (F-P) isoperibolic calorimetry using a Dewar type cell evolved through various designs dating back to the early 1980's. The major changes involved the dimensions selected for the cell as well as incorporating the silvering of the top portion of the cell [1,2]. Proper scaling of the system is critical because the cell diameter and length determine the volume of electrolyte used, the rate of change of the electrolyte level, the effectiveness of stirring by the electrolysis gases, the dynamic range for power input, and the magnitude of the calorimetric constants. These changes led to the ICARUS (Isoperibolic Calorimetry: Acquisition, Research and Utilities System) series of cells used in later experiments.

The ICARUS 1 to 3 calorimeters were for lower temperatures up to boiling, and the ICARUS 4 to 9 calorimeters allowed long-term maintenance of boiling conditions. Results of ICARUS 9 experiments have been presented [3]. The ICARUS 10 to 13 were designed and constructed for further studies of boiling, but they were never put in use [4]. A schematic diagram for the ICARUS-14 calorimeter is available, but this calorimeter was never constructed[4]. An example of the ICARUS-1 type cell used at the New Hydrogen Energy (NHE) laboratory at the Sapporo, Japan from 1994 to 1998 had a filled electrolyte volume of 90 cm³, an inner diameter of 2.5 cm, an outer diameter of 4.2 cm, and a length of 25.0 cm with the top 8.0 cm silvered. A similar Fleischmann-Pons Dewar cell was used in France by Longchamp and Bonnetain [5].

The modeling and mathematical equation of the Fleischmann-Pons Dewar isoperibolic calorimeter have been previously presented [1,2,4,6,7]. A detailed version of this present paper containing all the equations is available electronically [8]. The correct equations for modeling isoperibolic calorimetry using open cells are now well established and can give highly accurate results [2,8]. There has been no challenge to these calorimetric equations in any refereed scientific publication even after nearly twenty years. Therefore any institution that performs accurate isoperibolic calorimetry using open cells must correctly account for all of the following power terms:

1. Power for the calorimetric system itself due to changes in the cell temperature.
2. Electrical power due to the electrochemical reactions.
3. Power due to the transfer of heat by electromagnetic radiation.
4. Power due to the transfer of heat by conduction.
5. Power carried out of the open system by the gases exiting the cell including D₂O vapor.
6. Power applied to any internal heater.
7. Power due to the rate of any pressure-volume work done by the electrogenerated gases.
8. Power due to any anomalous source (Excess Power).

Isoperibolic calorimetric measurement in 1989 at three influential institutions prematurely squashed the public and scientific considerations of the Fleischmann-Pons (F-P) Effect. These

three institutions (Caltech, M.I.T., Harwell) did not account for many of the power terms listed above.

California Institute of Technology Calorimetry

The initial publication by Caltech on the F-P effect was received by Nature on 23 May 1989 [9]. This means that all work was completed in less than two months after the initial announcement of the F-P effect (March 23, 1989). It is remarkable that Caltech claimed completion of multiple calorimetric experiments in this short time span because completion of a single F-P experiment generally requires 4 to 8 weeks or more of electrolysis.

The first step in evaluating this Caltech calorimetry is to look for the required power terms in the modeling equations. The Caltech paper is almost devoid of equations for these power terms. Only terms for the electrochemical power and an expression for the total power could be identified [8]. The Caltech calorimetric cell consisted simply of a Dewar flask containing 30 mL of electrolyte, but the Dewar walls contained 1 atm of air, hence there was no vacuum and heat conduction would dominate over electromagnetic radiation. The most disturbing aspect of the Caltech report concerns the heating coefficient that was allowed to change with time to give zero excess power. This heating coefficient should have a nearly constant value as found in their control study using ordinary water. The Caltech heavy water experiment is more correctly interpreted as an excess power effect [8].

Massachusetts Institute of Technology Calorimetry

The two M.I.T. calorimeters used glass wool thermal insulation in the compartment between the cell and water bath [10], thus their main heat transfer pathway was by conduction rather than by electromagnetic radiation as in the F-P Dewar cells. The sensitivity of the Phase II M.I.T. calorimeters was stated as ± 40 mW [10] contrasted to ± 0.1 mW sensitivity for the F-P Dewar calorimeters [1,2]. From the dimensions of the M.I.T. Pd rod cathodes (0.1×9 cm), the expected excess power of about 70 mW would not easily be distinguished from the large calorimetric error reported. The M.I.T. laboratory reported their key calorimetric measurements over a rather short time period (100 hours). The observation of excess power with Pd cathodes in heavy water generally requires 6 days or more of electrolysis.

To M.I.T.'s credit, most of the required power terms were considered in their analysis. The main problem with the M.I.T. experiments is that there is a serious discrepancy between the unpublished raw data showing a small excess power effect and the final published data for their heavy water cell [8]. The data points appear to have been arbitrarily shifted down to make the excess power vanish [8]. Because a "wake" to ridicule cold fusion at M.I.T. was already planned before the experiments were completed, it would have required unusual honesty for M.I.T. to have correctly reported a small excess power effect.

The Harwell Calorimetry

The Harwell (U.K.) laboratory investigated the F-P effect using Dewar calorimetric cells during the early stage (1989) of the cold fusion controversy [11]. These Harwell experiments were hastily performed, and the reported calorimetric error of $\pm 15\%$ falls far short of the $\pm 0.01\%$ error reported by Fleischmann [1,2]. The Harwell publication [11] provides only fragmental information about the power terms and equations used in their calculations for their Dewar cell. Most of the required power terms are missing in their analysis of the data [8]. To the credit of the Harwell group, their raw experimental data was made available to other groups. Several independent analyses of this raw data have reported that excess enthalpy generation was in fact observed in the Harwell study contrary to the conclusions reached by the authors [8].

Summary

The correct equations for modeling isoperibolic calorimetry using open cells are now well established and can give highly accurate results. These calorimetric equations were used to evaluate the Caltech, M.I.T., and Harwell calorimetry performed in 1989. It appears that scientific objectivity was sacrificed by these three influential institutions in order to obtain their desired result of no anomalous excess power effects.

Acknowledgement

One of us (M.H.M.) received financial help from an anonymous fund at the Denver Foundation. Dixie State College and the Dixie Foundation, especially Kalynn Larson, assisted in the administration of this fund.

References

1. M. Fleischmann and M.H. Miles, "The Instrument Function of Isoperibolic Calorimeters: Excess Enthalpy Generation Due to Parasitic Reduction of Oxygen" in *Condensed Matter Nuclear Science: Proceedings of the 10th International Conferences on Cold Fusion*, Cambridge, MA, August 24-29, 2003, P.L. Hagelstein and S.R. Chubb, Editors, World Scientific Publishing Co., Singapore, 2006, pp. 247-268.
See also <http://lenr-canr.org/acrobat/Fleischmantheinstrum.pdf>
2. M.H. Miles and M. Fleischmann, "Accuracy of Isoperibolic Calorimetry Used in a Cold Fusion Control Experiment" in *Low Energy Nuclear Reactions Sourcebook*, ACS Symposium Series 998, 71. J.Marwan and S. Krivit, Editors, ISBN 978-0-8412-6966-8, Oxford University Press, Fall 2008 (in press).
3. T. Roulette, J. Roulette and S. Pons, "Results of ICARUS 9 Experiments Run at IMRA Europe", in *Progress in New Hydrogen Energy*, Vol. 1, ICCF-6 Proceedings, Lake Toya, Hokkaido, Japan, October 13-18, 1996, M. Okamoto, Editor, pp. 85-92.
See also <http://lenr-canr.org/acrobat/RoulettTresultsofi.pdf>
4. M.H. Miles, M. Fleischmann and M.A. Imam, "Calorimetric Analysis of a Heavy Water Electrolysis Experiment Using a Pd-B Alloy Cathodes", Naval Research Laboratory Report Number NRL/MR/6320-01-8526, Washington, DC, March 26, 2001, pp. 1-155.

5. G. Lonchamp, L. Bonnetrain and P. Hicter, "Reproduction of Fleischmann and Pons Experiments" in *Progress in New Hydrogen Energy*, Vol. 1, ICCF-6 Proceedings, Lake Toya, Hokkaido, Japan, October 13-18, 1996, M. Okamoto, Editor, pp. 113-120.
See also <http://lenr-canr.org/acrobat/LonchampGreproducti.pdf>
6. M. Fleischmann, "Simulation of the Electrochemical Cell (ICARUS) Calorimetry", in *Thermal and Nuclear Aspects of the Pd/D₂O System*, Vol. 2, SPAWAR Systems Center, Technical Report Number 1862, S. Szpak and P.A. Mosier-Boss, Editors, February 2002, pp. 1-180.
See also <http://lenr-canr.org/acrobat/MosierBossthermalanda.pdf>
7. S. Szpak, P.A. Mosier-Boss, M.H. Miles, M.A. Imam and M. Fleischmann, "Analysis of Experiment MC-21: A Case Study" in *Thermal and Nuclear Aspects of the Pd/D₂O System*, Volume 1, SPAWAR Systems Center, Technical Report Number 1862, S. Szpak and P.A. Mosier-Boss, Editors, February 2002, pp. 31-89.
See also <http://lenr-canr.org/acrobat/MosierBossthermaland.pdf>
8. The full version of the present paper with complete mathematical equations is available electronically.
Please see: <http://lenr-canr.org/acrobat/MilesMisoperibol.pdf>
9. N.S. Lewis et al., "Searches for Low-Temperature Nuclear Fusion of Deuterium In Palladium", *Nature*, 1989, 340, pp. 525-530.
10. D. Albagli et al., "Measurements and Analysis of Neutron and Gamma-Ray Emission Rates, Other Fusion Products, and Power in Electrochemical Cells Having Pd Cathodes", *J. Fusion Energy*, 1990, 9, pp. 133-148.
11. D.E. Williams et al., "Upper Bounds on Cold Fusion in Electrolytic Cells", *Nature*, 1989, 342, pp. 375-384.

The Method and Results Using Seebeck Calorimetry

Edmund Storms
KivaLabs, Santa Fe, NM

ABSTRACT

The characteristics of and errors associated with Seebeck calorimeters, as applied to the Fleischmann-Pons Effect, are described. This type of calorimeter as well as a flow type calorimeter were used to measured apparent excess energy from the same sample of platinum plated with palladium and other materials.

I. INTRODUCTION

Acceptance of the Pons-Fleischmann effect¹ has depended on acceptance of anomalous heat production. Proving this claim involves use of a calorimeter. At least five different basic kinds have been used. Naturally, each design has its own set of errors and characteristics needing evaluation. Besides having only a small error, a calorimeter used to study cold fusion also must be very stable because the studies usually last for a long time. In addition, heat generated by the electrolytic process needs to be removed to avoid having the cell get too hot. Because this background energy can be large and the anomalous energy can be small, the calorimeter needs to be very sensitive over a wide range of heating power. No single design is ideal in meeting these requirements. Nevertheless, the Seebeck- or Kelvin-type comes close. This type of calorimeter measures power. Energy of a reaction is obtained by integrating the power over a period of time. This paper will describe the construction, operation, evaluation, and some results obtained using such a calorimeter. Other authors have also used and described the method.²⁻¹⁶

II. DESCRIPTION OF THE METHOD

Heating power can be measured by causing the heat to pass through a thermal barrier, a process that generates a temperature difference across the barrier. When this method is used, the calorimeter is called an isoperibolic type. This temperature difference can be measured using various detectors, but usually only at a few locations. In contrast, a Seebeck calorimeter has a thermal barrier containing many temperature sensors, even to the extent of using a barrier made from a commercial thermoelectric converter assembly. When thermocouples are used, they are electrically connected in series so that their generated voltages add, thus providing a voltage having easily measured magnitude. This arrangement provides an accurate measurement of temperature difference at every location on the surrounding enclosure. When the outside is kept at constant temperature by flowing water, the generated voltage is proportional to the average power flowing through the walls. As a result, the calorimeter is relatively insensitive to where the source of heat is located. However, use of a fan within the envelope is advised to insure uniform temperature.

The amount of power (W) being generated within the Seebeck envelope is equal to

$$W = A + BV + CV^2 \quad \text{Equation 1}$$

where A, B, and C are constants obtained from a calibration using a known source of heat and V is the generated voltage. The simplicity of this defining equation makes the measurement easy to understand and to evaluate. Normally, the “A” term is very close to zero. However, small errors in the voltage measurement or small heat leaks into the envelope through penetrating wires can produce a small value. The “B” value gives the sensitivity of the calorimeter in units of watt/volt. The C term corrects for the nonlinearity of the thermal barrier, thermoelectric converter or thermocouples. Normally, the contribution of this term is very small.

Although the temperature is well known, accurate values for power can only be obtained after the temperature within the calorimeter has reached a constant value. The time required for the temperature to become constant after a change in produced power is called the time constant of the calorimeter, which is usually between 1 and 2 hours. An apparent power calculated using the calorimeter is not accurate until sufficient time has lapsed for the temperature within the cell to become constant.

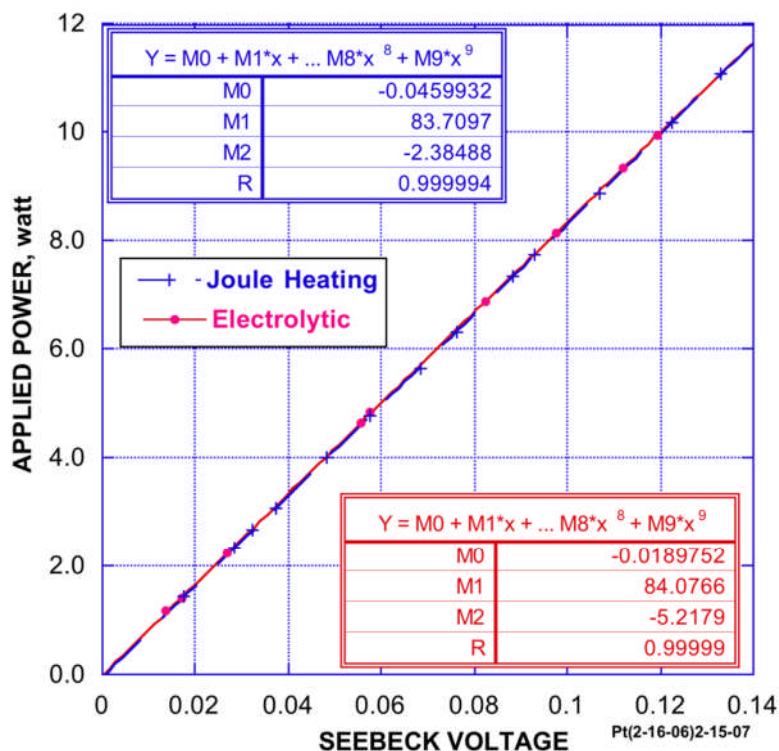


Figure 1. Typical calibration

Figure 1 shows a typical calibration using two sources of heat. One set of calibration values was obtained using an electrical heater located within the electrolytic cell (Joule). The second resulted from heat generated by electrolytic action in a cell containing a recombining catalyst and an inert cathode. Notice that these two independent sources of heat show only a small difference. At 1 watt total power, the difference is about 32 mW and about 35 mW at 8 watts total power. Temperature gradients are not the cause because the difference is nearly independent of applied power. If temperature gradients were the cause, bubble action, which increases with applied electrolytic power, would cause the gradients to change, hence cause the difference between the two calibrations to change. Nevertheless, the persistence difference over a wide range of applied power gives the final calibration an uncertainty of perhaps 35 mW. Because this difference is variable and not clearly related to any particular condition, a comparison should be made in an attempt to find the cause. If the source of bias cannot be identified, a doubt is created as to which of the two methods for calibration is correct. Consequently, the resulting excess power will contain an unknown bias. The existence of excess power can only be accepted if the amount is significantly greater than this bias.

Excess power is determined by subtracting the amount of applied electric power (cell volt x current) from that calculated using Equation 1. If the same resistors and measuring circuits are used for both the calibration and the measurement of excess power, many errors cancel, resulting in much less uncertainty. If different resistors and/or measuring circuits are used, the bias that is generated can give a false indication of excess power that can be hard to identify. Consequently, a dual calibration using both Joule and electrolytic power is important.

III. CALORIMETER DESIGN

A picture of an open Seebeck envelope (7" × 7" × 7") containing a small electrolytic cell and several small fans is shown in Fig. 2a. This version is available from Thermonetics (<http://www.thermoneticscorp.com/>). Figure 2b shows a small Seebeck made by cementing commercial thermoelectric panels together. In this case, the top is a simple insulator. Constant-temperature water circulates around the outside of the converters.

Figure 2c shows a Seebeck calorimeter using 1000 thermocouples placed in a polyethylene water pipe that serves as the thermal barrier. A fan is provided on the lid to circulate air within the enclosure. Water flows outside of the thermal barrier. A water-proof paint is used to electrically insulate the thermocouples from the cooling water.

Figures 2d and 2e show the outside and inside of a calorimeter made using commercial thermoelectric converter plates having high efficiency. In this design, the top is also active and water-cooled. This is only an example of possible designs. The method can be used to create enclosures of any size and a sensitivity greater than any other method.

When constructing such a calorimeter, it is important to have all walls as identical as possible with respect to thermal conductivity and conversion efficiency from heat to voltage. In addition, the entire surface of the thermal barrier outside of the enclosure must be held at the same constant temperature regardless of the amount of power being generated within the enclosure. Therefore, water cooling, in contrast to air cooling, is the better method. If these conditions are not met, the calorimeter will be nonlinear and will be sensitive to where within

the enclosure heat is generated. Water cooling also allows the temperature within the box to start well below room temperature if this should provide an advantage.

When used to measure heat generated by an electrolytic cell, the sensitivity and accuracy will be reduced somewhat by random variations in applied power caused by bubble formation. Bubbles change the resistance of the electrolyte, which causes random variations in voltage measured across the cell. Hence random variations in applied power are produced, especially at high applied current.

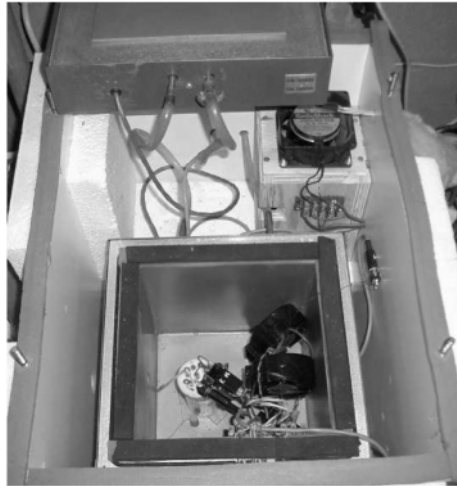


Figure 2a. Picture of commercial Seebeck Calorimeter. The calorimeter is contained in a constant temperature environment.

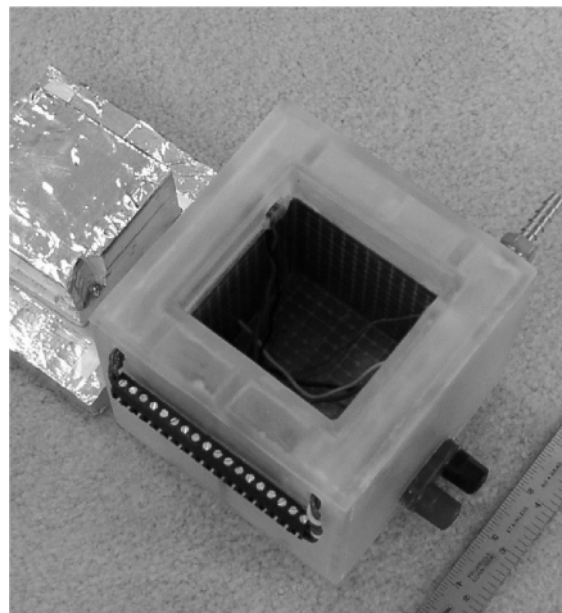


Figure 2b. Picture of small Seebeck calorimeter using thermoelectric converters as the thermal barrier, but with an inactive, insulating lid.

Although a well constructed Seebeck is relatively insensitive to changes in the room temperature, higher accuracy can be obtained by placing the Seebeck enclosure and all parts of the voltage and current measuring circuits in a constant temperature environment.

In general, the smaller and more compact the enclosure, the better. In general, a smaller enclosure has a faster response time and a higher sensitivity. In addition, it will have a lower cost.



Figure 2c. A Seebeck calorimeter made using 1000 thermocouples.

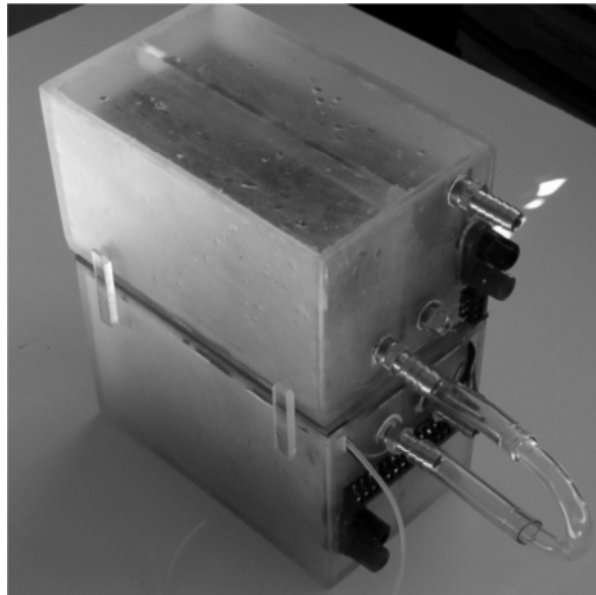


Figure 2d. Assembled calorimeter.

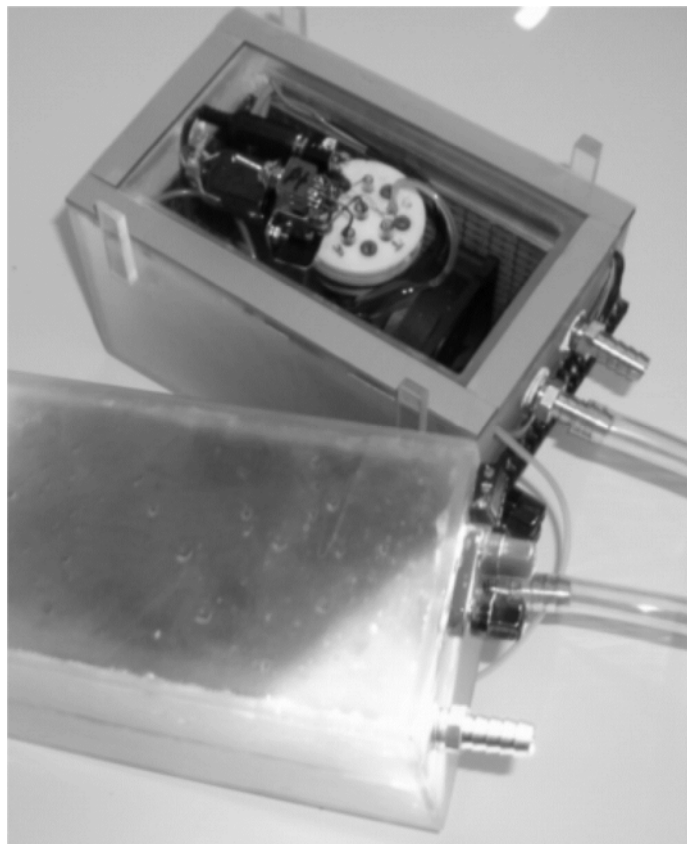


Figure 2e. Open calorimeter showing the electrolytic cell and a small fan. The cell has a universal design so that it can be exchanged with other cells when different experiments are undertaken.

IV. SOURCES OF ERROR

Although the measurement is not sensitive to where heat is generated within the electrolytic cell, it can be sensitive to where the cell is located within the Seebeck envelope. This effect arises when the outside of the thermal barrier is not cooled uniformly by constant-temperature water flow or if it does not have a uniform thermal conductivity. Consequently, better results are obtained if a small fan is placed in the envelope to distribute the heat. In addition, the fan cools the cell, resulting in a smaller temperature increase within the cell for the same amount of generated power. In the examples shown here, a 12V DC fan is used that consumes about 0.75 watts. This power is added to that being generated within the cell when the system is calibrated.

Unexpected differences in behavior can result when a large difference in the temperature at the cathode is produced by the same electrolytic power, such as results when different calorimeter designs are used. For example, Fig. 3 compares the temperature difference of the cathode in a flow-type and Seebeck calorimeter as a function of applied electrolytic power. This behavior is universal and needs to be acknowledged when results obtained using different calorimeters are compared. A special cell can be designed to lose heat more rapidly and reduce the cathode temperature, as pictured in Fig. 4.

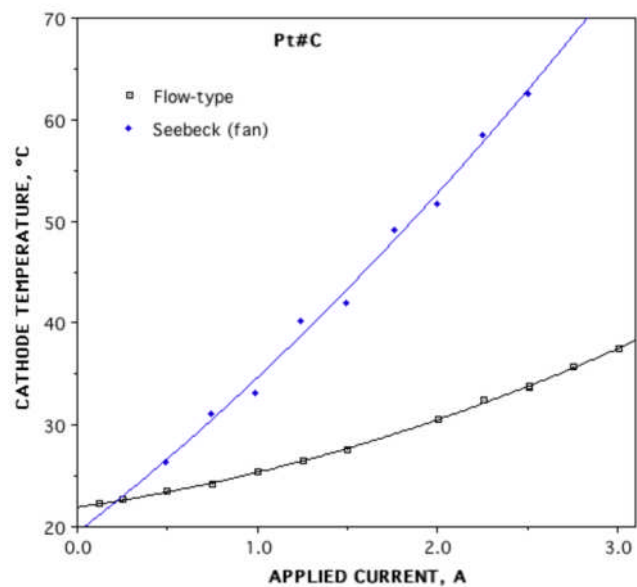


Figure 3. Comparison of cathode temperature vs applied current for a Seebeck and flow-type calorimeter.



Figure 4. Cell with cooling fins to reduce cathode temperature.

As long as power supplied to the fan and electrolytic action is constant, its value can be accurately measured. However, most fans of this type exhibit small variations in wattage that introduce about a ± 5 mW ripple on the value of calculated power (W). Bubble action adds an additional variation on the power being supplied for electrolysis. An example of how this rapid variation in applied power affects the apparent excess power is shown in Fig. 5. Other calorimeter types are expected to show the same behavior, the magnitude of which will depend on long the signal is averaged to obtain the reported value. In this case, points are taken every six minutes and the data are averaged for about 30 sec.

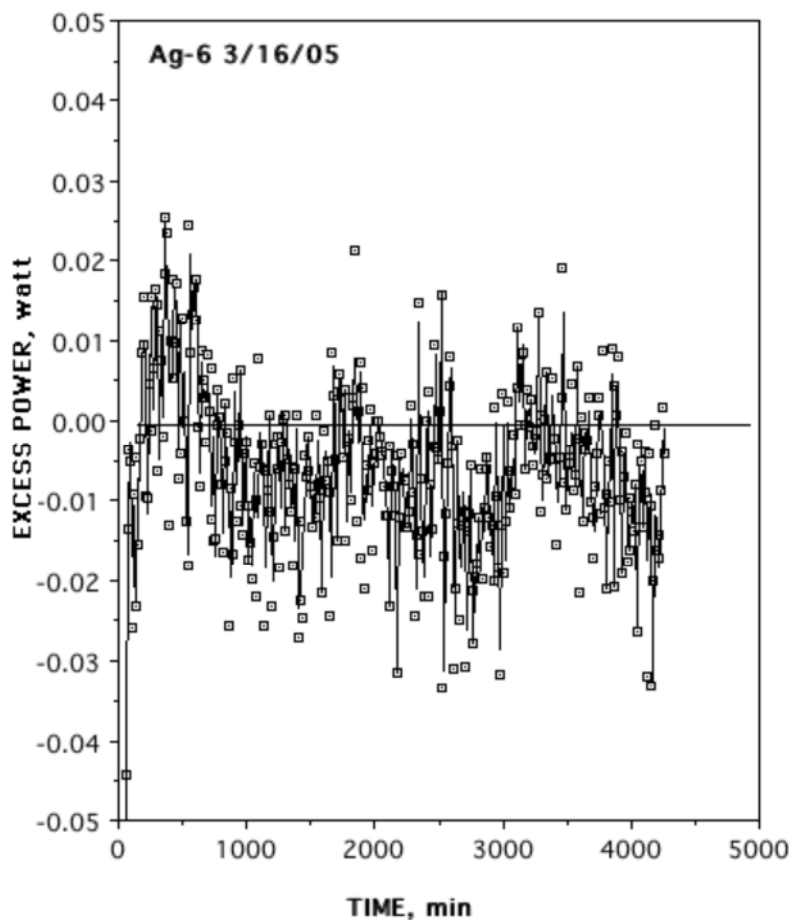


Figure. 5. Examples of variations in apparent excess power.

Apparent excess power can also be produced when applied power changes too rapidly for the calorimeter to remain in equilibrium. For example, if applied power is reduced as shown in Fig. 6, perhaps because the resistance of the cell changes, the calculated apparent power will have the behavior shown in Fig. 7. Unless this change in applied power were recognized, the result might be interpreted as a sudden burst of excess power. In fact, the calculated excess is only accurate when applied power and the resulting temperature within the cell are constant or

change slowly compared to the time constant of the calorimeter. Similar behavior will be observed in all calorimeters that measure power production.

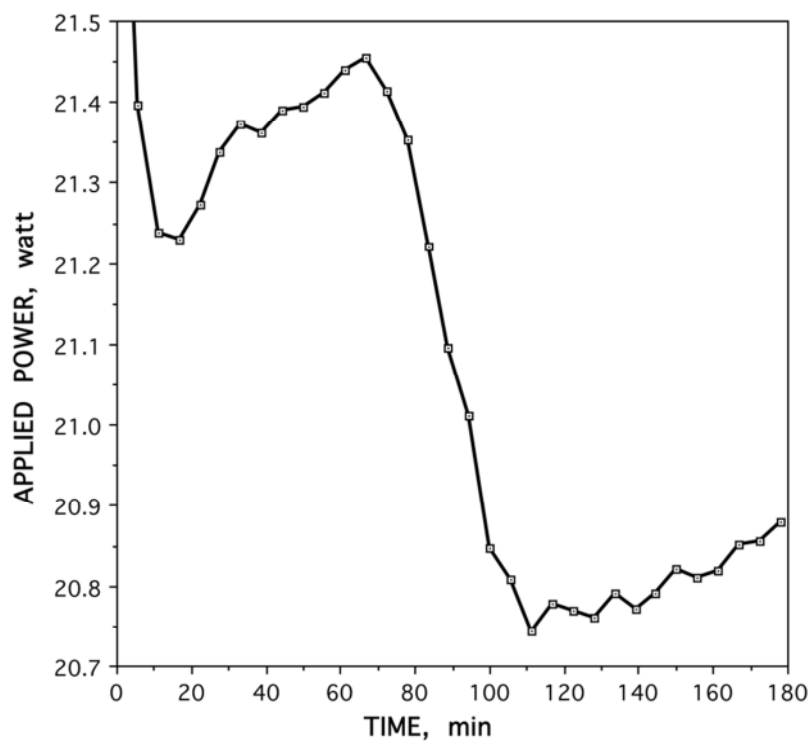


Figure 6. Example of a change in power applied to an electrolytic cell.

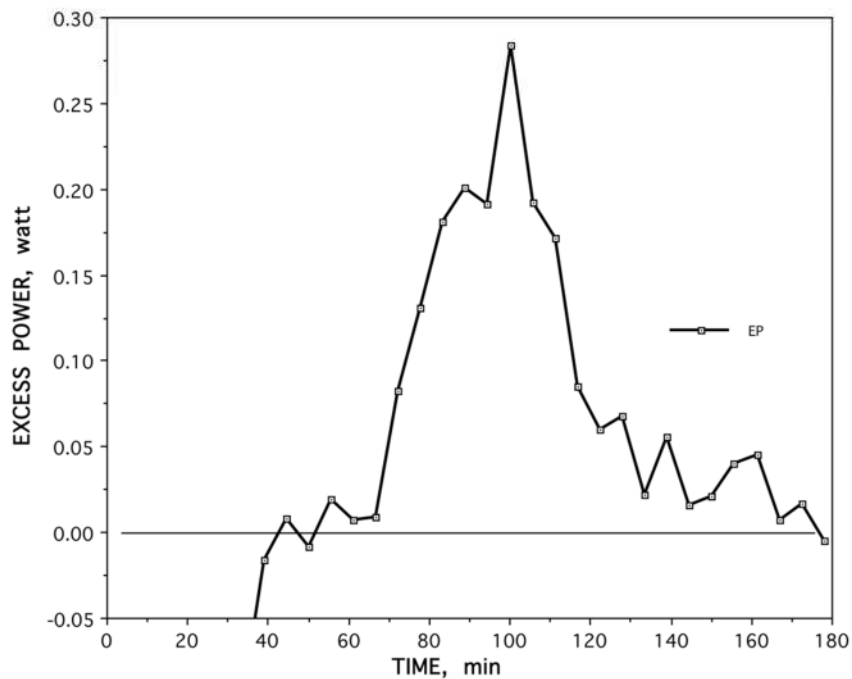


Figure 7. Result of power change shown in Fig. 6.

Apparent excess power can also be caused by a drift in the calibration constant. Unfortunately, this drift produces a behavior exactly like the one produced by production of excess energy. This error can be identified by changing applied current, first up and then down in value. Because the excess is a function of applied current, this change should show a repeated behavior. An example of several studies showing this effect is provided in Fig. 8. Some samples show a very reproducible effect of current and some do not. If the apparent excess returns to near zero when current is reduced to zero, confidence in the calorimeter can remain high. On the other hand, if the excess does not return to zero, the data should be ignored even though life after death might be the explanation. At the very least, a recalibration needs to be done when expected behavior is not produced.

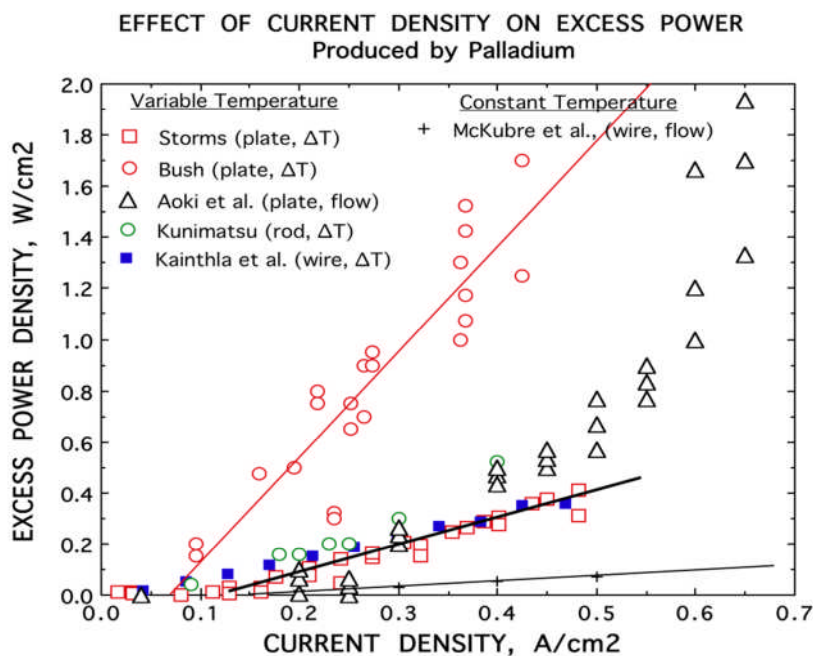


Figure 8. Change in apparent excess with applied current.

Another error results when the amount of recombination of D_2 and O_2 is unknown. If recombination is complete, because a catalyst has been placed in the cell, no error is introduced in the measured heat because all gas will be converted to the original D_2O . However, in the absence of a catalyst, the amount of recombination can be variable and must be measured. When applied current is above about 0.1 A, the amount of recombination is always small, as shown in Fig. 9. In contrast, smaller currents show a significant and variable amount of recombination that needs to be measured directly. This measurement can be made by attaching an oil reservoir to the sealed cell that captures gas leaving the cell, as shown in Fig. 10. By dividing the amount of gas leaving the cell by the number of electrons passing through the cell, the amount of recombination can be determined. When a constant value independent of current is found, it is safe to assume that no recombination is occurring in the cell, i.e. all generated gas

is leaving the cell. However, when recombination occurs, the amount of gas leaving the cell is reduced and the calculated ratio is no longer constant. This behavior can be easily seen in Fig. 11 for various conditions. Stirring the cell, thereby causing bubbles to impact the electrodes, has no significant effect on this behavior. Therefore, bubble contact with the electrodes does not cause recombination.

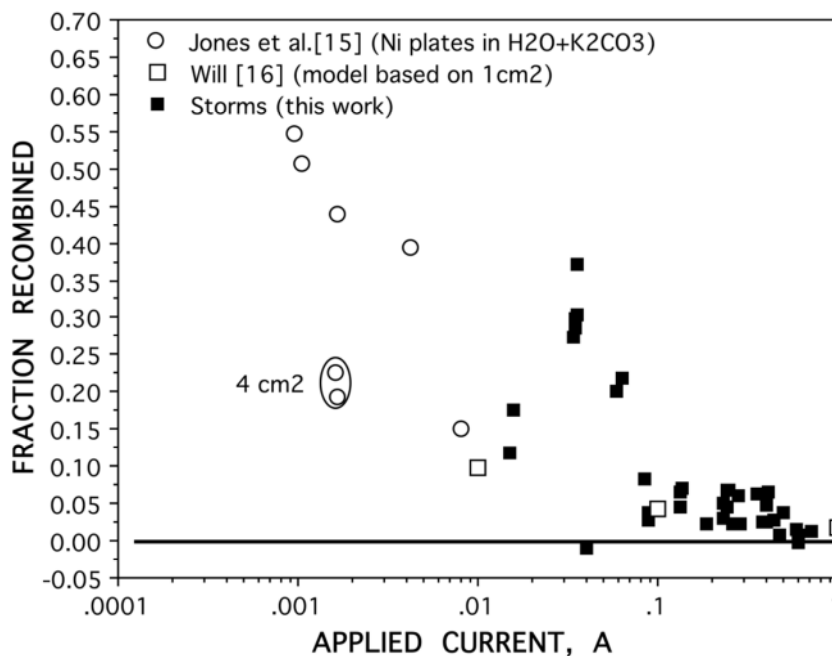


Figure 9. Fraction of gas recombined vs log of applied current.

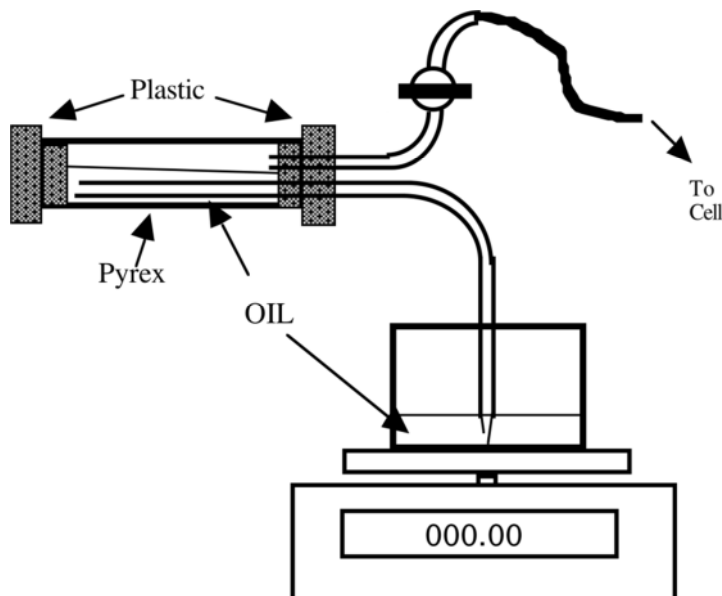


Figure 10. Drawing of oil system. Mineral oil is used.

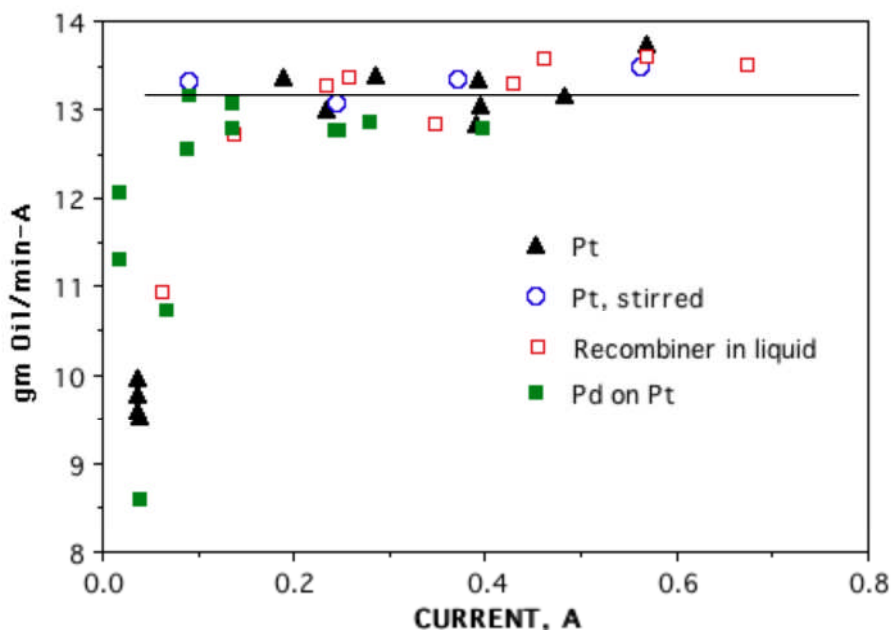


Figure 11. Oil weight/ampere*minute vs current for various conditions.

Recombination can also be determined less accurately by weighing the amount of D_2O lost from the cell or by measuring the change in electrolyte volume.

Errors can't be avoided, but techniques can be used to separate a real behavior from one produced by error. These techniques involve measuring two independent behaviors or by using two different kinds of calorimeters as discussed below.

When extra heat is produced by a reaction at the cathode, the cell temperature will increase. If this increase is associated with excess heat being produced, as shown in Fig.12, confidence in the reality of the excess heat is increased. As the figure shows, a slow initial drop in cell temperature caused no change in excess power. However, when an increase in cell temperature was detected at 1200 min, a corresponding increase in excess power was also measured. This excess remained constant while the cell temperature remained constant at the higher temperature. Because cell temperature is not used to calculate excess power, these values result from two completely independent measurements showing extra heat production.

If a sample shows similar behaviors using two different calorimeters, each having different errors, the reality of the measurement also increases. Figure 13 shows such a comparison using a flow-type and a Seebeck calorimeter. Figure 14 shows a different data set for the same sample using two different methods. During the study labeled "sweep" a data point was taken after which the current was changed. After a delay sufficient to allow the calorimeter to stabilize for about 90 minutes, another data point was taken. In contrast, each data point labeled "constant" is an average of data taken over several hours at constant current. As a result, random errors are reduced. In Fig. 14, the excess power obtained using the Seebeck, which had a larger cell temperature, was slightly greater than that produced in the flow-type in which the cathode had a lower temperature.

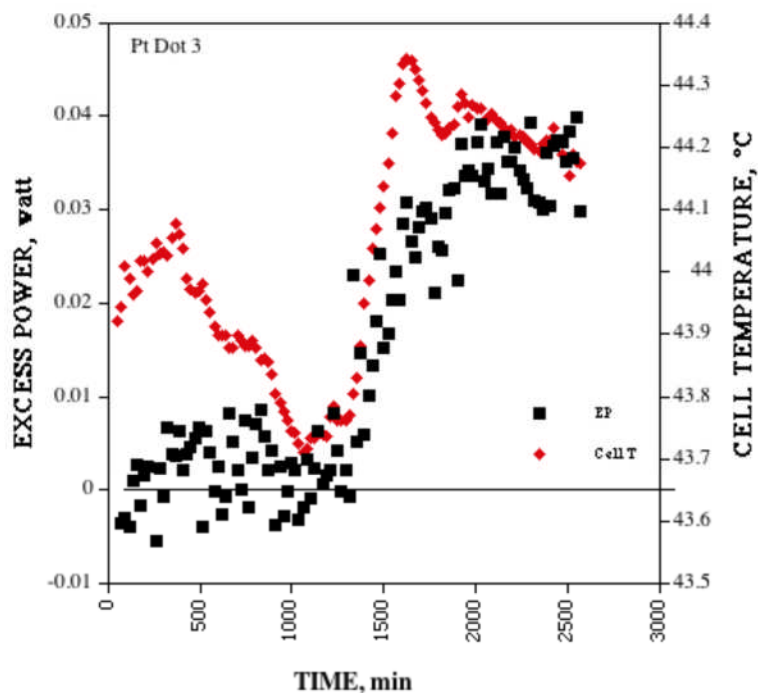


Figure 12. Simultaneous measurement of excess power and cell temperature using a Seebeck calorimeter.

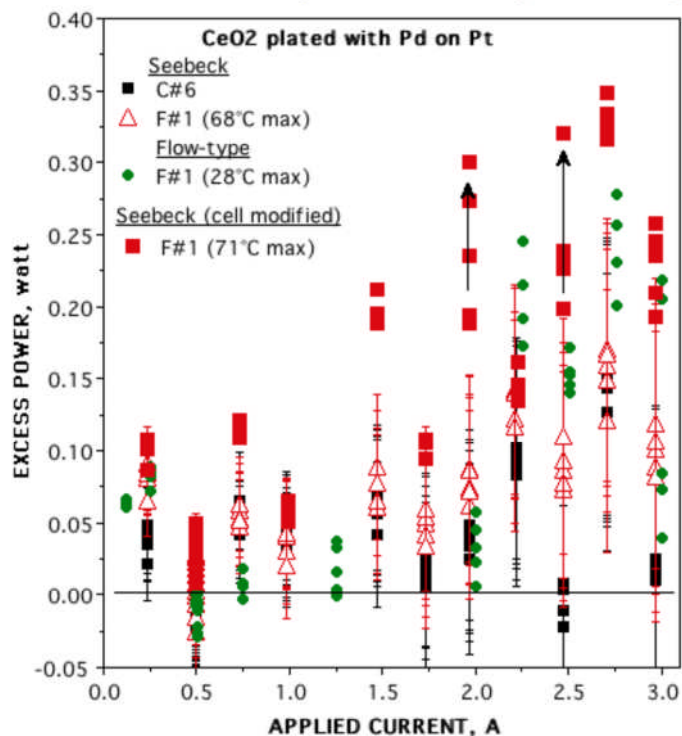


Figure 13. A comparison between excess power obtained by using a flow-type and a Seebeck calorimeter. The cathode was platinum plated with palladium using a bath containing a suspended powder of mixed oxides including CeO_2 , TiO_2 , SiO_2 , Al_2O_3 and CaO .

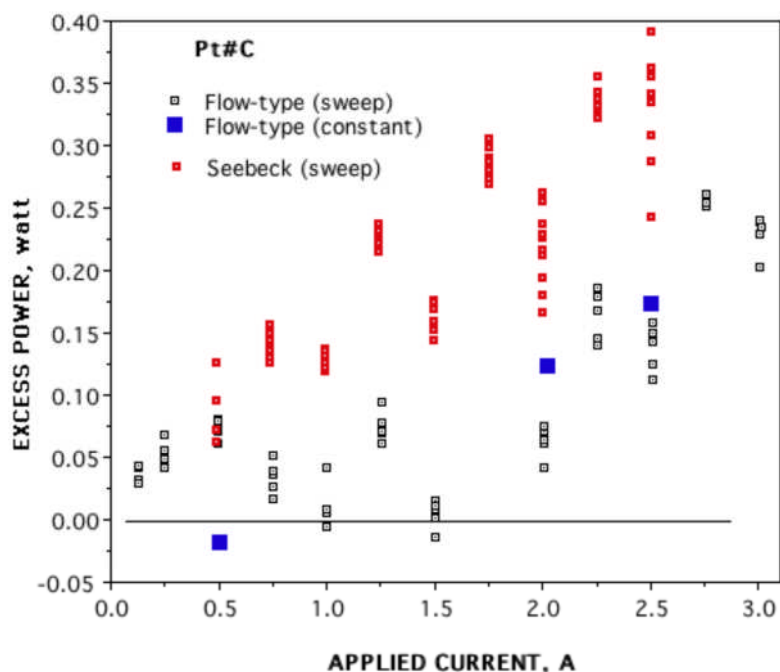


Figure 14. A comparison between excess power obtained by using a flow-type and a Seebeck calorimeter using the same cathode studied in Fig. 13.

V. CONCLUSION

The Seebeck calorimeter is simple to use and to understand. It is very stable and is capable of accepting a wide range of power production within its envelope. The absolute accuracy depends on the design and the skill of the operator, as is required of all measurement methods. Nevertheless, this calorimeter allows the error to be easily identified and evaluated. Proper design of a measurement can reduce the absolute error in a power measurement to less than 30 mW and the relative error to less than 15 mW.

A study of the same sample using two different types of calorimeter demonstrates production of excess energy using an electrolyte containing D₂O and a platinum cathode on which palladium and other materials have been plated. The behavior has the characteristics attributed to the Fleischmann-Pons Effect.

REFERENCES

1. Storms, E. K. *The science of low energy nuclear reaction* (World Scientific, Singapore, 2007).
2. Bush, B. F. & Lagowski, J. J. in *The Seventh International Conference on Cold Fusion* (ed. Jaeger, F.) 38 (ENECO, Inc., Salt Lake City, UT., Vancouver, Canada, 1998).
3. Oriani, R. A., Nelson, J. C., Lee, S.-K. & Broadhurst, J. H. Calorimetric measurements of excess power output during the cathodic charging of deuterium into palladium. *Fusion Technol.* **18**, 652 (1990).

4. Zhang, Z. L., Yan, B. Z., Wang, M. G., Gu, J. & Tan, F. in *Anomalous Nuclear Effects in Deuterium/Solid Systems, "AIP Conference Proceedings 228"* (eds. Jones, S., Scaramuzzi, F. & Worledge, D.) 572 (American Institute of Physics, New York, Brigham Young Univ., Provo, UT, 1990).
5. Bertalot, L. et al. in *Second Annual Conference on Cold Fusion, "The Science of Cold Fusion"* (eds. Bressani, T., Del Giudice, E. & Preparata, G.) 3 (Societa Italiana di Fisica, Bologna, Italy, Como, Italy, 1991).
6. Olofsson, G., Wadsoe, I. & Eberson, L. Design and testing of a calorimeter for measurements on electrochemical reactions with gas evolution. *J. Chem. Thermodyn.* **23**, 95 (1991).
7. Barrowes, S. C. & Bergeson, H. E. in *Fourth International Conference on Cold Fusion* (ed. Passell, T. O.) 21 (Electric Power Research Institute 3412 Hillview Ave., Palo Alto, CA 94304, Lahaina, Maui, 1993).
8. Zhang, Z. et al. Precision calorimetric studies of H₂O electrolysis. *J. Thermal Anal.* **45**, 99 (1995).
9. Oriani, R. A. An investigation of anomalous thermal power generation from a proton-conducting oxide. *Fusion Technol.* **30**, 281 (1996).
10. Zhang, Z. L., Zhang, W. S., Zhong, M. H. & Tan, F. in *8th International Conference on Cold Fusion* (ed. Scaramuzzi, F.) 91 (Italian Physical Society, Bologna, Italy, Lerici (La Spezia), Italy, 2000).
11. Tian, J. et al. in *The 9th International Conference on Cold Fusion, Condensed Matter Nuclear Science* (ed. Li, X. Z.) 353 (Tsinghua Univ. Press, Tsinghua Univ., Beijing, China, 2002).
12. Warner, J., Dash, J. & Frantz, S. in *The Ninth International Conference on Cold Fusion* (ed. Li, X. Z.) 404 (Tsinghua University, Beijing, China: Tsinghua University, 2002).
13. Zhang, W.-S., Zhang, Z.-F. & Zhang, Z.-L. in *The 9th International Conference on Cold Fusion, Condensed Matter Nuclear Science* (ed. Li, X. Z.) 431 (Tsinghua Univ. Press, Tsinghua Univ., Beijing, China, 2002).
14. Li, X. Z. et al. Correlation between abnormal deuterium flux and heat flow in a D/Pd system. *J. Phys. D: Appl. Phys.* **36**, 3095 (2003).
15. Storms, E. K. in *Tenth International Conference on Cold Fusion* (eds. Hagelstein, P. L. & Chubb, S. R.) 269 (World Scientific Publishing Co., Cambridge, MA, 2003).
16. Zhang, W.-S., Dash, J. & Wang, Q. in *Condensed Matter Nuclear Science, ICCF-12* (eds. Takahashi, A., Ota, K. & Iwamura, Y.) 86 (World Scientific, Yokohama, Japan, 2005).

Construction of a Seebeck Envelope Calorimeter and Reproducibility of Excess Heat

Wu-Shou Zhang¹, John Dash² and Zhong-Liang Zhang¹

¹ *Institute of Chemistry, Chinese Academy of Sciences*

P.O. Box 2709, Beijing 100190, China

² *Low Energy Nuclear Laboratory, Portland State University
Portland, OR 97207-0751, U.S.A.*

Abstract

A Seebeck Envelope Calorimeter (SEC) was designed and built. The inner volume is 17.6 L. Its outer wall temperature was controlled within 0.01°C. The device constant was 6 W/V and its time constant was 5 minutes. Dash-type cells were tested. Both an isoperibolic calorimeter and the SEC measured excess heat with the same Pd cathode of $25 \times 25 \times 0.3 \text{ mm}^3$. The SEC showed excess heat ranging from 0.15 ± 0.02 to $0.41 \pm 0.03 \text{ W}$ (average value 0.22 W) at applied current of 3 to 3.5 A (0.24 to 0.28 A cm^{-2}).

1. Introduction

A Seebeck Envelope Calorimeter (SEC) is a powerful tool for measuring excess heat in low energy nuclear reaction experiments [1–3]. In previous works we used an SEC made by Thermoionics Corporation [1,2]. However, this device had some intrinsic defects in our experience: (1) The device constant was unstable. We found that it shifted by 20% in three months; the SEC had to be calibrated before and after every experiment. (2) The heat insulation around the calorimeter was insufficient; thus the baseline and output signal shifted daily with the ambient temperature. This SEC had to be put into another, larger insulated box to prevent temperature fluctuations [1,2].

In this paper, we will describe a new SEC; its merits are simplicity, stability, and accuracy. Preliminary results on reproducibility of excess heat in the Pd-D₂O system are also reported.

2. Construction of calorimeter

A schematic of the calorimeter and accessories is similar to that which was published previously [1]. The calorimeter core consists of two aluminum alloy boxes. The inner box is the measuring vessel with interior dimensions of $26 \times 26 \times 26 \text{ cm}^3$ (17.576 L). The thicknesses of inner and outer box walls are 4 mm and 6 mm, respectively. Thermoelectric modules (TM, $5.4 \times 40 \times 40 \text{ mm}^3$), each with 127 thermocouples, are mounted between the inner and outer walls with screws. Thermal conductive silicone is wiped on both sides of each TM to improve thermal conductivity. 25 TMs are distributed uniformly on each wall, except for the two facing sidewalls which have 24 TMs because there is one hole in the center of each wall. Altogether, 148 TMs with a total of 18,796 thermocouples are used in this calorimeter. All of the TMs are connected in series. The heat flow during experiments is proportional to the measured emf

(electromotive force) of the TMs. The two holes ($\phi = 2\text{cm}$) in the two sidewalls mentioned above permit multi-functionality of this calorimeter; i.e., measurements of temperature, internal resistance and voltage of the unit-under-test (UUT). The thermal emf of the calorimeter and other signals of UUT are measured with a Keithley 2000 multimeter which is connected to a PC through a GPIB card, to automatically register the data.

The outer aluminum box is wired with copper tubing ($\phi_{\text{in}} = 8\text{ mm}$, $\phi_{\text{out}} = 10\text{ mm}$). Thermal conductive adhesive is used to mount the copper tubing and the aluminum walls. The outlet of the copper tubing is connected with the hose of a refrigerating/heating circulator (PolyScience 9112). The temperature range of this circulator is -20 to 200°C ; the temperature stability is $\pm 0.01^\circ\text{C}$; and the pump outlet flow rate of the working fluid is 15 to 22 liters per minute. The inlet of the copper tube around the outer box is connected with a small cylindrical heat sink ($\phi_{\text{in}} 20\text{ mm} \times h_{\text{in}} 50\text{ mm}$); a remote, circular temperature probe is placed in it. This arrangement of the temperature probe ensures that the fluctuation of ambient temperature does not affect the calorimeter. The inlet of the small heat sink is connected to the circular probe with another hose. The hoses are wrapped with a polystyrene foam tubing to prevent heat losses. The calorimeter core is placed in a larger box with inner dimension of $70 \times 70 \times 70\text{ cm}^3$. Heat insulation materials fill the gap between these two boxes.

3. Calibration of the calorimeter

Calibration is conducted with a 6 ohm electrical heater. The four-wire Kelvin bridge method was used to eliminate lead resistance in the measurements. Applied current was measured with a $0.1\ \Omega$ ($\pm 0.01\%$) standard resistor as shunt. A Sanyo Denki brushless fan ($12\text{ V} \times 0.21\text{ A}$, 2.5 W) was used to make the temperature in the vessel homogeneous. The power of the fan was also measured in a similar manner. The calibration results are shown in Fig. 1. These results are simulated by a quadratic equation:

$$P/W = -0.0743 \pm 0.0038 + (5.899 \pm 0.0053)E/V + (0.0017 \pm 0.0014)(E/V)^2 \quad (1)$$

with $\chi^2 = 1.2 \times 10^{-4}$, $R^2 = 1$. P is the input power, and E is the output emf of the SEC. The device constant is about 6, or about 30 times more sensitive than the Thermonetics SEC. The device constant changed only 1.7% over a 9 month period. The time constant of this SEC is 5 minutes.

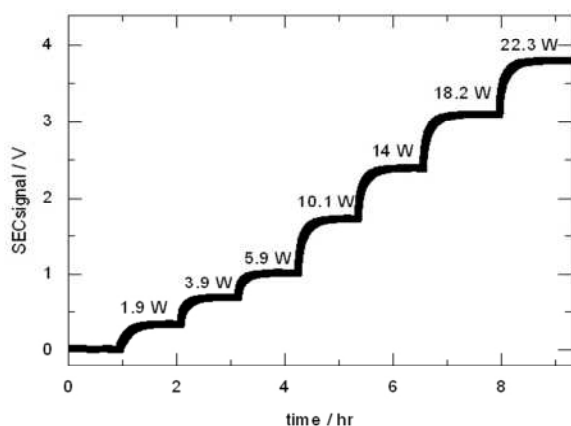


Figure 1 (a) SEC calibrations at 25°C.

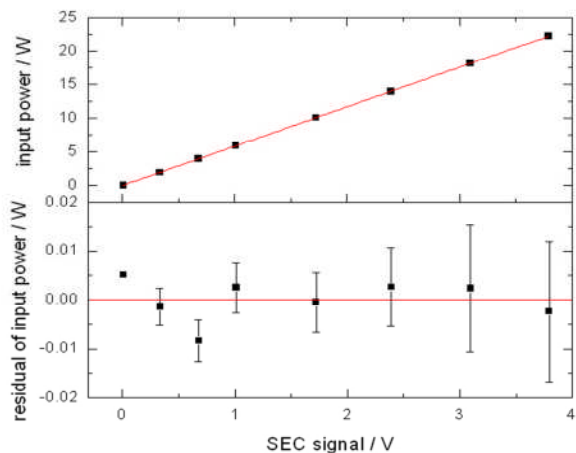


Figure 1(b) Simulation of calibrations.

4. Excess heat of Pd-D₂O system

A schematic of the electrolytic cell is shown in Fig. 2(a). The cell is a cylinder of borosilicate glass (capacity is about 250 ml, $\phi_{in} = 42$ mm and $\phi_{out} = 45$ mm, wall thickness = 1.5 mm, $h = 180$ mm). A PTFE male cap is tapered from $\phi 47 \times 5$ mm² at the top, and $\phi 41 \times 15$ mm² at the bottom. A groove of 4 mm width and 2.5 mm depth is made for O-ring in the middle of bottom part. The O-ring ($\phi_{in} = 31.5$ mm, width = 3.55 mm) made of nitrile butadiene rubber (NBR, resistant to acid) is used to seal the top cap against the top inner wall of glass cylinder. The top cap has two holes, 7 mm diameter each, for the electrode lead wires. A PTFE plate ($\phi 41$ mm \times 8 mm) is used to suspend the recombination catalyst above the electrode. It has 24 holes of $\phi 2$ mm for fluid (D₂, O₂, D₂O and its vapor) passing, and also has two holes, 7 mm diameter each, for the electrode lead wires. A PTFE rod ($\phi 6 \times 90$ mm²) is fastened to the perforated plate and the top cap ensures that the perforated plate is at a fixed distance above the electrolyte.

The Pd cathode was prepared from Alfa Aesar Stock # 11514, Lot # G15Q17, 99.9% purity palladium foil (metals basis). It was cold rolled from $15 \times 25 \times 0.5$ mm³ to $25 \times 25 \times 0.3$ mm³. Its surface area is 12.5 cm² and weight is 2.1891 g. The same Pd cathode was used for all experiments, with both isoperibolic calorimetry (IPC) and SEC.

Three platinum electrodes (two anodes and one cathode) are foils $22 \times 28 \times 0.02$ mm³, 11.5 cm² surface area. Four electrode lead wires are made of Pt ($\phi 1$ mm \times 40 ~ 60 mm). The Pt foils (99.95% Pt) are from General Research Institute for Nonferrous Metals. These Pt leads are connected with copper tubes and encapsulated with glass tubes ($\phi_{in} = 2$ mm, $\phi_{out} = 7$ mm, length = 170 mm) as shown in Fig. 2(a). The gaps between the glass tubes and the PTFE cap are filled with glass cement.

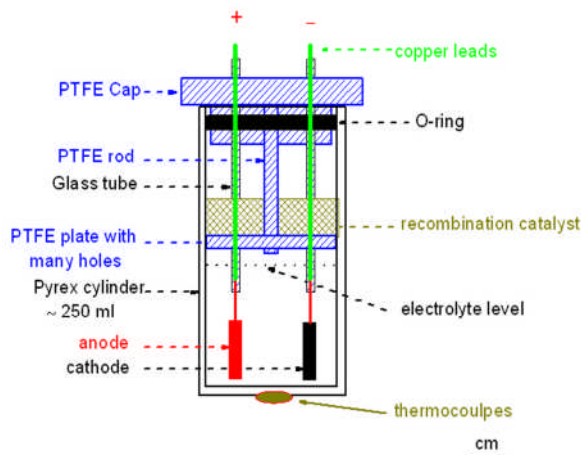


Figure 2(a) Schematic of cell.

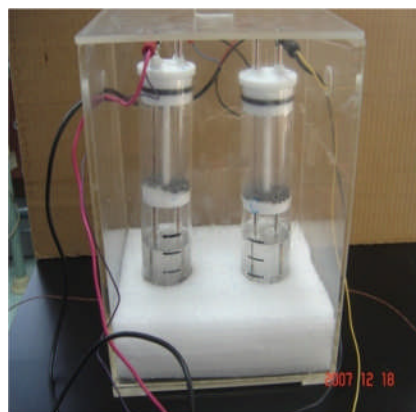


Figure 2(b) Photo of isoperibolic calorimeter.

The electrolyte contains heavy water (Beijing Chemical Reagent Company, > 99.9% isotopic purity) mixed with H_2SO_4 in the mass ratio of 110:27.5 (20:3 of volume ratio or 20% of mass concentration). The catalyst contains 0.5% Pt on 1/8 inch diameter alumina pellets (Alfa Aesar). Three grams (62 to 64 pellets) are used in each cell.

4.1. Excess heat measured by isoperibolic calorimetry (IPC)

Before samples were tested with the SEC, excess heat production from the samples was first verified with an isoperibolic calorimeter (IPC) shown in Fig. 2(b). Two cells were connected in series: the E cell (experimental cell, heavy water electrolyte and Pd cathode) and C cell (control cell, light water electrolyte and Pt electrodes) [2,4]. The mass concentration of H_2SO_4 in light water electrolyte is 13%. The distance between two electrodes in the C cell is adjusted to make its voltage close to that of the E cell. These two cells are embedded in a 5 cm thick polystyrene block in a plexiglass box ($14 \times 18 \times 23 \text{ cm}^3$, 4 mm wall thickness) as shown in Fig. 2(b). One K-type thermocouple was attached on the bottom of each cell to measure the temperature. The output power of the E-cell was calculated using the temperature difference between it and ambient, and the device constant deduced from the C-cell, as described in Refs. [2,4]. One example of excess heat is illustrated in Fig. 3(a) and all results are summarized in Table I. The excess power is 0.22 to 0.79 W in 7 runs. These results indicate this sample can produce excess heat during electrolysis at 0.24 A cm^{-2} .

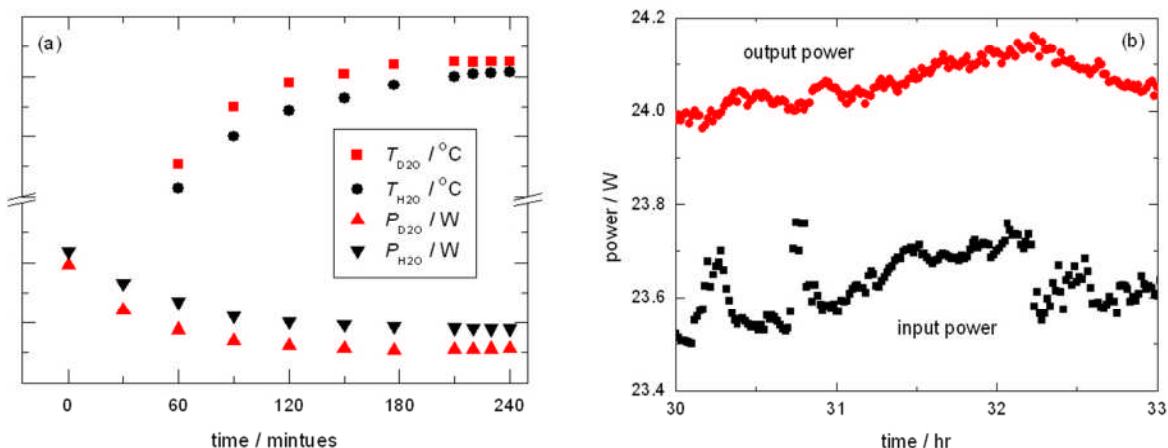


Figure 3(a) Excess thermal power measured by IPC (Run #2 in Table I); (b) Excess thermal power measured by SEC at 0.28 A cm^{-2} (Run #6 in Table II).

Table I. Summary of excess thermal power measured by IPC.

No.	System*	Current and time	$T_{\text{room}}/^{\circ}\text{C}$	P_{C}/W	$T_{\text{C}}/^{\circ}\text{C}$	P_{E}/W	$T_{\text{E}}/^{\circ}\text{C}$	P_{ex}/W
1	OC	-3A×2hr, 3A×3hr	22.0	4.77	59.5	4.21	60.4	0.44
2	OC	3 A × 5 hr	25.3	4.91	60.3	4.56	61.3	0.49
3	OC	3.5 A × 3.3 hr	24.9	5.84	67.3	5.66	67.0	0.22
4	CC	3 A × 4 hr	22.0	10.08	73.6	8.87	71.6	0.79
5	CC	-3 A × 1 hr 3 A × 7 hr	24.1	9.51	70.4	8.69	70.1	0.67
6	CC	3 A × 4 hr	30.8	9.86	77.0	9.18	76.2	0.50
7	CC	-3A×1hr, 3A×7hr	30.0	8.59	69.4	8.53	72.0	0.63

* OC is open cell; CC is closed cell; C is the control cell; E is the experimental cell.

4.2. Excess heat measured by SEC

After excess heat was verified with the IPC method, the entire isoperibolic calorimeter with the two cells installed in it (shown in Fig. 2(b)) was placed inside the SEC, where calorimetry was again performed. One example of excess heat is shown in Fig. 3(b). We performed 11 experimental runs. Six of these produced excess heat, ranging from 0.15 to 0.41 W, as shown in Table II. Run #3 had only the E (experimental) cell and not the C (control) cell; it also showed the excess heat. The total excess heat was 54 kJ and average excess power was 0.22 W in these 6 positive runs. Excess power measured by IPC and SEC were qualitatively consistent as shown in Table II.

Table II. Summary of 6 positive excess heat run measured by SEC at 25°C.

No.	System*	Current, time	$\Delta Q/\text{kJ}$	P_{in}/W	P_{ex}/W	P_{in}/W		$T/^\circ\text{C}$	
						P_{C}	P_{E}	T_{C}	T_{E}
1	OC, E+C	3 A \times 6.33 hr	4.29	9.60	0.28 ± 0.02			59.6	58.9
2	OC, E+C	3 A \times 7 hr	4.04	9.50	0.23 ± 0.02			59.8	59.6
3	OC, E	3 A \times 7 hr	5.04	8.20	0.15 ± 0.02				59.9
4	OC, E+C	3.5 A \times 6 hr	3.63	12.97	0.29 ± 0.02	6.55	5.48	66.2	66.1
5	OC, E+C	-3.5 A \times 1 hr, 3.5 A \times 5.5 hr	8.18	13.16	0.22 ± 0.04	6.93	5.29	66.8	66.7
6	CC, E+C	3 A \times 24 hr, 3.5 A \times 36 hr	28.63 [#]	23.67	0.41 ± 0.03	12.19	10.55	76.5	75.4

Note: All power and temperature values were taken when the values were stable.

* OC is open cell; CC is closed cell; E is E cell, C is C cell.

[#] Because the catalyst in the E cell did not work after 34 hrs electrolysis (mass losses of E cell and C cell were 32.7 and 0.4 g, respectively), this is a conservative evaluation.

5. Conclusion

A Seebeck Envelope Calorimeter was designed and constructed. It is sensitive; it has a fast response, and a stable device constant. Excess heat in Dash-type cells was verified with this calorimeter. Further work on this subject is in progress in our lab.

Acknowledgment

This research was supported by NSFC (20673129).

References

1. W.-S. Zhang, J. Dash, Q. Wang, Proc. ICCF12, Yokohama, Nov 27 to Dec 2, 2005, p. 86.
2. W.-S. Zhang, J. Dash, Proc. ICCF13, Dagomys, Sochi, Russia, June 25 to July 1, 2007.
3. E. Storms, Proc. ICCF12, Yokohama, Nov 27 to Dec 2, 2005, p. 108.
4. Q. Wang, J. Dash, Proc. ICCF12, Yokohama, Nov 27 to Dec 2, 2005, p. 140

Mass Flow Calorimetry

Michael C. H. McKubre and Francis Tanzella
Materials Research Laboratory
SRI International, Menlo Park, California

Abstract

Discussion of the Mass Flow first principles calorimeter in this paper is based primarily on the analysis and experience gained at SRI in answering the question: “is there a Fleischmann Pons heat effect (FPE)”?. Subsequently other mass flow calorimeters, or more generically heat balance calorimeters, were designed to answer this same question and some comment will be directed to the technical differences resulting from different design philosophies, specifically those designed and operated by ENEA, and Energetics Technologies.

Discussion will be undertaken of ideal and non-ideal calorimeter operation, design principles and practical implementation including long and short term accuracy and sensitivity as well as limitations of heat balance calorimeters as the vehicle chosen to study the FPE.

Introduction

The needs of so-called “cold fusion” calorimeters are so different from those intended for use studying brief chemical reactions that, apart from basic principles, very little of value can be learned from studying that community, and little reference will be made to them here.

First a few words about the special purpose that constrains the design. The generation of mass flow or more generically heat balance calorimeters under discussion were constructed to achieve confidence and give credence to a result that was not believed. Fleischmann *et al.* [1], and others had reported results of a nuclear level heat effect resulting from the extensive electrochemical insertion of deuterium into palladium cathodes over an extended period of time by means of electrolysis of heavy water in heavily alkaline conditions. This effect has subsequently become known as the “Fleischmann Pons Effect” or FPE.

If true, this result was seen by some as a potential energy source, or at the very least a new potentially interesting physical effect. By others it was viewed as an unwelcome diversion of attention which was criticized as “irreproducible” or the result of unspecified “inaccuracies”. With regard to the second, apparently informed statements were made that “all calorimeters” were “intrinsically inaccurate”, an assertion that early pioneers of chemical thermodynamics in the early 20th and even late 19th century would have found puzzling. In this climate, however, the challenges to the second-generation FPE calorimeters were threefold:

- i. To allow reproducible demonstration of the effect – whether it be real or the consequence of (unidentified) systematic error,
- ii. To exhibit proven levels of accuracy, over sufficient periods to quantify heat generation consistent with the FPE,

- iii. The operating principal must be sufficiently simple to allow an open-minded non-specialist to visualize the full range of potential error.

Design Principles

With these needs well in mind a group of senior physical scientists was convened at SRI¹ to consider the design of a simple, first-principals calorimeter with high and stable accuracy, capable of accommodating a sufficient volume and input power range without compromising the electrochemical needs, or the need to know the chemical state of the system under test. The first result of this design exercise was presented with results at ICCF2 [2] and states:

“Our calorimeters were designed with the philosophy that in precise calorimetry, and in the search for unusual reaction products, it is desirable to have a closed system, and a knowledge at all times of the composition of the reacting system. All experiments were performed with closed and sealed electrochemical cells operating from 40 to 10,000 psi above atmospheric pressure. Axial resistance measurements were made to monitor the D/Pd or H/Pd ratio.”

This covers the requirements of physical operating condition and the perceived needs for both calorimetric and reaction diagnostic, reasons to retain products in a closed cell and to measure the chemical (and electrochemical) state of the system under test at all times. Additional constraints were imposed by points i to iii above. The calorimeters were designed and constructed according to the following ten requirements:

1. As conceptually simple, first-principals devices based on the first law of thermodynamics².
2. With a requirement to maintain complete control of the critical chemical and electrochemical operating parameters, including cell temperature.
3. To accommodate a large dynamic range of heat input and output anticipated to be ~100 mW – 100 W (later extended to 500 W).
4. To permit complete, on-line monitoring of all important physical, chemical, electrochemical and thermal variables.
5. With multiple measurement redundancy of variables critical to calorimetry (*e.g.* temperature).
6. So that heat was measured accurately, equally and completely, independent of its source position within the calorimeter.
7. To allow high precision (the greater of 10 mW or 0.1% of power input) and high and stable accuracy for operating times as long as 1000 hours.
8. To operate as closely as possible to the (thermal) steady state, thus simplifying calorimetric data analysis.

¹ The authors are very much indebted to this group, which expanded with time, but had as its core: Jason Chao, Bindi Chexal, Steve Crouch-Baker, Jon McCarty, Tom Passell, Joe Santucci, Stuart Smedley, Robert Weaver and Sharon Wing.

² It is interesting to note that our widespread and deep trust in this law is based exactly on our confidence in calorimetric accuracy.

9. With sufficient time resolution to permit simple non steady state correction allowing source reconstruction of possible thermal transients.
10. To be operated in such a way that known sources of potential systematic error yield conservative estimates of “excess” heat.

Heat balance calorimetry

One means of calorimetry was considered (in 1989) best able to meet the above-listed requirements. Often called mass flow calorimetry because of its emphasis on heat convected by a moving fluid mass, Heat Balance Calorimetry is accomplished by monitoring the heat gained or lost by the heat transfer fluid as follows:

$$Q_o = \delta m / \delta t C_{ps} (T_i - T_o) \quad [1]$$

where:

Q_o = process heating (output) power (W)

$\delta m / \delta t$ = mass flow of heat transfer fluid (kg/s)

C_{ps} = specific heat of heat transfer fluid (J/(kg K))

T_i = inlet temperature of heat transfer fluid (K)

T_o = outlet temperature of heat transfer fluid (K)

Heat balance calorimetry has been described as “*the ideal method of measuring heat since the heat entering and leaving the system through the heating/cooling jacket is measured from the heat transfer fluid (which has known properties). This eliminates most of the calibration problems encountered by heat flow and power compensation calorimetry*” [3].

As written, equation [1] has no calorimeter dependent calibration requirements. Given independent, fundamental calibrated references for mass and time (hence $\delta m / \delta t$) and temperature (or temperature difference), and independent accurately known properties of the mass transport fluid, then the measurement of Q is absolute. This calibration independence is very important. Drifts in calorimeter “calibration constant” are the greatest cause of concern and error in FPE experiments which must last hundreds of hours before the effect is seen, and may last thousands¹.

Input power to an electrochemical cell operating thermodynamically closed is simply the product of the electrochemical current and the voltage measured at the calorimetric boundary (i.e. at a point on the surface that is neither inside nor outside). To meet requirements 2 and 8

¹ The effect of drift was eliminated and turned to advantage in the heat flow calorimeters designed by Fleischmann and Pons by daily, automated Joule calibration pulses. The presence of drift and rather clumsy handling of it essentially invalidated several early “negative” results as the position of the “baseline” was adjusted daily by arbitrary assertion that the “excess power” was zero.

above allowing independent control of electrolyte temperature and steady state operation it is necessary to add an input electrical Joule heater to complement the electrochemical power input. In this configuration,

$$Q_i = I_{EC} V_{EC} + I_J V_J \quad [2]$$

and we define as excess power the difference between the calorimetrically determined heating output power and the sum of power input,

$$Q_{XS} = Q_o - Q_i \quad [3]$$

Note that Q_{XS} may have either sign. Negative “excess” is possible, although this condition has never been observed in any mass flow calorimetry performed at SRI in studies of the FPE except during transient conditions as will be discussed shortly.

Departures from ideality:

To obtain accuracies higher than ~1%, two factors affecting calorimeter performance must be taken into account:

1. Thermal efficiency

Equation [1] accounts for heat removed from the calorimeter by convection of the thermal transfer fluid. Heat may also penetrate the calorimeter boundary by conductive exchange with the ambient. Of particular concern are metallic wires and pipes. If the environment is configured in such a way that the ambient is the inlet temperature, then equation [1] can be simply rewritten to include a conductive loss term, k ,

$$Q_o = (\delta m / \delta t C_{ps} + k) (T_i - T_o) \quad [4]$$

Since k is a calorimeter specific constant that does require calibration, it is important that it be kept small to preserve first principals operation. By careful insulation, controlled geometry and selection of the fluid flow rate, k was typically less than 1% of $\delta m / \delta t C_{ps}$ in the SRI mass flow calorimeters. Because k is defined by geometry, it is also very unlikely to change and was observed to be stable.

In high temperature operation one should expect radiative in addition to conductive transport. No such non-linear tem has been observed or required in the mass flow studies so far performed at SRI or by our close collaborators. In high temperature studies [4] performed at Energetics Technologies reflective surfaces were used to minimize radiative heat transport.

2. Thermal time constant

Input power is measured effectively instantaneously while the calorimetric output thermal power responds with the thermal time constant(s) of the calorimeter. To make accurate subtraction of $Q_o - Q_i$ in order to calculate Q_{XS} at the same instant and thus improve (instantaneous) accuracy and permit study of thermal transients, it is necessary to apply one or a series of exponential filters to Q_i so that the terms on the right side of equation [3] refer to the same time of measurement.

Although other heat transfer processes might be considered, three terms dominate the transfer of electrochemical cell heat out of the calorimeter:

- The conduction communication of electrochemical cell heat to the moving heat transfer fluid
- Convective transport of the heated fluid element to the outlet temperature sensors
- Convective thermal dilution of this heat due to the incoming mass flow at constant rate and constant (cooler) temperature.

Terms “a” and “c” depend exponentially on time. In all calorimeters studied at SRI the time constant for “a” and “b” were substantially less than for “c” and it was found sufficient to adopt a single level of exponential filtering with the following form.

$$\Delta Q = \sum_{\Delta t = 0}^t \Delta Q_{i,\Delta t} \left(1 - e^{-\Delta t/\tau} \right) \quad [5]$$

where Δt is the time interval of measurement and τ is the composite time constant.

In this way the output power was corrected using the sum of the exponential decay response to each stepped change in Q_i from the preceding $t/\Delta t$ measurement intervals (6 hours) of P_{In} . At this point the response of P_{Out} has achieved >99.99% of its steady-state value for $\tau_2 = 0.33$ h. For some data sets, particularly those in which the bath temperature was changed, corrections were also made for the effect on P_{Out} caused by the heat capacity and changing temperature of the cell contents. The mathematical form of this correction is given by equation [6].

$$\Delta P_{Out} = [M_{Water} C_{ps,Water} + M_{Solid} C_{ps,Solid}] \Delta \bar{T} / \Delta t \quad [6]$$

where subscripts “Water” and “Solid” refer to the liquid (*i.e.* heavy or light water) and solid components of the electrochemical cell and M is the mass of these cell components.

In practice, because \bar{T} (the average temperature of the cell and its contents) is a slow-moving function of time, $\Delta \bar{T} / \Delta t$ can be calculated as the slope at the respective time series functions, $\delta T / \delta t$, at each point in the data series.

It is important to remember that the form of the non-steady-state corrections is such that, while these can significantly improve calorimetric precision, they do not affect the accuracy of total excess energy generation. The round trip integral effect of both the $\delta Q / \delta t$ and $\delta T / \delta t$ corrections expressed by Equations [5] and [6] is zero for the same initial and final conditions.

The consequences of the non-idealities of mass flow calorimetry expressed in equations [4] and [5] are represented graphically in Fig. 1. For an arbitrary stepped increase in input power of 1 W at time $t=0$ the response of the output temperature sensors respond exponentially with time constant τ . For a calorimeter with 100% thermal efficiency ($k = 0$) shown by the black line in

Fig. 1, the output responds asymptotically to the input step, but to a lower value at lower thermal efficiency. The effect of “a” above is to add a second (faster) exponential response, the effect of “b” above is to add a (short) onset delay.

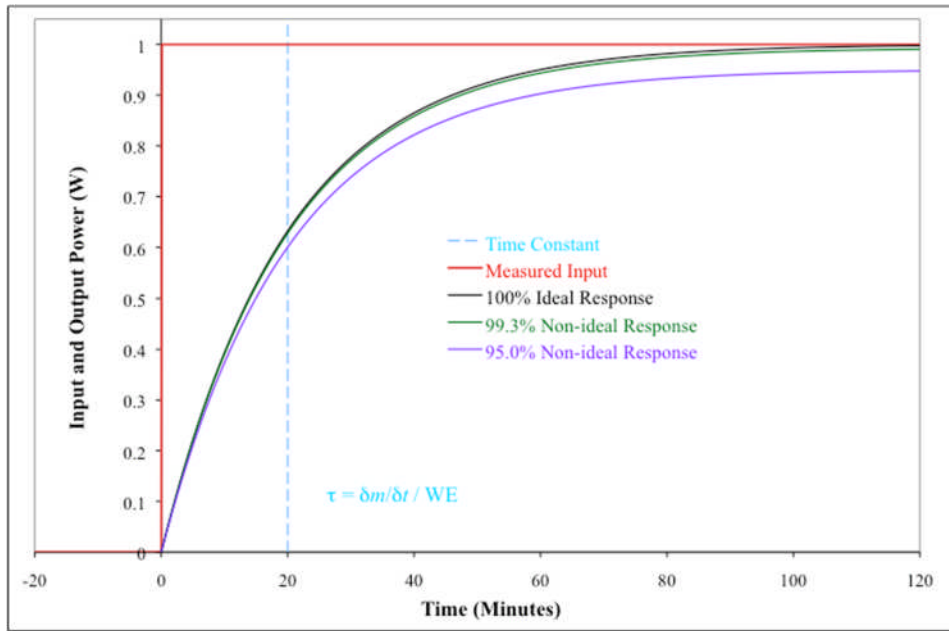


Figure 1. Non-ideal response of mass flow calorimeters

Practical implementation

To preserve first principles operation as closely as possible as one of the major strengths of mass flow or heat balance method, we are concerned to keep conduction and radiation losses (k) to a minimum. Several methods have been evolved in FPE calorimeters. One of the simplest methods is to incorporate a high efficiency heat exchanger within the electrolyte and heavily insulate the perimeter. This method has been used successfully by Arata [5], Violante [6] and others [7]. An important figure of merit for all configurations of mass flow calorimeters is the thermal efficiency, Φ , which reflects the fraction of the total heat removed by convective flow.

$$\Phi = Q_{Convection} / [Q_{Convection} + Q_{Conduction} + Q_{Radiation}] \quad [7]$$

Figure 2 shows an implementation of this method at ENEA [see Ref. 8, p. 238] with the calibration of the thermal efficiency using a Pd electrode in LiOH shown in Fig. 2. The mass flow coils can be observed in section inside the electrochemical cell. For this example the attained thermal efficiency was 97.5%. While relatively low for a mass flow calorimeter, this is an impressive value for this “inside out” geometry because of the relatively small exposed surface area of the immersed heat exchanger compared with the outer surface. Another limiting constraint is the need to use insulating, or insulation covered materials for the heat exchanger to prevent chemical contamination of the electrolyte thus compromising the cathode electrochemistry.

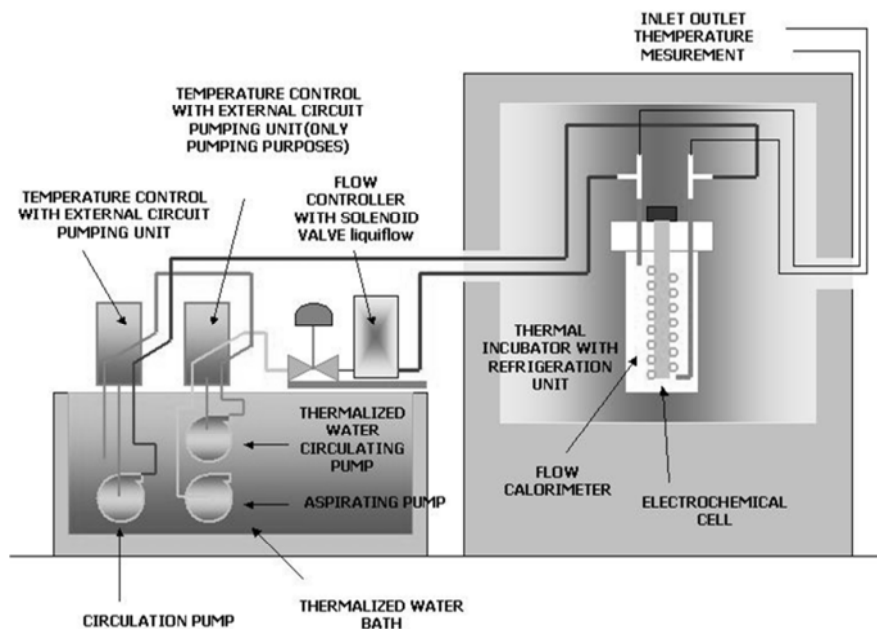


Figure 2. ENEA Mass Flow calorimeter with internal heat exchanger

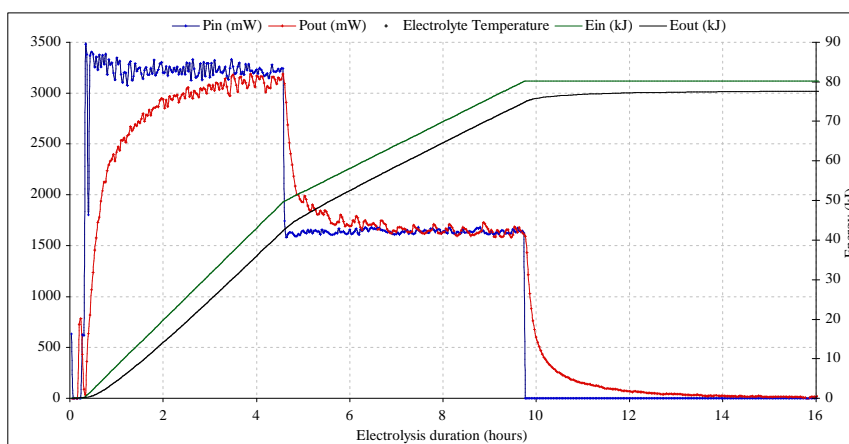


Figure 3. Calibration of ENEA calorimeter using Pd cathode in 0.1M LiOH

In general higher thermal efficiencies can be achieved with the inverse geometry which positions the heat exchanger to cover as much as possible of the cell external area. Particularly elegant designs have been implemented by Energetics Technologies in which the heat exchanger is a helical flow channel machined into the external surface of the cell to ensure intimate thermal contact. An early design with the heat exchanger covering the cylindrical walls in 2π geometry with insulating end caps was used to study heat production from a glow-discharge FPE [4].

A thermally more efficient design was recently implemented by Energetics Technologies to study SuperWave[®] stimulated electrolytic FPE heat production in helium leak tight,

thermodynamically closed cells. In this design, shown in Fig. 4, the bottom and cylindrical sides of the cell are fitted with spiral and helical water flow channels. This design resulted from extensive engineering development efforts at Energetics Technologies, and elaborate finite element thermal modeling at ENEA. Because the top is not actively cooled, however, and due to thermal conduction out along numerous electrical power and sensor wires and gas lines, the maximum thermal efficiency so far achieved with this design is only ~95%.

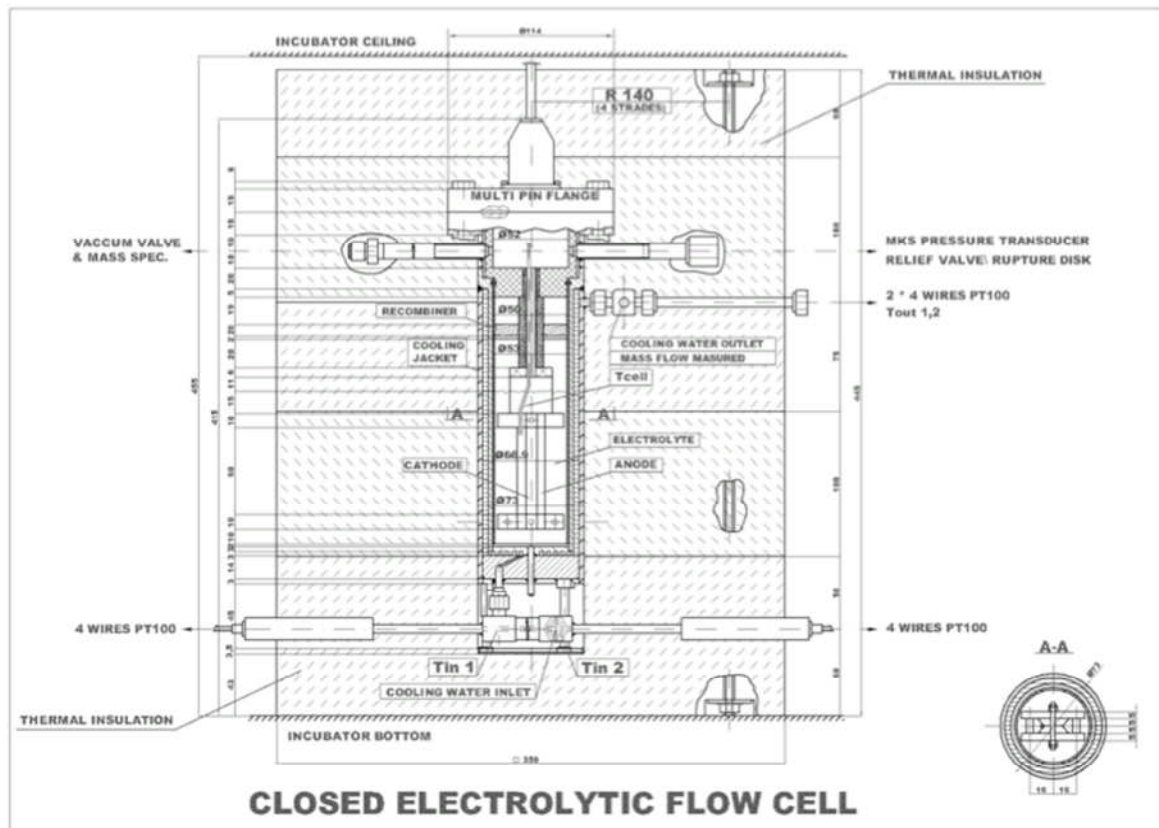


Figure 4. Energetics Technologies closed electrolytic mass flow calorimeter cell¹

To achieve values of Φ higher than 99%, very particular attention must be paid to numerous details of design. The labyrinth calorimeter developed at SRI and shown in Fig. 5, achieved $\Phi > 99.3\%$. Higher values were attainable at higher mass flow rates, but with decreased sensitivities. We will examine this design more closely as a way to highlight these design details. The contained electrochemical cell, capable of operating autonomously, is shown in Fig. 6.

¹ The authors are indebted to S. Lesin and A. Godfrey of Energetics Technologies for permission to reproduce this Figure.

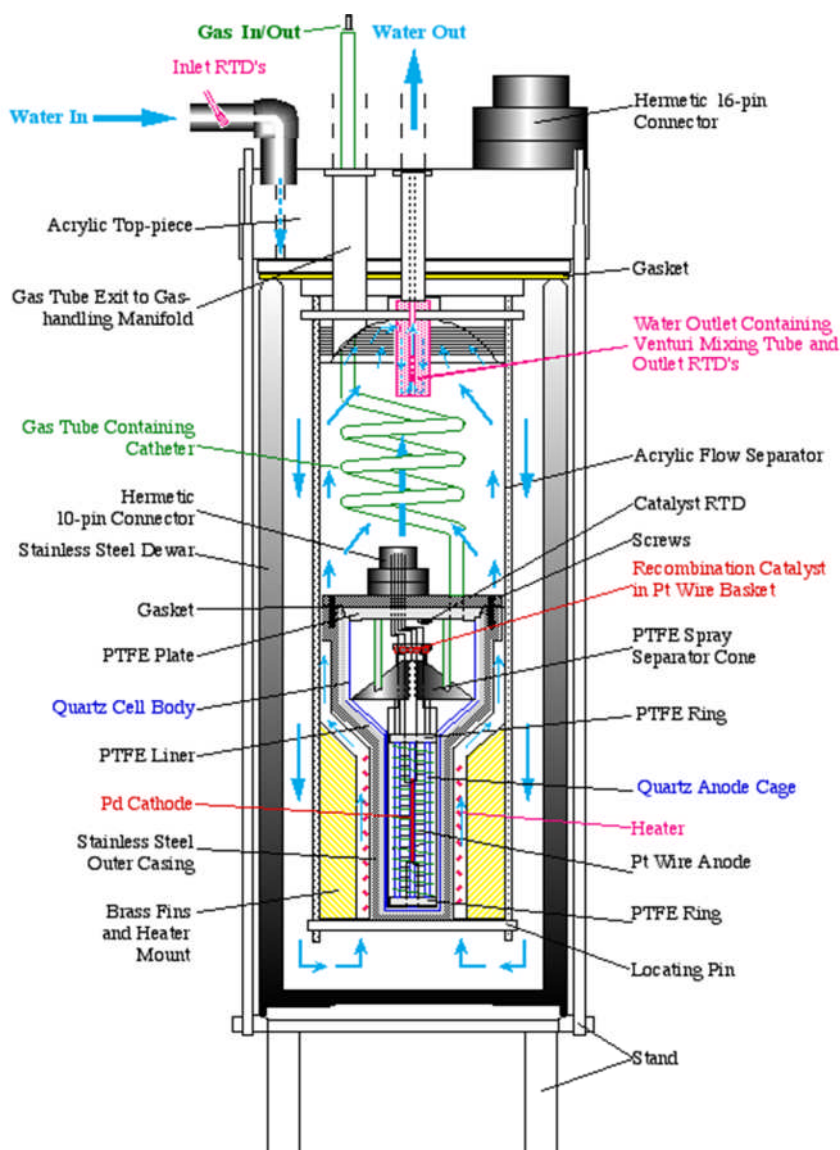


Figure 5. SRI Labyrinth Mass Flow Calorimeter circa 1992

Due to issues of irreproducible interfacial kinetics and bulk deuterium loading [see companion paper, ref. 9] experiments were started in a “farm” of 12 DoL cells sometimes intentionally identical. Only those cells that exhibited acceptable loading and interfacial dynamics were promoted to the calorimeter shown in Fig. 5. The DoL cells therefore needed to exhibit two different sets of characteristics:

- i. To be consistent with the needs of good electrochemistry and maintain scrupulous cleanliness for long periods of time in strong basic electrolytes and at the high current levels demanded of FPE experiments
- ii. To be compatible with the needs of good calorimetry and maintain hermeticity for long periods of time.

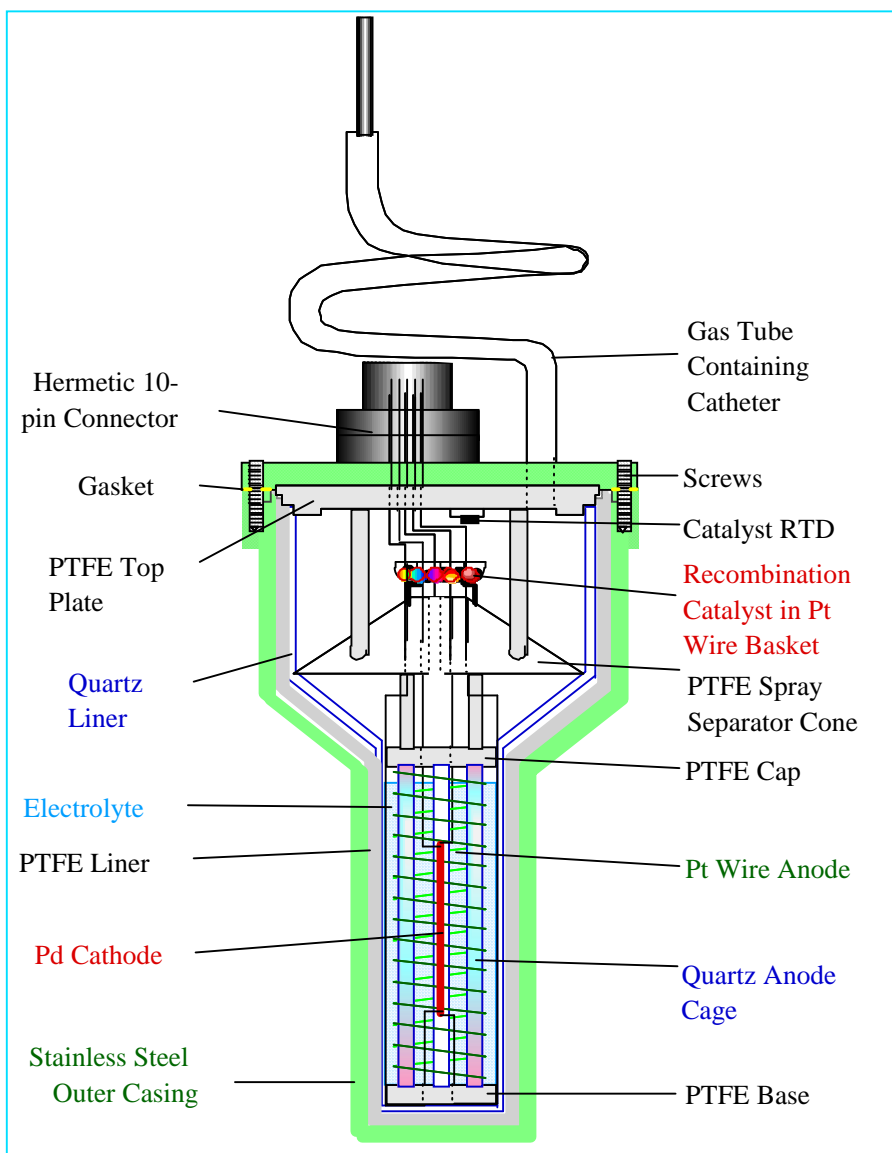


Figure 6. SRI Degree of Loading (DoL) and Calorimeter Cell

The first was accomplished by using a quartz (fused silica) cell body with fitting PTFE head. All components structural or otherwise inside the cell in contact with either electrolyte or vapor were manufactured of SiO_2 , Al_2O_3 , PTFE, Pt or Pd. Internal recombination and thus thermodynamic closure, was provided by either Pt or Pd on Al_2O_3 recombination catalyst suspended above a PTFE conic section designed to prevent electrolyte splash damage and allow the condensed recombine (either H_2O or D_2O) to wash deposits back into the electrolyte. The working volume was $\sim 30 \text{ cm}^3$. Using this materials selection and design geometry these cells are capable of sustained operation in 1 M base at currents above 1 A for period over 1000 hours.

The hermetic design of the DoL cell allows for full immersion in the mass flow fluid so that the moving mass of calorimetry fluid (in this case air saturated water) can remove heat efficiently from each of 5 geometrically disperse heat sources:

1. The product of the electrochemical current flow and the cathode interfacial impedance and any excess heat source located at the cathode (in the case shown at the axial center of the cell)
2. The product of the current flow and the electrolyte resistance path due to and located within the electrolyte volume between cathode and anode (or anodes)
3. The product of the current flow and the anode interfacial impedance located in an axially symmetric cylindrical shell relatively close to the cell wall
4. The heat of recombination of H_2 and O_2 or D_2 and O_2 at the recombination catalyst located in the volume of the recombiner near the top of the cell
5. The product of the current in the Joule heater used for power compensation and calibration, located in an axially symmetric cylindrical shell immediately outside and intimately contacting¹ the cell wall.

All of these terms are significant and differently couple to the calorimeter and outside environment. In a well-stirred electrolyte as exists above relatively modest current densities, the first three terms constitute effectively a single volume source. In the steady state the recombination thermal power is equal to the electrochemical current times the thermoneutral voltage of 1.48 V for H_2O or 1.23 V for D_2O . The Joule heater, while axially symmetric with the electrolyte volumetric heat source, is closer and therefore temporally and thermally better coupled to the convecting mass flow fluid.

By enveloping the whole DoL cell in the flow as shown in Fig. 5, we were able to establish within better than 0.1% (1 ppt) that the measurement of heat (the output thermal power) was independent of its source within the calorimeter. This degree of position insensitivity is very difficult to achieve with the “inside out” mass flow calorimeter design of the type shown in Fig. 2, or by the use of an external heat exchanger as shown in Fig. 3.

Several other features of the calorimeter shown in Fig. 5 merit further discussion. In employing equation [6] with a single conductive loss term, k , it is necessary to ensure that the calorimeter experiences a single, stable thermal ambient environment. The calorimeter shown in Fig. 5 was submerged inside a large ($\sim 1\text{ m}^3$), water bath that was well stirred and well regulated². This bath was placed in the center of an isolated, temperature controlled room. The mass flow fluid (water) was drawn from the bath past two inlet RTD sensors placed directly in the flow stream. The flow entered to head of the calorimeter through a flow distribution header

¹ In calorimetric operation the Joule heater is held in place by a push-fit, finned brass heatsink that fills the radial space between the outside of the cell and the inside of the flow channel to ensure rapid coupling of the heat from all sources to the moving mass flow fluid.

² Temperature gradients and variability both short and long term were maintained below ± 3 mK. A Quartz Crystal reference thermometer [HP Model 2804A was maintained as a temperature standard in this bath.

and was channeled down through the annular volume between the inner wall of a 2 liter stainless steel Dewar and a thermally insulating barrier to form a flow labyrinth reversing direction at the bottom to flow past the submersed electrochemical cell. The electrical leads from the cell were dressed in the reverse direction from a hermetic connector at the top of the cell to another at the top of the calorimeter. The purpose of this arrangement is to minimize conductive heat loss radially from the cell and along the electrical leads used for electrochemical control and measurement. In the labyrinth configuration heat leaving by these paths is picked up in the incoming fluid and delivered to the outlet sensors for measurement.

The final feature of the calorimeter is the hemispherically domed insulating head that houses the outlet temperature sensors. The hemispherical shape was designed to minimize the formation of thermal “pockets” at higher or lower temperature than the average. The mass flow fluid flows through a small hole at the highest accessible point of the hemisphere to enter the outer annulus of a small flow labyrinth containing a venturi (helical) flow mixer. Turning the corner this flow enters a small axial flow channel designed to ensure good mixing at the operating mass flow rate (typically ~1 g/s).

These flow precautions were taken to ensure that the outlet temperatures measured represent an accurate average value in the fluid flow. The outlet temperature sensors were situated within the axial outflow channel, directly in contact with the outgoing fluid. Two RTD sensors were used, identical to the two at the inlet, to provide a redundant measurement of ΔT . In some experiments two additional thermistor sensors were used at the outlet to provide a redundancy of measurement method.

An FMI QV-OSSY constant displacement pump was used to draw water from the top of the calorimeter through a standard heat exchanger to ensure constant mass flow. This flow was then pumped directly into a reservoir placed on a Setra 5000L electronic balance that was polled regularly by the data acquisition system to measure the mass flow rate as $\Delta m/\Delta t$. When the balance reservoir is filled a siphon automatically forms and empties the vessel rapidly¹.

Brief evaluation of errors

Excess power is calculated as the difference between the output power and the input power

$$Q_{XS} = Q_o - Q_i = (\Delta m/\Delta t C_{ps} + k) (T_i - T_o) - I_{EC} V_{EC} - I_J V_J \quad [8]$$

Temperatures were measured using 100 Ω platinum resistance temperature devices (RTD's) so that to first order,

$$T = T^\circ + (R - R^\circ) / \alpha R^\circ \quad [9]$$

where α is the (known) temperature coefficient of resistance for Pt, and R° is the sensor resistance at some known temperature (typically 0°C).

¹ This normally disrupts only one, and at most two determinations of $\Delta m/\Delta t$. In general the flows were very stable but redundant mass flow measurements occasionally were used for added accuracy.

A complete error propagation model has been developed for the calorimeter shown in Fig. 5; the basic elements are reproduced below. Errors propagate from mis-measurement of each of the terms. The constants and variables needed to measure Q_{XS} and its uncertainty may be divided into three classes:

1. Measured variables: Δm , Δt , R , I and V .
2. Predetermined constants: C_{ps} , α and R° .
3. The calorimeter inefficiency: k .

Measurements of mass, time, resistance, current and voltage rely on the calibration accuracy of the devices being used. At SRI the instruments used were periodically calibrated to accuracies better than 1 part per thousand (<1 ppt) and typically better than 1 part in ten thousand. Measuring R° with the same instrument used to measure R further increases measurement accuracy. Systematic errors in the calorimetry critical temperature difference tend to cancel since this depends on the difference of resistances measured with the same meter at almost identical times.

The heat capacity of air-saturated water and the temperature coefficient of Pt resistance are well-measured constants. It should be noted that these are not constant with temperature; for accuracies better than 1 ppt it is necessary to take account of the fact that the outlet temperature may vary over of a considerable range, affecting both C_{ps} and α .

What remains is the conductive loss term or calorimeter thermal inefficiency, k . Three factors contribute to reducing the inaccuracy in this term and increase its long-term stability and thus influence on overall calorimeter accuracy.

- a. By design and selection of mass flow rate k is maintained to be a small fraction of $\Delta m/\Delta t C_{ps}$. Typically this constant was held to contribute ~1% or less of the output power and it can be measured easily with better than $\pm 10\%$ accuracy thus contributing <1 ppt to the overall measurement.
- b. The method of calibration using a Joule heater pulse determines k in terms of the other predetermined constants. In this way the cumulative error is reduced and recalibration can be performed at any time (in the absence of excess power) using a Joule heater pulse.
- c. The value of k is determined by the geometry and materials properties of heat conduction pathways. With the calorimeter isolated in the constant temperature bath these are not likely to change, and were not observed to do so.

For the Labyrinth Mass Flow Calorimeter shown in Fig. 5 the maximum error in the typical operating range of input power and mass flow rates ($Q_i = 5 - 20$ W, $\partial m/\partial t \sim 1$ g/s) was $\pm 0.35\%$ of Q_i . The largest source of error in practice is mis-measurement of the average temperature of the outgoing fluid stream due to flow streaming. Care must be taken to ensure good flow mixing and the avoidance of particulates in the flow stream.

Conclusions

With some attention to detail heat balance calorimeters based on the mass flow of water are capable and robust instruments that combine the desirable features of simplicity of design and calorimetric analysis, adequate accuracy, high long-term stability and low initial materials and operating costs. By these criteria such devices are well suited to studies of the FPE and have been widely employed with considerable success [7, 11]. Mass flow calorimeters are conceptually simple, first principles devices based on the first law of thermodynamics. They are able to accommodate and operate nearly linearly over a large dynamic range of heat input and output, extending easily to 500 W while maintaining better than 1% accuracy. Designs are available to permit the measurement of heat accurately, equally and completely, independent of its source position within the calorimeter.

Several potential disadvantages and undesirable features nevertheless are implicit in the mass flow principle and subject operation to added complexity. Designs needed to maintain high accuracy, such as those shown in Figures 2, 4 and 5 are not cheap to develop or implement. Highest accuracy (closest to first principles) operation with enveloping mass flow renders the cells opaque and inaccessible, increasing the difficulty of identifying and rectifying technical issues within the cell. To achieve accuracies approaching or exceeding 0.1% it is necessary to take account of the (known) temperature variability of the heat capacity of air-saturated water and the temperature coefficient of Pt resistance.

A final point is perhaps pertinent only to FPE studies. Fleischmann and Pons exploited a positive temperature coefficient of the excess heat phenomenon [10] to produce large effects, and several authors have noted [7, 11, 12] that to initiate or stimulate the effect sometimes required a step or abrupt change in conditions. Mass flow calorimeters are by design and nature thermally sluggish. They are not capable of responding quickly to a rapid change in input conditions. The steady state method favored at SRI actually opposes thermal change by maintaining the total input power constant. To the extent that changes in thermal condition are necessary to produce or intensify the effect under test then the heat flow design of Fleischmann and Pons [1] offers clear advantage.

Acknowledgment

As specified in “Design Principles” this paper summarizes briefly knowledge and experience accumulated by a very large number of contributors over a period of nearly 20 years. The authors would like to acknowledge and thank each of those who have contributed and recognize that in doing so the somewhat opaque and outmoded science of calorimetry may have been rendered less so. None of this change and innovation would have occurred without the stimulus provided by Martin Fleischmann and Stanley Pons to whom we offer our final and ultimate acknowledgment.

References

1. Fleischmann, M., Pons, S., and Hawkins, M., *J. Electroanal. Chem.*, **201**, p.301 (1989); Errata, **263**, p. 187 (1990). See also M. Fleischmann, S. Pons, M. W. Anderson, L. J. Li and M. Hawkins, *J. Electroanal. Chem.*, **287**, p. 293 (1990).

2. McKubre, M. C. H., Rocha - Filho, R. C., Smedley, S. I., Tanzella, F. L. , Crouch - Baker, S., Passell, T. O. and Santucci, J., “*Isothermal Flow Calorimetric Investigations of the D/Pd System*” in *The Science of Cold Fusion*, eds. T. Bressani, E. Del Giudice and G. Preparata, Conference Proceedings Vol. 33, Italian Physical Society, Bologna, p. 419 (1992).
3. <http://en.wikipedia.org/wiki/Calorimeter>
4. Dardik, I., Branover, H., El-Boher, A., Gazit, D., Golbreich, E., Greenspan, E., Kapusta, A., Khachatorov, B., Krakov, V., Lesin, S., Michailovitch, B., Shani, G., and Zilov, T., “*Intensification of low energy nuclear reactions using superwave excitation*”, in *Tenth International Conference on Cold Fusion*, Hagelstein, P. L. World Scientific Publishing Co., Cambridge, MA, 2003, pp. 61.
5. Arata, Y., and Zhang, Y-C., “*Helium (^4He , ^3He) within deuterated Pd-black*”, Proc. Japan Acad. 73B (1997). p. 1.
6. Violante, V., M. Apicella, E. Castagna, L. Capobianco, L. D’Aulerio, G. Mazzitelli, F. Sarto, A. Rosada, E. Santoro, M. McKubre, F. Tanzella, C. Sibilia, Proceedings XII International Conference on Cold Fusion, Yokohama (Japan) 27 Nov. 2 Dic. 2005, p.117.
7. Storms, E., The science of low energy nuclear reactions, World Scientific, 2007.
8. McKubre, M. C. H., Tanzella, F. L., Dardik, I., El Boher, A., Zilov, T., Greenspan, E., Sibilia, C., and Violante, V., Replication of Condensed Matter Heat Production, in *Low-Energy Nuclear Reactions Sourcebook*, Marwan, J., ACS Symposium Series 998, Oxford University Press, 2008, p. 219.
9. McKubre, M. C. H., “*The Importance of Replication*”, in *14th International Conference on Cold Fusion*, 2008, submitted.
10. Fleischmann, M., and Pons, S., “More About Positive Feedback; More About Boiling”, in *5th International Conference on Cold Fusion*, Fleischmann, M., and Pons, S., Monte Carlo, Monaco, 1995.
11. Hagelstein, P. L., McKubre, M. C. H., Nagel, D. J., Chubb, T. A., and Hekman, R. J., “*New Effects in Metal Deuterides*”, in *11th International Conference on Cold Fusion*, Biberian, J-P., Marseilles, France, 2004, pp. 23.
12. McKubre, M. C. H., Tanzella, F. L., Hagelstein, P. L., Mullican, K., and Trevithick, M., “*The need for Triggering in Cold Fusion Reactions*”, in *10th International Conference on Cold Fusion*, Hagelstein, P. L., Cambridge, USA, 2003, p. 199.

MOAC – A High Accuracy Calorimeter for Cold Fusion Studies

Scott R. Little, George A. Luce, Marissa E. Little
EarthTech International, Inc., 11855 Research Blvd
Austin, TX 78759, USA

Abstract

Calorimetry is conceptually simple but considerable effort is required to reduce systematic errors to acceptable levels. Since 1989, we have designed and constructed a dozen calorimeter systems for cold fusion research. Each of these systems provided valuable experience in error detection and correction. The culmination of our efforts, an instrument with a design accuracy of 0.1% relative, is nicknamed MOAC (Mother Of All Calorimeters). This paper provides a brief description of MOAC.

1. Introduction

One of the most important effects associated with cold fusion is excess heat. In order to measure excess heat a special calorimeter is required; one that simultaneously measures both the electrical power into the cell and the heat power out of the cell. Most of the calorimeters routinely used in chemical studies are unsuitable for this purpose because they only measure the heat power or energy released by the specimen.

For cold fusion research it is desirable to have a calorimeter with high accuracy so that small effects can be studied. Unfortunately, high-accuracy calorimetry is not easily achieved. It is especially difficult to realize accuracy better than 1% relative. Compared to a calorimeter with 1% accuracy, at least an order of magnitude more effort is required to achieve 0.1% accuracy.¹

2. Measurement Strategy

MOAC operates on a simple principle. Flowing water is used to extract the heat from the cell. The flow rate and the temperature rise of the water are measured. The product of the temperature rise, the flow rate, and the specific heat of water yields the heat power being extracted from the cell. This approach is commonly referred to as flow calorimetry. In addition, MOAC simultaneously measures the heat output of the cell by isoperibolic calorimetry. In this technique, which is based upon Newton's Law of Cooling, the heat output power is assumed to be proportional to the temperature difference between the electrolyte and the gently stirred air that surrounds the cell. These two independent methods of heat power measurement provide important insights into the thermal behavior of cold fusion cells.

3. Construction

Despite its simple concept, MOAC is not a simple instrument. Two independent computer-based data acquisition systems monitor a total of forty-five parameters, including twenty-two

separate temperatures. Fourteen analog outputs, driven by proportional-derivative feedback algorithms, control various critical parameters.

Figure 1 shows a simplified block diagram of the system.

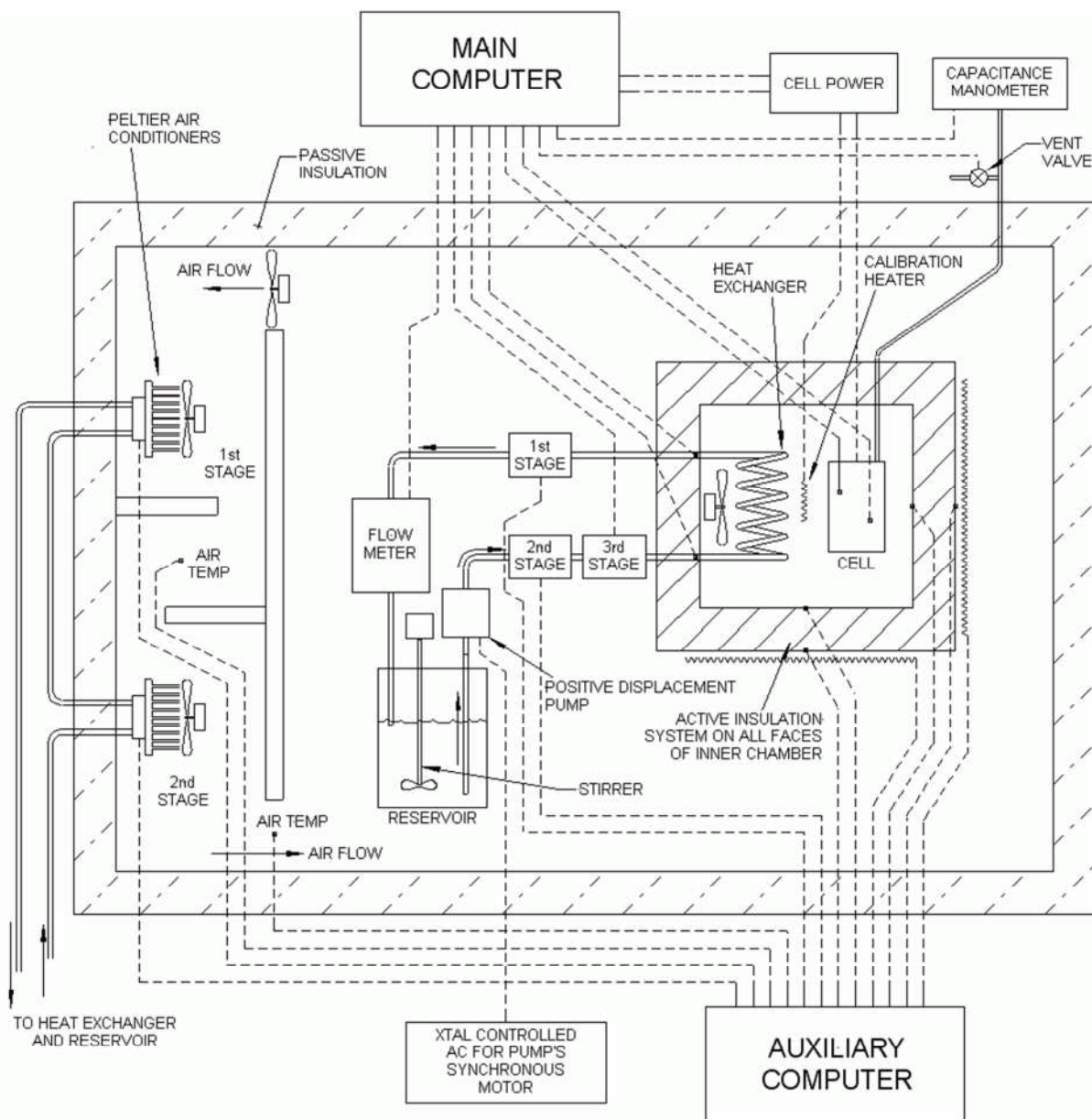


Figure 1. Block Diagram of MOAC

The cell is placed in the calorimetry chamber (CC) with a liquid-air heat exchanger and a small fan. The CC walls are active insulation (AI) panels made almost perfectly insulating by a system that heats the outer surface of each of the six wall panels so that its temperature matches that of the corresponding inner surface.

A three-stage Peltier temperature regulator controls the temperature of the water entering the heat exchanger. A positive-displacement pump produces a stable flow of about 2.5 gm/s. This flow rate gives MOAC a nominal sensitivity of about 10 W/°C. A flowmeter consisting of an automated batch weighing system measures the flow rate periodically. A large insulated environmental enclosure (EE) houses the entire system. Air circulates over the calorimetry apparatus and then is ducted to a two-stage Peltier air conditioner where its temperature is tightly regulated before it re-enters the enclosure.

Figure 2 is a photograph of the entire system. The CC is the light blue box visible inside the wooden environmental enclosure. Also visible through the door window is the water reservoir and the flowmeter. Under the computer bench is a bank of DC power supplies. Under the bench that supports the EE is the water reservoir and heat exchanger for the Peltier air conditioners.

Figure 3 shows the interior of the CC. On the right is the cell, in this case our standard calibration cell. On the left is the liquid-air heat exchanger and fan. Between the heat exchanger and the cell is the permanent calibration heater. In the foreground at the bottom is a trap that collects any liquid ejected from the cell.



Figure 2. Overall View of MOAC

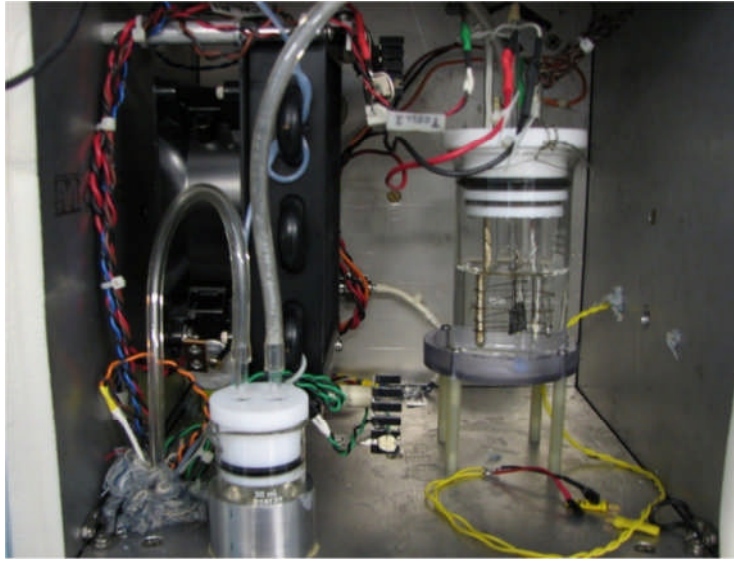


Figure 3. Calorimetry Chamber

3.1. CC Input Power

Input power is determined by the input voltages and currents of the devices within the CC:

$$P_{in} = V_{in} \cdot I_{in} \quad (1)$$

where V_{in} is the voltage at the boundary of the CC, and I_{in} is the current through the device. In the case of multiple devices, the total power is the sum of the individual device dissipations.

3.2. CC Output Power

The rise in water temperature across the heat exchanger and the mass flow of the water are used to determine the power dissipated in the CC:

$$P_{flow} = \Delta T \cdot \Gamma \cdot c \quad (2)$$

where: $\Delta T = T_{out} - T_{in} + \text{Sensor Offset}$; Γ = the mean flow rate in gm/s; and $c = 4.1796 \text{ J/gm} \cdot ^\circ\text{C}$ at 25°C . The values T_{out} and T_{in} are the averages of the temperatures indicated by the individual sensors in each dual-thermistor sensor assembly at the boundaries of the CC.

For calibration, accurately known electrical power levels are applied to any or all of several devices inside the CC: the permanent calibration heater in the air (R1); a standard control electrolysis cell (E); and a second calibration heater immersed in the electrolyte (R2). These three heat sources are operated singly and in combination at different power levels for extended periods to acquire the calibration data. The readings are used in a statistical regression analysis to obtain the coefficients **a** (intercept: watts) and **b** (slope: dimensionless) which are then used in the calorimeter power equation:

$$P_{flow(cal)} = a + b \cdot P_{flow} + \text{wire loss} \quad (3)$$

The term *wire loss* is the measured heat loss due to the thermal conductivity of the copper wires entering the CC through the bottom ports. When 10 W is dissipated in the chamber, the wire loss is typically about 60 mW.

4. Performance

The primary measure of MOAC's performance is its overall measurement accuracy. When recently calibrated, MOAC can achieve the original design goal of $\pm 0.1\%$ relative accuracy.

A typical value for **b** is 1.0005, which reflects the fundamental nature of this approach to calorimetry and also shows that MOAC's thermal design is successful in removing heat from the chamber only via the flowing water.

Another important aspect of performance is specimen versatility. MOAC excels in this area by producing precisely the same reading on a wide variety of heat sources. The size, shape, temperature, and location within the chamber have very little effect on the measurement.

A clear demonstration of this specimen versatility is the observed deviation of three heat sources (R1, R2, and E) about the calibration line; typically ± 5 mW. A study was conducted in which a calibration heater was operated at 15 watts at several different locations within the CC. For all the reasonable locations, the difference between electrical input power and heat output power was 12 mW or less (i.e. within 0.1% relative). When the calibration heater was placed in one of the extreme corners of the chamber, the heat output power read 25 mW lower than the electrical input power (i.e. a 0.2% error).

4.1. Errors

MOAC exhibits both random and systematic errors. The random errors appear to be a combination of electrical noise and digital granularity in the temperature measurements. This conclusion is supported by the fact that fixed precision resistors located within the environmental enclosure report about the same jitter as the thermistors. Even with 100-reading averages comprising each observation, these errors produce a jitter in the temperature signals of about ± 0.0005 °C. Given MOAC's 10 W/°C sensitivity and the fact that inlet and outlet water temperatures are measured independently, this jitter corresponds to almost ± 10 mW in the heat output power signal. Fortunately, MOAC's thermal time constant is about one hour so it is permissible to apply additional averaging to the signals to reduce this jitter to negligible levels.

The systematic errors are more complex. When MOAC was first commissioned in the summer of 2004, it readily achieved 1% relative accuracy. However, numerous systematic errors prevented it from approaching the design goal of 0.1% accuracy. It took nearly 2 years of intensive testing and evaluation to find and eliminate these errors.

For the first few months of operation we observed mysterious perturbations in the heat output power reading. We finally determined that these perturbations were due to the sudden expulsion of an air bubble in the liquid-air heat exchanger in the CC. We solved this problem by installing three air traps at strategic locations in the calorimetry water loop.

Another problem that caused noticeable short-term drift was instability in the water flow rate. We initially constructed MOAC with a pump system from FMI that was advertised to provide a highly stable flow rate. Once we identified pump speed variations as the problem we abandoned the FMI controller and tried a custom closed-loop speed control that employed a digital tachometer. That worked better but the brushes in the DC pump motor caused undesirable speed perturbations. After trying another type of DC motor with similar results we abandoned DC motors altogether and installed a synchronous AC motor powered by the 120VAC 60Hz mains. Small line frequency variations were clearly visible in the measured flow rate. Finally we conquered the flow rate stability problem by constructing a crystal-based 60Hz power supply for the synchronous motor. The result is a flow rate whose stability is typically $\pm 0.02\%$ relative.

For the first 6 months of operation, MOAC required a **b** calibration coefficient of approximately 1.01. In other words, we were losing 1% of the heat from the chamber. We tracked this loss down to the power and signal wires passing through the walls of the chamber. Our wire bundles were not adequately thermally clamped at each wall so ambient air temperatures were having an unexpected influence. We solved this problem by instrumenting the wire bundles with temperature probes located at each wall of the CC. The measured temperature difference from these probes is used to calculate the wire loss term used in equation 3. After this correction was implemented, the **b** coefficient typically comes out between 0.999 and 1.001; in other words, within 0.1% of unity.

At the time of this writing, MOAC is quite reliable and readily achieves 0.1% accuracy when recently calibrated. The largest remaining source of error is the drift exhibited by the thermistors used for the critical inlet and outlet water temperature measurements. The observed drift is usually quite slow and is only a fraction of the manufacturer's specification. That is, the thermistors are performing significantly better than the manufacturer's guarantee but we can still see their drift. Because of this drift, MOAC requires recalibration, usually only a change in the **a** term, once every month or two.

A longer version of this paper, including construction details and interesting calorimetric results, is located at http://www.earthtech.org/experiments/ICCF14_MOAC.pdf

References

1. McCullough & Scott, "Experimental Thermodynamics, Calorimetry of non-reacting systems", D.W. Butterworth, London, p. 9, Vol. 1, 1968

Constant Heat Flow Calorimeter

T. V. Lautzenhiser, D. W. Phelps and M. Eisner
Science Associates

Abstract

A constant heat flow calorimeter is described and its application to a Fleischmann-Pons experiment is detailed. In this calorimeter the electrolytic cell is contained in an isothermal chamber into which electrical power is fed from two separate sources. One source feeds biasing power P_{aux} to an auxiliary resistive element located in the chamber while the other source provides, P_e , the electrochemical power requirements for the cell. The cell temperature T_1 is maintained at its set point by varying P_{aux} as needed. Clearly power needs to be removed from the cell if a steady state is to be maintained and this is accomplished by inducing heat flow through a thermal link to a reference body whose temperature T_2 is less than T_1 . The heat flow is a function of the thermal gradient, which needs to be closely controlled, which in turn requires active control of T_2 . This is accomplished by coupling the reference body to an external heat reservoir through a Peltier element. Power to the Peltier element is varied to maintain the temperature of the reference body at T_2 . Heat stored in the cell requires an increase in P_{aux} to the cell while heat generated in the cell results in a decrease in P_{aux} , to the cell. The details of the operation of the system over a period of 53 days is presented along with evidence for heat production.

1. Introduction

The Constant Flow Calorimeter discussed is an outgrowth of an experiment requiring precise temperature control. It entails essentially a classic double oven approach where because of the layered temperature control around the experimental volume several potential error sources such as radiation leaks, conductive heat losses, etc to first order are constant as long as the two thermal shells are held constant at their individually controlled temperatures. This allows relatively precise measurement of the heat generated within the experimental volume by knowing that the sum of the energy within the volume from both a resistive heater and the experiment is a constant as determined by the calibration. The use of this calorimeter is illustrated using data from one of our early experiments into Pons - Fleishman cold fusion. Incidentally, this experiment was one of the few that did show excess heat and also a supporting creation of tritium. Ironically, we were not able to reproduce this phenomenon and we have no firm ideas as to what change in chemicals, palladium, or preparation (cleaning, etc) was fatal to the process. However, the calorimeter also showed quite clearly that we did not produce any excess heat in further experiments.

2. Calorimeter Design

The design premise is to create measuring and feedback systems that will establish and maintain a temperature gradient which sustains a constant heat flux from a calorimetric cell chamber (Fig. 1).

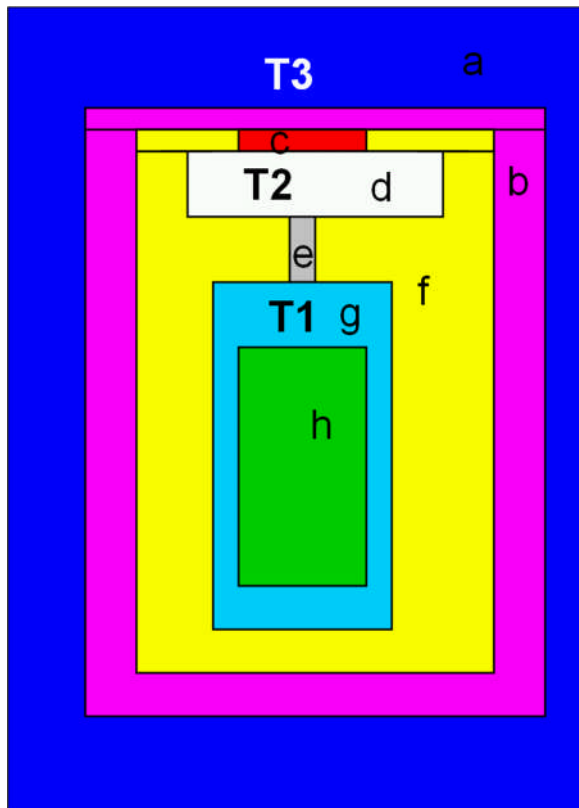


Figure 1. Schematic of Constant Heat Flow Calorimeter. a. Water bath b. Dewar Flask c. Peltier Element d. Aluminum Plate e. Heat Leak f. Insulation g. Experimental Enclosure h. Experimental Volume. Power to T1 and T2 are measured by HP-2804A Quartz thermometers (Accuracy Limit: $\pm 0.0001^{\circ}\text{C}$). T3 is controlled by the circulating water bath system (Accuracy Limit: $\pm 0.01^{\circ}\text{C}$).

The calorimeter cell temperature T1 is maintained constant at a preset value by varying the power delivered to an auxiliary electrical heater located in the experimental chamber. A thin-walled stainless steel channel serves as a heat leak connected to a heat sink formed by the aluminum plate at temperature T2. To insure the constancy of the heat flux, temperature T2 of the aluminum plate is precisely controlled at a constant preset value by a Peltier cell which in turn discharges heat to a thermal reservoir at temperature T3. The entire apparatus is enclosed by the circulating water bath which is maintained at temperature T3 through its own control system.

Calibration

The system was assembled with the electrochemical cell in the calorimeter and the heat leak was calibrated. Setting operating temperatures of 30°C for T1, 20°C for T2 and 28°C for T3

and with the electrolysis current set to zero, the auxiliary power required to maintain the system at the fixed points was found to be 2.486 W.

The stability of the heat leak calibration over a period of 24 hours is shown in Fig. 2.

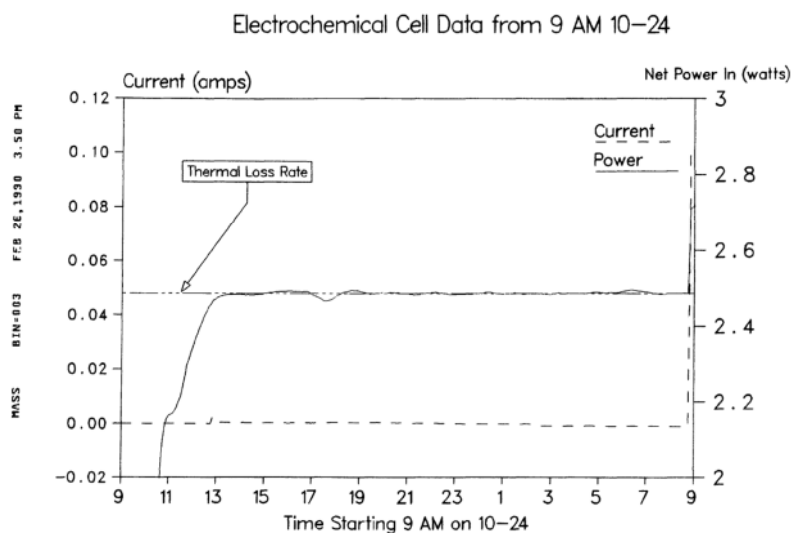


Figure 2. Initial Calibration Data

3. RESULTS

The system was operated for a period of 56 days with varying electrolytic cell currents. Over this period of time a constant flow of 2.486 W exited the cell through the heat leak while electrical power provided by the auxiliary source and the electrolytic cell flowed into the cell. Integrating the total input power over time gives the energy delivered to the cell over this period of time. Similarly the integrated power outflow, through the heat leak, is the energy leaving the cell over the same period of time. If more energy enters the cell than leaves it, the cell is storing energy essentially getting charged like a battery; however if the reverse is true, the cell is generating energy by some internal process.

Figure 3 is a plot of the time history of energy over the 56 days' operation of the cell along with the operating cell current. Positive energy indicates cell storage of energy while negative energies indicate a release of energy from the cell. As seen in Fig. 3, the cell stored 20 kJ during the first 29 days of operation. At Day 29 the cell current was reduced to 40 mA from 400 mA and a period of energy release followed. Initially, a rapid release of 5 kJ was followed by a more moderate release rate over the next eight days. An increased rate is seen for almost all the remainder of the experiment even after the cell current was reduced to zero. The experiment was terminated after the energy release ended. Although the system initially stored 20 kJ, it generated 50 kJ of new energy.

Electrochemical Cell Data

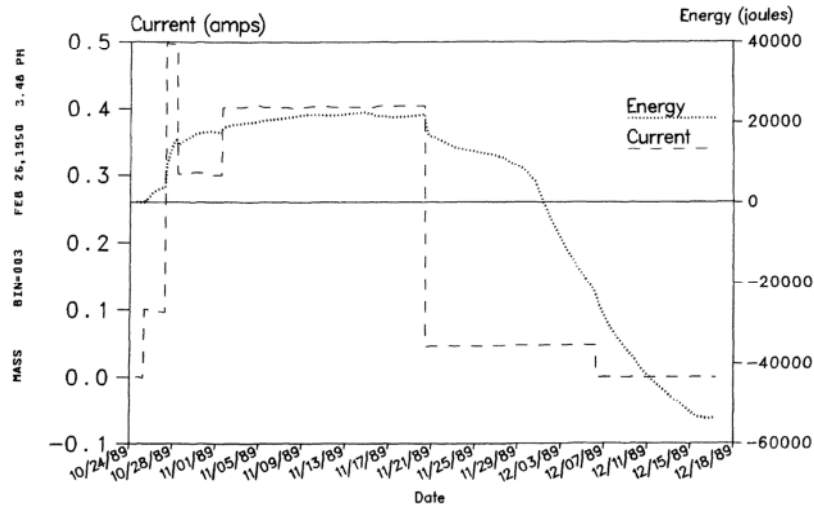


Figure 3. Energy Production and Cell Current for Entire Experiment 10/24/89 to 12/18/89 (56 days)

Figure 5 displays a time history in which energy and power input plotted as a function of time. Although the energy plot is relatively smooth, the power plot shows both transients associated with changes in cell current as well as fluctuations associated with processes inherent in the electrolysis process.

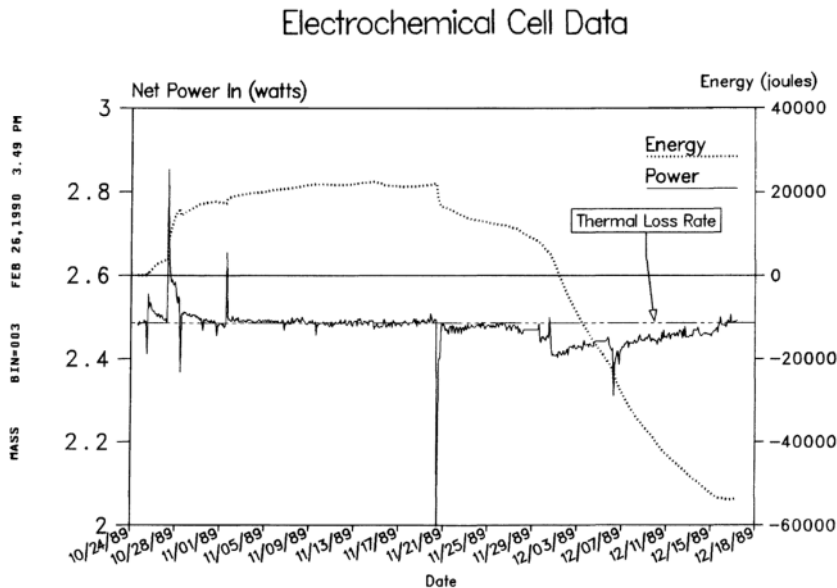


Figure 4. Energy and Power for Entire Experiment 10/24/89 to 12/18/89

4. Discussion

The plot of the system energy E shown in Figure 5 reveals the existence of three phases in the experiment. Initially, there is a storage phase in which deuterons are being absorbed into the palladium lattice. The rate of storage depends initially on the magnitude of the electrolysis current, however, after about 20 kJ have been stored, the system enters the second phase in which the electric power fed into the system is essentially balanced by the power flowing through the heat leak with no further increase seen in the stored energy. The third phase is initiated by the reduction of electrolysis current from 400 mA to 40 mA on 11-21. This stimulates the release of energy from the cell. Data for the cell behavior on 11-21 is given in Fig. 6, showing the current and power for 11-21 time period. The oscillations at a period of the order of one hour are associated with the functioning of the control circuit maintaining the temperature T_1 . There is about an eight hour period in which about 3 MJ of energy are released.

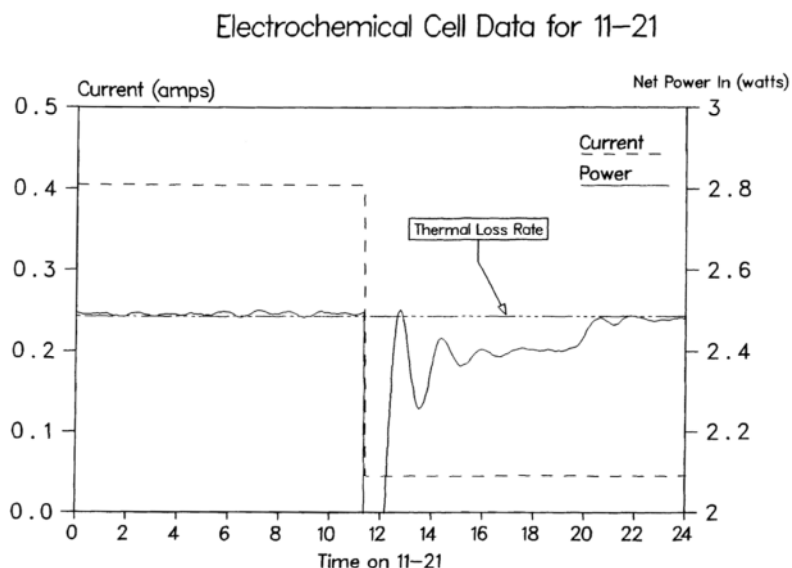


Figure 5. Electrochemical Cell Data for 11-21

Following this steep reduction energy, there follows a period of a more moderate release – about 7 kJ over a two-week period. A further increase in the rate of energy release occurs spontaneously around 12-04, although as seen in Fig. 6, there is a modest decrease in energy release following the transient which appears in the cell power plot.

Electrochemical Cell Data for 12-04

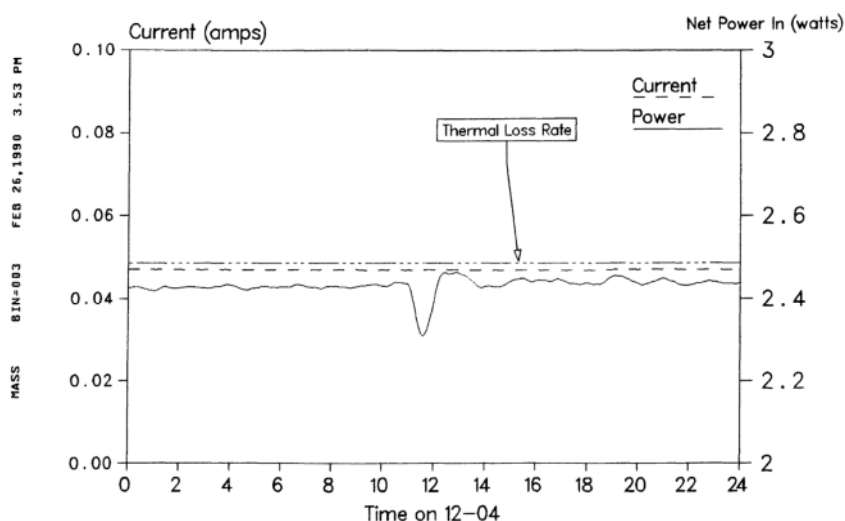


Figure 6. Electrochemical Cell Data for 12-04

The cell continued to release energy even after the cell current was set to zero on 12-07. Although the rate decreased slowly, it finally leveled off on 12-15, after releasing a total of 50 kJ. Figure 7 shows the system data for 12-17. The power supplied to the auxiliary heater is balanced by the power exiting the system through the heat leak.

We note that the fluctuations of the power in Fig. 4 appear to increase after the electrolysis current has been cut off, indicative of the existence of continuing sporadic events in the cathode. The process which started around 12-01 produced an initial sharp burst of power followed by a linear rate of decay for the next two weeks. The transient related to the current shut off seems to have only a small effect on the decay rate. This observed behavior seems to be consistent with a model in which the energy production process is being controlled by a diminishing fuel supply.

Electrochemical Cell Data from 10 AM 12-17

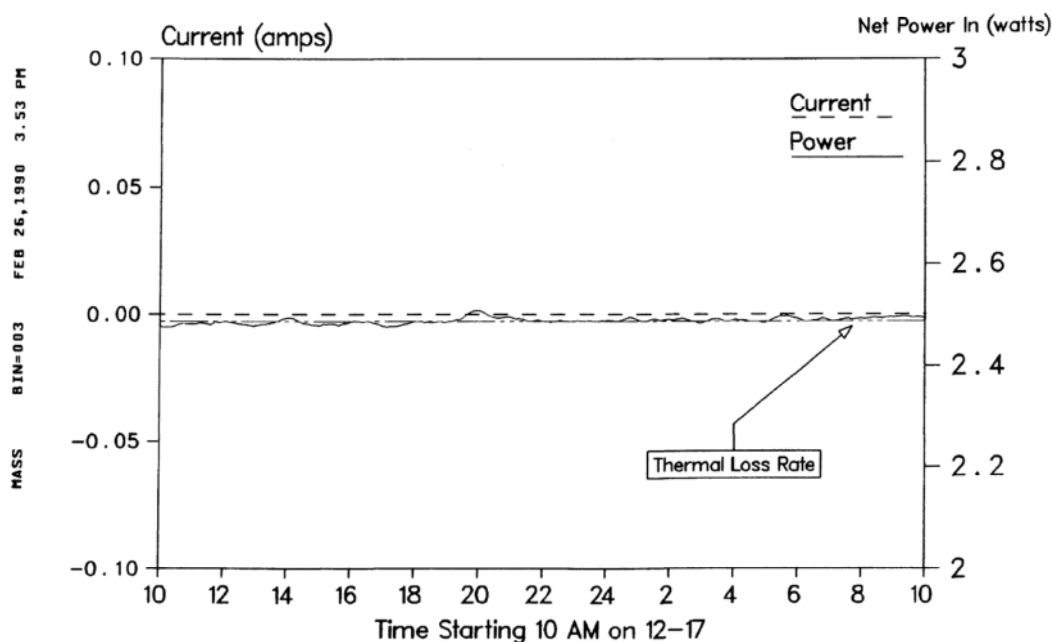


Figure 7. Final Calibration Curve

5. Conclusions

The system performed well within the design parameters. Although the system was operated at input powers of a few watts it would be relatively simple to modify the system to operate with a tenfold increase in power.

The operating temperatures used here can be changed, permitting the cell operating temperature to be varied while maintaining the same temperature gradient. Although the input power to the cell over the life of the experiment results in a large transfer of energy to the cell compared with the 50kJ of heat, the accuracy with which this power was measured is the basis for concluding that the heat effect is real.

Over the 56 day lifetime of the experiment (about 4 million seconds), the heat leak carried away a total of 10 MJ +/- 100 J. It is apparent the 50 kJ measured release is well within the limits of the performance of the system. The key point in support of this analysis rests on the accuracy and stability of the heat leak.

Finally, the tritium level in the electrolyte, initially at 2.5 +/- 1.0 picocuries/ml, increased after the experiment to 7.4 +/- 1.1 picocuries/ml. Although this level of tritium is insufficient to account for the 50 kJ of energy production observed, the apparent production of tritium increases the perception that the heat may be of nuclear origin.

A Simple Calorimetric Method to Avoid Artifacts in a Controversial Field: The Ice Calorimeter

Jacques Dufour, Xavier Dufour, Denis Murat and Jacques Foos
CNAM - Laboratoire des sciences nucléaires - CC304A - 75141 Paris Cedex 03

Introduction

The idea of the ice calorimeter is rather old. Antoine Lavoisier (1743-1794) developed in 1783 a calorimetric method based on the measurement of the mass of the ice that melts when heated. Robert Bunsen (1811-1899) improved this method in 1870 and designed a calorimeter based on the measurement of the volume rather than the mass of ice melted. Nowadays this method is still used [1] because it is simple, accurate, sensitive and most of all rather insensitive to interference, which is a key point in order to have convincing experiment in a controversial field. Moreover, an ice calorimeter is adiabatic and isotherm (0°C) thus suppressing the problem of heat transfer in wires and tubing connecting the experiment to the outside of the calorimeter. It is an integrating calorimeter that measures enthalpy.

Principle of the measurement

At 0°C, 1 gram of ice occupies 1.0908 cm³, 1 gram of water 1.0001 cm³. Thus, when 1 gram of ice melts, its volume shrinks by $\Delta V = 0.0907 \text{ cm}^3$. The measured reduction in volume of a mixture of melting ice and water thus indicates the number of grams of ice which have melted, and thus the amount of energy deposited in the calorimeter. To measure the volume of melted ice, an automatic sensing unit has been designed that weights a reserve of the indicator liquid, mercury (see below, description of the calorimeter).

$$(d_{\text{Hg}})_{0^\circ\text{C}} = 13.595 \text{ g/cm}^3$$

being the mercury density at 0°C

$$\Delta H_w = 6.01 \text{ kJ} \cdot \text{mol}^{-1} = 333.7 \text{ J} \cdot \text{g}^{-1}$$

being the latent enthalpy of fusion of ice

The total energy deposited in the calorimeter is:

$$H = \left(\Delta H_w \cdot \frac{m}{(d_{\text{Hg}})_{0^\circ\text{C}} \cdot \Delta V} \right) \cdot \chi$$

where m is the weight of mercury which is transferred from the reserve tank during the experiment and χ a correction factor due to the buoyant force on the capillary tube (see Figure 1). χ was measured to be 0.998.

Thus for $m = 1$ gram, the constant of the calorimeter is $H_0 = 270.085 \text{ J} / g_{\text{Hg}}$

Description of the calorimeter

A cylindrical insulated container, 40 cm diameter and 75 cm high, is filled with a mixture of ice and water (melting ice). The ice is generated through an ice machine from very pure water (distilled and then passed through resins) so that the temperature of the melting ice is very close to 0°C.

The calorimeter itself is placed inside the container and is completely surrounded by the melting ice. All tubes and electrical wires connecting the reactor inside the calorimeter are immersed in the melting ice (for a length of about 1 m), thus avoiding exchanges of heat with the outside. The calorimeter is made from Pyrex (or alternatively stainless steel). Its total volume is some 3000 cm³, which is filled with ultra pure water. Figure 2 shows a detailed description of the calorimeter: the well inside the calorimeter (36 mm diameter, 340 mm high) contains the experiment where energy is released. It is filled with a mixture of water and ethanol. This well is surrounded by an ice layer, formed prior to the experiment by inserting a tube in the well, where water mixed with ethanol flows at a temperature of around -15°C. At the bottom of the calorimeter, a 5 kg reserve of pure mercury is placed. The mercury is hydraulically connected to an Erlenmeyer through a Pyrex (or alternatively stainless steel) capillary tube. The Erlenmeyer is placed on a scale where its weight can be recorded. The mercury in the Erlenmeyer is covered by a layer of water for safety reasons. No mercury can thus be detected on top of the water layer, and it has been shown that the rate of evaporation of this water is sufficiently low not to have any influence on the measurements. In first approximation, the whole measuring system is thus isotherm and adiabatic. Checking the constancy of the temperatures of the melting ice during an experiment is of prime importance. This is done by four temperature sensors (Pt 100) one in the middle of the container, a second one at the bottom of the container, a third one at 5 cm of the bottom and the last one at 10 cm. These sensors were not calibrated (what is important is that their indication remains constant during an experiment). An increase of the bottom temperature indicates the formation of a water layer transferring heat from the outside to the calorimeter. The measurements are then no longer valid. The calorimeter is placed in a temperature regulated room and the outer container is surrounded by a temperature regulated water jacket.

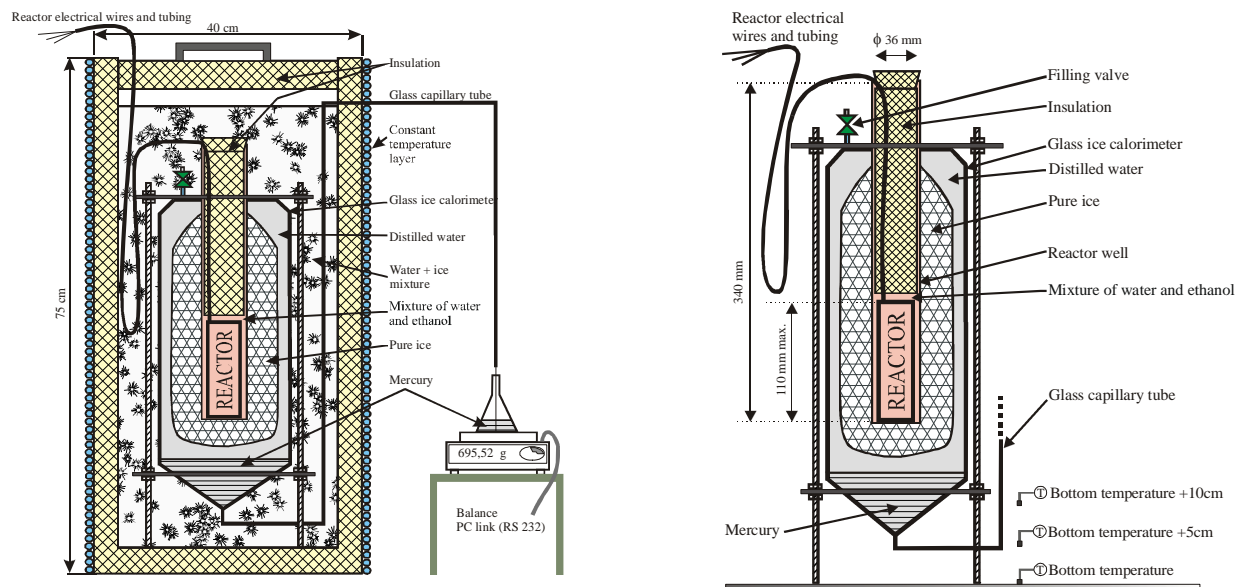


Figure 1. The calorimeter setup.

The detailed conditioning procedure of the calorimeter is not given here. An important step is the complete degassing of the ultra pure water filling the calorimeter.

Description of an experiment

The cylindrical container is first replenished with fresh ice and water. The reactor is placed in the well, after the ice layer has been formed and the calorimeter is left until the weight of the mercury reaches the base line (nearly horizontal straight line). The baseline value “before the experiment” is recorded for 3000 seconds. The reaction to be studied is then initiated: heating, electrolysis, electrical discharge or hydrogen admission.

Figure 2 shows a typical example of mass as a function of time. Due to the energy released, part of the ice layer melts and the mercury reenters the calorimeter, thus showing a decrease of the recorded weight. The experiment phase is recorded for 6000 seconds (for a typical energy input of 8000 J), after which the calorimeter reaches the "after experiment" baseline, which is then recorded for 3000 seconds. The total mass m of the mercury transferred is then measured (as shown in Fig. 2) and the energy released calculated from the calibration curve of the calorimeter (see below). The mass of the mercury is recorded every 30 seconds during the 2 base lines. This mass, together with the electrical energy injected (intensity and voltage) and H_2 / D_2 flow rate (for gas admission) are recorded every second during the experiment phase.

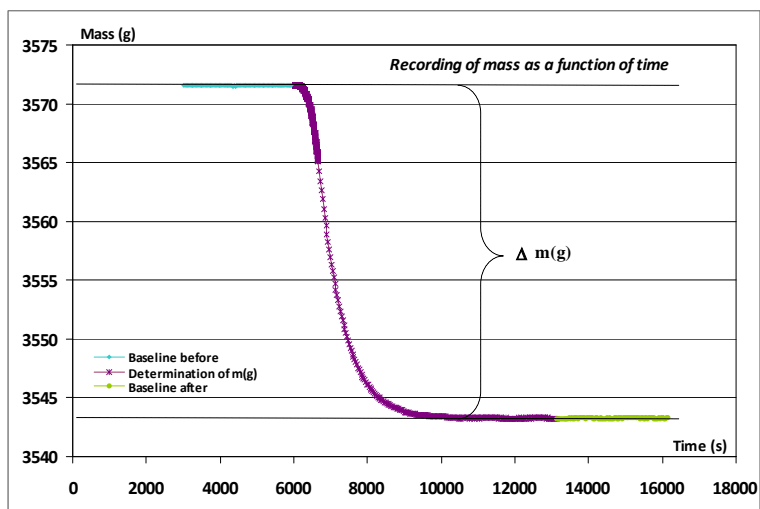


Figure 2. Typical example of mass as a function of time.

Calibration of the calorimeter

The calorimeter has been calibrated using resistors heated by direct current (DC), placed in various positions in the well and in reactors fitting the well. The results of these calibrations are shown on the following graph 2, where the amount of energy entering the calorimeter as electrical energy is plotted against the weight of mercury transferred. 32 measurements were performed, for P_{in} varying from 350 to 10000 J.

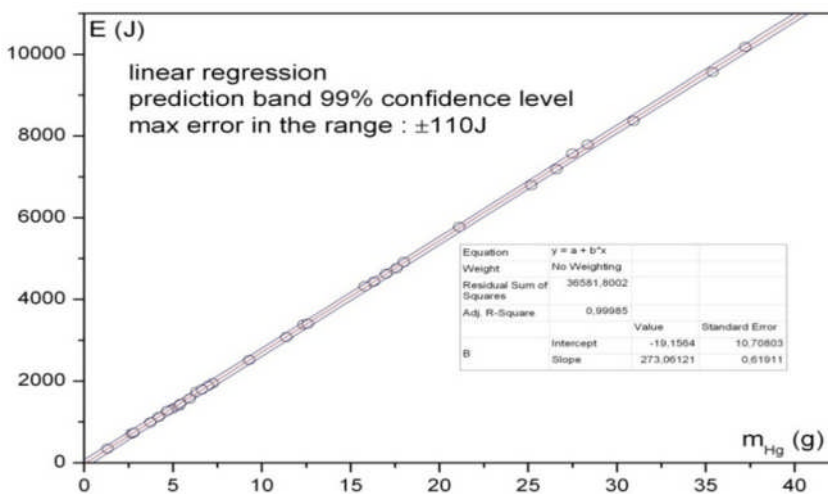


Figure 3. Calibration with direct current resistors.

The linear regression prediction band at 99% confidence level has been calculated (Fig. 3) and shows that, at this level of confidence, the maximum error is in the range ± 110 J.

In this regression, the constant of the calorimeter has been calculated to be 273.06 J/g_{Hg}, in good agreement with the value of 270.085 J/g_{Hg} calculated from published values of the thermodynamic properties of pure water and mercury.

Based on the fact that the direct current electrical energy input, is measured with a precision of 0.5%, it can be seen that at the level of 10000 J, the precision of the calorimeter is $\pm 1.5\%$.

The duration of an experiment is limited by the melting of the ice in the cylindrical container that surrounds the calorimeter. As a result of this melting, a layer of pure water forms at the bottom of the cylindrical container and the temperature of this layer starts increasing (the maximum density of water occurs at 4°C). For an experiment to be valid, this layer must not reach the level of the mercury capillary. The upper limit of the energy that can thus be measured is 15000 J.

An example of application of the ice calorimeter: unexplained heat effects during palladium gas loading with hydrogen isotopes

Scope of the experiment

It has been reported [2] and [3], that unexplained heat effects occur when gas loading palladium with hydrogen isotopes. The palladium used is in a very dispersed form and deposited either on carbon black [2] or on Zr oxide [3]. These effects are characterized by the evolution of the temperature taken at one representative point of the palladium under loading. A comparison is made of this evolution for both isotopes. In [3], the effect shows up, only in the case of deuterium, as a long delay for the representative temperature to go back to base line. The ice calorimeter has shown this effect with such a sensitivity, that only 1 g of unsupported palladium black, activated at 450°C for 4 h under 3 Pa, gave a response.

Description of the experimental set-up

A schematic of the experiment is shown in Figure 4. A cylindrical reactor, fitting the well of the calorimeter is connected through flexible tubing, to a manifold. This manifold connects a bottle of hydrogen (deuterium) to a vacuum pump. A metering valve allows controlled injection of the isotope of hydrogen from the bottle. A flow-meter (Brooks 5860 E) measures the flow of hydrogen entering the reactor and a Pt 100 the temperature of the reactor. The pressures in the manifold (and the reactor) are measured. A heater (regulated up to 500°C) is placed close to the calorimeter.

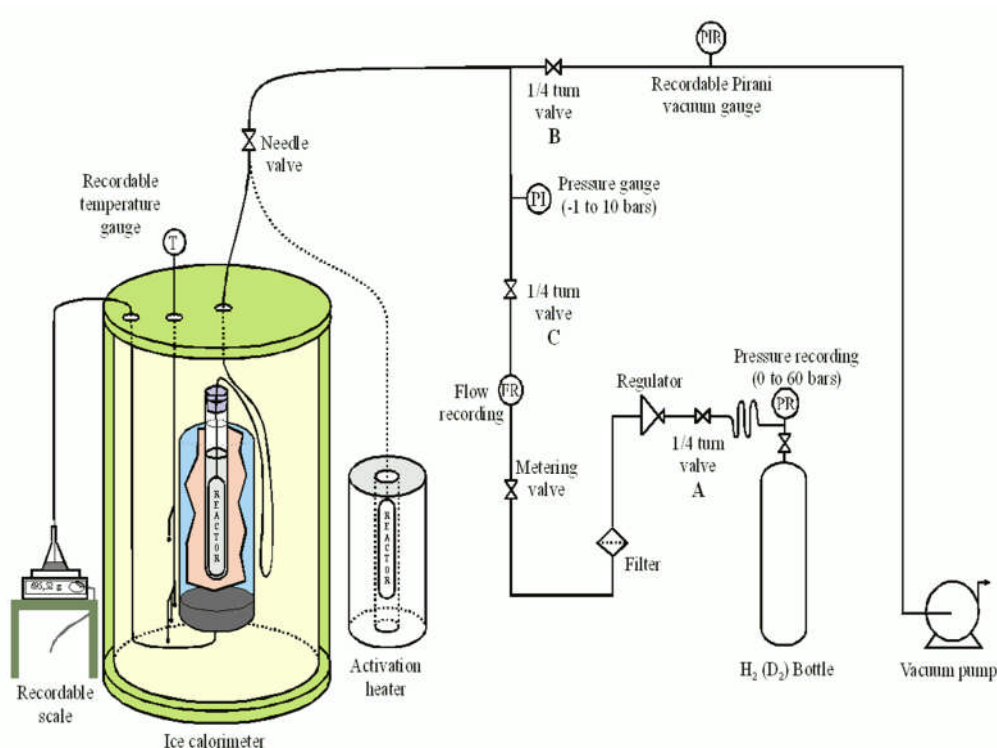


Figure 4. Schematic of experiment.

Description of an experiment

1 g of palladium black (Alpha Aesar 00659 Lot 0109400, purity 99,9%) is placed in a Pyrex tube in the reactor. The reactor is closed and placed in the heater where the palladium black is activated (450°C , 3 Pa for 4 hours). After cooling, the reactor is placed in the calorimeter without opening it. It is maintained under vacuum. After the base line registration, hydrogen (deuterium) is admitted in the reactor. The calorimeter then reaches the "after experiment" base line and the mass m is measured.

Results of the experiments

The main result is illustrated in Fig. 5. It can be seen that, for deuterium, the mass m of mercury reabsorbed by the calorimeter does not stabilize and goes on decreasing well after the usual base line should have been reached, although the temperatures of the melting ice in the container (bottom, bottom + 5 cm and bottom + 10 cm) have remained perfectly stable. This unexplained decrease is observed well after the end of the deuterium loading and corresponds to an extra power of some 2 mW (which could be heat after death [4]).

This result is not observed when hydrogen is used instead of deuterium.

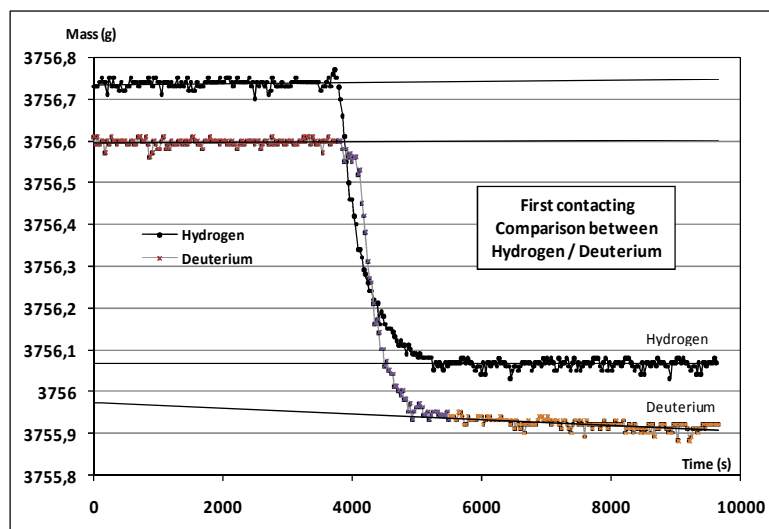


Figure 5. Main result of the experiment.

Conclusion

Ice calorimetry is a first principle method. It measures enthalpy with high absolute precision and sensitivity. This calorimeter is specially adapted to gas loading experiments.

References

1. Ditmars, D.A., *Measurement of the average total decay power of two plutonium sources in a Bunsen ice calorimeter*. International Journal of applied radiation and isotopes, 1976. **27**: p. 469-490
2. M. McKubre *Review of experimental measurements involving dd reactions: Case cells study*. Short course on LENR for ICCF-10 August 23, 2003
3. Y. Arata and Yue-Chang Zhang *Development of "DS Reactor" as a practical reactor of "Cold Fusion" based on the "DS –Cell" with "DS-Cathode*. ICCF12. Yokohama-Japan Nov. 27 - Dec. 2, 2005
4. S. Pons M. Fleischmann *Heat after death*, Proceedings ICCF4 1993 EPRI, Vol. 2 p. 81

Introduction to Heat Measurements

The reported production of heat in an electrochemical cell of apparently non-chemical origin was a main feature of the first report by Fleischmann and Pons in 1989. Experiments to measure energy production have been a mainstay of the field since then. The last section described five different calorimeters for measuring heat with adequate sensitivity and good signal-to-noise ratios. Each type has been used in LENR experiments and measured heat from the Fleischmann-Pons Effect. This section deals with the results of such measurements, which were reported at ICCF-14. First, we provide a brief overview of the character and importance of heat measurements. Then, we preview the results provided in the papers of this section.

Most low energy nuclear reaction experiments aimed at heat measurements are done by measuring both the power input to the electrochemical cell and the power from the cell as a function of time. If the output power exceeds the input power, then the cell is said to produce “excess” or “anomalous” power. The integral of this excess power over the duration of the experiment gives the “excess energy” from the cell during its operation. There has been some confusion associated with the term “excess heat,” which is simply the difference between the output and input energies, and is often termed “anomalous” heat. Unknown chemical reactions can produce “excess heat”. It can be very challenging experimentally to establish that the heat is not from chemistry. In many FPE (LENR) heat experiments, the amount of excess heat seen, when normalized to the number of atoms in the sample, the volume of the sample or the mass of the sample in various units, is so large that known chemistry is excluded. Thus, excess heat in these experiments begs to be explained because of its anomalously large value.

The net (excess) absolute powers and energies from LENR cells have been modest in comparison to values routinely encountered in daily life. Incandescent light bulbs generally consume a few tens to a few hundreds of watts of power. Most LENR experiments have produced powers in or below this range of values. Those measurements did have good calibrations and signal-to-noise ratios, so there should be little concern about the reality of these relatively small values. Nevertheless, the measured powers to date are modest. The duration of the periods of power production are also not practical when contemplated for routine applications. They range from a few hours to a few weeks, with some few exceptions. And, the reproducibility and controllability of the power production is sorely wanting in almost all experiments. In short, the power production capabilities of LENR sources are now far from practical. Absent the most rudimentary quantitative theoretical understanding, it is not clear when power production at significant values, with adequate reproducibility and control will be available. Having a theory is, of course, not necessary, but engineering without good models becomes Edisonian in the development of systems with the attendant high cost in effort and time.

It is conceivable that useful energies could be produced even from small power sources. This is done increasingly in electronic systems, which “scavenge” energy from their environments and charge batteries for their occasional operational periods. Light, vibrational and even radio-frequency energy sources are employed commercially for ambient energy harvesting. The total excess energies from LENR experiments are also relatively small. There are some experiments

that have produced excess heat energies exceeding mega Joules. While this sounds like a lot of energy, it is only enough to power a 100 watt light for about three hours. (Note a lead acid battery weighing about 15 kg would store this amount of energy.) It is likely that uses will be found for LENR sources with the current modest powers and energies. But, there is a significant need to scale up both the power and energy levels from LENR systems before they will be commercially significant, that is, sufficient for many applications.

These considerations might deflate hopes that LENR energy sources will ever prove to be widely useful. However, achievement of reproducibility and control, even without understanding, might lead to useful scaling up of the outputs. Once understanding is achieved, it is very possible that both scaling and optimization of LENR power and energy sources will follow. The histories of some technologies offer examples of dramatic scaling. The increase in the number of cars during the past century is one of them. In the past half century, the number of transistors on a single chip has grown from a few hundred to a half billion. In the past ten years, the number of phones in the world has also skyrocketed because of mobile phone technologies. There are 6.8 billion people living now and almost 5 billion mobile phones. Hence, it is reasonable to expect that LENR sources of power and energy will grow significantly in capabilities and, with that growth, increase in the numbers of applications.

Besides the chronic need for energy, especially in the face of rapid population growth, there are some reasons that compel interest in relatively small sources of nuclear energy. They include:

- Such small nuclear energy sources might be mobile, even to the point of powering personal electronic devices.
- Stationary, but still small LENR sources could be geographically distributed and, hence, relieve stress on power grids. They might power homes, for example.
- Experiments to date have shown that LENR energy sources do not produce dangerous radiation during operation, in stark contrast to current fission and hypothetical hot fusion sources, which require very heavy shielding.
- It is also known experimentally, that the operation of LENR sources does not produce significant radioactive waste materials, again in contrast to fission and hot fusion sources.
- LENR sources do not emit greenhouse gases during operation. Their production and the management of waste from defunct LENR sources could also be done in a “green” fashion.

There is a major question concerning the characteristics of the heat, which might be obtained from commercial LENR sources. If the temperatures put out by such sources are modest, notably below the boiling point of water, there will still be significant applications. Home water heaters provide one example. However, if temperatures of hundreds of degrees C are available, then efficient production of electricity becomes possible using currently available technologies.

In addition to these possibilities, there are emerging technologies for the direct production of electricity from thermal sources. The best known of these are devices based on thermoelectric materials. When these devices have a thermal gradient across their sides, they produce a

voltage (power). The reverse is also true, that is, application of a voltage causes the devices to be heat pumps. There is a tremendous interest in making efficient thermoelectric devices because of refrigeration. Such devices could enable solid-state refrigeration, that is, cooling systems for homes and other places without compressors and working fluids. Such systems, which would not have moving parts, should require less maintenance and last longer than the present systems with their moving parts.

There is a newer technology for direct conversion of heat to electricity. It is called micro-gap thermo photovoltaics (MTPV). This technology is a relatively recent development and a long way from practical commercialization. The efficiency of both thermoelectric and MTPV technologies improves with operating temperatures and gradients. It could turn out that both commercial LENR sources, and either thermoelectric or MTPV materials, will be developed in the same time frames, and then mated for production of electricity from LENR power.

The papers on heat production presented at the conference and given on the following pages are research studies. They are not yet technology developments or engineering designs. However, these papers have three key features. First, they add to the considerable experimental database for the production of net power and energy by LENR. Second, results from these papers help point to the possibilities for practical LENR heat sources. So, finally, the range of potential applications for LENR sources becomes somewhat clearer.

The first paper by Cravens and Letts was commissioned to provide an overview of papers reporting excess heat results. They provide four “enabling criteria” for generation of excess energy. These are based on earlier experiments, and they appear to be necessary but not sufficient conditions for energy production by LENR.

The paper from Energetics Technologies reports some remarkable results. Their electrolytic experiments included both “SuperWaves” to drive the electrolysis and the presence of ultrasonic excitation. Excess powers as high as 34 watts were achieved. In the best case, the excess power was about 30 times larger than the input power to the experiment. The longest duration experiment gave excess power for 40 days. The largest excess energy was 3.5 MJ. In one case the ratio of the excess energy to the number of Pd atoms in the system was an incredible 27,000 eV/Pd. Specific excess powers of 70 W/gm Pd were measured. They compare favorable with fission fuel rod specific powers of 20 to 50 W/gm of U. This paper is one of the most important experimental papers in the field.

Swartz has prosecuted one of the most instructive experimental efforts on LENR over the years. One of his key discoveries is the existence of “optimal operating points” (OOP) for electrolytic LENR cells, which are expressed in terms of the output power vs. input power in his systems. In his analytical paper, he links the characteristics of OOPs to three sites within deuterium-loaded Pd where excess heat originates. Data from published experiments, in addition to his own measurements, is analyzed with a quasi-one-dimensional model.

Mizuno and Sawada have a university-industry collaboration, but their experiments are both very different and diverse compared to other papers at ICCF-14. They subjected a heavy oil (phenanthrene) to both high pressure and high temperatures in a reactor with a metal catalyst. Heat generation of 100 W was observed for several hours. Gamma rays were also measured,

and a “reasonably significant” correspondence between heat generation and gamma emission was reported. Mass spectroscopy measurements after runs showed what appears to be ^{13}C .

Karabut and Karabut reported the results of both electrolysis and plasma (glow discharge) loading of Pd with deuterium. In the electrolysis experiments, controls with light water and Cu and Pd cathodes were performed. Both mass flow and heat capacity calorimetry were employed for the electrolytic experiments. Excess heat was observed for both electrolytic and plasma loading. In the case of plasma loading, excess powers in the range of 5-15 W were reported.

The experimental and analytical papers on production of excess power and heat, given at ICCF-14 and in this section, added considerably to the database and knowledge for LENR. Given the several types of loading, the many experimental parameters and the diversity of calorimeters, there remain numerous opportunities for LENR power and heat measurements. Both replication of reported experiments by other experimenters, and the performance of new types of experiments, are needed. More and better chemical analyses of materials both before and after experimental runs are also critically needed.

The Enabling Criteria of Electrochemical Heat: Beyond Reasonable Doubt

Dennis Cravens¹ and Dennis Letts²

¹ *Amridge University Box 1317*

Cloudcroft, NM 88317 USA

² *12015 Ladrido Lane*

Austin, TX 78727 USA

Abstract

One hundred sixty seven papers from 1989 to 2007 concerning the generation of heat from electrochemical cells were collected, listed, and digitally posted to a CD for reference, review and study. A review showed four criteria that were correlated to reports of successful experiments attempting replication of the Fleischmann-Pons effect. All published negative results can be traced to researchers not fulfilling one or more of these conditions. Statistical and Bayesian studies show that observation of the Fleischmann-Pons effect is correlated with the criteria and that production of “excess heat” is a real physical effect “beyond a reasonable doubt.”

Introduction

The field of Condensed Matter Nuclear Science began March 23, 1989 when Fleischmann, Pons and Hawkins reported the generation of electrochemical heat intense enough to be classified as nuclear in origin [1]. Mainstream science embraced the possibility briefly but soon the embrace turned into a strangle hold that has marginalized the field. Funding, patents and acceptance have been denied for 19 years due mainly to early failed experiments, conducted before the most conducive experimental conditions and criteria were widely known. This work is a telling of how those criteria came to be known and how we have become certain beyond reasonable doubt that the Fleischmann-Pons Effect is real.

Enabling criteria

In their seminal paper, *Electrochemically Induced Nuclear Fusion of Deuterium* [1], Fleischmann and Pons reported electrode power densities in excess of 10 watts per cubic centimeter and figures of merit normally associated with nuclear reactors. (See Table 1.)

Table 1. From Ref. 1. The results shown here pushed the limits of credibility but the science community suspended its disbelief, owing mainly to the reputation of Martin Fleischmann.

Generation of excess enthalpy in Pd cathodes as a function of current density and electrode size

Electrode Type	Dimensions /cm	Current density /mA cm ⁻²	Excess rate of heating /W	Excess specific rate of heating /W cm ⁻³
Rods	0.1 × 10	8	0.0075	0.095
		64	0.079	1.01
		512 ^a	0.654 ^a	8.33
	0.2 × 10	8	0.036	0.115
		64	0.493	1.57
		512 ^a	3.02 ^a	9.61
	0.4 × 10	8	0.153	0.122
		64	1.751	1.39
		512 ^a	26.8 ^a	21.4
Sheet	0.2 × 8 × 8	0.8	0.153	0
		1.2	1.751	0.0021
		1.6	26.8	0.0061
Cube	1 × 1 × 1	125	WARNING! IGNITION? See text	
		250		

^a Measured on electrodes of length 1.25 cm and rescaled to 10 cm.

The four enabling criteria found in most successful Fleischmann-Pons experiments were present in their first paper. Their presence is subtle but clear when viewed with the advantage of hindsight. We use the term “criteria” to indicate some condition believed to influence the probability of the desired result of observing excess heat. One should remember that these are used in a statistical sense and that correlation is not causation. That is, they seem to help enable a researcher trying to reproduce the effect. Exact operational definitions were used to evaluate the papers; however their exact forms are too lengthy for this paper. For example, the lowest current density used in any runs within each paper was used when multiple cells were reported. Also, terms like “care in selection” was given an arbitrary operational definition for evaluation of the criteria. In that case, the term depended not on what the material was but that the paper included a statement on its source and or purity. All decisions were reduced to Boolean logical 1 or 0. Here is the abbreviated description of the criteria that entered our statistical analysis.

Criterion 1 is deemed fulfilled when at least one of these conditions is met:

1. Cathode is likely or claimed to be loaded to at least 0.85 D/Pd
2. Cathode loading was slow and current density below 100 mA/cm² ⁽¹⁾
3. Open cell voltage was measured during loading
4. Loading was done at or below 15°C ⁽²⁾
5. Cathode resistance was monitored during loading

(1) As Storms points out, loading at a low current density does not necessarily lead to high loading or excess heat; however the authors have observed that there is a statistical correlation between loading at a low current density and excess heat (~ 55%).

(2) Loading the cathode at a low temperature does not necessarily lead to high loading or excess heat; however, the authors' combined experience in loading approximately 1,000 cathodes suggests that it is helpful in producing the excess heat effect. Other factors such as the nature of the palladium are likely to be more important than loading temperature but are difficult to measure in small laboratories.

Criterion 2 is deemed fulfilled when any of these conditions is met:

1. The source, preparation or purity of cathode is stated.
2. The purity, source or handling of the heavy water is stated.
3. The preparation or formulation of the electrolyte is stated.
4. The chemical procedures used were stated or documented.
5. Additives were used to poison recombination or to seal the cathode against D.

Criterion 3 is deemed fulfilled when at least one of these conditions is met:

1. The cell was operated at current density of at least 200 mA/cm²
2. Special current systems were used (for example, current pulses, hi-low loading)

Criterion 4 is deemed fulfilled when this condition is met:

1. Non-equilibrium conditions are applied to cathode (i.e. heat pulse, current pulse, lasers, magnets, RF, acoustic energy, superwaves)

Criterion 1 was met in their seminal paper because Fleischmann and Pons loaded at a low current density and ran “long duration” experiments (page 304 of their paper [1]). This is now thought to produce a loading ratio sufficient to produce excess power in many cases (D/Pd >0.85). Also they state:” Electrode potentials were measured with respect to a Pd-D reference electrode charged to the α - β -phase equilibrium” which can be use to give a lower bound to their loading ratios.

Criterion 2 was met because Lithium ions were present in the electrolyte and because of their clear statement: “0.1 M LiOD in 99.5% D₂O + 0.5% H₂O solutions.”

Criterion 3 was met because Fleischmann and Pons operated some cells at a current density of 512 mA/cm² which is above the 200 mA/cm² current density threshold.

Criterion 4 was met because Fleischmann and Pons used calibration heaters that were periodically pulsed, providing non-equilibrium thermal conditions. Also the act of rapidly increasing the current density served to produce non-equilibrium conditions.

These four enabling criteria were not widely known in 1989 but their importance cannot be overstated. Every failed experiment in 1989 and 1990 was lacking in one or more of the criteria and it was the early failed experiments that isolated Condensed Matter Nuclear Science (CMNS) from mainstream science.

An early D-Pd replication attempt of the Fleischmann-Pons experiment was made by Armstrong et al published June 23, 1989 [2], exactly 3 months after the original publication of Fleischmann and Pons. The Armstrong experiment failed because it only met Criterion 2. A total of five replication attempts failed before Kainthla published a successful replication of the Fleischmann-Pons Effect. Kainthla's paper was an early replication but likely not the first [170].

Table 2. Positive experiments compared with negative experiments

Experiment	Criterion 1	Criterion 2	Criterion 3	Criterion 4	Excess
F&P	Yes	Yes	Yes	Yes	Pos.
Armstrong	No	Yes	No	No	Neg.
Armstrong	No	Yes	No	No	Neg.
Balej	No	Yes	No	No	Neg.
Blaser	No	Yes	No	Yes	Neg.
Chu	No	Yes	No	No	Neg.
Kainthla	Yes	Yes	Yes	Yes	Pos.

The five failed experiments (Table 2) had several deficiencies in common. The failed experiments did not load at a low enough current density to meet criterion 1. The later failed experiments that actually measured the loading ratio reported D/Pd ratios less than 0.8. Although a few systems have worked at lower ratios, we know that 0.8 is too low to produce the FPE reliably. Four out of five negative experiments in Table 2 failed to increase the current density above the loading current density. In short, the failed experiments used a current density too high for a good load and too low to trigger the FPE.

Summarizing the enabling criteria¹

The four criteria can best be understood and remembered by thinking in terms of four questions:

1. Criterion 1 asks “was there a demonstrable statement that showed concern about the loading ratios of the palladium?”

¹ Please note that the four criteria mentioned in this paper are correlated with excess heat production but correlation is not causation; it is possible that an experimenter can meet all four criteria and still not produce the excess heat effect. Based on many experiments from many diverse researchers, these criteria will increase the probability of a successful experiment but they will not guarantee the success of a single experiment.

2. Criterion 2 asks “was there a demonstrable statement that showed concern about cathode and electrolyte purity and were chemical procedures documented?”
3. Criterion 3 asks “Was the cathode operated at a high enough current to be above some current density threshold (note: some researchers find much higher densities are required to see the effect)
4. Criterion 4 asks “was a trigger applied to provide non-equilibrium conditions at the cathode to change the flux of the deuterium?”

Two failed experiments that mattered

Later in 1989, two failed experiments (Table 3) produced the most important papers in the field of Condensed Matter Nuclear Science; they were important not for what they contributed to the field but for what they took away: funding, patents and access to the mainstream scientific community.

In August 1989 Nathan Lewis’ group from Caltech published a negative paper *Searches for Low-temperature nuclear fusion of deuterium in palladium* [10] in the mainstream science journal, Nature. In November 1989, D.E. Williams’ group at Harwell Laboratory published a negative paper *Upper bounds on cold fusion in electrolytic cells* [15] in Nature. Mainstream science writers and patent agents have referred to these papers for years when seeking to deny scientific legitimacy or patent protection for CMNS researchers. The failed papers have made a lasting impression since Nature refuses to publish more recent experimental results. The editors consider the matter settled: the Fleischmann-Pons Effect is not real.

By the time the Caltech and Harwell experiments were conducted, a few of the required experimental factors were known from the Kainthla and Fleischmann-Pons papers. The lead investigators chose to follow their own protocol resulting in two failed experiments and a negative image for CMNS.

Table 3. The Caltech (Lewis) and Harwell (Williams) papers

Experiment	Criterion 1	Criterion 2	Criterion 3	Criterion 4	Excess
Lewis	No	No	No	No	No
Williams	No	No	No	Yes	No

The Lewis experiment failed in a manner very similar to the earlier 1989 papers: they did not load to a high D/Pd ratio and they didn’t run for extended periods of time – two or three months. The Harwell experiment was a larger effort and did change the current from low to high in some but not all experiments. The Harwell and Caltech experiments tended to load at higher levels and to run for fairly short periods. They also used large area cathodes and small currents. Cravens & Letts work with small cathodes on the order of 0.15 g. The authors recommend loading for 10E7 coulombs per atomic mole atom of Pd. Our cathodes load for 120 hours and run for a minimum of 60 days (1440 hours). Harwell’s longest run was 917 hours on a cathode that weighed 1.4 grams – 10 times the mass of our cathodes – and was tested for about half as long. On page 380 of their paper, the Harwell group reports the D/Pd ratios were in the 0.76 to 0.84 range – too low to produce the FPE reliably. In summary, both experiments failed to achieve high loading.

Teaching Papers

In the early nineties, CMNS researchers began to build on the foundation laid by Fleischmann and Pons; the enabling criteria were learned and taught to others at a rapid rate. From the digital databases, we identified seventeen positive electrochemical heat experiments in 1990, compared to just two in 1989. The enabling criteria identified in this review paper were discovered and quantified by several key researchers and then taught by conference papers and personal communications. Table 4 contains a listing of CMNS researchers who we believe made key contributions to identifying / quantifying the enabling criteria or taught methods to fulfill them.

Table 4. Papers that identified enabling criteria or taught how to fulfill them (bulk loaded Pd-LiOD)

Year	Author	Criteria
1989	Fleischmann & Pons [1]	Criteria 2- 4
1989	Kainthla [8]	Criteria 2-4
1990	Appleby [17]	Criterion 2-4
1990	Guruswamy [26]	Criteria 1-4
1990	Lautzenhiser (Amoco) [28]	Criteria 2-4
1991	McKubre [49]	Criterion 2-4
1992	McKubre [56]	Criterion 1
1992	Takahashi [60]	Criterion 1 Low-high loading
1993	Bockris [62]	Criteria 2, 4
1993	Cravens [63]	Criteria 2-4
1993	Storms [71]	Criterion 3
1996	Celani [90]	Criterion 1 Pulse loading
1996	Miles [96]	Criterion 1 Boron alloy
1996	Storms [100]	Criteria 1-4
1998	Arata & Zhang [107]	Criterion 1 Double cathode
1998	Storms [119]	Criterion 1 OCV method
1999	Storms [121]	Criterion 1 Lattice expansion
2000	Miles [125]	Criterion 4 Current trigger
2001	Miles [131]	Criterion 1 Boron alloy
2003	Dardik [148]	Criteria 1,4 Superwave
2003	Letts & Cravens [149]	Criterion 4 Laser trigger
2004	Apicella [155]	Criterion 4 Laser trigger
2005	Violante [162]	Criterion 4 Laser trigger

Discussion of the Teaching papers

Fleischmann & Pons [1] laid the foundation for a scientific field of study that has endured 19 years. Their first paper has motivated 14 international conferences, thousands of experiments, papers and many books. Most of all, their paper inspired many to believe that important science could still be done by dedicated individuals.

Criterion 1 (Bulk loading considerations)

In 1990 an excellent positive experiment was reported by Guruswamy and Wadsworth in their paper, *Metallurgical Aspects of Cold Fusion Experiments* [26]. This appears to be a superior paper but is perhaps underappreciated. Criteria 1 is fulfilled in this paper by measurement of cathode enlargement as the cathode filled with deuterium. The authors reported a D/Pd ratio of 0.93. Criteria 1 was fulfilled. The loading current density used was higher than one might normally use – 100 mA/cm². The authors reported the use of arsenate to poison the surface. This may have helped seal the palladium surface and reduce the loss of deuterium, resulting in a high D/Pd ratio even with a higher-than-normal current density.

This 1992 paper, *Excess Power Observations in Electrochemical Studies of the D/Pd System: the Influence of Loading* [56], is one of the great teaching experiments that came from McKubre's group at SRI in the early to mid-nineties. If these high quality experiments had been available in mid 1989 to support the seminal work of Fleischmann and Pons, perhaps the Caltech and Harwell experiments would have succeeded and our history might have been written differently.

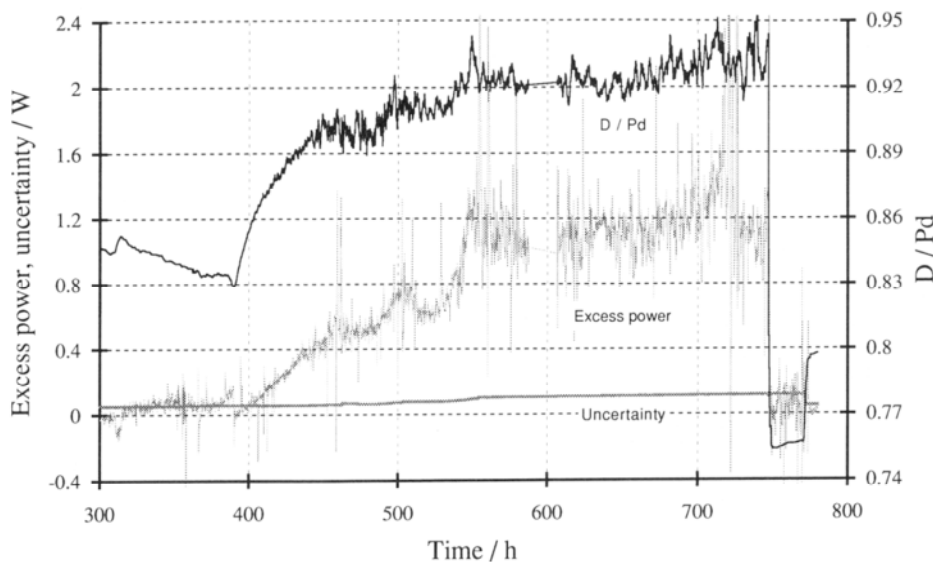


Figure 1. Output from SRI experiment showing that excess power appears at a D/Pd ratio of 0.8 but is more robust above 0.85.

In 1992, Takahashi produced an interesting paper, *Anomalous Excess Heat by D₂O/Pd Cell under L-H Mode Electrolysis* [60], about how to achieve Criterion 1; the Takahashi method taught that the anode should be a square geometry evenly spaced around the cathode. The cathode was a large 2.5 cm square plate. Counting both sides, its effective area was 12.5 cm².

Takahashi loaded the cathode low, at 20 mA/cm² for 6 hours, and then high at 336 mA/cm² for 6 hours. He repeated this for about two weeks, at which time excess power began to appear. Takahashi estimated that the loading ratio was ~ 0.9. The high loading drove the cell to boil and produced excess power of approximately 90 W.

In 1993 at ICCF4, Cravens presented a conference paper, *Factors Affecting The Success Rate of Heat Generation in CF Cells* [63], that listed in detail all of the techniques that he had learned from others and methods that he had discovered in his own lab. The paper was unique enough to prompt Martin Fleischmann to comment that if any investigators were having reproducibility problems, they should read the Cravens paper. Quoting his 1993 abstract is instructive:

A series of low cost, low precision experiments were conducted to screen for factors which may affect the successful observation of heat from palladium/heavy water electrolytic cells. Critical factors include the selection of the palladium and the experimental protocol during the initial loading to the beta phase. It was found that bubble patterns, volume expansion, and surface appearance can be used as early predictors of ultimate success. Since large scale defects are detrimental, methods of avoiding cracking are discussed. These include alloying, preparing a uniform surface, loading at a slow rate at low temperatures, delaying use of additives to the electrolyte, and uniform loading techniques. Methods of achieving the later and larger heat releases were found to include: rapid increase in the current density above a threshold value and raising the temperature. A reflux calorimeter design is presented that allows for continuous studies at boiling temperatures of the electrolyte. Unexpected and unexplained occurrences of heat bursts by magnetic fields and radio frequency fields are reported.

It can be clearly seen that a self-funded researcher had taught himself how to do the Fleischmann-Pons experiment successfully; he learned by reading other papers and noting the common factors in successful experiments. Over the years since then, these common factors have become the four “criteria” or “conditions” we are discussing in this work. When Letts began experimenting in 1992, it was Cravens who taught him how to produce a successful Fleischmann-Pons experiment by using the “Cravens criteria.” We tend to forget that many excellent CMNS researchers are also excellent teachers, so it was natural that colleagues would learn from colleagues.

In 1996, Celani and his group produced a paper, *Reproducible D/Pd Ratio > 1 and Excess Heat Correlation by 1 Micro-Second Pulse, High Current Electrolysis*, which described a novel method to fulfill Criterion 1 by using pulsed current to load palladium with deuterium to a D/Pd ~ 1 or slightly above. The method seemed to involve the surface and did produce a high D/Pd ratio reproducibly. However, even with high loading, not all cathodes produced excess power. The investigators concluded that the deuterium absorption rate seems related to excess power production more than just the loading ratio. High absorption rates of deuterium by palladium seem to be related to excess power production.

Also in 1996, Miles and his collaborators produced a paper, *Electrochemical Loading of Hydrogen and Deuterium Into Palladium and Palladium-Boron Alloys* [96], proposing that a small amount of boron alloyed with palladium helps fulfill Criterion 1, producing a high loading ratio. In a personal communication, Miles explained that he thought that Pd-B is a two

phase material and high loading may exist in small regions, perhaps reducing the need for a bulk loading ratio near 0.85.

Storms contributed a paper in 1996, *How to Produce the Pons-Fleischmann Effect* [100], that like the Cravens “Factors” paper provided an experimental handbook on how to produce the Fleischmann-Pons effect (FPE). On page 3 of this paper Storms identifies the critical deuterium content as the most important requirement in order to produce the FPE. Fulfillment of Criterion 1 is the same as achieving the critical deuterium content. In this paper Storms identifies loading at 20 mA/cm^2 as the best loading current density to use. Storms’ paper [100] is an excellent resource for new researchers wanting to avoid a high number of failures before seeing the Fleischmann-Pons heat effect. Had this paper been available in mid 1989, many CMNS image problems would have been avoided.

In 1998 Arata & Zhang proposed a new type of cathode design to improve the chances of fulfilling criteria 1. Their paper, *Anomalous Difference between Reaction Energies Generated within D_2O Cell and H_2O Cell* [107] reported results from their new design called a double structure cathode. The methods are meant to fulfill Criterion 1 with high reproducibility. A small amount of finely divided (nano) particles of palladium was sealed inside of a palladium cylinder. The cylinder was evacuated and then run as a cathode in a traditional Pd-LiOD electrolytic system. Deuterium diffused through the palladium cylinder and entered the inner evacuated region of the cylinder. Pressure increased as more deuterium diffused into the cylinder’s inner space. The nano palladium black absorbed the deuterium to a very high D/Pd ratio. The Fleischman-Pons effect self-triggered and the entire palladium cylinder heated up, producing large amounts of excess power/energy. The effect was reported to be 100% reproducible. A new version of this experiment was conducted as a working demonstration in Japan during the spring of 2008 and produced positive results.

Storms contributed a useful paper in 1998, *Relationship between Open-Circuit-Voltage and Heat Production in a Pons-Fleischmann Cell* [119]. In this paper, Storms explores how the open circuit voltage predicts the fulfillment of Criterion 1. According to Storms, open circuit voltage of 1 to 1.2 Volts indicates a D/Pd ratio around 0.8 to 0.9, the minimum requirement to fulfill Criterion 1 and produce the Fleischmann-Pons effect. An excellent discussion of the mechanics of hydrogen loading and loss through a network cracks in a palladium cathode is also presented in this paper. A graphic from the paper (Fig. 2) is instructive.

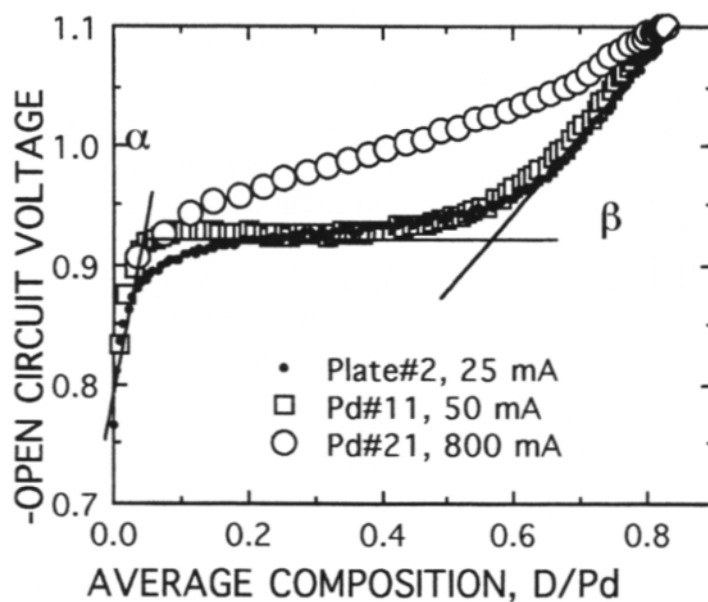


Figure 2. OCV versus D/Pd ratio

The following year, 1999, Storms contributed another excellent teaching paper, *Anomalous Heat Generated by Electrolysis Using a Palladium Cathode and Heavy Water* [121], reporting how lattice expansion may serve as an indicator of Criterion 1 fulfillment. Storms teaches that high loading is not likely when the palladium cathode expands more than about 13% during formation of the deuteride, as illustrated in Fig. 3. Cracks are likely to form.

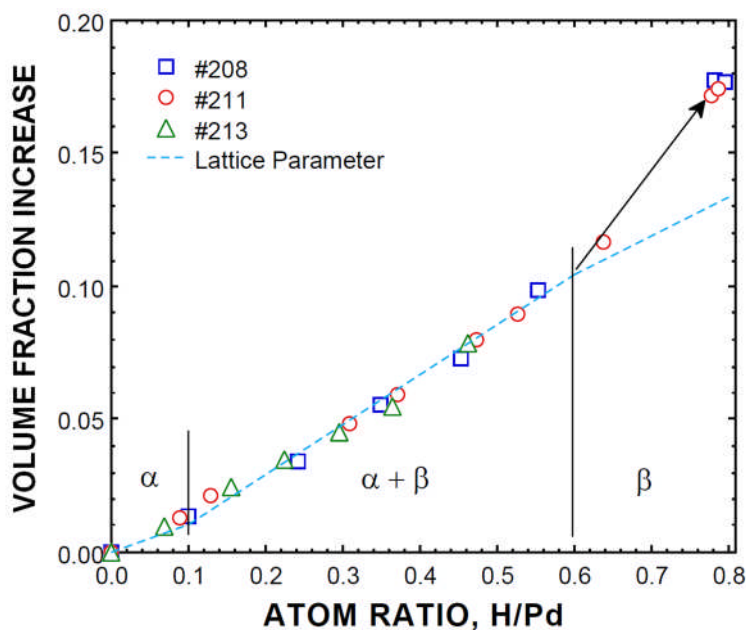


Figure 3. Vertical scale is cathode volume fraction increase

The next Criterion 1 teaching paper, *Calorimetric Analysis of a Heavy Water Electrolysis Experiment using a Pd-B Alloy Cathode*, [131], was contributed by Miles, Imam and Fleischmann in 2001. This paper taught that Criterion 1 could be fulfilled by adding boron to the palladium cathode. This paper is another study of the importance of boron when alloyed with palladium, confirming the observations reported in the 1996 paper by Miles and collaborators [96]. Again, Miles reported to the authors that the Pd-B alloy may produce high local loading, reducing the need to load the bulk cathode to 0.85 D/Pd or above. Storms also reported to the authors that he was unable to load bulk Pd-B above 0.67 D/Pd. So there appears to be the need for some more detailed work to clarify the issue of high loading in a bulk Pd-B cathode.

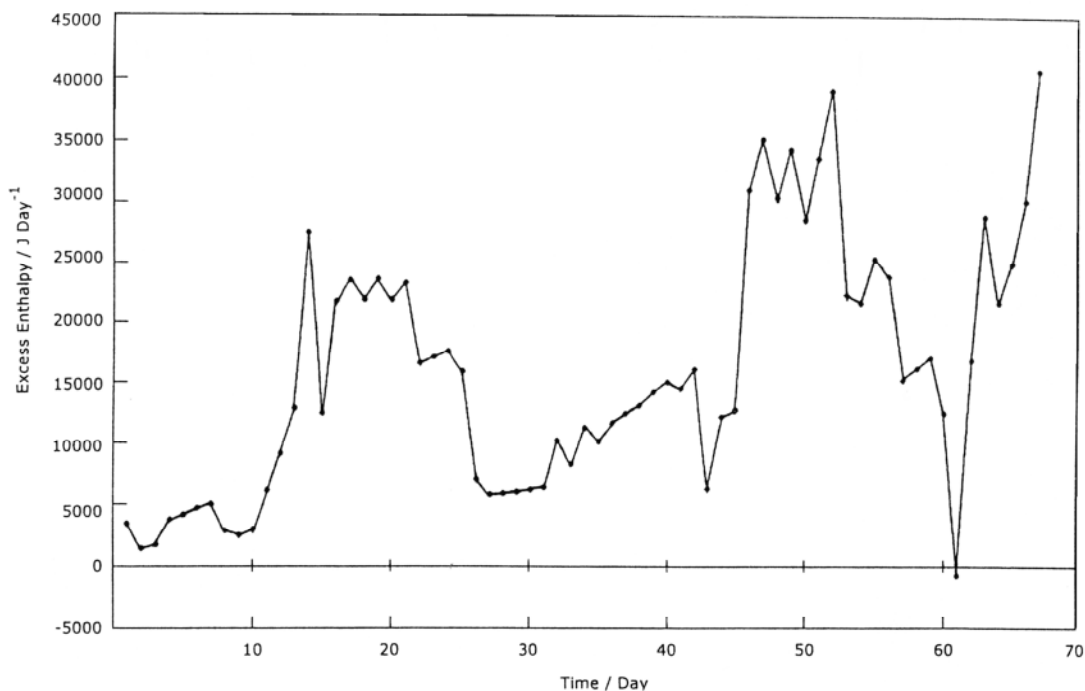


Figure 4. Excess enthalpy produced by Pd-boron cathode

In 2003, Dardik and his collaborators produced the final Criterion 1 teaching paper in Table 4, *Intensification of Low Energy Nuclear reactions Using Superwave Excitation* [148]. Figure 5 shows an image of the Superwave applied to a palladium cathode that resulted in much higher loading at 0.96 D/Pd.

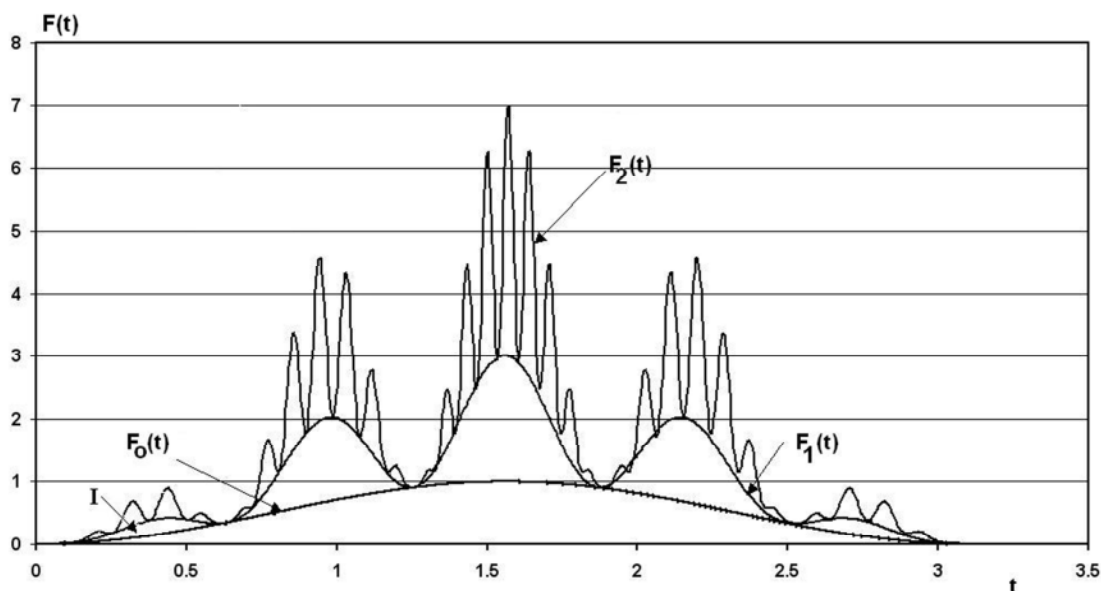


Figure 5. Application of a Superwave to a palladium cathode resulted in a D/Pd ratio of 0.96 compared to 0.88 for DC.

Criterion 2 (Chemical considerations)

Criterion 2 is concerned with providing a chemical environment that improves the chances of producing the excess heat effect; criterion 2 was met in Fleischmann and Pons' first paper because of their clear statement regarding electrolyte composition: "0.1 M LiOD in 99.5% D₂O + 0.5% H₂O".

The next paper in Table 4 teaching Criterion 2 is the paper from Bockris' group, *Sporadic Observation of the Fleischmann-Pons Heat Effect* [8] by Kainthla. This paper fulfilled Criterion 2 by reporting the electrolyte composition as "0.1 M LiOD" and by stating the cathode purity was 99.9%. The last three cells (out of 10) produced excess power, which shows that being concerned about chemical purity might be helpful in producing the excess heat effect. (Storms told the authors that as little as 1-2% of H contamination in the electrolyte can terminate the excess heat effect.)

Appleby's 1990 paper, *Anomalous Calorimetric Results During Long-Term Evolution of Deuterium on Palladium from Alkaline Deuterioxide Electrolyte* [17], is an excellent example of paying attention to Criterion 2. Note that Appleby reported that LiOD worked but NaOD did not (Fig. 6). The chemical environment is important.

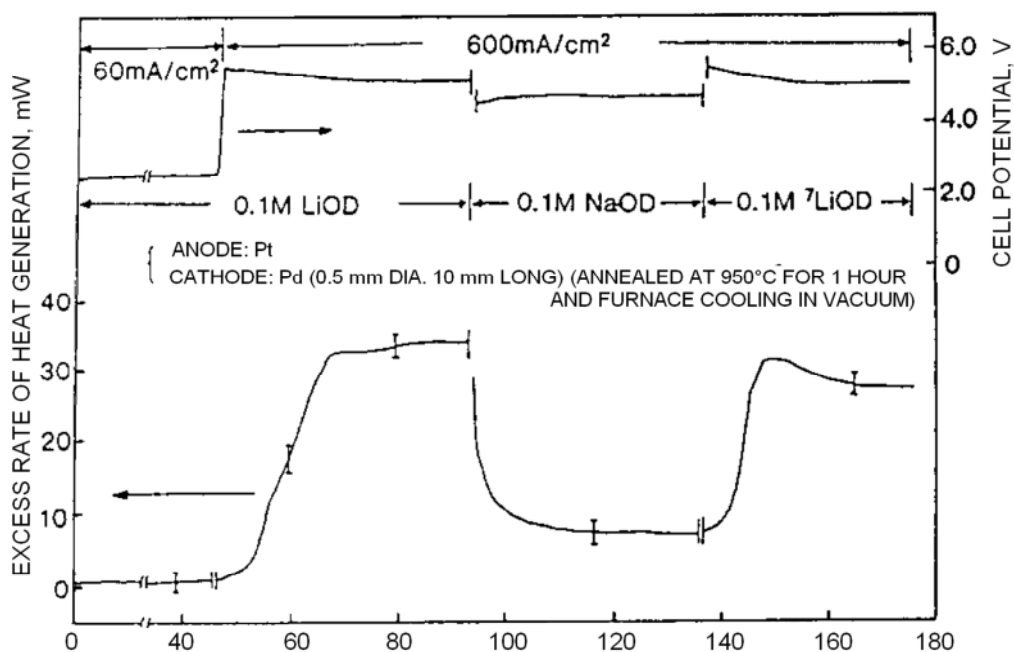


Figure 6. From Ref. 17, shows the importance of Criterion 2 with regard to ions. LiOD produces the FPE but NaOD does not.

Another paper that demonstrates consideration of Criterion 2 is the paper by Guruswamy and Wadsworth, *Metallurgical Aspects of Cold Fusion Experiments* [26]; this early paper from 1990 loaded at a relatively low current density and produced excess power while anticipating many of the issues that would become important in the field of CMNS over the next decade: electrode purity, electrolyte purity, electrode geometry and triggering. This insight is collected in the authors' Table 1 and is shown here in Table 6.

Table 6. From Ref. 26. Guruswamy and Wadsworth's insight into Criterion 2, especially points 2, 3 and 4.

1. EXPERIMENTAL CONDITIONS
 - CURRENT DENSITY
 - TEMPERATURE
 - ELECTROLYTE COMPOSITION
 - POISONS IN ELECTROLYTE
 - NEED FOR INITIATION (ELECTRICAL, MAGNETIC, THERMAL or ULTRASONIC SHOCK)
 - H, CO₂ PICK UP
 - CELL DESIGN
2. ELECTRODE PURITY
 - SUBSTITUTIONAL IMPURITIES
 - PRIMARY Pd (Cu, Ni, Fe, Zr, Te, As, Sb, Cd, Mg, Ca, Li...)
 - RECYCLED Pd (LARGE NO. OF ALLOYING ELEMENTS)
 - INTERSTITIAL IMPURITIES
 - PICKED UP DURING PROCESSING & HANDLING (C, O, N, H)
3. IMPURITIES IN ELECTROLYTE
 - IMPURITIES FROM PROCESSING & HANDLING (C, S, Cu, Zr...)
4. ELECTRODE MICROSTRUCTURE
 - GRAIN SIZE, DISLOCATION DENSITY & DISTRIBUTION

POSSIBLE ROLE OF A THIRD ELEMENT IN THE NUCLEAR REACTION

CELL DESIGN: ELECTRODE GEOMETRY, ELECTRODE SPACING, ETC.

The next paper in Table 4 that fulfilled Criterion 2 was the Lautzenhiser and Phelps paper, *Cold Fusion: Report on a Recent Amoco Experiment* [28]; the experimenters reported the purity of their heavy water and the purity of their palladium cathode in the materials section. They also reported many of the impurities present in the cathode, showing concern for criterion 2.

The next paper in Table 4 that met criterion 2 is the paper by Bockris and his collaborators, *Triggering of Heat and Sub-surface Changes in Pd-D Systems* [62] from 1993. This paper reported electrolyte and cathode purity on page 3 in the material science section.

The Cravens paper, *Factors Affecting The Success Rate of Heat Generation in CF Cells* [63], discloses the importance of chemical considerations. On page 8, Cravens recites the importance of contamination avoidance in producing the excess heat effect. He reported the use of a dummy cathode to remove contaminants and the importance of avoiding H contamination.

Cravens also reported the importance of surface chemistry - a polished cathode worked best (Fig. 7).

Surface conditions – use a smooth surface

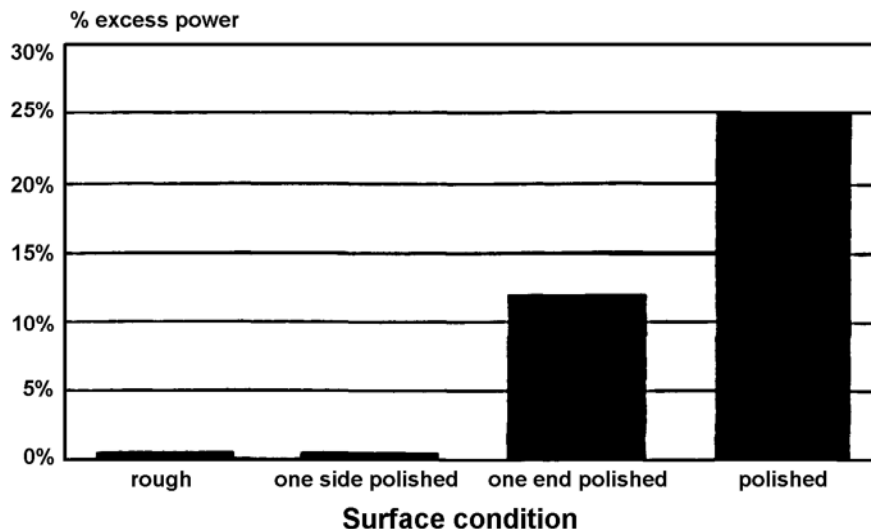


Figure 7. A polished cathode works best to produce the FPE.

Storms, in his well known paper from 1996, *How to Produce the Pons-Fleischmann Effect* [100], succinctly describes the importance of cathode surface conditions: (quoted from page 5)

. . . Aluminum metal (2-20 ppm) added to the electrolyte after the palladium has achieved its maximum deuterium content is sometimes useful in initiating excess heat production. Thiourea also has been used with limited success. Preoxidizing the surface at 600-750°C in air improves the loading rate because the very thin layer of oxide is quickly reduced to a pure, very chemically active layer of palladium once electrolysis starts. Absence of certain surface impurities such as copper, lead or silver (from solder) is also important. However, a thin film of gold ($\approx 7000 \text{ \AA}$) on the palladium surface can increase the limiting D/Pd ratio.[34] The benefits of lithium and platinum, two impurities normally observed on and within the surface region, are still unknown. Other impurities not yet studied may have both good and bad effects.

Cravens and Storms are in agreement that cathode surface conditions are vital to consider when attempting reproduction of the Fleischmann-Pons Effect (FPE).

Criterion 3 (high operating current density)

Table 1 from the 1989 Fleischmann and Pons paper, *Electrochemically Induced Nuclear Fusion of Deuterium* [1], shown above, demonstrates that operating current density is proportional to observed excess power. The importance of loading at a low current density and running at a much higher current density was known to only a few researchers in 1989.

As mentioned earlier in this review paper, investigators began to learn or discover the current density requirements; In June, 1989 the Kainthla paper, *Sporadic Observation of the Fleischmann-Pons Heat Effect* [8], reported modest excess power production after loading at 60 mA/cm² for 18-30 days, followed by running above 400 mA/cm².

The Guruswamy and Wadsworth paper, *Metallurgical Aspects of Cold Fusion Experiments* [26] reported excess power production after loading at the somewhat high current density of 100 mA/cm². Later they increased current density to 200 mA/cm² and saw bursts (Fig. 8).

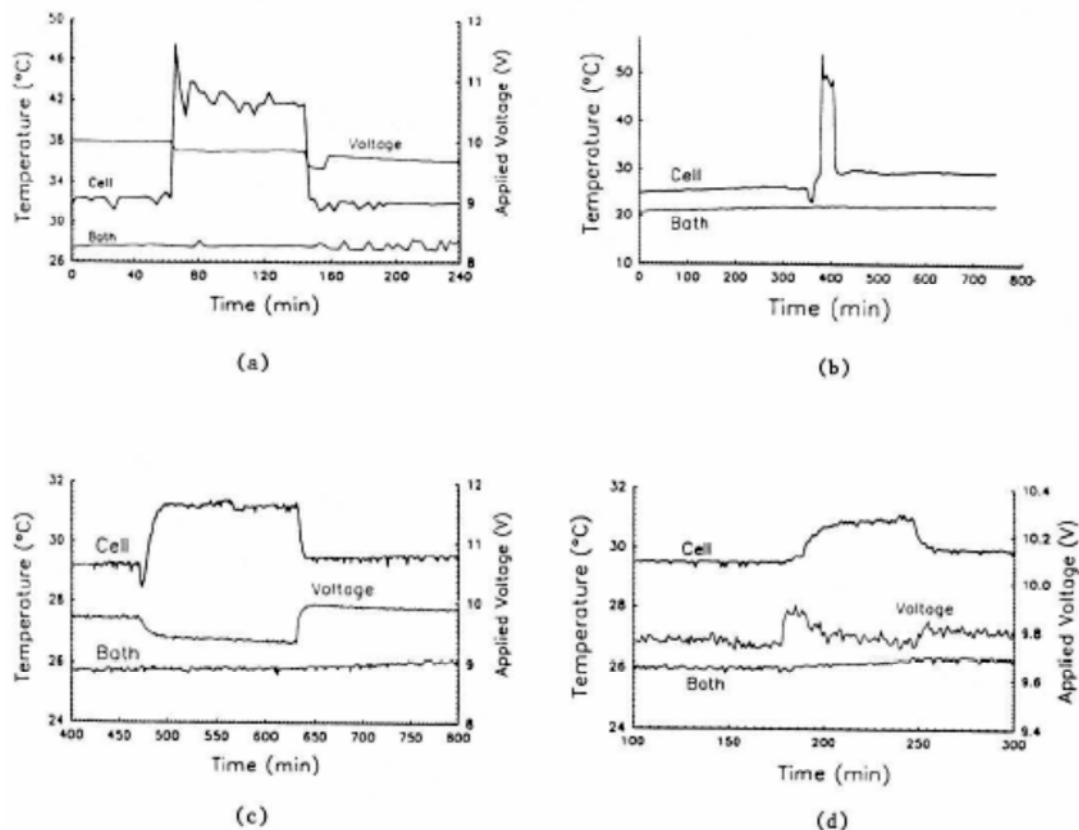


Figure 8. Unexpected heat spikes

With respect to current density, the Lautzenhiser (Amoco) paper, *Cold Fusion: Report on a Recent Amoco Experiment* [28], is unusual. The cathode for that experiment loaded at 3 mA/cm² and ran at only 15 mA/cm². The paper reported a small amount of excess power – 40-90 mW, seen in a high-precision micro calorimeter. We would not expect that a current density of only 15 mA/cm² would trigger excess power, yet it did. Notice that they saw a small amount of excess heat even though they did not fulfill the criterion. It is important to notice the difference in the statistical terms of correlation and saying that something is “essential”. Adherence to the criteria does not guarantee success nor does ignoring criteria doom an experiment. The criteria are only “enabling” in that they increase the probability of the desired outcome.

In 1991 SRI and EPRI collaborated to produce an excellent paper, *Isothermal Flow Calorimetric Investigation of the D/Pd System* [49]; this paper quantified the current density threshold of about 200 mA/cm². We usually recognize that 500 mA/cm² is a good target current density to maximize the chances of triggering the FPE. The current density threshold is clearly visible in Fig. 9.

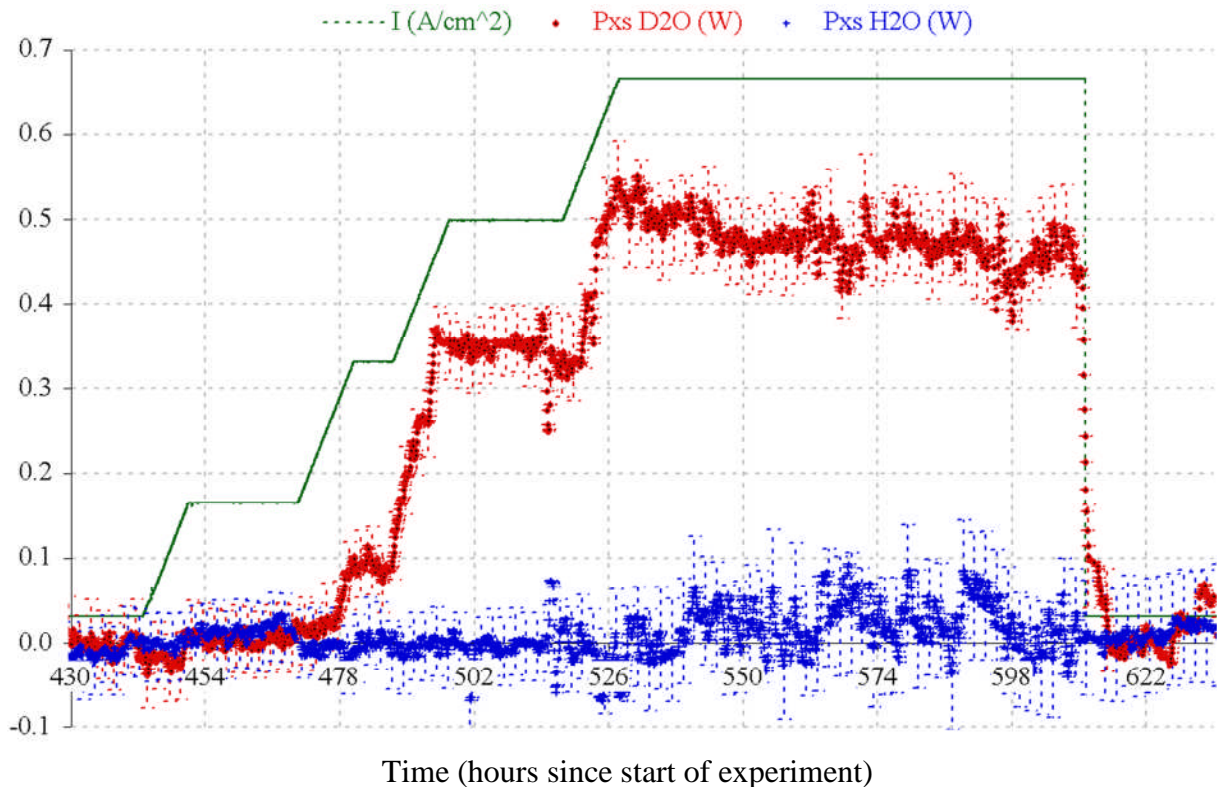


Figure 9. Excess power “switches on” at ~ 200 mA/cm²

In 1992 Takahashi demonstrated the importance of Criterion 3 by running a cell in the low current-high current mode for many hours, as reported in his paper, *Anomalous Excess Heat by D₂O/Pd Cell under L-H Mode Electrolysis* [60]. After a loading period, the cathode produced ~ 90 W of excess power when running at high current density of 336 mA/cm². There was no excess power at low current density of 20 mA/cm².

The importance of Criterion 3 (current density) is also addressed in Cravens’ 1993 conference paper, *Factors Affecting The Success Rate of Heat Generation in CF Cells*, [63]; in this multi-faceted paper, Cravens shows that an operating current density greater than 120 mA/cm² is required to produce the FPE (Fig. 13).

Initial loading – use a slow initial loading

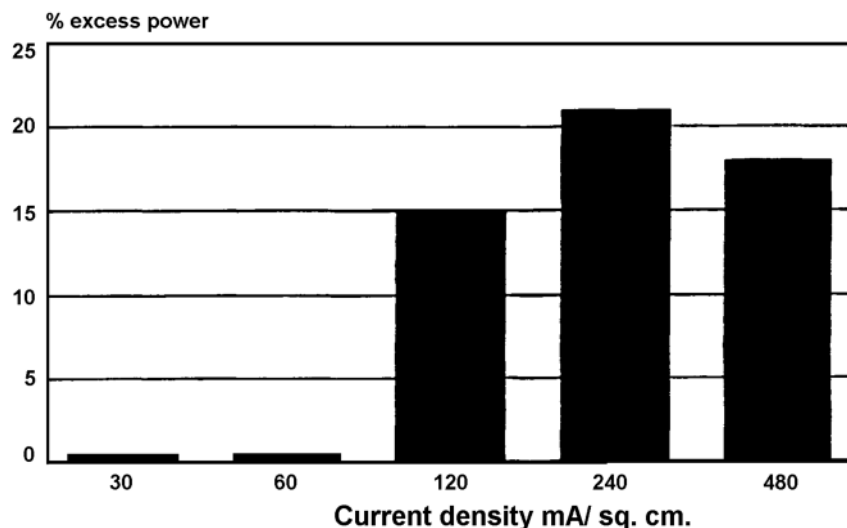


Figure 10. Cravens shows that low operating current densities will not normally produce the FPE.

The final paper in Table 4 discussing Criterion 3 (current density) issues was contributed by Storms in 1993 titled, *Some Characteristics of Heat Production Using the “Cold Fusion” Effect* [71]. In Fig. 11 Storms plots his experimental data with three other data sources. Storms shows that some cathodes “switch on” at a lower current density than many others – perhaps because those cathodes have fewer cracks and can load hydrogen more readily. A more typical value in Storms data appears to be $\sim 100 \text{ mA/cm}^2$.

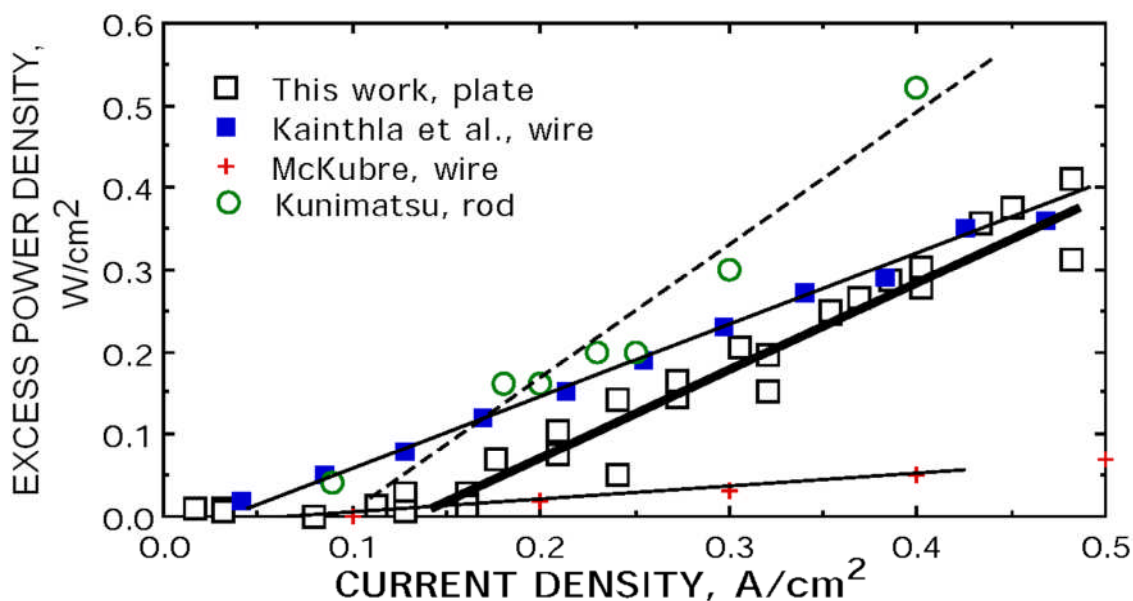


Figure 11. Vertical column is excess power density, W/cm^2

Criterion 4 (External factors – triggering)

In the early years of CMNS (1989-1992), long incubation periods were often required to produce the Fleischmann-Pons effect. It seemed all that was required to produce the FPE was a long, low current loading period followed by an even longer high current loading period. As the Lautzenhiser (AMOCO) paper [28] demonstrated, patience was important. This paper, *Cold Fusion: Report on a Recent Amoco Experiment* [28] reported, “It is important to note that if this experiment had been terminated after only one month, the results would have shown no positive energy production.”

The 1990 Guruswamy & Wadsworth paper, *Metallurgical Aspects of Cold Fusion Experiments* [26] anticipated the possibility of triggering as mentioned in Table 6 (“need for initiation”) but was not attempted.

As far as we could determine, external triggering of the D-Pd system was not reported until 1993. The Bockris paper, *Triggering of Heat and Sub-surface Changes in Pd-D Systems* [62] and the Cravens paper, *Factors Affecting The Success Rate of Heat Generation in CF Cells* [63] reported triggering the FPE with RF at three specific frequencies of 82,365 and 533 MHz and by imposition of magnetic fields greater than about 200 gauss. One to two watts of excess power was observed within a few minutes following cell stimulation.

Two new types of cell stimulation appeared in 2003. Letts and Cravens reported excess power production in their ICCF10 conference paper, *Laser Stimulation of Deuterated Palladium: Past and Present* [149] and Dardik reported excess power from cell stimulation by Superwaves in the ICCF10 conference paper, *Intensification of Low Energy Nuclear reactions Using Superwave Excitation* [148]. Both types of stimulation appear to create dynamic conditions at the cathode surface favorable to triggering the Fleischmann-Pons effect.

The laser effect has been replicated by Storms [151], McKubre & Tanzella [172] and advanced by Apicella [155] and Violante [162]. Swartz reported observation of the laser effect before 2003 and reported excess power from laser stimulation in his ICCF10 conference paper, *Photo Induced Excess Heat from Laser-Irradiated Electrically Polarized Palladium Cathodes in D₂O*. [173].

The Dardik Superwave trigger has been replicated at SRI, with help from Energetics Technologies. The Superwave is built up using a series of rectified sine waves. The idea is to begin with a base frequency and then add harmonics to the base such as 2x, 3x...6x. The Superwave is designed to rise to its peak quickly and decay back to base frequency slowly. Dardik’s idea is based on how natural systems oscillate. This same rapid up, slow down cycle is apparently effective in providing a flux of deuterium at the cathode surface. Dynamic surface conditions are evidently effective because the Superwave has been reported to trigger excess power of 100-300% over input power. A few 25 to 1 power gains have been reported using the Superwave trigger.

In 2004, Apicella and collaborators reported in their paper, *Some Recent Results at ENEA* [155] that laser stimulation increased excess power reproducibility from 30% to 90% and that ⁴He is detected in amounts commensurate with D+D fusion. It was also reported that P polarization of the laser was required to see the benefits of laser stimulation.

In 2005, Violante and collaborators reported in their paper, *Progress in Excess of Power Experiments with Electrochemical Loading of Deuterium in Palladium* [162] that the P polarization is effective because it creates charge separation on the cathode surface. Charge separation on the cathode implies the possibility of creating surface Plasmons (Polaritons) that can interact with the laser. This may be very important as it could provide a connection with Hagelstein's theory and laser stimulated excess power.

Section 4 has discussed several of the papers that demonstrated fulfillment of the four criteria we believe are required to produce the Fleischmann-Pons Effect. These papers are a subset of a larger number of papers that we considered in a statistical analysis of the four enabling criteria.

Statistical Analysis of Papers and Enabling Criteria

The authors selected 167 papers (see references) for this study. These papers reported heat generation from electrolytic systems. As many may recall, it was very difficult for CMNS researchers to get their work published in the two years following the Fleischmann and Pons announcement. We are aware that many viable papers from that period were not included in this study, mainly because they are not yet available in a digital format. Exclusion from this study should not be taken as a judgment about the importance of excluded papers but only their availability. The 167 papers in this study span 18 years, come from vastly different laboratories and were performed by dedicated researchers from a number of political and cultural backgrounds. The diversity of this work is almost as amazing as its consistency, serving as a fair representative sample for statistical input.

Only electrochemical heat papers from the Pd-LiOD system were included in the statistical survey to make the statistics meaningful. Although we directed our efforts to identifying which criteria were fulfilled by each paper, it was not always clear if the criteria were met or not. In those cases, the papers were excluded from the final statistical analysis. Our guiding premise was to allow data into the analysis only if it was clear and unambiguous. We had several alternative ways to signal achievement of each criteria so that more papers could be included. This resulted in 122 papers entering our statistical analysis. The papers were segregated by criterion and each paper was assigned a 1 or 0 based on observation of excess power or not. There were 34 papers in our study that actually measured the D/Pd ratio; there were 49 papers that reported the loading current density; there were 59 papers that reported the operating current density and 122 papers that reported enough data to determine if triggering was used either by increasing the current, the temperature, applying external fields or electromagnetic radiation.

Our analysis shows that there is a 76% overall correlation (Rank) between the four enabling criteria and observation of the Fleischmann-Pons Effect (FPE).

Our analysis of 122 papers shows that if an experimenter met these requirements:

1. Loads below 100 mA/cm^2
2. Achieves a loading ratio > 0.8
3. Runs above 500 mA/cm^2
4. Applies a trigger to the cathode

Then the probability of producing the FPE was ~ 76%. It is obvious that there is a high degree of correlation between the four enabling criteria and the observation of excess power. It was less obvious to us before completing this study that the measured D/Pd ratio was only correlated to excess power by 26% . We noted several papers in our study that achieved a high measured D/Pd ratio but still failed to produce excess power (see the Isobe paper #138). Further, the operating current density was only correlated with excess power production by 21%. The loading current density was negatively correlated with excess power at -55%, confirming that a low loading current density makes excess power more likely. Triggering was correlated with excess power at 65%. All negative papers were seen to have failed in fulfilling one or more of the enabling criteria. If we define a Fleischmann-Pons experiment as one that fulfills all four criteria, then none of the early researchers who published negative papers actually performed the Fleischmann-Pons experiment as we know it today.

Statistical Analysis of Papers Reporting Measured Parameters

In order to include a maximum number of papers in our study, we had to rely on indirect methods to determine if a cathode had achieved a high degree of loading. In this section we discuss our results when only measured parameters are included to more fully investigate the roles of various conditions and to provide a more quantitative view.

Although there is not room to describe in detail our operational definitions used in the statistics, it is important to note that the authors tried to assure objective definitions that lead to unambiguous Boolean binary logical notation for each criterion. This approach was taken to span the greatest number of papers. For example, no attempt was made to evaluate “goodness” of chemical protocols or material sources, only that a protocol was mentioned in the paper. If the material source was mentioned then the paper received a binary 1.

The grading for excess heat was based on any claims of excess heat within the paper and not individual cells or cathodes within a series of runs. Thus, each paper was scored by a single binary number based on objective “operational definitions” (specific statistical term) for each of the 4 criteria and the claim of excess heat.

The original individual criteria were scored as a logical 1 if any of the items existed within the paper. This permitted inclusion of 122 papers out of the original 167 papers investigated. The following analysis was done with restricted single element criteria to provide statistical data based on measured parameters only. Since only a few papers addressed all of the specific issues with measurements, this approach results in only 17 papers entering the analysis. There are very few papers which report specific loading ratios, loading current densities, operational current densities and triggering information. This restricted view is presented here, however the authors caution that it may not be desirable to discard over one hundred papers based on a restricted view of what factors are generally thought to be relevant.

The criteria used for this more restricted statistical study are:

- Criterion 1: Is the loading ratio measured at 0.85 D/Pd or greater?
- Criterion 2: Was the initial loading done below 100 mA/cm²? (lowest listed when several are reported)
- Criterion 3: Was the cell operated at current densities at or above 200mA/cm² (highest listed for multiple listings)
- Criterion 4: Was some triggering or event imposed that would alter the deuterium flux or cause a non-equilibrium condition?
- Excess Heat: Was there any claim of excess heat within the paper?

When these were used, the following correlations between criteria and excess heat were found:

- Criterion 1: 0.3
- Criterion 2: -0.5 (negative correlation indicates lower current densities are beneficial)
- Criterion 3: 0.2
- Criterion 4: 0.7

Correlation of average of criteria for individual papers: 0.6

Note that significant figures were decreased to reflect more uncertainty due to the reduced number of papers in the restricted study. It is interesting to note that our analysis shows that the loading ratios may not be as significant as many would expect and that the presence of dynamic conditions appears more significant than many would expect. It is important to repeat that “correlation is not causation” and that some researchers have used conditions and materials that result in excess heat at lower ratios and that some fail to see excess at higher ratios. However it remains important for researchers to consider materials, loading, running currents and dynamic conditions.

As we have stated previously, not all experiments that fulfill all enabling criteria will produce the FPE. However, the most likely outcome of an experiment that failed to meet one or more criteria was failure; the most likely outcome for an experiment meeting all criteria was success.

The 122 paper subset we used for this study clearly addressed the criteria used for statistical input; however, they are just a representative sample of the field of electrochemical heat production. It is important to note that our results were statistically significant across many different calorimeters, different cathode geometries, electrolyte concentrations, research groups and spanned 18 years. The criteria are difficult to achieve but once achieved there is a high correlation with the expected outcome of excess power production. There is a clear indication that there is a reproducible Fleischmann-Pons effect but in the minds of some there is still more doubt than certainty.

Quantifying Certainty for the Fleischmann-Pons Effect

As experimentalists, we believe what we can measure but how do we measure what we believe? How do we compute the certainty level of what we believe to be observational fact? This problem is not new.

History teaches that Laplace used probability theory in conjunction with five or six independent astronomical observations to show that Newton's laws govern celestial mechanics with a certainty of 99% [168]. Colleagues have recently suggested to us that perhaps a similar approach could be used to estimate the certainty associated with the Fleischmann-Pons Effect.

Modern seekers of truth use a computerized version of Laplace's approach. The method is based on Bayesian network analysis and is well outside of our realm of experience and the scope of this review. We will, however, quote some interesting results [169].

The Bayesian Network

Johnson and Melich developed a Bayesian network over the last 3 years that captures the basic relationship among the key logic elements of the Fleischmann-Pons experiments to be considered in the Bayesian network.

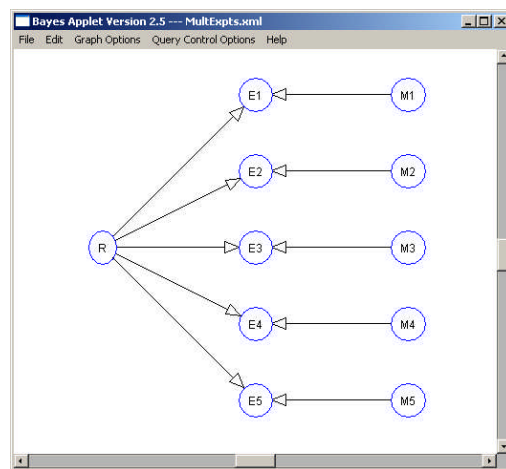


Figure 12. Bayesian logic network for quantifying belief in the Fleischmann-Pons Effect

Figure 12, above, shows the logical relationships between the propositions that the FPE is real, given a number of confirming experiments. The starting assumption is that the FPE is only 10% certain to be a real effect and the experimenters are reliable only 75% of the time. Bayesian software from the Laboratory of Computer Intelligence, University of British Columbia was used to carry out the calculation.

Output from the software package is tabulated in Table 9 as positive experiments were reported.

Table 9. Certainty of the FPE over time as replications are reported

Author	Year	Real	Not Real
F&P	1989	10%	90%
Kainthla	1989	31%	69%
Appleby	1990	64%	36%
Arata & Zhang	1990	87%	13%
Guruswamy	1990	96%	4%
Lautzenhiser(Amoco)	1990	99%	1%

With the Amoco experiment, the certainty that the FPE is a real effect has reached 99%; Since the Amoco experiment, more than one hundred positive electrochemical heat experiments have been reported. It is clear that more than one hundred positive experiments from several countries, using isoperibolic, mass flow and Seebeck calorimetry methods suggest a very high degree of certainty in the Fleischmann-Pons Effect [FPE].

A colleague, Dr Tom Grimshaw, suggests that the quality of evidence for the FPE surpassed the 90% certainty level 18 years ago and should now be considered “beyond a reasonable doubt” – a well known phrase from our criminal justice system. [171]

Another Form of Certainty

While we recognize the value of Bayesian analysis, as experimentalists we respond to experimental results more than probabilities. We would like to close with a result from our experimental history (Fig. 13). As experimentalists, we believe these three results suggest certainty in the fact that the Fleischmann-Pons Effect is real. These three independent experiments produced nearly identical results in three vastly different calorimeters, in three very different laboratories and spanned 17 years. Further, all three experiments reproduced perfectly the endothermic precursor to the Fleischmann-Pons heat effect.

Note the sudden dip in cell temperature or excess power just before each cell goes exothermic. We have observed this effect many times since the early nineties and consider it to be a reliable marker for the FPE.

Three Independent Experiments Showing the Fingerprint of the FPE

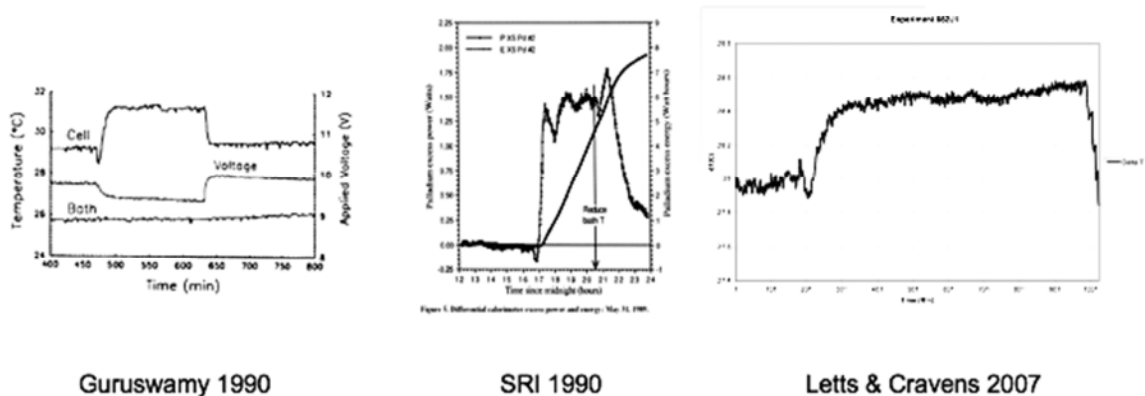


Figure 13. Three independent experiments show nearly identical results and span 17 years. The Guruswamy experiment shows cell temperature, the SRI experiment shows excess power and the Letts-Cravens experiment shows delta T. All three experiments show the endothermic precursor to the FPE.

Summary

Our review has attempted to show that more than one hundred electrochemical heat experiments have taught us that there are basically four criteria that must be fulfilled in order to see the Fleischmann-Pons effect with any degree of reliability. We also showed rather clearly that many of the early experiments failed because they did not fulfill one or more of the required criteria.

We have shown that there is a high degree of statistical correlation between fulfillment of the four criteria and success in producing the FPE. We briefly quoted a method to estimate how certain we are that the Fleischmann-Pons Effect is real. The Bayesian method tells us that by 1990 the Fleischmann-Pons effect had attained a certainty of 99%. This suggests to us that our field of CMNS deserves admission to the mainstream scientific community as a legitimate field of study – as an idea whose time has come.

Acknowledgments

We would like to acknowledge and thank Jed Rothwell, Ed Storms, Dieter Britz, Bill Collis and Steve Krivit for their diligent archival/historical work in preserving the record of CMNS. Our review was based largely upon their work. We also thank Dave Nagel and Mike Melich for this opportunity to share our common history.

References 1989-2007

1. 1989, Pons and Fleischmann, Electrochemically Induced Nuclear Fusion of Deuterium. *Journal of Electroanalytical Chemistry*, 261 (March, 1989) 301-308.
2. 1989, Armstrong et al., Some Aspects of Thermal Energy Generation During the Electrolysis of D₂O Using a Palladium Cathode, *Electrochimica Acta*, Vol. 34, pp1319-1322 1989.
3. 1989, Armstrong et al., A Long-Term Calorimetric Study of the electrolysis of D₂O Using Palladium cube Cathodes, *Journal of Electroanalytical Chemistry*, 272 (1989) 293-297.
4. 1989, Balej et al., Energy Balance of D₂O electrolysis with a Palladium Cathode Part II, Experimental Results, *Journal of Electroanalytical Chemistry*, 278 (1990) 99-117.
5. 1989, Blaser et al., Experimental Investigation of Cold Fusion Phenomena in Palladium, *Chimia* 43 9(1989) 22-268.
6. 1989, Chu et al., Search for the Proposed Cold Fusion of D in Pd, *Modern Physics Letters B* Vol. 3, No 10 (1989) 753-760.
7. 1989 Ikeya and Miyamaru, Chemical Heat Production of Pd Electrode Electrolytically Charged with Deuterium and Hydrogen, *Chemistry Express*, Vol. 4 No. 9, pp 563-566 (1989).
8. 1989, Kainthla et al., Sporadic Observation of the Fleischmann-Pons Heat Effect, *Electrochimica Acta*, Vol. 34, No. 9, pp 1315-1318, 1989.
9. 1989, Kainthla et al., Eight Chemical Explanations of the Fleischmann-Pons Effect, *Int. J. Hydrogen Energy*, Vol. 14, No. 11, pp 771-775, 1989.
10. 1989, Lewis et al., Searches for Low Temperature Nuclear Fusion of Deuterium in Palladium, *Nature*, Vol. 340 August 17, 1989.
11. 1989, Ohashi and Morozumi, Decoding of Thermal Data in Fleischmann and Pons Paper, *Journal of Nuclear Science and Technology*, 6(7), pp729-732.
12. 1989, Santhanam et al., Electrochemically Initiated Cold Fusion of Deuterium, *Indian Journal of Technology*, Vol. 27, April 1989, pp 175-177.
13. 1989, Santhanam et al., Excess Enthalpy during Electrolysis of D₂O, *Current Science*, October 20, 1989, Vol. 58, No. 20.
14. 1989, Shapovalov, Test for Additional Heat Evolution in Electrolysis of Heavy Water with Palladium cathode, *JETP Lett.*, Vol. 50, No. 3, 10 Aug 1989.
15. 1989, Williams et al., Upper Bounds on "Cold Fusion" in Electrolytic Cells, *Nature*, Vol. 342 – 23 November 1989.
16. 1990, An et al., Calorimetric Investigation of Electrochemically Induced Nuclear Fusion of Deuterium, *Thermochimica Acta*, 183 (1991) 107-115
17. 1990 Appleby et al., Anomalous Calorimetric Results During Long-Term Evolution of Deuterium on Palladium from Alkaline Deuterioxide Electrolyte, 1st Annual Conference on Cold Fusion, May 1990.
18. 1990, Arata and Zhang, Achievement of Intense "Cold" Fusion Reaction, *Proc. Japan Acad.*, 66 Series B (1990).
19. 1990, Arata and Zhang, "Cold" Fusion Caused by a Weak "On-Off" Effect, *Proc. Japan Acad.*, 66, Series B (1990).

20. 1990, Arata and Zhang, Corroborating Evidence for “Cold” Fusion Reaction, Proc. Japan Acad., 66, Series B (1990).
21. 1990, Birgul et al., Electrochemically Induced Fusion of Deuterium Using Surface Modified Palladium Electrodes,
22. 1990, Bosch, Electrochemical Cold Fusion Trials at IPP Garching, Journal of Fusion Energy, Vol. 9, No. 2, 1990.
23. 1990, Brudanin et al., Does Cold Nuclear Fusion Exist? Physics Letters A. Vol. 146, No 6.
24. 1990, Fleming et al., Calorimetric Studies of electrochemical Incorporation of Hydrogen Isotopes into Palladium, Journal of Fusion Energy, Vol. 9, No. 4 1990.
25. 1990 Gozzi et al., Evidences for Associated Heat Generation and Nuclear Products Release in Palladium Heavy-Water Electrolysis, IL. Nuovo Cimento, Vol. 103A, N. 1.
26. 1990 Guruswamy and Wadsworth, Metallurgical Aspects of Cold Fusion Experiments, First Annual Conference on Cold Fusion, 1990.
27. 1990, Jow et al., Calorimetric Studies of Deuterated Pd electrodes.
28. 1990, Lautzenhiser and Phelps, Cold Fusion: Report on a Recent Amoco Experiment, unpublished company report 1990.
29. 1990, Lewis and Skold, A phenomenological Study of the Fleischmann-Pons Effect, Journal of Electroanalytical Chemistry, 294 (1990) 275-288.
30. 1990, Longhurst et al, An Investigation of Energy Balances in Palladium Cathode Electrolysis Experiments, Journal of Fusion Energy, Vol. 9, No. 3 1990.
31. 1990, McCracken et al., In Search of Nuclear Fusion in Electrolytic Cells and in Metal/Gas Systems, Journal of Fusion Energy, Vol. 9, No. 2, 1990.
32. 1990 McKubre et al., Calorimetry and Electrochemistry in the D/Pd System, First Annual Conference on Cold Fusion 1990.
33. 1990, Miles et al., Electrochemical Calorimetric Studies of the Cold Fusion Effect, First Annual Conference on Cold Fusion, 1990.
34. 1990, Miles et al., Electrochemical Calorimetric Evidence for Cold fusion in the Palladium-deuterium System, Journal of Electroanalytical Chemistry, 296 (1990) 241-254.
35. 1990, Noninski & Noninski, Determination of the Excess Energy Obtained during the Electrolysis of Heavy Water, Fusion Technology, Vol. 19, p 364, Mar 1991.
36. 1990, Oriani et al., Calorimetric Measurements of Excess Power Output during the Cathodic charging of Deuterium into Palladium, Fusion Technology, Vol. 18 Dec 1990.
37. 1990, Oyama et al., Electrochemical Calorimetry of D₂O Electrolysis using a Palladium Cathode – an Undivided, Open Cell System, The Chemical Society of Japan, 63, 2659-2664 (1990).
38. 1990, Fleischmann et al., Calorimetry of the Palladium-Deuterium-Heavy Water System, J. Electroanalytical Chemistry, 287 (1990) 293-348,
39. 1990, Redey et al., Calorimetric Measurements on Electrochemical Cells with Pd-D Cathodes, Fusion Energy, Vol. 9, No. 3 1990.
40. 1990, Rock et al., Energy Balance in the Electrolysis of Water with a Palladium Cathode, Journal of Electroanalytical Chemistry, 293 (1990), 261-267.

41. 1990, Schreiber et al., Recent Experimental Results on the Thermal Behavior of Electrochemical cells in the Hydrogen-Palladium and Deuterium-Palladium Systems, 8th World Hydrogen Energy Conference, 1990.
42. 1990 Scott et al., Measurement of Excess Heat and Apparent Coincident Increases in the Neutron and Gamma-Ray Count Rates During the Electrolysis of Heavy Water, *Fusion Technology*, Vol. 18, P 103, Aug 1990.
43. 1990, Scott et al., Preliminary Investigation of Possible Low-Temperature Fusion, *Fusion Energy*, Vol. 9, No. 2, 1990.
44. 1990, Stillwell et al., Electrochemical Calorimetric Studies on the Electrolysis of Water and Heavy Water (D₂O), *Fusion Energy*, Vol., 9, No. 3, 1990.
45. 1990, Szpak et al., Electrochemical Charging of Pd Rods, *Journal of Electrochemistry*, 309 (1991) 273-292.
46. 1990 Szpak et al., On the Behavior of Pd Deposited in the Presence of Evolving Deuterium, *Journal of Electroanalytical Chemistry*, 302 (1991).
47. 1990, Wiesmann, Examination of Cathodically Charged Palladium Electrodes for Excess Heat, Neutron Emission, or Tritium Production, *Fusion Technology*, Vol. 17, March 1990.
48. 1991, Lewis, Some Regularities and Coincidences in Thermal, Electrochemical and Radiation Phenomena Observed in Experiments at Studsvik o the Fleischmann-Pons Effect, *Journal of Electroanalytical Chemistry*, 316 (1991) 353-360.
49. 1991, McKubre et al., Isothermal Flow Calorimetric Investigation of the D/Pd System, Second Annual Conference on Cold Fusion.
50. 1991, Noninski and Noninski, Determination of the Excess Energy Obtained During the Electrolysis of Heavy Water, *Fusion Technology*, Vol., 19, March 1991.
51. 1991, Shirai et al., Some Experimental Results Relating to Cold Nuclear Fusion, *Bull. Inst. Chem. Res., Kyoto University*, Vol. 69, No. 5-6, 1991.
52. 1991, Szpak et al., Charging of the Pd/nH System: role of the Interphase, *Journal of Electroanalytical Chemistry*, 337 (1992) pp 147-163.
53. 1992, Celani et al., Measurements of Excess Heat and Tritium during Self-Biased Pulsed Electrolysis of Pd-D₂O, Third International conference on Cold Fusion, Nagoya, Japan 1992.
54. 1992, Kunimatsu et al., Deuterium Loading Ratio and Excess Heat Generation During Electrolysis of Heavy Water by a Palladium Cathode in a Closed Cell Using a Partially Immersed Fuel Cell Anode, Third International Conference on Cold Fusion, Nagoya, Japan 1992.
55. 1992, Fleischmann and Pons, Calorimetry of the Pd/D₂O System: from Simplicity Via Complications to Simplicity, Third International Conference on Cold fusion, Nagoya, Japan, 1992.
56. 1992, McKubre et al., Excess Power Observations in Electrochemical Studies of the D/Pd System: the Influence of Loading, Third International Conference on Cold Fusion, Nagoya, Japan 1992.
57. 1992, Noninski, Excess Heat during the Electrolysis of a Light Water Solution of K₂CO₃ with a Nickel Cathode, *Fusion Technology*, Vol. 21, March 1992.

58. 1992, Ray et al., The Fleischmann-Pons Phenomenon – a Different Perspective, *Fusion Technology*, Vol. 22, Nov. 1992.
59. 1992, Takahashi, A. et al., Excess Heat and Nuclear Products by D₂O/Pd Electrolysis and Multibody Fusion, *International Journal of Applied Electromagnetics in Materials* 3 (1992) 221-230.
60. 1992, Takahashi et al., Anomalous Excess Heat by D₂O/Pd Cell under L-H Mode Electrolysis, *Third International ICCF*, Nagoya, Japan, 1992.
61. 1993, Bertalot et al., Study of Deuterium Charging in Palladium by the Electrolysis of Heavy Water: Excess Heat Production, *Il Nuovo Cimento*, Vol. 15 D N 11, Nov 1993.
62. 1993, Bockris et al., Triggering of Heat and Sub-surface Changes in Pd-D Systems, *Fourth International Conference on Cold Fusion*, Maui, Hawaii 1993.
63. 1993, Cravens, Factors Affecting The Success Rate of Heat Generation in CF Cells. *Fourth International Conference on Cold Fusion*, Maui, Hawaii 1993.
64. 1993, Hasegawa et al., Observation Of Excess Heat During Electrolysis of 1M LiOD in a Fuel Cell Type Closed Cell, *Fourth International Conference on Cold Fusion* 1993.
65. 1993, Lyakov et al., Anomalous Heat Release in the Pd/PdO System Electrolytically Saturated with Hydrogen, *Russian Journal of Physical Chemistry*, Vol. 67, No. 3, 1993.
66. 1993, Miles et al., Correlation of Excess Power and Helium Production during D₂O and H₂O Electrolysis using Palladium Cathodes, *Journal of Electroanalytical Chemistry*, 346 (1993) 99-117.
67. 1993, Notoya, Cold Fusion by Electrolysis in a Light Water-Potassium Carbonate Solution with a Nickel Electrode, *Fusion Technology* Vol. 23 Sept 1993.
68. 1993, Ohmori and Enyo, Excess Heat Evolution during Electrolysis of H₂O with Nickel, Gold, Silver and Tin Cathodes, *Fusion Technology*, Vol.24 Nov 1993.
69. 1993, Pons and Fleischmann, Heat after Death, *Fourth International Conference on Cold Fusion*, Maui, Hawaii 1993. (No digital Copy)
70. 1993, Quickenden and Green, A Calorimetric Study of the Electrolysis of D₂O and H₂O at Palladium Cathodes, *Journal of Electroanalytical Chemistry*, 344 (1993) 167-185.
71. 1993, Storms, Some Characteristics of Heat Production Using the “Cold Fusion” Effect, *Fourth International Conference on Cold Fusion*, Maui, Hawaii 1993.
72. 1993, Storms, Measurements of Excess Heat from a Pons-Fleischmann-Type Electrolytic Cell Using Palladium Sheet, *Fusion Technology*, 1993, 23, p 230.
73. 1993, SUN Da-Lin et al., An Explanation for the Abnormal Temperature Rise of Palladium Cathode During Electrochemical Deuterium Charging, *Science in China (Series A)*, Vol. 36, No. 12.
74. 1994, De Ninno and Violante, Study of Deuterium Charging in Palladium by Electrolysis of Heavy Water, *Fusion Technology*, Vol. 26, Dec. 1994.
75. 1994, Focardi et al., Anomalous Heat Production in Ni-H Systems, *Il Nuovo Cimento, Note Brevi*, Vol. 107A N 1.
76. 1994, McKubre, Isothermal Flow Calorimetric Investigations of the D/Pd and H/Pd Systems, *Journal of Electroanalytical Chemistry*, 1994, 368, p55.
77. 1994, Miles et al., Anomalous Effects Involving Excess Power, Radiation and Helium Production during D₂O Electrolysis Using Palladium Cathodes, *Fusion Technology*, Vol. 25, 1994.

78. 1994, Szpak et al., Absorption of Deuterium in Palladium Rods: Model vs. Experiment, LENR-CANR.org, 1994.
79. 1994, Szpak et al., Deuterium Uptake during Pd-D Codeposition, Journal of Electroanalytical Chemistry, 379 (1994) 121-127.
80. 1995, Celani et al., Study of Deuterium Charging Behavior in Palladium and Palladium Alloy Plates, Changing Surface Treatments, by micro-second Pulsed Electrolysis, ICCF5 Conference, Monte Carlo 1995.
81. 1995, Jones et al., Faradaic Efficiencies Less than 100% during Electrolysis of Water Can Account for reports of Excess Heat in "Cold Fusion" Cells, Journal of Phys. Chem. 1995, 99, 6973-6979.
82. 1995, Lipson et al., The Nature of excess Energy Liberated in a Pd/PdO Heterostructure Electrochemically Saturated with Hydrogen (Deuterium), Russian Journal of Physical Chemistry, Vol. 69, No. 11, 1995 pp 1810-1813.
83. 1995, Shkedi, Calorimetry, Excess Heat and Faraday Efficiency in Ni-H₂O Electrolytic Cells, Fusion Technology, Vol. 28, Nov 1995.
84. 1995, Szpak et al., Anomalous Behavior of the Pd/D System, Technical Report 1696, Office of Naval Research 1995.
85. 1995, Szpak and Mossier-Boss, Calorimetry of Open Electrolysis Cells, Office of Naval Research 1995.
86. 1995, Szpak et al., Cyclic Voltammetry of Pd + D Codeposition, Journal of Electroanalytical Chemistry 380 (1995) 1-6.
87. 1996, Bockris and Minevski, Two Zones of "Impurities" Observed after Prolonged Electrolysis of Deuterium on Palladium, Infinite Energy Magazine, November 1995, p67.
88. 1996, Celani et al., Deuterium Overloading of Palladium Wires by Means of High Power Micro-Second Pulsed Electrolysis and Electromigration: Suggestions of a "Phase Transition" and Related Excess Heat, Physics Letters A 214 (1996) 1-13.
89. 1996, Celani et al., Observations of Strong Resistivity Reduction in a Palladium Thin Long Wire Using Ultra High Frequency Pulsed Electrolysis at D/Pd>1, ICCF6, Sapporo, Japan 1996.
90. 1996, Celani et al., Reproducible D/Pd Ratio>1 and Excess Heat Correlation by 1 Micro-Second Pulse, High Current Electrolysis, Fusion Technology, Vol. 29 p 398, May 1996.
91. 1996, Dominguez et al., The Effect of Microstructure on Deuterium Loading in Palladium Cathodes, Sixth International Conference on Cold Fusion, Lake Toya, Japan 1996.
92. 1996, Hagans et al., Surface Composition of Pd Cathodes, Sixth International Conference on Cold Fusion, Lake Toya, Japan 1996.
93. 1996, Lonchamp et al., Reproduction of Fleischmann and Pons Experiments, Sixth International Conference on Cold Fusion, Lake Toya, Japan 1996.
94. 1996, Miles et al., Anomalous Effects in Deuterated Systems, Naval Air Warfare Center Weapons Division, China Lake, CA, 1996.
95. 1996, Miles and Johnson, Electrochemical Insertion of Hydrogen Into Metals and Alloys, Infinite Energy Magazine, 1996 1(5&6): p68.

96. 1996, Miles et al., Electrochemical Loading of Hydrogen and Deuterium Into Palladium and Palladium-Boron Alloys, Sixth International Conference on Cold Fusion, Lake Toya, Japan 1996.
97. 1996, Notoya, Cold Fusion Arising from Hydrogen Evolution Reaction on Active Metals in Alkali Ions' Solutions, Environmental Research Forum, Vols. 1-2 (1996) pp 127-140.
98. 1996, Roulette and Pons, Results of Icarus 9 Experiments Run at IMRA Europe, Sixth International Conference on Cold Fusion, Lake Toya, Japan 1996.
99. 1996, Storms, A Study of those Properties of Palladium That Influence Excess Energy Production by the "Pons-Fleischmann" Effect, Infinite Energy, 2 #8, 50 (1996).
100. 1996, Storms, How to Produce the Pons-Fleischmann Effect, Journal of Fusion Technology, 29 (1996) p261.
101. 1996, Storms, Some Thoughts on the Nature of the Nuclear-Active Regions in Palladium, Sixth International Conference on Cold Fusion, Lake Toya, Japan 1996.
102. 1996, Tanzella et al., Parameters Affecting the Loading of Hydrogen Isotopes Into Palladium Cathodes, Sixth International Conference on Cold Fusion, Lake Toya, Japan 1996.
103. 1997, Dash et al., Excess Heat and Unexpected Elements from Aqueous Electrolysis with Titanium and Palladium Cathodes, Proceedings of the 32nd Intersociety Energy Conversion Engineering Conference, vol. 2, pp 1350-1355 (1997).
104. 1997, Little and Puthoff, Calorimetric Study of Pd/Ni Beads from the CETI RIFEX Kit, EarthTech International lab report, 1997.
105. 1997, Swartz, Consistency of the Biphasic Nature of excess Enthalpy in Solid-State Anomalous Phenomena with the Quasi-One-Dimensional Model of Isotope Loading into a Material, Fusion Technology, Vol. 31, Jan. 1997.
106. 1997, Swartz, Codeposition of Palladium and Deuterium, Fusion Technology, Vol. 32, Aug. 1997.
107. 1998, Arata and Zhang, Anomalous Difference between Reaction Energies Generated within D₂O Cell and H₂O Cell, Japanese Journal of Applied Physics, Vol. 37 (1998), L1274-L1276. Part 2 No 11a Nov. 1998.
108. 1998, Bush and Lagowski, Methods of Generating Excess Heat with the Pons and Fleischmann Effect: Rigorous and Cost Effective Calorimetry, Nuclear Products Analysis of the Cathode and Helium Analysis, Seventh International Conference on Cold Fusion, Vancouver, Canada 1998.
109. 1998, Gozzi et al., X-Ray, Heat Excess and ⁴He in the D/Pd System, Journal of Electroanalytical Chemistry 452 (1998).
110. 1998, Little et al., the Incandescent W Experiment, EarthTech International Lab Report, August 1998.
111. 1998, Lonchamp et al., Excess Heat Measurement with Patterson Type Cells, Seventh International Conference, Vancouver, Canada 1998.
112. 1998, Lonchamp et al., Excess Heat Measurement with Pons and Fleischmann Type Cells, Seventh International Conference on Cold Fusion, Vancouver, Canada 1998.
113. 1998, McKubre and Tanzella, Materials Issues of Loading Deuterium Into Palladium and the Association with Excess Heat Production, Seventh International Conference on Cold Fusion, Vancouver, Canada 1998.

114. 1998 Mengoli et al., Anomalous Heat Effects Correlated with Electrochemical Hydriding of Nickel, *Il Nuovo Cimento*, Vol. 20 D, N. 3 March 1998.
115. 1998, Mengoli et al., Calorimetry Close to the Boiling Temperature of the D₂O/Pd Electrolytic System, *Journal of Electroanalytical Chemistry* 444 (1998) pp 155-167.
116. 1998, Ota, Effect of Boron for the Heat Production during the Heavy Water Electrolysis using Palladium Cathode, *International Journal of the Society of Materials Engineering for resources* Vol. 6 No 1 26-34 (1998).
117. 1998, Oya et al., The Role of Alkaline Ions in Dynamic Movement of Hydrogen Isotopes in Pd, *Seventh International Conference on Cold Fusion*, Vancouver, Canada 1998.
118. 1998, Storms, Formation of -PdD Containing High Deuterium Concentration Using Electrolysis of Heavy Water, *Journal of Alloys and Compounds*, 268 (1998)89.
119. 1998, Storms, Relationship between Open-Circuit-Voltage and Heat Production in a Pons-Fleischmann Cell, *Seventh International Conference on Cold Fusion*, Vancouver, Canada 1998.
120. 1998, Takahashi, A. et al., Experimental Study on Correlation between Excess Heat and Nuclear Products by D₂O/Pd Electrolysis, *Int. J. of the Soc. Of Mat. Eng. For Resources*, Vol. 6, No. 1 4-13 (1998)
121. 1999, Storms, Anomalous Heat Generated by Electrolysis Using a Palladium Cathode and Heavy Water, *APS Meeting*, Atlanta, Georgia 1999.
122. 2000, Bernardini et al., Anomalous Effects Induced by D₂O Electrolysis of Titanium, *Eighth International Conference on Cold Fusion*, Lerici, Italy 2000.
123. 2000, Celani et al., High Hydrogen Loading into Thin Palladium Wires Through Precipitate of Alkaline-Earth Carbonate on the Surface of Cathode: Evidence of New Phases in the Pd-H System and Unexpected Problems Due to Bacteria Contamination in the Heavy Water, *Eighth International Conference on Cold Fusion*, Lerici, Italy 2000.
124. 2000, McKubre et al., The Emergence of a Coherent Explanation for Anomalies Observed in D/Pd and H/Pd Systems; Evidence for ⁴He and ³He Production, *Eighth International Conference on Cold Fusion*, Lerici, Italy 2000.
125. 2000, Miles, Calorimetric Studies of Pd/D₂O+LiOD Electrolysis Cells, *Journal of Electroanalytical Chemistry*, 2000, 482, p. 56.
126. 2000. Miles, Report on the Calorimetric Studies at the NHE Laboratory in Sapporo, Japan, *Infinite Energy*, 2000, 5(30), p, 22.
127. 2000, Mizuno, Confirmation of Heat Generation and Anomalous Element Caused by Plasma Electrolysis in the Liquid, *Conference Proceedings Vol. 70, ICCF8, Societa Italiana Di Fisica*, Bologna, Italy, 2000, p75.
128. 2000, Mizuno, Production of Heat during Plasma Electrolysis in Liquid, *Japanese Journal of Applied Physics*, Vol., 39 (2000) pp 6055-6061.
129. 2000, Storms, Excess Power Production from Platinum Cathodes Using the Pons-Fleischmann Effect, *LENR-CANR.org*, 2000.
130. 2000, Zhang, Measurement of Excess Heat in the Open Pd/D₂O Electrolytic System by the Calvet Calorimetry, *Conference Proceedings*, Vol. 70, ICCF8, F. Scaramuzzi (Ed.) SIF, Bologna, Italy 2000.
131. 2001, Miles et al., Calorimetric Analysis of a Heavy Water Electrolysis Experiment using a Pd-B Alloy Cathode, *Electrochemical Society Proceedings Volume 2001-23*.

132. 2001, Storms, Ways to Initiate a Nuclear Reaction in Solid Environments, APS Meeting, March 15, 2001, Seattle WA.
133. 2002, Castano et al., Calorimetric Measurements During Pd-Ni Thin Film-Cathodes Electrolysis in $\text{Li}_2\text{SO}_4/\text{H}_2\text{O}$ Solution, Ninth International Conference on Cold Fusion, Beijing, China 2002.
134. 2002, Celani et al., Electrochemical D Loading of Palladium Wires by Heavy Ethyl-Alcohol and Water Electrolyte, Related to Ralstonia Bacteria Problematics, Ninth International Conference on Cold Fusion, Beijing, China 2002.
135. 2002, Chicea, On Current Density and Excess Power Density in Electrolysis Experiments, Ninth International Conference on Cold Fusion, Beijing, China 2002.
136. 2002, Del Giudice et al., Production of Excess Enthalpy in the Electrolysis of D_2O on Pd Cathodes, Ninth International Conference on Cold Fusion, Beijing, China 2002.
137. 2002, Fujii et al., Heat Measurement During Light Water Electrolysis Using Pd/Ni Rod Cathodes, Ninth International Conference on Cold Fusion, Beijing, China 2002.
138. 2002, Isobe et al., Search for Multibody Nuclear Reactions in Metal Deuteride Induced with Ion Beam and Electrolysis Methods, Japanese Journal of Applied Physics, Vol. 41(2002) 00. 1546-1556, part 1, No. 3A March 2002.
139. 2002, Kirkinskii et al., Experimental Evidence of Excess Heat Output During Deuterium Sorption-Desorption in Palladium Deuteride, Ninth International Conference on Cold Fusion, Beijing, China 2002.
140. 2002, Luo et al., In-Situ Characterization of Sputtered Pd Thin Films Undergoing Electrolysis, Ninth International Conference on Cold Fusion, Beijing, China 2002.
141. 2002, Miles et al., The Elevation of Boiling Points in H_2O and D_2O Electrolytes, Ninth International Conference on Cold Fusion, Beijing, China 2002.
142. 2002, Miles et al., Thermal Behavior of Polarized Pd/D Electrodes Prepared by Co-Deposition, Ninth International Conference on Cold Fusion, Beijing, China 2002.
143. 2002, Spallone et al., Experimental Studies to Achieve H/Pd Loading ratio Close to 1 in Thin Wires, Using Different Electrolytic Solutions, Ninth International Conference on Cold Fusion, Beijing, China 2002.
144. 2002, Warner et al., Electrolysis of D_2O with Titanium Cathodes: Enhancement of Excess Heat and Further Evidence of Possible Transmutation, LENR-CANR.org.
145. 2002, Zhang et al., Primary Calorimetric Results on Closed Pd/ D_2O Electrolysis Systems by Calvet Calorimetry, Ninth International Conference on Cold Fusion, Beijing, China 2002.
146. 2003, Celani et al., Thermal and Isotopic Anomalies When Pd Cathodes are Electrolyzed in Electrolytes Containing Th-Hg Salts Dissolved at Micro molar Concentrations in $\text{C}_2\text{H}_5\text{OD}/\text{D}_2\text{O}$ Mixtures, Tenth International Conference on Cold Fusion, Cambridge, MA 2003.
147. 2003, Cravens & Letts, Practical Techniques in CF Research - Triggering Methods, Tenth International Conference on Cold Fusion, Cambridge, MA 2003.
148. 2003, Dardik et al., Intensification of Low Energy Nuclear reactions Using Superwave Excitation, Tenth International Conference on Cold fusion, Cambridge, MA 2003.
149. 2003, Letts and Cravens, Laser Stimulation of Deuterated Palladium: Past and Present, Tenth International Conference on Cold fusion, Cambridge, MA 2003.

150. 2003, Miles, Fluidized Bed Experiments Using Platinum and Palladium Particles in Heavy Water, Tenth International Conference on Cold Fusion, Cambridge, MA 2003.
151. 2003, Storms, Use of a Very Sensitive Seebeck Calorimeter to Study the Pons-Fleischmann and Letts Effects, Tenth International Conference on Cold Fusion, Cambridge, MA 2003.
152. 2003, SUN Yue et al., The Crystal Change and “Excess Heat” Produced by Long time Electrolysis of Heavy Water with Titanium Cathode, Chinese Journal of Atomic and Molecular Physics, Vol. 20, No. 1, Jan., 2003.
153. 2003, Szpak et al., Polarized D+/Pd-D₂O System: Hot Spots and Mini-Explosions, Tenth International Conference on Cold Fusion, Cambridge, MA, 2003.
154. 2003, Wei et al., Excess Heat in Heavy Water-Pd/C Catalyst Cathode (Case-Type) Electrolysis at Temperatures near the Boiling Point, Tenth International Conference on Cold fusion, Cambridge, MA 2003.
155. 2004, Apicella et al., Some Recent Results at Enea, Eleventh International Conference on Cold Fusion, Marseille, France 2004.
156. 2004, Dash and Ambadkar, Co-Deposition of Palladium with Hydrogen Isotopes, Eleventh International Conference on Cold Fusion, Marseille, France 2004.
157. 2004, Miles, Electrochemical Calorimetric Studies of Palladium and Palladium Alloys in Heavy Water, NEDO Final Report,
158. 2004, Szpak et al., Thermal Behavior of Polarized Pd/D Electrodes Prepared by Co-Deposition, *Thermochimica Acta* 410 (2004) 101-107,
159. 2005, Dardik, Progress in Electrolysis Experiments at Energetics Technologies, 12th International Conference on CMNS, Yokohama, Japan 2005.
160. 2005, Gimpel, Multi Cell Reactors, WSPC Proceedings, July 2005.
161. 2005, Mizuno and Toriyabe, Anomalous Energy Generation During Conventional Electrolysis, 12th International Conference on CMNS, Yokohama, Japan 2005.
162. 2005, Violante et al., Progress in Excess of Power Experiments with Electrochemical Loading of Deuterium in Palladium, 12th International Conference on CMNS, Yokohama, Japan 2005.
163. 2005, Wang and Dash, Effect of an additive on Thermal Output during Electrolysis of Heavy Water With Palladium Cathode, 12th International Conference on CMNS, Yokohama, Japan 2005.
164. 2005, Zhang et al., Seebeck Envelope Calorimetry With a PD/D₂O+H₂SO₄ Electrolytic Cell, 12 International Conference on CMNS, Yokohama, Japan 2005.
165. 2007, Kozima et al., Precision Measurement of Excess Energy in Electrolytic System Pd/D/H₂SO₄ and Inverse-Power Distribution of Energy Pulses VS. Excess Energy, 13th International Conference on CMNS, Sochi, Russia 2007.
166. 2007, Storms, Anomalous Heat Produced by Electrolysis of Palladium Using a Heavy-Water Electrolyte, Submitted to *Thermochimica Acta*, May 2006, LENR-CANR.org.
167. 2007, Zhang and Dash, Excess Heat Reproducibility and Evidence of Anomalous Elements after Electrolysis in Pd/D₂O+H₂SO₄, 13th International Conference on CMNS, Sochi, Russia 2007.
168. Michael Melich, personal communication, May 2008
169. Rod Johnson, personal communication, May 2008

170. John O'M Bockris, personal communication, June 2008
171. Thomas Grimshaw, personal communication, May 2008
172. 2003, McKubre et al., The Need for Triggering in Cold Fusion Reactions, Tenth International Conference on Cold Fusion, Cambridge, MA, 2003.
173. 2003, Swartz, Photo Induced Excess Heat from Laser-irradiated Electrically Polarized Palladium Cathodes in D₂O, Tenth International Conference on Cold Fusion, Cambridge, MA 2003.
174. 2005, Dardik et al., Progress in Electrolysis Experiments at Energetics Technologies (PowerPoint Slides), in the 12th ICCMNS, Yokohama, Japan, 2005.

Ultrasonically-Excited Electrolysis Experiments at Energetics Technologies

I. Dardik, T. Zilov, H. Branover, A. El-Boher, E. Greenspan, B. Khachaturov, V. Krakov, S. Lesin, A. Shapiro and M. Tsirlin
Energetics Technologies
P.O.Box 3026
Omer Industrial Park
Omer, Israel

Abstract

Three electrolysis cells with built-in ultrasonic transmitters were developed by Energetics Technologies. The ultrasonic transmitters induce cavitation in the electrolyte in the vicinity of the palladium cathode for in-situ cleaning and activation of the cathode surface, generation of dislocations, assistance in loading and excitation of the Pd-D system. The ultrasonically assisted electrolysis cells are described and excess heat generating experiments using these cells are illustrated. All of these experiments used the Dardik's modified SuperWaves to drive the electrolysis. The reproducibility of excess heat generation obtained using the ultrasonically assisted electrolysis experiments approaches 80%, which is the highest of all types of electrolysis experiments performed at Energetics Technologies.

A significant amount of excess heat was generated and a very large Coefficient Of Performance (COP) was obtained in several experiments. The largest excess power obtained is 34 watts; the largest total excess energy is 3.5 MJ; the largest COP achieved is 3000%; and the longest duration of excess heat generation in a single experiment is 40 days. The largest amount of specific excess energy is 27 KeV per Pd or D atom. This is at least three orders of magnitude larger than the specific energy that can be generated by chemical reactions or that can be stored in the cell in the form of mechanical energy. The largest specific power generated is 70 W/g of Pd. For comparison, the average specific power in commercial nuclear fission reactors is between 20 to 50 W/g of uranium.

1. Introduction

The primary near-term objectives of the Energetics Technologies experimental program in the quest for developing commercial cold fusion energy sources are: (1) Improvement of the reproducibility of high power gain and high energy gain excess heat generation, and (2) Extension of the duration of excess heat generation. The program focuses on experiments with electrolytic cells that are driven by SuperWaves. [1-3]. The idea of using SuperWaves to enhance LENR (Low Energy Nuclear Reactions) was proposed by I. Dardik based on his vision of nature described in [4].

Several experimental approaches are being pursued in an attempt of achieving the near-term objectives, including the following:

- Optimization of the SuperWave pattern
- Modification of the cathode surface by special annealing-etching procedures jointly under development with ENEA Frascati and the University of Rome [5]
- Modification of the cathode surface by SuperWave glow discharge etching [3]
- Development of new types of cathodes [3]
- Use of ultrasound cavitation in the electrolyte in the vicinity of the cathode for in-situ cleaning and activation of the cathode surface, generation of dislocations, assistance in loading and inducing excitation in the Pd-D system.

This paper is an overview of the latter approach. The other approaches listed above were reported upon in preceding conferences [1-3]. Successful replication of earlier Energetics Technologies excess heat generating electrolysis experiments were achieved at both the SRI and the ENEA laboratories as reported in reference [6].

A description of the SuperWave principle can be found in previous publications [1-4] and will not be repeated here. Section 2 describes the electrolysis cells with ultrasonic transmitters developed and used by Energetics Technologies. Examples of excess heat generated in ultrasonic excited electrolysis cells are presented in Section 3. That is followed by a discussion, in Section 4, of the functions of the ultrasound cavitation. A summary of high excess heat generation results obtained so far in our experiments is given in Section 5.

2. Electrolysis Cells with Ultrasonic Excitation

Since its early days, Energetics Technologies planned to conduct experiments that combine ultrasonic excitation with electrolysis [1]. The designs of our electrolysis cells with ultrasonic excitation have undergone a number of conceptual variations.

Presently we have three cylindrical electrolysis cells designed to allow ultrasonic cavitation excitation. These cells are immersed in a water bath that incorporates a flow calorimeter. The ultrasonic transmitter or transmitters are located outside of the water bath. The entire system is housed in an incubator that maintains the experimental setup in a tightly regulated ambient temperature. The uncertainty in the determination of the excess heat, P_{ex} , using the calibrated mass-flow calorimeter is approximately 20 mW.

Experimental cells #1 and #2 use an annular piezo ceramic ultrasonic transmitter surrounding the water bath as shown in Fig. 1. The cathode-anode assembly used in these cells is shown in Fig. 2. The cathode is a palladium foil, $60 \times 3.0 \times 0.03$ mm. It is made at Energetics Technologies by rolling a 0.5 or 1.0 mm thick Pd wire. The anode is a helical platinum wire wound around the cathode over a perforated cylinder of Teflon (See Fig. 2).

Cell #3 uses four tubular ultrasonic transmitters located 90 degrees from each other as shown in Figs. 3 and 4. The design of the anodes was modified for this geometrical arrangement, as shown in Fig. 6 (compare with Fig. 2).

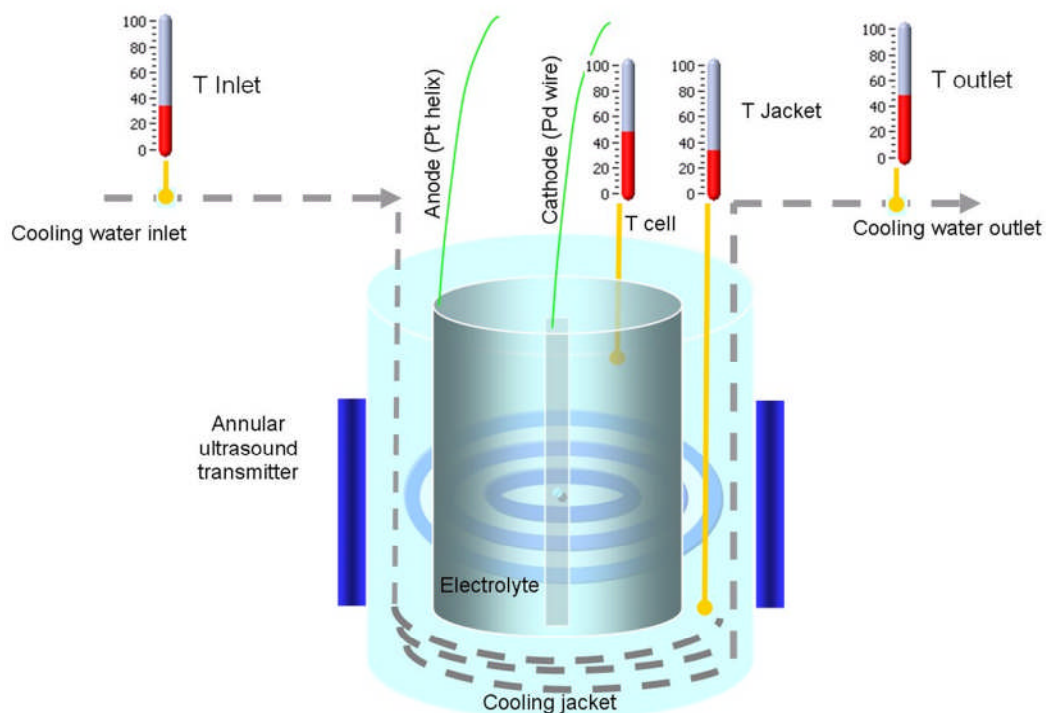


Figure. 1. Schematic of the Energetics Technologies electrolytic cell system with an annular ultrasonic-transmitter; Cells #1 and 2. Flow calorimetry is performed by comparing temperatures T Inlet and T Outlet

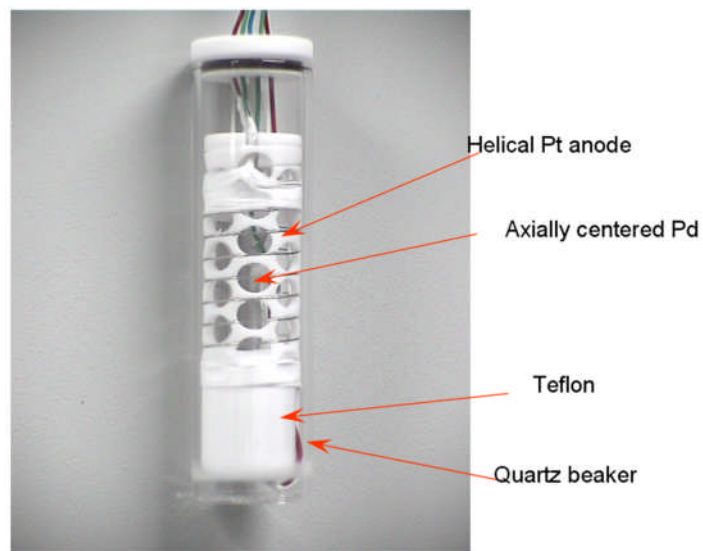


Figure 2. The cathode-anode assembly used in the Energetics Technologies electrolytic cells #1 and #2 that have annular ultrasonic-transmitters

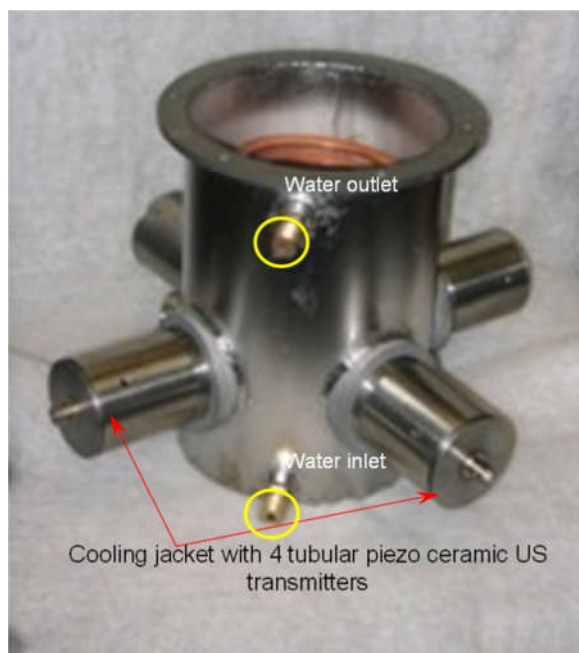


Figure 3. The hardware of the flow calorimeter of Energetics Technologies electrolytic cell #3 that incorporates four tubular ultrasonic transmitters



Figure 4. Energetics Technologies electrolytic cell #3 assembly installed inside a constant temperature incubator.

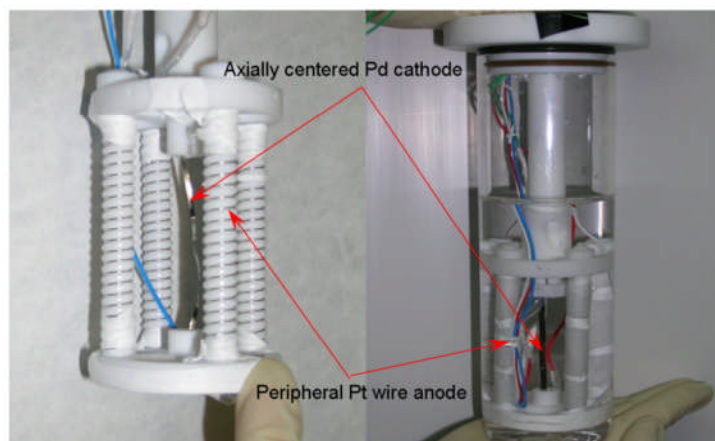


Figure 5. The cathode-anode assembly of Energetics Technologies electrolytic cell #3

The maximum power level and frequencies that the ultrasonic transmitters can operate at in the three electrolytic cells are summarized in Table 1.

Table 1. Characteristics of Energetics Technologies Electrolysis Cells with Ultrasonic Transmitters

Cell #	Type of transmitter	Frequency [KHz]	Max power [W]
1	Ring	16	15
2	Ring	38	15
3	Four tubes	30	60

3. Results

Table 2 gives a statistical summary of the electrolysis experiments performed during 2007 and 2008 using the three ultrasonic excitation electrolysis cells. Seventeen additional experiments failed because of mechanical problems: mainly palladium foil rupture caused by cavitation. The reproducibility of excess heat generation is quite high; it is higher than the reproducibility obtained in our previous electrolysis experiments that did not incorporate ultrasonic cavitation.

Table 2. Summary of Energetics Technologies Electrolysis Experiments Using Ultrasonic Excitation

Cell	Number of experiments	Number producing excess heat	Success rate
1	8	6	75%
2	5	4	80%
3	6	4	67%
Total	19	14	74%

Figures 6 through 11 show examples of excess heat generation measured in electrolysis experiments with ultrasonic excitation. In these experiments, ultrasonic excitation was applied for several periods, each lasting as long as 24 hours, while electrolysis power was continuously applied. The figures show: net input power, P_{inet} – the power delivered to the cell from the

external power supply driving the electrolysis (P_{in}) minus the power consumed for decomposition of heavy water molecules; and P_{out} – the power transferred out from the cell as measured by the calorimeter. The Coefficient Of Performance (COP) is defined as $(P_{out} - P_{in})/P_{in}$.

Figure 6 shows that excess heat started in experiment ETUS3-5 about 5 days after the beginning of the experiment. The vertical pink spikes in the figure are heating effects due to the application of the ultrasonic transmitter and are ignored in the excess-heat analysis. Sometime between day 20 and day 30 of the experiment, the excess heat level was ~ 0.2 W, while the net input energy was ~ 1 W. Around the 31st day, electrolysis was turned off, but excess heat generation continued and even increased up to ~ 0.5 W. This “heat-after-death” lasted for about 4 days, at which time (around the 35th day) the electrolysis current was turned on again. At day 56, after ramping P_{in} up and down in a stepwise manner, P_{in} was turned off again but P_{out} continued for several days at a level of ~ 0.6 watts, before it started dropping. On the 60th day the Pd cathode was replaced with a Pt cathode, following which P_{out} became zero. This proves that our calorimeter was well calibrated. It also proves that the excess heat measured after electrolysis was turned off was, indeed, heat-after-death.

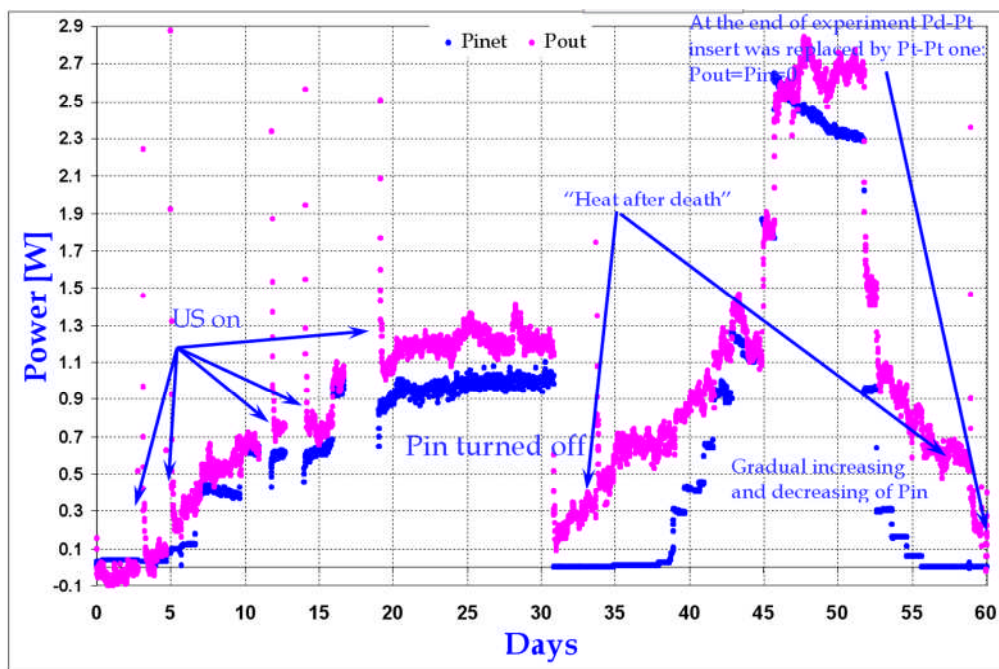


Figure 6. Net input power (P_{in} – in blue) and output power (P_{out} – in violet) in ultrasonically excited electrolysis experiment #ETUS3-5 in cell #3

Figure 7 shows the evolution of P_{in} and P_{out} in experiment #ETUS3-6. The ultrasonic transmitters were turned on 4 times, for 24 hours each time, while the electrolysis power was set at a low P_{in} level of less than 0.2 W. After the first session of ultrasonic excitation the output power gradually dropped to zero. After the second session of ultrasonic excitation P_{out} dropped

to zero and then started increasing. The third session was soon started¹. After the 3rd session of ultrasonic excitation P_{out} dropped to zero at which time the 4th session of ultrasonic excitation was applied. P_{in} dropped to zero, then increased up to ~1 W, and then gradually declined. The duration of excess heat generation was 17 days and the maximum COP exceeded 500%. At about 2,400,000 seconds (approximately 28 days) P_{in} was turned off. Following this P_{out} dropped to zero. Applying P_{in} again did not succeed in reviving the excess heat generation. These last two steps again provide strong evidence that the excess heat recorded earlier in this experiment is real, and not a result of improper calibration.

Similar features are observed in the three additional experimental results shown in Figs. 8 through 10.

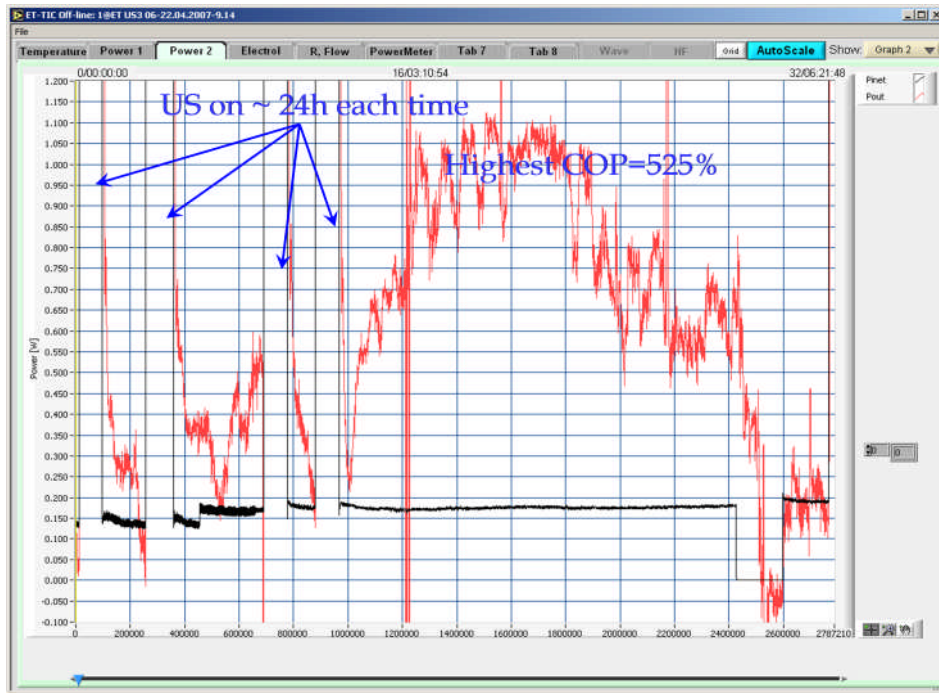


Figure 7. Net input power (P_{in} – in black) and output power (P_{out} – in red) in ultrasonically excited electrolysis experiment #ETUS3-6 in cell #3. Ultrasound (US) was applied in 4 sessions, each lasting about 24 h

¹ In retrospect, it would have been preferable to wait longer before applying the 3rd session.

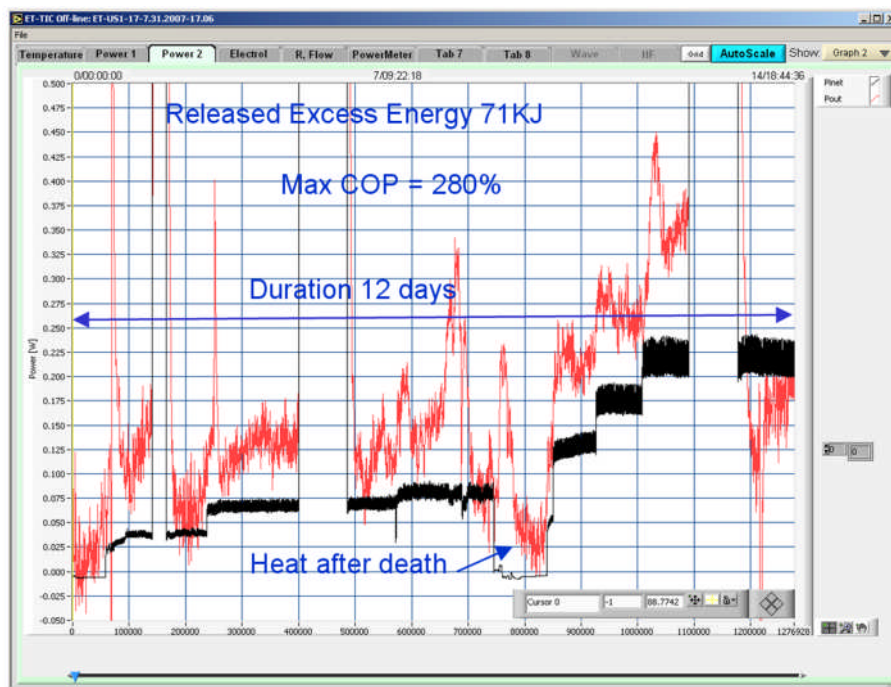


Figure 8. Net input power (Pinet – in black) and output power (Pout – in red) in ultrasonically excited electrolysis experiment #ETUS1-17 in cell #1

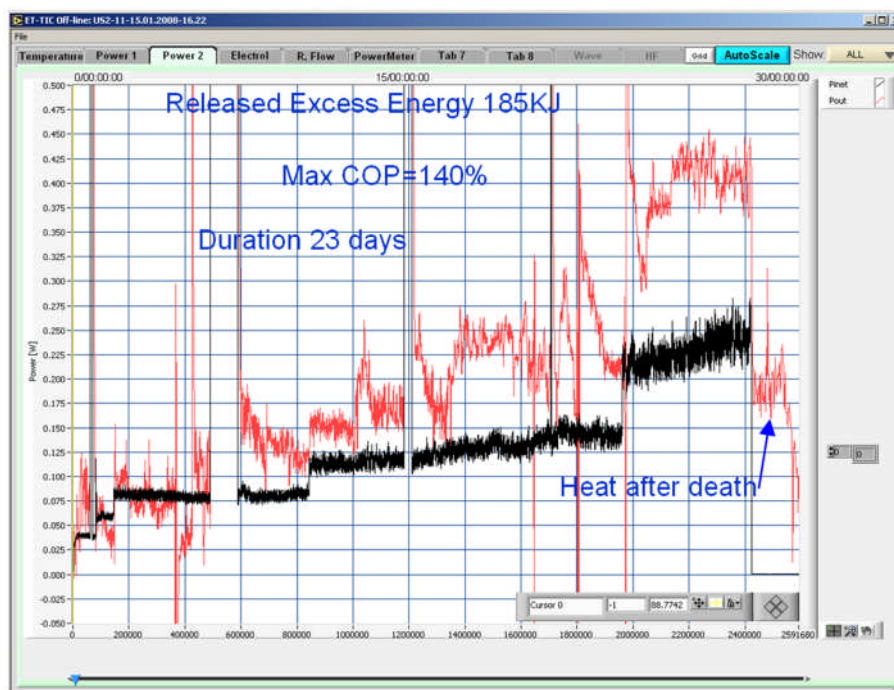


Figure 9. Net input power (Pinet – in black) and output power (Pout – in red) in ultrasonically excited electrolysis experiment #ETUS2-11 using cell #2

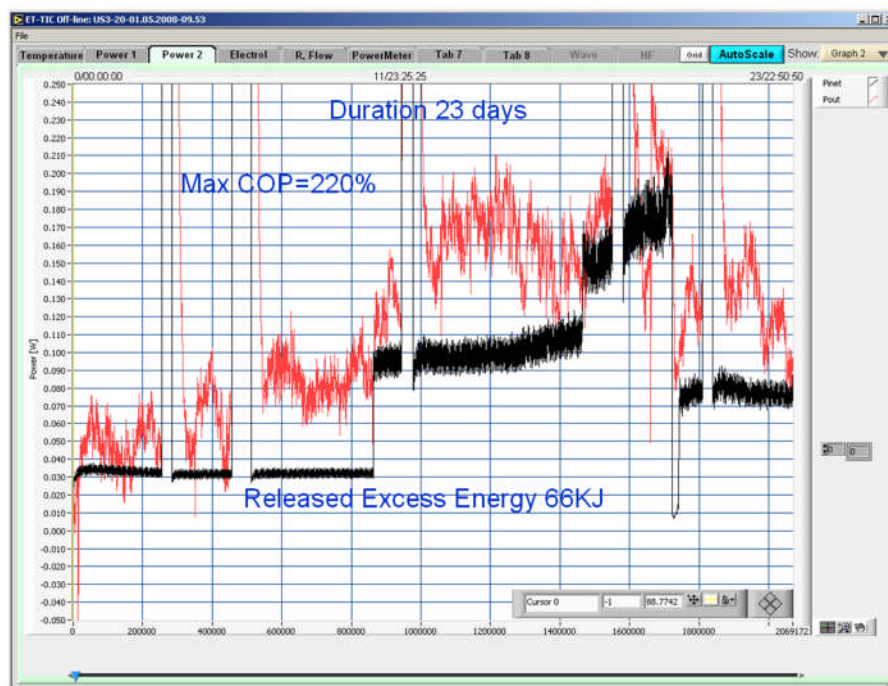


Figure 10. Net input power (Pinet – in black) and output power (Pout – in red) in ultrasonically excited electrolysis experiment #ETUS3-20 using cell #3

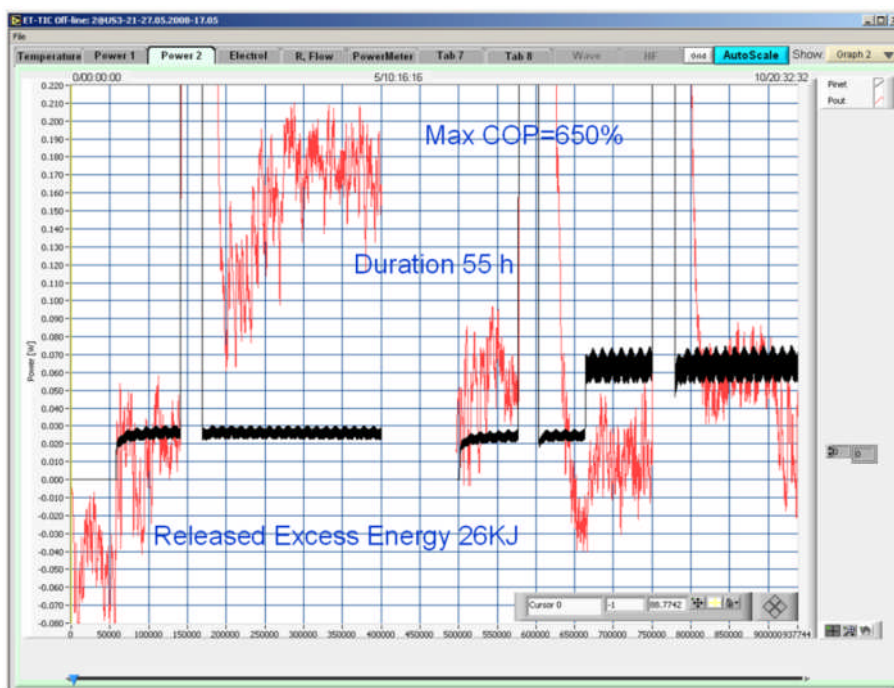


Figure 11. Net input power (Pinet – in black) and output power (Pout – in red) in ultrasonically excited electrolysis experiment #ETUS3-21 using cell #3

4. Unique Characteristics of Ultrasonic Excited Electrolysis

Unique characteristics of ultrasonic excited electrolysis experiments include the following:

- Very high deuterium loadings ($D/Pd > 0.95$) is achieved, while applying low current density
- The deuterium stays in the palladium a long time after shutdown (the β phase is stable)
- Sub-micron sized pits are found on the surface of palladium cathode, in high density
- Craters with signs of melting (and some craters without melting) are found on the surface of the palladium cathodes

A comparison between Figs. 12 - 14 and Figs. 15 and 16 illustrate the fact that the application of ultrasonic cavitation, together with the application of SuperWaves electrolysis, enables very high deuterium loading using exceptionally low current densities. This remarkable increase in the deuterium loading may be attributed to the following phenomena induced by cavitation:

- Cleaning various deposits from the cathode surface
- Activating the cathode surface
- Increasing the cathode effective surface area

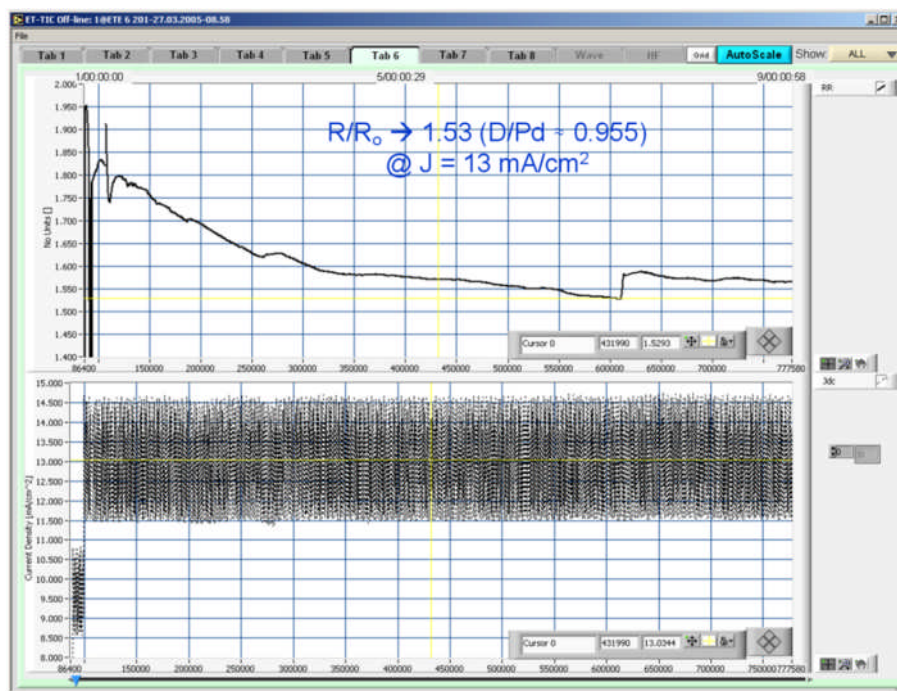


Figure 12. Very high D loading in Pd is obtained in ultrasonically excited electrolysis when driven with low current density – example 1

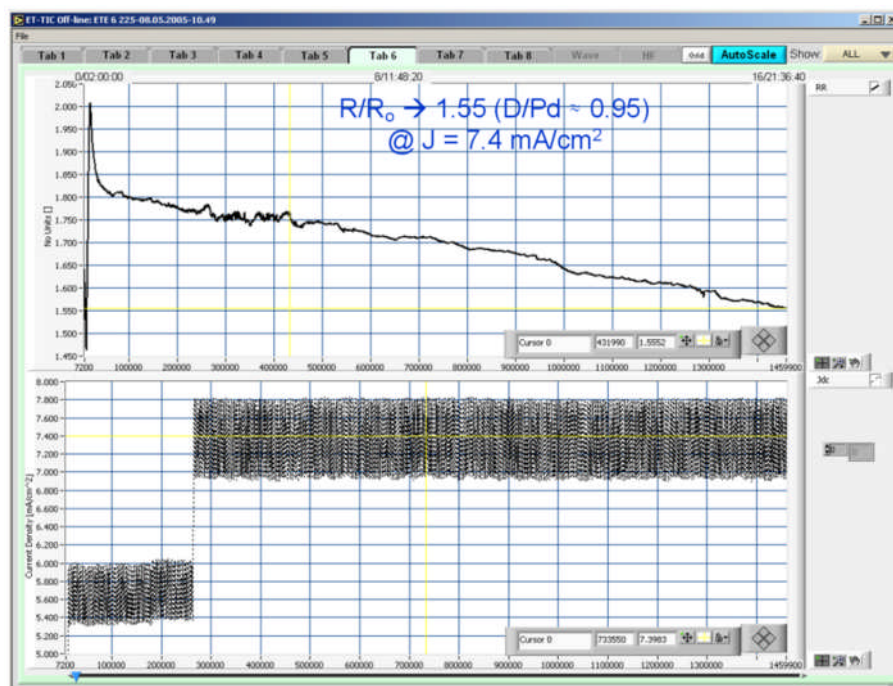


Figure 13. Very high D loading in Pd is obtained in ultrasonically excited electrolysis when driven with low current density – example 2

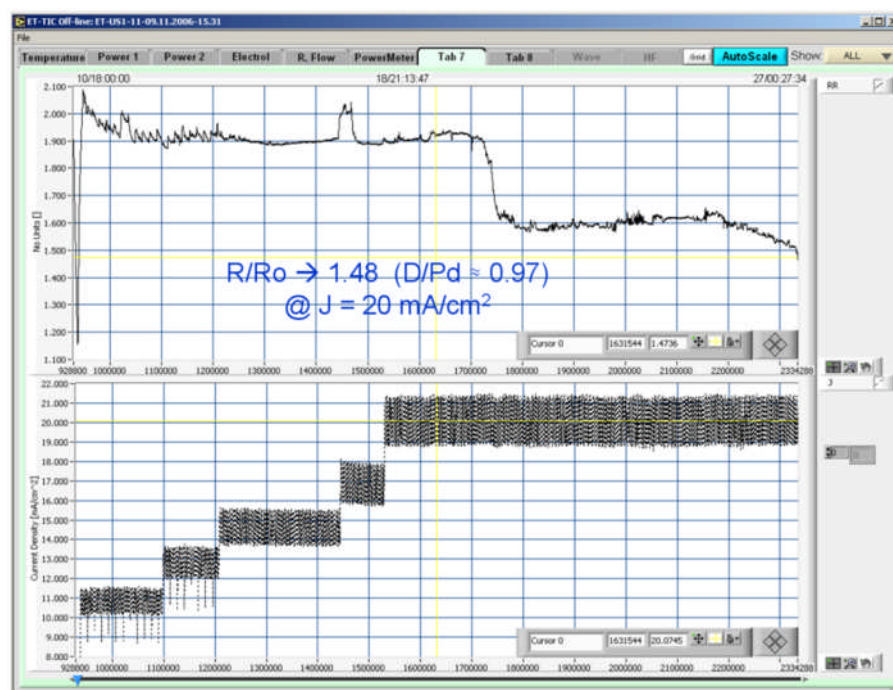


Figure 14. Very high D loading in Pd is obtained in ultrasonically excited electrolysis when driven with low current density – example 3

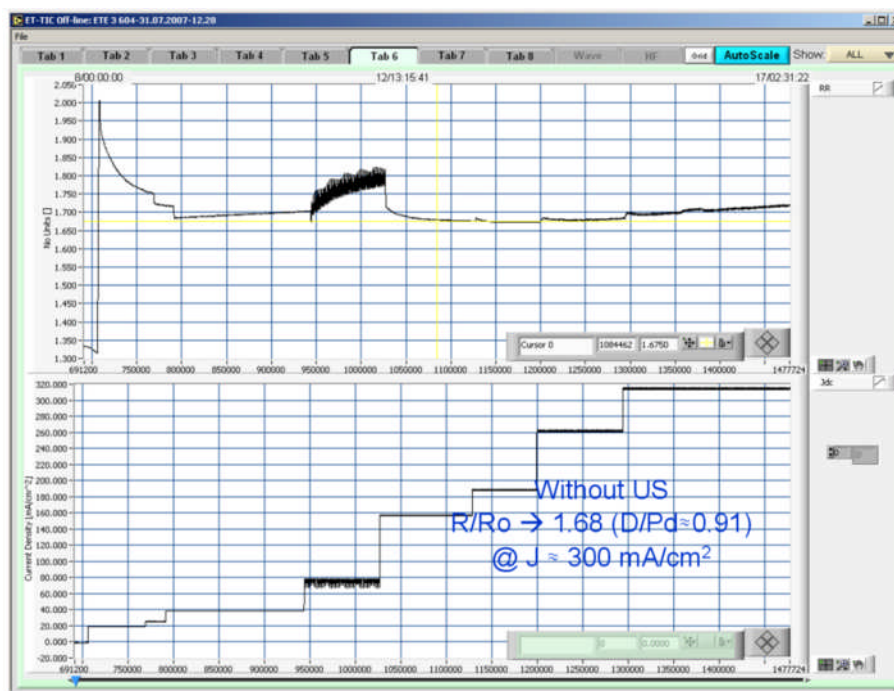


Figure 15. D loading in Pd without ultrasonically excited electrolysis experiment is lower even at significantly higher current density – example 1

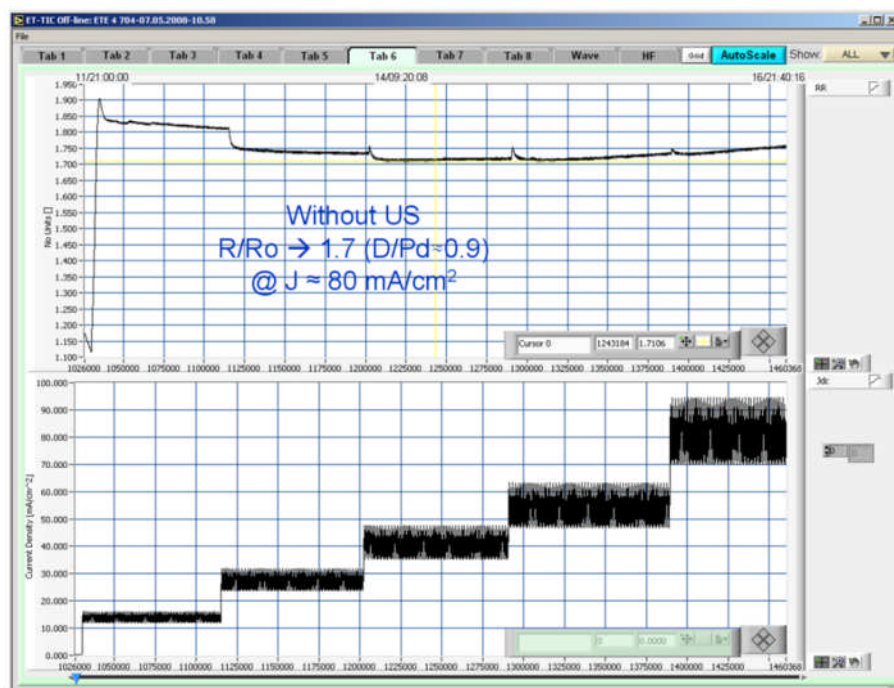


Figure 16. D loading in Pd without ultrasonically excited electrolysis experiment is lower even at significantly higher current density – example 2

Figure 17 compares the rate of deuterium desorption from two Pd cathodes after turning electrolysis off. The sample in the top plot was subjected to ultrasonic excitation, while the sample in the bottom plot was not. The difference is remarkable. Note that from the time the Pd foil was removed from the cell to the beginning of the X-Ray diffraction analysis used to measure the D/Pd atom ratio, the D/Pd ratio in the palladium foil in the bottom plot dropped from more than 0.9 to ~0.4, while the D/Pd ratio in top plot (palladium foil exposed to ultrasonic cavitation) remained close to 1.0. During the D/Pd analysis period, the rate of desorption from the palladium foil that was exposed to cavitation is far slower: the β phase appears to be stable for over 100 days. This unique phenomenon may be due to the formation, by cavitation, of a high concentration of defects in the palladium. These defects can act as potential deuterium traps causing slow deuterium desorption.

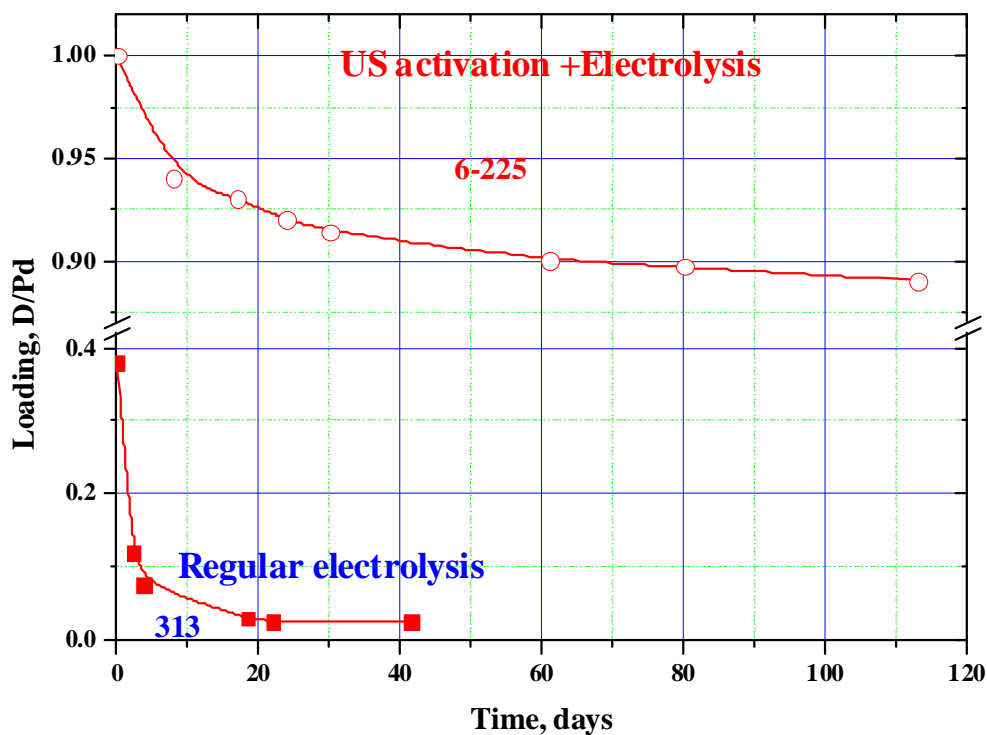


Figure 17. Rate of deuterium desorption from a Pd cathode that was subjected to ultrasonic cavitation (“US activation”) (top), versus a Pd cathode that was subjected regular electrolysis (bottom)

Figure 18 compares the surface of the Pd cathode after ultrasonic assisted electrolysis experiment #ETUS3-6 (left) with the surface of the cathode of electrolysis experiment #64 (right) that was not exposed to ultrasonic cavitation. The morphology of the two cathodes is very different. The cavitation introduces considerable changes in the structure of the Pd surface. Regular electrolysis (right) produces a structure consisting of slip bands formed in the course of plastic deformation of the palladium, due to deuterium absorption and resulting lattice expansion. Cavitation plus electrolysis (left) leads to the formation of a cellular structure. This

effect results in activation of a surface and creates a high concentration of defects – potential deuterium traps.

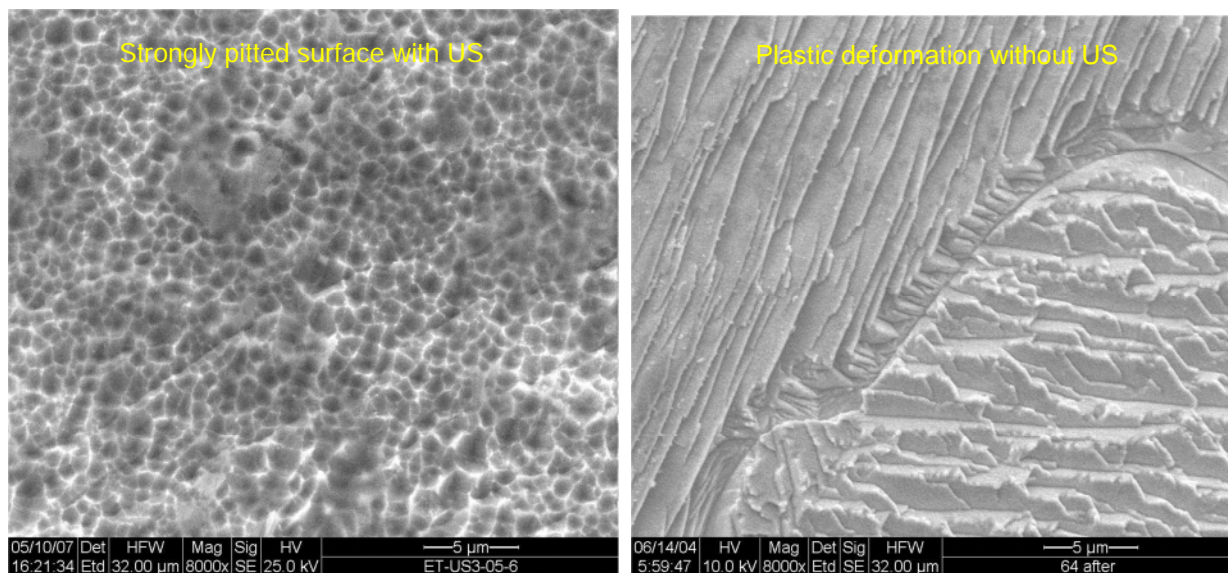


Figure 18. Comparison of Pd cathode surface after experiment ETUS3-6 (left) and ETE-64 (right; no ultrasonic) – both gave excess heat. Secondary electron microscope image magnification of x8000

Craters of various shapes and dimensions were formed on the surfaces of several of the palladium cathodes subjected to ultrasonic excited electrolysis. Figure 19 shows samples. Some of the craters show clear signs of palladium melting on and near the surface. The craters are typically several microns in diameter and several microns deep.

Consider, for example, the crater at the top center of Fig. 19. It is ~4 microns in diameter and ~6 microns deep. The amount of energy required to melt the mass of palladium from this crater (ignoring heat losses via conduction to the surrounding palladium and to the electrolyte) is on the order of 0.1 milli-Joules. This is many orders of magnitude smaller than the measured excess heat, which was on the order of tens to thousands of kilojoules. Remember, though, that the palladium is in direct contact with the electrolyte, and the heat transfer rate from the palladium to the electrolyte should be very high. So it is surprising that some spots in the cathode even reach the melting point of Pd (1554°C).

The craters identified so far have been found in a very small fraction of the total cathode surface that can be scanned using a SEM. Better diagnostics will be needed to obtain statistically significant information on the number and types of craters, and their spatial distribution.

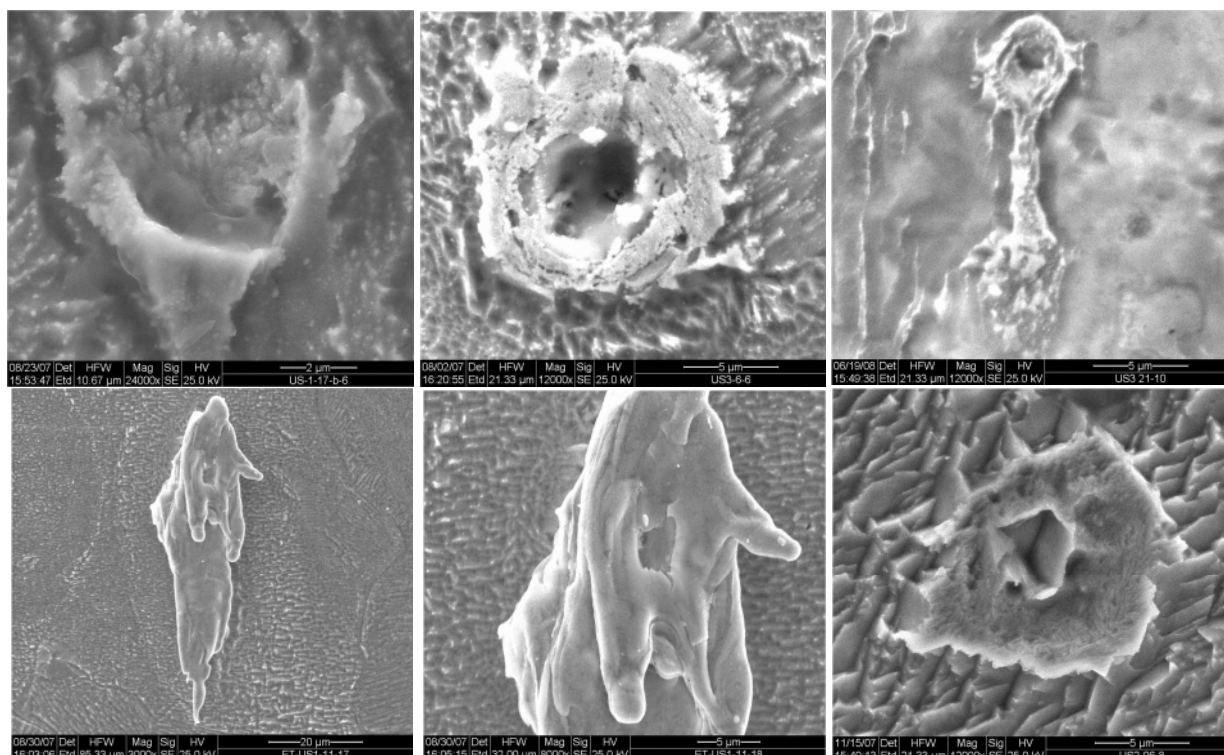


Figure 19. Example of craters found on the surface of palladium cathodes that were subjected to electrolysis with intermittent application of ultrasound cavitation.

5. Summary of Best Excess Heat Generating Experiments at Energetics Technologies

Table 3 summarizes selected performance characteristics of the eight electrolysis experiments that so far generated the largest amount of excess power, P_x (previously referred to as excess heat), or excess energy, E_x . The average “specific excess power,” given in watts per gram of palladium that was exposed to the electrolyte, is a measure of the utilization effectiveness of the palladium. The largest average specific excess power obtained so far – nearly 70 W/g of Pd, is even higher than the typical specific power in commercial fission reactors – 20 to 50 Watts per gram of uranium. The “specific excess energy,” expressed in kilo-electron-volt generated per palladium atom or per deuterium atom in the cathode (the ratio of D to Pd atoms in the cathode is nearly 1), is an indicator of whether or not the excess heat could be chemical or mechanical (stored energy) in origin.

The maximum specific excess energy obtained in our electrolysis experiment is over 20 KeV per Pd or D atom. This is to be compared with heat of desorption of D from the Pd lattice of ~ 0.3 eV per D atom; heat of D oxidation of ~ 1.3 eV per D atom; heat of molarization of ~ 2.2 eV per D atom; heat of melting (an upper bound on the possible mechanical energy storage in the Pd lattice) of ~ 0.2 eV per Pd atom and heat of evaporation of Pd of ~ 4 eV per Pd atom. All of these are three to four orders of magnitude smaller than the specific excess energy measured.

This provides a strong yet indirect indication that the excess energy generated in the experiments reported above is, indeed, of nuclear origin.

Table 3. Selected Characteristics of the Eight Energetics Technologies (ET) Electrolysis Experiments that Generated Largest Amount of Excess Power or Excess Energy. The highest value in each row is highlighted.

Experiment	56	64a	64b	GD-141	US1-15	US3-05	US3-06	US3-21
Cathode source	ENEa	ENEa	ENEa	ET	ET	ET	ET	ET
Excess energy (MJ)	3.1	1.1	>3.5	2.4	0.19	1.1	1.32	0.026
Maximum excess power (W)	3.6	34	32	14	0.25	0.7	0.9	0.165
Maximum COP (%)	80	2500	>1500	75	600	3000	525	650
Duration of excess power (hr)	300	17	80	90	280	960	445	55
Average excess power (W)	2.9	18	> 11	7.5	0.19	0.3	0.82	0.13
Average specific excess power (W/gm Pd)	11	71	>43	29	4	6	15	24
Specific excess energy (KeV/Pd atom)	13	5	>15	11	4	22	27	13

6. Conclusions

In-cell exposure of palladium cathodes to ultrasound cavitation, combined with SuperWave electric current driven electrolysis, was found to enable remarkably high deuterium loading with surprisingly low current density. The rate of deuterium desorption from palladium cathodes removed from ultrasonic-assisted electrolysis cells was found to be remarkably slow: the palladium remained in beta phase loading for many days. The outer layer of palladium foils exposed to ultrasonic cavitation experiences a large plastic deformation that is characterized by a highly pitted rough surface. Craters showing clear signs of palladium melting were found on palladium cathodes that underwent ultrasonic excitation during electrolysis. Better diagnostics will be required to analyze these craters.

The most reproducible excess heat generation of all experiments performed so far at Energetics Technologies has been obtained with ultrasonic excitation. Several episodes of “heat-after-death” were observed during some of the ultrasonically excited experiments. It is necessary to optimize the application of the ultrasound to minimize the energy needed to generate the cavitation versus the amount of excess energy generated. The mechanism by which ultrasonic excitation intensifies the excess heat also needs to be thoroughly investigated.

Significant amounts of excess power and excess energy were generated and very large Coefficient Of Performance (COP) were obtained in several of Energetics Technologies experiments. The best performance parameters obtained so far are:

- Excess energy 3.5 MJ
- Excess power 34 W
- COP 3000%
- Duration 40 days
- Specific energy 27 KeV per Pd or D atom
- Specific power 70 W/g Pd

The latter can be appreciated when compared against the 20 to 50 W/g of uranium that is achieved in large commercial fission power reactors.

Acknowledgment

This work was funded by Mr. Sidney Kimmel.

References

1. I. Dardik, H. Branover, A. El-Boher, D. Gazit, E. Golbreich, E. Greenspan, A. Kapusta, B. Khachaturov, V. Krakov, S. Lesin, B. Michailovitch, G. Shani And T. Zilov, "Intensification of Low Energy Nuclear Reactions Using SuperWaves Excitation," Proc. of the Tenth International Conference on Cold Fusion ICCF-10, Cambridge, MA, August 2003.
2. I. Dardik, T. Zilov, H. Branover, A. El-Boher, E. Greenspan, B. Khachaturov, V. Krakov, S. Lesin and M. Tsirlin, "Excess Heat in Electrolysis Experiments at Energetics Technologies," Presented at the 11th International Conference on Cold Fusion, ICCF-11, Marseilles, France, November 1 - 6, 2004.
3. I. Dardik, "SuperWaves Reality," Proc. of the Tenth International Conference on Cold Fusion ICCF-10, Cambridge, MA, August 2003.
4. I. Dardik, T. Zilov, H. Branover, A. El-Boher, E. Greenspan, B. Khachaturov, V. Krakov, S. Lesin, A. Shapiro and M. Tsirlin, "Report on Electrolysis Experiments at Energetics Technologies," Proc. of the 13th International Conference on Cold Fusion ICCF-13, Sochi, Russia, June 25-July 1, 2007.
5. V. Violante, F. Sarto, E. Castagna, C. Sibilia, M. Bertolotti, R. Li Voti, G. Leahu, M. McKubre, F. Tanzella, K. Grabowski, G. Hubler, D. Knies, T. Zilov and I. Dardik, "Calorimetric Results of ENEA Cooperative Experiments," Proc. of the 13th International Conference on Cold Fusion ICCF-13, Sochi, Russia, June 25-July 1, 2007.
6. M. C. H. McKubre, F. L. Tanzella, I. Dardik, A. El Boher, T. Zilov, E. Greenspan, C. Sibilia and V. Violante. "Replication of Condensed Matter Heat Production," in American Chemical Society Low Energy Nuclear Reactions Sourcebook, Oxford University Press, August 2008.

Excess Power Gain using High Impedance and Codepositional LANR Devices Monitored by Calorimetry, Heat Flow, and Paired Stirling Engines

Mitchell Swartz
JET Energy, Inc. Wellesley, MA 02481 (USA)

Dr. Mitchell Swartz does not wish to have his papers uploaded to LENR-CANR.org. A copy of this paper can be found here:

<http://www.iscmns.org/iccf14/ProcICCF14a.pdf>

This page intentionally left blank

This page intentionally left blank

This page intentionally left blank

This page intentionally left blank

This page intentionally left blank

This page intentionally left blank

This page intentionally left blank

This page intentionally left blank

This page intentionally left blank

This page intentionally left blank

This page intentionally left blank

This page intentionally left blank

This page intentionally left blank

This page intentionally left blank

This page intentionally left blank

This page intentionally left blank

This page intentionally left blank

This page intentionally left blank

This page intentionally left blank

This page intentionally left blank

This page intentionally left blank

This page intentionally left blank

This page intentionally left blank

Anomalous Heat Generation during Hydrogenation of Carbon (Phenanthrene)

Tadahiko Mizuno¹ and Shigemi Sawada²

¹ *Graduate School of Engineering, Hokkaido University*

Division of Energy Environment

Kita-ku Kita 13 Nishi 8, Sapporo 060-8628, Japan

² *Sequence Co. Ltd, Yamanote 1-22-11, Hakodate 041-0836 Japan.*

Abstract

When phenanthrene (a heavy oil fraction) is subjected to high pressure and heat in a reactor with a metal catalyzer, it produces a markedly anomalous reaction. It produces excess heat and weak radiation, specifically x-rays and gamma-rays. Furthermore, after the reaction finishes, mass spectroscopy reveals what appears to be ^{13}C . It is very difficult to explain the total energy generation as a conventional chemical reaction. After the experiment, almost all phenanthrene and hydrogen gas remains in the same condition they were initially. There are few reaction products such as other chemical compounds. However, the formation enthalpies for these compounds are all negative. The heat generation sometimes reaches 0.1 kW and has continued for several hours. There is a reasonably significant correspondence between the heat generation and the gamma emission. We have confirmed the same result with high reproducibility by controlling temperature and pressure.

1. Introduction

In 1989, Fleischmann and Pons ⁽¹⁾ reported that palladium electrolyzed in heavy water produces the anomalous heat generation reaction (the cold fusion reaction). Reproducibility and control of the reaction have been difficult, and although many researchers attempted to replicate, most failed. If we assume the reaction is some form of a normal d-d reaction, there should be a much higher neutron flux. However, there are few reports of the neutron observations ⁽²⁻⁸⁾. The authors have examined many of the reports of neutrons and have reached the following conclusions:

- First, neutrons and excess heat are rarely observed, but when they are observed, they occur suddenly after electrolysis or discharge have continued for a long time.
- Second, many instances have been reported in which these effects began when some triggering reaction occurred.
- Third, almost all cold fusion experiments have been performed by absorbing the deuterium into the reaction system at first; the electrolyte contains almost pure deuterium gas.

Based on these considerations, we conclude that the cold fusion reaction must be something quite different from conventional d-d fusion. Furthermore, the reaction must involve factors other than absorption of deuterium. After electrolysis has continued for a long time and the deuterium has been replenished, some trigger is likely to occur. We predict that certain triggers are needed to give rise to the reaction.

Many people have asserted that if nuclear reactions are induced by electrochemical reactions using solid electrodes there should also appear clear evidence of the generation of radioisotopes and radiation. Moreover, the evolution rates of reaction products should be quantitatively explained in terms of well-established nuclear reaction mechanisms. These expectations would be valid only if the reaction mechanism is in accord with accepted nuclear theory. There is little reason to believe that is the case.

Mizuno⁽⁹⁾, Miley⁽¹⁰⁾, Ohmori⁽¹¹⁾, Iwamura⁽¹²⁾ and others have reported anomalous production of radiation-less foreign elements (Fe, Cr, Ti, Ca, Cu, Zn, Si and so on) on cathode metals (mainly Pd) with heavy water or light water electrolysis experiments. These elements sometimes have drastically non-natural isotopic ratios. These reports present evidence that a nuclear reaction takes place during electrolysis that produces isotopically changed elements on the cathode surface. These elements are generated by a mechanism that does not induce any detectable radiation. The anomalous isotopic abundances of these elements show that they do not come from contamination. Again, the operative nuclear mechanism appears to be completely different from any known nuclear reaction. Whatever it is, if it can be controlled, it appears likely to probably produce tremendous amounts of energy.

The hydrogenation of hydrocarbons has been studied for decades. Song et al.⁽¹³⁾ examined the hydrogenation reaction of naphthalene using zeorite supported Pd and Pt catalysts at low temperatures. In particular, they investigated the effect of the catalyst poisoned by sulfur. Fedorynska et al.⁽¹⁴⁾ studied the H₂ transfer reaction between phenanthrene and H₂ in the presence of K/MgO from 250°C to 350°C. Durland et al.⁽¹⁵⁾ tested the hydrogenation of phenanthrene by Raney Ni and CuCrO from 370 K to 573 K. Burger et al.⁽¹⁶⁾ performed pioneering work of the hydrogenation of phenanthrene at ~227°C under 136 to 218 atm of hydrogen gas, which is considered high pressure by the standards of this field. Qian et al.⁽¹⁷⁾ used an alumina supported Pt and Pd catalyst for the hydrogenation of phenanthrene, and they obtained a very high conversion rate, up to 100%. Mahdavi et al.⁽¹⁸⁻²¹⁾ and Menini et al.⁽²²⁾ developed another technique of electrocatalytic hydrogenation that showed a comparably high conversion rate. This study was stimulated by Soejima's research circa 1930 into methods of changing coal to oil by a liquefying reaction. Soejima observed abnormal heat generation during hydrogenation of creosote oil heated in high pressure hydrogen gas. The heat generated was larger than the largest estimated chemical reaction that can occur with few drop of creosote and a little hydrogen gas. Soejima concluded that it could not have come from a conventional chemical reaction.

2. Experimental

2.1 reaction cell

Figure 1 shows a photograph of the two reaction cells used in this study, and experimental setup. The reactors are the cylinders shown in the left side of Fig. 1. The large one is made from Inconel 625. It has a 56 mm outer diameter, 26 mm inner diameter, 160 mm height and the volume is 0.1 L. The smaller one is made from SUS316L, with a 15 mm outer diameter, 9 mm inner diameter and 300 mm height with 0.02 L capacity. The Inconel cylinder can sustain 500 atm of pressure, while the SUS cylinder is limited to less than 200 atm. Both can be heated up to 850°C.

Each cylinder has a hydrogen inlet, gas outlet, and housing for a thermocouple used to measure the internal cell temperature. The cylinder is placed in an electric furnace. A thermocouple to measure the temperature of the outside wall of the reactor cylinder is inserted between the reactor wall and the inner wall of the heater.

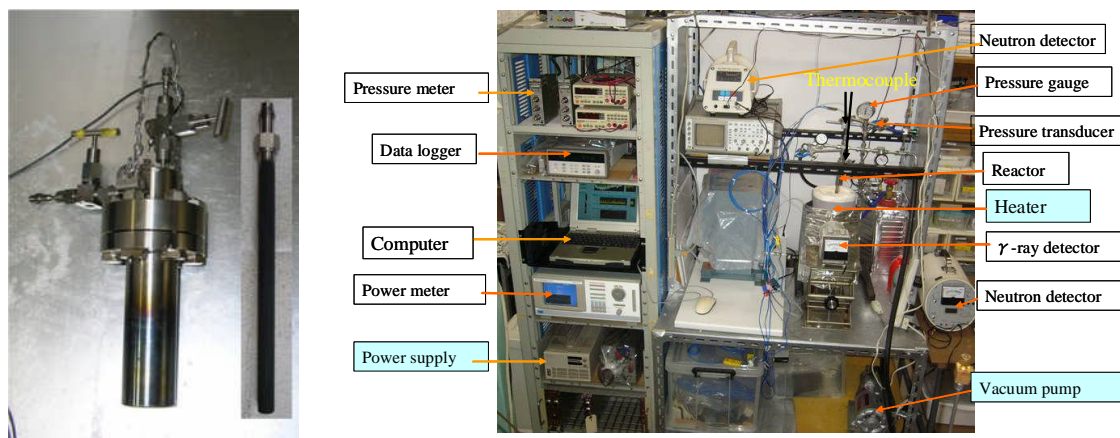


Figure 1. Cell and experimental setup.

2.2 Measurement system

Figure 2 shows a schematic drawing of the measurement setup. The reaction cylinder placed in the heater is shown in gray. An electric power supply is shown in the bottom right, connected to a data logger and recorder.

After the metal catalyzer is put in the reaction container, a few grams of phenanthrene are placed in the cell, and the cover is bolted tightly shut. The reactor is then evacuated to 10^{-3} mmHg. Hydrogen gas is supplied from the gas cylinder up to a constant pressure through a pressure regulator. The electric furnace (Tokyo Technical Lab.: PH, Mo13763A1) was supplied by a 2 kW of power supply. The temperature inside the reactor and the temperature between the reactor and the furnace are continuously measured by R-type thermocouples.

Gamma-ray emission was detected by a detector (Aloka TCS-161) set 15 cm from the reactor, and continuously recorded by a digital multi-meter (Advantest, TR-6845). Temperatures of the heater wire, in the reactor, out of the reactor wall, surface of the gamma detector, and the room were also recorded in the computer through the multimeter.

The mass spectrometer used in this study (ULVAC REGA201) can detect mass numbers up to 400.

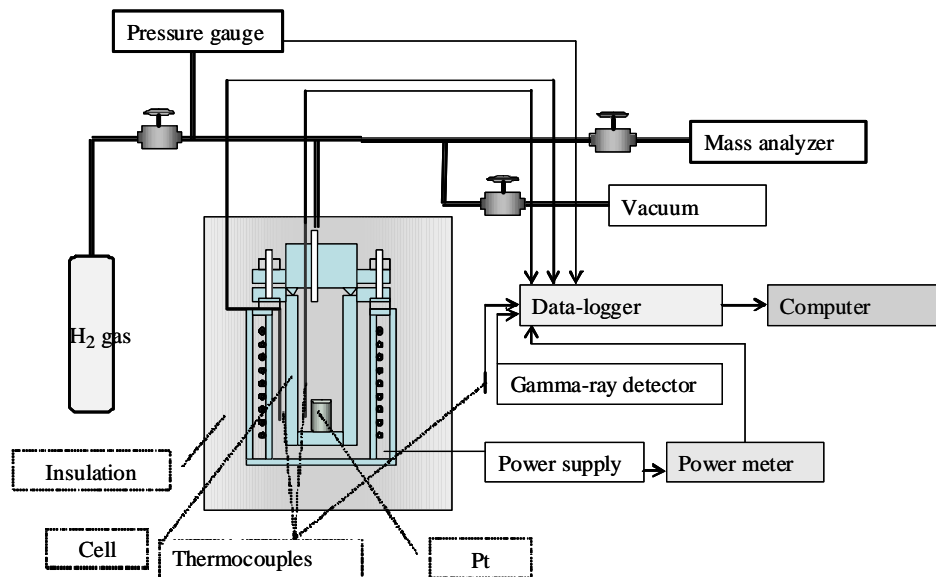


Figure 2. Schematic drawing of the measurement setup.

2.3 Experimental procedures

The fluorescent grade (99.5%) of phenanthrene was supplied by Kanto Chemical Co. LTD. The Pt catalyzer was a high purity Pt mesh (99.99%) supplied by Tanaka Noble Metal Co. LTD. It is rectangular, 5 cm × 10 cm, 50 g. At the beginning of this series of experiments, the Pt catalyzer was activated once in an atmosphere of hydrogen gas for 100 ks at 850°C. When the Pt catalyzer was inactive, it was prepared by oxidizing it in air with an electric heater at 850°C for one hour. As noted, 1 g of phenanthrene and the Pt catalyzer were put in the reactor; the reactor lid was bolted shut. The reactor was connected to the vacuum system and pumped out. The exhaust valve was left open for several minutes to remove residual air. Then the exhaust valve was closed, and hydrogen gas was supplied. The reactor was then heated.

Calibrations for temperature and radiation emission were performed by changing the hydrogen gas pressure from vacuum to 80 atmospheres. The gamma detectors were calibrated by a 3.7×10^5 Bq source of ^{226}Ra that was set at various distances from the detectors, and in the reactor cylinder. The background level of the surroundings was 0.05 ± 0.008 $\mu\text{Sv/h}$.

3. Results

3.1 temperature calibration

We can estimate the anomalous heat caused from the calibration curve obtained from the relationship between input power and the stable temperature of the reactor cylinder.

Figure 3 shows a calibration with the Inconel cell. In this case, a platinum catalyst was placed in the cell, and hydrogen pressure was raised to 50 atm, but there was no phenanthrene in the

cell. The heater was turned on and set to 65 W, and the temperatures at the heater, the cell wall and inside the cell were measured, along with the cell gas pressure. When the heater was turned on, heater temperature rose rapidly at first, followed by the temperature at the cell wall and, after a lag, the temperature inside the cell. After 10 ks the temperature inside the cell drew even with the temperature at the cell wall, and after that the two remained the same as they continued to increase. The cell temperature was never higher than the cell wall temperature. After 15 ks both temperatures reached the same, stable value. In the example shown here, the final temperature inside the cell, at the cell wall and at the heater were all 140°C hotter than the ambient room temperature. The final temperature depends upon various factors such as the heater power, hydrogen pressure, whether or not the phenanthrene or the catalyst are present in the cell, and the size and type of cell selected.

Figure 4 shows the relationship between input power of the heater and the temperature in the reactors. The data was taken under varying conditions of pressure and temperature, with phenanthrene and an inactivated metal catalyzer. Each point represents the final stable temperature achieved when a power setting is maintained; that is, the temperature difference between the reactor and the room. The cell takes about 5 ks (83 minutes) to reach the set temperature with constant input power. The graph shows log-log relationship between the input and the temperature at various hydrogen pressures. The relationship varies with hydrogen gas pressure. The heat conductivity for the gas is nearly constant over a wide range of pressure, from 10^{-3} atm to 10 atm. However, the stable temperatures for each input are decreased at high pressure of H_2 , indicating that the gas conductivity increases at more than 10 atm.

The calibration curve derived for the Inconel reactor showed a similar relationship, with the same slope but ten times different input power per degree of temperature. The heat release caused by gas in the reactor is not significant with the Inconel reactor: the temperature deviation stays within $\pm 3^\circ\text{C}$ while the hydrogen gas pressure increased from 1 to 100 atm. Because the Inconel reactor height is 160 mm, the walls of the reactor fit inside the heater envelope (which is 220 mm deep), although the top surface is exposed to air. The SUS reactor has a small diameter and it is longer; 300 mm, so the top 80 mm of the reactor walls protrudes. Some heat release from the exposed portions of the reactors occurs.

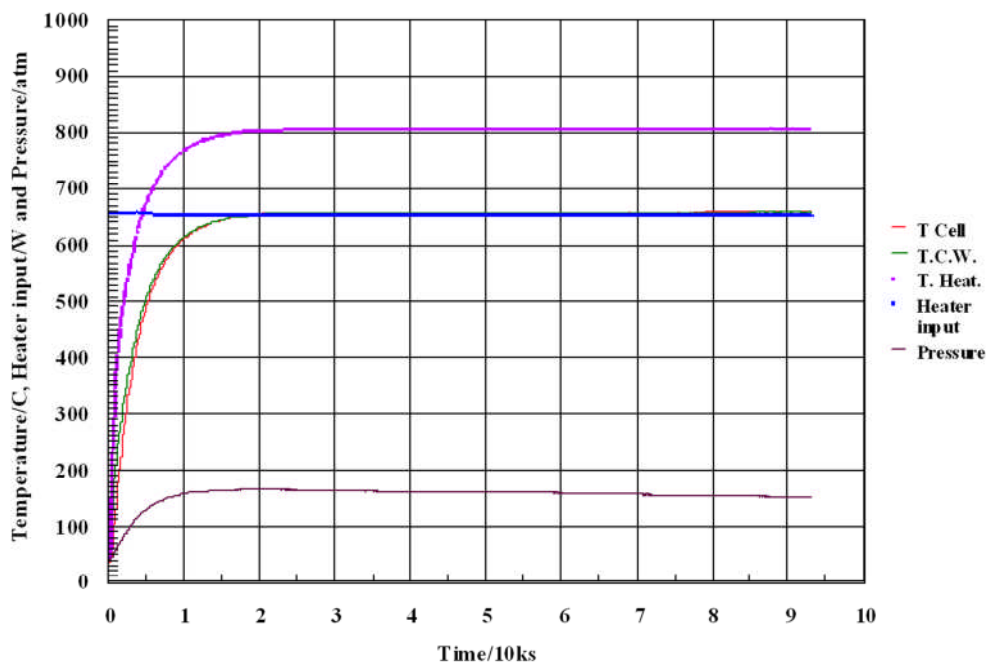


Figure 3. Temperature, pressure and heater power with the Inconel reactor at 650 W input and H₂ at 50 atm with no phenanthrene sample. Three temperatures are measured in this test: inside the cell (T cell) at the cell wall (T.C.W), and at the heater (T. Heat.).

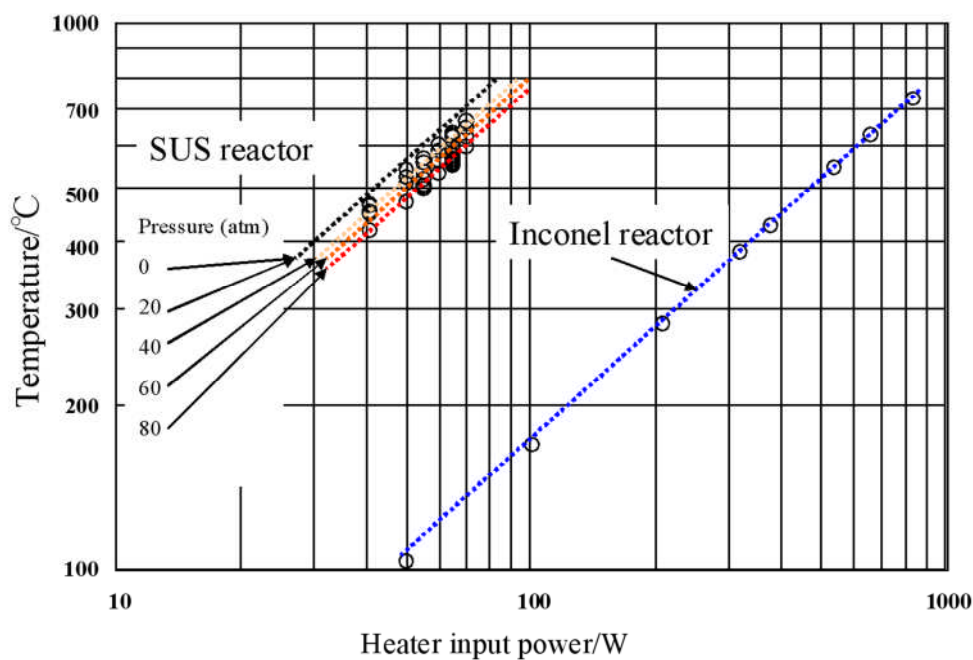


Figure 4. Heater input dependence of reactor temperature at various H₂ pressure settings.

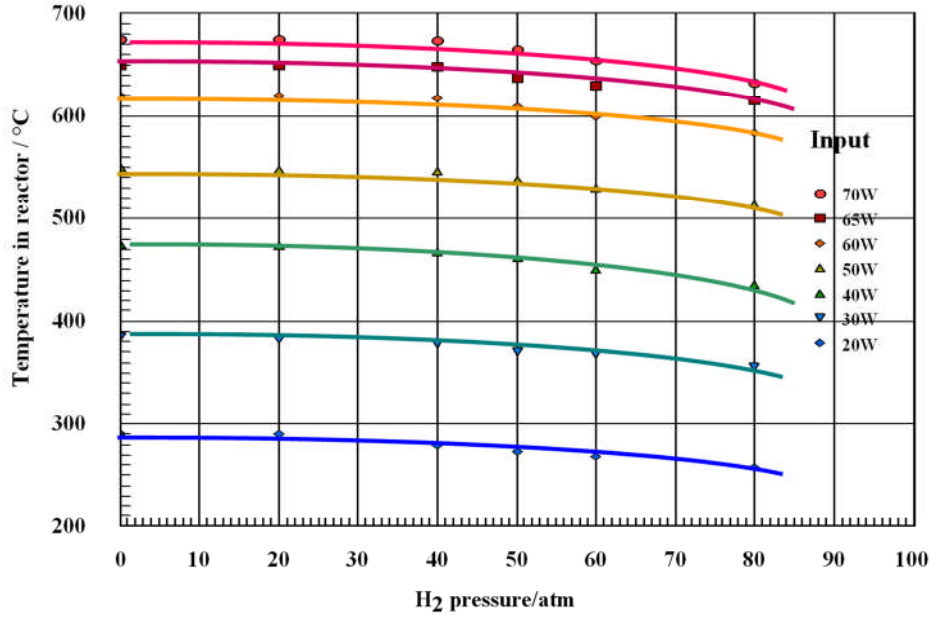


Figure 5. H₂ pressure dependence of reactor temperature at various input power.

The relationship between temperature (T) and input heat (W) is represented by a simple equation $T = CW^k$ in the temperature region of this experiment. The constant of the exponent k for the relationship is nearly the same for all the calibration conditions, at 0.6. The heat conductivity of hydrogen is 0.18 W to 0.42 W m⁻¹ K⁻¹ from 373 K to 1273 K and is almost constant at the pressure range from 1 to 100 atm^(23, 24). However, heat conductivity of the gas increases at the high pressure range, as indicated in Fig. 4. The heat release radiation is described by the equation below. This is non-linear. The coefficient k is 0.6 because the process of heat release depends on conductivity and radiation. Conductivity increases with temperature. The heat release also depends on the radiant process at high temperature region:

$$P = \sigma \varepsilon A(T_s^4 - T_a^4)$$

Here, P is heat release (W m⁻¹ K⁻¹), σ is Stefan-Boltzmann constant (5.67×10^{-8} W m⁻² K⁻⁴), ε is the radiant constant, T_s is absolute temperature of the body and T_a is ambient room temperature. With both the Inconel and SUS cells, the area above the heater exposed to air is roughly 30 cm². The radiation rate from a metal surface is about 0.9. In this experiment, the highest temperature achieved is 700°C, or 1000 K. According to the above equation, at this temperature the exposed metal surface radiates 40 W. At 500 K, it would radiate 10 W, and at 300 K 1.4 W. This heat loss amounts to a rate of around 50% with the small SUS cell, and 10% with the Inconel cell. The heat loss rate grows larger as the temperature rises. Figure 3 shows that with the SUS cell above 600°C the calibration curve peak is reduced. But with the Inconel cell, even above 700°C no significant heat loss to radiation is observed.

If anomalous heat is generated, the calibration will clearly show that this occurred.

3.2 Gamma ray calibration

Figure 6 shows background gamma activity, and the intensity spectrum for the gamma activity is shown in Fig. 7. The background is steady at $0.05 \mu\text{Sv/h}$, in a Poisson distribution, as shown in the blue line.

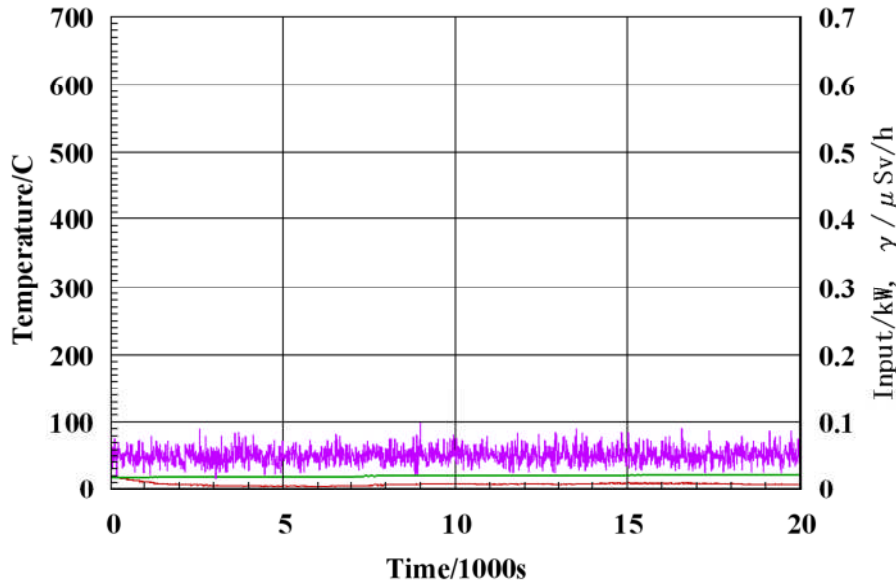


Figure 6. Background gamma emission.

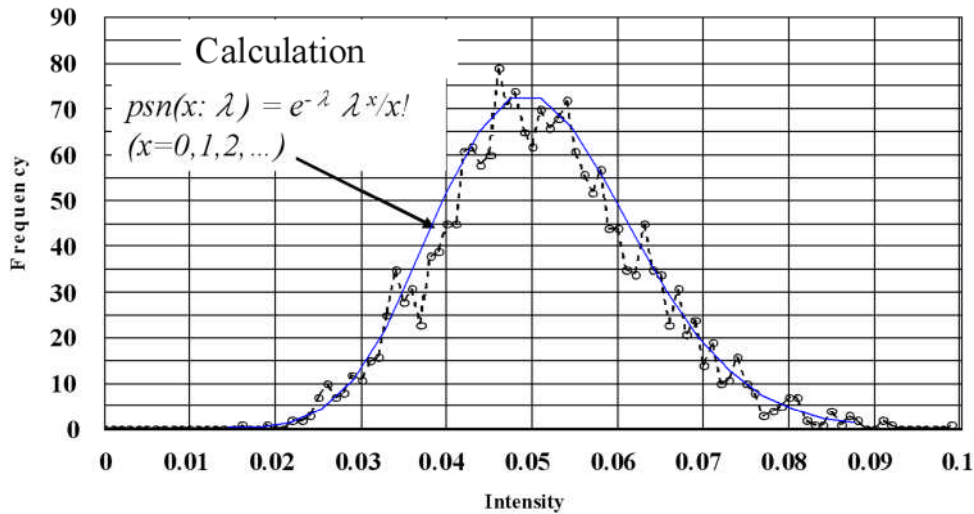


Figure 7. Intensity spectrum for background gamma emission.

Figure 8 shows gamma emission change with $0.1 \mu\text{Ci}$ ($= 3.8 \text{ kBq}$) of Ra-226. This graph shows data over 1.57 ks, with the gamma source placed 10 cm from the detector. The source was first placed near the detector at 1.8 ks, and removed at 4 ks. The times before and after this show the background gamma ray levels.

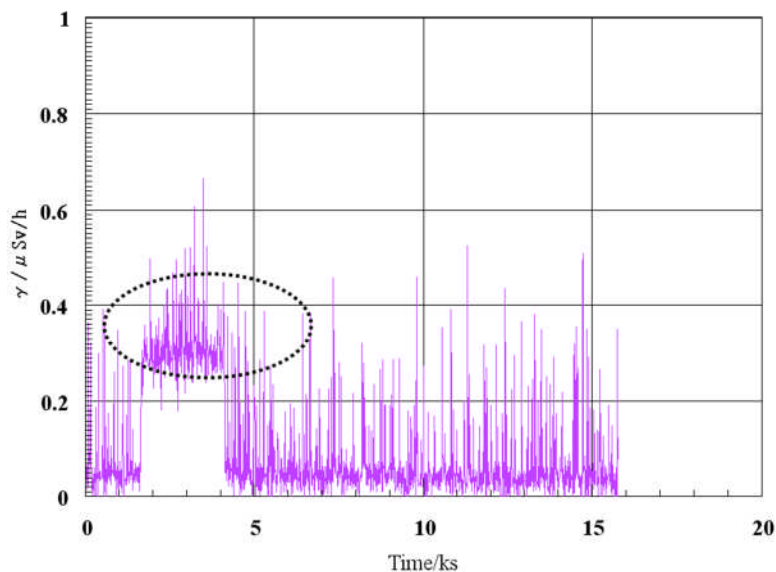


Figure 8. A calibration with Ra-226 placed 10 cm from the cell. Data from the Geiger counter.

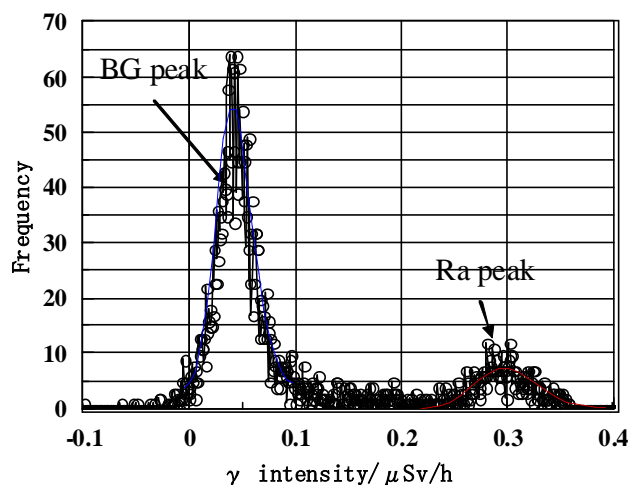


Figure 9. Intensity spectrum for gamma emission during calibration with Ra-226. Data from the ionization chamber.

Figure 9 shows the intensity distribution of gamma emission of Fig. 8. Two peaks are shown in the intensity distribution: at $0.05 \mu\text{Sv/h}$ from the background; and at $0.3 \mu\text{Sv/h}$ from a gamma source. The solid red line shows the computed distribution. In this example, the gamma peak is pronounced and easy to separate from the background, but when the Ra-226 gamma source is farther from the detector, or when it is left in place for a shorter time, the separation is not clear.

Figure 10 shows a calibration with the gamma source placed 10 cm from the detector for 1.2 ks. This produces an extra peak above the $0.22 \mu\text{Sv/h}$ background peak. Figure 11 shows a

calibration with the gamma source placed 30 cm from the detector. A weak peak of 0.04 $\mu\text{Sv/h}$ can be seen.

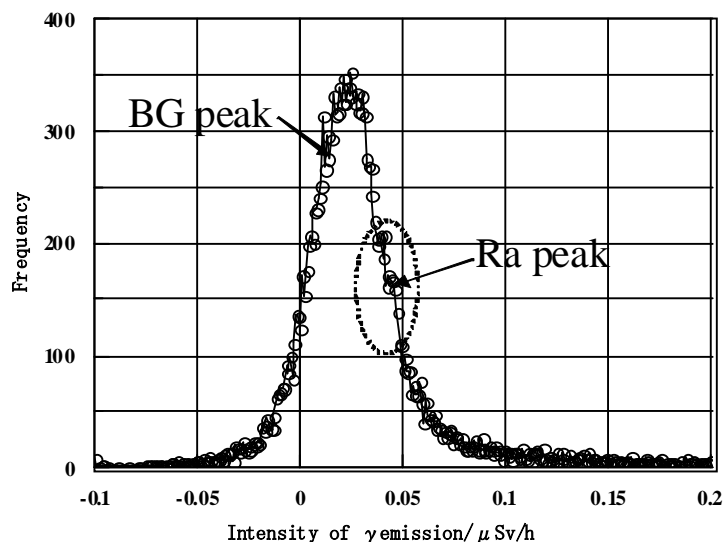


Figure 10. Calibration with gamma source 10 cm from detector

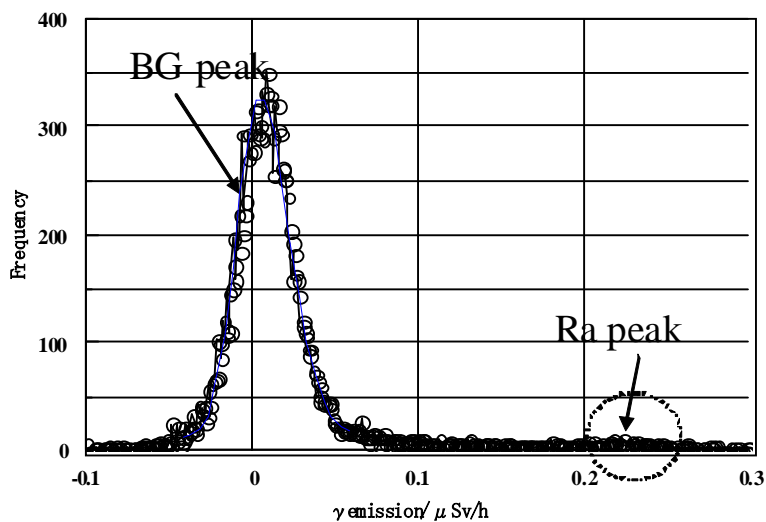


Figure 11. Calibration with gamma source 30 cm from detector

3.3 control experiments

The following control experiments have been performed:

- Hydrogen gas, and a platinum mesh, but no phenanthrene.
- Helium gas, a platinum mesh, and phenanthrene.
- Vacuum only; no gas.

These tests did not produce measureable anomalous heat, gamma rays or a change in mass 13.

4. Results

4.1 Excess heat generation

Figure 12 shows an example of anomalous excess heat. In this test, 1 g of phenanthrene was exposed to a mixture of 1 atm of hydrogen and 70 atm of helium gas. Heater power is initially set for 1.4 kW, then after 3 ks it is reduced to 700 W. Finally, it is reduced to 640 W. The heater temperature (T_2) rises faster than the cell temperature (T_1). At 10 ks they both stabilize at around 640°C, which is where the calibration curve (Fig. 4) predicts they will settle if there is no anomalous heat. However, they both soon begin to rise above the calibration point. Figure 13 is a magnification of Fig. 12 at the peak of heat production. At 9 ks the cell temperature T_1 stabilizes for about 2 ks as the heater temperature continues to rise. The cell temperature begins rising again and at 12 ks it exceeds the heater temperature T_2 . This temperature reversal is definitive proof that heat is being produced inside the cell. When power is turned off, at 16 ks, the heater temperature T_2 peaks at 670°C and the cell temperature T_1 has reached 690°C (20°C higher than T_2). Input heater power is 640 W. The cell wall temperature at T_2 peaks at 670°C which is only as high as the calibrated point for this power level; unlike T_1 , it does not indicate any excess heat.

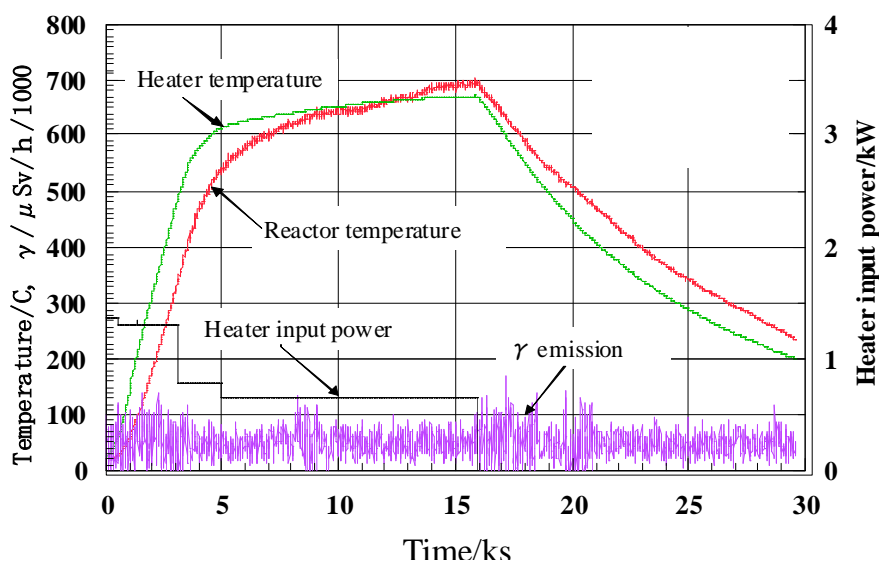


Figure 12. An example of anomalous excess heat.

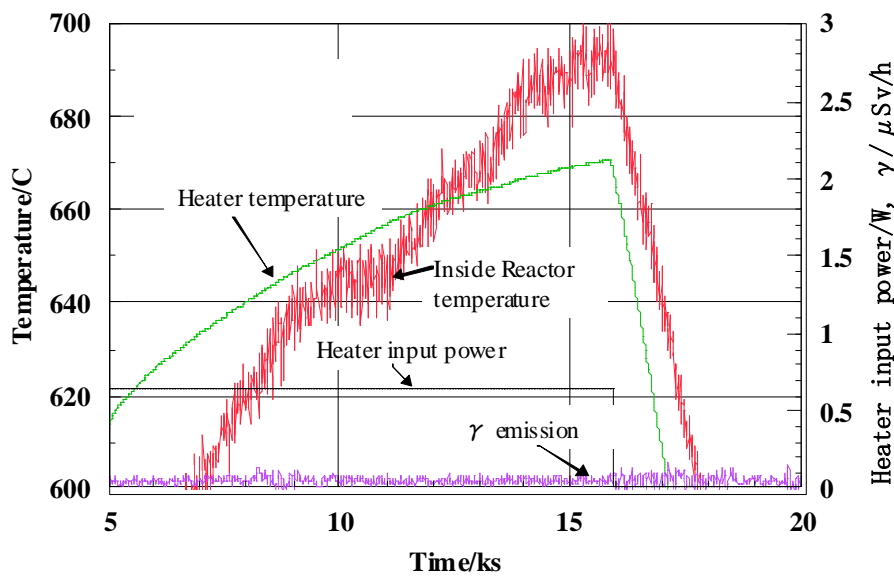


Figure 13. Magnification of Figure 7 data at peak of anomalous power output.

Total energy is more difficult to estimate than power, but given that the excess power persisted for 6 ks (100 min.) it was at least 120 kJ, for this test. Other tests have produced more energy.

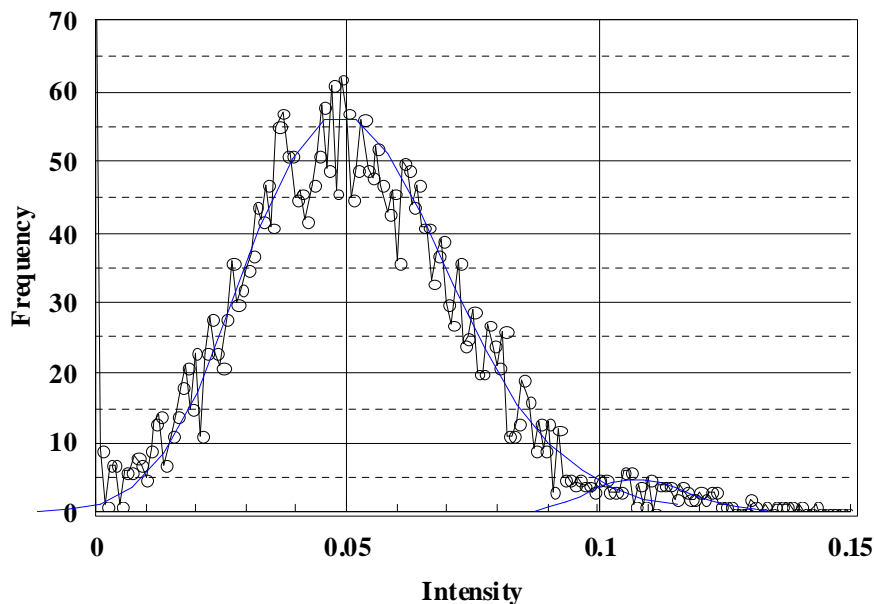


Figure 14. Intensity spectrum for the foreground gamma emission in Figure 11.

Figure 14 shows the energy intensity spectrum from the ionization chamber gamma detector. After mathematical treatment it is clear that a 0.11 $\mu\text{Sv/h}$ peak is superimposed on the 0.05

$\mu\text{Sv/h}$ background. Similar large gamma peaks are rare but they have been observed during high excess heat production.

Figure 15 shows another example of anomalous heat production. In the first stage, 1 atm of hydrogen and 70 atm of helium are admitted into the cell, and the temperature is raised to 680°C . After 10 ks, the temperature reaches the calibrated point. After that the temperature inside the cell goes well above this point. At 60 ks in this graph, it goes above 700°C , 20°C above the calibration.

At 74 ks the heater power is lowered, but the cell temperature actually rises abruptly. Later, as the temperature fall, the cell temperature fluctuates a great deal.

During this time, gamma ray activity is much larger than background, especially when intense heat is generated.

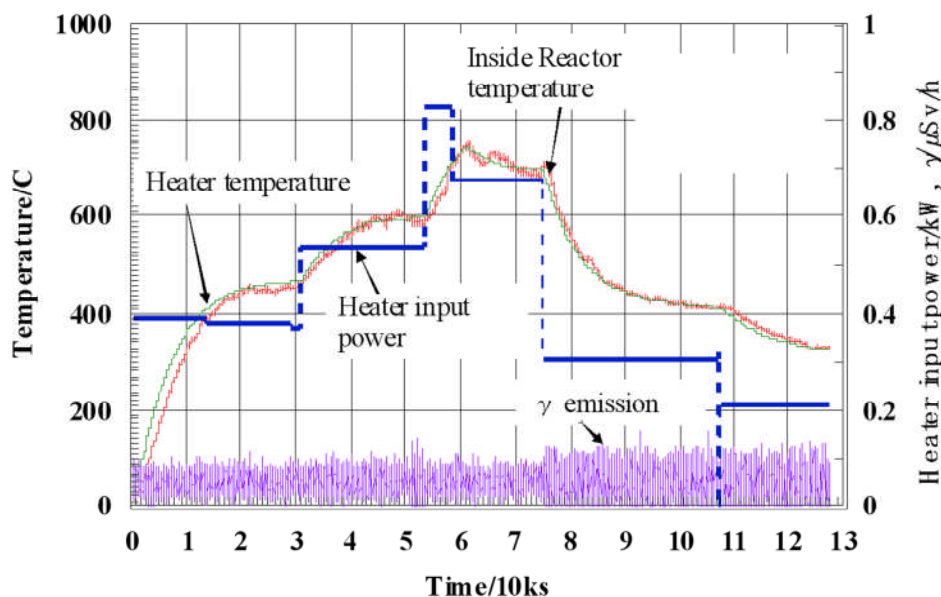


Figure 15. Anomalous heat production, example 2.

Figure 16 shows the calculated and measured intensity distributions for the gamma-ray emission detected with the ionization chamber. There are three peaks: two in the foreground data at 0.07 and $0.11 \mu\text{Sv/h}$, and another of the background at $0.05 \mu\text{Sv/h}$. All have a Poisson distribution. In this case, one of the peaks is at $0.11 \mu\text{Sv/h}$, the same as case shown in Fig. 14. The intensity of the gamma radiation is more than two times that of the background although the peak height of the spectrum is very weak compared with the background.

Figure 17 shows an enlargement of data from the heat generation experiment shown in Fig. 15. The cell temperature begins to rise rapidly at 74.5 ks. At 75 ks, the furnace heater input power is reduced from 700 to 300 W. The furnace heater temperature immediately begins to fall, yet the cell temperature continues to rise. Eventually it rises to 40°C above the previous furnace heater temperature. The only heat being supplied to the system comes from the furnace

heater, so if there is no anomalous heat within the cell, it is thermodynamically impossible for the cell temperature to rise above the furnace heater temperature, and it is also impossible for it to continue to rise as the furnace heater temperature drops.

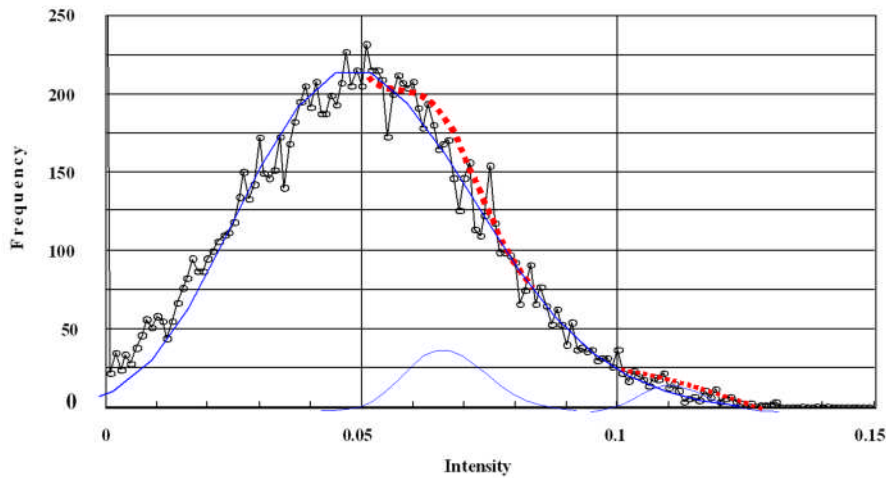


Figure 16. Intensity spectrum for the foreground gamma emission in Figure 15.

With this technique, unlike electrochemical cold fusion, there is no electrolysis power or other direct input power. The only input is to the heater, so once high-temperature triggers a reaction, all of the anomalous heat is self-sustaining. The reaction could be sustained without electricity by insulating the cell to maintain the temperature, but this would make it difficult to control the temperature.

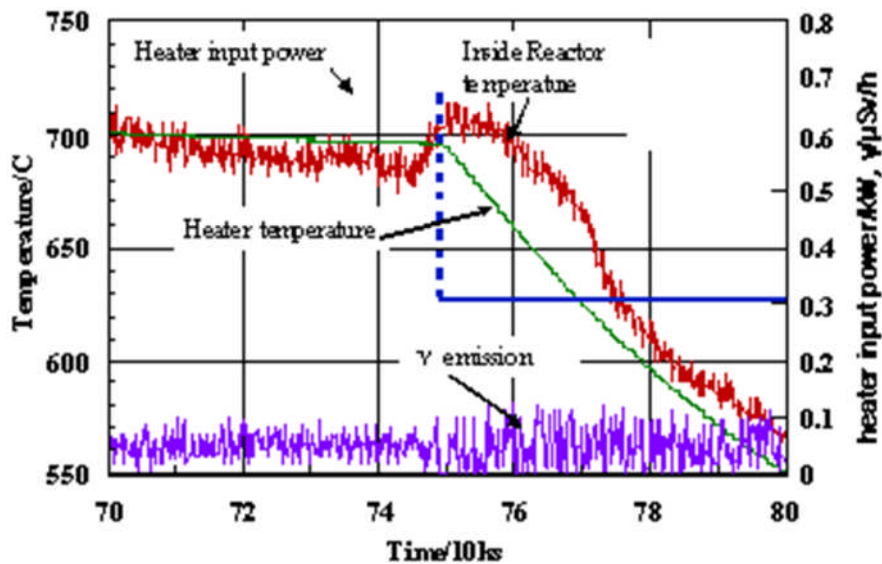


Figure 17. At 75 ks input heating power is lowered, but the cell temperature rises.

4.2 Coincidence between gamma emission and heat generation

As shown above, with the Inconel cell we were able to confirm anomalous heat production. Furthermore, we confirmed that gamma-rays were produced while anomalous heat was produced. However, with the large 0.1 L cell, we are only able to measure heat in part of the cell, and we cannot be sure what part of the cell the heat originates from. Response is slow because the thermal mass of the cell is large. To alleviate this problem, we constructed a smaller cell, and we took other steps to correlate heat production with gamma ray production. The smaller cell is made from the SUS alloy, with 9 mm diameter. The phenanthrene sample and platinum catalyst are placed at the bottom of the cell, and the thermocouple is placed in direct contact with the catalyst, so that temperature changes can be rapidly detected. With this arrangement, gamma-ray emission and changes in temperature can be directly compared.

Figure 18 shows an example of data from the SUS cell. The platinum catalyzer and 1 g of phenanthrene are placed at the bottom of the cell, and 50 atm of hydrogen gas is admitted to the cell. The cell is heated and changes in temperature and gamma ray emission are recorded. Heater power is set at 55 W, so the temperature is expected to reach 595°C according to the calibration. The figure shows data between 30 and 82 ks. The temperature reaches 595°C as expected, and then gradually exceeds it. Furthermore, when this happens, the temperature inside the cell (the red line) rises before the temperature at the cell wall (green line). Note that both of these temperatures are below the heater temperature, which is 700°C, and not shown in this graph. Note also that the temperature fluctuations inside the cell are large. Detailed data from the right portion of this graph is shown below, in Fig. 19.

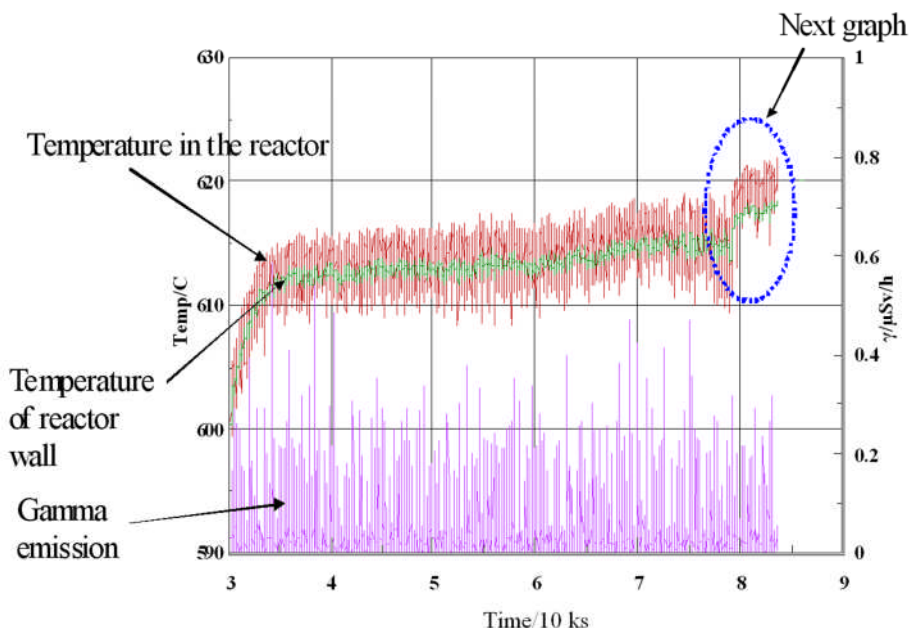


Figure 18. Change in temperature and gamma emission during hydrogenation.

Figure 19 shows high resolution data, with individual data points taken at 5-second intervals. The purple line indicates gamma rays. It can be seen that immediately after gamma ray bursts,

the temperature rises. Especially after a large gamma ray burst, a corresponding temperature rise can be seen. Many other examples of this have been observed. In this case, the calibrated temperature for the heater input is 600°C but the cell temperature rapidly and repeatedly rises to 620°C before returning to the equilibrium temperature of 600°C.

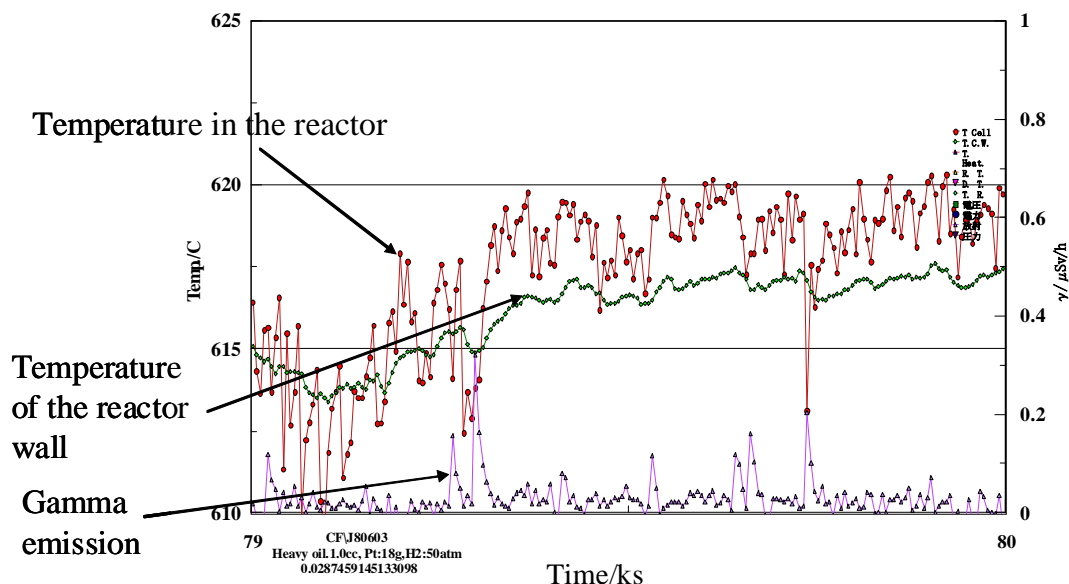


Figure 19. Gamma activity at the onset of anomalous heat.

4.3 Mass analysis after experiment

Figure 20 shows the normalized mass spectra for five runs with different starting conditions and outcomes. The red points show the gas after excess heat generated. The other colors show the gas after various null experiments. In these tests, the phenanthrene sample (when present) is 1 g; the platinum catalyst is 27.8 g; hydrogen is at 54 atm, the temperature was held at 600°C for 10 days. The M/e numbers were measured up to 100.

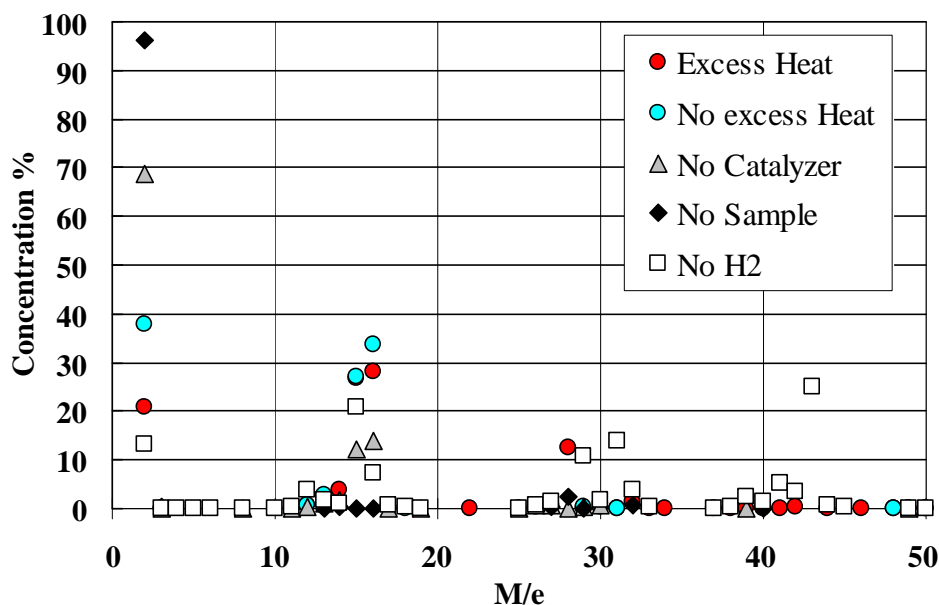


Figure 20. Mass spectrum of gas sample taken after the experiment.

The values in this graph were computed by the following method:

- (1) The value was normalized to the pressure measured during the test.
- (2) Background values for the elements already present in the cell are measured at the time the gas was admitted to the cell, and subtracted from the values measured after the experiment.
- (3) The species with the highest concentration was H_2^+ which was 96.2% of the gas in the test with no phenanthrene present. This is shown as the black diamond on the top right.

The symbols in Fig. 20 are described in Table 1. This shows, for example, that the red circles (data taken when excess heat was produced) represent different species. The red circle at mass number 2 (M/e 2 on X-axis) indicates H_2^+ which is 21% of the total. The red circle at mass number 12 represents C^+ , which is 0.7% of the total mass of the sample.

Table 1. Cell conditions for the five runs shown in Fig. 20.

Symbol, meaning	Cell conditions		
	Pressure	Temperature	Gas volume
● Excess heat produced	37 atm	650°C	0.33 L
● No excess heat	60 atm	605°C	0.56 L
▲ No catalyzer in cell	54 atm	645°C	0.48 L
◆ No sample phenanthrene in cell	38 atm	660°C	0.33 L
□ No H_2 gas in cell	0.33 atm	350°C	0.004 L

Table 2. Percent of each species found for the five runs shown in Fig. 20.

Mass number	Species	Percent of all gas				
		● Excess heat produced	● No excess heat	▲ No catalyzer in cell	◆ No sample phenanthrene in cell	□ No H ₂ gas in cell
2	H ₂ ⁺	21	37	68	96.2	13
12	C ⁺	0.7	0.7	0.3	0	3.7
13	¹³ C ⁺	2.5	2.6	1.0	0	1.8
14	CH ₂ ⁺	3.8	1.0	1.6	0.36	1.1
15	CH ₃ ⁺	27	27	12	0	21
16	CH ₄ ⁺	28	34	12	0.1	7.5
17	OH	0.3	0	0.1	0	0.8
28	N ₂	12.5	0	0.1	0.25	0
29	C ₂ H ₅	—	—	—	—	11
43	C ₃ H ₇	—	—	—	—	25

Based on the analysis of the gas, in all four tests with the sample phenanthrene present in the cell, hydrocarbon species were found, including C1 species (CH₂, CH₃, CH₄), C₂ (C₂H₃, C₂H₄), and C₃ (C₃H₃, C₃H₄, C₃H₅, C₃H₆, C₃H₇).

The above analysis is for the relative amounts of gas, not the absolute amounts. The actual amount of gas present in the cell varies with gas pressure and temperature. Total cell volume is 0.03 L, but the equipment in the cell such as the catalyst take up 0.01 L, leaving 0.02 L free space for the gas. After taking into consideration the gas pressure and temperature, the total gas volume of ¹³C⁺ at STP for the 5 tests is estimated as follows:

- Excess heat produced, 8.25 ml
- No excess heat, 14.6 ml
- ▲ No catalyzer in cell, 4.8 ml
- ◆ No sample phenanthrene in cell, 0 ml
- No H₂ gas in cell, 0.0072 ml

ICP mass spectroscopy (Finnigan Mat Element: outsourced) was performed, with the following parameter settings. ICP settings: high frequency 27 MH, 2.0 kW, earth potential; analyzer: double-focus; mass range: 5 – 260; mass resolution, variable: 300, 3000 or 7500; slit: variable resolution; analysis acceleration voltage: 8 kV; magnetic field radius: 16 cm; electric field orbital radius 10.5 cm; detector: dual mode SEM – analog/ion counter; detection limit 0.1 ppt; internal standard calibration element: ¹¹⁵In. Current measurement or ion counting uses an electron multiplier.

Solids found in the cell after the reaction were analyzed. Before the experiment, the carbon in the cell was 99% ¹²C, but after heat was produced in the example shown in Fig. 20, more than 50% of the carbon in the phenanthrene sample was ¹³C⁺.

The largest mass of carbon products from the reaction were found after the experiment shown in Fig. 18 in which no excess heat was found (●). This was followed by:

- Excess heat produced, with all necessary elements in the cell; the catalyzer, phenanthrene and gas.
- ▲ No catalyzer in cell
- No H₂ gas in cell, no reaction
- ◆ No sample phenanthrene in cell, no reaction

In the test that produced no heat, and the test with no catalyst, ¹³C⁺ was detected. There does not appear to be a correlation between the amount of heat produced and the amount of ¹³C⁺. Also, in tests without the catalyst, it is possible that the nickel in the cell wall alloy may act as a catalyst for the reaction.

5. Discussion

We used only 1 g of phenanthrene as the reactant. We have checked the weight of phenanthrene in the reactor after the experiment. Due to the high temperature of the experiment, a portion of the reactant evaporated and was adhered on the reactor inner surface and on the Pt catalyzer. This reactant was collected by wiping it off with filter paper. The phenanthrene recovered from the cell weighed 0.99 g; the reactant weight decreased by 0.01 g. However, it was difficult to weigh the loss of the reactant exactly, because it was impossible to completely recover the reactant.

The addition of hydrogen to a carbon-carbon double bond is called hydrogenation. The overall effect of such an addition is the reductive removal of the double bond functional group. Although the overall hydrogenation reaction is exothermic, high activation energy prevents it from taking place under normal conditions. This restriction may be circumvented by the use of a catalyst, such as Pt.

Catalysts act by lowering the activation energy of reactions, but they do not change the relative potential energy of the reactants and products. Finely divided metals, such as platinum, palladium and nickel, are among the most widely used hydrogenation catalysts.

Usually the reaction of hydrogenation of carbon hydride is exothermic, and heat is released corresponding to the ΔE. For example, ΔE is around -125 kJ/mole. Another case, for example, hydrogenation reaction for benzene is:



But the enthalpy of the hydrogenation reaction of phenanthrene is different depending on the temperature. It is a reaction of heat generation less than 300°C⁽²⁵⁾. However, it is an endothermic reaction consuming kilojoules per mole at temperatures higher than 300°C. We observed that less than 0.01 g of phenanthrene reacted with the high pressure H₂ gas. So, the molar value of the reactant phenanthrene was only 5.6×10⁻⁵. Thus, the heat of the reaction can be estimated as 11.2 J. Total heat observed during the experiment was on the order of 10² kJ,

10^4 times higher than a chemical reaction would allow. Therefore, a chemical reaction is ruled out.

The amount of anomalous heat was lower than with hydrogen alone than it was with hydrogen mixed with helium. Hydrogen is a significant constituent in phenanthrene, so it seems likely that this constituent hydrogen was involved in the reaction.

A weak gamma line discharge is observed during the experiment. This indicates that some sort of nuclear reaction occurred, although the correlation of the heat generation and this gamma line radiation was low. The gamma emission increased somewhat on average when anomalous heat was generated, occasionally to levels several times background, but not dramatically. The gamma emission was sporadic, which may indicate that the reaction causing the gamma emission and the heat occurs in very short time.

6. Conclusions

The anomalous energy generation cannot be the product of a conventional chemical reaction for the following reasons:

- At these temperatures, hydrogenation reactions are endothermic, not exothermic.
- The total heat release far exceeded any known chemical reaction with this mass of reactants.
- There is virtually no chemical fuel in the cell.
- There were no chemical reaction products. The components and chemical species in the cell including phenanthrene and hydrogen gas remained essentially as they were when experiment began, except that the platinum screen was coated with carbon.
- Gamma emissions are characteristic of a nuclear reaction.

The reaction is reliably triggered by raising temperatures above the threshold temperature of $\sim 600^\circ\text{C}$ and the hydrogen pressures above 70 atm. It can be quenched by lowering the temperature inside the cell below $\sim 600^\circ\text{C}$.

When the necessary conditions are achieved, generation of heat is observed with high reproducibility. However, the amount of heat generated is not stable. Only a small amount of reactant is consumed during the experiment, presumably by conventional chemical reactions. We conclude the following:

1. Anomalous heat generation was confirmed during heating of phenanthrene in high pressure of H_2 gas.
2. Sporadic gamma emission was confirmed during high temperature experiment.
3. A weak correlation was observed between heat and gamma ray emissions.

Acknowledgements

We thank Brian Scanlan of Kiva Labs for support.

References

1. M. Fleischmann and S. Pons: J. Electroanal. Chem. 261 (1989) 301.
2. Chicea, D. and D. Lupu, *Low-intensity neutron emission from TiDx samples under nonequilibrium conditions*. Fusion Technol., 2001. **39**: p. 108.
3. Choi, E., H. Ejiri, and H. Ohsumi, *Application of a Ge detector to search for fast neutrons from DD fusion in deuterized Pd*. Jpn. J. Appl. Phys. A, 1993. **32A**: p. 3964.
4. Mizuno, T., et al., *Neutron Evolution from a Palladium Electrode by Alternate Absorption Treatment of Deuterium and Hydrogen*. Jpn. J. Appl. Phys. A, 2001. **40**(9A/B): p. L989-L991.
5. Klyuev, V.A., et al., *High-energy Processes Accompanying the Fracture of Solids*. Sov. Tech. Phys. Lett., 1986. 12: p. 551.
6. Dickinson, J.T., et al., *Fracto-emission from deuterated titanium: Supporting evidence for a fracto-fusion mechanism*. J. Mater. Res., 1990. 5: p. 109.
7. Preparata, G., *A new look at solid-state fractures, particle emission and 'cold' nuclear fusion*. Nuovo Cimento A, 1991. 104: p. 1259.
8. Fateev, E.G., *Possibilities for establishing the mechanism of neutron generation in deuterated materials under mechanical loading*. Tech. Phys. Lett., 1995. 21(5): p. 373.
9. Tadahiko Mizuno, Tadayoshi Ohmori, Kazuya Kurokawa, Tadashi Akimoto, Masatoshi Kitaichi, Kohichi Inoda, Kazuhisa Azumi, Sigezo Shimokawa and Michio Enyo, "Anomalous isotopic changes for the elements induced by cathodic electrolysis of Pd electrode" *Denki Kagaku*, **64**, No.11 (1996) 1160-1165 (in Japanese).
10. George H. Miley, and James A. Patterson, "Nuclear transmutations in thin-film nickel coatings undergoing electrolysis" *J. New Energy*, **1**, No.3 (1996) 5-39.
11. Tadayoshi Ohmori, Tadahiko Mizuno, Yoshinobu Nodasaka and Michio Enyo, "Transmutation in A Gold-Light Water Electrolysis System" *Fusion Technology*, **33** (1998) 367-382.
12. Y. Iwamura, M. Sakano and T. Itoh, *Elemental Analysis of Pd Complexes: Effects of D₂ gas permeation*. Jpn. J. Appl. Phys. **41** (2002) 4642-4648.
13. Chunshan Song and Andred D. Schmitz, "Zeolite-Supported Pd and Pt Catalysts for Low-Temperature Hydrogenation of Naphthalene in the Absence and Presence of Benzothiophene" *Energy & Fuels*, 11(1997) 656-661.
14. Elzbieta Fedorynska and Piotr Winiarek, "Influence of gaseous hydrogen on the hydrogen transfer reaction between phenanthrene and hydrogen donors", *Reaction Kinetics and Catalysis Letters* 63 (2) (1998) 235-239.
15. John R. Durland and Homer Adkins, "Hydrogenation of Phenanthrene" *J. Am. Chem. Soc.*, 59 (1937) 135-137.
16. Alfred Burger and Erich Mosettig, "Studies in the Phenanthrene Series, XIII. 9,10-Dihydrophenanthrene and Amino Alcohols Derived from It" *J. Am. Chem. Soc.*, 58 (1936) 1857-1860.
17. Weihua. Qian, Yosuke Yoda, Yoshiki Hirai, A. Ishihara and T. Kabe, "Hydrodesulfurization of Dibenzothiophene and hydrogenation of phenanthrene on Alumina-Supported Pt and Pd Catalysts", *Appl. Catal., A: General* 184 (1999) 81-88.
18. Behzad Mahdavi, Jean Marc Chapuzet and Jean Lessard. "The electrocatalytic

- hydrogenation of phenanthrene at Raney nickel electrodes: the effect of periodic current control". *Electrochim. Acta* 38 (1993) 1377-1380.
19. Behzad Mahdavi, P. Los, M. Jean Lessard and Jean Lessard. "A comparison of nickel boride and Raney nickel electrode activity in the electrocatalytic hydrogenation of phenanthrene". *Can. J. Chem.* 72 (1994) 2268-2277.
 20. Jean Mark Chapuzet, Behzad Mahdavi and Jean Lessard. "The electrocatalytic hydrogenation of phenanthrene at modified Raney nickel electrodes". *J. Chim. Phys.* 93 (1996) 1252-1261.
 21. Behzad Mahdavi, Jean Marc Chapuzet, M. Jean Lessard and Jean Lessard. "Determination of intrinsic electrode activity in the electrocatalytic hydrogenation of phenanthrene". 76th CSC Conference, Sherbrooke, May 30-June 3, 1993.
 22. Richard Menini, Anna Martel, Hugues Ménard, Jean Lessard and Olivier Vittori "The electrocatalytic hydrogenation of phenanthrene at Raney nickel electrodes: the influence of an inert gas pressure". *Electrochim. Acta*, 43 (1998) 1697-1703.
 23. "Materials of Engineering of Heat Conductivity" Edited by Japan Society of Mechanical Engineering, pressed by Maruzen, (1986) 337.
 24. Ikuji Takagi, Kouhei Toyoda, Masaaki Katayama, Haruyuki Fujita and Kunio Higashi, *J. Nucl. Mater.* Vol.258-263 (1998) pp.1082-1086.
 25. Wendell H. Wiser and Alex G. Oblad "High conversion of coal to transportation fuels for the future with low HC gas production" Progress Report No. 2, (Covering the period January 1 – March 31, 1993) April 1993.

Electric and Heat Measurements in High Voltage Electrolysis Cell Experiments

A. B. Karabut¹ and E. A. Karabut²

¹*FSUE "LUCH" 24 Zheleznodorozhnaya St, Podolsk, Moscow Region, 142100, Russia.*

Tel. (095) 5508129; Fax (095) 5508129

²*Moscow Power Engineering Institute (Technical University)*

Abstract

Experimental research of the heat and high-energy processes occurring in the cathode solid medium in the high voltage electric discharge system (electrolysis cell and glow discharge device) is presented. Excess heat was observed in experiments with high-voltage electrolysis (1000 V or more). Three sets of experiments were carried out: electrolysis in light water with a Cu cathode, electrolysis in light water with a Pd cathode, and electrolysis in heavy water with a Pd cathode. X-rays were registered during the glow discharge and after deuterium glow discharge current was switched off. Presumably, the observed X-ray emission occurs as a result of relaxation of excited energetic levels in the cathode solid medium. A hypothetical process (phenomenological model) of Low Energy Nuclear Reaction (LENR) in the cathode solid medium of the electric discharge systems that may trigger the energy (ranging from 10 - 100 eV and up to 3000 eV) is discussed.

1. Introduction

Previously reported experiments showed that excess heat value from cathodes in electric discharge systems depends of the discharge voltage value (ion flux energy). For most electric discharge experiments (typically electrolysis, or electric discharge electrolysis) are done with low voltage (10 - 100 V). High voltage was used in high current glow discharge experiments [1] and high-voltage electrolysis experiments[2]. These results allow us to estimate the values of excess heat and efficiency. An X-ray emission experiment was made to elucidate the LENR triggering process.

2. Calorimetry in High Voltage Electrolysis (HVE) experiments

Three sets of the experiments were carried out at the different HVE cell operating parameters [1] with light and heavy water. Three methods of calorimetry were used to measure excess heat: calorimetry based on the time it took to bring the electrolyte to boiling; heat capacity calorimetry; and flow calorimetry. These are described in the following sections.

2.1. Calorimetry by the start time of electrolyte boiling

HVE open-type cells were used. The time the electrolyte began boiling was recorded in two experiment data sets with light and heavy water, with equal electrolysis power. It was observed

that the heavy water started boiling 4 to 5 times sooner than the light water control cell. This indicates that much more heat was produced in the heavy water cells.

2.2. Heat capacity calorimetry

A HVE device consisting of a quartz tube with an additional circuit for the working fluid (Fig. 2a) was constructed. The anode and cathode units were placed inside the tube. To circulate the working fluid (40 ml) a mixer was installed inside the circuit. The quartz tube was also provided with a thermocouple.

Four sets of experiments were carried out at the following HVE operating parameters: electrolysis in H₂O with a Pd cathode; electrolysis in H₂O with a Cu cathode; electrolysis in D₂O with a Pd cathode (not pre-treated Pd and pre-treated Pd cathode by saturation in D₂O for a month).

The following experimental procedure was used: In all the experiments the electric power input into the cell was constantly maintained at the same level for all types of cathodes and working liquids. Electrolysis was stopped when the electrolyte temperature reached 80°C. Four different tests were performed, with different electric power levels: 20 W; 40 W; 60 W and 80 W were carried out for each experimental system (with different cathode materials and electrolyte). The electrolyte temperature/time gradient (the electrolyte heating rate) was determined. The data shows that with two systems – D₂O with Pd cathode and D₂O with Pd cathode (pre-treated Pd cathode by saturation in heavy water for a month) – the electrolyte heating rate was several times higher than H₂O. Presumably, this difference of temperature gradient for heavy water with Pd cathode is accounted for by the production of excess heat in the cell.

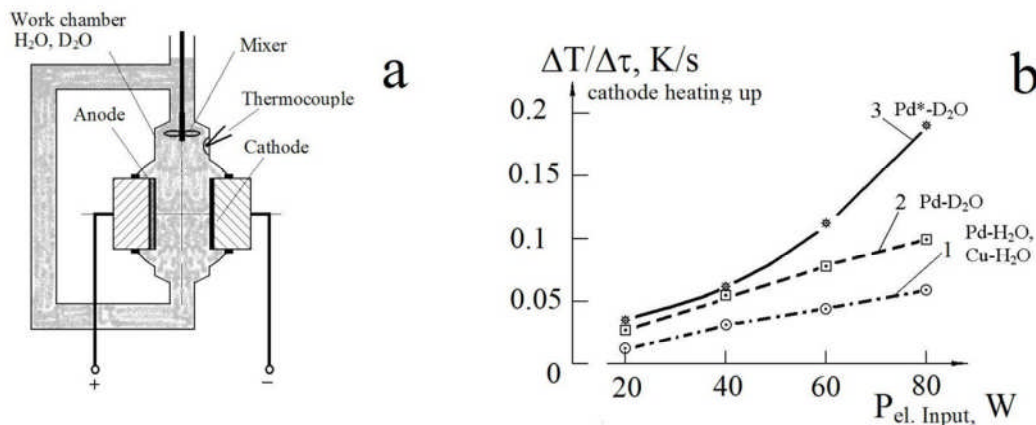


Figure 1. a – A schematic of a High Voltage Electrolysis (HVE) device, set up as a heat capacity calorimeter; b – Dependence of the water heat up value $\Delta T/\Delta \tau$ (in the circuit with the working liquid, (H₂O or D₂O)) upon the input electric power. 1 – electrolysis in H₂O with the Pd and Cu cathode; 2 – electrolysis in D₂O with a Pd cathode (not pre-treated); 3 – electrolysis in D₂O with a Pd cathode (pre-treated Pd).

2.3. Flow calorimetry

The HVE device (as a water-cooled flow calorimeter), consisted of a quartz tube with an additional circuit for a working fluid (Fig. 2a). The anode and cathode units were placed inside the tube. To circulate the working fluid a mixer was installed inside the circuit. One side of the

flat cathode was washed by the working liquid, while the other side of it was cooled by the water flowing in a cooling tube. Thermocouples connected differentially were placed inside the water-cooling passage to take the difference in the cooling water temperature input and output. The cooling water flow rate on the cathode was the same in all the experiments. The experiments were carried out using light and heavy water as a working liquid. By various techniques the voltage in the working liquid between the cathode and the anode was brought up to 800-1000 V. Three sets of experiments were carried out at the following High Voltage Electrolysis operating parameters: electrolysis in H_2O with a Pd cathode; electrolysis in D_2O with a Pd cathode; electrolysis in D_2O with a Pd cathode (pre-treated Pd cathode by saturation in heavy water for a month).

Electrolysis powers were equal in the light and heavy water experiments.

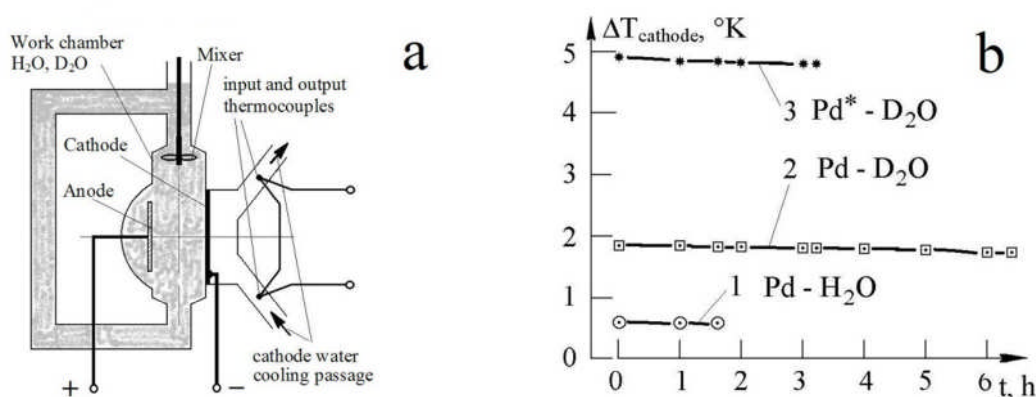


Figure 2. a – The outline of High Voltage Electrolysis device (flow calorimeter); b – Dependence of the cooling water heat up (value Δt in the cathode system) upon the experimental time

3. Estimates of Excess Heat and Heating Efficiency in High Voltage Electrolysis (HVE) Experiments

The above experimental results may be represented in terms of excess heat and efficiency values. The term Heat Efficiency implies correlation between the heat power output into the cathode water cooling system and the electric power input into electrolytic cell during electrolysis.

3.1. Results from calorimetry by the start time of electrolyte boiling

The estimate of Heat Efficiency gives the value up to 800 – 1000% and excess heat up to 80 W.

3.2. Results from heat capacity calorimetry

The following procedure was used to evaluate excess heat and Heat Efficiency: the change in thermal energy of electrolytic cell (ΔQ_{heat}) relative to time ($\Delta \tau$) occurs due to (results from) the

input electric power (P_{el}) and the excess heat power (P_{EH}) produced in the cell.

$$\frac{\Delta Q_{heat}}{\Delta \tau} = m \cdot c_p \frac{\Delta T}{\Delta \tau} = P_{el} + P_{EH}$$

Here m stands for the effective mass of the cell-calorimeter; C_p represents the efficiency coefficient of the calorimeter mass heat capacity; ΔT shows the electrolyte temperature change relative to time $\Delta \tau$.

Assuming that no excess heat is produced in using H_2O with Pd and H_2O with Cu cathode systems we arrive at $P_{EH} = 0$.

Excess heat and Heat Efficiency values are lower in experiments with cell-calorimeter without thermal insulation (from the environment) (Fig. 3a, 3b).

3.3. Results from flow calorimetry

The above experimental results may be represented in terms of excess heat and Efficiency values. The term Heat Efficiency implies correlation between the heat power output into the cathode water cooling system and the electric power input into electrolytic cell during electrolysis. It may be assumed that the electric power input into the electrolytic cell, and the heat power produced in the cell are carried away by the water of the cathode cooling system.

The Heat Efficiency of relative heat output was used:

$$\eta = \frac{\Delta t_{D2O} \cdot P_{el.H2O}}{\Delta t_{H2O} \cdot P_{el.D2O}}$$

Here $\Delta t = (t_{out} - t_{in})$ represents water heat up in the cathode water cooling passage; $P_{el.}$ stands for the electric power input into the electrolytic cell in the experiments with heavy and light water, respectively.

Excess heat produced in the electrolytic cell is determined by the following expression:

$$P_{EH} = P_{el} \cdot (\eta - 1)$$

Experimental data treated with this method is presented in the graphs shown in Fig. 4a and 4b.

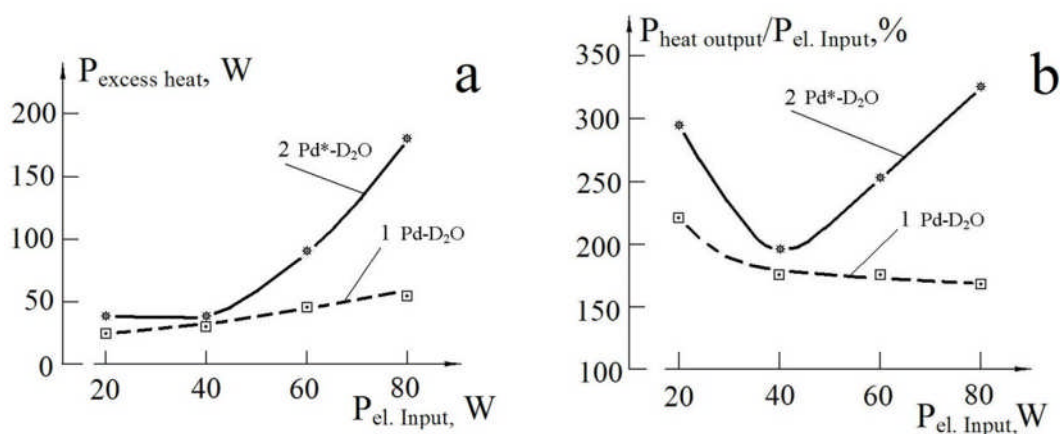


Figure 3. Heat Capacity Calorimeter. a -Excess heat value as a function of the input electric power. b- Dependence of Heat Efficiency value the input electric power. 1 – D₂O with a Pd cathode (not pre-treated Pd); 2 – D₂O with a Pd cathode (pre-treated Pd).

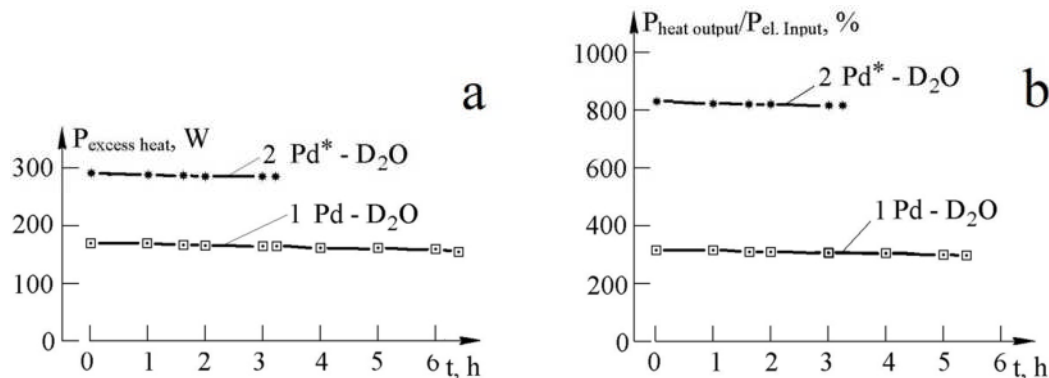


Figure 4. Flow Calorimeter. a – Excess heat value as a function of experimental time. b – Dependence of Heat Efficiency value of experimental time. 1 – D₂O with a Pd cathode (not pre-treated Pd); 2 D₂O with a Pd cathode (pre-treated Pd).

4. Excess Heat in Glow Discharge Experiments

Measurements of excess heat were carried out in experiments with high-current Glow. The excess heat registration experiments were carried out using the glow discharge device. A pulse-periodic electric power supply was used. The big values of excess heat (5 – 15 W) and Efficiency (160%) were observed in conditions when the glow discharge operational voltage ranged from 1000 V to 1300 V (Fig. 5a, 5b). The glow discharge voltage area (D₂ ion energy) with maximum efficiency heating corresponding to the inverse X-ray emission energy area on the Pd cathode (Fig. 5b).

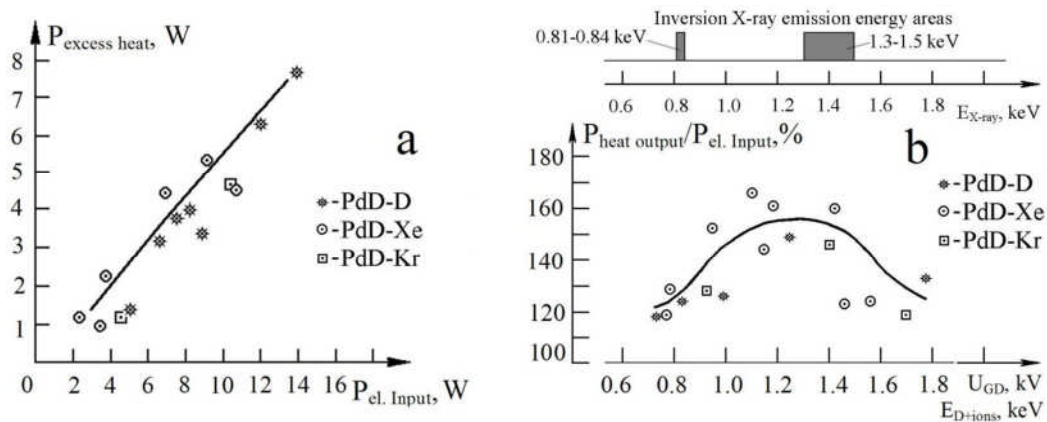


Figure 5. a – The relationship of excess heat to input electric power (glow discharge experiments); b – Dependence of the output heat power and the input electric power ratio of the glow discharge voltage (deuterium ion energy). Deuterium pre-charged Pd cathode samples in D_2 , Xe and Kr discharges. Inversion X-ray emission energy by the curved mica crystal X-ray spectrometer.

5. LENR PHENOMENON THEORY

The totality of experimental results (excess heat production, production of ^4He , nuclides with unnatural isotopic ratios, and X-ray emission) are clues to developing a theory to explain LENR in the solid medium of the electric discharge systems cathodes. One can single out the following electric discharge systems areas and physical phenomena observed within them:

- 1) Ion flux generation in electric discharge systems near cathode area plasma or electrolyte. The transfer of electric discharge energy (1000-2000 eV) to ion flux of deuterium plasma. The cathode surface is bombarded with the ion flux.
- 2) The soft collision D^+ ions flux with surface of Pd cathode solid causes the following processes:
 - a) Low energy modes transfer in solid volume;
 - b) Anharmonic processes of low energy modes conversion to high energy modes (P. Hagelstein process);
 - c) Creation of excited long-lived states with 1000-3000 eV and more energy in solid medium;
 - d) Loading deuterium in Pd solid.
- 3) Triggering and realization of Low Energy Nuclear Reactions in the solid.
- 4) Conversion of nuclear reaction energy into the crystal lattice heat.

6. Conclusion

The development of new nuclear engineering is possible based on low energy nuclear reactions (LENR) in the solid-state medium of the high voltage electric discharge system.

References

1. G. Kazyonov et al., “Experiments of anomalous output heat registration by electrolysis in heavy water ”, Proceedings of the 10-th Russian Conference on Cold Nuclear Transmutation of Chemical Element and Ball Lighting, DAGOMYS, CITY OF SOCHI, September 29 – October 6, 2002, RUSSIA, pp. 41 – 49.
2. A. B. Karabut, “Research into Low Energy Nuclear Reactions in Cathode Sample Solid with Production of Excess Heat, Stable and Radioactive Impurity Nuclides”, Proceedings of the 12th International Conference on Cold Fusion, December 2 – 7, 2006, JAPAN, pp 214 – 230.

Introduction to Nuclear Reaction Products

As noted in the Preface, there are four classes of measurements that have been made to show that it is possible to trigger nuclear reactions with chemical energies. They involve the detection of heat, nuclear reaction products, energetic particles and low-energy (infrared or sound) phenomena. That is, there are measurements that deal with energy (heat or particle kinetic energy or low-energy emissions) or with matter (slow reaction products or fast particles). The production of heat at levels which simply cannot be explained by known chemical reactions was addressed in the last section. Now we consider the measurement of reaction products that are left behind after the occurrence of LENR. Energetic particle measurements are the subject of the next section.

Before dealing directly with reaction products, we should pause to note the wide variety of nuclear reactions. They are not as numerous as chemical reactions, but still run to the thousands of possibilities. In principle, any exothermic nuclear reaction can be a source of energy. The problem is that to stimulate most nuclear reactions, the amount of total energy that is needed exceeds the energy from the reactions. That is, most nuclear reactions are not viable energy sources. Note that a similar situation, overcoming “energy barriers,” is the focus of the search for catalysts in chemistry. Catalyzing nuclear reactions is a phrase sometimes associated with LENR.

It happens that elements near both extremes of the periodic table are either actual or candidate energy sources. Heavy isotopes of U and Pu, impacted by neutrons, fission to produce the power currently extracted from over 400 reactors around the world. Fission reactors have the drawback requiring radioactive fuels, producing dangerous radiations during operation, and generating significant amounts of radioactive waste after operation. At the low mass end of the periodic table are isotopes of hydrogen (notably deuterium and tritium), plus a few other isotopes, which can produce energy by fusion, if they collide with sufficient energy. Such energies can be attained for large numbers of reactant particles by heating them in plasmas that have temperatures in the range of 100 million K. The fusion reaction products are generally not dangerous, but the fast neutrons that result from many fusion reactions are dangerous and they activate radioactivity in nearby materials, and create a waste problem.

Many people, Martin Fleischmann included, think it was a mistake to term nuclear reactions stimulated by low energy phenomenon as “cold fusion.” Aside from the relative nature of the term “cold,” it was, and is even more so now, unclear that fusion is the only, or even dominant LENR. There is a great deal of experimental evidence, and some theoretical concepts, regarding the possibility of nuclear reactions involving elements across the periodic table. This is not to say that all LENR are something other than fusion reactions. It is, rather, an assertion that many other nuclear reactions fall under the heading of “LENR.”

When atoms of one element are changed into atoms of another, the process is called transmutation. There is a long history of interest in such processes. It includes alchemy, the many efforts by some well-intentioned experimenters and numerous charlatans to turn various substances into gold. When particle accelerators with enough energy to induce nuclear reactions became available early in the last century, transmutation reactions became possible

and even routine in physics laboratories. However, the amounts of new materials produced in beam experiments are small and not economical.

Global interest in valuable materials, such as gold and silver, dates to antiquity. But, after the filling of most of the slots in the periodic table and since the industrial revolution, many other elements came to be valuable. Uses range from alloying metals to increase their useful properties to doping of semiconductors for microelectronics. For decades after WW II, the US had a strategic stockpile of elements. Arranged by atomic number, they included He, Be, diamonds, Cr, In, Co, Ge and Mo. This stockpile has been sold off. However, the vagaries of geology and politics might lead again to the hoarding of some technologically valuable elements. The point is that, if transmutations of one element to another by LENR were both controllable and greatly scaled up in rates, it is conceivable that needed elements could be produced on demand.

There is one particular isotope of hydrogen, namely tritium, which is a basic material for nuclear weapons. It boosts the performance of fission bombs, either as separate weapons (A Bombs), or as the primaries in fusion devices (H bombs). But, it has a half life of only 12.3 years. Hence, its production is of interest to countries with nuclear weapon stockpiles. The US last produced tritium for weapons in 1988 when a reactor production facility in South Carolina was closed. Since then, the need for tritium to top off weapons has been satisfied by using tritium from decommissioned devices. In 1998, it was decided to employ two light water reactors in Tennessee for tritium production. The question of whether or not LENR could be used to provide tritium for nuclear weapons arose early in the field. Production rates demonstrated to date are dramatically lower than what is needed. However, that does not rule out this possibility in the future. Tritium also finds uses in self-powered lighting for watches and firearm night sights, controlled nuclear fusion, analytical chemistry and tracing of oceanic currents.

Most of the attention to transmutations in LENR experiments has involved heavier elements. The reports that it is possible to produce nuclear reactions involving heavy elements startled even researchers already studying LENR. Some people in the field reacted with incredulity to reports of transmutations as did most scientists in 1989 after the Fleischmann-Pons announcement. There are two reasons for this amazement. One was the fact that the original name “cold fusion” was taken quite literally by many people, and transmutations were entirely outside of that vision. The second was that the coulomb barrier, already high for fusion of light atoms, is immense for nuclear reactions in atoms with heavier nuclei. That is, according to normal two-body picture of nuclear collisions and reactions, much greater kinetic energies are required to overcome the mutual repulsion of two positively-charged heavy nuclei.

The critical fact is that, despite skepticism, many laboratories reported the appearance of new elements in LENR experiments. In 2003, George Miley compiled a list of 15 laboratories in six countries, which had reported transmutations. He summarized the appearance of elements across the periodic table in LENR experiments. His data on the increase in the amounts of elements showed peaks as a function of atomic mass. Mizuno also took such data, which showed peaks in elemental production close to those found by Miley and his colleagues. The data in both cases are quite scattered. However, the fact that two independent and different

experiments lead to the same picture of elemental production is one of the more enticing facts in the field.

Widom and Larsen later computed nuclear reaction probabilities as a function of atomic mass, that is, nuclear size. They found that peaks occurred at each nuclear size for which one more wavelength for neutrons in nuclear matter fit into the nucleus. The positions of their peaks agreed reasonably with Miley's data, and hence with Mizuno's results. This is one of very few direct comparisons (over plots) of experiment and theoretical computations in the entire field.

The conduct of transmutation experiments is very challenging. If elements are observed with some instrument after an experiment, it does not guarantee that they were not there prior to the run. Before an experiment, the element of interest might have been widely distributed and below the detection threshold for the instruments being used. If the experiment served to concentrate the element at some locations on a cathode, moving it above the minimum detectable limit of an analytical instrument, it would be measurable without any increase of the number of atoms of interest in the entire experiment. In several electrochemical experiments, the authors argue that some of the newly observed elements could not have been deposited electrochemically at the sites where they were found. This is a useful argument, although it does not preclude some concentration mechanism.

Logically, an experiment that purports to show increase in the amount of any element during a run should have analyses for that element done in all the phases and materials that went into the experiment. This is doubly challenging. First, there is a sampling problem. That is, materials are not homogeneous at the nanogram level and it is not possible to consume all of the experimental material for analysis before it is run! Second, even if a defensible procedure for adequate sampling without unduly changing the experiment is possible and accomplished, the analyses that are needed to quantify low-levels of the elements of interest are costly and time consuming. Analyzing for parts per million, billion, or trillion levels of impurities is challenging. The analyses would generally have to be done by analytical specialists with the needed and usually expensive equipment and considerable expertise. There are dozens of analytical methods for specific elements, so the selection of which technique to use for each of the elements of interest is not easy. In experiments like Miley's and Mizuno's, where a few dozen elements are germane, there is the added difficulty of making an analytical choice many times. In general, many of the LENR experiments reporting transmutations have not included adequate chemical analyses.

One of our goals in ICCF-14 was to focus attention on how LENR transmutation experiments should be conducted from the perspective of scientists who specialize in trace element analyses. David Kidwell was invited to present a paper on trace analysis of elements in a Pd matrix. His expertise is in inductively-coupled plasma mass spectroscopy (ICP-MS). The message is not that you can find evidence of changes in the measured isotopic content of a sample, but rather how does one establish what was the source of the changed content.

There were two new and related reports of transmutation research at the conference. Both followed the earlier reports of Iwamura *et al* in which deuterium permeation of multi-layered Pd foils resulted in the transmutation of Cs to Pr and Sr to Mo. The two new works involved

the second of these reactions. The first was by Yamaguchi and his colleagues. Four beam analytical methods were employed, including Proton Induced X-ray Emission, Elastic Recoil Detection Analysis, Nuclear Reaction Analysis and Rutherford Backscattering. An increase in the amount of Mo was observed in 25% of the runs. The authors now seek to improve both the sample uniformity and the deuterium permeation rate.

The second permeation and transmutation paper was by Hioki and his collaborators. The Sr was implanted into the Pd and multi-layered foils. The analyses for Mo were performed with Time-of-Flight Mass Spectroscopy and X-Ray Photoelectron Spectroscopy. Mo was clearly seen with the XPS technique. However, the mass spectroscopy data was not yet conclusive. Work is continuing.

Interest in transmutations in the LENR field is appropriately high for both scientific and practical reasons. Hence, a workshop on transmutations was organized immediately after the conference by George Miley. About fifty people attended the half-day workshop, another measure of the interest in transmutations. A summary of that workshop by Miley is also included in this section.

Trace Analysis of Elements in a Palladium Matrix

David A. Kidwell
Chemistry Division
Naval Research Laboratory
Washington, DC 20375

Abstract

Inductively Coupled Plasma Mass Spectrometry (ICP-MS) is a technique for trace elemental analysis and isotopic distribution determination at trace levels, but ICP-MS cannot handle directly high concentrations of ions. Dimethylglyoxime will selectively precipitate palladium from acid solutions leaving most of the impurities in solution and allowing their quantitation by ICP-MS without dilution. By avoiding dilution, the sensitivity and precision of the analysis can be increased to sub-PPM levels. A convenient method for controlled etching of palladium is also described.

Introduction

The exact requirement(s) for the Fleischmann-Pons Effect (FPE)¹ is not clear, but it may be dominated by surface effects. Trace contaminants on the surface influence the uptake and recombination of deuterium (or hydrogen) by blocking or enhancing certain catalytic centers or causing certain crystalline phases to form during processing that may influence the FPE. A classic example in organic synthesis is Lindlar's catalyst.¹ Normally, palladium in the presence of hydrogen will completely hydrogenate triple and double bonds to the saturated alkanes. However, in the case of Lindlar's catalyst the palladium is poisoned with lead and further deactivated with either quinoline (an amine) or a thiol. This deactivated catalyst has a sufficiently slow hydrogenation rate to allow stopping the hydrogenation at the double-bond stage. Lindlar's catalyst allows the preparation of many cis-alkenes from acetylenes. For example, several steps in the multi-step preparation of Vitamin E are accomplished on an industrial scale with this catalyst.²

To fully understand the FPE requires analysis of the palladium before and after various processes to determine if either:

- (1) An impurity is present that inhibits or enhances some chemical or other process. The impurity may come from the surface, bulk of the palladium, or from the reagents or equipment used in the reaction; or,

¹ Although the mechanisms may be completely different, I use the term Fleischmann-Pons Effect in this a paper to refer to a palladium matrix exposed to deuterium and production of excess heat, elements, or isotopes. The method of introduction of deuterium need not be only through electrolysis, as in the original Fleischmann-Pons experiments.

- (2) Transmutation had occurred where a new element or isotope was formed that was not initially present in either the bulk starting palladium, solutions, or equipment used for the reaction.

Inductively Coupled Plasma Mass Spectrometry (ICP-MS) is a technique for trace elemental analysis. The Thermo-Finnigan Element 2 instrument used in this work will detect most elements that form positively charged ions.³ For use in ICP-MS, a sample is dissolved in high-purity acid (generally a strong oxidant such as nitric acid), diluted to 2-5% acid with high-purity water and sprayed through a nebulizer into a desolvation chamber that removes most of the water. The semi-dry droplets are carried into an Argon plasma torch that dissociates and ionizes all molecules such that only the elements are left.⁴ The ions are then extracted from the plasma through a series of differently-pumped chambers, which reduces the pressure, into a magnetic mass-separator that allows mass analysis of the extracted ions. Once mass separated, the positive ions are detected with an electron multiplier that can be automatically switched from ion counting to analog modes. Because of the analysis process – dissolution, dissociation, and ionization – it is highly unlikely that any molecule could survive intact. Furthermore, the acid and water used to prepare the samples are not isotopically enriched, so any initial deuterium compounds (for example PdD) that may be present are diluted to normal isotopic abundance.

ICP-MS has three limitations: adduct formation, isotopic ratios, and overloading. They are discussed below.

Adduct Formation

During the extraction of the ions from the Argon plasma, ion-atom recombination can occur. I will refer to this as adduct formation.⁵ The primary adducts that form are those with the main constituents of the plasma: Argon and Oxygen⁶ (from the water solution). Other adducts may be present if the sensitivity is increased – *i.e.* into the PPT¹ and PPQ range. As the ion-atom recombination occurs in the region after the plasma, the proportions of adducts formed varies with the plasma conditions, the exact placement of the plasma torch relative to the extraction lens (as this affects the residence time of the ions in the plasma), the extraction voltages, and the ion concentrations in the test solution. The Ar+matrix ions may interfere with other desired analytes, especially if the host matrix is sufficiently high in concentration (>1 PPM). With analysis of palladium solutions, one often observes Pd+Ar adducts as shown in Figure 1. Scanning over a narrow window without considering adducts may lead to the false conclusion that some element is present that a wider scan would correctly identify as an adduct (Figure 1a vs. 1b). Palladium has the advantage that its adducts will reflect the isotopic ratio of palladium plus Argon making them easy to identify. Other elements are not so easy to identify, so caution is called for when interpreting the presence of unexpected elements.

ICP-MS uses two techniques to reduce interferents from adduct formation: collision cells and high resolution. For a collision cell instrument, after extracting the ions from the plasma but

¹ Units used: PPM = parts per million ($1:10^{-6}$), PPB = parts per billion ($1:10^{-9}$), PPT = parts per trillion ($1:10^{-12}$) and PPQ = parts per quadrillion ($1:10^{-15}$).

before mass analysis, the ions are collided with an inert gas where the energy of collision is sufficient to break apart weakly held complexes. A collision cell is often used on ICP-MS instruments that use a quadrupole as the mass resolving element. The Element 2, used in this work, is a high-resolution ICP-MS. The resolution can be greater than 10,000, which can resolve many, but not all, adduct ions. In addition to reducing interferences directly, interferences from adducts may be mathematically removed with reduced precision (described below).

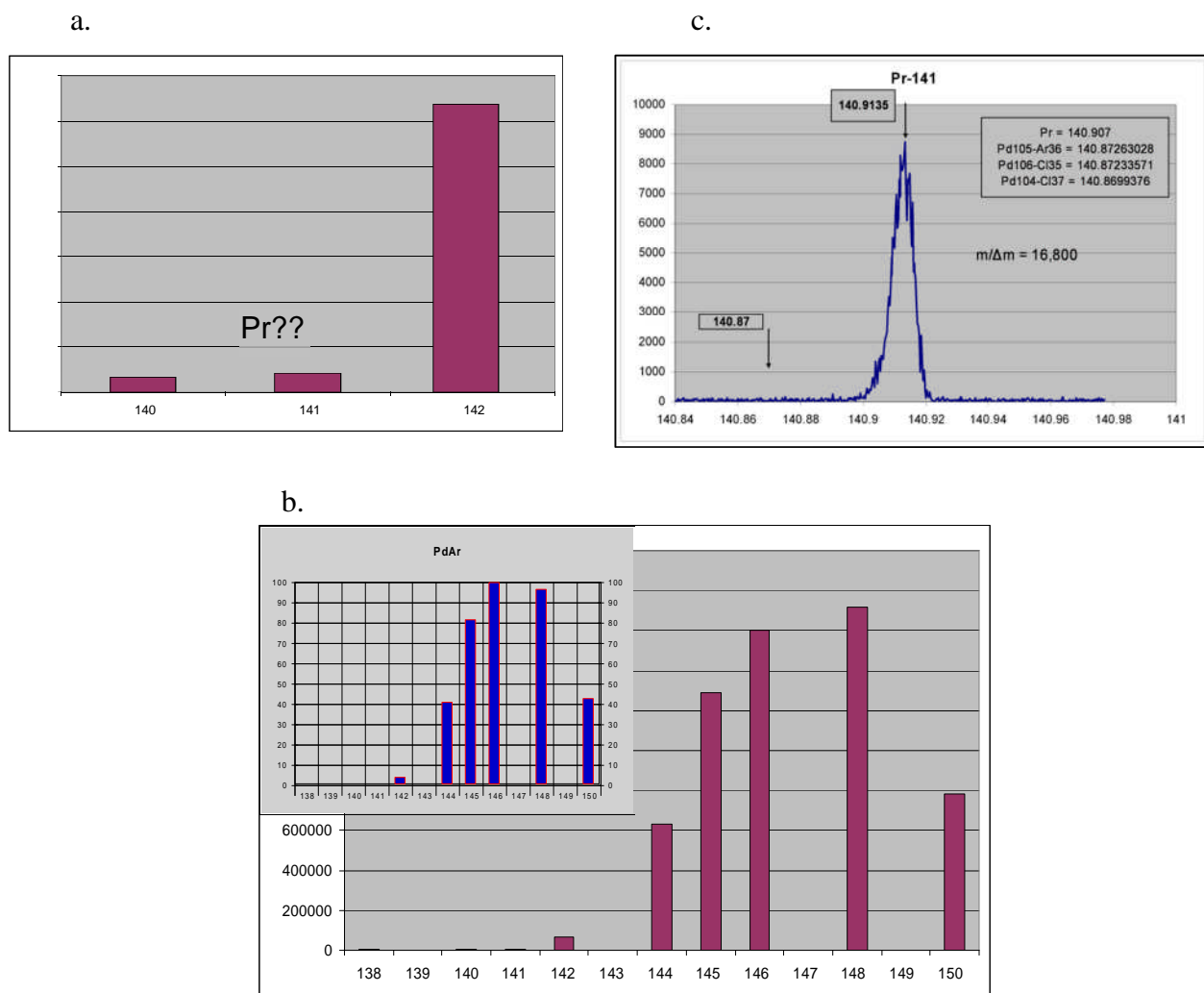


Figure 1. Examples of an Argon-Palladium adduct. Figure 1a: A minor peak in the Ar-Pd adduct occurs at m/z 141 (Pd-105 + Ar-36) and interferes with the detection of Pr (which is mono isotopic). Scanning a narrow mass window may miss the characteristic isotopic envelope of Palladium, which would indicate an adduct ion. **Figure 1b:** A larger scan range of the top spectra indicating the Pd-Ar adduct, with the inset showing the expected isotopic distribution. Argon is mostly mono-isotopic (Ar-40 99.6%) but palladium has six stable isotopes. For the analysis of Pr, if other adducts are absent, one can use the expected distribution of the ions for the Ar-Pd adduct to calculate what the intensity should be at m/z 141 and subtract that intensity from what is observed with the remaining intensity attributed to Pr. Such a correction can correct up to a 20 fold interferent. The use of multiple isotopes increases the confidence in the correction. Higher corrections are suspect because the isotopic ratios vary due to plasma conditions. Note that the calculated ion distribution, shown in the insert, and the measured distribution do not agree exactly (m/z 148 should be smaller than m/z 146). This is due to rapid scanning of the ICP-MS, and the discrepancy can be decreased by scanning a narrow range of ions. **Figure 1c:** This spectrum shows the unambiguous identification of Pr by high resolution. The Pd-Ar adduct interferent (not observed here) can be separable from Pr with higher resolution (>4000) as they have slightly different mass (140.8726303 vs. 140.907648). The preferred method to confirm the presence of some unique element is to both reduce the palladium concentration (to reduce the interference) and use higher resolution rather than a mathematical correction.

Although adducts form in ICP-MS, they form in greater abundance in Secondary Ion Mass Spectrometry (SIMS). Adduct ions in the SIMS analysis may complicate the identification of an unexpected element.⁷ SIMS readily analyzes surface impurities but can have several orders of magnitude discrimination among the materials on the surface. Furthermore, the ionization efficiency and discrimination can change depending on what is present on the surface, making accurate quantitation difficult. Species that form cations readily are enhanced in SIMS, and this has been used to advantage for selectively detecting one species in the presence of others.^{8,9} Not having a surface present to influence the ionization process makes ICP-MS more quantitative than SIMS. Not having large amounts of adduct ions make isotopic ratios easier to determine.

Isotopic Ratios

When the ions are extracted from the plasma, they are not all extracted with the same efficiency. ICP-MS shows about a 1% per AMU discrimination in the intensities.¹⁰ The raw intensities should not be directly compared to published values but may be corrected by analysis of known standards. A scanning instrument may not measure isotopic ratios with great precision because the plasma can fluctuate slightly even over a scan. This is partially mitigated with the Thermo-Finnigan Element 2 by rapid scanning using an electric sector over a narrow mass range. Nevertheless, for more precise work, instruments used for isotopic ratios often have multiple collectors that simultaneously detect all ions. Even with multiple collectors, the isotopic ratios may be affected by other elements present in the matrix slightly altering the plasma conditions and the ion extraction efficiency.¹¹ For the most precise work, all matrix conditions should be as identical as possible to known standards or other techniques be employed, such as thermal ionization mass spectrometry.

Overloading

ICP-MS is a trace analytical procedure that can analyze PPB levels routinely and PPQ levels in carefully prepared samples. Because ICP-MS is a trace technique, high amounts (PPM) of analyte can interfere. Worse than interference, high amounts can irreversibly contaminate the instrument – especially the sample introduction nebulizer that is frequently made of glass and can absorb materials. The contamination from a sample with high concentrations of species provides a constant background for subsequent analysis that can be a substantial problem if one wished to analyze the same element at trace levels.

One may ask: If ICP-MS can detect routinely PPB levels of elements, why do we need to reduce the matrix? Can it be analyzed directly? To answer these questions, one needs to consider how the whole procedure is performed using an example analysis. One mg of palladium dissolved in 1 mL of acid would correspond to 1000 PPM of palladium. To reach 1 PPM of palladium so as to avoid instrumental contamination, this solution must be diluted 1:1000. This also dilutes any impurity that was being sought in the original palladium sample the same 1:1000. If your sensitivity were 1 PPT for that impurity, the concentration in the original palladium would correspond to 1 PPM.¹² Quantitation at lower levels would either require a smaller dilution and potential contamination of the instrument, or use of another technique. Besides sensitivity, the precision that can be claimed for the absence of some

element is also affected by the dilution, mainly due to the blanks. For example, assume the blanks had signal levels for the impurity Praseodymium, maybe due to adduct ions, which corresponded to 1 PPT level with some precision. Because of the 1:1000 dilution and precision in the blank measurement, one could not say with confidence that the original palladium sample had less than 1 PPM of Pr present, or 1 µg of Pr/g Pd. If the palladium matrix could be reduced 100-10,000 fold, without reducing the analyte, then the dilution could be reduced and the sensitivity proportionally increased.

This report describes a procedure to reduce the main matrix element – palladium – to PPM levels so that one can observe trace levels (PPB-PPQ) of other elements in the palladium matrix without grossly contaminating the ICP-MS or requiring excessive dilution of the matrix. Precautions in interpreting ICP-MS data are also emphasized.

Experimental

Reagents and Supplies

JT Baker Ultrex[®] II nitric acid (cat #6901-05) and hydrochloric acid (cat #6900-05) were used in preparing solutions. Fischer Optima nitric acid (cat #A467-500) has also been used with success. Only pasticware was used for preparing samples and reagents, as glass quickly leaches trace elements. All samples were prepared in 15 mL Falcon[®] Blue Max[®] (cat #352097) polypropylene test tubes. These tubes have unlined plastic caps that are not completely resistant to concentrated nitric acid – they discolor after a few days, but they appear to be resistant to 5% nitric acid for long periods of time. Other brands may have linings in some caps with traces of impurities that are extracted and cause high blanks. Blanks of the starting solutions are always done, often before samples are prepared, to insure that contamination is minimized. Some analysts soak their plasticware in 5% nitric acid before use. For the elements of interest, this was not necessary but may be necessary for some of the more common, first-row transition metals. Dimethylglyoxime (DMG) was purchased from Sigma-Aldrich (cat #162574-500g). Distilled water was triply distilled directly into PTFE bottles in-house using a quartz still. Transfer of solutions was made by either direct pouring, where possible, or using disposable plastic transfer pipettes (PGC Scientifics Cat #304-001)). ICP-MS standards were purchased from Alfa Aesar. A hood was dedicated to sample preparation and was scrubbed, sampled for blanks, lined with bench paper, and several layers of disposable paper towels (Techwipes) placed on top of the bench paper. A layer was renewed between each sample. A Teflon hood is recommended for elements in the first row of the transition metals. Pall VM-1 5.0 µm (cat #60693) filters were used for environmental surveys, extracted with 5% nitric acid, and analyzed without dilution. The white disks are the filters and the blue disks are spacers. The ICP-MS analysis was performed on a Thermo-Finnigan Element 2 running in both low resolution (300 AMU) and medium resolution (4000 AMU) modes. Selected ions were collected in both modes. For confirmation of an element, high resolution (nominally 10,000 AMU) was used.

Surface Analysis

The goal of surface analysis is to look for impurities that may have migrated to the surface during processing. To preserve sensitively, use of minimal amounts of solutions and prevention

of dissolution of the palladium is desirable. For surface analysis, approximately 120 mg of palladium foil or a few mg of palladium powder was placed in a polypropylene tube and 5 mL of 5% nitric acid was added. The acid was allowed to react at least 30 min. at room temperature, decanted into another tube or analyzed directly by ICP-MS (the fewer the steps, the less likely the contamination). The solution should be colorless or only light yellow in color – yellow being the color of the palladium ion in water. For some samples, after this initial surface analysis, the 5% nitric acid was decanted and 500 μ L - 1 mL of concentrated nitric acid was added to the palladium. This was allowed to stand for 30 min., diluted with distilled water to 5-10% nitric acid, and analyzed. If chloride is present, then the nitric acid will slowly dissolve the palladium. If the solution becomes yellow, due to dissolution of the palladium, then too much palladium is present and the sample must be diluted.¹³ Generally, the 5% nitric acid initial exposure removes most of the halides and prevents nitric acid from attacking the palladium but allows a stronger etch for other impurities. A survey scan by ICP-MS of most of the elements was made on these surface extracts.

Bulk Analysis

After the surface analysis, bulk analysis is performed on the same sample. The palladium foil is dissolved in minimal amounts of *aqua regia* (3:1 HCl:HNO₃). For recovery experiments, the solution is spiked with 5 ng of Sm and varying amounts of rare earths. For most analysis, no internal standard is added because the composition is unknown and the elements used as an internal standard may be present as an impurity. Alternatively, the palladium may be dissolved more slowly in concentrated nitric acid with 1% or less HCl. This procedure avoids excess chloride in the final solution that may interfere with certain elements by forming cluster ions. The excess acid may be removed by evaporation under nitrogen and 7 mL of 0.1M HCl added (2 % nitric acid may be used if the chloride needs to be minimized). After dissolving the palladium, 300 mg of DMG was introduced (for 120 mg of palladium – this was a 14% excess over a 2:1 DMG-Pd complex), the tubes capped, shaken, and rocked overnight at room temperature. Occasional shaking is helpful to disperse the DMG as its water solubility is low. The amount of DMG was varied depending on the amount of palladium analyzed and the amount added must be known for correction of the blank, as DMG contains traces of certain elements. Large excess of DMG should be avoided as uncomplexed DMG will float on the acid and make decantation in the next step more difficult. The samples were centrifuged to separate the DMG-Pd complex and the supernatant decanted into another tube (3-5 mL generally recovered). This solution was analyzed by ICP-MS directly. The supernatant will be yellow due to a decomposition products and the color is not reflective of the palladium concentration. The removal of the acid under nitrogen can be eliminated if the acid is kept to a minimum as evaporation takes time and the nitrogen stream may introduce contaminants. Some samples of supernatant were filtered through Whatman[®] Autovial[®] 0.45 μ m PTFE membranes (cat # AV125UORG). This filtration appears to introduce barium, likely from the glass prefilter present in the assembly. To avoid filtration, the solutions may just be decanted from the precipitate. If care is taken in decanting the supernatant from the DMG-Pd complex, no particles (which can plug the ICP-MS nebulizer) will be transferred to the second tube. DMG was not fully characterized for its ability to precipitate Pd selectively in the presence of traces of other elements as the focus of this work was on analysis of rare earths and silver.

Results and Discussion

Dimethylglyoxime (DMG) is known to precipitate only nickel and palladium by forming a 2:1 (DMG:metal) complex. This precipitation has been used to separate palladium from other platinum group metals for analysis of the palladium.¹⁴ The focus of this work was on analysis of rare earths and silver in a palladium matrix rather than the palladium itself. Figure 2 shows a typical tube containing the DMG complex with palladium. Although some of the DMG floats, the solution can be carefully poured into another tube without any precipitate being transferred. Direct transfer eliminates filtering, which can introduce contamination. The nebulizer on the ICP-MS has not been plugged by particles of DMG or the complex even though many samples have been analyzed. The DMG-Pd complex solubility varies with the acid strength (Figure 3), but the solubility does not appear to be affected by the type of acid used. Acid concentrations below 0.6M provide palladium levels sufficiently low (<1 PPM) to allow the solutions to be analyzed directly by ICP-MS without dilution.

For reproducibility of the precipitation, ten separate palladium foils were cut and analyzed. The amount of palladium remaining had a relative standard deviation of 2% and as the acid concentration was high, the palladium concentration averaged 6.5 PPM. Ayres and Berg used 1M HCl and found about 100 PPB of palladium in solution compared to 2.5 PPM in this work.¹⁴ Their solution, being cold, may account for the lower palladium levels, so further improvement in the present method could be envisioned.

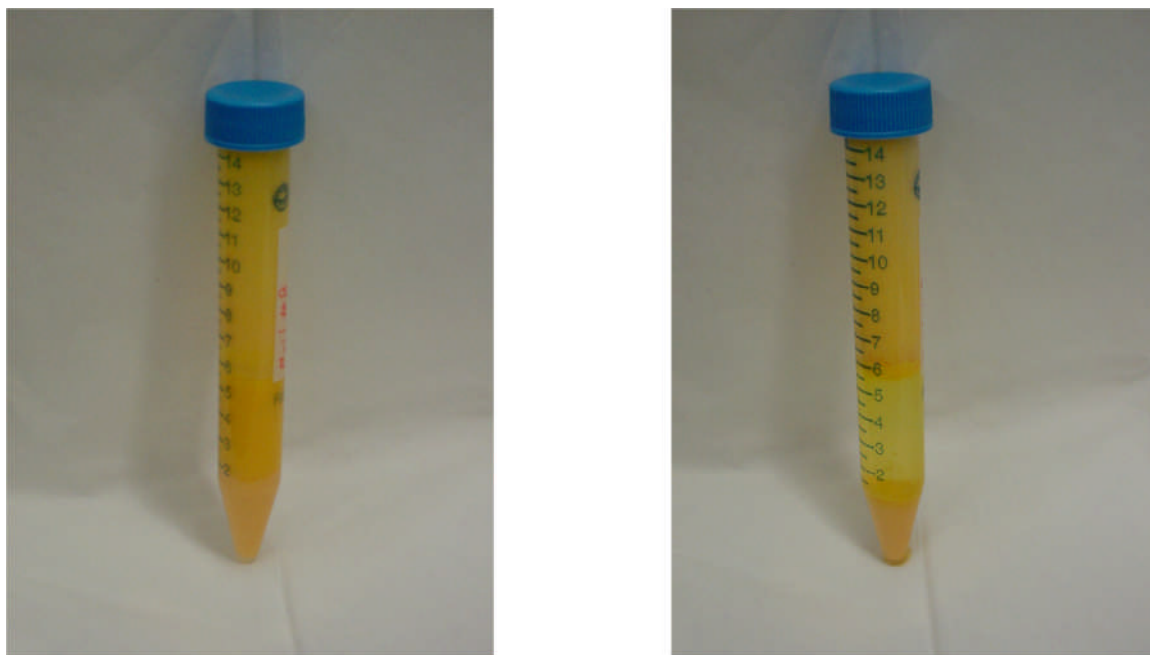


Figure 2. A typical reaction of DMG with palladium. (a) shows the tube before centrifugation and (b) shows the tube after centrifugation. The solution turns yellow, which is due to the palladium complex or impurities. In this case, only 6 mL of 0.1M HCl was used for reconstituting the dissolved palladium.

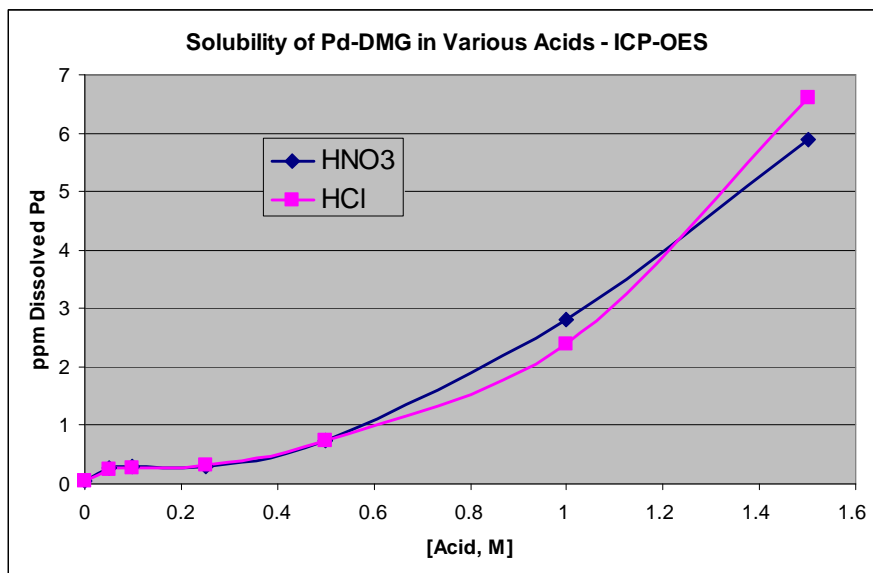


Figure 3. Amount of dissolved Pd vs. acid concentration. Recovered DMG-Pd complex was recrystallized from ethanol and air dried. This was shaken in the various media overnight before analysis. The quantitation was done by Inductively Coupled Plasma Optical Emission Spectroscopy (ICP-OES).

Example of Surface Analysis

One common occurrence when investigating the FPE is variation in heat production for different lots of palladium. Anecdotally, some electrolysis process will be working well, producing heat in excess of input power repeatedly for many runs. However, the palladium stock material is eventually exhausted and the replacement material no longer produces heat. The FPE may be dominated by surface impurities which may affect surface morphology and loading or unloading of deuterium. Selected data from the surface analysis on two lots of palladium are shown in Figure 4. L-25 was working in a process for many years, whereas L-40 was a newer lot that no-longer produced heat even though the production process was unchanged.¹⁵ Figure 4 shows a limited mass range of the typical broad scan run during bulk analysis. L-40 has substantial amounts of Zirconium relative to L-25, which cannot even be seen on this scale. Discussions with the manufacturer indicated that they had melted L-40 in a Yttrium stabilized Zirconium crucible. Likely the Zirconium arose from this source as traces of Yttrium were also observed. Although not demonstrated in this work, it is possible that there will be within lot variations on impurities that are not reflected in any certificate of analysis issued by the manufacturer. If palladium is poured in large amounts – say 25 kg at a time – then liquid near the center of the crucible should have a different composition than that near the walls. The effects of these impurities on the reproducibility of the FPE remain to be delineated.

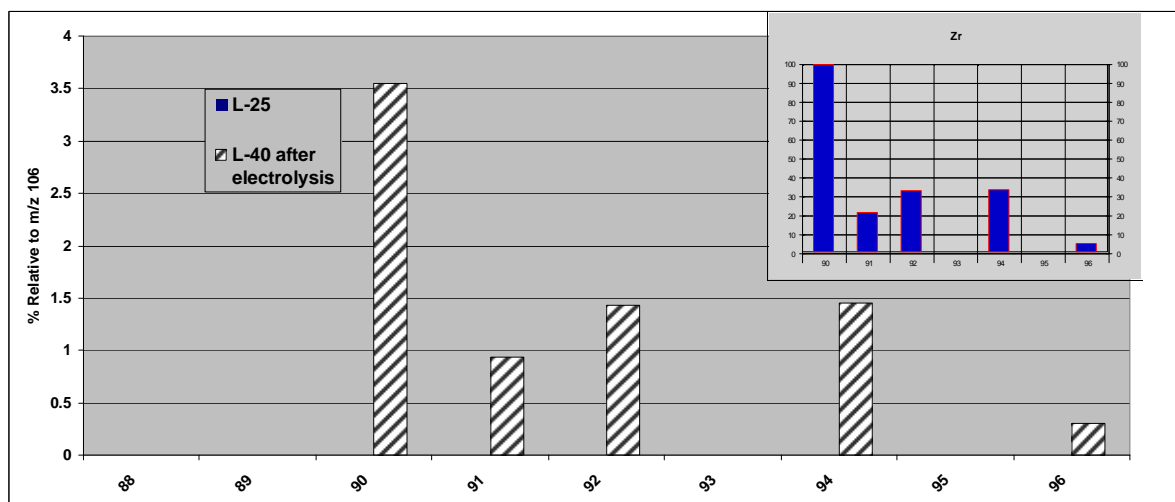


Figure 4. Examples of surface analysis. A limited mass range is shown. L-25 was working for heat production for many years, whereas L-40 was newly purchased material and showed no heat production. The Zirconium signal from L-25 is so low (at least $100 \times$ less) as not to be visible. The signal levels are reported relative to raw ion intensities of Palladium, but this is NOT an accurate measure of concentration as the relative dissolution rate of Zirconium vs. Palladium is unknown. The insert shows the expected isotopic distribution for Zirconium.

Example of Bulk Analysis

Bulk and surface analysis can help confirm if other measurements have correctly identified a change in impurity level of some element. In one Arata-type experiment,¹⁶ carried out in another laboratory independently of Arata, palladium black was pressurized inside a palladium cathode electrochemically. Analysis of the palladium black before and after use by Neutron Activation Analysis (NAA) suggested that there was an increase in silver level. A hypothesis was that the reaction $^{105}\text{Pd} + \text{D} \rightarrow ^{107}\text{Ag}$ could be occurring. If this reaction were to take place and produce all the silver increase observed, then the ^{107}Ag to ^{109}Ag isotopic ratio would be greatly changed from the natural 52:48 ratio. NAA is not ideally suited to this type of analysis because of background radiation from activated palladium takes years to decay to levels that can reveal trace amounts of silver. Surface analysis by ICP-MS indicated similar levels in silver between the two samples with the natural isotopic ratio for silver. Bulk analysis showed a 13x increase in silver (to 140 PPM) but with a natural isotopic ratio. Unfortunately, the palladium tube used for the cathode during electrolysis was unavailable so the source of the silver increase in the palladium undergoing pressurization is still unknown. However, the hypothesis that the silver was a transmutation product from palladium is unlikely since the isotopic ratio is what would be expected from natural abundance silver.

Reporting Limits of Detection

A typical calibration curve for DMG separations is constructed by spiking standards into a palladium solution (Figure 5). For accurate work, the amounts of palladium should be standardized. The blanks with DMG were always higher than that for DMG alone or for stock solutions likely reflecting impurities in the palladium used for preparing the standard curves. This makes answering the question – Is element X in the bulk palladium? – difficult because

the answer depends on what element is being sought, what are the blank levels, and how low a number is needed. To provide a better answer to that question, limits of the concentration of an element should be calculated in three ways:

- (1) With no blank subtraction. In this case the raw ion intensity is converted to concentration using only the slope of the calibration curve. This is the most conservative method and likely overestimates the presence of element X.
- (2) With the intercept of the DMG-Pd calibration curve subtracted from the ion counts. This is equivalent to subtracting a blank and accounts for both the purity of the DMG and the purity of the palladium making the standards. This procedure could underestimate the amount of element X in the bulk as element X may also be present in the palladium used to make the standard curve.
- (3) With blank subtraction of the DMG blanks without added palladium. This method does not take into account an untested hypothesis that the DMG may complex elements as impurities during manufacture and only have them released if they are displaced by palladium. If this hypothesis is correct, then this subtraction method will overestimate the amount of some target element.

The reporting of the absence of some element is only relevant if the absence of element X (*i.e.* the lower amount that some element was present) in the bulk starting material was a concern. If this case, blank subtraction using method 3 is preferred. For example, if some process was claimed to be producing element X, one might want to know if element X were in the bulk and just migrating to the surface during a chemical process rather than a true transmutation event. Obviously, if all three reporting methods produce limits on the amount of element X substantially below that found during the process being tested, then elements X cannot come from the bulk palladium. Of course, other sources of element X, such as contamination during handling, are not eliminated.

Figure 5 shows a calibration curve for Silver and Indium in a palladium matrix after DMG precipitation. Normally 8 point calibration curves are employed for quantitation and have correlation coefficients >0.999. The concentration on the X-Axis refers to the concentration in the liquid sample. For example, 1 PPB would be prepared by adding 5 ng to a 5 mL solution of palladium in 2.5% nitric acid. In parallel experiments without DMG or palladium, the slopes are about 12% higher, indicating that some silver and indium are lost in the DMG precipitation. The intercept corresponds to a Limit of Detection (LOD) of 3 PPT. If 10 mg of Pd powder were analyzed without dilution, a 3 PPT LOD would correspond to 3.3 PPB in the Pd powder. Where possible, quantitation (and calibration) is done with multiple isotopes (^{107}Ag and ^{109}Ag in this example) and at multiple mass resolutions (LR = low resolution of 300 AMU). If no interferents are present, then the various calculations should agree. The calibration plots for both isotopes of silver overlay each other.

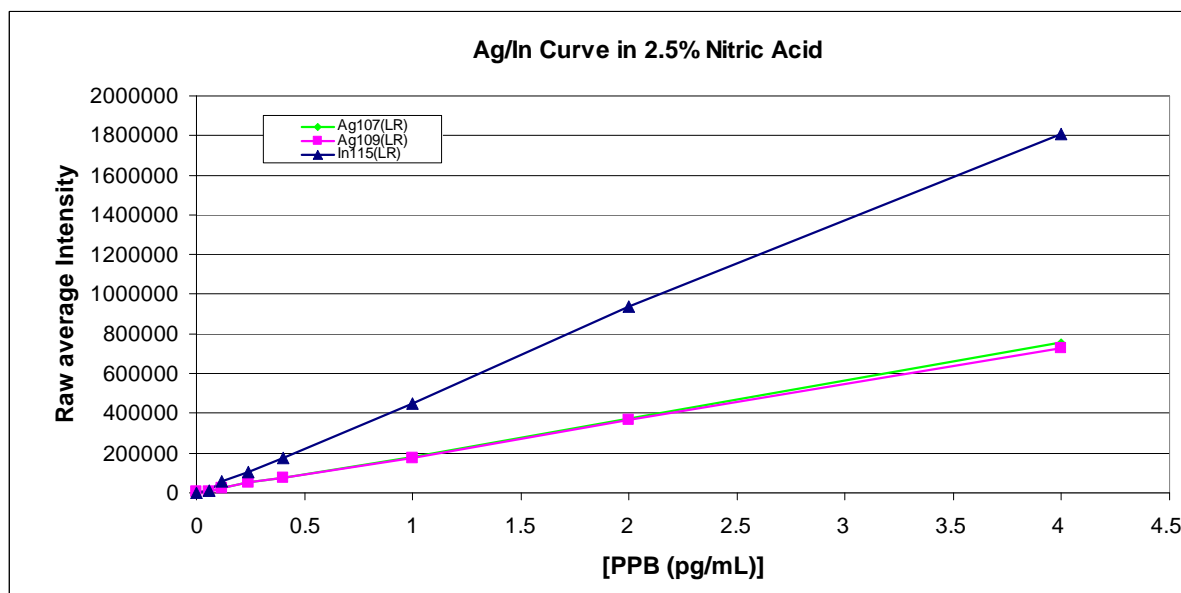


Figure 5. Calibration curve for Silver and Indium in a palladium matrix after DMG precipitation

Controlled Etching of Palladium

Palladium is often dissolved in *aqua regia*, a 3:1 mixture of HCl and HNO₃. For the noble metals, *aqua regia* is thought to oxidize a small amount of metal on the surface and then complex the ion with the excess chloride. The complex shifts the reaction to the dissolved metals otherwise nitric acid alone should not completely dissolve gold, platinum, or palladium. Palladium is often cleaned with concentrated nitric acid. In this process substantial palladium is sometimes removed as the acid turns yellow. Yet, no chloride is intentionally added. We have used that observation to both control the etching rate and measure the amounts of chloride (or likely other halides) present on the surface as impurities. The chemistry in *aqua regia* is complex and other oxidants, such as chlorine and nitrosyl chloride may be present, being produced from nitric acid reacting with the chloride from the HCl. These other oxidants could oxidize the palladium directly and in the process be reduced back to chloride that can be reoxidized by the nitric acid in a catalytic cycle. Figure 6 shows how the rate of oxidation can be translated into the amount of chloride present on the surface. Sample 1 was a multilayered sample and appeared to have buried chloride as its slope was substantially different than the controls after adding the HCl. Through control of the nitric acid concentration and chloride content, one can slow down the etching to remove impurities without greatly etching the palladium. For surface analysis, 5% nitric acid without chloride appears satisfactory as an initial cleaning.

Figure 6 shows the effects of controlled etching of palladium and measuring chloride content. The control samples had been previously etched with high-purity nitric acid and rinsed before use with 5% nitric acid. Etching was done with 25% nitric acid (to slow the etching rate) under constant sonication. Aliquots (200 μ L) were removed at each time point and diluted to 4 mL for analysis by ICP-MS. UV spectroscopy could have also been employed with reduced sensitivity.¹⁷ After 30 min., 5 μ L of concentrated HCl was added. Comparing the slopes with

the known addition of chloride to the initial slopes estimates the original chloride surface contamination as shown in the insert.

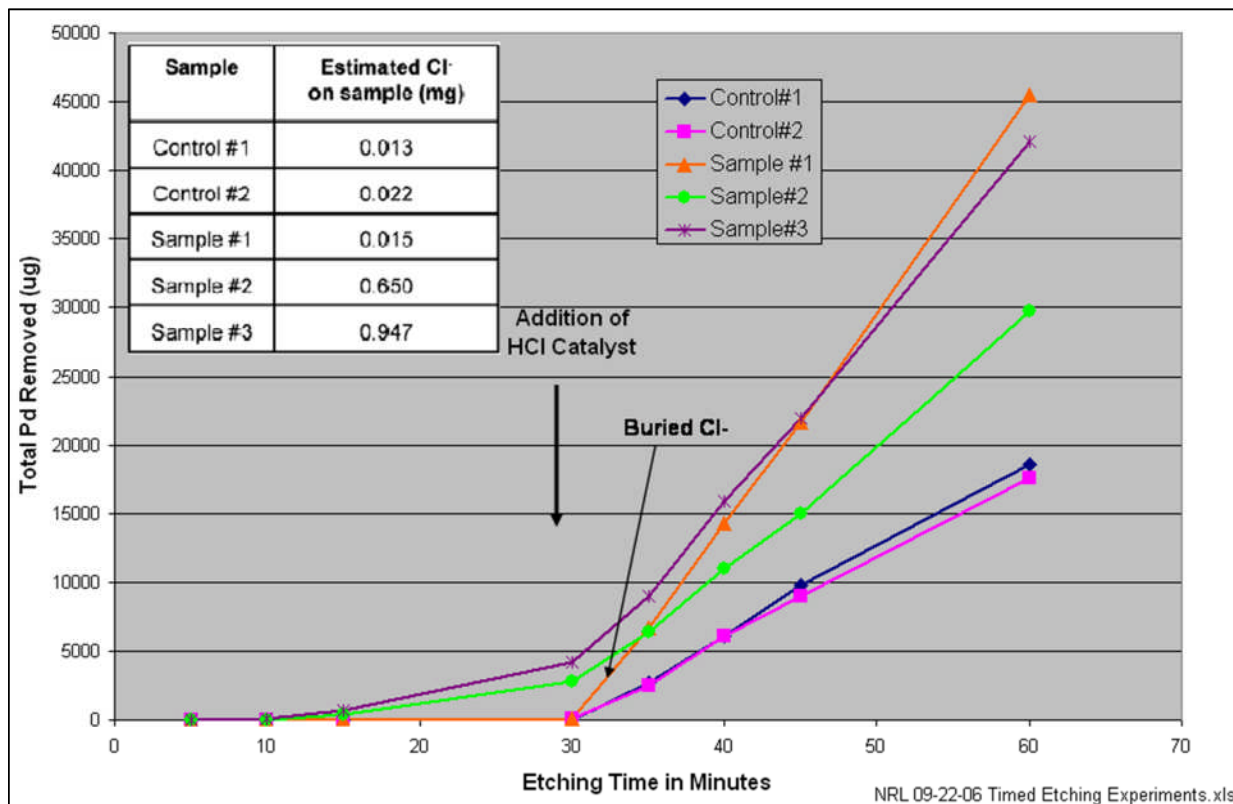


Figure 6. Controlled etching of palladium and measuring chloride content

Conclusions

If the Fleischmann-Pons Effect is dominated by impurities, then surface and bulk analysis can help identify those impurities. Dimethylglyoxime will precipitate selectively palladium from acid solutions leaving most of the impurities and allow analysis by ICP-MS without dilution. By avoiding dilution, the sensitivity and precision of the analysis can be increased. By controlling the amount of chloride in the nitric acid used to etch palladium, a controlled etch is possible, which may be useful to prepare certain structures on the palladium surface.

Acknowledgements

Funding from ONR and DARPA is gratefully acknowledged. The original concept of using DMG for precipitation of palladium was suggested by Ken Rubenstein. I also would like to thank Robert Mowery for the analysis of the DMG-Pd complexes by ICP-OES. Approved for Public Release, Distribution Unlimited.

References and Notes

1. H. Lindlar and R. Dubuis, "Palladium Catalyst for Partial Reduction of Acetylenes", *Organic Syntheses, Collected Volume 5*, p.880.
2. W. Bonrath, M. Eggersdorfer, and T. Netscher, "Catalysis in the industrial preparation of vitamins and nutraceuticals", *Catalysis Today*, **121** (2007) 45-57.
3. Nitrogen, Carbon, Oxygen, and all the Inert Gases cannot be measured due to their presence in the matrix or ionization gas. Also, other elements are difficult if they have masses that overlap adducts or dimers of the main matrix or ionization gas. For example, Sulfur-32 has an interference from an O₂ adduct ion.
4. The Argon plasma is at approximately 10,000°K.
5. I use the term adduct formation to refer to any ion not elemental in nature irrespective of the mechanism of formation. The process of formation of adducts is different in ICP-MS than in SIMS. In SIMS the molecules may come from the surface as an intact molecular ion or a neutral and subsequently have attached a cation, such as sodium, in the gas phase. In ICP-MS the adducts may arise though recombination between the plasma torch and the ion extraction optics.
6. M.A. Vaughan and G. Horlick, "Oxide, Hydroxide, and Doubly Charged Analyte Species in Inductively Coupled Plasma/Mass Spectrometry", *Applied Spectroscopy*, **40** (1986) 434-445.
7. For a discussion of some adduct ions in SIMS see: T. Hioki, J. Gao, N. Takahashi, S. Hibi, A. Murase, T. Motohiro, and J. Kasagi, "Influence of Deuterium Gas Permeation on Surface Elemental Change of Ion-Implanted Pd", Abstract #29, 14th International Conference on Condensed Matter Nuclear Science, Hyatt Regency, Washington, DC, August 10-15, 2008.
8. D.A. Kidwell, M.M. Ross, and R.J. Colton, "The Mechanism of Ion Production in Secondary Ion Mass Spectrometry", *Int. J. Mass Spectrom. Ion Proc.*, **78** (1987) 315-328.
9. D.A. Kidwell, "Selective detection of species in complex matrices by chemical derivatization and secondary ion mass spectrometry", U.S. Patent #4,902,627 issued February 20, 1990.
10. These authors observed a 4.7% mass bias/AMU using a quadrupole instrument. Generally it is in the 1%/AMU range. See: A.R. Warren, L.A. Allen, H.M. Pang, R.S. Houk, and M. Janghorbani, "Simultaneous Measurement of Ion Ratios by Inductively-Coupled Plasma-Mass Spectrometry with A Twin-Quadrupole Instrument", *Applied Spectroscopy*, **48** (1994) 1360-1366.
11. J. Barling and D. Weis, "Influence of non-spectral matrix effects on the accuracy of Pb isotope ratio measurement by MC-ICP-MS: implications for the external normalization method of instrumental mass bias correction", *Journal of Analytical Atomic Spectrometry*, **23** (2008) 1017-1025.
12. Generally, ICP-MS can detect 1 PPT of an element, which would correspond to 1 PPM in the original sample if a 1:1000 dilution were made. Other techniques, such as glow discharge mass spectrometry, can also detect 1 PPM impurity levels directly.
13. Diluted *aqua regia* can also be used for surface analysis. However, it is yellow in color and makes visual estimation of the palladium content difficult.

14. G.H. Ayres, and E.W. Berg, "Separation of Palladium from Platinum, Iridium, and Rhodium with Dimethylglyoxime", *Analytical Chemistry*, **25** (1953) 980-981.
15. Palladium samples were kindly provided by Vittorio Violante.
16. Y. Arata, and Y.C. Zhang, "Anomalous production of gaseous ^4He at the inside of 'DS cathode' during D_2O -electrolysis", *Proc. Jpn. Acad., Ser. B*, **75** (1999) 281.
17. M. Balcerzak and K. Pergol, "Selective Determination of Platinum and Palladium in Iodide Media by Derivative Spectrophotometry", *Chem. Anal. (Warsaw)*, **48** (2003) 87.

Investigation of Nuclear Transmutation Using Multilayered CaO/X/Pd Samples Under Deuterium Permeation

T. Yamaguchi¹, Y. Sasaki¹, T. Nohmi¹, A. Taniike¹, Y. Furuyama¹, A. Kitamura¹ and A. Takahashi²

¹ Division of Marine Engineering, Graduate School of Maritime Sciences, Kobe University
5-1-1 Fukaeminami-machi, Higashinada-ku, Kobe 658-0022, Japan

² Osaka University
2-1 Yamadaoka, Suita, Osaka 565-0871, Japan

Abstract

We constructed an experimental system in which accelerator analyses by PIXE, ERDA, NRA and RBS can be made *in situ* under deuterium (D) gas permeation through multilayered CaO/X/Pd samples to induce nuclear transmutation in the element X. Furthermore, to examine the effect of flow direction, we made a D gas permeation system separated from the accelerator beam-line chamber for *ex-situ* accelerator analysis. We report the results of recent experiments in this paper.

1. Introduction

It has been claimed that the forced permeation of D through Cs(Sr)-deposited multilayered Pd/(CaO/Pd)₅ samples induces nuclear transmutations from ¹³³Cs(⁸⁸Sr) to ¹⁴¹Pr(⁹⁶Mo) [1]. To confirm the nuclear transmutation and to study the mechanism, we constructed an experimental system in which accelerator analyses by PIXE, ERDA, NRA and RBS can be made *in situ* under D gas permeation through the samples. Furthermore, we have done experiments using a separate D gas permeation system and an *ex-situ* accelerator analysis.

In our previous work [2], we used XPS to characterize the CaO/Sr/Pd sample. The XPS method has a high sensitivity of detection limit 7×10^{12} atoms/cm², but it is applicable only for the near-surface (< 3 nm) region, and is necessarily destructive when measurement of the depth distribution over tens of nm is required. Therefore we have used PIXE to measure nondestructively the time-dependent concentration of the elements in the sample *in situ*, at the cost of increasing the sensitivity limit to 1×10^{14} atoms/cm².

2. Experimental apparatus and procedure

The major system is an *in-situ* system shown in Fig. 1. The film was mounted on a vacuum flange with an O-ring seal, and the rear surface was exposed to D gas at a pressure of 0.1 MPa typically. The sample temperature was kept at 70°C during D permeation. We performed *in situ* analyses to characterize the sample before, during and after D permeation; we used the 3-MeV proton PIXE for elemental analysis, the 2.5-MeV ³He NRA or 4-MeV ⁴He ERDA for D distribution analysis.

The other system is a D-absorption apparatus with an *ex-situ* accelerator analysis system, shown in Fig. 2. In the analysis, we intended to make a large incident angle (85°) measurement to increase PIXE sensitivity. First, we made samples and did PIXE analysis. Next, the samples were mounted on a vacuum flange and the rear surfaces were exposed to D_2 gas at a pressure of 0.1 MPa similarly to the *in-situ* system. Finally, after D permeation we did PIXE analysis again. In *ex-situ* experiments, we skipped NRA and ERDA for D distribution analysis.

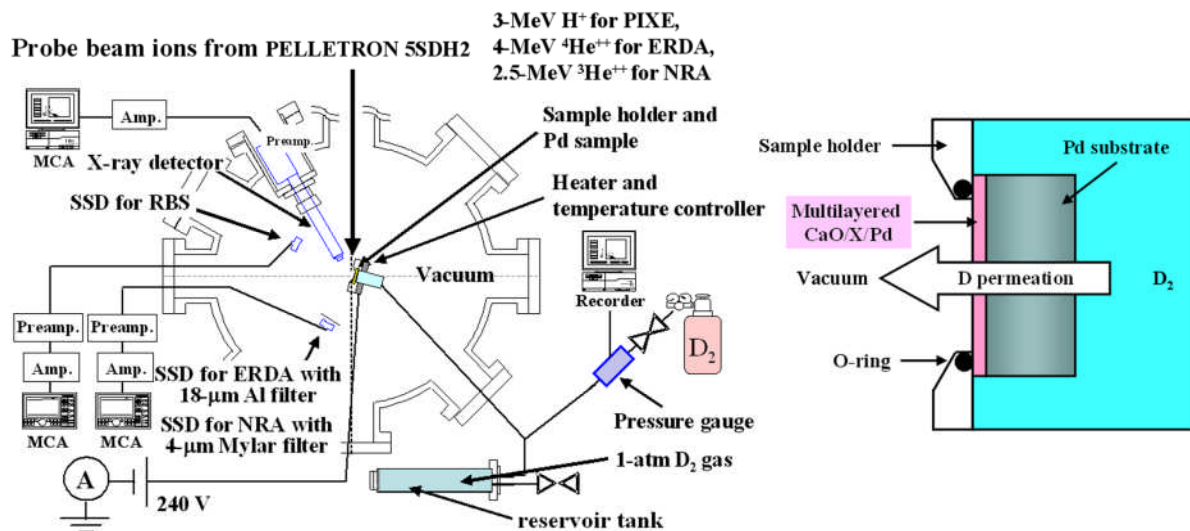


Figure 1. *In-situ* system.

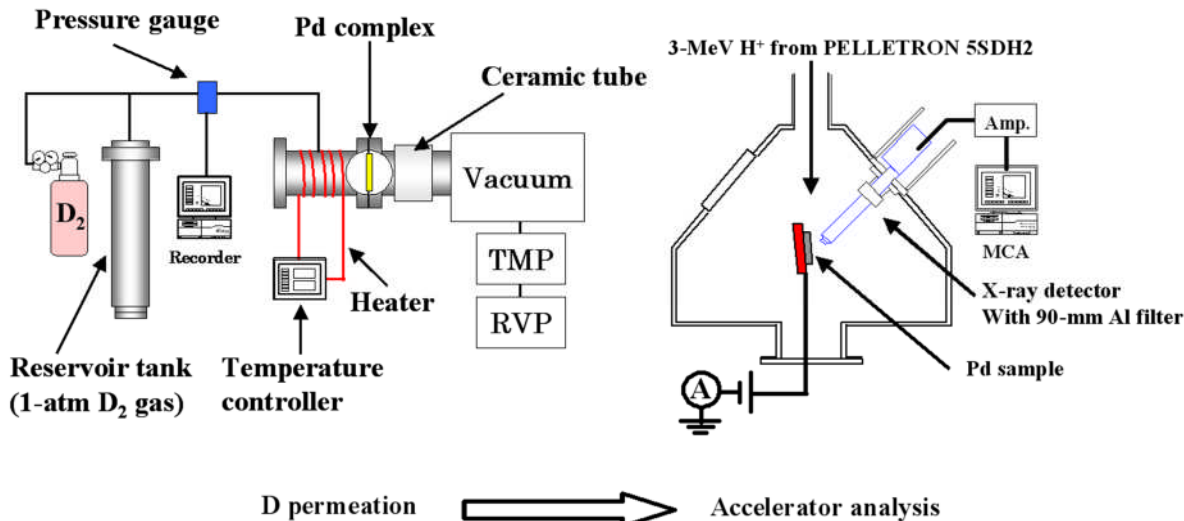


Figure 2. *Ex-situ* system.

3. *in-situ* experiments

3-1. D permeation through monolayer samples

A 0.1 mm thick Pd bulk plate was annealed for 3 to 10 hours at 570 - 1170 K, and then immersed in aqua regia/H₂O or aqua regia/D₂O for 100 seconds. Sr atoms were deposited on one side of the Pd bulk surface using electrochemical deposition, by carefully placing the Pd bulk plate on the surface of the 10-mM Sr(NO₃)₂/D₂O solution. Finally, a CaO layer with a thickness of 2 - 8 nm was deposited on the Sr/Pd samples.

The results of Run 9 are shown in Table 1. We observed some increase in molybdenum areal density. Run 9 is discussed in more detail below.

Table 1. Temporal variation of the areal densities of detected element during the permeation process in Run 9.

Run 9	0.05 sccm	
Vacuum/CaO/Sr/Pd/D ₂		
D fluence [10 ²¹ cm ⁻²]	Areal density [10 ¹⁵ cm ⁻²]	
	Sr	Mo
0	2.5 ± 0.3	0
18.8	2.3 ± 0.3	1.8 ± 0.8
21.6	2.1 ± 0.4	1.7 ± 1.1
31.1	2.1 ± 0.3	2.1 ± 0.9
33.7	2.7 ± 0.3	1.8 ± 0.9
34.9	2.3 ± 0.3	1.1 ± 0.9
40.9	1.9 ± 0.3	2.5 ± 0.9
43.9	2.4 ± 0.2	1.1 ± 0.7

The PIXE spectra are shown in Fig. 3. An increase ($2.5 \times 10^{15} \text{ cm}^{-2}$) in Mo areal density and a slight decrease ($0.6 \times 10^{15} \text{ cm}^{-2}$) in Sr areal density were observed until after the 2160 hour permeation run. Typical examples of ERDA spectra obtained at 1650 hours after initiation of D permeation are shown in Fig. 4. We notice small humps at the recoil particle energy of 1.3 MeV, below which recoil hydrogen atoms (H) are detected. Depth profiles of the D and H densities deduced from them are shown in Fig. 5. The D density at 1650 hours of $3.9 \times 10^{22} \text{ cm}^{-3}$ averaged over the surface region up to depths of 0.5 μm corresponds to the mean composition of PdD_{0.58}.

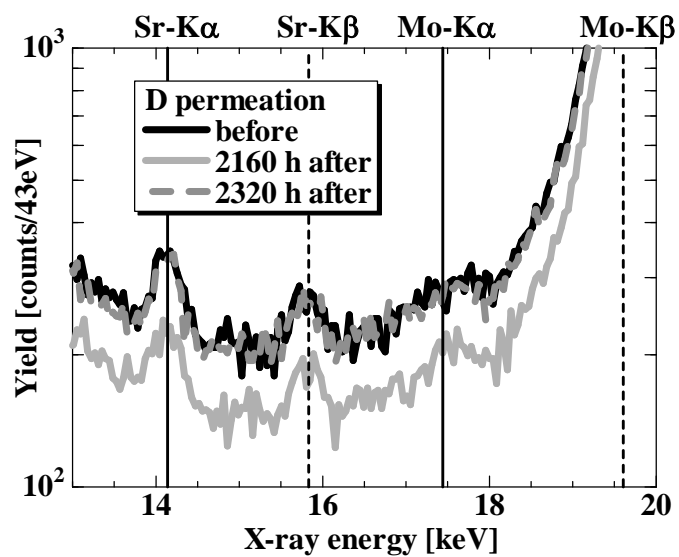


Figure 3. PIXE spectra in Run 9.

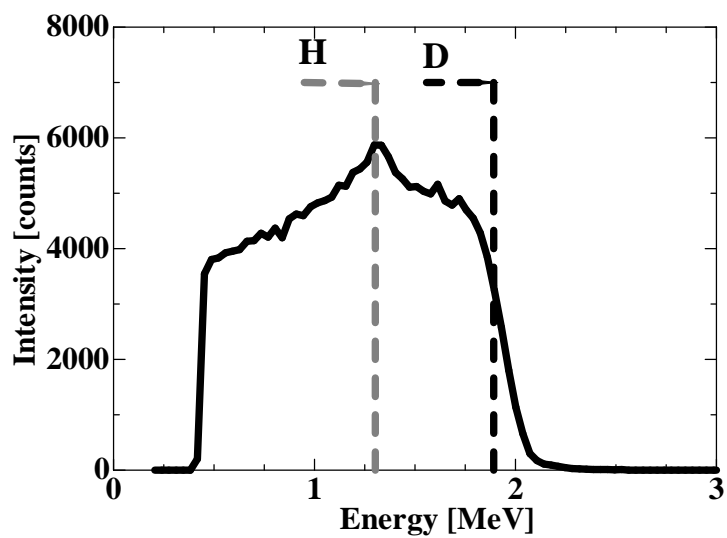


Figure 4. Typical ERDA spectrum.

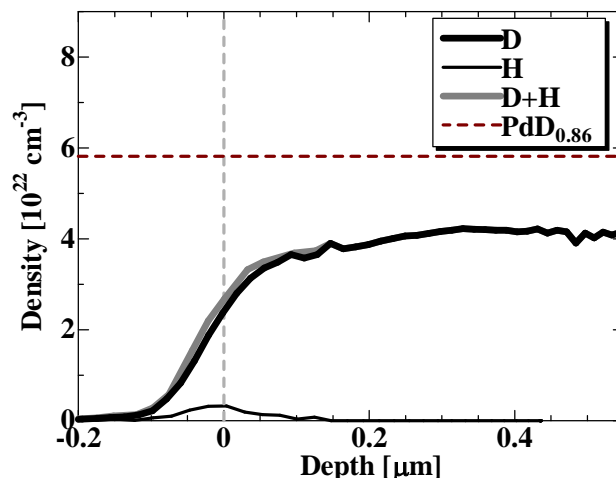


Figure 5. Depth profiles of the D and H densities in run 9.

3-2. D permeation through multilayered samples

Next, we discuss the results of Runs 4, 10 and 11 using multilayered samples prepared for the purpose of increasing the number of the atoms to be transmuted. For the sample of Run 4, a Pd layer with a thickness of 54 nm was deposited on the Sr/Pd surface by RF sputtering. We repeated the process of Sr deposition followed by Pd sputtering nine times to make a (Sr/Pd)₉/Sr/Pd sample. The multilayered samples used in Run 10 and 11 were prepared by means of sputtering deposition of CaO and Pd layers with a thickness of 2 nm and 18 nm, respectively, in addition to electrochemical deposition of Sr. The results of Run 10 and 11 are summarized in Table 2. The PIXE spectra in Run 4 are shown in Fig. 6. In this Run 4, the identification of Mo was satisfactory.

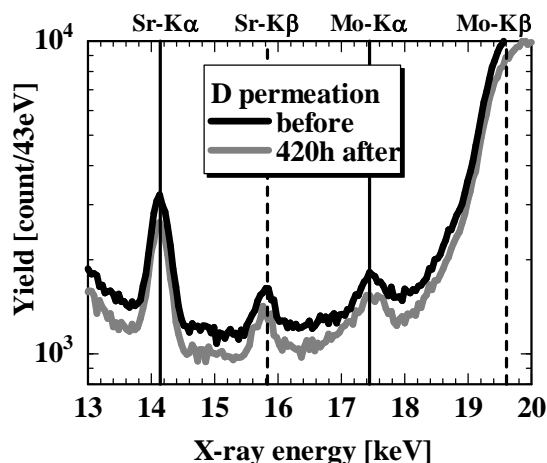


Figure 6. PIXE spectra.

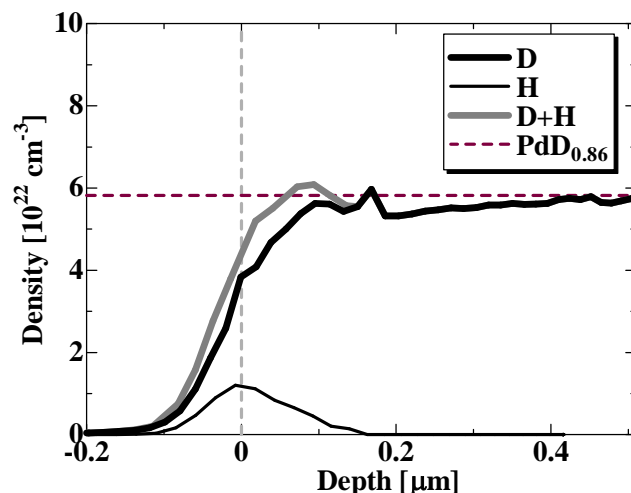


Figure 7. Depth profiles of the D and H densities in Run 10.

In Run 10, we saw hardly any change in the areal densities of Sr and Mo. The ERDA was successfully applied to reveal the D density approaching the saturation value in this sample. The depth profiles of the D and H densities deduced from them are shown in Fig. 7. The D density at 189 hours of $5.8 \times 10^{22} \text{ cm}^{-3}$ averaged over the surface region up to the depth of 0.5 μm corresponds to the mean composition of $\text{PdD}_{0.86}$.

Finally, in the Run 11, a slight increase in Mo areal density and a decrease in Sr areal density were observed until the end of the 971-hour permeation. The depth profiles of the D and H densities deduced from them are shown in Fig. 8. The D density at 189 hours of $1.5 \times 10^{21} \text{ cm}^{-3}$ averaged over the surface region up to the depth of 0.5 μm corresponds to the mean composition of $\text{PdD}_{0.02}$. The D density is very small in this sample. There is a rather large amount of contaminant H atoms.

Table 2. Temporal variation of the areal densities of detected element during the permeation process in Run 10 and 11.

Run 10	0.47* sccm		Run 11	0.03 sccm	
Vacuum/(CaO/Sr/Pd) ₉ /CaO/Sr/Pd/D ₂			Vacuum/Pd/(CaO/Sr/Pd) ₉ /CaO/Sr/Pd/D ₂		
D fluence [10 ²¹ cm ⁻²]	Areal density [10 ¹⁵ cm ⁻²]		D fluence [10 ²¹ cm ⁻²]	Areal density [10 ¹⁵ cm ⁻²]	
	Sr	Mo		Sr	Mo
0	49.5 ± 0.4	0.2 ± 0.1	0	24.1 ± 0.4	0
9.0	50.5 ± 0.4	0.7 ± 0.3	1.9	24.3 ± 0.4	0
31.6	49.4 ± 0.5	0.3 ± 0.1	7.8	20.1 ± 0.3	0
95.0	50.1 ± 0.6	0.4 ± 0.3	10.2	21.0 ± 0.3	1.2 ± 0.5
126.0	52.0 ± 0.5	0.4 ± 0.2	13.3	21.2 ± 0.3	0.7 ± 0.4

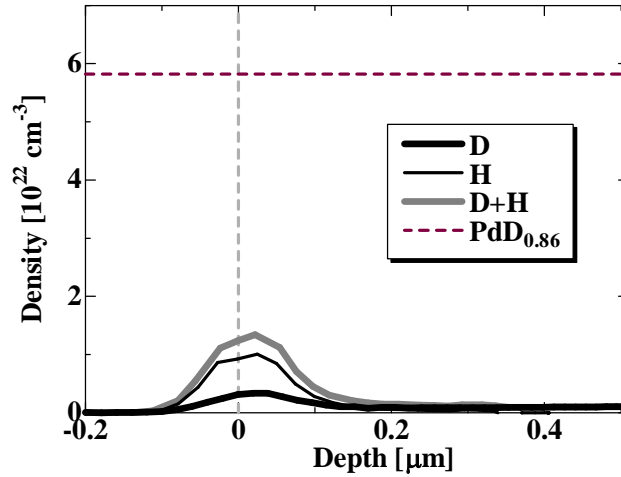


Figure 8. Depth profiles of the D and H densities in Run 11.

3-3. D permeation through multilayered samples (surface version)

We made the monolayer sample again to examine whether a nuclear transmutation was caused at the surface. At first a CaO layer with a thickness of 2 nm was deposited on the Pd substrate. And a Pd layer with a thickness of 18 nm was deposited on the CaO/Pd sample. Finally, Sr atoms were deposited on Pd/CaO/Pd sample.

The results of Run 12 are shown in Table 3. An increase ($4.5 \times 10^{14} \text{ cm}^{-2}$) in Mo areal density and a decrease ($9.4 \times 10^{14} \text{ cm}^{-2}$) in Sr areal density were observed under D fluence of $111.4 \times 10^{21} \text{ cm}^{-2}$ for permeation. However, a null Mo areal density was obtained in the succeeding measurement with the D fluence of $123.7 \times 10^{21} \text{ cm}^{-2}$, which prevents a definite conclusion.

Table 3. Temporal variation of the areal densities of detected element during the permeation process in Run 12

Run12	0.64 sccm	
Vacuum/Sr/Pd/CaO/Pd/D ₂		
D fluence [10 ²¹ cm ⁻²]	Areal density [10 ¹⁵ cm ⁻²]	
	Sr	Mo
0	3.5 ± 0.1	0
68.5	2.3 ± 0.1	0.2 ± 0.2
111.4	2.6 ± 0.1	0.5 ± 0.2
123.7	2.2 ± 0.1	0

3-4. Summary of the *in-situ* experiments

Results of Run 9 and Run 12 suggested occurrence of the nuclear transmutation, and Run 11 showed marginal increase in Mo, while the other runs (4, 6, 7, 8, and 10) showed no significant

increases in Mo. However, identification of Mo by PIXE was not definite. We need Mo atoms with areal density larger than $3 \times 10^{15} \text{ cm}^{-2}$ to make a clear identification by PIXE analysis. In summary, we observed what appear to be positive results in two out of eight cases, but with weak identification.

4. *en-situ* experiments

For Run B1 and B2, we made a CaO/Sr/Pd and a Pd/CaO/Sr/Pd sample. D gas permeates from the palladium substrate side to the multilayer side. The sample used in Run B3 has the same structure as the sample for Run 12, but with a reversed flow direction of D. Results of the PIXE analysis in Run B1 through B3 are shown in Table 4. We could identify Sr with areal density as low as $7.2 \times 10^{13} \text{ cm}^{-2}$ by measurements with large incident angle. A decrease in Sr areal density was observed clearly. However, an increase in Mo areal density to compensate the decrease in Sr areal density was not observed.

Table 4. Temporal variation of the areal densities of detected element during the permeation process in Run B1 - 3.

Run B1	0.05 sccm		Run B2	0.07 sccm		Run B3	0.09 sccm	
Vacuum/CaO/Sr/Pd/D ₂			Vacuum/CaO/Sr/Pd/D ₂			Vacuum/CaO/Sr/Pd/D ₂		
Areal density [10 ¹⁵ cm ⁻²]			Areal density [10 ¹⁴ cm ⁻²]			Areal density [10 ¹⁴ cm ⁻²]		
	Sr	Mo		Sr	Mo		Sr	Mo
Before	5.6 ± 0.1	0.1 ± 0.1	Before	8.1 ± 0.1	0.3 ± 0.2	Before	3.4 ± 0.2	0.3 ± 0.2
After	0.7 ± 0.04	0.2 ± 0.1	After	1.5 ± 0.1	0.4 ± 0.2	After	1.4 ± 0.1	0.2 ± 0.1

5. Concluding Remarks

An increase in Mo areal density was seen in deuterium permeation. Apparently positive results in the present transmutation experiments were obtained in about 25% of the runs. However, the identification of Mo resolved peaks was not definite, and needs to be improved.

We have at least two problems to be solved in future research: to improve the sample uniformity, and to increase the D permeation rate.

References

1. Y. Iwamura, M. Sakano and T. Itoh; Jpn. J. Appl. Phys. 41 (2002) 4642-4650.
2. A. Kitamura, et al.; Proc. ICCF12 (World Scientific Publ. Co. Pte. Ltd, 2006) 272-277.

Influence of Deuterium Gas Permeation on Surface Elemental Change of ^{88}Sr Ion-Implanted Pd and Pd/CaO Multi-layer System

T. Hioki¹, J. Gao¹, N. Takahashi¹, S. Hibi¹, A. Murase¹, T. Motohiro¹ and J. Kasagi²

¹ Toyota Central Research and Development Laboratories Inc., Japan

² Laboratory for Nuclear Science, Tohoku University, Japan

Abstract

The selected nuclear transmutation $^{88}\text{Sr} \rightarrow ^{96}\text{Mo}$ reported by Iwamura et al. was studied by combining $^{88}\text{Sr}^+$ ion implantation with time-of-flight secondary ion mass spectrometry (TOF-SIMS) measurements of the isotopic abundance ratio for Mo. For both the Sr ion implanted Pd and Pd/CaO multilayer foils, Mo was clearly observed after D_2 gas permeation, when the foils were subsequently heat-treated in air in order to remove S which condensed at the surface during the permeation treatment. For the Sr implanted Pd, the isotopic abundance ratio for the observed Mo was similar to that of natural Mo. For the Sr implanted multilayer foil, a strong peak at a mass close to ^{96}Mo was observed, although the peak was contaminated with an unknown peak, probably from GaAl or Ca_2O . An analysis of the TOF-SIMS data cannot be used to rule out the possibility of existence of “excess ^{96}Mo ” exceeding the amount of ^{96}Mo of nature. To obtain a definite conclusion, further studies on the mechanism of the appearance of natural Mo and the origin and the behavior of the unknown peak are required.

1. Introduction

Nuclear transmutation with deuterium gas permeation through a Pd/CaO multilayer foil was first reported by Iwamura et al.¹ Using X-ray photoelectron spectroscopy (XPS), they demonstrated that Sr and Cs deposited on the surface of the multilayer foil changes to Mo and Pr, respectively, with D_2 gas permeation for a period of a week or so at a temperature as low as 343 K. The isotopic abundance ratio for the induced Mo was quite different from that for natural Mo; this observation with secondary ion mass spectrometry has suggested that the change is caused by a nuclear process. Using the D_2 gas permeation method, they have further found that Ba changes to Sm.²

It has been assumed that these results will be easily replicated in different laboratories. However, only a limited number of replication experiments have been reported so far.³⁻⁵ One of the difficulties is to reproduce the high D_2 gas flow rate.⁶ A D_2 gas flow rate through Pd is sensitive to the state of surface. Therefore, appropriate pretreatments of Pd as well as clean experimental environment are required to produce a high D_2 flow rate. We have reported that commercially available Pd foils are often contaminated with S⁷ and a segregation of the S impurity on the surface during D_2 gas permeation results in a lowering of the flow rate.⁸

Furthermore, if S is on the surface, it is difficult to examine the generation of Mo by using XPS, because a S_{2s} peak in the XPS spectrum overlaps with Mo_{3d} peaks.⁷

In this study, both pure Pd foils and Pd foils with five Pd/CaO layers were implanted with 65-keV ⁸⁸Sr⁺ ions, these foils were subjected to D₂ gas permeation treatments at 343 K, and XPS and TOF-SIMS measurements were performed to examine the change of surface elements before and after D₂ gas permeation.

2. Experimental

2.1. Sample Preparation

Pd foils of 50 μm (purity: 99.97%) and 100 μm (99.95%) in thickness were obtained from Nilaco Corporation for substrates of the complex foils. Three types of sample were prepared as summarized in Table 1. Sample #3, for example, was prepared as follows. An as-purchased foil was first ultrasonically cleaned with ethanol and heat-treated in vacuum (5×10^{-5} Pa) at 1223 K for 5 hours and subsequently in air at 873 K for 10 minutes. Layers of CaO and Pd were piled up alternately on the substrate foil, using the RF sputter deposition method. The structure of the multilayer was the same as reported by Iwamura et al.: Pd (40 nm) / CaO (2 nm) / Pd (18 nm) / CaO (2 nm) / Pd (18 nm) / CaO (2 nm) / Pd (18 nm) / CaO (2 nm) / Pd (18 nm) / CaO (2 nm) / Pd (100 μm). Then ⁸⁸Sr was implanted in the multilayer foil with 65-keV ⁸⁸Sr⁺ ion bombardment, with a dose of 1×10^{16} ions/cm². Subsequently the foil was treated in air at 573 K for 10 minutes in order to remove carbonaceous materials deposited during the ion implantation. The sample was then subjected to D₂ gas permeation treatments at 343 K for 230 h.

Table 1. Procedures for sample preparation

	#1 (Sr- implanted Pd)	#2 (Pd)	#3 (Sr- implanted multilayer system)
Pretreatments	• 50μmPd : ultrasonic cleaning with ethanol	• 50μmPd : ultrasonic cleaning with ethanol • 1273K × 10min in air	• 100μmPd : ultrasonic cleaning with ethanol • 1223K × 5h in vacuum • 873K × 10min in air
Multilayer formation	—	—	• Pd(40nm) / 4 × [CaO(2nm) / Pd(18nm)] / CaO(2nm) / Pd(100μm)
Ion implantation	• 65keV ⁸⁸ Sr ⁺ 1×10^{16} / cm ²	—	• 65keV ⁸⁸ Sr ⁺ 1×10^{16} / cm ² • 573K × 10min in air
Heat treatments	• 1223K × 5h in vacuum • 873K × 10min in air	—	—
D ₂ permeation	• 260h at 343K, 200kPa	• 70h at 343K, 200kPa	• 230h at 343K, 200kPa
Heat treatment after D ₂ permeation	• 1273K × 10min in air	• 1273K × 10min in air	• 1273K × 10min in air

2.2 Elemental Analysis

The XPS method was employed to examine the change of surface elements with D₂ gas permeation. The system used was ULVAC-PHI, Inc. model Quantera SXM (20 kV, 100 W). The X-ray used to excite the photoelectrons was the monochromatic Al-K_α line (1.438 keV). The size of the incident X-ray beam was 100 × 1500 μm². A TOF-SIMS (ULVAC-PHI, Inc. model TRIFT II) was used to measure isotopic abundance ratios. The primary ion was ⁶⁹Ga⁺ (15 keV, 2 nA) generated from an enriched ⁶⁹Ga metal. The pulse width and frequency were 12 ns and 10 kHz, respectively. The raster area was 50 × 50 μm² and the analysis time 120 s.

3. Results and Discussion

3.1. Depth profile of ion implanted Sr

The depth profile of the implanted Sr was measured by XPS for a Pd foil bombarded by a 65-keV ⁸⁸Sr⁺ beam with a dose of 3 × 10¹⁶/cm². The data showed that the concentration of Sr is almost constant from the surface to 8 nm inside the foil, and below that gradually decreases with the depth. The concentration at the surface was about 5 at%. The depth profile was examined by a simulation using TRIM code. However, the simulation indicated that the profile has a marked peak at 13 nm from the surface and the concentration at the surface is about 1/5 of the peak concentration. This disagreement suggests that redistribution of the implanted Sr occurs during the ion implantation. From these data, the concentration of Sr at the surface for the samples #1 and #3 was roughly estimated to be about 1 at%.

3.2. ⁸⁸Sr⁺-implanted Pd

Figure 1 shows obtained XPS spectra for the sample #1. The curve A is the one before D₂ permeation; neither Mo nor S exists on the surface. The curve B is after the D₂ permeation. Two peaks are clearly observed at 227.5 eV and 233.0 eV; this indicates the existence of a sulfate and a sulfide.⁹ Sulfur is often contaminated in Pd as an impurity. Although its concentration is less than 1 ppm, it concentrates and forms sulfuric compounds at the surface during D₂ permeation. In order to remove the sulfuric compounds, the sample was subsequently annealed in air at 1273 K for 10 min. The curve C is the spectrum obtained after the D₂ permeation and the subsequent annealing. It shows two peaks at 232.4 eV and 235.5 eV. The energy difference is 3.1 eV, which agrees well with that between Mo_{3d5/2} and Mo_{3d3/2}.⁹ The intensity ratio is about 1.5, which also agrees with that for Mo_{3d5/2} / Mo_{3d3/2}. Therefore, the two peaks correspond to Mo_{3d5/2} and Mo_{3d3/2}, respectively. The observed binding energy for Mo_{3d5/2} indicates that the chemical state of Mo is MoO₃.⁹ The oxidation is probably caused by the annealing in air after the permeation. Thus the appearance of Mo after D₂ permeation was clearly observed. Similarly, the appearance of Mo was confirmed for two other samples prepared following the same procedure as #1.

The TOF-SIMS spectrum for the observed Mo is shown in Fig. 2. All of the isotopes of Mo are observed and the isotopic abundance ratio is similar to that of natural Mo, as seen in Fig. 3.

We considered the possibility that the natural Mo comes from impurities in the Pd bulk, and these impurities concentrate on the surface during D₂ permeation. To examine this idea, the XPS measurement was performed for the sample #2. However, no Mo peak is observed, as

shown in Fig. 4. Thus, the cause of the natural Mo on the surface of the Sr implanted Pd foil is presently not clear.

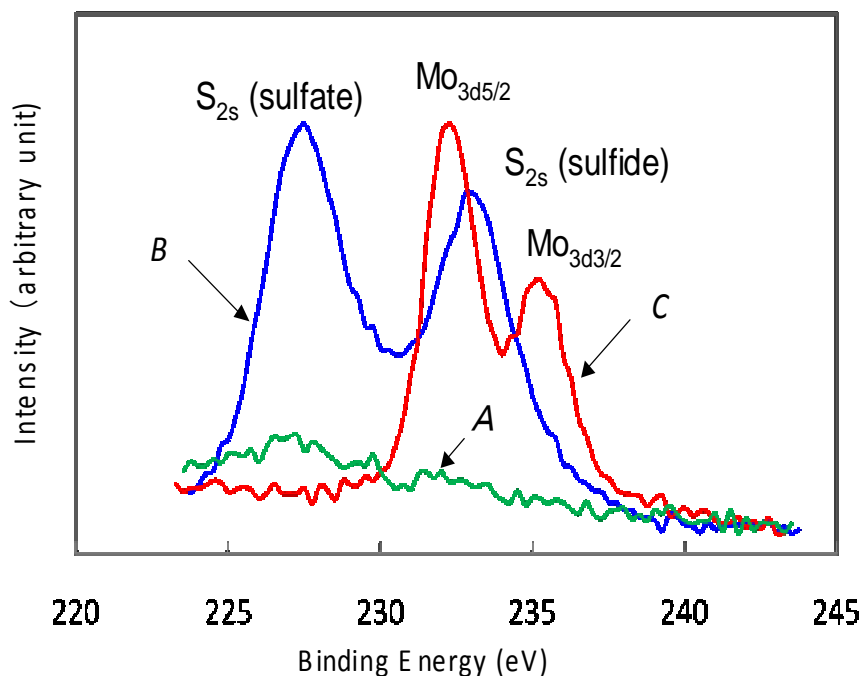


Figure 1. XPS spectra around Mo3d for sample #1; A: before permeation, B: after permeation, C: after permeation followed by annealing in air.

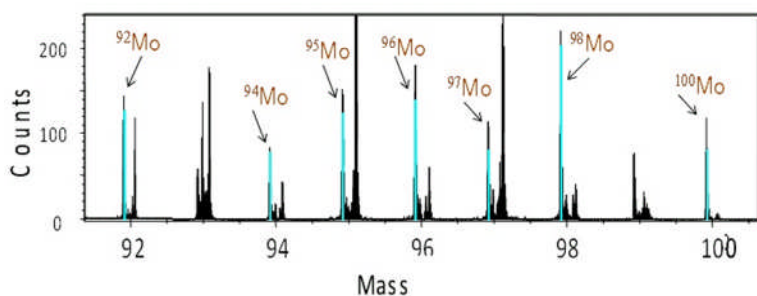


Figure 2. TOF-SIMS spectrum for sample #1.

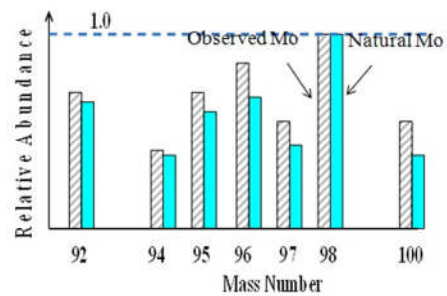


Figure 3. Isotopic abundance ratio

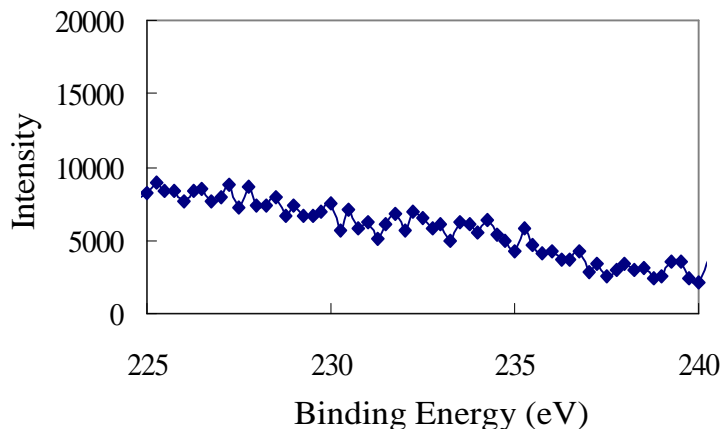


Figure 4. XPS spectrum around Mo_{3d} for sample #2 after permeation followed by annealing in air.

3.3. ⁸⁸Sr⁺- implanted Pd/CaO multilayer foil

For sample #3, Mo peaks are again clearly observed in the XPS spectrum when the sample is annealed in air after the permeation, as shown in Fig. 5.

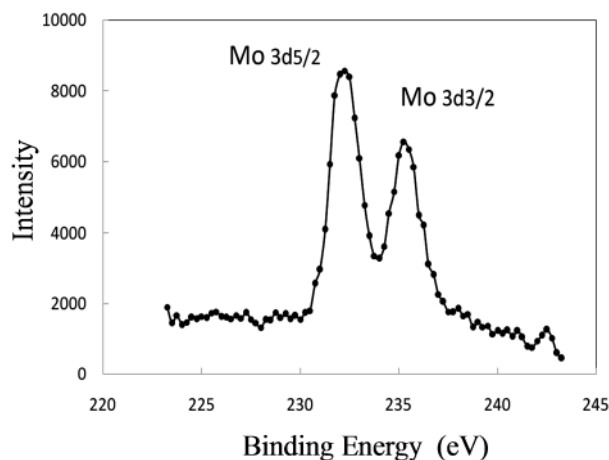


Figure 5. XPS spectrum around Mo_{3d} for sample #3 after permeation followed by annealing in air.

Figure 6 shows TOF-SIMS spectra of the sample #3 after the permeation. On the surface of #3, the existence of ⁸⁸Sr is confirmed by a peak at Mass = 88 in Fig. 6-a, and all the isotopes of Mo appear as shown in Fig. 6-b. Inside sample #3, however, a stronger peak is observed at the mass of ⁹⁶Mo as is shown in Fig. 6-c, which show the spectrum after the 60-sec sputtering of Ga ions which removes a surface layer of about 2-3 nm in depth. As seen in Fig. 6-c, the peak at the mass of ⁹⁶Mo is strongest among the isotopes of Mo and the spectrum is similar to that reported by Iwamura et al.¹

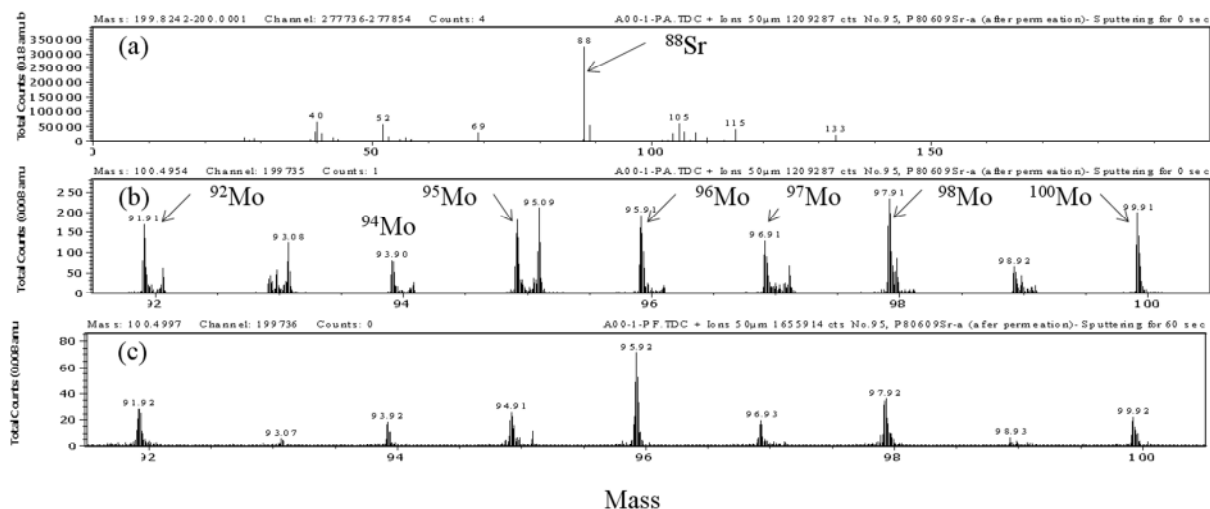


Figure 6. TOF-SIMS spectra for sample #3; (a) wide scan spectrum at surface; (b) spectrum around Mo at surface, (c) spectrum around Mo after sputtering for 60 s.

Figure 7 shows the spectra before D_2 permeation. They were taken for the area where Sr^+ ions had not been implanted. On the surface, neither Sr nor Mo isotopes are observed as shown in Figs. 7-a and 7-b, respectively. However, when the outermost surface layer is removed by sputtering for 60 sec, a peak at a mass close to ^{96}Mo is observed, as shown in Fig. 7-c. The peak cannot be due to natural ^{96}Mo , because no other Mo isotopes are seen, especially not the most abundant isotope ^{98}Mo . We refer to this peak as ^{96}X . Candidate materials for X are GaAl and Ca_2O as shown in Table 2.

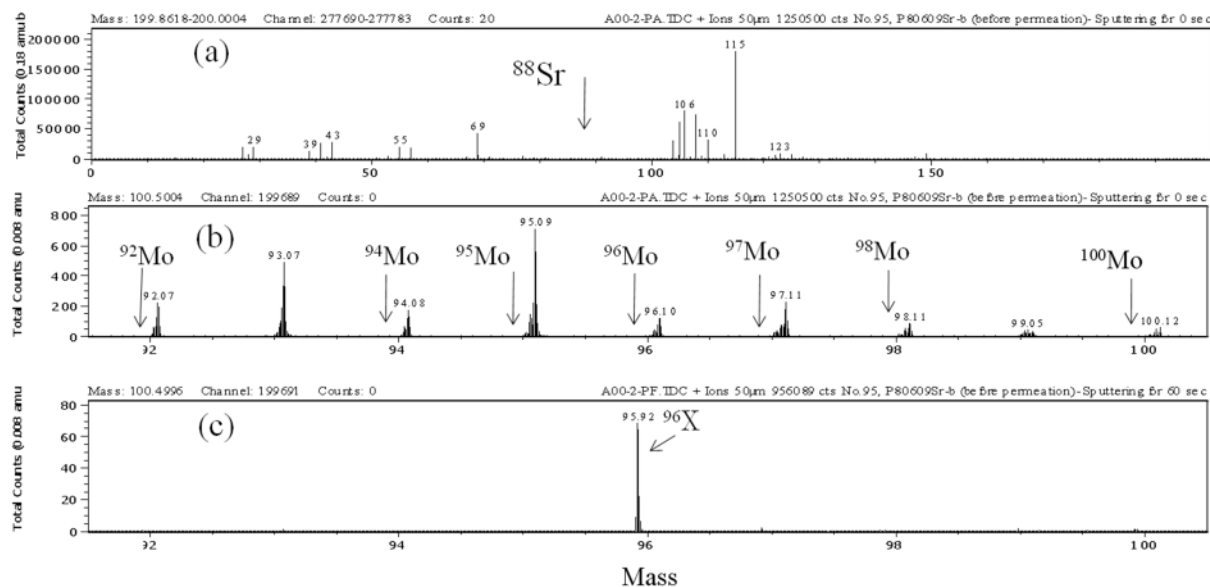


Figure 7. TOF-SIMS spectra for sample #3 (un-implanted area) before permeation; (a) wide scan spectrum at surface; (b) spectrum around Mo at surface, (c) spectrum around Mo after sputtering for 60 s.

Table 2. Candidates for X

Molecule	Mass	Source Material
Ca ₂ O	95.920	Ca \leftrightarrow CaO/Pd multilayer
GaAl	95.907	Ga \leftrightarrow ⁶⁹ Ga ⁺ : Primary ion for SIMS Al \leftrightarrow impurity in Pd
⁹⁶ Mo	95.905	

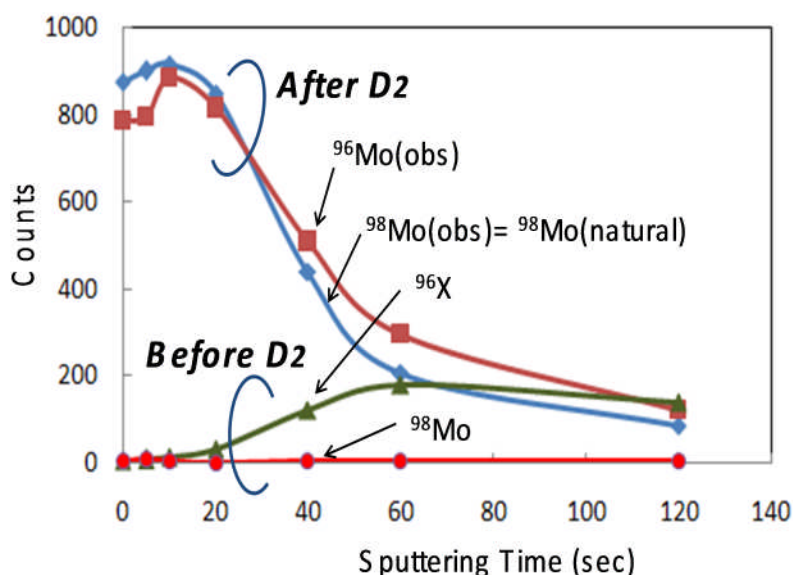


Figure 8. TOF-SIMS counts vs. sputtering time (depth).

Figure 8 shows total counts of each peak in TOF-SIMS spectra as a function of sputtering time before and after the D₂ permeation. It is noted that the intensity of ⁹⁶X is very small before the permeation, especially when the sputtering time is small, and after the permeation, the intensity of ⁹⁶Mo is larger than or comparable to that of ⁹⁸Mo. The natural isotopic abundance of ⁹⁶Mo is 69% of ⁹⁸Mo. Thus the intensity of ⁹⁸Mo should always be larger than that of ⁹⁶Mo, if the intensity of ⁹⁶Mo is only due to ⁹⁶Mo of nature. Therefore, we assume that the observed intensity of ⁹⁶Mo is the sum of those of ⁹⁶Mo of nature, ⁹⁶X, and excess ⁹⁶Mo, i.e.,

$${}^{96}\text{Mo}(\text{observed}) = {}^{96}\text{Mo}(\text{natural}) + {}^{96}\text{X} + {}^{96}\text{Mo}(\text{excess}) \quad (1)$$

where ${}^{96}\text{Mo}(\text{natural}) = 0.69 \times {}^{98}\text{Mo}(\text{natural}) = 0.69 \times {}^{98}\text{Mo}(\text{observed})$, because the observed ⁹⁸Mo is natural, as shown in Fig. 8. We estimate the intensity of ⁹⁶Mo(excess) as shown in Fig. 9, assuming further that the intensity of ⁹⁶X has the same time dependence as the curve shown in Fig. 8 and is equal to that of ⁹⁶Mo(observed) at a sputtering time of 120 s. The intensity of

excess ^{96}Mo is about 1/4 of ^{96}Mo of nature, and it exists only in the surface layer within 6 nm. Because the total concentration of Mo is estimated to be about 0.3 at% from the XPS measurement, the concentration of excess ^{96}Mo is of order 0.01 at %. It should be stressed, here, that the intensity of the excess ^{96}Mo depends strongly on the behavior of the unknown peak ^{96}X . Therefore, a definite conclusion on the nuclear transmutation $^{88}\text{Sr} \rightarrow ^{96}\text{Mo}$ cannot be made without clarifying the origin of the ^{96}X .

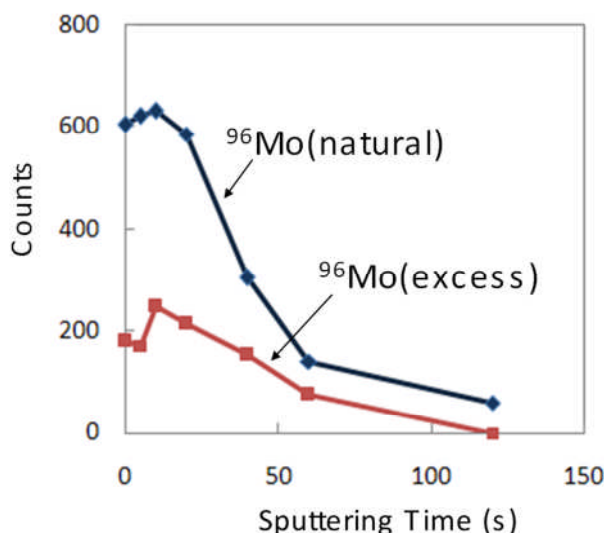


Figure 9. $^{96}\text{Mo}(\text{excess})$ and $^{96}\text{Mo}(\text{natural})$ versus sputtering time (depth).

4. Summary

For both ^{88}Sr ion implanted-Pd and ^{88}Sr ion implanted-Pd/CaO multilayer foils, segregation of S onto the surface during D_2 permeation at 343 K was observed. When S on the surface was removed by annealing in air, Mo was clearly observed by XPS measurement.

For the ^{88}Sr ion implanted Pd foil, the TOF-SIMS analysis showed that the isotopic abundance ratio of observed Mo was similar to that of natural Mo. For the multilayer sample, however, the peak at the mass of ^{96}Mo was stronger than ^{98}Mo (or comparable to it). At the mass of ^{96}Mo , an unknown peak ^{96}X , probably arising from GaAl, or Ca_2O , was also found. An analysis of the peak intensity as a function of sputtering time cannot be used to rule out the possible existence of excess ^{96}Mo that exceeds the amount of ^{96}Mo in nature.

Further studies on the behavior of the unknown peak or trials to eliminate ^{96}X are required to confirm the existence of excess ^{96}Mo .

Acknowledgments

The authors would like to thank Y. Iwamura, H. Azuma, and A. Itoh for discussion.

References

1. Y. Iwamura, et al., Jpn. J. Appl. Phys.41, (2002) pp. 4642-4648.

2. Y. Iwamura, et al., *Proc. ICCF11*, Marseilles, France, 31 October-5 November (2004) pp. 339-350.
3. T. Higashiyama, et al., *Proc. ICCF10*, Cambridge, USA, 24-29 August (2003) pp. 447-454.
4. A. Kitamura, et al., *Proc. ICCF12*, Yokohama, Japan, 27 November-2 December (2005) pp. 272-277.
5. F. Celani, et al., *Proc. ICCF10*, Cambridge, USA, 24 -29 August (2003) pp. 379-397.
6. Y. Iwamura, et al., *Proc. ICCF10*, Cambridge, USA, 24 -29 August (2003) pp. 435-446.
7. T. Hioki, et al, *Proc. ICCF13*, Sochi, Russia, 25 June-1 July (2007) in press.
8. J. Gao, et al., submitted to *J. Vac. Sci. Tech.*
9. J. F. Moulder, et al., *Handbook of X-ray Photoelectron Spectroscopy*, Perkin-Elmer Corporation, 1992.

Summary of the Transmutation Workshop Held in Association with ICCF-14

George H. Miley

*Dept. of Nuclear, Plasma and Radiological Engineering University of Illinois, Urbana, IL
This paper was prepared with input from panel chairs and participants. It was published in
Infinite Energy magazine, Issue 82, November/December 2008*

Abstract

The purpose of this workshop was to exchange technical information and insights on the emerging field of nuclear transmutations associated with LENRs. Transmutations have been observed under a variety of conditions (various electrode designs and a range of loading techniques, including electrolytic, gas loading, laser excitation, electric arcs and biological media, among others.). Discussions covered most of these situations, with the goal of identifying unifying aspects the fundamental reaction mechanism.

The workshop was held Friday afternoon following the closing of the main ICCF-14 Conference. It was conducted in the Gordon Research Conference style with short presentations, plus panel and participant discussions. Over 35 persons participated while another dozen indicated interest but had to leave due to flight times. George H. Miley, University of Illinois, served as the organizer with assistance from panel chairs Xing Zhong Li, Akito Takahashi, and Ed Storms. The schedule for the half day workshop (Friday, August 15, 2008) was as follows:

- 1:30 – 1:50pm Introduction and Brief Overview of the Field – George H. Miley
- 1:50 – 2:30pm Short Presentations and Panel Discussion of Prior Experiments - Xing Zhong Li Panel chair
- 2:30 – 2:45pm Break
- 2:45 – 3:25pm Short Presentations and Panel Discussion of Theory – A. Takahashi, Panel Chair
- 3:25 – 4:05pm Panel Discussion of Key Issues for Experiments and Theory, and Future Directions – all panel chairs plus participants.
- 4:05 – 4:45pm Panel Discussion of Scientific Implications and Potential Commercial Applications – Ed Storms, panel chair
- 4:45 – 5:00pm Discussion and Summary Remarks. – George H. Miley

In the spirit of the Gordon Conferences, specific discussion and presentations from the workshop are not published. This provides participants with more freedom to discuss recent results. In this spirit, the present summary is intentionally quite general but hopefully provides the reader with a broad view of the discussion and general conclusions coming out of the workshop.

Comments About Discussion

Brief presentations (~ 3 min each) were volunteered by 6-10 participants prior to each panel discussion. These presentations, combined with remarks by the panel chair, provided background for the following panel discussion. Panel members stated some points and then the discussion was open to the floor. The questions posed to the panel were; Is the transmutation phenomenon real? What reactions occur? How can they occur in view of the high-Z columbic barrier involved? Is heat produced? What elements undergo transmutation and can these be identified in advance through the experiment design? What are the potential applications?

Participants were referred back to the ICCF-10 paper by Miley and Shrestha titled: “Overview of transmutation reactions” which documents literature where such reactions have been reported by a number of research groups worldwide. Indeed, when asked for a show of hands, over 20 participants at the workshop said they had personally observed various transmutation reactions in experiments. The scientific characteristics of LENR open a whole new interdisciplinary field of nuclear physics. Potential applications such as unique power sources, transmutations, isotope production, and waste management were discussed. A general view, however, was that such applications represent great potential. However, much more research and development is needed to get transmutation type cells to a state where therein practicality can be fully evaluated. Some points from the Miley-Shrestha review paper were presented at the opening of the workshop and are briefly summarized here.

Transmutations reactions observed to date can be divided into two different types. The first type is direct reaction to single products. Early electrolysis based transmutation experiments frequently reported one or more isolated products, i.e. “direct transmutations” vs. product arrays. In several cases radioactive products were observed. Most recently Mitsubishi Corp. researchers reported a precision real-time measurement using built-in XPS diagnostics. An atomic layer of Sr-88 coated on a thin-film Pd substrate was transmuted into Mo-96 over 200 hours.

The experiment used 1 atm of deuterium on one side of the thin film to force deuterium diffusion through a multi-layer thin-film Pd/CaO substrate. Cs-133 was also transmuted into Pr-141 in a similar experiment. The second type is product array, illustrated from early studies by Miley, Mizuno, Bockris, and others. Such a result is illustrated from Miley’s work in the following figures.

These figures illustrate some common features observed in these types of reactions. Large reaction rates occur for key products lying in 4 mass zones, the lack of energetic gamma or neutron emission but low level emission of low energy x-ray or beta radiation production and MeV protons and alphas. The reaction leads to productions of nearly stable elements. Non-natural isotopic ratios for many products were observed (Fig. 2), as might be expected, and gives further evidence against mistaking transmutation products with impurities. Such features need further experimental definition since they should provide key signatures that theory must explain. Indeed several theorists (e.g. A. Takahashi, L. Larson, X.Z. Li, and Widon) have already used data from the experiments noted here as a test of their models. Indeed, they have achieved some degree of success in reproducing major trends.

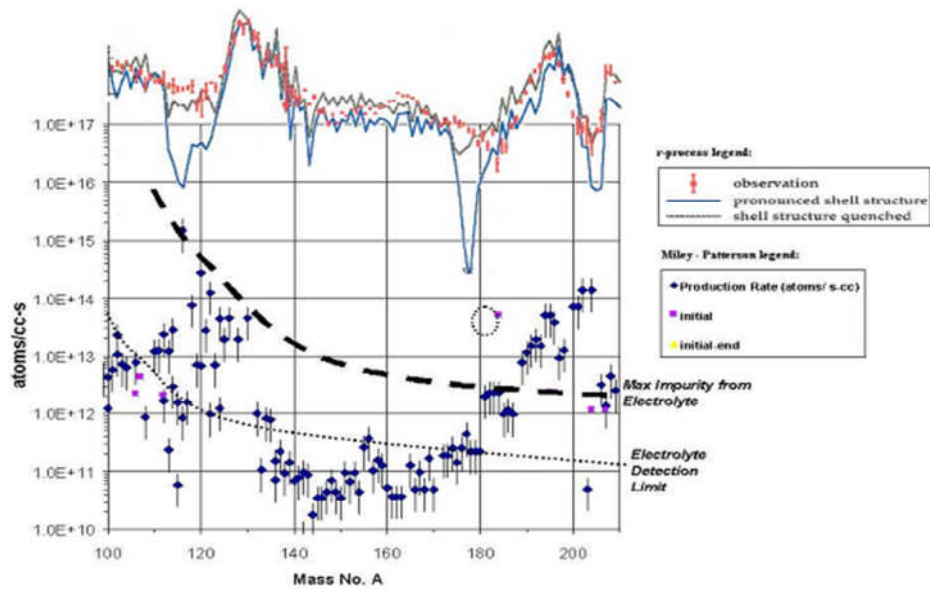


Figure 1. Comparison of mass number abundance in Miley-Patterson & r-process results. Extreme care was taken to rule out potential impurities from the electrolyte and cell components.

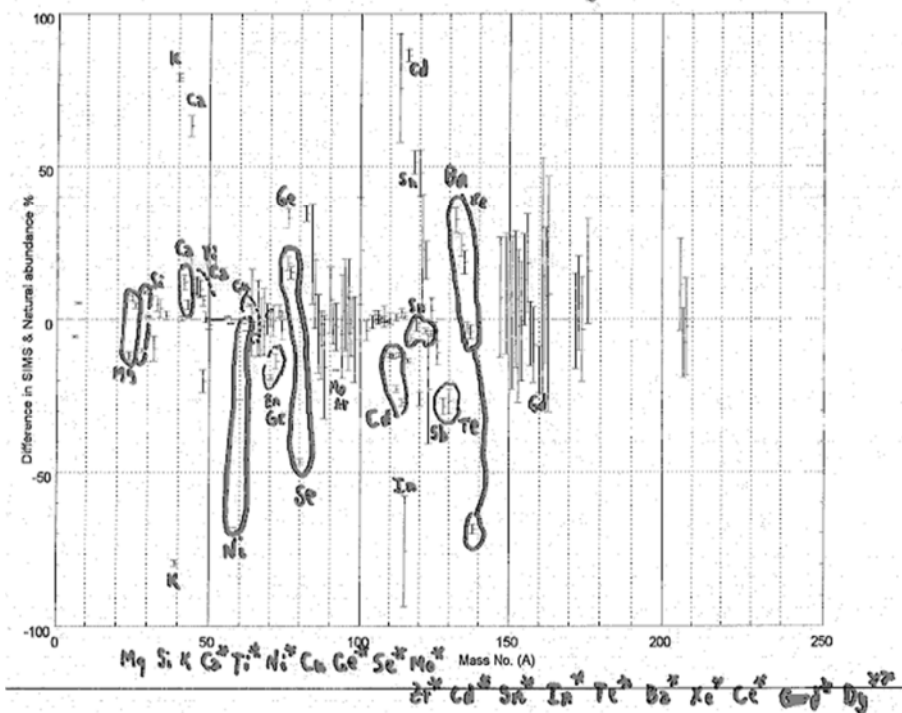


Figure 2. Many transmutation products have isotope densities that show distinct deviations from natural elements. The differences were found to be larger for some rare elements as opposed to larger yield common elements. Detailed study of Ag and Cu using neutron activation analysis confirms the SIMS results shown here.

Ed Esko, Quantum Rabbit LLC provided new information about carbon arc and also biological transmutation studies, video, and points. Following this brief review, the panels' convened to discuss issues related to experiment, theory, and science/applications.

Workshop discussions of experiments covered various topics including: What are the key experiments to date that have the most decisive evidence of transmutation products? Which have been reproduced? What key features/signatures come from these that theory must benchmark against? What is the most urgent next step in experiments? What diagnostics have provided the best analysis, and what new diagnostics should be brought in? Ed Storms summarized the theory discussion by citing physics issues that must be explained in a comprehensive theory. These were summarized, including Columbic barrier penetration - rates, Z-dependence, H vs D, "agent" involved reactions following penetration - unique stable products, lack of high energy radiation, non-natural isotope ratios, Energy and mass balances, fuel and ash, role of solid-state lattice, loading effects, coherent QED effects, irreproducibility, trigger, non-equilibrium effects. With the limited time available, the general consensus was not reached, but the feeling frequently expressed was that the experiments highlighted here represent a strong start towards addressing these questions. One added comment was that a reviewed effort should be made to find transmutations that lead to easily detected radioactive products. While reported by some workers, e.g. R. Bush, Cal Poly, this has not been achieved in recent experiments. Another possible experiment proposed by X.Z. Li and others (e.g. Stoppimi, U. Pisa) would be to attempt measure of neutrons from transmutation cells. Several prominent theories suggest neutrino emission. However, some participants charged that leading current underground neutrino detector facilities do not have the required sensitivity to undertake such measurements until a high reaction rate cell is developed. Several participants discussed potential triggers with lasers, ultrasound, and "super wave" input.

Some issues concerning theory were then discussed: What are the key theories now, and which have been successfully benchmarked against experiment? Is there any consensus about how the high Z barrier is overcome and how multi-body reactions occur to form heavy products? Are there theoretical predictions about reactions/experiments that should be pursued?

Questions mentioned about science/applications were: What new science is brought out by LENR transmutations and can this work contribute to advancing basic science? Are there potential practical applications, or is this premature to decide? Do any applications appear to be competitive cost-wise with other approaches, for example neutron irradiation transmutations?

Unknown factors were also emphasized by several speakers during the discussion. A Benchmarked theory is not available. Range of experimental conditions and possible reactions possible is not yet clear. The character of the nuclear-active-state for transmutations (otr for cold-fusion in general) is not well defined. Initiation methods; the role of non-equilibrium flows, the dependence on temperature and limiting conditions were discussed, but no conclusions reached. Cell operational lifetime considering fueling requirements and ash buildup need attention. The question of how to benchmark theory to experiments in view of the variety of reaction conditions and irreproducibility encounter in work to date was discussed, and viewed a key goal needed to advance this field forward.

Conclusion and Future Plans

Overwhelmingly participants reported that they felt the workshop was very successful and long overdue in view of the world-wide work in the field. At the close of the meeting there was a brief discussion of the need for and possible organization of future meetings or workshops devoted to this topic. The present workshop served the purpose of bringing the community together and opening a dialogue on issues plus identifying key issues for future study. But the time was too short to explore topics in any detail, so the participants overwhelmingly agreed that a longer follow-up meeting is desirable. One possibility is a meeting dedicated to John Bockris who started the well received series on this topic while at Texas A&M. The series ended with his retirement, but could now be revived. Several locations in the US were mentioned as possible as well as a site in India. Alternately many participants thought the formation of a Gordon Conference series would greatly help to move the field forward. However, these meetings are costly for participants, so they may not be practical until more funding enters the area. Several stated that in the interim, holding another workshop as a satellite meeting to ICCF meeting may be most attractive. It was agreed that this discussion would continue among participants via e-mail in an effort to formalize a next meeting or workshop.

Introduction to Energetic Particle Measurements

The last two sections dealt with two of the three main types of measurements that establish the ability to initiate nuclear reactions with chemical energies. We now turn to the third, namely the measurement of energetic particles immediately given off by LENR. For some scientists in the field, these provide the best evidence of nuclear reactions. The large values of excess heat can be explained only as due to nuclear reactions. However, that logical path is inferential, a matter of eliminating other possible explanations of the heat. And, for many researchers, there are two main problems with looking for new elements (transmutation products) that result from LENR. First, many of the experiments have not been as rigorous as is desired. And, there is the nagging possibility that the elements measured after an experiment were there at the beginning, albeit with very different spatial distributions.

The detection of the prompt emission of energetic particles is thought by many scientists to be the only ironclad means of proving that LENR occur. Such detection, and the quantification, identification and determination of the energy, of neutrons, protons and alpha particles (Helium nuclei), constitute important diagnostics in many LENR experiments. The operation of chemistry does not generate neutrons or ions, such as protons and alpha particles, with energies in excess of 1 MeV. For this reason, the measurement of neutrons and ions has been a part of this field since 1989.

The remarkable fact, now widely known, is that the number of neutrons is dramatically less than would be indicated by the amount of heat produced, if the branching ratios applicable to hot fusion also applied to LENR. The rate of tritium production is also orders of magnitude less than would be consistent with the energy production in the case of hot fusion. In fact, the rate of tritium production is very highly variable, and sometimes tritium is undetectable after a LENR experiment. A compilation by Storms from 15 papers reporting both quantitative neutron and tritium production gives ratios of neutrons to tritium ranging from 10^{-4} to 10^{-9} . Unlike hot fusion, there is no fixed ratio of neutrons or tritium to heat, or to each other. Researchers have struggled to get neutron background levels low enough to confidently detect neutrons from LENR experiments. Many experiments have been done deep in mines, away from the neutrons that come from space.

The other problem with neutron measurements is their small interaction cross sections with matter, liquids and solids included. That is why energetic neutrons are so penetrating, and why the shielding around fission reactors and planned fusion reactors must be heavy and thick. The interaction of neutrons with small detectors is relatively weak. Generally, it is necessary to degrade the energies of neutrons, a process called thermalization. This is done by having the energetic neutrons pass through a material, such as plastic, which has a high fraction of hydrogen atoms. Collisions between fast neutrons and protons share energy due to their similar masses. Hence, the neutrons lose energy relatively quickly in hydrogenous materials. Then, the thermal neutrons have a much higher interaction probability with some elements, notably boron. Such interactions lead to ionization that can be detected electronically. One alternative approach is to cause the thermal neutrons to interact with a scintillation material. Those

interactions produce light that can be detected with an optical sensor. Of all the active detectors for neutrons, BF_3 and scintillation detectors have been used most widely in LENR experiments.

In contrast to neutrons, which penetrate long distances through matter, energetic particles have very short ranges. Their charged character leads to strong interactions with the electrons in material, which slows them quickly. Protons with MeV energies have ranges in air of about 1 cm and in plastic of about 10 micrometers. MeV alpha particles can be stopped by a sheet of paper. In the case of these energetic particles, the experimental challenge is to configure experiments and detectors such that the particles can enter the sensitive parts of the detectors. Semiconductor detectors for ions are most widely used in LENR experiments, especially those conducted in low pressure conditions. Such detectors directly produce electrical pulses that are measured to indicate energetic particles. Active electronic detectors require critical downstream electronics, which can quickly register their output. This can be done by a variety of means depending on the type of signal the detector puts out.

In contrast to the active detectors just described for measuring energetic neutrons and ions, there are also passive sensors for both neutrons and ions. Passive detectors, such as photographic film, track detectors (including the polymer CR-39 and some minerals like mica), thermoluminescent detectors and bubble detectors, can be used for particle detection. They have the advantage of integrating over time during an experiment. However, most, but not all of the passive detectors require some type of chemical development or other processing, after exposure. These processes can introduce many variables into the use of the otherwise simple passive detectors.

CR-39 is a type of plastic that is used in some lenses for eyeglasses. It has been quite widely used for particle detection in LENR experiments. Passage of an energetic particle through this material produces chemical changes, sort of like the latent images in exposed but undeveloped photographic film. Neutrons can also cause such changes, if they first interact strongly with some nucleus, which can then move at high speeds through the CR-39 and cause similar latent effects. Chemical etching of exposed CR-39 will preferentially remove the damaged materials, leaving pits, structures that are called tracks. The geometry of the track depends on the type of fast particle and its energy. Calibration data relating track diameters and lengths to the particle type and energy are available, and have been employed to interpret tracks from LENR experiments. In general, there is considerable need for more calibration data for energetic particles and all types of sensors used to detect them.

This conference included a few papers dealing with the measurement of energetic particles or instrumentation for such measurements. They are briefly summarized in the following paragraphs. Then, some general comments are offered.

Lipson and his colleagues measured particle emission from electron irradiated samples of deuterated Pd and Ti using CR-39 covered with foils to provide energy discrimination. Protons with energies near 3 MeV and alpha particles with energies in the 11-20 MeV range were detected in statistically significant numbers.

Oriani also used Cr-39 in two dozen electrolysis experiments. The detectors were in air and close to the cathode for both light and heavy water solutions, but separated from the electrolyte

by 6 micrometers of mylar. Significant track densities were found in all cases. In some instances, the tracks were clustered near each other within an area of about one millimeter squared. Sometimes, the orientations of the tracks were such that the particles causing them appeared to be radiating from a small region.

Storms and Scanlan sought to measure energetic particle emission and x-rays from low-voltage discharges in deuterium gas with cathodes of several materials, including Pd. They employed two active detectors, one a gas-filled Geiger-Mueller counter and the other a solid-state silicon surface barrier detector. Many combinations of materials and conditions were explored. They found evidence for both deuterons with energy in the 0.5 to 3 MeV range and for x-rays emitted at rates about 10,000 times the particle emission rates. The particle data is certainly anomalous because the voltages applied to the discharge cell did not exceed 900 V.

Cantwell and McConnell sought to replicate experiments reported earlier by Storms and Scanlan. Two types of radiation had been measured. The paper at this conference reported observations of radiation similar to one of the earlier findings. Low energy x-rays would produce the newly observed behavior.

The work reported by Jiang and his colleagues was motivated by their interest in the geophysical origin of ^3He and ^3H in the earth. They used gas loading to deuterate samples of foil and powder of Ti and Ti-Mo. Ratios of D to Ti atoms in excess of 1.2 were achieved. The samples were then measured with an energy-sensitive silicon detector. Evidence for proton emission with energies of 2.8 MeV was obtained.

The paper by Toriyabe and Kasagi described a new detector system for charged particle detection in high-temperature gas permeation LENR experiments. The detector consists of two scintillators viewed by a photomultiplier tube. Individual pulses were recorded for off-line pulse shape discrimination to eliminate extraneous counts. Cosmic ray events were excluded by use of large scintillator veto counters. The result was a system with the ability of measure charged particle emissions at the remarkably low rate of 3 counts per day. Permeation of a Pd multilayer foil gave a slight difference in count rates between hydrogen and deuterium at high energies. This might be due to alpha particle emission.

In summary, the evidence for particle emission presented at ICCF-14 added to the database that indicates it is indeed possible to stimulate nuclear reactions at low input energies. As with heat and transmutation measurements, there is great need for additional experimental work on energetic particle emission measurements. The many combinations of materials, loading methods, measurement techniques, and particle types and energies call for exploration. More work is also needed on the development and calibration of detectors and systems to detect and quantify the characteristics of particles emitted from LENR experiments.

Charged Particle Emission during Electron Beam Excitation of Deuterium Subsystem in Pd and Ti- Deuteride Targets

Andrei Lipson¹, Ivan Chernov², Alexei Roussetski³, Yuri Chardantsev², Boris Lyakhov¹,
Eugeny Saunin¹ and Michael Melich⁴

¹ *A.N. Frumkin Institute of Physical Chemistry and Electrochemistry, Russian Academy of Sciences, 119991 Moscow, Russia*

² *Tomsk Polytechnic University, 634050 Tomsk, Russia*

³ *P. N. Lebedev Physics Institute, Russian Academy of Sciences, 119991 Moscow, Russia*

⁴ *Naval Postgraduate School, Monterey, CA 93943-5000 USA*

Abstract

Energetic charged particle emissions accompanying deuterium desorption from specially prepared Pd/PdO:D_x and TiD_x targets in vacuum, stimulated by electron beam ($J \sim 0.6$ mA/cm², $U = 30$ keV) have been studied using a set of CR-39 plastic track detectors covered with various metal foil filters. It was found that the electron bombardment of those targets is caused by statistically significant emissions of DD-reaction product (3 MeV protons), as well as high energy alpha particles (11-20 MeV). At the same time the Pd/PdO:D_x and the TiD_x samples show no sign of nuclear emissions during vacuum exposure without e-beam stimulation. Extrapolation of both the DD-reaction cross section and the enhancement factor (consistent with calculated screening potential $U_e = 750$ eV) to very low deuteron energy allowed us to satisfactorily describe the detected DD-reaction yield in Pd/PdO:D_x target, assuming “hot” deuteron ($E_d \sim 3.0$ eV) generation under e-beam bombardment. This result strongly supports the theoretical prediction [1,2] with regards to electron excitation of the D- subsystem in Pd- deuterides

1. Introduction

Recent *ab-initio* theoretical studies of hydrogen desorption from metal hydrides/deuterides with a high hydrogen solubility have shown that excitation of the hydrogen subsystem in those deuterides results in plasmon formation leading to electron density oscillations producing a strong electric field ($F \sim 10^8$ V/cm) within a lattice parameter scale ($a \sim 0.3$ - 0.4 nm) [1,2]. As a result, a mean energy of desorbed protons/deuterons (E_d), escaping from the hydride surface would effectively be increased from kT to the several eV values ($E_d = F \times a \sim 3$ - 4 eV) or two orders of magnitude, effectively producing “hot” deuterons. This deuteron acceleration mechanism, alongside a possible large electron screening in the metal targets with high hydrogen diffusivity [3-5] could potentially strongly enhance the yield of DD-reaction in metal deuterides, even at the extremely low energy of their excitation. In order to verify the hypothesis on the role of excitation of the hydrogen subsystem in metal deuterides to enhance the yield of low energy nuclear reactions (LENR), we have carried out a series of experiments

on charged particle detection with plastic track detectors CR-39, using electron-beam (in vacuum) stimulation of various metal deuterides during spontaneous deuterium desorption (if any) from the deuterated samples.

Here we show that electron beam stimulation of the D-desorption process from specially prepared Pd/PdO:D_x and TiD_x targets is caused by statistically significant emissions of DD-reaction product (3 MeV protons), as well as high energy alpha particles. It is important that the same Pd/PdO:D_x and TiD_x samples show no sign of nuclear emissions in vacuum without e-beam stimulation. Extrapolation of both DD-reaction cross section and the enhancement factor (consistent with calculated screening potential $U_e = 750$ eV) to very low deuteron energy ($E_d \sim 1.0$ eV) allowed to describe satisfactorily the detected DD-reaction yield in Pd/PdO:D_x target under e-beam excitation. This result strongly supports the theoretical prediction [1,2] with regards to electron excitation of the D- subsystem in Pd/PdO deuteride.

2. Experimental

The experiments with e-beam stimulation have been performed in TPU, Tomsk. The samples for the experiments were synthesized in the Frumkin Institute of RAS. The Pd-based samples were prepared from Nilaco (Japan) Pd foil (99.95% purity) of 50 μm thick with dimensions $S = 30 \times 10 \text{ mm}^2$. The TiD_x samples were prepared from laboratory grade pure titanium foils of 30 and 300 μm thick. The Pd/PdO heterostructure samples served as cathodes during their electrochemical loading in 0.3 M-LiOD solution in D₂O with a Pt anode. The loading has been carried out at $j = 10 \text{ mA/cm}^2$ at $\sim 280 \text{ K}$ (below room temperature) in a special electrolytic cell with split cathode and anodic spaces. After the loading up to $x = \text{D/Pd} \sim 0.73$ (about 40 min required) the samples were rinsed in pure D₂O and then were put in the Dewar glass to cool them down to $T = 77 \text{ K}$. Those cooled samples were then rapidly mounted (during 1 min) in sample holder in front of two or three CR-39 detectors covered with various metal foils (filters) and put in a vacuum chamber of SEM using a special handle-manipulator (Fig. 1). In the first series of experiments the e-beam bombarded the sample in one fixed position in the center (the scanning has been carried out within the beam spot). In the second series of experiment, it was possible to move e-beam along the sample surface in three fixed position, producing 15 min irradiation in each position. The mean fraction of the deuterium desorbed from the sample during e-beam irradiation in vacuum has been determined by anodic polarization of the samples after termination of the irradiation. This measurement showed about 10% of residual deuterium remaining in the Pd/PdO:D_x sample after its 50 min of 30 keV e-beam irradiation with current density $J = 0.6 \mu\text{A/cm}^2$. This desorption rate is consistent with a mean D⁺ desorption current from the Pd/PdOD_x sample during e-beam action $J_D \sim 3.3 \times 10^{15} \text{ D/s-cm}^2$. This number of desorbed deuterons is consistent with the rate of D-desorption in air at ambient conditions (Fig. 1).

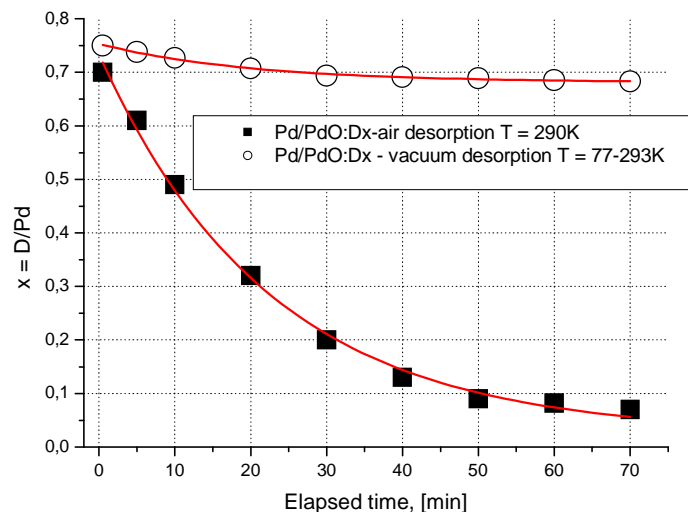


Figure 1. D-desorption rate from the Pd/PdO:Dx samples in vacuum (electrolysis at $T=280$ K with cooling down to $T = 77$ K after electrolysis termination)) and in air at ambient conditions (electrolysis at $T=290$ K).

In contrast to Pd/PdO samples, the Ti samples have been loaded in a 1 M solution of D_2SO_4 in D_2O during $t = 35$ hr at $J = 30$ mA/cm², in order to dissolve the TiO_2 oxide layer at the Ti-surface and to provide D-penetration. This technique is able to provide TiD_1 compound formation at the Ti cathode surface layer of several microns thick. The average loading here has been determined by weight balance of the sample before and after e-beam irradiation. It was found that the D-desorption rate in case of TiD_1 irradiation is consistent with the $J_D \sim 1.0 \times 10^{14}$ D/s-cm². Important that TiD_1 compound is very stable and does not loose deuterium below $t = 400$ C. Thus, all desorbed deuterons in TiD has been caused only by e-beam irradiation.

The set of noiseless plastic track detectors has been used to detect charged particles emitted during exposure of deuterated samples under electron excitation. In order to identify type and energy of emitted particles we used simultaneously two or three CR-39 detectors covered with various foils with known stopping ranges (this arrangement can be considered as a simple dE-E detector without a temporal data channel). Similar reference experiments were performed in the Frumkin Institute. These were carried out in vacuum with open and Cu-covered CR-39 detectors, but with no electron beam excitation.

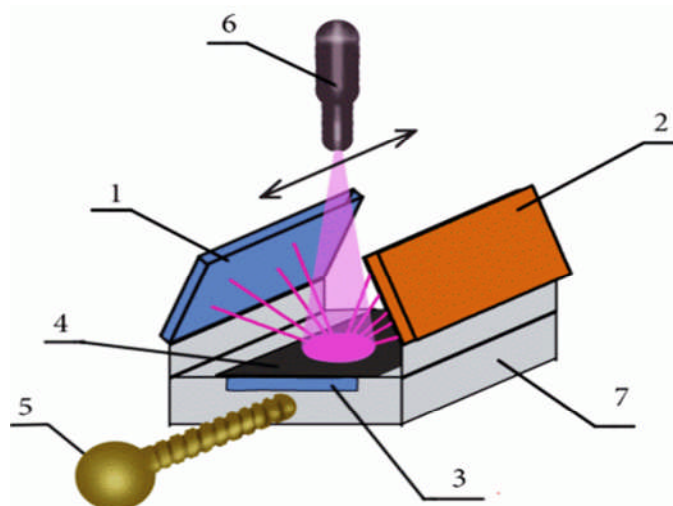


Figure 2. Experimental sample-detector holder mounted in the SEM vacuum chamber ($p = 10^{-6}$ torr) and irradiated by collimated electron beam of EDS electron gun ($J = 100\text{-}300$ nA, $E = 30$ keV): where 1,2 and 3 – are the CR-39 detectors covered with the $11\text{ }\mu\text{m}$ Al (1), $25\text{ }\mu\text{m}$ Cu (2) and $33\text{ }\mu\text{m}$ Al (3) foil filters, respectively, 4 – is the deuterated sample. 5-manipulator, 6-electron gun, 7- stainless steel support

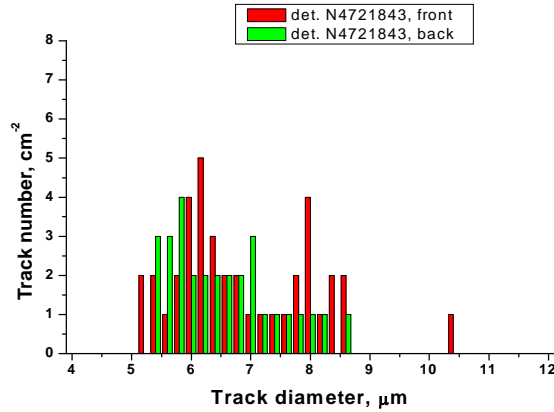
The desorbed deuterium and generated charged particles reach the detectors from the spot produced by e-beam with dimensions $S = 8 \times 6\text{ mm}^2$. The effective distance between the center of the spot and the detectors 1 and 2 is about $\langle R_{\text{eff}} \rangle = 12\text{ mm}$. The background counts are always taken from the rear side of CR-39 (opposite to the side directed to the sample's surface). The Foreground counts have been read out from the CR-39 surface of detectors 1, 2 and 3 faced the sample, while the background counts have been taken from the rear sides of these same detectors faced to the vacuum chamber (1, 2) or to the stainless support (3). The resulting counts caused by charged particle emission from the sample, were thus derived by subtracting of the background read out data (rear side) from the foreground (the front side faced to the sample) of the same CR-39 detector. The subtracting of the rear side reading data could provide more precise result in case if CR-39 detectors are irradiated by fast neutrons. Unfortunately, this batch of CR-39 track detectors was irradiated by weak fast neutron flux en route to Moscow from USA, most probably in an airport security facility. As a result, the background level in the track diameter range of interest ($4\text{-}8\text{ }\mu\text{m}$) was found to be 4-5 times above the usual $4\text{-}8\text{ }\mu\text{m}$ track diameter background, which is normally show $N < 10\text{ track/cm}^2$.

Only tracks close to the normal incidence (with respect to the CR-39 surface, such that incidence angle with respect to the perpendicular to the detector's surface would be $\Theta = 0 \pm 10^\circ$). The effective read out area of the CR-39 detector chips with dimensions $2 \times 1\text{ cm}^2$ was normally of 1 cm^2 (to avoid severely defective edge detector's sites).

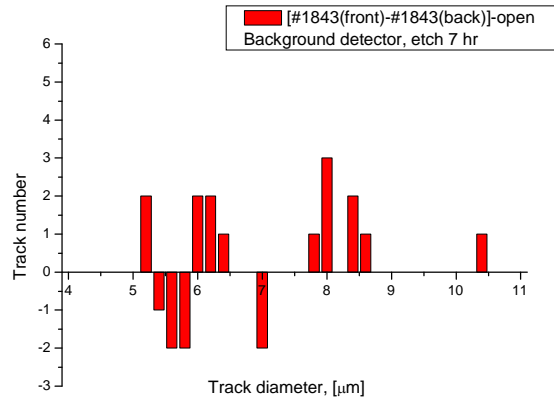
In such a condition the effective geometrical efficiency of the detectors 1 and 2 was calculated as following: $\varepsilon_g = 1/4\pi \langle R_{\text{eff}} \rangle^2 S = 2.6 \times 10^{-2}$, where $S = 0.48\text{ cm}^2$ is the effective area of the irradiated spot at the surface of the sample, which is taken equal to the area of the e-beam.

Earlier we showed that the efficiency of the detectors that are in tight contact with sample (the #3 detector case) is calculated as $\varepsilon \cong \frac{1}{2}(1-\cos\Theta_c)$, where Θ_c is the critical angle for charged particle of the given type and energy, the $\varepsilon \sim 1/2$ is the numerical coefficient counting for the including into consideration also the “non-circular” tracks, (i.e. the tracks with the small deviations from their circular shape). The detectors were etched in 6 N NaOH at $t = 70^\circ\text{C}$ with the rate of $\sim 1.3 \mu\text{m/hr}$.

The negative results showing absence of the charged particle emissions in the background measurements are shown in Fig. 3.



(3a)



(3b)

Figure 3 a,b background in the vacuum chamber (Tomsk). As seen, in the diameter range of interest (5-8 μm) the deviation of track number difference between the front and the rear side of the detector is about ± 2 . The tracks at the detector’s surface are due to a weak fast neutron irradiation and radon exposure (see the “maximum” at $\varnothing = 8 \mu\text{m}$).

3.1. Experimental Results: Pd/PdO:D_x

In order to evaluate contribution of the electron beam stimulation it was important to carry out CR-39 measurements in the spontaneous vacuum D-desorption mode at T=290 K (upper curve in Fig. 1). To increase efficiency of measurements the detection here has been performed using two detectors (one open, another filtered with 25 μm thick Cu-foil) attached to the Pd/PdODx samples from their both sides. The results presented in Fig. 5 (a-d) show a null effect.

3.1.1. Pd/PdO:Dx exposure without e-beam stimulation: no proton and alpha effects

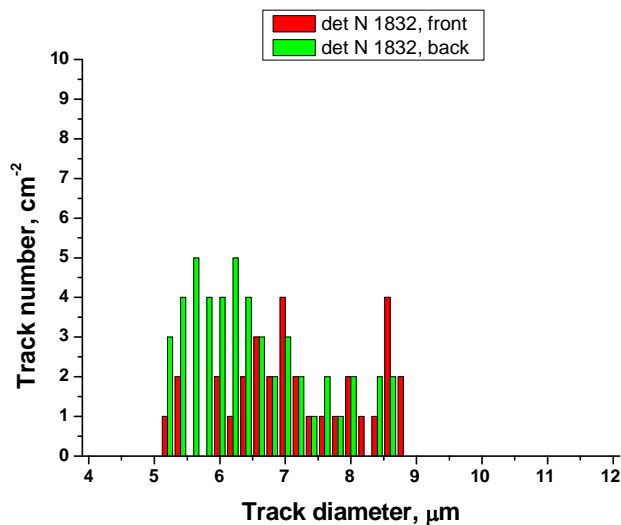


Figure 4a: Open detector results- the front and the back sides counts

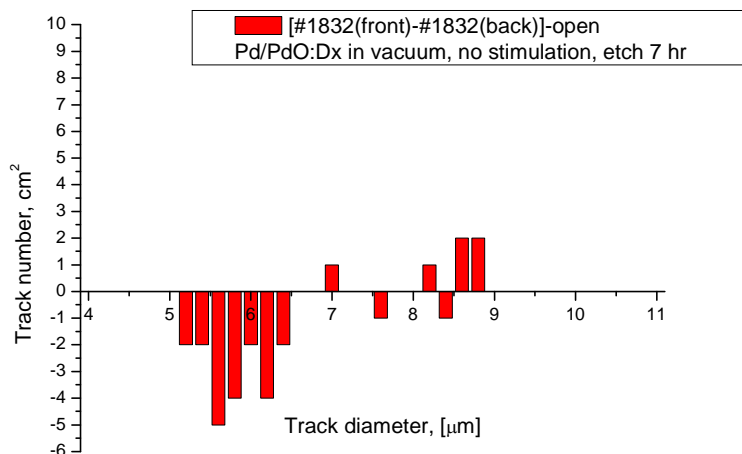


Figure 4b: Open detector- the difference between the front (attached to the sample) and back (i.e. opposite to the front one) sides of the CR-39 detector.

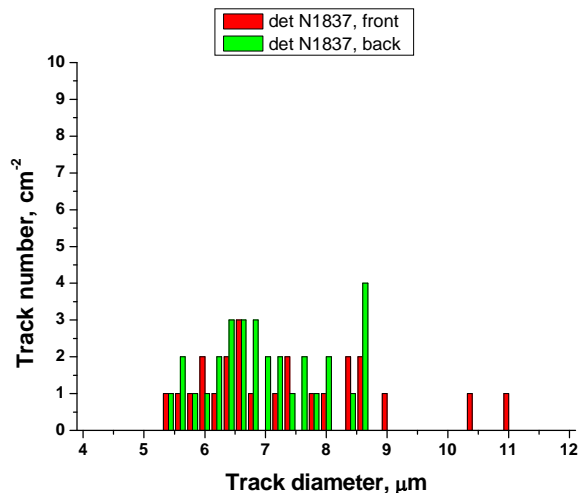


Figure 4c. 25 μm Cu covered CR-39 detector results: - the front and the back sides counts

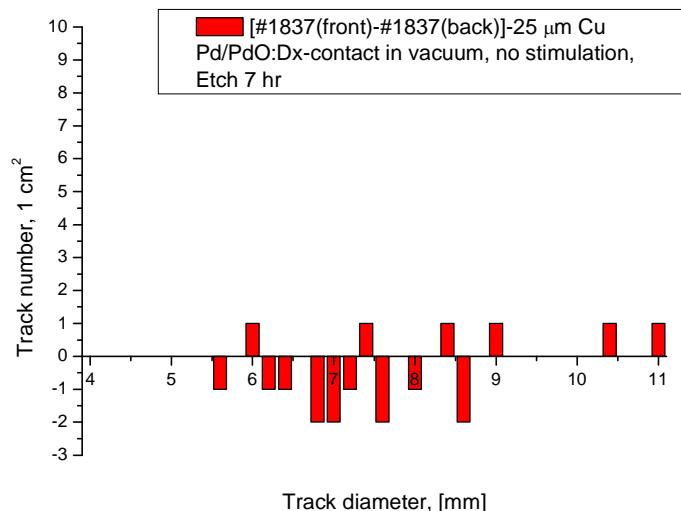


Figure 4d. 25 μm Cu covered CR-39 detector; the difference between the front (attached to the sample) and back (no contact with the sample, i.e, opposite to the front side) sides of the CR-39 detector

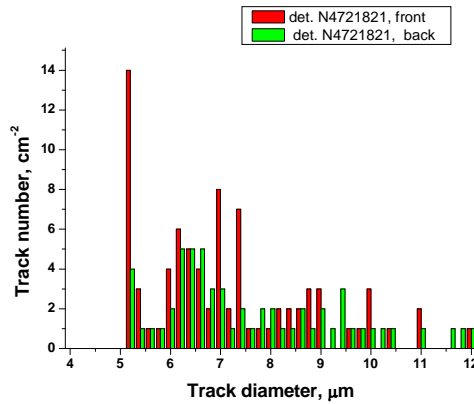
3.1.2. Electron beam irradiation of the Pd/PdO/Pd:D_x

The statistically provided results have been obtained in two separate series of experiments with Pd/PdO/Pd:D_x samples consisting of 16 and 20 runs, respectively exposed in vacuum under electron beam stimulation. In these experiments we used 3 CR-39 detectors in each series (as shown in Fig. 2). Two of them (covered with 11 μm Al and 25 μm Cu foils) have been placed under the free face of the sample irradiated by e-beam; the third detector (covered with

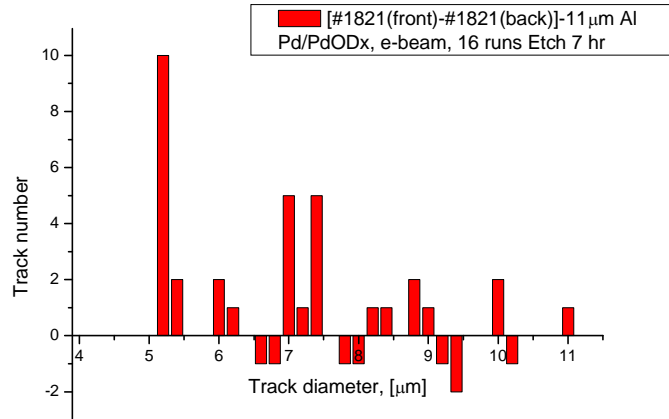
33 μm Al) has been placed at the rear side of the sample that has nor been irradiated by electrons.

The results of the first (16 runs) series containing 16 consecutive runs (the run duration is $\tau = 50$ min) with 4 Pd/PdO:Dx samples irradiated by 30 keV electron beam ($J = 0.3 \mu\text{A}/\text{cm}^2$) are shown in Figs. 5-7.

In contrast to the experiments without stimulation carried out with the Pd/PdO:Dx samples, the data obtained in Tomsk using 3 independent CR-39 detectors (the diagram is shown in Fig. 2) showed statistically significant counts of 3 MeV protons from DD-reaction as well as the energetic alphas.

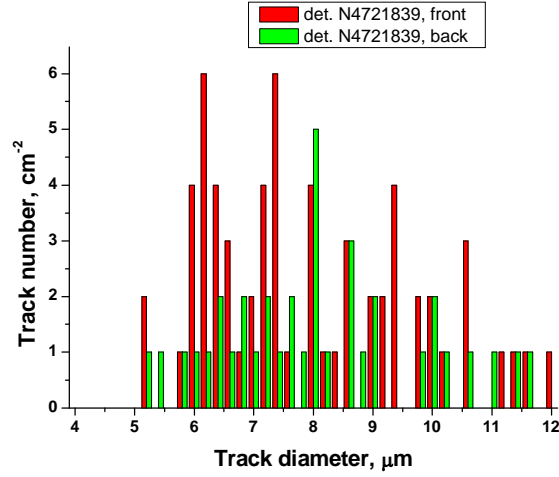


(5a)

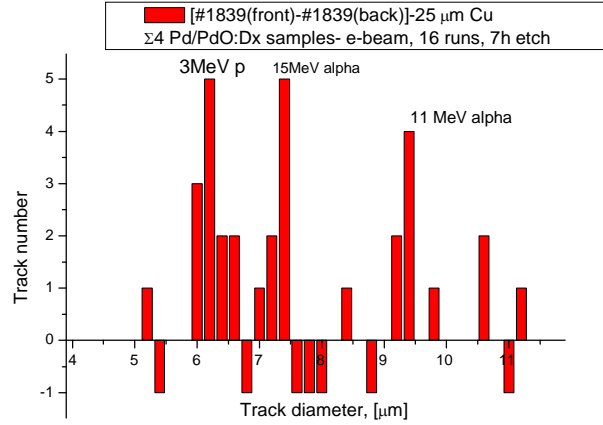


(5b)

Figure 5. a, b. Foreground and background (a) and differential (b) spectra of 11 μm Al covered CR-39 detector (position 1 in Figure 1). Total time of 16 runs with the 4 Pd/PdO:Dx samples is 16 hr. The intensity of 3MeV proton counts ($d \sim 5.2 \mu\text{m}$), taking into account the detector efficiency is $\langle N_p \rangle = (8.0 \pm 3) \times 10^{-3} \text{ p/s-cm}^2$, The high energy alpha ($10 < E < 16 \text{ MeV}$, $d \sim 7\text{-}7.4 \mu\text{m}$) intensity would be $\langle N_\alpha \rangle = (1.0 \pm 0.4) \times 10^{-2} \text{ p/s-cm}^2$.

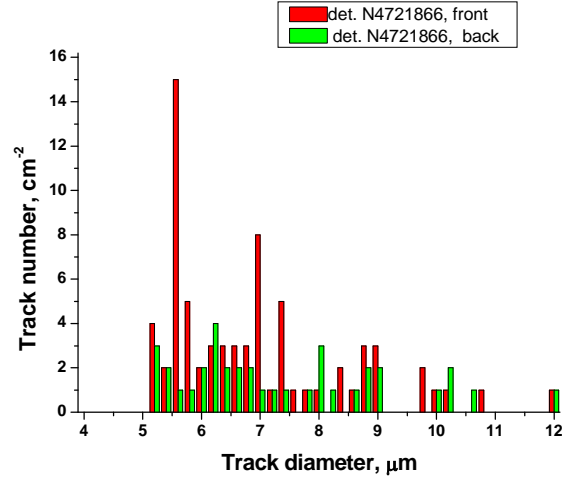


(6a)

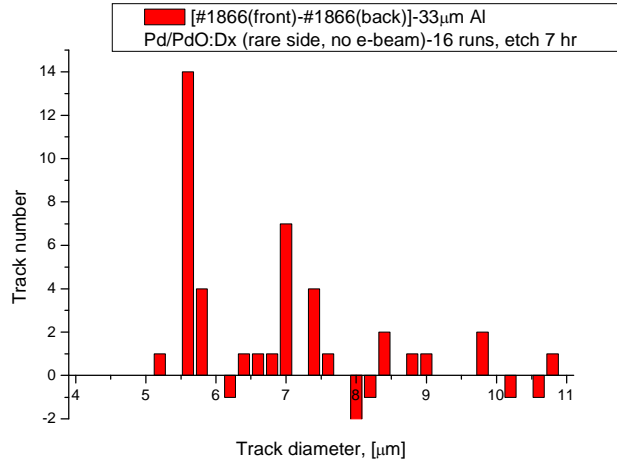


(6b)

Figure 6, a,b. Foreground and background (a) and differential (b) spectra of the 25 μm Cu covered CR-39 detector (position 2 in Figure 1). The intensity of the incident 2.5-3MeV proton counts ($d \sim 6.0$ - $6.6 \mu\text{m}$), taking into account the detector efficiency is $\langle N_p \rangle = (8.0 \pm 2.6) \times 10^{-3} \text{ p/s-cm}^2$; The high energy alpha (incident energies are split in two bands of $12 < E < 20 \text{ MeV}$, $d \sim 7$ - $7.4 \mu\text{m}$ and $10 < E < 12 \text{ MeV}$ $d = 9$ - $11 \mu\text{m}$) intensity would be $\langle N_\alpha \rangle = (1.0 \pm 0.3) \times 10^{-2} \alpha/\text{s-cm}^2$.



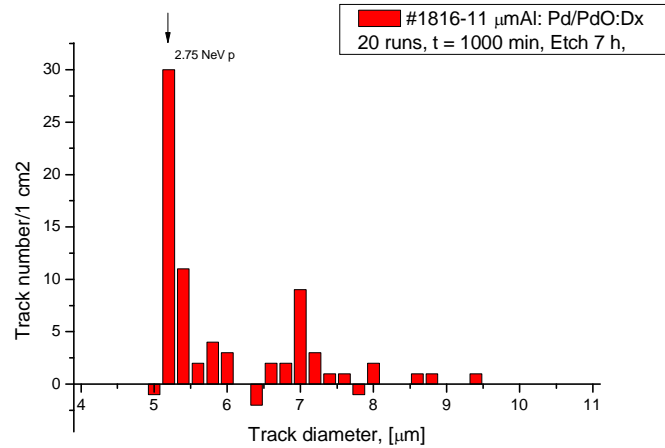
(7a)



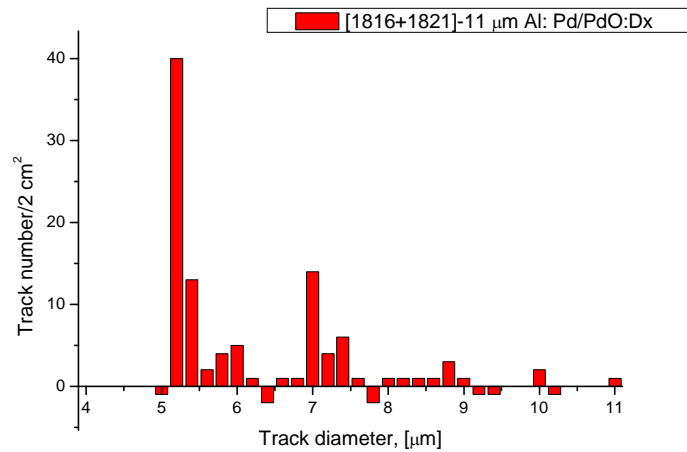
(7b)

Figure 7 a, b. Foreground and background (a) and differential (b) spectra of the 33 μm Al covered CR-39 detector attached to the Pd/PdO:Dx sample from its rear side (position 3 in Figure 1). The intensity of the incident 2.5-3 MeV proton counts ($d \sim 5.6\text{-}5.8 \mu\text{m}$), taking into account the detector efficiency (with the critical angle of $\sim 35^\circ$ for 2.1 MeV protons taking into account of 0.9 MeV energy losses of 3.0 MeV protons in 33 μm Al foil) is $\langle N_p \rangle = (3.5 \pm 0.9) \times 10^{-3} \text{ p/s-cm}^2$; The high energy alpha (incident energies are split into $12 < E < 16 \text{ MeV}$, $d \sim 7\text{-}7.6 \mu\text{m}$ and $10 < E < 11 \text{ MeV}$ $d \sim 10 \mu\text{m}$) intensity would be $\langle N_\alpha \rangle = (1.6 \pm 0.6) \times 10^{-3} \alpha/\text{s-cm}^2$.

Even more statistically significant results have been obtained in the second series (20 runs with duration 50 min each) of experiments with 6 freshly prepared Pd/PdO:Dx samples using twice as higher e-beam current ($J = 0.6 \mu\text{A}/\text{cm}^2$) as it was in the first series and also producing a scanning of the e-beam along the sample. The results for three detectors (1,2,3 - Fig. 2) and the total sum of the first (16 runs) and second (20 runs) series results are shown below.

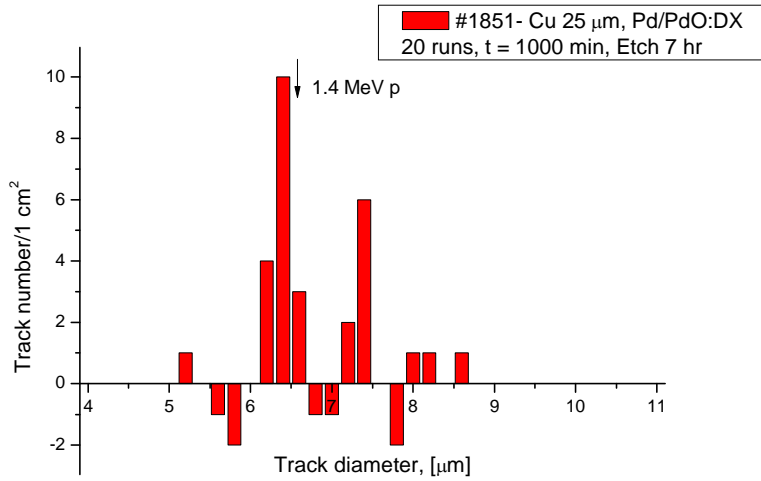


(8a)

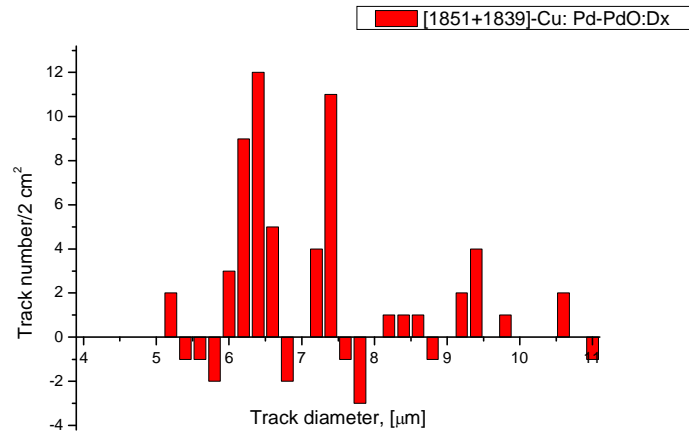


(8b)

Figure 8. a. Differential spectra of the 11 μm Al covered CR-39 detector (position 1 in Figure 2) obtained in the second series (20 runs) of experiments with the 6 Pd/PdODx samples b. The sum obtained in both first (16 runs, Fig. 5b) and second (20 runs) series of experiments. Total time of 1+2 series is $\tau = 1800$ min, using 10 similar Pd/PdO:Dx. As seen both highly statistically significant 2.75 MeV proton (5.2-5.4 μm track diameter) and 11-20 MeV alphas (7.0-7.6 μm track diameter) bands are appeared in the second series of experiments

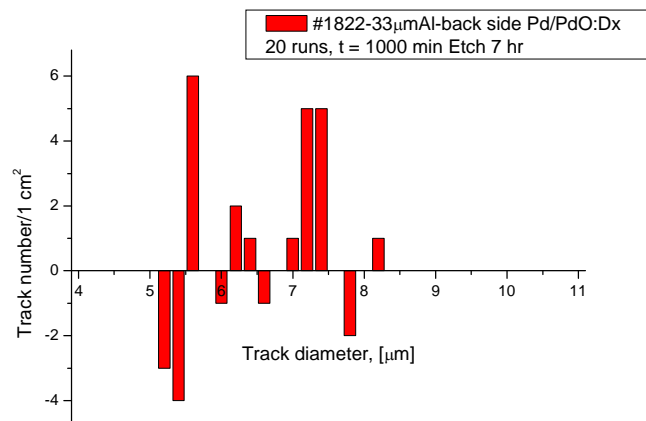


(9a)

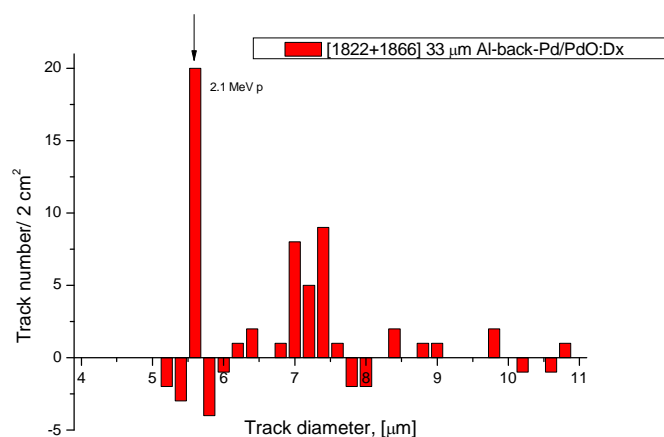


(9b)

Figure 9. a. Differential spectra of the 25 μm Cu covered CR-39 detector (position 2 in Figure 2) obtained in the second series (20 runs) of experiments with the 6 Pd/PdODx samples. b. The sum obtained in both first (16 runs, Fig. 6b) and second (20 runs) series of experiments. Total time of 1+2 series is $\tau = 1800$ min, using 10 similar Pd/PdO:DX. The statistically significant bands of 1.4 MeV protons (track diameter in the range of 6.0-6.6 μm , consistent with the 3 MeV proton losses in 25 μm Cu foil) and 15 MeV alphas (track diameter near 7.4 μm , consistent with ~ 19 MeV alpha losses in 25 μm Cu foil) are appeared in the sum spectra (b).



(10a)



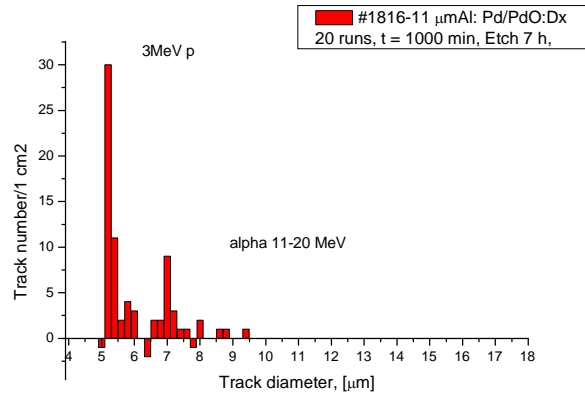
(10b)

Figure 10. a,b Differential spectra of the 33 μm Al covered CR-39 detector placed below the rear (non-irradiated by e-beam) side of the Pd/PdO:Dx sample (the position #3 in Figure 2) obtained in the second series (20 runs) of experiments with the 6 Pd/PdODx samples (a) and the sum obtained in both first (16 runs, Fig. 10 b) and second (20 runs) series of experiments (b). Total time of 1+2 series is $\tau = 1800$ min, using 10 similar Pd/PdO:Dx. The statistically significant bands of 2.1 MeV protons (track diameter near 5.6 μm , consistent with 3 MeV proton losses in 33 μm Al foil) and 14 MeV alphas (track diameter 7-7.4 μm , consistent with ~ 14 -19 MeV alpha losses in 33 μm Al foil) are appeared in the sum spectra (b).

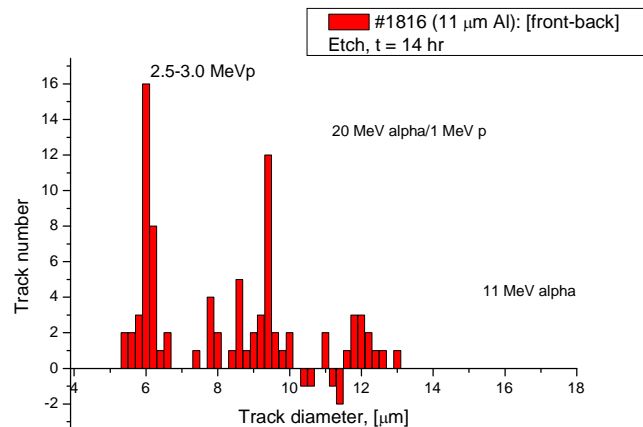
3.1.3. Sequential Etching of the Detectors #1 and #2

In order to get additional unambiguous proof that emissions of DD-reaction product (3 MeV protons) and energetic alphas are really observed in our experiments, a sequential etching of the detectors 1 (11 μm Al foil covered, # 1816) and 2 (25 μm Cu foil covered, # 1851) faced to the open surface of the sample (Fig. 2) in the second series of experiment has been performed. This procedure included 14, 21 and 28 hr etching and analysis in addition to the analysis of the same detectors shown in section 3.1.2 for the 7 hr etched detectors. The diameters of tracks obtained

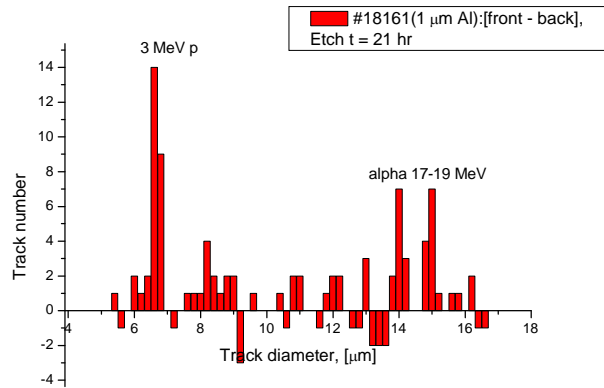
during sequential etching in main peaks (of lower $d \sim 5.2 \mu\text{m}$ and higher $d \sim 7.0 \mu\text{m}$ diameter at etch time $t=7 \text{ hr}$) have been compared with that of proton and alpha tracks extracted from similarly etched calibration detectors. The sequential etching data for p and α accelerator bombardment are presented in Ref. [6].



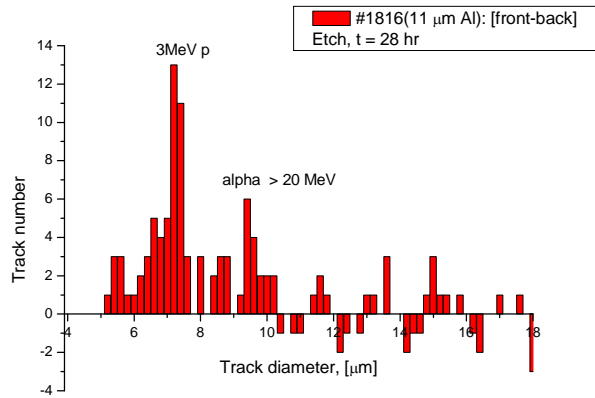
(11a)



(11b)



(11c)



(11d)

Figure 11 (a-d). Differential spectra (with subtracting of the background (the rear detector's face tracks) of #1816 CR-39 detector (exposed during e-beam irradiation of 6 Pd/PdO:Dx samples during 1000 min) after its etching during 7 (a), 14(b), 21(c) and 28(d) hours. The shift of the “peaks” in a larger track diameter side with increase in etching time is well seen.

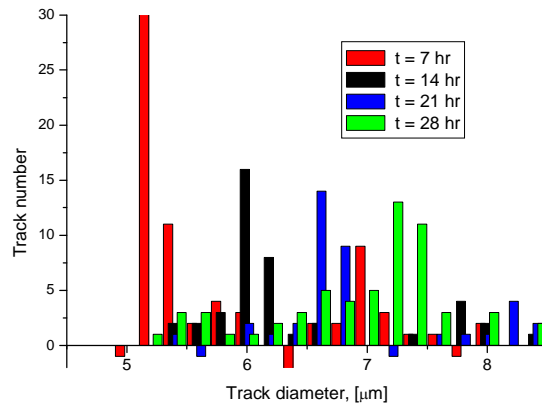
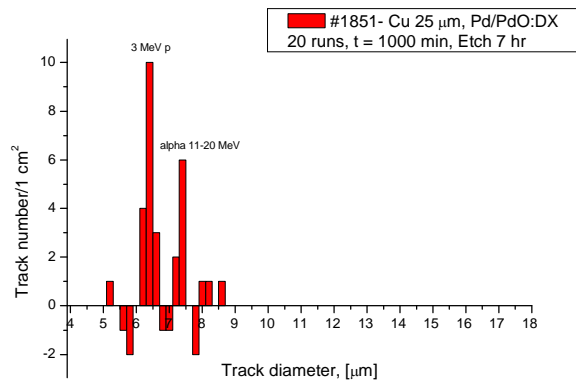
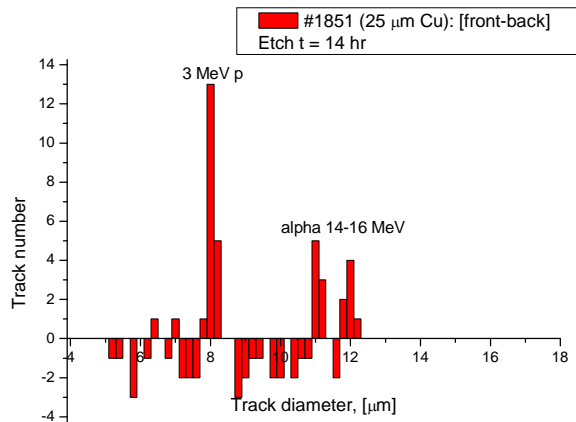


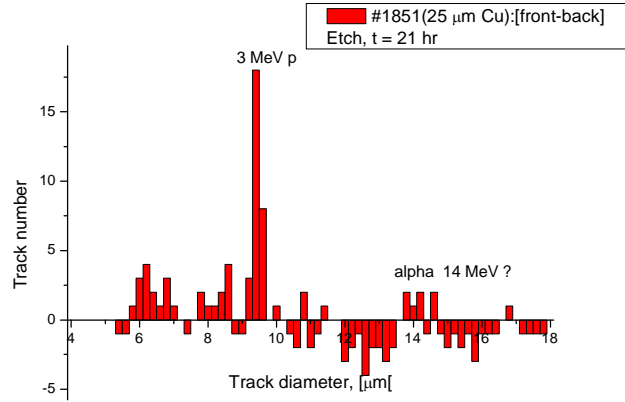
Figure 12. Shift in track diameter for the a main peak (3 MeV protons) obtained during sequential etching of #1816 detector covered with 11 μm thick Al foil



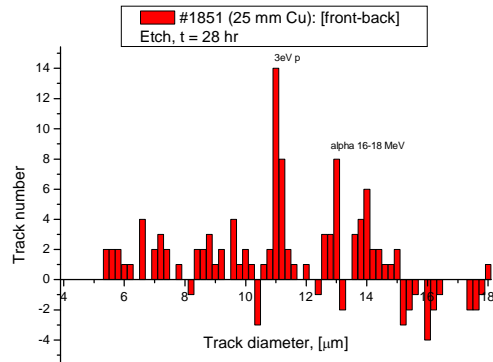
(13a)



(13b)



(13c)



(13d)

Figure 13. Differential spectra (with subtracting of the background rear face results) of #1851 CR-39 detector (exposed in front of the free surface of the 6 Pd/PdO:Dx samples during their e-beam irradiation during 1000 min) after its etching during 7 (a), 14(b), 21(c) and 28(d) hours. The shift of the “peaks” in a larger track diameter side with increase in etching time is well seen.

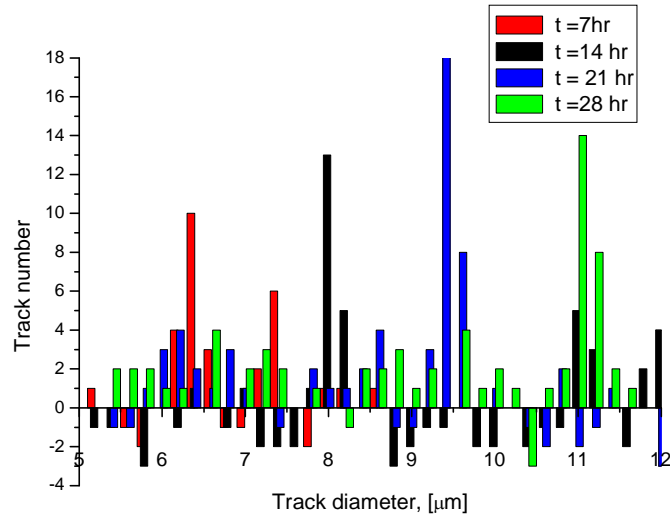


Figure 14. Shift in a main peak track diameter (1.4 MeV protons) following by sequential etching of #1816 detector covered with 25 μm thick Cu foil

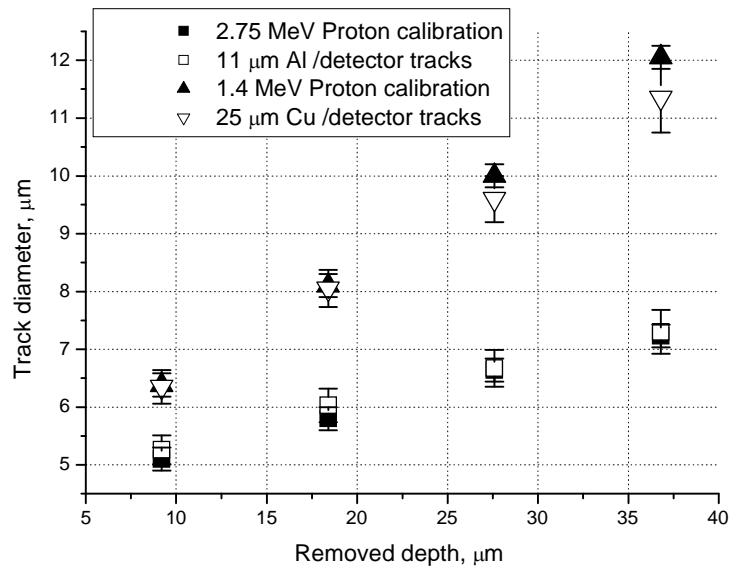


Figure 15. Track diameter vs. removed depth ($d(h)$) dependences for “proton” tracks detected during sequential etching of the detectors 1 and 2, respectively. The black squares and triangles represent fit of experimental tracks from detectors 1 and 2 (empty squares and triangles, respectively) with $d(h)$ functions obtained using normal incidence accelerator CR-39 bombardment at proton energies 2.75 (consistent with 3 MeV proton after its passage through 11 μm thick Al foil) and 1.4 (consistent with 3 MeV proton after its passage through the 25 μm thick Cu foil) MeV, respectively.

The sequential etching data (Fig.11-14), including track diameter fit shown in Fig.15 represents an additional unambiguous evidence for 3 MeV proton emission during vacuum electron beam bombardment of the Pd/PdO:Dx heterostructure. Indeed, the shift of tracks in a main (lower diameter track) peak to the larger diameter for both #1 and #2 detectors (Figs. 12 and 14) is consistent (within the standard deviation) with those shifts obtained for 2.75 and 1.4 MeV normal incidence proton tracks, respectively (Fig. 15). Notice that these chosen proton energies of 2.75 and 1.4 MeV are associated with the 3.0 MeV protons from DD-reaction, passed through the 11 μm thick Al and 25 μm thick Cu foils, respectively. Exactly these foils were used as filters in detector #1 and #2, respectively.

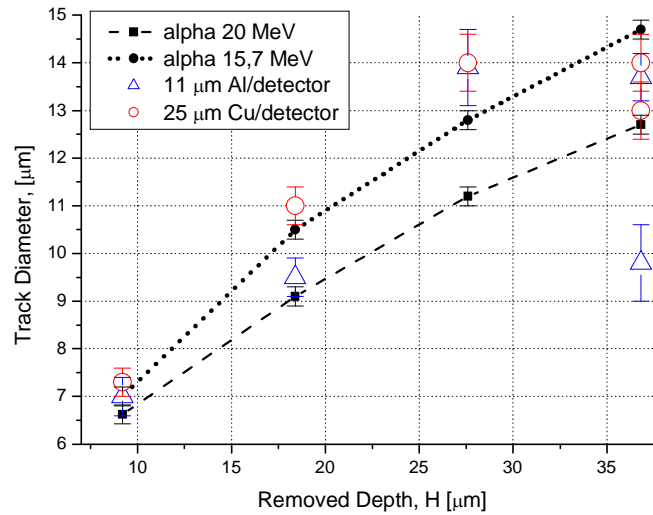


Figure 16. Track diameter vs. removed depth ($d(h)$) dependences for alpha tracks detected during sequential etching of the detectors 1 and 2, respectively. The dashed and dotted lines represent fits of experimental tracks from detectors 1 and 2 with $d(h)$ functions obtained using normal incidence accelerator CR-39 bombardment at alpha energies 20 and 15.7 (corresponding to 20 MeV alpha after its passage through 25 μm thick Cu foil) MeV, respectively.

Due to lower statistics, the sequential etching data (shown in Figs. 11 and 13) obtained for the second main peak (located at $d \sim 7.0$ -7.6 μm track diameter at etch time $t = 7$ hr) and their fit with normal incidence accelerator alpha beams of 20 and 15.7 MeV energies (Fig.16) are less impressive than those shown in Fig. 15 for 3.0 MeV protons. The lower statistics of energetic alphas is defined by strong track spread at their larger diameter during CR-39 etching in depth leading to the spread of the second peak. The last circumstance is mainly due to the fact that the emitted alphas do not produce monoenergetic beam, in contrast to DD- protons. The spread is larger at larger track diameter, making it not possible to identify alphas with energy located near 11 MeV.

Despite larger statistical errors (especially with regards to detector 1 covered with 11 μm thick Al foil) in Fig. 16, this data eventually confirm the emission of high energy alphas. Indeed, the track diameter vs. removed depth function $d(h)$ for the detector 2 is satisfactorily

fitted with the d(h) function of 15.7 MeV alphas (Fig. 16 dashed line) At the same time, expecting that alpha particles with mean incident energy of ~ 20 MeV will pass then through the 25 μm thick Cu foil, the energy losses in this foil would be of 4.3 MeV, such that the energy of the alpha-particle decreases to 15.7 MeV. Note that the detector 1 data presented in Fig. 16 could be also fitted with 1.2 MeV proton curve. However in this case one have to expect that Pd/PdO:Dx sample would emit 1.6 MeV protons that are detected by the CR-39 alongside with 3.0 MeV particles. This, however, cannot be occurred because the 25 μm thick Cu foil covering the detector 2 will stop all protons with the energies $E < 2.4$ MeV. This is why the tracks obtained in the second main peak should only be considered as high energy alpha particles in the range of 11-20 MeV, and cannot be ascribed to 1-2 MeV protons.

Thus, the sequential etching data shows that during e-beam irradiation of the Pd/PdO:D_x heterostructure the 3 MeV protons and high energy alphas (in the range, roughly of 11-20 MeV) really have been emitted.

3.1.4. Charged particle emission rate in the Pd/PdO:D_x

The results for e-beam irradiated face of the Pd/PdO:D_x heterostructure sample, obtained by averaging of 11 μm Al and 25 μm Cu data, taken for detectors 1 and 2 respectively in total 36 runs ($t = 1800$ min) are following:

- a. For 3 MeV protons $\langle \Delta N_p \rangle = (3.71 \pm 0.48) \times 10^{-4}$ cps/cm² of CR-39, or taking into account total efficiency of the detection ($\varepsilon = 0.026$) $N_p = (1.39 \pm 0.18) \times 10^{-2}$ p/s-cm² of Pd/PdO:D_x sample. (the significance level above the background is $L = 7.7 \sigma$)
- b. For alpha particles with the energy in the range of 11-20 MeV. $\langle \Delta N_\alpha \rangle = (1.87 \pm 0.32) \times 10^{-4}$ cps/cm² of CR-39 or taking into account total efficiency of the detection ($\varepsilon = 0.026$), $N_\alpha = (0.71 \pm 0.12) \times 10^{-2}$ α /s-cm² of Pd/PdO:D_x sample. (the significance level is $L = 6.0 \sigma$)

The yield of DD-reaction in the Pd/PdO:D_x target under e-beam bombardment, taken only for movable deuterons (the desorbed flux $J_d = 3 \times 10^{15}$ D/s-cm²) is found to be $\lambda_{DD} \sim 3.3 \times 10^{-18}$ p/D.

For the detector in position #3 (Fig 2) placed under the rear (non-irradiated by e-beam) side of the Pd/PdO:D_x sample the average result in total 36 runs ($t = 1800$ min) during e-beam irradiation of the front side of the Pd/PdO:D_x:

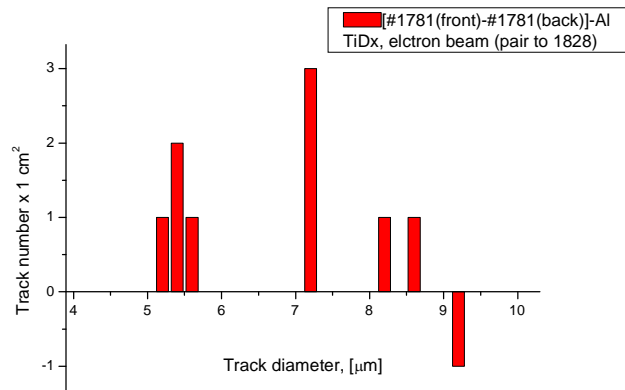
- a. For 3 MeV protons $\langle \Delta N_p \rangle = (1.81 \pm 0.40) \times 10^{-4}$ cps/cm² of CR-39, or taking into account total efficiency of the track detection for 1.9 MeV protons after permeation of 3 MeV p through 33 μm Al ($\varepsilon = 0.11$), $N_p = (1.68 \pm 0.37) \times 10^{-3}$ p/s-cm² of the Pd/PdO:D_x sample. (significance $L = 4.5 \sigma$)
- b. For alpha particles with the energy in the range of 11-19 MeV $\langle \Delta N_\alpha \rangle = (2.49 \pm 0.45) \times 10^{-4}$ cps/cm² of CR-39 or taking into account total efficiency of the track detection for high energy (> 11 MeV) alphas ($\varepsilon = 0.17$) $N_\alpha = (1.46 \pm 0.27) \times 10^{-3}$ α /s-cm² of the Pd/PdO:D_x sample. (significance $L = 5.5 \sigma$).

The count rate calculation results show that the front side of the sample irradiated by electron beam provides an excess (5-8 times) in the absolute intensity of the proton and alpha emissions compared to that detected at the rear side of the sample, which has not been irradiated directly. At the same time both the front and the rear side of the Pd/PdO:Dx sample under e-beam stimulation show a large excess in the proton and alpha emission bands, compared to the same Pd/PdO:Dx target that have been run in vacuum without excitation of their D-subsystem (i.e. in the spontaneous D-desorption mode). Observation of nuclear emissions from the rear side of the target, under e-beam irradiation of its front side, indicates some D-desorption enhancement in vacuum also at the rear side of the e-irradiated Pd/PdO:Dx sample

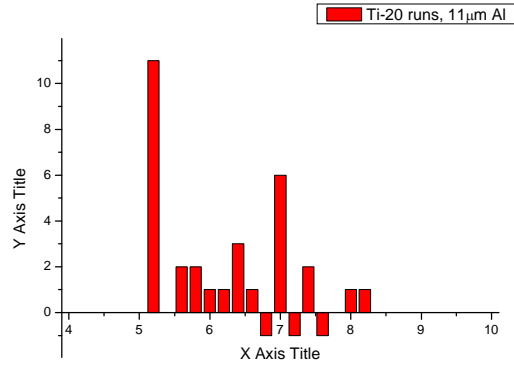
3.2. Experimental Results: TiD_x

Experiments with the TiD_x samples have been carried out similarly to that performed with Pd/PdO:Dx. In contrast to Pd/PdO heterostructure, ready-to- use Ti deuteride samples were put in vacuum chamber. The one surface of the samples have been scanned by electron beam ($J = 0.6 \mu\text{A}/\text{cm}^2$). Then in other run the sample has been turned around and the other surface of the TiD_x was scanned too. In total there were carried out 26 runs with duration of 50 min each. (total Foreground time is 1300 min, including 300 min (6 runs) in first series and 1000 min (20 runs) in a second series). Three CR-39 detectors (with 11 and 33 μm Al filters and with 26 μm Cu filter), accordingly to diagram depicted in Fig. 2 were used in each series of experiments with the TiD_x .

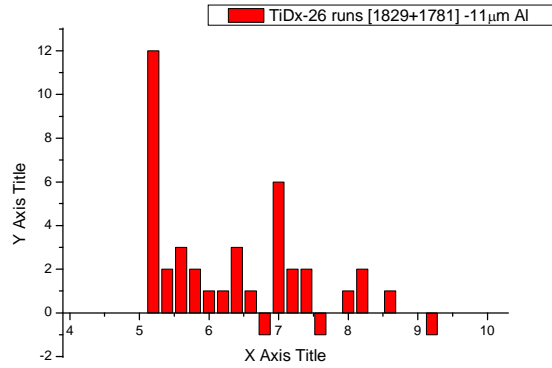
The results on nuclear particle detection for CR-39 covered with Al and Cu filters are shown below.



(17a)

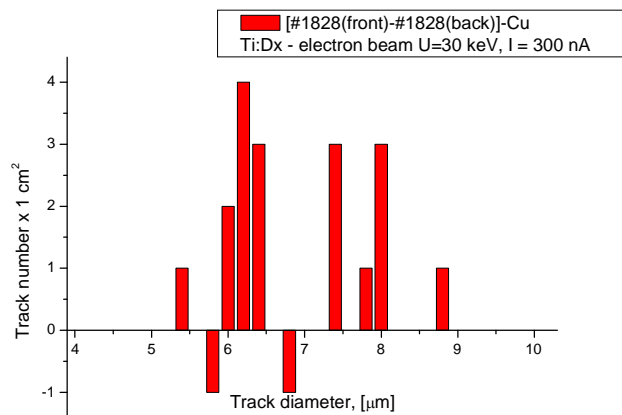


(17b)

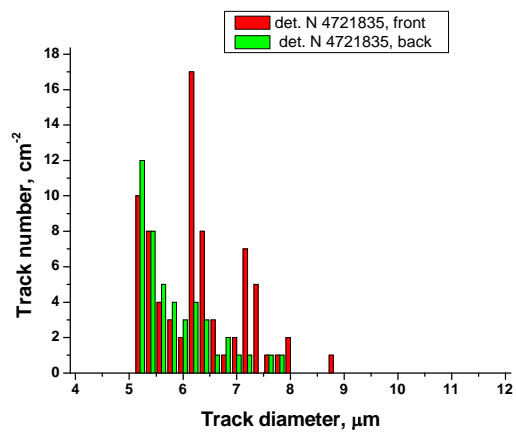


(17c)

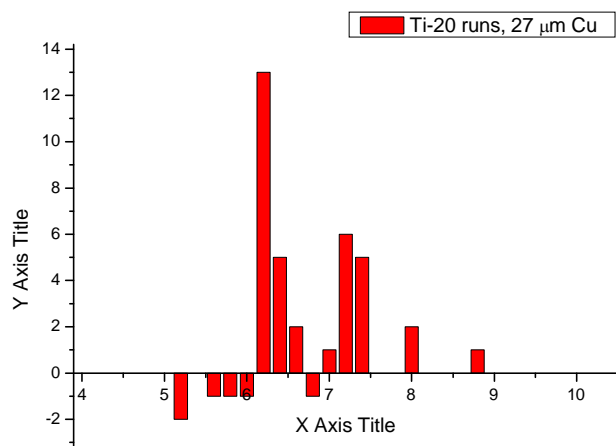
Figure 17. a-c Differential spectra of the 11 μm Al covered CR-39 detector (position 1 in Figure 2) obtained in the first series (6 runs) of experiments with the 5 TiDx samples (a), the similar data obtained in the second series (20 runs) of experiment with the TiDx results (b) and the sum obtained in both first (6 runs) and second (20 runs) series of experiments (c). Total time of 1+2 series is $\tau = 1300$ min, using 10 similar TiDx samples. As seen from the data (c), both statistically significant 3 MeV proton (5.2-5.4 μm track diameter) and 11-19 MeV alphas (7.0-7.6 μm track diameter) bands are appeared in the TiDx-electron beam excitation experiments.



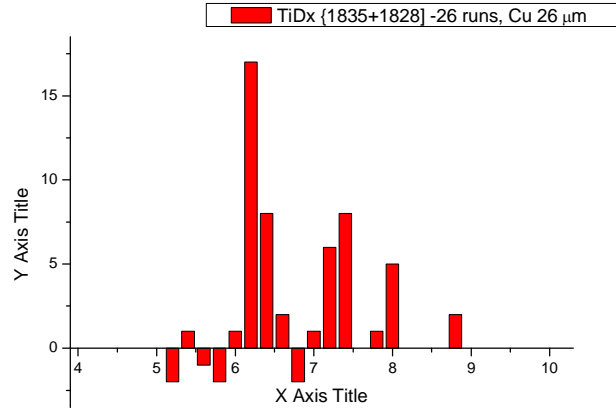
(18a)



(18b)

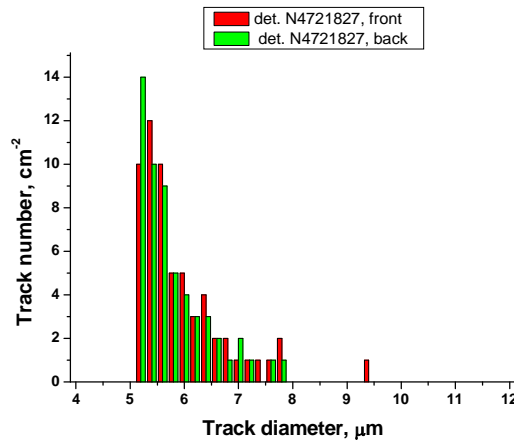


(18c)

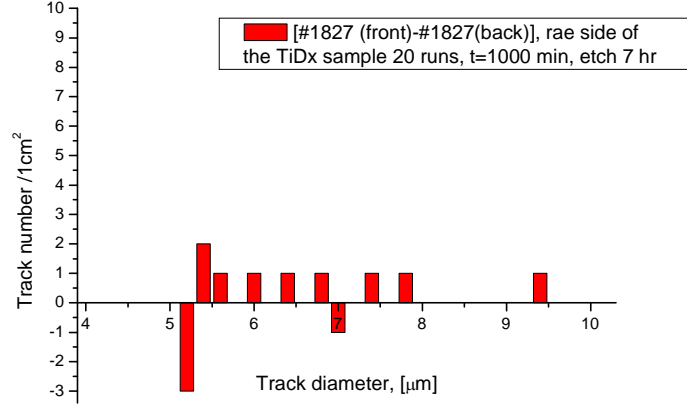


(18d)

Figure 18(a-d) The spectra of the 25 μm Cu covered CR-39 detector (position 2 in Figure 2) obtained in the first series (6 runs) of experiments with the 5 TiDx samples (a); Foreground and background (b) and differential (c) spectra obtained in the second series (20 runs) experiments ; the summary spectrum for total 26 runs obtained by summarizing the spectrum (a) and the spectrum (c). The statistically significant bands of 1.5 MeV protons (track diameter in the range of 6.0-6.6 μm , consistent with the 3 MeV proton losses in 26 μm Cu foil) and 14 MeV alphas (track diameter near 7.4 μm , consistent with ~ 17 MeV alpha losses in 25 μm Cu foil) are appeared in the sum spectra (b).



(19a)



(19b)

Figure 19. a,b The Foreground and the background spectra (a) and the differential spectrum (b) of the 33 μm Al covered CR-39 detector placed below the rear (non-irradiated by e-beam) side of the TiDx sample (the detector with the position #3 in Figure 2) obtained in the second series (20 runs) of experiments with the 5 TiDx samples. No statistically significant results have been found over all differential spectrum (b) of the rear side of the TiDx sample.

The results for e-beam irradiated face of the TiDx sample, obtained by averaging of 11 μm Al and 25 μm Cu data, taken for detectors 1 and 2 respectively in total 26 runs ($t = 1300$ min) are following:

- a. For 3 MeV protons $\langle \Delta N_p \rangle = (2.87 \pm 0.61) \times 10^{-4}$ cps/cm² of CR-39, or taking into account total efficiency of the detection ($\varepsilon = 0.026$) $N_p = (1.10 \pm 0.23) \times 10^{-2}$ p/s-cm² of TiDx sample. (the significance level of the result above the background is $L = 4.74 \sigma$)
- b. For alpha particles with the energy in the range of 11-19 MeV $\langle \Delta N_\alpha \rangle = (1.60 \pm 0.38) \times 10^{-4}$ cps/cm² of CR-39 or taking into account total efficiency of the detection ($\varepsilon = 0.026$), $N_\alpha = (0.61 \pm 0.15) \times 10^{-2}$ α/s-cm² of the TiDx sample (the significance level is $L = 4.3 \sigma$).

The non-irradiated by e-beam face of the TiDx sample show no signatures of nuclear emission.

The yield of DD-reaction in the TiDx target under e-beam bombardment, taken only for movable deuterons (the desorbed flux $J_d = 10^{14}$ D/s-cm²) is found to be $\lambda_{DD} \sim 1.1 \times 10^{-16}$ p/D.

Thus, the e-beam excitation of the TiDx samples results in initiation of DD-reaction (producing 3 MeV protons) as well as high energy alpha particles. The intensity of the nuclear emissions is quite comparable to that of the Pd/PdO:Dx samples, but provide lower statistical significance. In contrast to Pd/PdO:Dx system the TiDx samples show no emissions from the face opposite to the e-beam irradiated side. This only proofs that no nuclear emissions occur without D-desorption from the rear face of the TiDx samples, while the Pd/PdO:Dx

heterostructure provides weak spontaneous D-desorption from its rear side. Such a desorption could be partially stimulated by e-beam interaction with the front (irradiated) face of the Pd/PdO:Dx sample.

4. Discussion

Thus, we have shown experimentally that charged particle emission in Pd/PdO:Dx and TiDx in vacuum can be stimulated by relatively weak ($J < 1 \mu\text{A}/\text{cm}^2$, $E = 30 \text{ keV}$) electron beam. We found that e-beam excitation of D-subsystem in those deuterides with a high affinity to hydrogen is resulted in origination of DD-reaction (3 MeV proton emission) as well as energetic alpha particles with energies in the range of 11-19 MeV. The yield of DD-reaction for Pd/PdO:Dx and TiDx targets taken per movable (desorbed) deuteron is found to be 10^{-18} - 10^{-16} per 1 D. This figure exceeds the so-called “Jones level” by 5 to 7 orders of magnitude.

The alpha particle emission effect has been observed previously in experiments on D-desorption from the Pd/PdO:Dx [7-9] system and high-current deuterium glow discharge bombardment of the Ti cathode [5]. The origin of energetic alphas still remains puzzling, and further experiments are required in order to shed a light on the mechanism of high energy alpha emission in deuterated solids. In this work we do not consider the alpha emission mechanism. Instead, we are going to discuss possible factors of the DD-reaction enhancement, providing a measurable 3 MeV proton yield.

In this connection, below we show that extrapolation of both DD-reaction cross section and the enhancement factor to very low deuteron energy ($E_d \sim 3.0 \text{ eV}$) with a reasonable screening potential $U_e = 750 \text{ eV}$, allowed to describe satisfactorily the detected DD-reaction yield in Pd/PdO:Dx target under e-beam excitation. This result strongly supports the theoretical prediction [1,2] with regards to electron excitation of hydrogen subsystem in Pd deuteride.

In order to estimate the DD-reaction rate in the Pd/PdO:Dx target under electron bombardment we use a simple model of the process, taking into account that D-desorption stimulated by e-beam results in deuterium flux moving toward the Pd/PdO:Dx surface. Thus the moving deuteron flux can be considered a low energy projectile or “deuteron beam,” while the deuterated surface of the Pd/PdO sample we consider a deuterated “target.” The deuteron (D^+) current, estimated via D-desorption rate (see Experimental part) would be of $J_d = 0.5 \text{ mA}/\text{cm}^2$, while the mean concentration of deuteron at the surface is corresponded to mean D/Pd ratio during e-beam bombardment ($\langle x \rangle \sim 0.15$ or $N_d = 1.1 \times 10^{22} \text{ cm}^{-3}$).

In order to estimate DD-reaction rate we use a so-called thick target yield expression, normally employed in accelerator physics [3-5], recently developed and modified for lower energy applications [10]:

$$Y_{DD} = J_d N_{\text{eff}}(T) \times \int_0^{E_d} f(E) \sigma_{DD}(E) (dx / dE) dE \quad (1),$$

where J_d – is the deuteron current on target, i.e. in our case, the desorbed deuteron flux from the surface of the Pd/PdO:D $_{\langle x \rangle}$; $N_{\text{eff}}(T) = N_0 \exp(-\varepsilon_d \Delta T / k_B T T_0)$ is the effective deuteron concentration in the target (here N_0 – is the bound deuteron concentration in the target, i.e. at

the Pd/PdO:Dx surface, corresponding to the $\langle x \rangle = D/Pd \sim 0.15 \pm 0.05$ at $T_0 = 290$ K, T – is the real target temperature, $\Delta T = T - T_0$, ε_d – is the activation energy of deuteron escape from the target, here $\varepsilon_d = 0.2$ eV = the activation energy of D-diffusion in Pd); $\sigma_{DD}(E)$ – is the “bare” cross-section of DD-reaction (e.g. without any enhancement) and dE/dx – is the deuteron stopping power in the target (here in the Pd); the $f(E)$ – is the enhancement factor, derived from the following equation:

$$f(E) = Y_{\text{exp}}(E)/Y_b(E) = \exp[\pi\eta(E)U_e/E] \quad (2),$$

where $Y_{\text{exp}}(E)$ – is the total experimental DD-reaction yield at deuteron energy E , taken in the center-of-mass system, $Y_b(E)$ – is the yield deduced with the standard cross-section approximation of Bosch and Halle [11] or bare yield (without taking into account the electron screening in the target); $2\pi\eta(E) = 31.29 Z^2(\mu/E)^{1/2}$ – is the Sommerfeld parameter (Z – is the charge of the particle, μ – is the reduced mass) and U_e – is the electron screening potential of deuterons in the target. Based on analysis of screening potentials for 60 elements of periodic table [8], it was shown that U_e depends on diffusivity of deuterons in the target and could be determined by semi-empirical formula [10]:

$$U_e = (T/T_0)^{-1/2}[a \ln(y) + b] \quad (3),$$

where $a = 145.3$ and $b = 71.2$ – are the numerical constants and $y = k \times y_0(J_d/J_0)$, (here $k = \exp(-\varepsilon_d \Delta T / k_B T T_0)$, $y_0 = Pd/D$ at $T_0 = 290$ K and $J_0 = 0.03$ mA/cm²). Substitution of $J_d = 0.5$ mA/cm², $T = 290$ K and $\langle Pd/D \rangle = 6.7$ in eq. (3) is resulting in $U_e = 750 \pm 50$ eV. Notice that this screening value falls roughly into the interval limited by Kasagi's (600 eV) [3,4] and Raiola's (800 eV) [12-14] estimates of U_e deduced from the 2.5-10 keV deuteron bombardment results of the Pd/PdO and the Pd targets, respectively.

In order to estimate the DD-reaction yield in the Pd/PDO:DX under e-bombardment, we extrapolate directly to lower energies both the integral $I(E) = \int_0^{E_d} \sigma_{DD}(E)(dx/dE)dE$,

(containing linear combination of the bare cross section and stopping power), and the enhancement factor, determined by eq (2) with the $U_e \sim 750$ eV (Fig. 20).

These extrapolations, as well as substituting of the deuteron flux and effective D-concentration values in eq. (1), allow us to conclude that the DD-reaction rate of ~ 0.01 p/s-cm² in 4π steradian could be reached in Pd/PdO:Dx target (with the $U_e \sim 750$ eV) only in case if the mean kinetic energy of the desorbing deuterons would be of the order of $E_d \sim 3-4$ eV (i.e. two orders of magnitude above the kT).

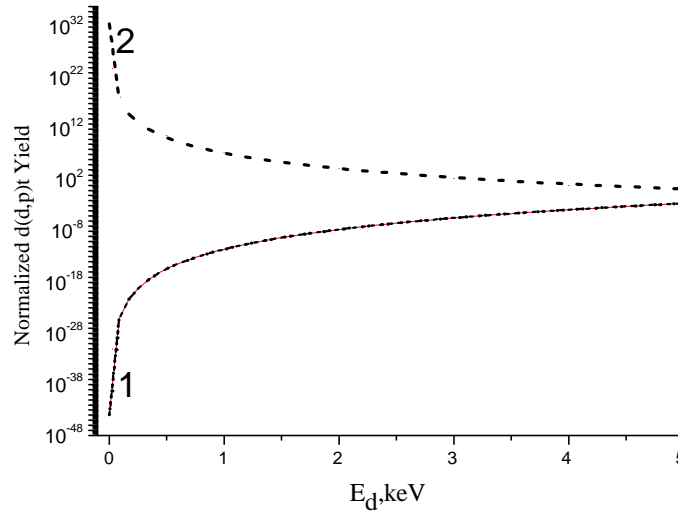


Figure 20. Extrapolation of the bare DD-reaction yield (assuming no enhancement) in Pd/PdO target normalized to that at $E_d = 10$ keV – (curve 1); and of the enhancement factor (see eq. (2) at screening potential value $U_e = 750$ eV) - (curve 2), respectively, to very low deuteron energy $E_d = 1.0$ eV.

Thus, a straight extrapolation of the DD-cross-section and enhancement factor to very low deuteron energy indicate a necessity of the eV range (“hot”) deuteron flux desorbed from the Pd/PdODx target in order to provide experimentally measured DD-yield in vacuum under electron beam irradiation. This result strongly supports the theoretical prediction [1,2] with regards to electron excitation of hydrogen subsystem in Pd deuteride. Indeed, the deduced from $d(d,p)t$ reaction rate 3-4 eV deuteron flux serve as a proof of the strong electric field ($F \sim 10^8$ V/cm) generation within a distance comparable with the lattice parameter ($a_0 = 0.39$ nm) caused by plasmon formation at the Pd/PdO:Dx surface during e-beam interaction with the D-subsystem of the deuteride.

In contrast to Pd/PdODx data, the results obtained for TiDx target under similar electron irradiation cannot be easily explained by eV deuteron kinetic energies, taking into account only the low energy extrapolation of the linear combination of the DD-reaction cross section and the enhancement factor. The problem is that due to very low D- diffusivity in Ti, the screening potential at the surface of TiDx would be also quite low. Indeed, using eq.(3) with $J_d = 0.015$ mA/cm² and $y_0 \sim 2.0$ (assuming that at the surface D-concentration is $x = D/Ti \sim 0.5$ during e-bombardment) one can obtain $U_e \sim 70$ eV (close to Kasagi’s value [4]). At this small screening potential, in order to produce DD-reaction rate of the order of ~ 0.01 p/s-cm², the kinetic energy of deuteron flux (in laboratory system) has to be rather higher, exceeding the value $E_d = 1$ keV.

The situation could be improved, assuming that main fraction of desorbed deuterium in TiD_x under e-beam irradiation would escape directly from the surface layer (of 1-2 lattice parameter thick), but not from the total 2-4 μ m thick area of D-localization. (This, actually, means that the energy transferred by electron beam would be effectively redistributed to the deuterons located

over the top of the TiD_x target - sort of inverse population). If, in this case, at the same D-flux $J_d = 0.015 \text{ mA/cm}^2$ the mean residual deuterium concentration at the surface would be $x = D/Ti < 0.1$ then at $E_d \sim 5\text{-}10 \text{ eV}$ and the screening potential $U_e \geq 600$ the deuteron yield, according to eq. (1), become similar to that in Pd/PdO:D_x derived above. It is also possible to speculate that thin TiO₂ strong dielectric layer (in contrast to semi-metallic PdO) always existing on top of the TiD_x target can be negatively charged under the electron bombardment. This macroscopic electric field would accelerate D⁺ ions passing through the surface, thus increasing their kinetic energy from several to hundreds eV. Such a process could certainly increase the yield of DD-reaction in TiD_x target. In order to make clear mechanism of high DD-reaction yield in the TiD_x target under electron bombardment, further experimental and theoretical studies are required.

5. Conclusions

- Taking into consideration total obtained experimental data, including vacuum experiments with and without e-beam irradiation, we come to the conclusion that electron beam ($J \sim 100\text{-}300 \text{ nA}$, $E = 30 \text{ keV}$) stimulation of the Pd and Ti based deuteride targets (cathodes) surface really can enhance the intensity of the emissions of nuclear charged particles.
- Both the products of DD-reaction (3 MeV protons) and high energy alphas (11-20 MeV) are clearly distinguished in e-beam stimulation experiment with the Pd/PdO:D_x and TiD_x targets.
- An important point is that signatures of 3 MeV and energetic alphas are appeared simultaneously at the surface of all (two or three) independent detectors used in the same experiment and covered by metallic foil filters with different stopping ranges/powers. To increase accuracy of measurements the rear detector side background results have been subtracted from the Foreground data obtained at the CR-39 side facing the sample's surface.
- Sequential etching of the detectors 1 and 2 during 7, 14, 21 and 28 hr show an appropriate track diameter shift (an increase), in accordance with the calibration curves obtained by CR-39 proton and alpha accelerator bombardment. This powerful technique allows us to identify unambiguously the emission of 3 MeV protons from DD-reaction as well as indicate a presence of energetic alpha particles with energies in the range 11-20 MeV.
- Total statistics obtained in experiments with the Pd/PdO:D_x heterostructure under e-beam irradiation show 3MeV/DD proton emission intensity in $4 \pi \text{ ster.}$: $N_p = (1.39 \pm 0.18) \times 10^{-2} \text{ p/s-cm}^2$ of the Pd/PdO:D_x sample, with the significance level above the background $L = 7.7 \sigma$. The intensity of energetic alphas is found to be: $N_\alpha = (0.71 \pm 0.12) \times 10^{-2} \alpha/\text{s-cm}^2$ of Pd/PdO:D_x sample (the significance level is $L = 6.0 \sigma$). The yield of DD-reaction in the Pd/PdO:D_x target under e-beam bombardment, taken only for movable deuterons (the desorbed flux $J_d = 3 \times 10^{15} \text{ D/s-cm}^2$) is found to be $\lambda_{DD} \sim 3.3 \times 10^{-18} \text{ p/D}$.
- Total statistics obtained in experiments with the TiD_x foils under e-beam irradiation show 3MeV/DD proton emission intensity in $4 \pi \text{ ster.}$: $N_p = (1.10 \pm 0.23) \times 10^{-2} \text{ p/s-cm}^2$ of the TiD_x sample. (the significance level above the background is $L = 4.74 \sigma$) and alpha intensity $N_\alpha = (0.61 \pm 0.15) \times 10^{-2} \alpha/\text{s-cm}^2$ of the TiD_x sample (the significance level is $L = 4.3 \sigma$).

- The yield of DD-reaction in the TiD_x target under e-beam bombardment, taken only for movable deuterons (the desorbed flux $J_d = 10^{14}$ D/s-cm²) is found to be $\lambda_{DD} \sim 1.1 \times 10^{-16}$ p/D.
- No signatures of nuclear emissions have been found in case of Pd/PdO:D_x and TiD_x samples exposed in vacuum at T=290K in absence of e-beam stimulation.
- The rear side of the Pd/PdO:D_x sample (opposite to e-beam irradiated side) show $N_p = (1.68 \pm 0.37) \times 10^{-3}$ p/s-cm² of the Pd/PdO:D_x sample. (significance $L = 4.5 \sigma$) and $N_\alpha = (1.46 \pm 0.27) \times 10^{-3}$ α /s-cm² of the Pd/PdO:D_x sample. (significance $L = 5.5 \sigma$). These values are 5-8 times less than charged particle emissions intensities from the e-beam bombarded side.
- The results presented here could be even more statistically significant; however, the batch of CR-39 track detectors used in this study has been irradiated by weak fast neutron flux on the route to Moscow from USA, most probably in an airport security facility. As a result the background level in the track diameter range of interest (4-8 μ m) was found to be 4-5 times above the usual 4-8 μ m track diameter background, which normally shows $N < 10$ track/cm². This important feature further convinces us that the CR-39 batches should be transported personally on board aircraft and cannot be placed in a baggage facility.
- Data analysis has been performed for Pd/PdO:D_x target. Extrapolation of both DD-reaction cross section and the enhancement factor to very low deuteron energy ($E_d \sim 3.0$ eV) with a reasonable screening potential $U_e = 750$ eV, allowed to describe satisfactorily the detected DD-reaction yield in Pd/PdO:D_x target under e-beam excitation. This result strongly supports the theoretical prediction [1,2] with regard to electron excitation of hydrogen subsystem in the Pd deuteride.

References

1. Yu. Tyurin and I. Chernov, Int. J. Hydrogen Energy **27**, 829 (2002).
2. V. Silikin, I. Chernov et al, Phys.Rev.B, **76**, 245105 (2007).
3. H. Yuki, J. Kasagi, A. G. Lipson et al, JETP Lett, **68**(11), 785, (1998).
4. J. Kasagi, H. Yuki, T. Baba, et al, J. Phys. Soc. Jpn., v. **71**(12), 2881 (2002).
5. A.G. Lipson, A.S. Roussetski, A.B. Karabut and G.H. Miley., JETP, **100**, 1175 (2005).
6. A.G. Lipson, A.S. Roussetski and E.I. Saunin, "Analysis of #2 W. Williams's detector after SPAWAR/Galileo type electrolysis experiment", Proc. of 8-th Int. Workshop on Anomalies in Hydrogen/Deuterium Loaded Metals, 13-18 Oct., 2007, Catania, Italy.
7. A.G. Lipson, A.S. Roussetski et al., "Observation of long-range alpha-particles during deuterium/hydrogen desorption from Au/Pd/PdO:D(H) heterostructure", Bulletin of the Lebedev Physical Institute (Russian Academy of Sciences) **#10**, pp. 22-29 (2001).
8. A.G. Lipson, G.H. Miley, A.S. Roussetski, Trans. Amer. Nuclear. Soc.. **88**, 638 (2003).
9. A.G. Lipson et al, ICCF-12 proc., Yokohama, Japan (2005).
10. A.G. Lipson et al, High Energy Chemistry, **42**(4), 361 (2008).
11. H.S. Bosch and G.M. Halle, Nuclear. Fusion **32**, 611, (1992).
12. F. Raiola, P. Migliardi, L. Gang, et al. Phys. Lett B **547**, 193 (2002).
13. F. Raiola, L. Gang, C. Bonomo et al, Europhys. J.A **19**, 283 (2004).
14. F. Raiola, B. Burchard, Z. Fulop et al, J. Phys. G: Nucl. Part. Phys., **31**, 1141 (2005).

Reproducible Evidence for the Generation of a Nuclear Reaction During Electrolysis

R. A. Oriani

*University of Minnesota, 151 Amundson Hall, 421 Washington Ave. SE
Minneapolis, MN 55455*

ABSTRACT

Past work in this laboratory has shown that nuclear particles generated during electrolysis can be registered by CR39 plastic detectors held within the electrolyte solution, suspended in the vapor above the solution, or placed just below the metal cathode that serves as the bottom of the electrolyte compartment of the electrolysis cell. However, not every electrolysis experiment produced nuclear particles so that total reproducibility was not achieved. Therefore another experimental technique has been developed which has shown the generation of nuclear particles in each of twenty five consecutive electrolysis experiments using heavy or light water solutions of lithium salts. The damage trails caused by the nuclear particles are made visible by etching in hot concentrated caustic solution, and the electrolysis experiments are accompanied by suitable blank, or control, experiments. The damage trails begin either at the surface of the CR39 chip that faces toward the electrolyte, at the opposite surface, or totally within the 0.83 mm thickness of the plastic detectors. It is demonstrated that the nuclear damage trails could not have been caused by ordinary radionuclides contaminating anything involved in the experimental procedure. The described phenomena pose a formidable challenge to nuclear theory.

1. INTRODUCTION

Energetic charged particles and very energetic neutrons can be detected and recorded by a high polymeric material called CR39, and its use is well known in the nuclear community [1]. Upon entering the plastic, a nuclear particle leaves a trail of disrupted chemical bonds which are more easily chemically attacked than those in undamaged material. The pit that results from etching by concentrated alkali solution is unambiguous evidence that a nuclear reaction has occurred because the energies required for such damage are much larger than can be provided by chemical reactions.

The integrating character and the relative simplicity of this technique have led the writer to use it within electrolysis cells. Control, or blank, experiments are necessary because radon in the air can produce etchable damage trails in CR39 detectors. Past work with this method in this laboratory has included immersion of CR39 chips in electrolyte solution, suspension of the chips in the vapor above the solution, and placement of chips in air just below the metal plate that serves both as cathode and as the bottom of the electrolyte compartment, with each of these configurations maintained during electrolysis. The count of nuclear tracks (pits) on the detector

chips used in the electrolyses and the pit counts on chips used as controls can be used to calculate the probability, P , that the two sets of pits belong to the same population, i.e., that the electrolysis has no effect on the number of pits. The results of prior research [2,3] are as follows. For detector chips immersed in $\text{H}_2\text{O}/\text{Li}_2\text{SO}_4$ electrolyte and with Pd as cathode $P = 1.2 \times 10^{-6}$, and with Ni as cathode $P = 5.8 \times 10^{-4}$. With $\text{D}_2\text{O}/\text{Li}_2\text{SO}_4$ and Pd as cathode $P = 2.5 \times 10^{-5}$. With detector chips suspended in the vapor above $\text{H}_2\text{O}/\text{Li}_2\text{SO}_4$ electrolyte and Ni or Pd as cathode material $P = 3.0 \times 10^{-10}$. Although these results reasonably demonstrate that electrolysis can indeed generate nuclear particles, it can not be claimed that every electrolysis experiment will produce the nuclear reaction since the data sets for the electrolysis chips and the control chips partially overlap. Consistent reproducibility was not achieved despite having kept constant all the controllable parameters. Therefore a different experimental approach has been adopted.

2. EXPERIMENTAL DETAILS

Investigators [4] at the SPAWAR Systems Center, San Diego California, initiated the strategy of having the cathode very proximate to the CR39 chip. The metal wire serving as cathode was wound tightly around the detector chip. Unfortunately, this configuration results in copious chemical attack on the detector plastic by ions generated by the electrochemical reactions at the cathode. The huge number of chemical pits produced makes it very difficult to verify the generation of nuclear pits if any. To maintain the desirable nearness of cathode to detector while avoiding the chemical attack, the obvious modification is the interposition of a thin Mylar film between the electrolyte and the detector chip. Preliminary experiments proved that 6 μm Mylar film permits the passage of nuclear particles emitted by pitchblende, initial energies of 4.1 to 5.8 MeV.

The cell design is shown in Fig. 1. Squares of CR39, roughly 3 cm \times 3 cm, cut from a sheet obtained from the Landauer Corp. are overlain by the Mylar films obtained from the Cemplex Industries, Inc., and the combination is pressed between Viton o-rings that fit into grooves in the glass o-ring joint purchased from the Fisher Scientific Corp. The joint is held together by a pinch clamp. The anode is a platinum wire the lower end of which forms a loop parallel to the plane of the detector chip. The cathode is usually a nickel wire whose lower end is bent into the shape of a W, the plane of which is parallel to the plane of the detector square. The vertical portion of the nickel wire is sheathed in heat-shrinkable plastic tubing and spot-welded to a titanium rod inserted in a glass tube. The electrode assembly is held together by a rubber stopper through which a hole permits the escape of the gases produced by the electrolysis. This describes the electrolysis cell designated by S. Another cell, constructed to enable more experiments to be done per week and designated by B, differs from the S-cell only in that the platinum anode wire ends in a crude spiral the plane of which is perpendicular to the plane of the detector chip.

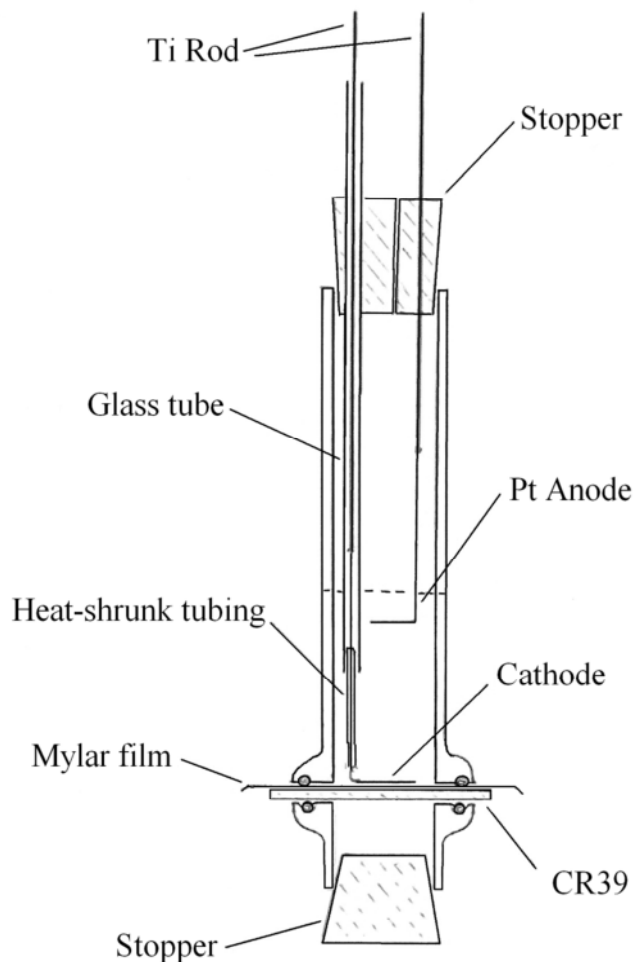


Figure 1. The electrolysis cell. The cathode assembly can be gently slid up and down to contact the Mylar film lying upon the detector chip.

The current to the S-cell was supplied and controlled by a potentiostat, and that to the B-cell by a constant-current power supply. To begin an experiment a square piece of CR39 is cut from the sheet from the manufacturer, a small hole is drilled at a corner of the detector chip to accommodate a nickel wire for the subsequent suspension of the chip, and an identification symbol is inscribed at another corner. The surface upon which the identifier is scratched is referred to as the front surface and is the surface upon which the Mylar foil is laid after the manufacturer-supplied blue protective film is removed. After the detector with the overlying Mylar film is clamped in the o-ring joint about 10 ml of electrolyte solution are poured into the cell and the electrode assembly is put in place. The cathode is then carefully lowered by sliding the supporting titanium rod within the supporting glass tube until the W-shaped foot of the cathode rests upon the Mylar film. Electrolysis is then started and the current is either kept constant for the entire duration of the electrolysis, or is increased once a day. The electrolyte

employed was usually of distilled H_2O with 0.022 g Li_2SO_4 per ml. To provide a comparison with the results of the SPAWAR team the first two experiments were done with silver cathodes in electrolyte of D_2O with LiCl plus PdCl_2 . Water was not added during the electrolysis to compensate for the loss due to dissociation. Four days of electrolysis was the usual duration, after which the cell was disassembled and the detector chip removed and washed. There was never any trace of pitting or abrasion on the detector chip before etching. Stirred sodium hydroxide solution of 6.5 M initial concentration was used as the etchant for various etching times at temperatures of 70°C or higher. This was followed by examination at 100X and 500X, applying experience gained from examining pits produced by exposure of CR39 to ^{241}Am and to pitchblende to distinguish nuclear pits from artifacts caused by manufacturing defects in the detector plastic. The nuclear pits were counted on the surface of the detector chip overlain by the Mylar foil (the front surface) as well as on the opposite surface (the rear surface). The pits were counted only within the area bounded by the outer perimeter of the o-ring, an area amounting to 4.5 cm^2 . This procedure avoided the counting of tracks that may have been caused by air-borne radon during the duration of electrolysis.

Because it was found that nuclear pits are produced on both sides of the detector chips, the possibility was investigated that nuclear tracks can be produced wholly within the thickness of the detector, i.e., that damage trails begin within the interior of the plastic. After completion of the electrolyses the chips were etched and examined at 100X magnification and the etch pits were counted. A second etching and microscopic examination were then carried out in which the etch pits were again counted. In a few experiments some ten markings were scratched on the front surfaces of the detector chips after the first etch, and the marked regions were photographed under the microscope. After the second etching exactly the same marked regions were again photographed. Efforts were made to protect the chips from exposure to air as much as possible during the entire course of the experiment. Between etchings the chips were kept tightly wrapped in aluminum foil.

3. CONTROLS AND POSSIBLE ARTIFACTS

Control experiments of four kinds were carried out to account for the nuclear tracks already present in the detectors as received from the supplier, as well as those produced during the entire experimental process by radon in the air, in the electrolyte, in the etching solution, and in the wash water. The control detector chips were handled in exactly the same way as were the experimental chips except that instead of being used in electrolysis they were either wrapped in Mylar film, immersed in stock electrolyte solution, pressed against as-received o-rings, or mounted in a newly constructed cell fitted with unused electrodes, electrolyte, Mylar film and stoppers, but in the absence of electrolysis. In each instance the same length of time as the electrolysis experiment was used. The results for the controls are presented in Table I. The number density of tracks in the as-received detector sheet varies from one shipment to another, and is not a constant for any one sheet. Therefore, it is appropriate to compare an experimental value of track number density with the mean value for the controls with due regard for the range of values for the controls. Electrolysis causes bubble generation which in turn causes convection currents that may bring daughter products from radon into close proximity to the CR39 detector, causing a larger number of etch pits than found in CR39 chips immersed in

quiescent electrolyte solution. This possibility was examined by injecting bubbles of H_2 or D_2 gas through a fritted glass sparger into H_2O/Li_2SO_4 solutions containing CR39 chips for periods of times of three or four days. After etching it was found that the chips did not display any statistically significant difference from the results obtained with quiescent electrolyte solution shown in Table I.

TABLE I. Results of Control Experiments

METHOD	FIRST SHEET				SECOND SHEET			
	N	RANGE	MEAN	σ	N	RANGE	MEAN	σ
CR39 in Mylar	16	7.6 - 47	26.4	12.1	13	5.3 - 31	13.6	6.8
New O - ring					10	4.9 - 20.7	16.2	6.0
Stock solution					14	3.3 - 11.7	5.9	2.7
In new cell					6	8.8 - 24.7	16.5	5.2

NOTES:

N = number of tests

σ = standard deviation

Controls for the experiments that looked for internally generated nuclear tracks were of two kinds. One of these consisted in mounting detector chips and Mylar films in a cell, a twin of the electrolysis cell that had never been used for electrolysis. The “virgin” cell was filled with H_2O/Li_2SO_4 solution from the same stock used for the electrolysis experiments, and was fitted with new Pt and Ni electrodes and new o-rings. Detector chips remained in the “virgin” cell without ongoing electrolysis for the same length of time as the electrolyses lasted in the experimental cell, after which the chips were etched, the etch pits examined and counted, and the chips re-etched and the resulting etch pits again counted. The second control experiment consisted in etching CR39 chips, counting the etch pits, and after a few days re-etching and again counting the pits. The two kinds of controls produced about the same increase in number density of pits between the two etchings, about 10 per cm^2 .

Consideration has been given to the possibility that the features seen after etching might have been caused by processes other than a nuclear reaction. For example, radioactive particles floating in the laboratory air may have adventitiously settled upon a detector chip and produced nuclear tracks. This possibility was examined by placing fine particles of pitchblende upon detector chips. Examination after etching showed that such particles produce “rosettes” of tracks. These track configurations, reputedly also produced by cosmic rays, have very occasionally appeared on detector chips during our research. They were not included in the counting of nuclear tracks. One may suspect that electrostatic charges produced by peeling off the manufacturer-supplied blue, protective plastic film from the CR39 might cause pits after etching. This possibility was explored by adhering Scotch tape to a detector chip then peeling it off. After etching nothing was visible that could be attributed to static charges. However, it is recognized that if after peeling off the protective film the bare chip is allowed to remain exposed to dry air for many hours, the electrostatic charges on the chip will attract daughter

products of air-borne radon so that nuclear tracks would be generated. This was prevented in our work by always mounting the detector chip in the electrolysis cell immediately after peeling off the protective film.

Manufacturing defects can make it difficult to discriminate between nuclear pits and artifacts. The polymerization process can leave poorly polymerized regions. As etching proceeds, the receding surface of the detector chip intersects with such regions which etch more rapidly than does well polymerized material and pits result. These pits are usually small, circular, and shallow, and most of them appear in groups. They can be distinguished from nuclear pits by the much darker appearance of the latter in the microscope when illuminated from above. Features whose identity remains ambiguous were not counted as nuclear pits. Scratches and other mechanical insults to the detector chips can also produce ambiguities. This problem was examined by a series of experiments in which various mechanical forces were applied to chips, followed by etching and examination. Light scratching produces linear arrays of pits, usually of uniform diameter. For this reason pits in linear arrays were never counted as nuclear pits. Etch pits are not produced by hard pushes against the chip surface with the point of metal tweezers or with the handle of an Exacta knife. On the other hand, a push with the point on the Exacta blade produces a very dark etch pit. Rubbing with a plastic rod has no effect, but rubbing with a metal spatula leaves a faint trace; and rubbing with the point of tweezers produces an etchable trail. Grasping a detector chip with metal tweezers using considerable force does not produce any effects. This is fortunate because the chips are manipulated with tweezers.

4. RESULTS AND DISCUSSION

The primary purpose of the first series of experiments was to establish whether or not the present technique repeatedly produces evidence that a nuclear reaction can accompany electrolysis. Table II displays the results of 25 consecutive experiments in which the counts of nuclear tracks, either on the front or on the rear surfaces or on both surfaces, are always considerably greater than those for the controls (Table I). Hence it can be concluded that the present technique has consistently produced evidence that a nuclear reaction of some sort has been generated in the course of electrolysis. It is significant that the generation of nuclear tracks is not limited to the use of one electrolyte composition, to one kind of cathode metal, or to one value of electrolysis current. The control experiments with CR39 chips immersed in quiescent electrolyte solution (Table I) and in stock solution stirred by hydrogen bubble injection have demonstrated that the results shown in Table II for track number density on the front surfaces of the chips can not have been produced by radioactive contaminants distributed throughout the volume of the electrolyte.

The experimental results listed in Table II indicate instances of nuclear tracks developing on both sides of the detector chips that had been mounted in the operating electrolysis cell. Indeed, often the track number density on the rear surface is larger than that on the surface that faced toward the electrolyte. This is significant because it is further evidence that ordinary radionuclides contaminating the electrolyte could not have been responsible for the observed tracks. Charged particles that caused the tracks on the rear surfaces could not have been

generated on the electrolysis side because the 0.83 mm thickness is much too large to be traversed by nuclear particles with energies of 15 MeV or less.

TABLE II. Summary of Consecutive Electrolysis Experiments. The first 11 experiments were done with the detector chips cut from the first CR39 sheet (see Table I), all of the rest were done with a second sheet.

Experiment	Cell	Current (mA)	Duration (hours)	Tracks/cm ²	
				Front	Rear
1 ^a	S	0.2-25	168	284	150
2 ^a	S	0.1-45	120	156 ^c	160
3 ^b	S	12-100	102	—	—
4	S	70-143	67	352	16
5	S	30-95	96	393 ^c	498 ^c
6	S	50	97	76	74
7	S	5-50	96.5	71 ^c	96
8	S	10-100	94	80	70 ^c
9	S	300	65	d	d
10	B	10, 25	98	98	40 ^e
11	S	12, 28	97	229 ^c	48 ^e
12	S	20	95	38 ^e	167 ^e , 163 ^e
13	B	27	95	193 ^e	298
14	S	20	94	11	81 ^c
15	B	19	94	195	49 ^{c,f}
16	S	40	94	36 ^e	9 ^c , 103
17	B	39	94	127	9 ^c , 32 ^f
18	S	60	93	28	102 ^c
19	B	60	93	47	35 ^f
20	S	80	117	72 ^c	41 ^c
21	B	80	117	60 ^c	132 ^c
22	S	100	93	426	207
23	B	101	93	62	51 ^f
24	S	50	96	102	38 ^f
25	B	50	96	26	344 ^f

- a. The electrolyte in these two experiments was LiCl plus PdCl. in D₂O with Ag as cathode material. For all other experiments Li₂SO₄ in H₂O with Ni as cathode was employed.
- b. In experiment 3, the detector chip was lost before a careful count of the clearly large number of tracks could be made.
- c. Some of the tracks appear in clusters.
- d. The number of tracks was so great that counting was impractical.

- e. The blue protective film supplied by the manufacturer was kept on the detector chip; in exps. 12, 16, and 17, only one-half of the detector surface was kept covered by the film.
- f. D_2O was maintained within the closed air space below the detector chip.

It is interesting that the nuclear pits are distributed bimodally, both as individual randomly distributed pits and as dense groups or clusters that are surrounded by areas relatively devoid of pits. The number densities in the clusters are much greater than the mean number densities listed in Table II. The clusters are of two kinds: one within which the pits are randomly distributed as to position and shape (Fig. 2), and one in which the elliptical or conical shape are radially distributed (Fig. 3). Pits of this shape result when the path of an impinging nuclear particle is other than perpendicular to the surface of the detector. By focusing the microscope up and down one can determine the direction and sense of the path [2]. Doing this for all of the elliptical or conical pits in the cluster one can determine that the nuclear particles that produced those pits emanated from a common origin away from the surface of the detector. In fact, by a careful analysis [5], one can estimate the distance above the detector surface where the shower of nuclear particles originated. Clusters such as the one shown in Fig. 3 can not be generated by a sequential decay of ordinary radionuclides dissolved in the electrolyte. Such a source of charged particles could not remain stationary in the convection currents caused by the bubbling during electrolysis long enough to produce a radial distribution of elliptical etch pits whose axes intersect at one common point. Such clusters furnish additional evidence that a nuclear reaction of unknown nature can develop during electrolysis.

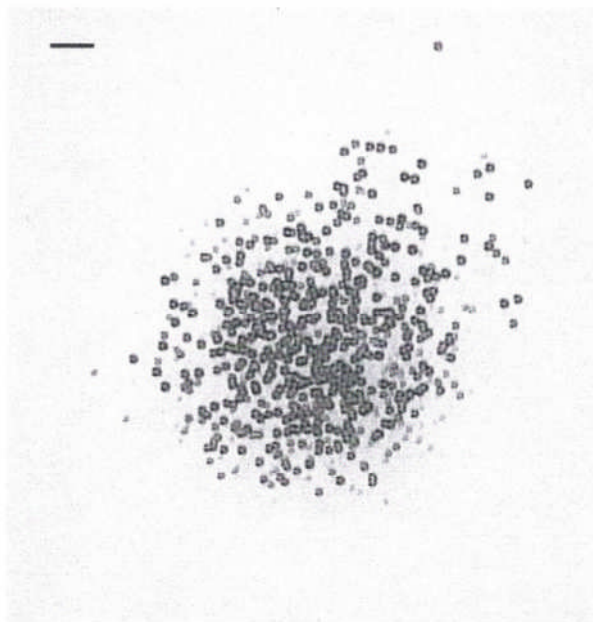


Figure 2. A typical group of etch pits here called a cluster. It is a high-density grouping of pits without any orientational arrangement among them, occupying an area of the detector chip otherwise fairly devoid of etch pits. (Scale line = 82 μm).

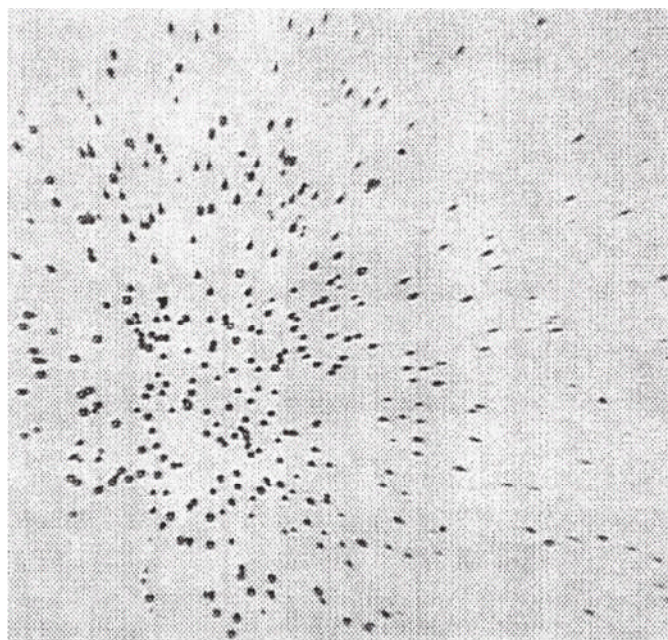


Figure 3. A radiating cluster typically containing pits of various shapes with the major axes of the non-circular pits radiating out from a common center. (Scale line=76 μm).

Further evidence that electrolysis can be accompanied by a nuclear process is provided by the re-etching experiments. The changes of etch pit counts on the detector chips that had been used in electrolysis experiments are shown in Table III. One sees that many of the re-etchings have produced large numbers of additional etch pits. The increases are to be compared with the pit count upon re-etching the control chips, about 10 pits/cm², reflecting only the effect of radon in the air, in the stock solution, and in the etching solution. The pits that appear after the second etch exhibit distributions of sizes and shapes very different from those of the pits that had appeared after the first etch. This is illustrated in Fig. 4. The large circular pit has resulted from the growth of a pit that was present after the first etch. The others appeared only after the second etch had caused the recession of the chip surface by 50 to 140 μm in from the original surface of the detector chip.

This latter set of pits could not have been the result of damage produced by nuclear particles that entered the plastic through the original surface of the detector chip because the mean free path of energetic protons and alpha particles in the plastic is considerably smaller than 50 μm . The lenticular shape of many of the etch pits show that the damage trails began many micrometers in from the original surface of the chip, so that the energetic charged particles that produced the damage trails must have been generated within the plastic material. Particularly interesting are the instances that show pitting of damage trails some 50 μm in from the original *rear* surfaces of the detector chips. These cases indicate that the energetic charged particles that produce the damage trails that lead to etch pits can originate at all depths within the 0.83 mm thickness of the plastic. This result is strong evidence against the hypothesis of contamination by radioisotopes in the electrolyte because the origins of the internal damage trails lie deeper

within the plastic than the penetration depth of protons or alphas from radionuclides in the electrolyte.

TABLE III. Change Of Etch Pit Count Upon Re-Etching

Experiment	Chip Side	Pits per cm ²		Thickness upon re-etching (mm)
		After 1 st etch	After 2 nd etch	
1	F	82	160	-----
2	F	71	75	-----
3	F	147	151	-----
4	F	55	TL	-----
	R	48	TL	-----
5	F	22	56	-----
6	R	8	194	-----
7	R	8	67	-----
8	F	38	295	0.71
	R	64	70	0.71
9	F	49	121	0.56
10	F	53	TL	0.69
11	F	11	700*	0.73
12	F	17	53	0.74
13	F	44	551	0.64
14	F	19	41	-----
	R	50	86	-----

NOTES:

* Estimated

F, R: Front, Rear surface of the detector chip

TL: The number of pits is too large for convenient counting

The original thickness of the detector chips is 0.83 mm.

The mean number of pits/cm² of the controls after re-etching is 10 with a range of 0 to 21 in 18 tests.

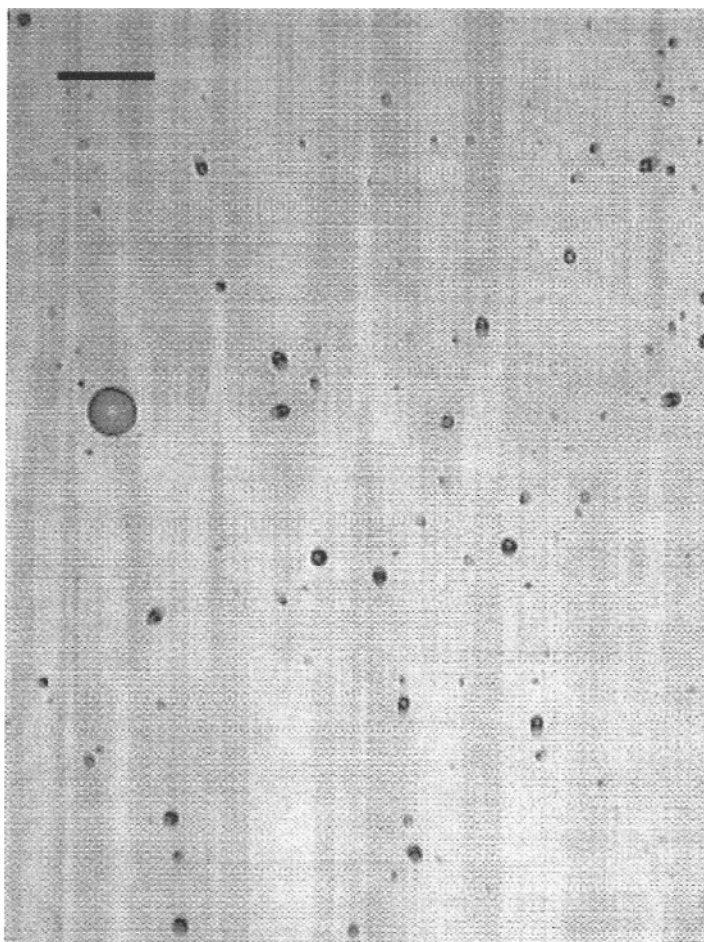


Figure 4. Photomicrograph (Scale line= 80 μm) of the front surface of a CR39 chip previously employed as a detector of nuclear particles generated during electrolysis. This chip showed 43.7 etch pits per cm^2 after the first etch and 551 after the subsequent etch. The second etch produced numerous smaller pits, in strong contrast with the single, large, circular pit made large by the re-etching of a pit already present after the first etch. The smaller pits appear classifiable into two families, probably associated with a distribution in depth of the starting points of the pits.

Several of the chips used in this study were marked after the first etch in order to be photographed at the marked locations both before and after the second etch. The marked chips showed large overall increases in pit count after the second etch, but the increases occurred in patches unevenly distributed over the area of the chip. Unfortunately, in only one case did one of these patches coincide with one of the marked and pre-photographed locations. Fig. 5a,b illustrates this instance. It is clear in Table III that not every second etch resulted in displaying internally generated damage trails. Either the phenomenon is of stochastic character, or all of the experimental parameters are not being controlled due to ignorance of their nature.

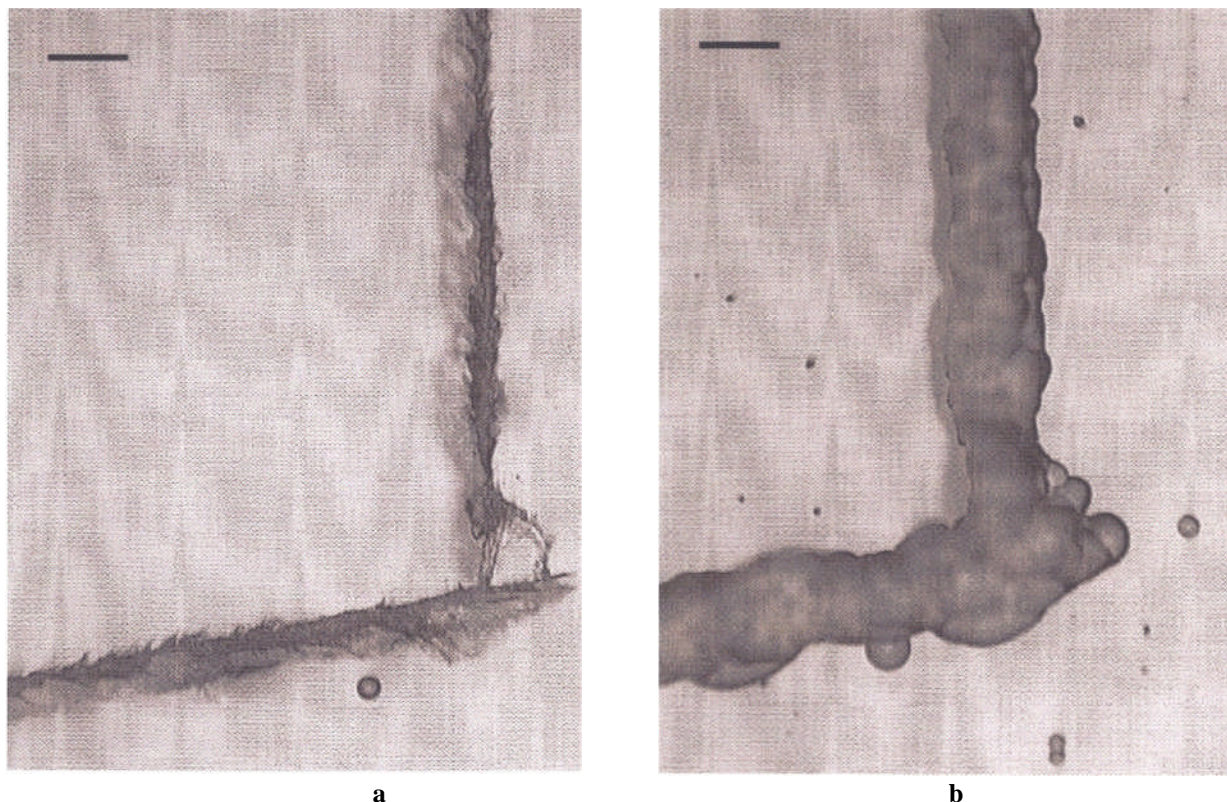


Figure 5a. Photomicrograph (Scale line= 80 μm) of a region of a CR39 chip after the first etch. The L-shaped figure was scratched after the first etch in order to be able to locate the same region after re-etching. Only one pit appeared after the first etch. **5b.** Photograph of the same region after the second etch. The scratch mark has thickened and almost covers the original single pit, and a new family of pits has appeared, produced by the second etch.

5. CONCLUSIONS

A technique has been developed that consistently produces evidence that a nuclear process can accompany electrolysis of solutions of lithium salts in either heavy or light water. The evidence is in the form of nuclear damage trails made visible by the etching of CR39 plastic chips. The damage trails can begin at either external surface of the chip placed within the cell during electrolysis as well as within the interior if the thickness of the chips. It is demonstrated that the nuclear damage trails could not have been caused by the decay of ordinary radionuclides contaminating anything in the experimental procedure. Rather, the nuclear damage is caused by a nuclear process of currently unknown nature.

The described experimental results can not be explained by nuclear physics as currently understood. Mechanistic interpretations should be the goal of future research. The aims of the present work have been only to develop an experimental technique that reproducibly shows that a nuclear process of a new kind can accompany electrolysis, to demonstrate some of the characteristics of the nuclear process, and to provide convincing evidence that would justify initiating intensive research in this new area of nuclear physics.

ACKNOWLEDGMENTS

Suggestions and discussions with J. C. Fisher are gratefully acknowledged. C. J. Stone is thanked for helping to prepare this paper for publication.

REFERENCES

1. R. L. Fleischer, P. B. Price, and R. M. Walker, Tracks in Solids, University of California Press, Berkeley, California (1975).
2. R. A. Oriani and J. C. Fisher, Jpn. J. Appl. Phys. Part 1, 41, no. 10, 6180, (2002); Erratum, *ibid.* 42, no. 3, 1498 (2003).
3. R. A. Oriani and J. C. Fisher, Proceedings of the 10th International Conference on Cold Fusion, p.577-584 (2003).
4. P. A. Mosier-Boss, S. Szpak, F. E. Gordon, and L. P. G. Forsley, Eur. Phys. J. Appl. Phys. **40**, 293-303 (2007).
5. R. A. Oriani and J. C. Fisher, Proceedings of the 10th International Conference on Cold Fusion, p.567-575 (2003).

Detection of Radiation Emitted from LENR

Edmund Storms and Brian Scanlan

Kiva Labs,

Santa Fe, NM and Greenwich, CT

ABSTRACT

A study was made to detect X-radiation and energetic particle emission from nuclear reactions that may be initiated during low-voltage gas discharge in deuterium. Evidence is presented for X-radiation having an energy nearly equal to the voltage applied to the discharge and energetic particle emission similar to deuterons having energy with peaks between 0.5 and 3 MeV. A study of radiation emitted from materials exposed to deuterium gas is underway.

I. INTRODUCTION

Emission of radiation is characteristic of nuclear reactions. Such radiation is required to carry away momentum and energy from the reaction and deposit it as heat in the environment. In contrast, the nuclear reactions associated with cold fusion appear to produce less radiation than expected when detection is attempted outside of the apparatus. This unexpected behavior has encouraged a search for low-energy radiation within the device. This search is important because detected radiation clearly shows that nuclear reactions are occurring and provides information about the process. Consequently, such observations are far more supportive of a nuclear reaction than the conventional measurement of heat.

In addition to heat energy, cold fusion is found to produce helium¹⁻¹² and occasionally tritium¹³⁻²¹. The helium is expected to originate as energetic alpha particles and the tritium as energetic tritons. A search for such energetic particles has been undertaken by other workers using CR-39 as the detector.²²⁻²⁶ However, energetic particles can also be detected using a silicon barrier detector (SBD), from which their energy can be obtained, or by use of a Geiger-Mueller (GM) counter, using absorbers to determine their energy. These methods are used in this study to measure the energy of the detected radiation. This paper further describes studies reported previously.^{27,28}

Two methods to initiate a fusion reaction have been explored. First, a discharge has been studied in low-pressure D₂ gas using various kinds of cathode materials. Second, fine powders of materials containing palladium have been exposed to pressurized D₂ gas. Both the SBD and GM detectors were used in the former study while only the SBD was used in the latter work.

II. EXPERIMENTAL

II.1. Gas Discharge

The gas discharge cell is shown in Fig. 1. The cathode is a water-cooled thin sheet of various metals including, Al, Cu, Pd, Pd+Pt, Pt Ti, bronze, brass, or stainless steel. The cathode is surrounded by a shroud consisting of various insulators including Teflon, Lavite, Al₂O₃ or BN

in order to force the discharge to occur within a well defined region of the metal surface. The anode is either a Pd or W rod located so as not to block the view of the cathode by the detectors. The system is evacuated using a turbomolecular pump capable of reaching pressures less than 1×10^{-7} Torr. After evacuation, the system is filled with deuterium gas (99.95% D + 0.05% H) to a pressure between 10 and 40 Torr, depending on the nature of the study. Gases consisting of N_2 , O_2 , Ar, H_2 , H_2O , or D_2O are used either alone or mixed with D_2 . A DC voltage between 500 V and 900 V is applied at a current between 0.05 A and 0.3 A, using current control. The various measurements are recorded using Labview (National Instruments) and Maestro (Ortec) programs with an iMAC computer running both Windows XP and OS10.5.4.

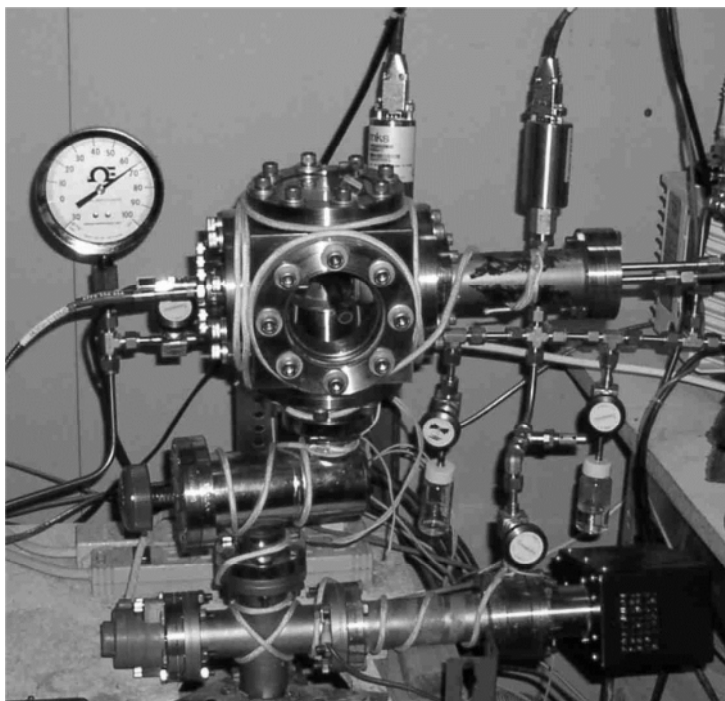


Figure 1. Picture of the gas discharge apparatus. The detectors are located on the left and the water cooled cathode is on the right. H_2O or D_2O vapor is supplied from small glass containers of the liquid as seen on the right.

The cathode surface is viewed by either a SBD, a GM, or both at the same time. Various SBD made by Ortec are used. Calibration of the SBD is done using Po^{210} in vacuum. The shape of the peak in vacuum (Fig.2) has a Gaussian relationship on the high-energy side but has slight broadening on the low-energy side caused by self-adsorption. Most of the peaks attributed to charged particles found in this study could be fit by a similar Gaussian equation. A study of energy vs. distance between the source and detector in air shows that the relationship between BIN number and energy is linear, as can be seen in Fig. 3. The BIN number was calibrated at lower energy by using a source of pulses (Ortec 419) having a linear relationship to energy that were fed into the preamp at the same location as the pulses from the SBD. An example of a

peak produced by these pulses is shown in Fig. 2. However, the apparent energy has to be modified because the SBD is covered by a thin aluminum light shield that removes some energy, depending on the kind of particle passing through it. The various corrections are listed in Table 1 for energy near 1 MeV based on the ASTAR tables. Because the kind of particle is not known initially, the apparent energies noted on the figures are the measured value without a correction for the light shield. The values are only used to compare the relative effects of absorbers and applied voltage. Once the particles have been identified later in the paper, actually energy will be assigned to each peak.

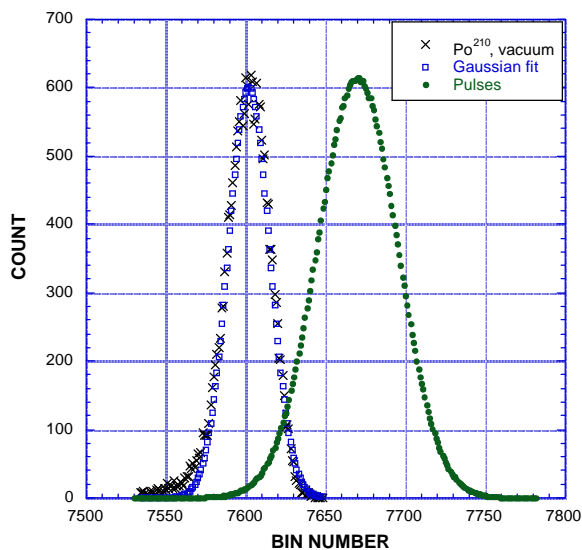


Figure 2. Count vs BIN number for Po^{210} compared to a Gaussian fit and output of the pulser.

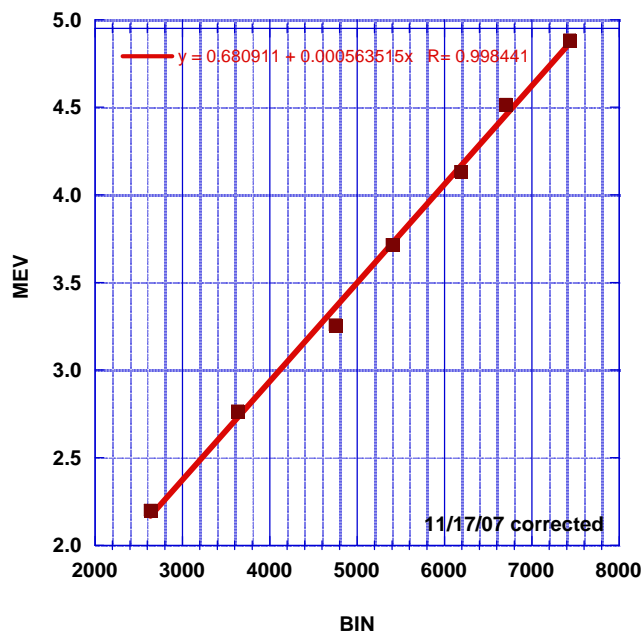


Figure 3. Typical calibration using air to change the energy of Po^{210} .

A system of moveable absorbers allows various thickness of Mylar, aluminum or copper to be imposed between the cathode and detectors. As many as three absorbers could be imposed during the same run in front of either the GM or the SBD. One of these absorbers is always a thickness of copper sufficient to completely stop the radiation. Only counts that are completely stopped by this absorber are accepted as being caused by actual radiation, in contrast to being caused by electrical noise in the counting circuit. Such noise was frequently generated by the electrical discharge when conditions had not been properly adjusted.

Two different GM tubes made by LND were used, one with a 2.5 mg/cm^2 window and the other with a 0.3 mg/cm^2 window. Because of its reduced absorption, the thin-window tube had a higher counting rate in spite of having a window only 1.5 mm in diameter compared to the 9 mm diameter of the other tube.

TABLE 1

Change in energy produced by passing 1 MeV particles
through absorbers based on ASTAR tables

	1.2 μm Aluminum	2.0 μm Mylar	3.0 μm Mylar
Alpha, MeV	0.39	0.54	0.81
Proton, MeV	0.075	0.095	0.14
Thickness, g/cm^2	0.000324	0.00028	0.00042

Calibration equation for SBD: $\text{MeV} = 0.000657 \cdot \text{BIN}$

III. RESULTS

III.1. Particle Measurement

Many peaks in the SBD spectrum were detected, some of which were clearly produced by electrical noise injected into the detection circuit by the discharge. Peaks that could be eliminated by imposing a thick absorber in front of the SBD are assumed to be caused by real particles. Further support for this conclusion is obtained when the intensity and energy are reduced by a thin absorber.

The sequence of the measurement is shown by the data number in each of the following figures. A few figures show the counting rate of a GM counter that detected the X-radiation emitted from the cathode along with the particles. The energy noted on the figures is uncorrected for the light shield. Therefore it can only be used to show relative changes in energy produced by the absorbers and voltage. The complete data set is listed in Table 2 along with corrected energies based on the particles being alpha or protons. A conclusion about the kind and energy of the particles is saved for the discussion section.

A gas mixture of approximately equal amounts of D_2 and D_2O produces the spectra shown in Figs. 7, 8, and 9. When 721 V is applied, a weak emission at 0.32 MeV is produced. Increasing the voltage to 771 V causes a peak to appear at 0.20 MeV, with an indication of a peak near 0.1 MeV that is partially overlapped by the noise region. A further increase to 800 V causes a peak at 0.26 MeV, with a decrease in intensity, and additional radiation near 0.1 MeV to form. Moving to Fig. 8, imposition of 3.0 μm of Mylar at 800 V reduced the peak at 0.26

MeV to 0.23 MeV without significantly changing the peak near 0.1 MeV. A thick copper absorber eliminated all peaks. When a 2.0 μm Mylar absorber is used instead of the 3.0 μm Mylar at 767 V, the peak shifts by 0.02 MeV showing the effect of 1.0 μm of Mylar, as seen in Fig. 9. Again, a thick absorber eliminates all peaks except for the noise below about BIN = 150.

TABLE 2

Summary of all data

Date	Absorber	Applied volt	BIN	Intensity for 1 min	Measured, MeV	Alpha, MeV	Proton, MeV	Gas composition
11/28/07	1.2 μm Al	823	640	65	0.42	0.81	0.50	D ₂ +D ₂ O
	1.2 μm Al	823	1430	5	0.94	1.33	1.01	D ₂ +D ₂ O
12/7/07	1.2 μm Al	760	300	4125	0.20	0.59	0.27	D ₂ +H ₂ O
	1.2 μm Al	760	680	400	0.45	0.84	0.52	D ₂ +H ₂ O
	1.2 μm Al	760	1100	50	0.72	1.11	0.80	D ₂ +H ₂ O
	1.2 μm Al	760	1500	25	0.99	1.38	1.06	D ₂ +H ₂ O
12/10/07	1.2 μm Al	721	480	10	0.32	0.71	0.39	D ₂ +D ₂ O
	1.2 μm Al	771	300	25	0.20	0.59	0.27	D ₂ +D ₂ O
	1.2 μm Al	800	400	12	0.26	0.65	0.34	D ₂ +D ₂ O
	1.2 μm Al+3.0 μm Mylar	801	350	25	0.23	1.43	0.44	D ₂ +D ₂ O
12/11/07	1.2 μm Al+3.0 μm Mylar	764	430	10	0.28	1.48	0.50	D ₂ +D ₂ O
	1.2 μm Al+2.0 μm Mylar	767	460	12	0.30	1.23	0.47	D ₂ +D ₂ O
	1.2 μm Al	767	340	29	0.22	0.61	0.30	D ₂ +D ₂ O
	1.2 μm Al	777	350	30	0.23	0.62	0.30	D ₂ +D ₂ O
	1.2 μm Al	788	390	50	0.26	0.65	0.33	D ₂ +D ₂ O
	1.2 μm Al	791	420	152	0.28	0.67	0.35	D ₂ +D ₂ O
	1.2 μm Al	791	1100	10	0.72	0.86	1.53	D ₂ +D ₂ O
	2*1.2 μm Al	777	590	10	0.39	1.17	0.54	D ₂ +D ₂ O
	2*1.2 μm Al	781	none					D ₂ +D ₂ O
	1.2 μm Al+3.0 μm Mylar	786	520	20	0.34	1.54	0.56	D ₂ +D ₂ O
12/12/07	1.2 μm Al+3.0 μm Mylar	766	350	10	0.23	1.43	0.44	D ₂ +D ₂ O
	1.2 μm Al	671	350	10	0.23	0.62	0.30	H ₂ +D ₂ +H ₂ O
	1.2 μm Al	756	330	400	0.22	0.61	0.29	H ₂ +D ₂ +H ₂ O
	1.2 μm Al	756	750	30	0.49	0.88	0.57	H ₂ +D ₂ +H ₂ O
	1.2 μm Al	756	1160	5	0.76	1.15	0.84	H ₂ +D ₂ +H ₂ O
12/13/07	1.2 μm Al+3.0 μm Mylar	785	300	2	0.20	1.40	0.41	H ₂ +D ₂ +H ₂ O
	1.2 μm Al	739	280	550	0.18	0.57	0.26	H ₂ +H ₂ O
	1.2 μm Al	739	690	40	0.45	0.84	0.53	H ₂ +H ₂ O
	1.2 μm Al	739	1100	10	0.72	1.11	0.80	H ₂ +H ₂ O
	1.2 μm Al	739	1550	5	1.02	1.41	1.09	H ₂ +H ₂ O
	1.2 μm Al	773	440	900	0.29	0.68	0.36	H ₂ +H ₂ O

	1.2 μm Al	773	950	75	0.62	1.01	0.70	H ₂ +H ₂ O
	1.2 μm Al	773	1520	15	1.00	1.39	1.07	H ₂ +H ₂ O
	1.2 μm Al	773	2050	5	1.35	1.74	1.42	H ₂ +H ₂ O
	1.2 μm Al	794	540	450	0.35	0.74	0.43	H ₂ +H ₂ O
	1.2 μm Al	794	1170	45	0.77	1.16	0.84	H ₂ +H ₂ O
	1.2 μm Al	794	1820	7	1.20	1.59	1.27	H ₂ +H ₂ O
	1.2 μm Al	794	2650	5	1.74	2.13	1.82	H ₂ +H ₂ O
	1.2 μm Al	794	3100	5	2.04	2.43	2.11	H ₂ +H ₂ O
					Measured, Alpha, Proton,			Gas
Date	Absorber	Voltage	BIN	Intensity	MeV	MeV	MeV	composition
12/18/07	1.2 μm Al	794	3600	2	2.37	2.76	2.44	H ₂ +H ₂ O
	2*1.2 μm Al	774	500	6	0.33	1.11	0.48	H ₂ +H ₂ O
	2*1.2 μm Al	774	250	33	0.16	0.94	0.31	H ₂ +H ₂ O
	1.2 μm Al	748	290		0.19	0.58	0.27	D ₂ +D ₂ O
	1.2 μm Al	785	420	7	0.28	0.67	0.35	D ₂ +D ₂ O
	1.2 μm Al	815	550	6	0.36	0.75	0.44	D ₂ +D ₂ O
	1.2 μm Al	845	730	30	0.48	0.87	0.55	D ₂ +D ₂ O

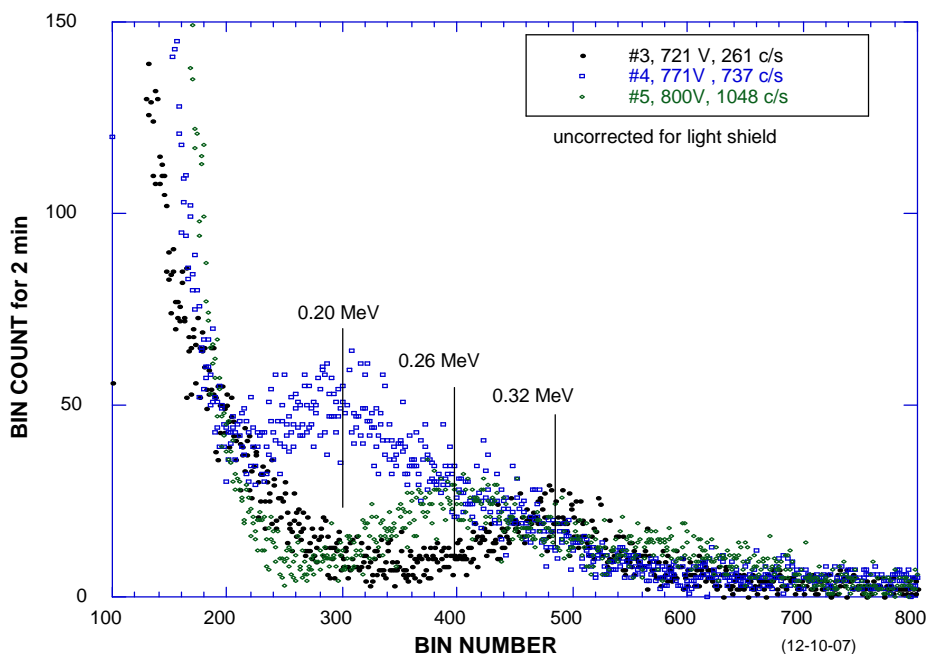


Figure 7. Spectrum produced using a Cu cathode, Al₂O₃ shroud, and a gas containing D₂ and D₂O at about 18 Torr. The count rate of the GM counter has a linear relationship to voltage and, in this case, extrapolates to zero at 695 V.

The next day, the system was opened to air and new absorbers were installed. The gas is again a mixture of D_2+D_2O . A clear peak can be seen in Fig. 10 at 0.28 MeV for 791 V and a smaller peak at 0.72 MeV. An energy of 0.34 MeV is produced at 786 V when 3.0 μm Mylar is inserted and this decreases to 0.39 MeV for 777 V when extra 1.2 μm Al is imposed. Imposition of 1.3 mm Cu stops all radiation below BIN=200, shown in Figs. 11 and 12. Counts below BIN=200 are assumed to result mainly from noise, although some counts in this region are removed by the thick absorber. Use of 3.0 μm Mylar at 766 V produces a peak at 0.23 MeV similar to the peak produced without Mylar at 777 V, as shown in Fig. 12.

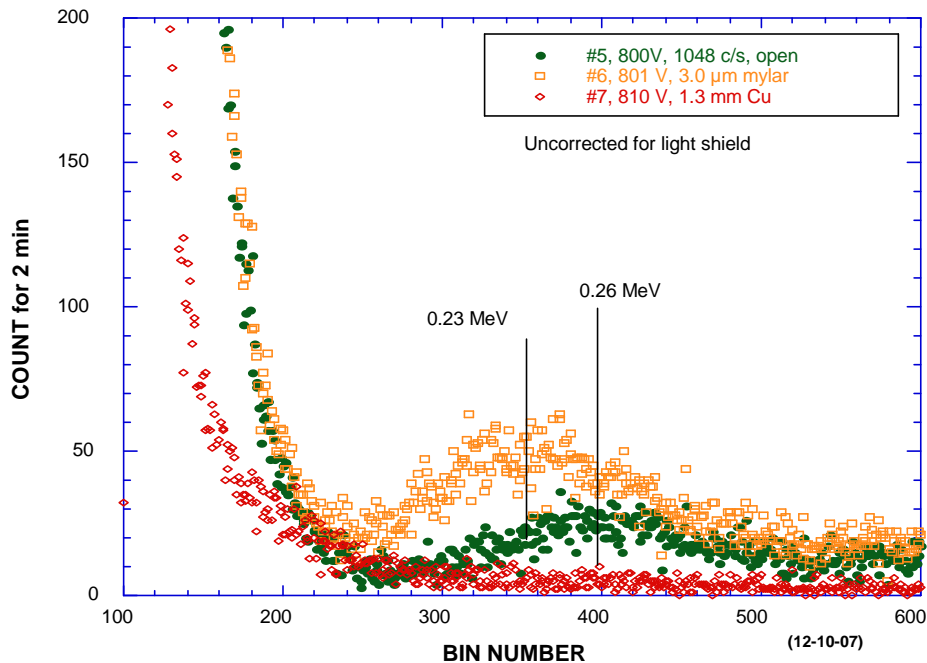


Figure 8. Spectrum produced using a Cu cathode, Al_2O_3 shroud, and a gas containing D_2 and D_2O at about 18 Torr.

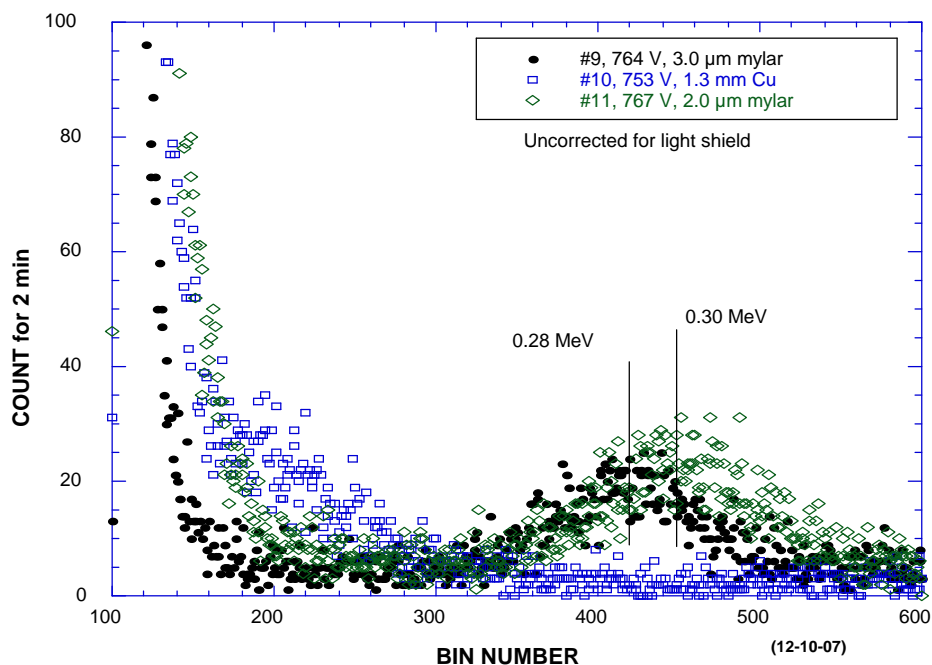


Figure 9. Spectrum produced using a Cu cathode, Al_2O_3 shroud, and a gas containing D_2 and D_2O at about 18 Torr.

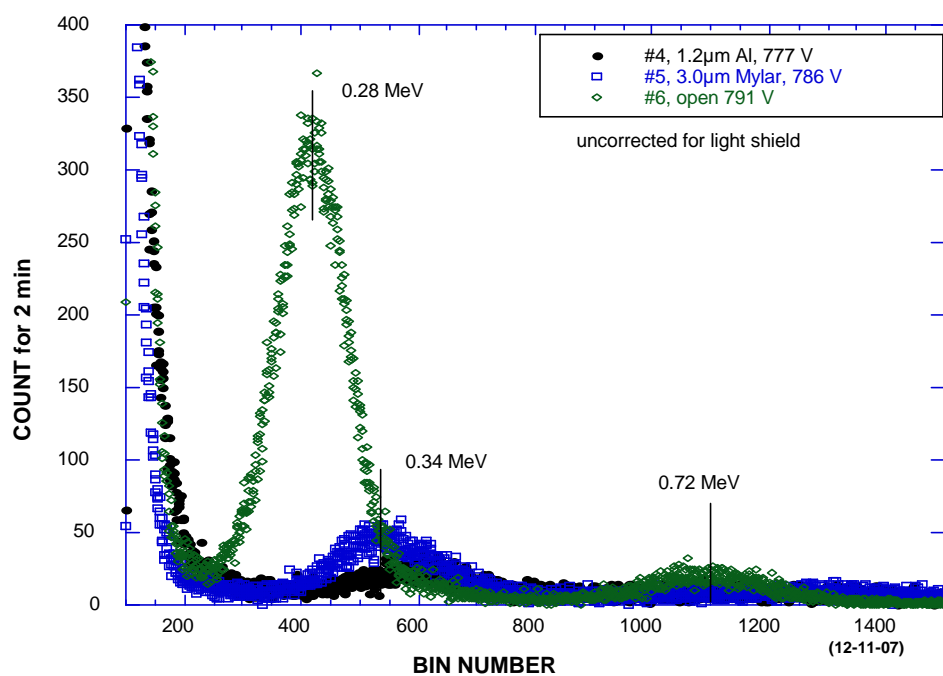


Figure 10. Spectrum produced using a Cu cathode, Al_2O_3 shroud, and a gas containing D_2 and D_2O at about 23 Torr.

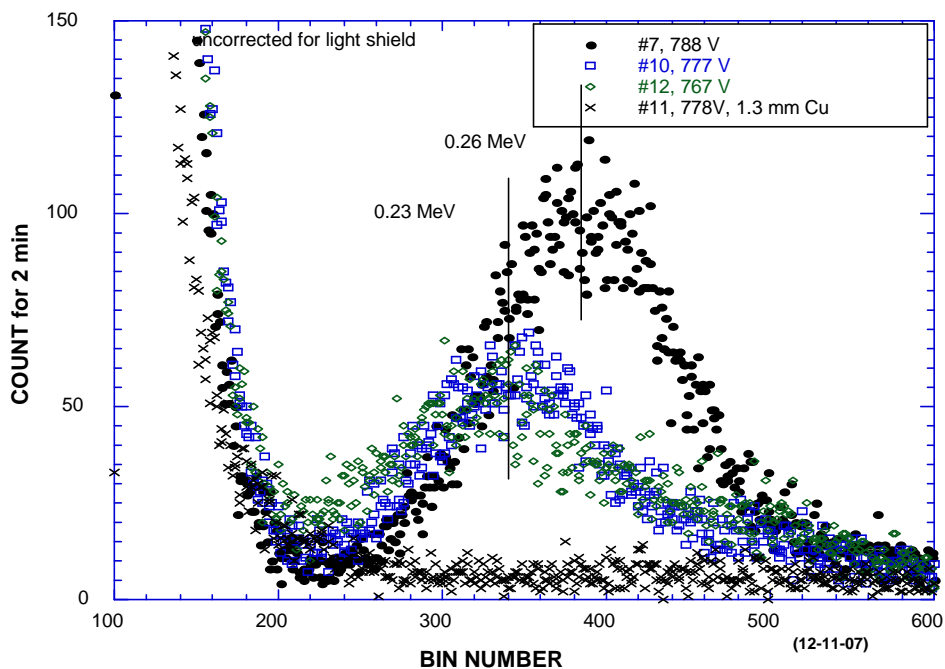


Figure 11. Spectrum produced using a Cu cathode, Al_2O_3 shroud, and a gas containing D_2 and D_2O at about 23 Torr.

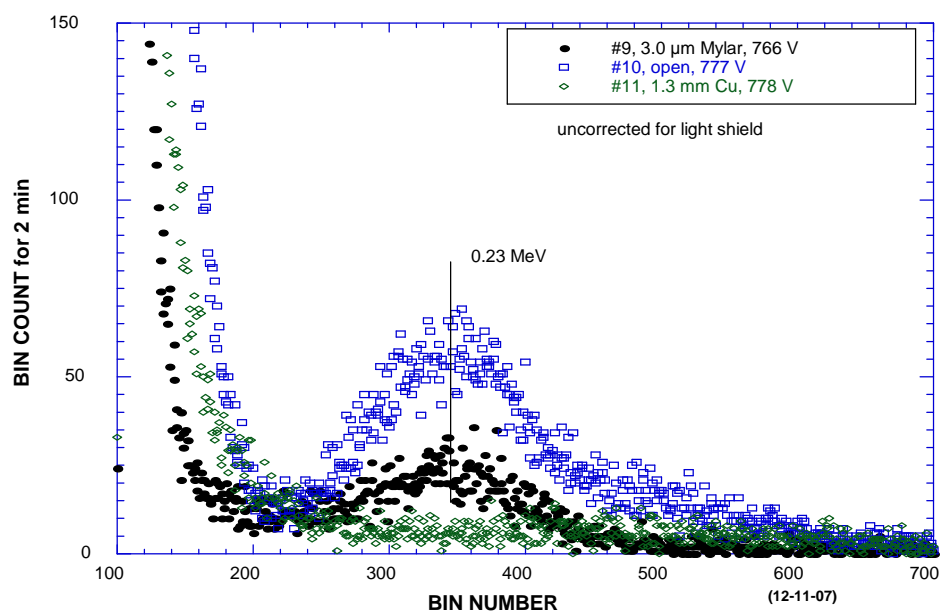


Figure 12. Spectrum produced using a Cu cathode, Al_2O_3 shroud, and a gas containing 12.0D_2 and $11.4\text{D}_2\text{O}$ at about 23 Torr.

The gas mixture was changed to D_2 , H_2 and H_2O , which causes the intensity of the radiation to increase. Imposition of 3 μm Mylar shifts the peaks near 0.1 MeV and 0.22 MeV off scale and shifts the peak at 0.49 MeV to 0.20 MeV, as shown in Fig. 13.

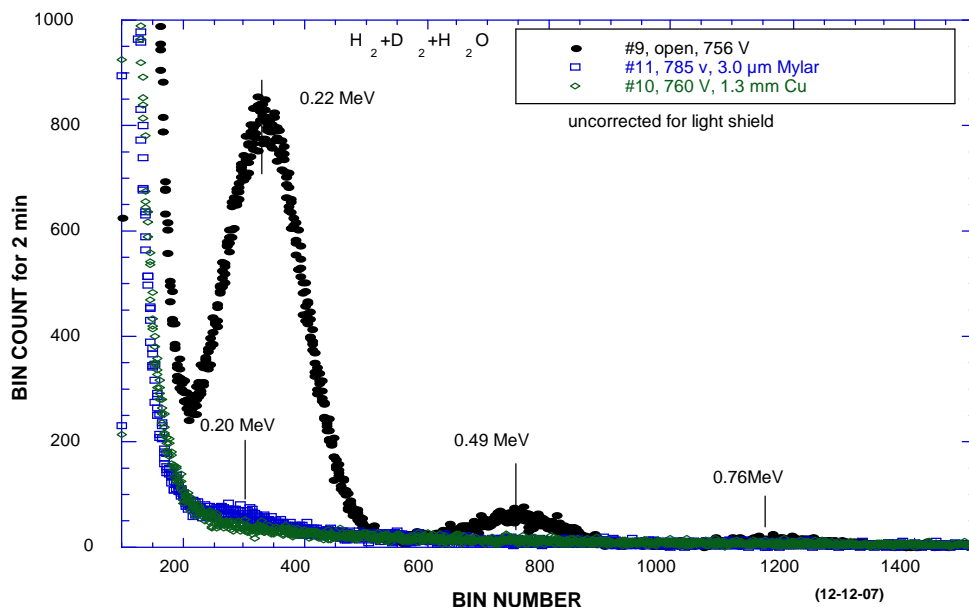


Figure 13. Spectrum produced using a Cu cathode, Al_2O_3 shroud, and a gas mixture of $2.8D_2$, $8.9H_2$, and $11.0H_2O$, with a total pressure of about 23 Torr.

When most D_2 is removed from the gas by using a mixture of H_2+H_2O , radiation intensity remains high and the spectrum becomes more complex, with additional peaks as shown in Figs. 14 and 15. The full spectrum of run #12 is shown in Fig. 16. Peaks at 2.37 MeV are visible. The energy of the peaks increases as applied voltage is increased. In contrast, no peaks fall on scale when the voltage is as low as 706 V.

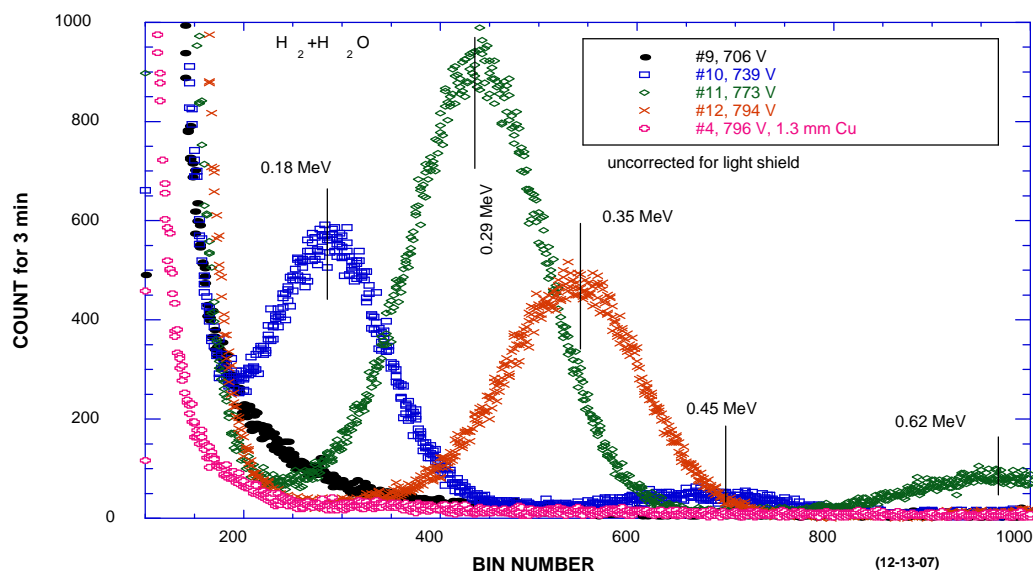


Figure 14. Spectrum produced using a Cu cathode, Al_2O_3 shroud, and a gas mixture of 8.5H_2 and $10.6\text{H}_2\text{O}$ with a total pressure of about 19 Torr. A small amount of D_2 is present in the gas, caused by release of absorbed gas after previous exposure to deuterium.

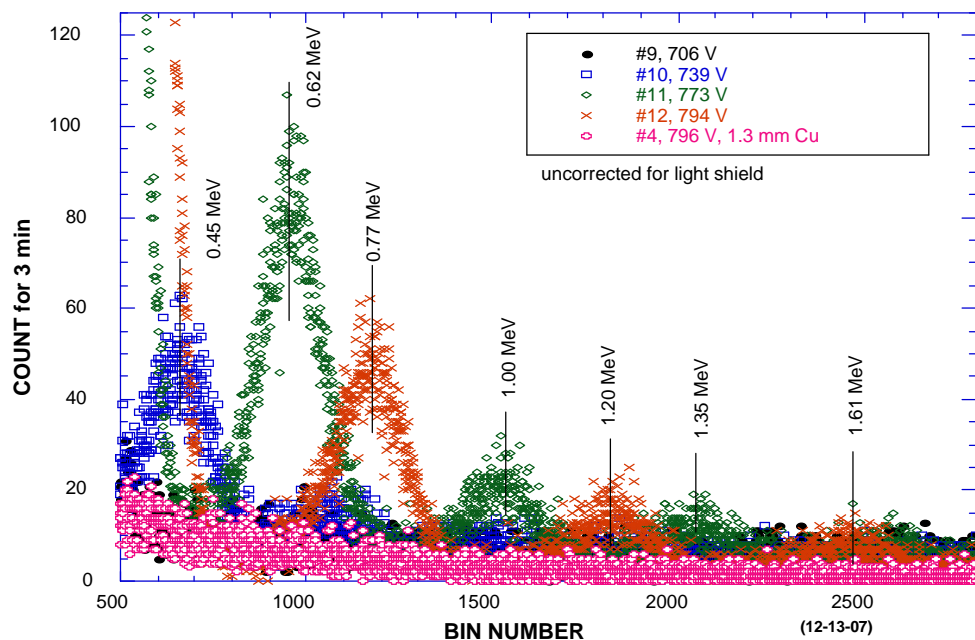


Figure 15. Spectrums shown in Fig. 14 from 500 to 2700 BIN number.

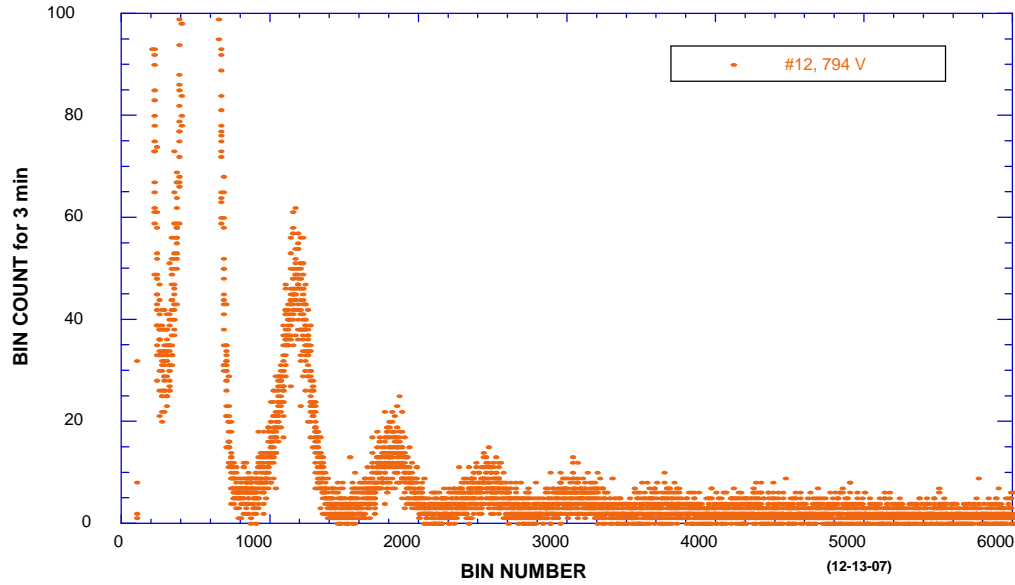


Figure 16. Full spectrum of run #12 from Figs. 14 and 15.

Imposition of 3.0 μm Mylar along with a reduction in voltage to 779 V eliminated all peaks. In contrast, 1.2 μm Al imposed at 774 V produced peaks at 0.16 MeV and 0.33 MeV.

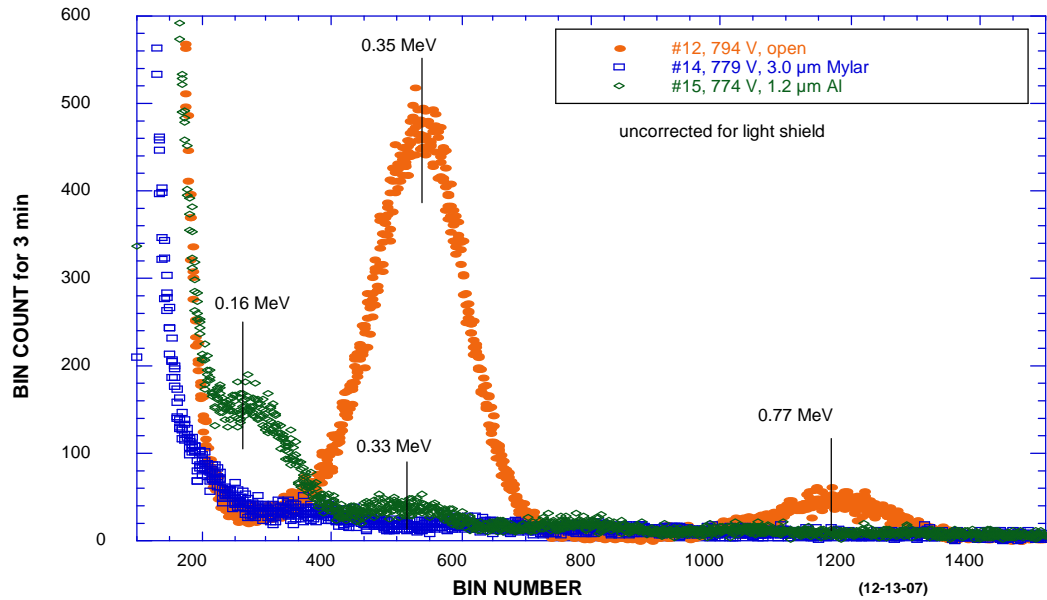


Figure 17. Effect of interposing 3.0 μm Mylar or 1.2 μm Al following run #12.

II.2. Gas Loading

Gas loading involves exposure of special materials to D_2 gas, as pioneered by Arata and Zhang²⁹, and Case³⁰. This method has been found to produce helium and excess heat when the proper materials are used. This method has several advantages over gas discharge for measuring radiation. For example, the background electrical noise generated by a discharge is not present, thereby allowing much lower energies and smaller fluxes of radiation to be measured. Absence of a light shield, as required during gas discharge, reduces the uncertainty in the measured energy. In addition, much greater control over the nature of the active material can be achieved.

Samples of various powdered materials are placed on a stage, shown in Fig. 18, that is within about 4 mm of a SBD, shown in Fig. 19. This stage is heated by passing current through an enclosed resistor and its temperature is measured using a type-K thermocouple located at the sample. An absorber made of 0.5 mm thick copper can be imposed between the SBD and the sample by moving an exterior rod. The assembly can be evacuated to less than 5×10^{-7} Torr and can be filled with purified D_2 or H_2 at pressures up to 100 psi.

A vacuum/hydrogen furnace used to purify the samples is shown in Fig. 20. This system can be evacuated to less than 5×10^{-7} Torr, pressurized with H_2 or D_2 up to 100 psi, and heated up to 500°C . The sample is contained in a thin Al cup that allows the powder to be removed and weighted after each treatment. The overall system is shown in Fig. 21.



Figure 18. A heated platen holds the powdered sample in the cup, into which a thermocouple is inserted. The white material is Teflon that is used to stabilize the source and to decrease gas volume.



Figure 19. Holder for the SBD. When assembled, the active area of the SBD is located about 4 mm directly above the cup in the heated platen shown in Fig. 16. The massive copper helps keep the SBD cool when the sample is heated.

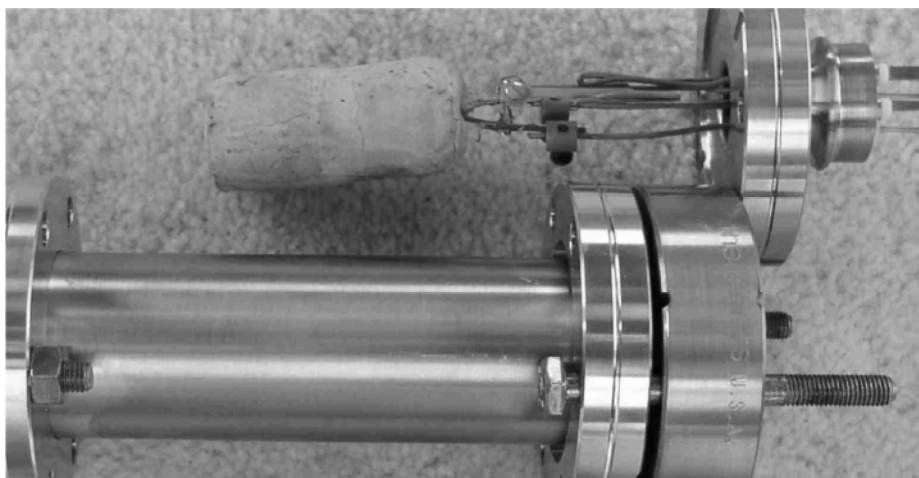


Figure. 20. Hydrogen furnace. The furnace consists of a brass tube wrapped with resistance wire imbedded in ceramic insulation. A thermocouple is inserted in the bottom.

A sample consisting of finely powdered ($\sim 2 \mu\text{m}$ particles) mixture of SiO_2 , TiO_2 , CaO , Al_2O_3 , and CeO_2 is mixed with a solution of $\text{Pd}(\text{NO}_3)_2$ in water. The liquid is evaporated to dryness at 120°C in air. After purification with D_2 using the hydrogen furnace described above, the material is examined using the SBD. Fig. 22 shows the spectrum obtained with and without the absorber in place. An identical spectrum is found using a sample of the same material, but without added Pd or exposure to D_2 . A sample of powdered KOH is also examined and found to produce the same spectrum as the mixed oxides.



Figure 21. Overview of vacuum system and gas handling system. The detector assembly is on the left and the hydrogen furnace assembly is on the right of the red vacuum valves. Vacuum is measured using a nude ion gauge and a 0-100 Torr Baratron gauge. A RGA allows the gas composition to be determined. Gamma and neutron detectors are located nearby. A hydrogen gas-purifier is located in the rear.

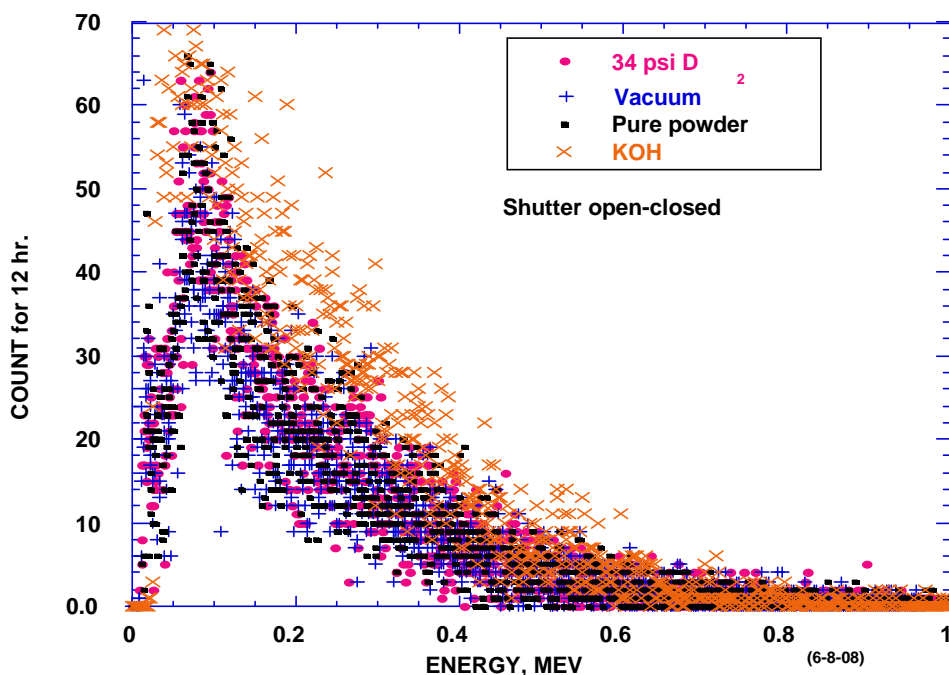


Figure 22. Difference between count for 12 hr with shutter open and closed using a sample of mixed oxides under various conditions. The pure oxide powder did not contain Pd nor was it exposed to D_2 . The data are compared to the radiation from KOH (1.33 MeV beta from K^{40}) measured using the same apparatus.

III.3. Preparation and characterization of materials

The materials are made by evaporating at 120°C a dilute solution containing PdCl₂ or Pd(NO₃)₂ mixed with a suspension of a powder. In one case, the powder consists of a mixture of various oxides. The palladium compound in the powder is reduced to Pd metal by heating it in H₂/D₂ followed by pumping out the resulting reaction products. Once activated, the powder is heated in D₂ gas. In the process, weight is increased by absorbed or reacted deuterium. If all of the deuterium is present as β-PdD, the added weight should be proportional to the Pd content of the powder. If this proportionally is not observed, the deuterium is assumed to be absorbed on the oxide surface either as D₂ molecules or spill-over D+. By determining the weight increase of a sample containing no Pd, the amount of absorbed deuterium as D₂ can be determined because in the absence of a catalyst the D+ cannot form. This type of study was done using the materials listed in Table 3. The SiO₂ samples are made by evaporating a solution of Pd(NO₃)₂ with a colloidal suspension of SiO₂ in H₂O.

TABLE 3

Composition wt. % Pd wt% D ₂ D/Pd				
DESCRIPTION	Wt.% Pd	Wt. % D ₂	D/Pd	TREATMENT
SiO ₂ (pure)	0.0	0.090	NA	40psi D ₂
SiO ₂ #7c	0.23	0.030	6.9	40 psi D ₂
SiO ₂ #9e	0.92	0.20	11.5	100 psi D ₂
SiO ₂ #9d	0.92	0.24	13.8	80 psi D ₂
SiO ₂ #10a	1.37	0.24	9.3	50 psi D ₂
SiO ₂ #10b	1.37	0.31	12.0	30 psi D ₂
Al ₂ O ₃ #1a	0.41	0.23	29.2	20 psi D ₂
ZrO ₂ #1a	0.39	0.09	12.5	30 psi D ₂

III.4 X-ray measurement

The X-ray measurements were described previously.^{27,28} The radiation originates at the cathode, which acquires a very complex surface. Consequently, emission is probably not uniform. Use of absorbers allows the energy of the X-rays to be determined. Figure 23 compares the counting rate as a function of applied volt for when various absorbers are placed between the GM tube and a Mo cathode using a gas mixture of D₂O and D₂ at 22 Torr. No absorber is used periodically during the study and these results are combined and fit by the equation

$$c/s = 0.002 * (V - 482)^3, \text{ where } V \text{ is the applied voltage.}$$

The form of this equation was chosen because it fits well the relationship between absorption coefficient and X-ray energy as provided by NIST. The counting rate (c/s) obtained using this equation is divided into the measured counting rate for each absorber to calculate I/I₀. An apparent absorption coefficient can be obtained using the equation

$$\mu/\rho \text{ (cm}^2/\text{g)} = -\ln(I/I_0)/t, \text{ where } t \text{ is the absorber thickness in g/cm}^2.$$

The calculated absorption coefficients for the aluminum absorbers are compared in Fig. 24 to the tabulated values provided by NIST. Apparently the X-ray energy is less than the applied voltage at low voltages, being about 400 eV when the applied voltage is 525 V. However, the X-ray energy and the applied voltage become equal as applied voltage is increased to about 600 V. The Mylar absorbers show results that are consistent with this behavior. Because the shape of the measured curve is very sensitive to the form of the equation used to calculate I_0 above 600 V, the effect of voltage on X-ray energy becomes increasingly uncertain at higher voltages. Nevertheless, as voltage is increased, the increased energy of the radiation allows more radiation to pass through the window of the GM tube resulting in an increasing counting rate when applied voltage is increased. The higher the oxygen content of the gas, the more rapidly the counting rate increases with applied voltage, as described previously.²⁷

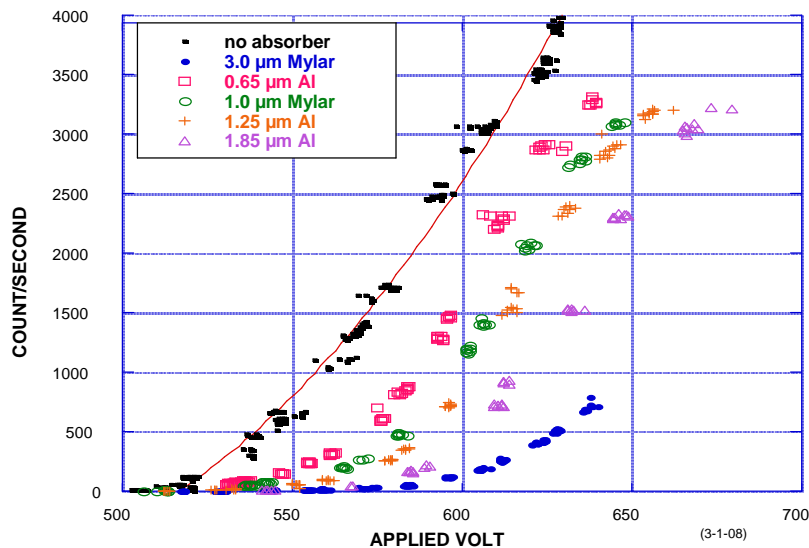


Figure 23. Effect of applied voltage on the counting rate measured when various absorbers are imposed.

The initial results suggested the radiation was energetic electrons. However, work done at Coalescence³¹ indicated the radiation is X-rays because it is apparently not deflected by a magnetic field. To test this conclusion, a large magnet is used in an attempt to deflect the radiation, a picture of which is shown in Fig. 25. Radiation originating in the cell on the right, as described previously, passes through a beam defining slit, through 3 inches of magnetic field, and into a small-window GM tube (1.5 mm dia.) on the left. An applied field strength up to 10,000 G is measured with a Gauss meter. Although significant counting rates are observed, at no time is this rate changed by a magnetic field, as would be expected if the radiation had an electric charge.

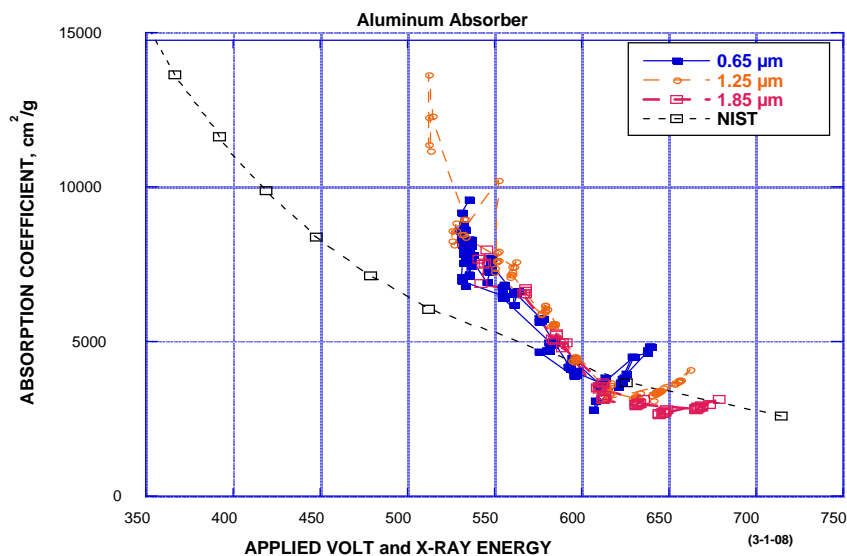


Figure 24. Comparison of absorption coefficients calculated using the aluminum absorbers and the tabulated values supplied by NIST for X-rays of the indicated energy.

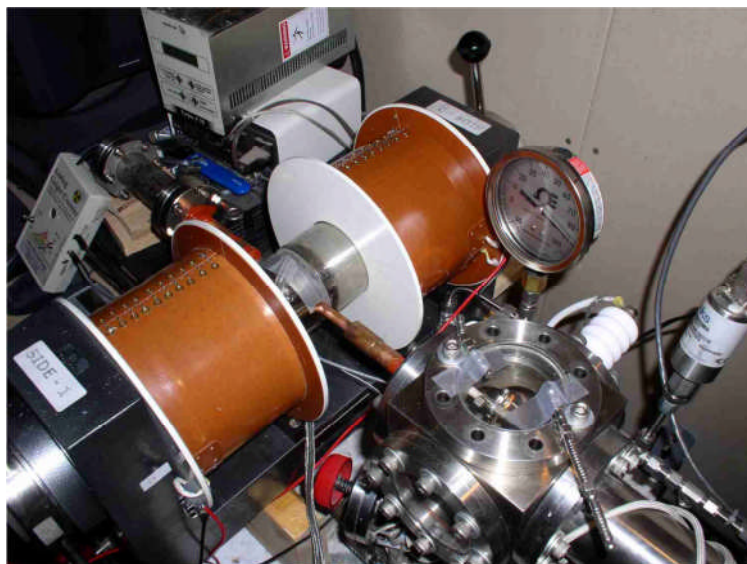


Figure 25. Picture of magnet used to deflect radiation from the gas discharge cell. The radiation is detected using a thin-window GM tube located at the left top.

IV. DISCUSSION

During gas discharge, X-radiation is always generated. In contrast, the particle radiation occurs infrequently, is often obscured by electrical noise generated by the discharge, and has a much lower flux compared to the X-ray emission. Nevertheless, both kinds of emission are sensitive to applied voltage and gas composition, which in each case cause changes in energy and intensity.

IV.1. Particle Emission

The intensity and characteristics of the spectrum is sensitive to composition of the gas, but less so to the basic material used as the cathode. The relationship between intensity and peak energy for the various energies is shown in Fig. 26 for different gas compositions. Apparently, addition of hydrogen causes the intensity of the various peaks to increase, thereby allowing the details of the spectrum to be more clearly seen in Fig. 12. The logarithmic behavior suggests that very large peaks might exist at an energy too low to be separated from the noise and much smaller peaks might exist at higher energies. As a result, only a small part of the full spectrum might be seen.

Each peak increases in energy as applied voltage is increased. This behavior can be seen in Fig. 27 where each peak at the same position in the spectrum is connected by a line. In general, the greater the energy of the emission, the greater the effect of applied voltage on its energy. When the gas contains only $D_2 + D_2O$ the intensity is too small to make the full spectrum visible. As a result, only the most intense peak is plotted and connected by a line. The observed effect of gas composition on energy and intensity encourages the belief that the peaks are produced by real emissions rather than by electrical noise.

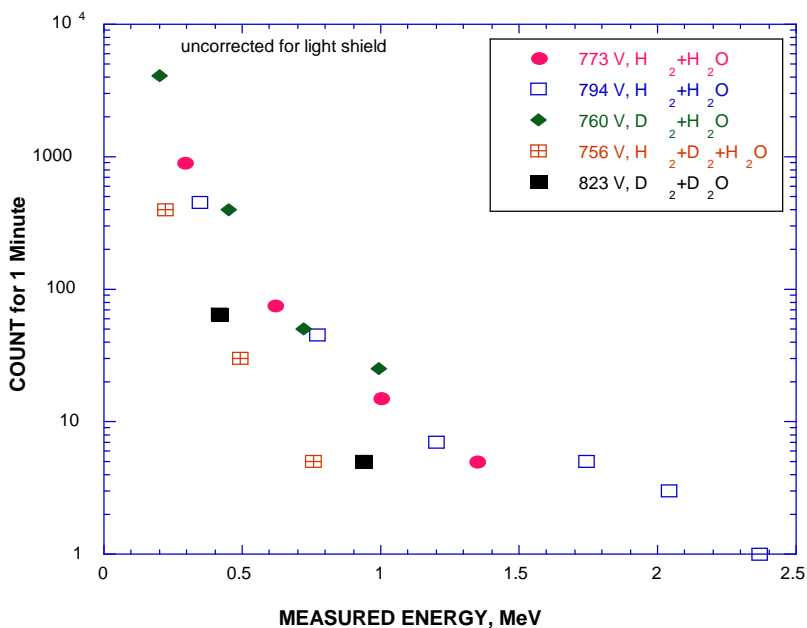


Figure 26. Effect of gas composition on the intensity of the various peaks.

What are the particles and what reaction causes their production? Because a light-shield is required, energy detected by the SBD needs to be corrected, depending on the kind of particle being measured. This requires the effect of this material be determined using published data from ASTAR. The effect of aluminum and Mylar are calculated from the data shown in Fig. 28 by dividing the slope at 1 MeV, an arbitrary energy near that of the particles, into the thickness density of the absorbers. The results are listed in Table 2. If the spectrum is produced by alpha particles, about 0.39 MeV must be added. If the particles are protons, addition of only 0.075

MeV is needed. The behavior of deuterons at this energy is very similar to that of protons. This information will now be used to identify the emission.

When a thin absorber is inserted, the energy of the particle is reduced without a significant reduction in intensity until an abrupt reduction is produced at the end of its range. Each kind of particle and absorbing material has a different behavior in this respect. Consequently, this behavior can be used to identify the radiation. For example, insertion of 3.0 μm Mylar (Fig. 10) shifts the peak designated 0.28 MeV off scale and moves the peak at 0.72 MeV to 0.34 MeV, a change of 0.38 MeV. Figure 13 shows a shift of 0.20 MeV when 3.0 μm Mylar is used in another study. The Mylar absorber has a density of 0.42 mg/cm^2 , which would reduce an alpha energy by 0.81 MeV. Apparently, the particle is not an alpha. In contrast, a proton would lose 0.14 MeV. Again, this is not consistent with the measurement, although the discrepancy is in the direction expected to be produced by a deuteron or triton. However, if a triton is produced by fusion, a proton having about 3 MeV should also be emitted, which is not detected. Consequently, while the data cannot be fit exactly by the behavior of a known particle, the most likely particle is a deuteron. The conflict between the expected behavior of deuterons and the measurements can be attributed to errors in the ASTAR data in this energy range, to an error in the expected thickness of the Mylar absorber, and to errors resulting from the detection of a very small number of particles. Nevertheless, alpha emission of any energy is ruled out by these studies. In addition, the measured energy is much greater than would be expected from a chemical reaction or as a result of normal processes occurring in the discharge.

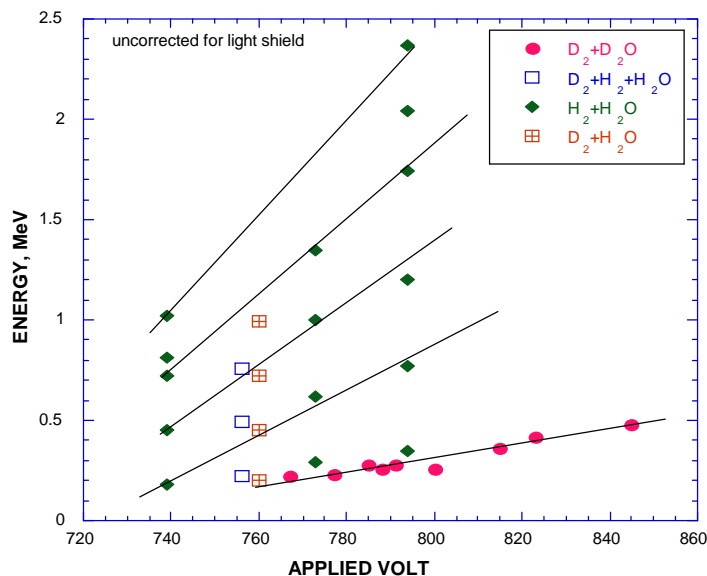


Figure 27. Effect of voltage on particle energy for various gas compositions and energy peaks. Lines are drawn between peaks of similar position in the spectrum.

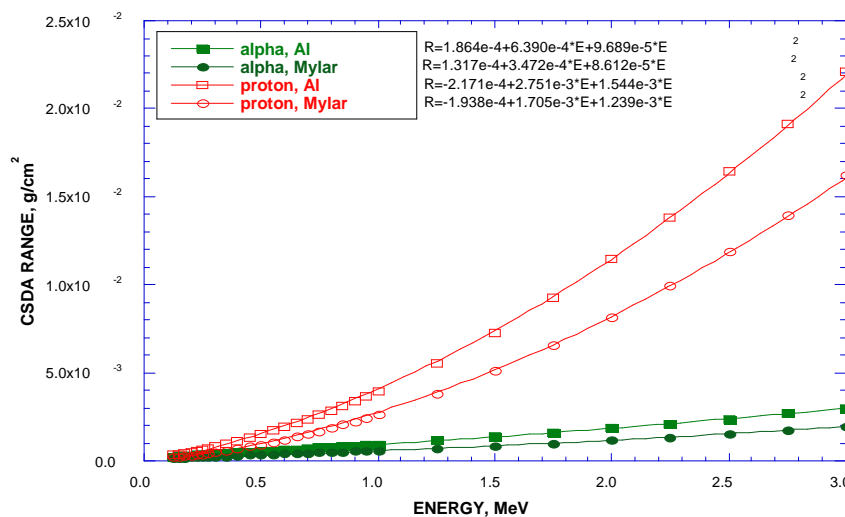


Figure 28. Range for alpha and proton in aluminum and Mylar from ASTAR.

How can these results be explained? The work of Iwamura et al.³² has shown that clusters of deuterons are involved in LENR reactions. Takahashi^{33,34} has explored how they might be made and proposed that members of the cluster carry away part of the energy. This conclusion follows if the cluster configuration is bound together tight enough to enter into a nuclear reaction as a unit. For such a nuclear reaction to occur, the unreacted members would have to be close enough to share in the energy released from the resulting reaction. In other words, the members of the cluster not actually involved in the nuclear reaction would carry away the energy resulting from a reaction between two of its members, as proposed by Takahashi. This work carries the idea further by finding that the energy is much lower than would be the case if the cluster had only a few members as proposed by Takahashi. Instead, the clusters appear to be large. For example, this work indicates that a cluster would have to contain nearly 20 deuterons for each to have an energy resulting from a fusion reaction near that found in this study. Because the clusters can have a variety of sizes, the resulting energy of deuterons emitted from a sample can have a variety of energies, but with a fixed relationship as is observed. In other words, each peak results from a cluster of a different size being the source of the nuclear reaction. Based on the intensity of the various observed energies, larger clusters appear to be more common than smaller ones with a distribution that is sensitive to the voltage applied to the discharge and to the gas composition. Apparently protium enhances this process without sharing the energy. If this mechanism and observations are correct, a search for emitted particles from the LENR process should focus on deuterons as the emitted particle with an energy between 0.5 and 3 MeV.

IV.2. Gas Loading

What appears to be anomalous radiation using a mixed oxide turns out to be radiation produced by potassium contamination. Nevertheless, this experience demonstrates the ability of the detector to find low-energy, low-intensity radiation. Further studies are underway.

Besides being a possible source of LENR, oxides containing finely divided palladium can absorb hydrogen in three ways. Before the hydrogen content can be related to the behavior or to theory, these three forms of hydrogen need to be determined separately. A preliminary study was done by determining the amount of deuterium that a sample takes up as a function of palladium content, as listed in Table 3. Although the data show significant scatter, some important patterns immerge. SiO₂ containing no Pd absorbed 0.09 wt % D₂, presumably as D₂ molecules. When a small amount of Pd (0.23%) was present, the amount of D₂ absorbed was less, but equally small. However, presence of 0.92% and 1.37% Pd caused a significant but similar increase in D₂ absorption. Although the Pd is present as very small particles, the average D/Pd ratio of about 12 is much greater than has been reported for similar particle size in the absence of a supporting oxide³⁵. Even palladium nanoparticles grown in zeolite only reach a composition near D/Pd=2.³⁶ A possible explanation for the unusually large amount of deuterium in the samples is that significant D+ is being retained by the oxide surface in addition to that being held by the Pd particles, as has been proposed previously.³⁷ Although this study is not complete, it shows evidence for the presence of the three kinds of D when Pd is mixed with an oxide. Similar studies need to be made for all such Pd-oxide combinations before any conclusions about the role of D in the fusion reaction can be determined in such materials. The enthalpy of reaction with D₂ will also be modified from that expected for pure Pd by these additional reactions.

IV.3. X-radiation

As can be seen in Fig. 24, the average energy of the X-rays emitted at 600 V is nearly equal to 600 eV. As applied voltage is reduced, the average energy of the X-rays is also reduced and becomes less than applied voltage. This change could result because as applied voltage is lowered, more of the smaller X-ray energy is removed by the window of the GM resulting in a smaller average. Nevertheless, the average energy is nearly equal to applied voltage. Because energy of the X-rays changes with applied voltage, this radiation cannot result directly from k-radiation because this emission has a fixed value. Even when oxygen, with a k-transition at 525 eV, and nitrogen, with a value of 392 eV, are largely absent, the typical X-radiation is still produced. If the X-radiation resulted from interaction between ions and/or electrons with the gas, the intensity would be sensitive to gas pressure, which it is not. If the radiation results from Bremsstrahlung, it appears to be produced by ions bombarding the cathode. The process is enhanced by the presence of oxygen in the gas.

V. CONCLUSION

Anomalous radiation is produced when a glow discharge is produced in deuterium gas. This discharge consists of low-energy X-radiation and occasional energetic particles.

The energy of the X-radiation increases as voltage applied to the discharged is increased, with an energy equal to applied voltage at 600 V. Intensity increases with applied voltage and with increase in O/D ratio. The source does not appear to be k-radiation from oxygen or nitrogen. The intensity of X-radiation is at least 1000 times greater than the particle flux.

Insertion of Mylar absorbers suggests the particles are deuterons with energy peaks having various values between 0.5 and 3 MeV. The energy is sensitive to voltage applied to the cell and to gas composition.

Samples consisting of Pd mixed with various oxides absorb hydrogen in three different ways. Therefore, all hydrogen in such mixtures cannot be assumed to have reacted only with the Pd.

When radiation is measured from such mixtures, the amount of potassium needs to be low to avoid radiation from K^{40} .

References

1. Bush, B. F., Lagowski, J. J., Miles, M. H., and Ostrom, G. S., Helium production during the electrolysis of D_2O in cold fusion experiments, *J. Electroanal. Chem.* 304, 271, 1991.
2. Miles, M., Bush, B. F., Ostrom, G. S., and Lagowski, J. J., Heat and helium production in cold fusion experiments, in *Second Annual Conference on Cold Fusion, "The Science of Cold Fusion"*, Bressani, T., Giudice, E. D., and Preparata, G. Societa Italiana di Fisica, Bologna, Italy, Como, Italy, 1991, pp. 363.
3. Miles, M. and Bush, B. F., Search for anomalous effects involving excess power and helium during D_2O electrolysis using palladium cathodes, in *Third International Conference on Cold Fusion, "Frontiers of Cold Fusion"*, Ikegami, H. Universal Academy Press, Inc., Tokyo, Japan, Nagoya Japan, 1992, pp. 189.
4. Gozzi, D., Caputo, R., Cignini, P. L., Tomellini, M., Gigli, G., Balducci, G., Cisbani, E., Frullani, S., Garibaldi, F., Jodice, M., and Urciuoli, G. M., Helium-4 quantitative measurements in the gas phase of cold fusion electrochemical cells, in *Fourth International Conference on Cold Fusion*, Passell, T. O. Electric Power Research Institute 3412 Hillview Ave., Palo Alto, CA 94304, Lahaina, Maui, 1993, pp. 6.
5. Miles, M. H. and Bush, B. F., Heat and helium measurements in deuterated palladium, in *Fourth International Conference on Cold Fusion*, Passell, T. O. Electric Power Research Institute 3412 Hillview Ave., Palo Alto, CA 94304, Lahaina, Maui, 1993, pp. 6.
6. Miles, M. H. and Bush, B. F., Heat and helium measurements in deuterated palladium, *Trans. Fusion Technol.* 26 (#4T), 156, 1994.
7. Gozzi, D., Caputo, R., Cignini, P. L., Tomellini, M., Gigli, G., Balducci, G., Cisbani, E., Frullani, S., Garibaldi, F., Jodice, M., and Urciuoli, G. M., Quantitative measurements of helium-4 in the gas phase of Pd + D_2O electrolysis, *J. Electroanal. Chem.* 380, 109, 1995.
8. Miles, M., Johnson, K. B., and Imam, M. A., Heat and helium measurements using palladium and palladium alloys in heavy water, in *Sixth International Conference on Cold Fusion, Progress in New Hydrogen Energy*, Okamoto, M. New Energy and Industrial Technology Development Organization, Tokyo Institute of Technology, Tokyo, Japan, Lake Toya, Hokkaido, Japan, 1996, pp. 20.
9. Arata, Y. and Zhang, C., Presence of helium (2He_4 , 2He_3) confirmed in deuterated Pd-black by the "vi-effect" in a "closed QMS" environment, *Proc. Japan. Acad. B* 73, 62, 1997.
10. McKubre, M. C. H., Tanzella, F. L., Tripodi, P., and Hagelstein, P. L., The emergence of a coherent explanation for anomalies observed in D/Pd and H/Pd system: evidence for 4He

- and ^3He production, in *8th International Conference on Cold Fusion*, Scaramuzzi, F. Italian Physical Society, Bologna, Italy, Lerici (La Spezia), Italy, 2000, pp. 3.
11. De Ninno, A., Frattolillo, A., Rizzo, A., Del Giudice, E., and Preparata, G., Report No. RT/2002/41/FUS, 2002.
 12. McKubre, M. C. H., Review of experimental measurements involving dd reactions, PowerPoint slides, in *Tenth International Conference on Cold Fusion*, Hagelstein, P. L. and Chubb, S. R. World Scientific Publishing Co., Cambridge, MA, 2003.
 13. Storms, E. and Talcott, C. L., Electrolytic tritium production, *Fusion Technol.* 17, 680, 1990.
 14. Sánchez, C., Sevilla, J., Escarpizo, B., Fernández, F. J., and Canizares, J., Nuclear products detection during electrolysis of heavy water with titanium and platinum electrodes, *Solid State Commun.* 71, 1039, 1989.
 15. Srinivasan, M., Shyam, A., Sankaranarayanan, T. K., Bajpai, M. B., Ramamurthy, H., Mukherjee, U. K., Krishnan, M. S., Nayar, M. G., and Naik, Y. P., Tritium and excess heat generation during electrolysis of aqueous solutions of alkali salts with nickel cathode, in *Third International Conference on Cold Fusion, "Frontiers of Cold Fusion"*, Ikegami, H. Universal Academy Press, Inc., Tokyo, Japan, Nagoya Japan, 1992, pp. 123.
 16. Sankaranarayanan, T. K., Srinivasan, M., Bajpai, M. B., and Gupta, D. S., Investigation of low-level tritium generation in Ni-H₂O electrolytic cells, *Fusion Technol.* 30, 349, 1996.
 17. Romodanov, V. A., Savin, V., Elksnin, V., and Skuratnik, Y., Reproducibility of tritium generation from nuclear reactions in condensed matter, in *Fourth International Conference on Cold Fusion*, Passell, T. O. Electric Power Research Institute 3412 Hillview Ave., Palo Alto, CA 94304, Lahaina, Maui, 1993, pp. 15.
 18. Claytor, T. N., Jackson, D. D., and Tuggle, D. G., Tritium production from a low voltage deuterium discharge of palladium and other metals, *J. New Energy* 1 (1), 111, 1996.
 19. Celani, F., Spallone, A., Tripodi, P., and Nuvoli, A., Measurement of excess heat and tritium during self-biased pulsed electrolysis of Pd-D₂O, in *Third International Conference on Cold Fusion, "Frontiers of Cold Fusion"*, Ikegami, H. Universal Academy Press, Inc., Tokyo, Japan, Nagoya Japan, 1992, pp. 93.
 20. Clarke, B. W., Oliver, B. M., McKubre, M. C. H., Tanzella, F. L., and Tripodi, P., Search for ^3He and ^4He in Arata-style palladium cathodes II: Evidence for tritium production, *Fusion Sci. & Technol.* 40, 152, 2001.
 21. Chêne, J. and Brass, A. M., Tritium production during the cathodic discharge of deuterium on palladium, *J. Electroanal. Chem.* 280, 199, 1990.
 22. Mosier-Boss, P. A., Szpak, S., Gordon, F. E., and Forsley, L. P. G., Use of CR-39 in Pd/D co-deposition experiments, *Eur. Phys. J. Appl. Phys.* 40, 293-303, 2007.
 23. Roussetski, A. S., Lipson, A. G., Lyakhov, B. F., and Saunin, E. I., Correct identification of energetic alpha and proton tracks in experiments on CR-39 charged particle detection during hydrogen desorption from Pd/Pd:Hx heterostructure, in *Condensed Matter Nuclear Science, ICCF-12*, Takahashi, A., Ken-ichiro, O., and Iwamura, Y. World Scientific, Yokohama, Japan, 2005, pp. 304.
 24. Lipson, A. G., Miley, G., Roussetski, A. S., Lyakhov, B. F., and Saunin, E. I., Reproducible nuclear emissions from Pd/PdO:Dx heterostructure during controlled exothermic deuterium

- desorption, in *Condensed Matter Nuclear Science, ICCF-12*, Takahashi, A., Ken-ichiro, O., and Iwamura, Y. World Scientific, Yokohama, Japan, 2005, pp. 293.
25. Roussetski, A. S., CR-39 track detectors in cold fusion experiments: Review and perspectives, in *11th International Conference on Cold Fusion*, Biberian, J.-P. World Scientific Co, Marseilles, France, 2004, pp. 274.
 26. Oriani, R. A. and Fisher, J. C., Nuclear reactions produced in an operating electrolytic cell, in *11th International Conference on Cold Fusion*, Biberian, J.-P. World Scientific Co., Marseilles, France, 2004, pp. 295.
 27. Storms, E. K. and Scanlan, B., Radiation produced by glow discharge in deuterium, in *8th International Workshop on Anomalies in Hydrogen / Deuterium Loaded Metals*. 2007. <http://www.iscmns.org/catania07/index.htm>, Catania, Sicily, 2007.
 28. Storms, E. K. and Scanlan, B., Radiation produced by glow discharge in a deuterium containing gas (Part 2), in *American Physical Society*, New Orleans, 2008.
 29. Arata, Y. and Zhang, Y.-C., The Establishment of Solid Nuclear Fusion Reactor, *J. High Temp. Soc.* 34 (2), 85, 2008.
 30. Case, L. C., Catalytic fusion of deuterium into helium-4, in *The Seventh International Conference on Cold Fusion*, Jaeger, F. ENECO, Inc., Salt Lake City, UT, Vancouver, Canada, 1998, pp. 48.
 31. Cantwell, R. and McConnell, M., Partial Replication of Storms/Scanlan Glow Discharge Radiation, in *American Physical Society*, New Orleans, 2008.
 32. Iwamura, Y., Sakano, M., and Itoh, T., Elemental analysis of Pd complexes: effects of D₂ gas permeation, *Jpn. J. Appl. Phys.* A 41 (7), 4642, 2002.
 33. Takahashi, A., Deuteron cluster fusion and ash, in *ASTI-5* www.iscmns.org/, Asti, Italy, 2004.
 34. Takahashi, A., Mechanism of deuteron cluster fusion by EQPET model, in *Tenth International Conference on Cold Fusion*, Hagelstein, P. L. and Chubb, S. R. World Scientific Publishing Co.g, Cambridge, MA, 2003, pp. 809.
 35. Everett, D. H. and Sermon, P. A., Crystallite size effects in the palladium/hydrogen system: A simultaneous sorption and X-ray study, *Zeit. Phys. Chem. Neue Folge Bd.* 114 (S), 109, 1979.
 36. Nishimiya, N., Kishi, T., Mizushima, T., Matsumoto, A., and Tsutsumi, K., Hyperstoichiometric hydrogen occlusion by palladium nanoparticles included in NaY zeolite, *J. Alloys and Compounds* 319, 312, 2001.
 37. Sermon, P. A. and Bond, G. C., *J. Catal.* 24, 467, 1974.

Partial Replication of Storms/Scanlan Glow Discharge Radiation

Rick Cantwell and Matt McConnell
Coolescence, LLC

Introduction

The Storms/Scanlan paper¹ presented at the 8th international workshop in Catania described two types of radiation produced in a deuterium glow discharge. One type was thought to be mono energetic electrons in the 0.8 MeV range. A second type of emission, obtained when oxygen was added to the D₂, was also described by Storms/Scanlan.

We have produced radiation with similar characteristics to this second type of emission. This radiation has been characterized with GM tubes, absorbers, silicon diode detector, and magnetic deflection. We propose that conventional low energy x-rays would produce behavior consistent with our observations.

Experimental Apparatus

A 1.8 liter chamber is evacuated with a turbomolecular pump as shown in Fig. 1. Gas pressure is measured with Baratron gauges. A 1 mm Pt rod, with all but the last 2-3 mm encased in glass, is used for the anode. The high voltage is supplied on the left hand side of the chamber. The cathode is driven with a negative voltage from a DC power supply capable of 2000 V at 100 mA. The chamber and anode are grounded. There is no provision for cooling the cathode or chamber. Radiation detectors and absorbers are mounted in the chamber through ports located on the right hand side of the chamber.

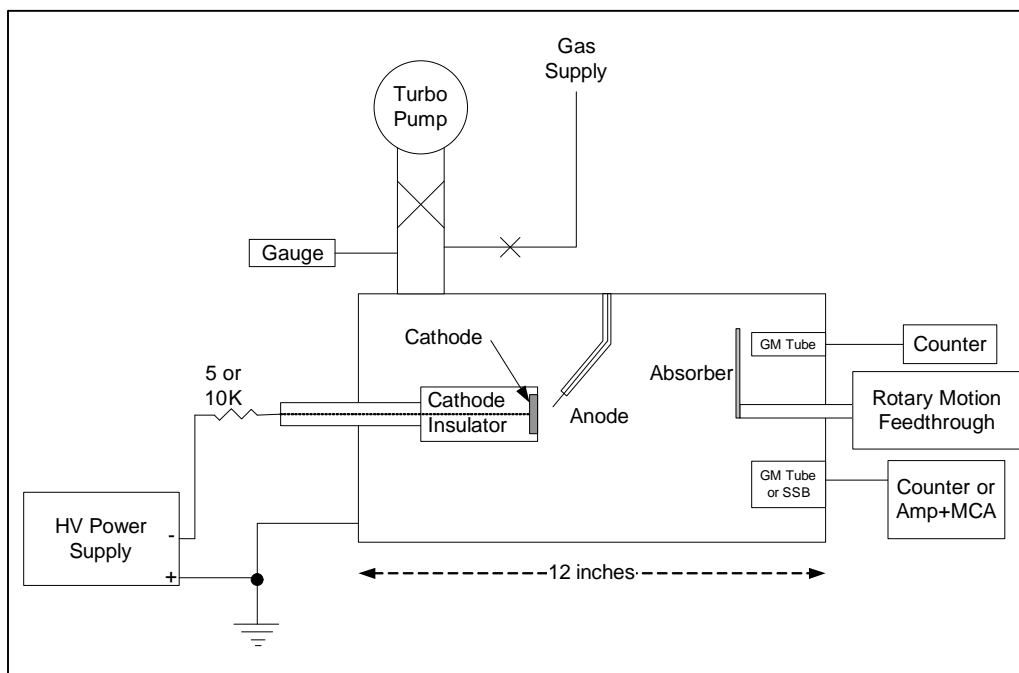


Figure 1. Diagram of experimental apparatus

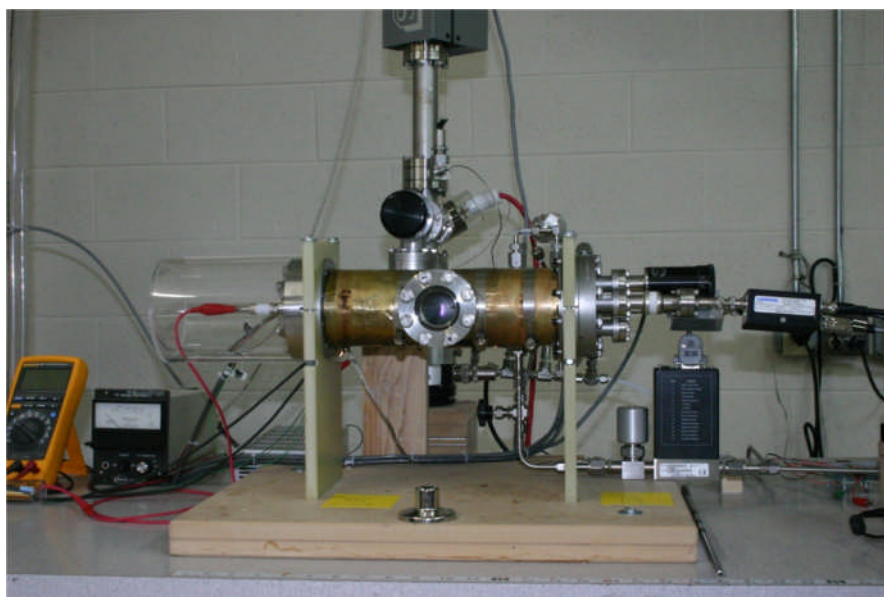


Figure 2. Vacuum chamber with high voltage supplied to cathode on the left, and ports for various detectors on the right

The cathode assembly is electrically insulated with glass and ceramic as pictured in Figure 3. Both copper and Pd cathodes have been used. The Pd cathodes are constructed by diffusion welding a 100 micron Pd foil to a copper substrate.

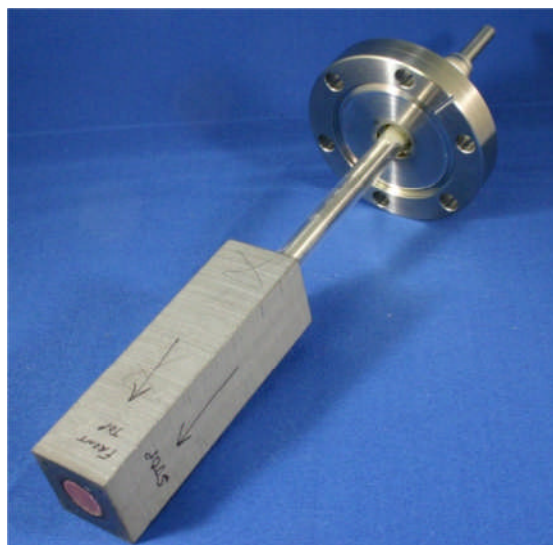


Figure 3. Cathode insulator assembly

GM detectors with 2mg/cm^2 windows (LND 712) and 10mg/cm^2 windows (LND 71221) have been used. A rotary feed through is used to move an absorber in front of the GM tubes. Figure 4 shows the detector end plate configured with 2 GM tubes and a plastic absorber.

In a different configuration one of the GM tubes is replaced with a silicon diode detector (25mm^2 , 1.5 mm thick) (Ortec BA-016-025-1500). Figure 5 shows the Si detector shielded from visible light with a 1.2 micron Al foil. In this configuration, a 1.8 micron Al foil absorber and a CR-39 nuclear track detector are mounted on the rotary feed through. The background noise of the Si detector limited the minimum detectable energy to about 50 keV.

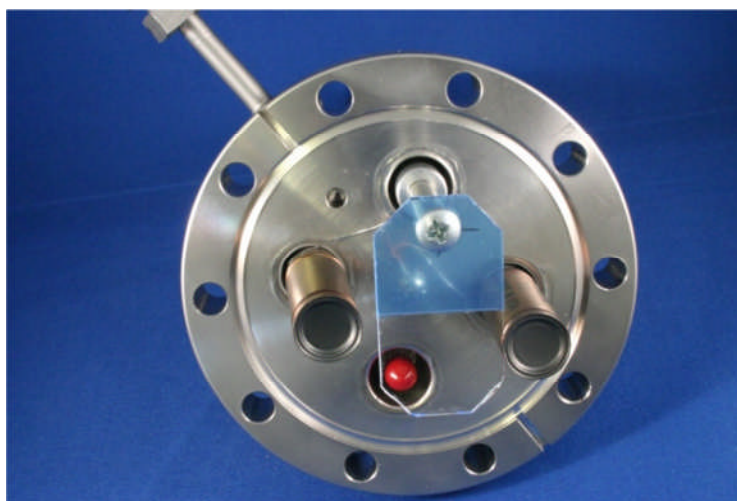


Figure 4. Detector end-plate configured with dual GM tubes and plastic absorber. (CR-39 is used here as a 100mg/cm^2 absorber.)

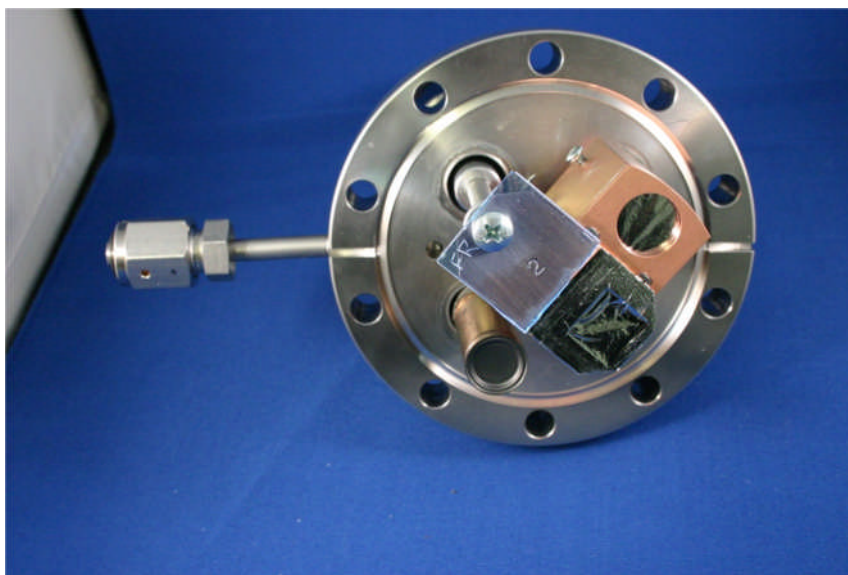


Figure 5. Detector end-plate configured with 2mg/cm² GM tube, Si detector, 1.8 micron aluminum absorber and CR-39 detector.

In another test configuration the absorber was replaced with an electromagnet assembly designed to deflect charged particles away from a slit placed in front of the GM tube. A toroidal transformer core, about 1 inch outside diameter, was cut to form a 0.4" gap. The core was wrapped with 100 turns of magnet wire. Currents up to 3A are possible without overheating the magnet assembly. The magnetic field was measured at 100 gauss per Amp. A diagram of the deflector assembly is shown in Figure 6.

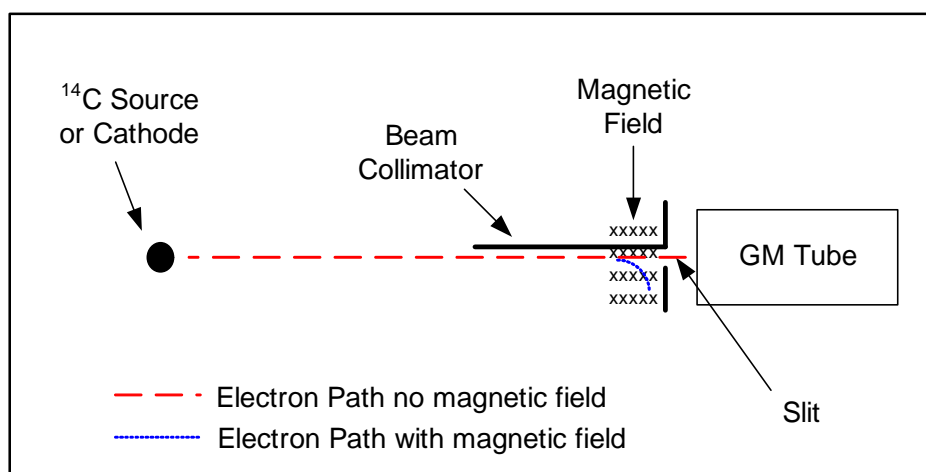


Figure 6. Magnetic deflection experiment schematic. (A simple half collimator is used to prevent off-axis particles from being deflected into the GM detector when the magnet is turned on.)

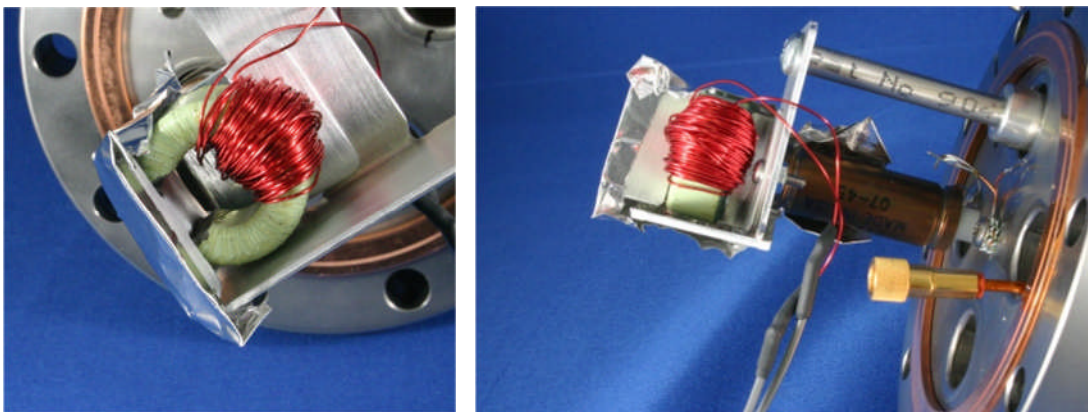


Figure 7. Photographs of deflection assembly using electromagnet with slit in front GM tube

Experimental Procedures

- **D₂+O₂ glow** - Equal parts of deuterium and oxygen are added to the chamber. These are then reacted with a glow lasting a few minutes. At this point the chamber pressure is typically between 1.5 and 3 Torr. A 25% duty cycle glow discharge is used, typically 4 seconds on and 12 seconds off, to keep the temperature of the cathode below 60 deg C. Average glow power is between 2 and 10 watts. Glow voltages are varied between 500 and 1200 volts.
- **H₂+O₂ and He+D₂ glow** – Same as above only with H₂ or He added to an equal amount of deuterium.
- **Single gas glow** – 2 Torr of O₂, D₂, H₂, He, or N₂ are added to the chamber. Glow as above.
- **Cathode** – Experiments were carried out with Pd cathodes as well as with copper cathodes.
- **Absorber** – GM tube counts are logged for 1 minute then the absorber is rotated in front of the GM tube. Counts are logged for another minute. The absorber is then rotated back to the starting position and counts are logged for an additional minute.
- **CR-39** – The CR-39 nuclear track detector is placed in the chamber. Numerous glow runs are done with D₂+O₂, the CR-39 is removed from the chamber and etched and inspected with a microscope for tracks.
- **Silicon detector** – 5-minute glows are done in D₂+O₂ while collecting the output of the Si detector with a multi-channel analyzer (MCA).
- **Magnetic deflector** – The deflector assembly was calibrated with a ¹⁴C beta (156 keV) source in vacuum as well as in 2 Torr of O₂ with electromagnet current being varied from .1A to 3A. The deflection test was done with a 5-minute glow in D₂+O₂ as well in O₂ with magnet currents varied from .1A to 3A.
- **Count timing test** – A digital storage oscilloscope is used to record the position of the GM counts vs. the glow waveform. The glow discharge is turned on for 500ms. Count positions from numerous 500ms glow pulses are collected.

Results

- In oxygen containing plasmas, counts from the 2 mg/cm² GM tube are seen whenever the glow voltage is greater than about 600V. In D₂, H₂, He, and N₂ plasmas counts start when the glow voltage is greater than 900-1000V. Count rates increase non-linearly with increasing voltage. See Figure 9.
- GM Counts are stopped by a 100mg/cm² plastic absorber; Counts are not seen with a 10 mg/cm² GM tube.
- Count rates for D₂+O₂ plasmas (V<900) are reduced by 66% with a 1 micron Mylar absorber (0.14 mg/cm²), by 75% with a 1.2 micron Al absorber (0.3 mg/cm²) and by 95% with a 1.8 micron Al absorber (0.5 mg/cm²). Counts are stopped by total areal density of 2.5 to 3.0 mg/cm².
- Similar count rate and absorber attenuation results are seen with D₂+O₂ using either Cu or Pd cathodes. Also, similar count rate and absorber attenuation results are seen with H₂+O₂ and D₂+O₂ discharges using a Cu cathode.
- The CR-39 detected no radiation above background.
- No counts above background have been observed with the Si detector.
- Transmission through a 1.8 micron Al or 1 micron Mylar absorber increases with increasing glow voltage for voltages greater than 900V. In an oxygen containing plasma, transmission through a 1.8 micron Al absorber or a 1 micron Mylar absorber is constant for voltages less than 900V. See Figures 10 and 11.
- Counts are observed during the on periods of the glow pulse, but do not occur (above background) during the off periods.
- An electromagnet deflector had no effect on GM count rates produced with a D₂+O₂ glow discharge on a Pd cathode or with an O₂ glow on a Pd cathode. The electromagnet did affect count rates of beta particles from a ¹⁴C source in vacuum as well as in 2 Torr of O₂. Count rates for ¹⁴C were reduced by 50% with 1A magnet current and by 80% with 2A magnet current.

Discussion

The absorber attenuation data showing particles are stopped by 2.5 – 3 mg/cm² could be explained by particles in the range (say +/-20%) of:

- 3 MeV alphas
- 0.7 MeV protons
- 30keV electrons
- 600 eV photons

based on stopping power data from NIST as shown below in Figure 8.

Since x-ray photons are never actually stopped by an absorber, we have used an attenuation figure of 10⁻⁵ to calculate an equivalent stopping distance for x-rays.

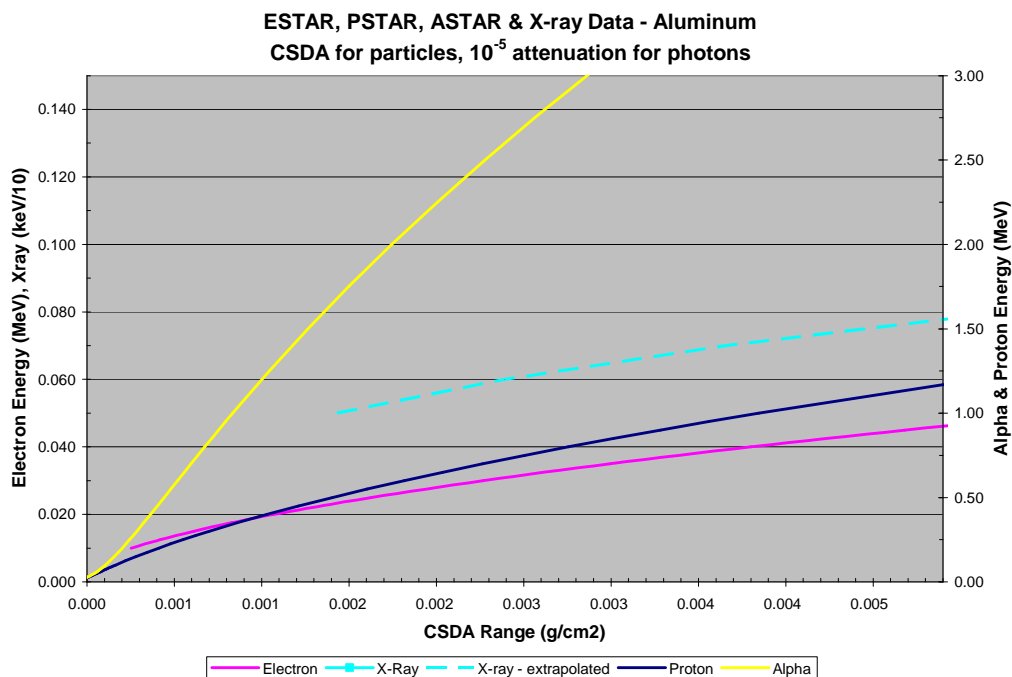


Figure 8. Energy vs. CSDA Range – taken from NIST databases. Photon “equivalent stopping power” calculated with 10^{-5} attenuation from extrapolated NIST photon mass attenuation data.

The lack of pits on CR-39 and the lack of counts with the Si detector rule out alphas and protons as the cause of the GM counts.

The lack of any effect on the radiation by a magnetic field rules out electrons as the cause of the GM counts.

The data observed appears consistent with conventionally produced low energy x-rays.

X-ray hypothesis

In an abnormal glow discharge most of the electrons leaving the cathode fall region have an energy corresponding to the glow voltage.² X-rays with energies as high as the plasma voltage will be produced in the glow discharge as a result of collisions between energetic electrons in the cathode fall region and atoms in the gas. Two types of x-ray emissions should be observed from gas mixtures containing oxygen: K-alpha x-rays at 525 eV and Bremsstrahlung emissions that increase in energy with increasing glow voltage.

Only the Bremsstrahlung radiation should be detected for the non-oxygen gases used. (The K-alpha photon for nitrogen is 392 eV and will be attenuated below the detector noise floor by the 2 mg/cm^2 GM tube window.) The energy of the Bremsstrahlung radiation should increase with increasing glow voltage.

Is it reasonable to generate enough k-shell x-rays to account for the observed counts? If we assume an x-ray generation efficiency of 0.1%, and an electron energy distribution where 0.1% of the electrons have sufficient energy, and factor in the attenuation of the 2 mg/cm^2 mica GM

tube window, and the collection efficiency of our apparatus we expect around 100 counts per minute per mA of glow. This is in line with the 50 or so counts per minute per mA we observe with a 700 V glow.

Figure 9 shows Count Rate vs. Voltage data collected for different gases. For oxygen containing gas mixtures, the count rate increases slowly from 600 volts to 900V as shown in the inset graph. Above 900V the count rate increases rapidly for all gases. We propose the counts in the sub 900V region are caused by the oxygen k-alpha x-ray (525 eV) and the counts above 900V are produced by Bremsstrahlung. (N₂ also produces a K-alpha (392 eV) but it is not energetic enough to pass through the 2mg/cm² GM window.)

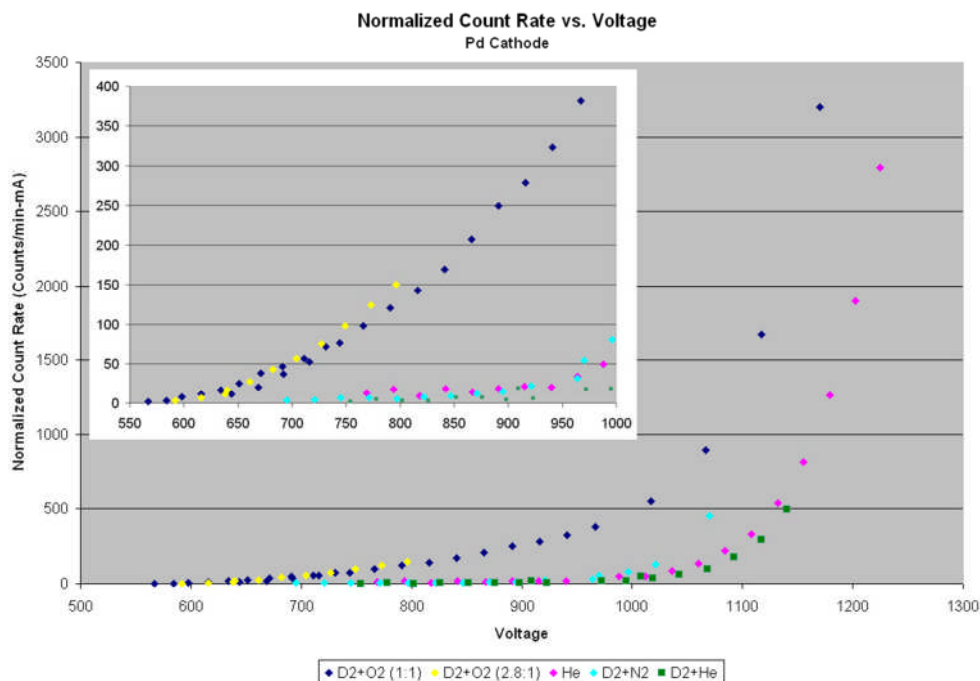


Figure 9. Normalized Count rate vs. Voltage of various gases. The insert shows the lower voltage and lower count region in more detail.

K-alpha radiation produced in gas mixtures containing oxygen will give constant absorber transmission (I/I_0) similar to observed transmission for lower voltages also seen in Figures 10 and 11.

An increase in Bremsstrahlung x-ray energy with increasing glow voltage will give rise to increased transmission through an absorber similar to observed aluminum and Mylar absorber transmission at higher voltages seen in Figures 10 and 11.

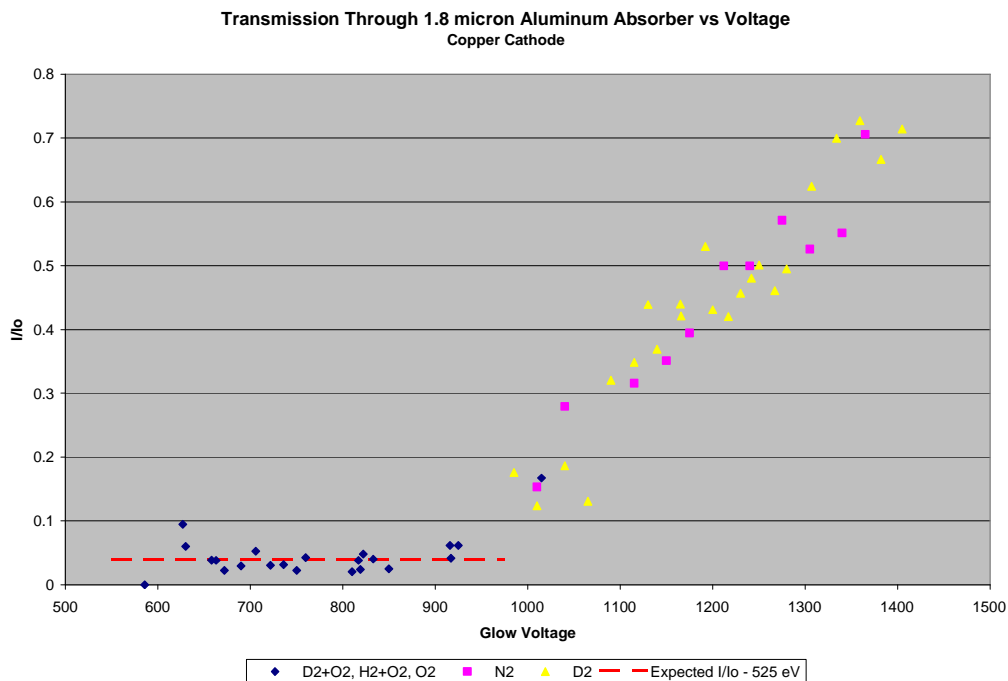


Figure 10. Transmission through a 1.8 micron Aluminum absorber vs. glow discharge voltage. Dashed line shows calculated attenuation of 525 k-alpha x-rays passing through the a 1.8 micron Al absorber.

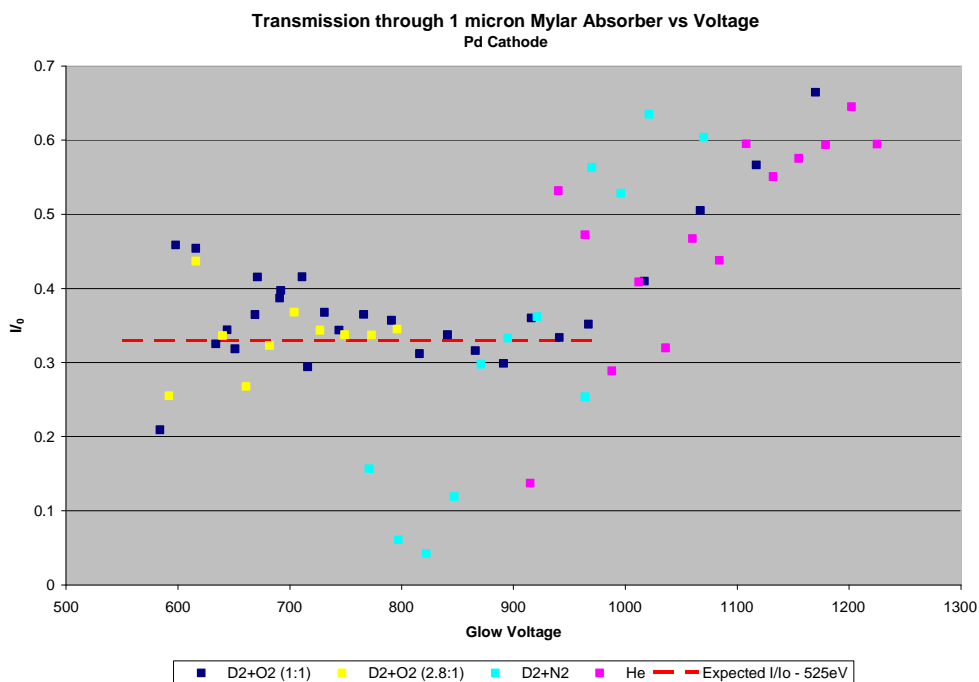


Figure 11. Transmission through a 1 micron Mylar absorber vs. glow discharge voltage. Dashed line shows calculated attenuation of 525 k-alpha x-rays passing through the a 1 micron Mylar absorber.

Finally, X-ray attenuation with different thickness Al absorber is similar to the observed attenuation curves as shown in Figure 12.

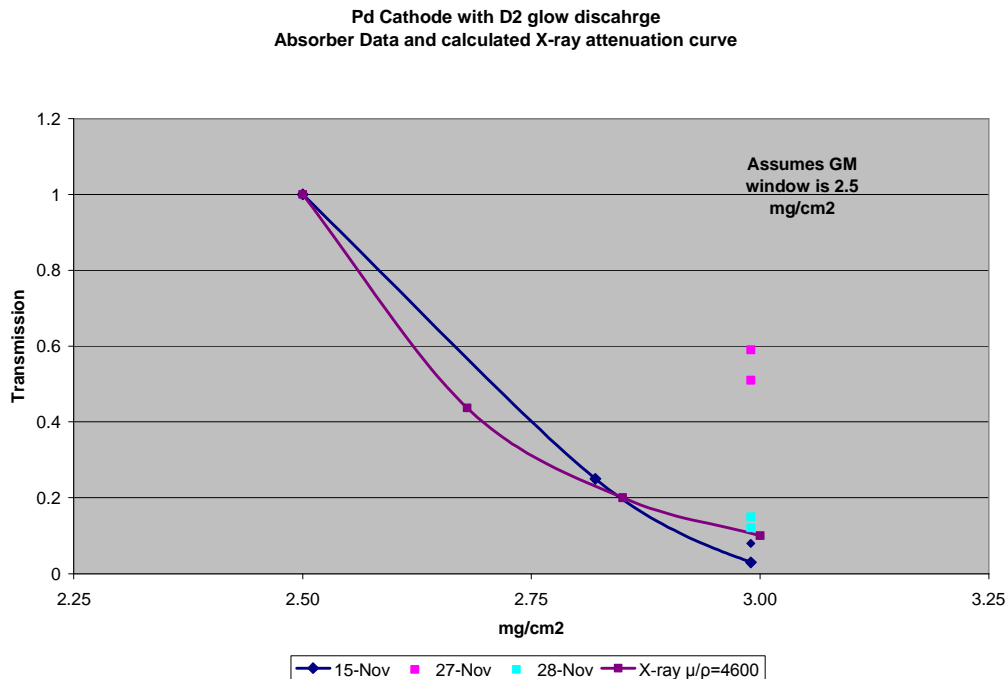


Figure 12. Attenuation vs. total absorber thickness. X-ray attenuation assumes an attenuation coefficient (μ/ρ) of 4600 cm²/gm which is obtained by extrapolating the NIST aluminum curve to 600 eV.

Conclusions

The repeatable results, consistent absorber behavior and count timing test have convinced us that our results are not caused by electrical noise. Radiation is being produced and detected in these experiments. The combination of properly grounded GM tubes and insertion of CR-39 inside the chamber provide an inexpensive and reliable way to detect a broad spectrum of radiation. If radiation is detected, a variety of other means must be used to identify it.

We believe the data observed in our series of experiments is consistent with the generally accepted mechanisms for production of Bremsstrahlung and Oxygen K-line x-rays. In particular, we are satisfied that the magnetic deflector tests rule out significant production of anomalous energetic electrons in our experiments, and that both our CR-39 results and Si barrier detector results rule out any significant production of heavier energetic particles. If any anomalous radiation was produced, it was below the sensitivity threshold of our detection systems.

A challenge for further investigations is to separate out the numerous low energy photons produced in the glow from any anomalous radiation that may be produced in a glow discharge initiated LENR.

Acknowledgements

Edmund Storms provided numerous suggestions as well as engaged in many helpful discussions with us. Scott Little read an early draft of this report and suggested changes that made this much more readable.

References

1. E.K. Storms and B. Scanlan, in *Radiation produced by glow discharge in deuterium*, Catania, Sicily, 2007 (<http://www.lenr-canr.org/acrobat/StormsEradiationp.pdf>)
2. B. Chapman, Glow Discharge Processes, (New York, John Wiley & Sons, 1980), 105

New Results of Charged Particles Released From Deuterium-Loaded Metal at Low Temperature

Songsheng Jiang⁺, Jinghuai Li, Ming He, Shaoyong Wu, Jianqing Wang, Hongtao Zhang,

Shunhe Yao, Yonggang Zhao and Chen Wang

China Institute of Atomic Energy, P.O. Box 275(49), Beijing, 102413

⁺ *Corresponding author, E-mail: ssjiang@ciae.ac.cn*

Abstract

We have suggested that the mantle ^3He and ^3H might have originated from natural nuclear fusion (d-d and d-p reaction, or other reactions) in deep Earth. Encouraged by this new idea, we tried to recreate nuclear fusion at low temperature in the laboratory. This paper describes charged particles emitted from the deuterium-loaded titanium foil and powder at low temperature. Although the counts are very low (about 0.13 counts/h), fortunately, broad and narrow peaks are observed for the deuterium-loaded titanium foil and TiD-Mo sample respectively. The charged particle is identified as proton having energy of about 2.8 MeV after exiting the sample. We suggest that the proton might originate from d-d reaction in the samples. Then the d-d reaction rate is calculated to be 1.4×10^{-24} fusion/d-d \cdot sec for the deuterium-loaded titanium foil sample. On the other hand, no charged particles were observed above the background level for deuterium-loaded titanium powder sample. Therefore, this work provides a positive result of nuclear fusion for the metal foil samples, but a negative result for the powder samples. The negative result of the deuterium-loaded titanium powder sample suggests that the reaction yield might be correlated with deuterium density, or it may be correlated with microscopic variations in the deuterium-loaded titanium materials. The negative result also indicates that d-d reaction catalyzed by μ -meson from cosmic ray can be excluded in this experiment. The present work may be helpful to the further study on the physical mechanism of nuclear fusion in deuterium (hydrogen)-loaded metals and also helpful to the study of origin of ^3He in the deep Earth.

1. Introduction

In the recent work ^{1,2}, we demonstrated that the excess ^3H in the volcanic Lakes Nemrut (Turkey) and Laacher (Germany) might be released from the mantle, based on the correlation of excess tritium (^3H) with mantle ^3He and other mantle gases. We have suggested that the mantle ^3He and ^3H might originate from natural nuclear fusion (d-d and d-p reactions, or other reactions) in the deep Earth, after ^3H originating from atmospheric and conventional nuclear reactions are excluded, and the correlation between constant $^3\text{He}/^4\text{He}$ ratio and $^3\text{He}/\text{heat}$ ratio in the hydrothermal vent fluids at Mid-Ocean-ridges is considered. ² Encouraged by this new idea, we tried to recreate natural nuclear fusion at laboratory. Since 1989, there have been a number of serious attempts to observe nuclear effect in metal deuterides. ^{3,4} Particularly relevant to the

present work are Jones *et al.*, Cecil *et al.* and Chambers *et al.*,⁵⁻⁷. However, particle identification was problematic and irreproducibility remained a significant issue.⁵ The results were not published in a mainstream journal. Our goal was to check these previous claims. We obtained a positive result for the deuterium-loaded titanium foil samples.

In the conventional view, the d-d fusion rate of deuterium molecule is exceedingly low at low temperatures, roughly on the order of 10^{-63} per D_2 molecule per second.⁸ However, recent theories, such as references [9] and [10], and experiment [5] and [7] show that nuclear fusion of the deuterium system is possible in metal lattices under strong restriction of the metal electrons. The measured fusion rates for the deuterium-loaded titanium foils were reported to be (10^{-21} - 10^{-25}) per D_2 per second at room temperature.⁵

In this experiment, charged particles emitted from the samples were measured using a low-level charged particle spectrometer, and the ΔE -E method was used for particle identification. The data acquisition was repeated several times and different samples were measured. Because of the very low counting rates, the measurements lasted for several months.

2. Experimental details

2.1. Sample preparation

Figure 1 shows a diagram of the system used to prepare the deuterium-loaded samples. Chemical-grade deuterium gas is stored in a depleted-uranium bed, inside the deuterium-storage chamber (50 mm diameter, 500 mm length). To load deuterium, the titanium sample is placed inside a reaction chamber (30 mm diameter, 300 mm length). The reaction chamber is evacuated to about 10 Pa and heated at 200-300°C to degas the sample. The temperature is increased to about 400°C, and the chamber is pressurized with deuterium gas, which was released from the uranium bed by heating it to about 400-500°C. When the pressure reaches about 5×10^4 Pa, the inlet valve of reaction chamber is closed. A drop in pressure clearly demonstrated that the titanium sample inside the reaction chamber become deuterided. Based on the change in gas pressure and the weight of titanium sample, the atomic ratio of D/Ti can be calculated. The average ratio depends on the thickness of Ti foil. For a thickness less than 5 μm , the atomic ratio of D/Ti is around 1.2-1.4, and the ratio reaches 1.6 for the powder sample. However, D/Ti ratio decreases to about 0.1 for the Ti foil with 0.5 mm thickness. The result suggests that most of deuterium can only be loaded near the Ti surface.

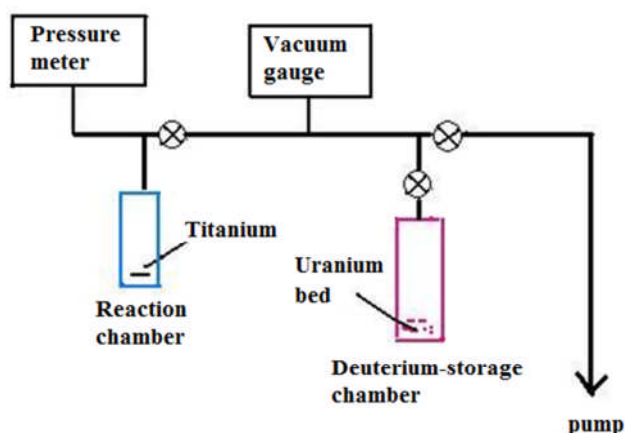


Figure 1. Systematic diagram for preparation of deuterium-loaded titanium samples.

2.2. Charged particle detection

Detection of charged particle was carried out using OCTETE low-level charged particle spectrometer. The silicon dioxide-passivated ion-implanted detectors with active-area of 600 mm² were used. The depleted layer of the detectors is 100 μ m. The detector and sample were located in a vacuum chamber (Fig. 2). The detector efficiency was calibrated using point sources to be about 30% at the detector when the source was less than 10 mm from the detector. The 1024-channel analyzer was calibrated with a ²⁴¹Am source (5.45 MeV α -particle) to be 8.52 keV per channel. During measurement, the chamber was evacuated to about 5 Pa. The spacing between detector and sample was about 5 mm.

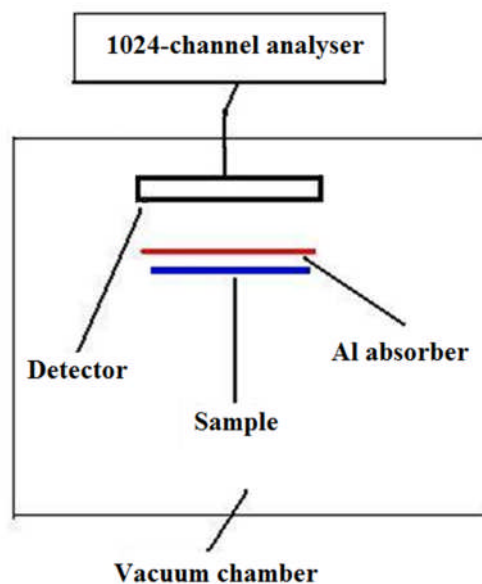
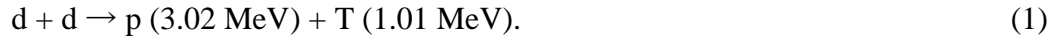


Figure 2. Outline of detection system for measurement of charged particle. The silicon dioxide-passivated ion-implanted detectors with active-area of 600 mm² are used. The depleted layer of the detectors is 100 μ m.

The aim of this experiment is search for proton from d-d reaction, as follows:



The range of 3.02 MeV proton in Si is calculated to be 91 μm using SRIM code ¹¹. While a 3-MeV proton penetrates the depleted layer of the Si detector, it should be stopped in the layer.

2.3. Charged particle identification

The ΔE -E method, based on Bethe-Bloch equation, is used for charged particle identification. The Bethe-Bloch equation can expressed simply as:

$$\Delta E \cdot E/M \propto Z^2 \quad (2)$$

Here ΔE and E is energy loss in the matter and overall energy of charged particle respectively. M and Z is the mass and atomic number of particle respectively.

In this experiment, we consider only how to identify protons, ^3He , tritons and α -particles. A 15 μm Al foil was used as energy absorber for ΔE measurement. The ΔE values for proton, ^3He , triton and α -particle are calculated using SIRM code. ¹¹ The energy loss for 3-MeV proton, triton, ^3He and α -particle in the Al foil is calculated to be about 0.35, 2.5, 2.9 and 3 MeV, respectively. Thus the type of particles can be identified from the measured ΔE (or residual energy) value. It can be seen that the residual energy of the proton, triton, ^3He and α -particle is 2.65, 0.5, 0.1 and 0 MeV respectively. The pronounced difference of the residual energies makes identification of those charged particles easy in the measurement.

3. Measurement

3.1. Deuterium-loaded titanium foil sample

Four runs were performed measuring deuterium-loaded titanium foil sample (0.1 mm thick). Two measurements were made in each of the first 3 runs, to test stability and repeatability. In the first run, the deuterium-loaded titanium foil sample was measured, and then in the third run it was measured again to check reproducibility. To identify particles, in the second run an Al foil of 15 μm thickness was inserted between the deuterium-loaded titanium foil sample and the detector. A fourth run was carried out with a blank sample; i.e., a titanium sample with no deuterium. The spectrum of the sample for run 1, 2 and 3 are shown in Figs. 3, 4 and 5 respectively.

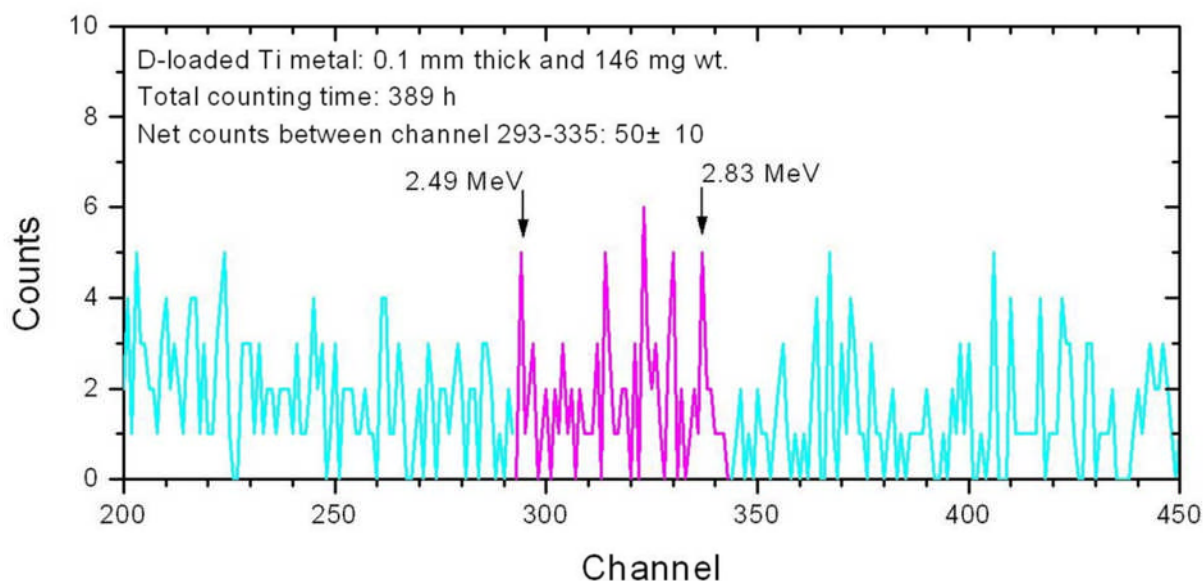


Figure 3. Spectrum of the deuterium-loaded titanium foil sample in run 1.

Although the counting rate is low, a broad peak above the background is observed, ranging from 2.49 to 2.83 MeV, with average energy of 2.66 MeV (Fig. 3). In this run another peak is observed around channel 370 (3.15 MeV) (Fig. 3). This peak might originate from contamination by other radioactive samples previously used in the detection chamber, because the peak did not appear again in the later runs. The background counts in the low energy region (less than ~ 2.0 MeV, or channel 250) are mainly induced by the tail effect of the electronic noise.

The background counts in the peak area are deduced from the average counts of the neighbouring channels close to the both sides of the broad peak. The total counts in the peak area after subtracting the deduced background counts is defined as net counts. The net counting rate in the broad peak is deduced to be 0.129 ± 0.032 counts/h in run 1. The same procedure is used to subtract the background counts in the following runs.

To identify the type of the particles in the peak, an Al foil was inserted between the sample and the detector in run 2 (Fig. 4). The energy loss of a 3-MeV proton in the Al foil is calculated to be 0.35 MeV. Therefore, the residual energy is about 2.65 MeV. A broad peak is also observed in run 2, but the peak is shifted and broadened (Fig. 4). Due to energy loss and dispersion of the charged particle in the Al absorber, the peak is shifted between 2.17 and 2.63 MeV and the peak width is broadened, ~ 0.12 MeV greater than in run 1. The average energy of the peak is 2.40 MeV, about 0.18 MeV smaller than the value in run 1. The net counting rate in the broad peak is 0.157 ± 0.046 counts/h.

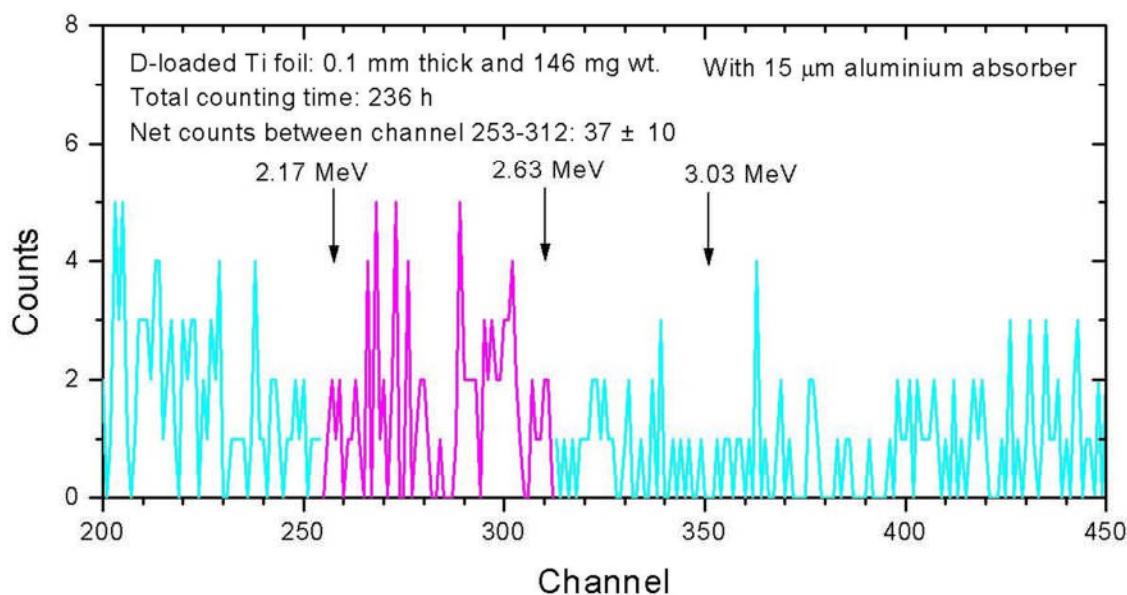


Figure 4. Spectrum of the deuterium-loaded titanium foil sample in run 2, with a 15 μm Al foil inserted between detector and the sample.

To test repeatability, the Al absorber was removed in run 3. It can be seen that the broad peak returns (Fig. 5a), close to the area it was observed in run 1. The peak ranges from 2.39 to 2.77 MeV, and average energy of the broad peak is 2.58 MeV. The net counting rate in the broad peak is 0.127 ± 0.036 counts/h (Fig. 5a). The spectrum of measurement in the first 94 hours in run 3 is also given in Fig. 5b. From Fig. 5a and 5b, it can be seen that the counting rates in the peak area is almost stable in the overall time of 189 hours, in run 3. The results indicate that after removing the Al absorber, the broad peak in run 1 was closely reproduced in run 3.

The shift of the peak in run 2 is well correlated with the insertion of the Al absorber. The residual energy of the charged particles in run 2 is measured at 2.40 MeV, and the mean value of the energy in run 1 and 3 is deduced to be 2.62 MeV. From the difference of the mean value of energy for the broad peak in run 1 and 3 (with no Al foil) and run 2 (with Al foil), the energy-loss of charged particle passing through the Al absorber is estimated to be 0.22 ± 0.15 MeV, a value that is consistent with the calculated value (0.35 ± 0.10 MeV) for 3 MeV proton. Therefore, the observed charged-particle should be 3 MeV proton released from the sample.

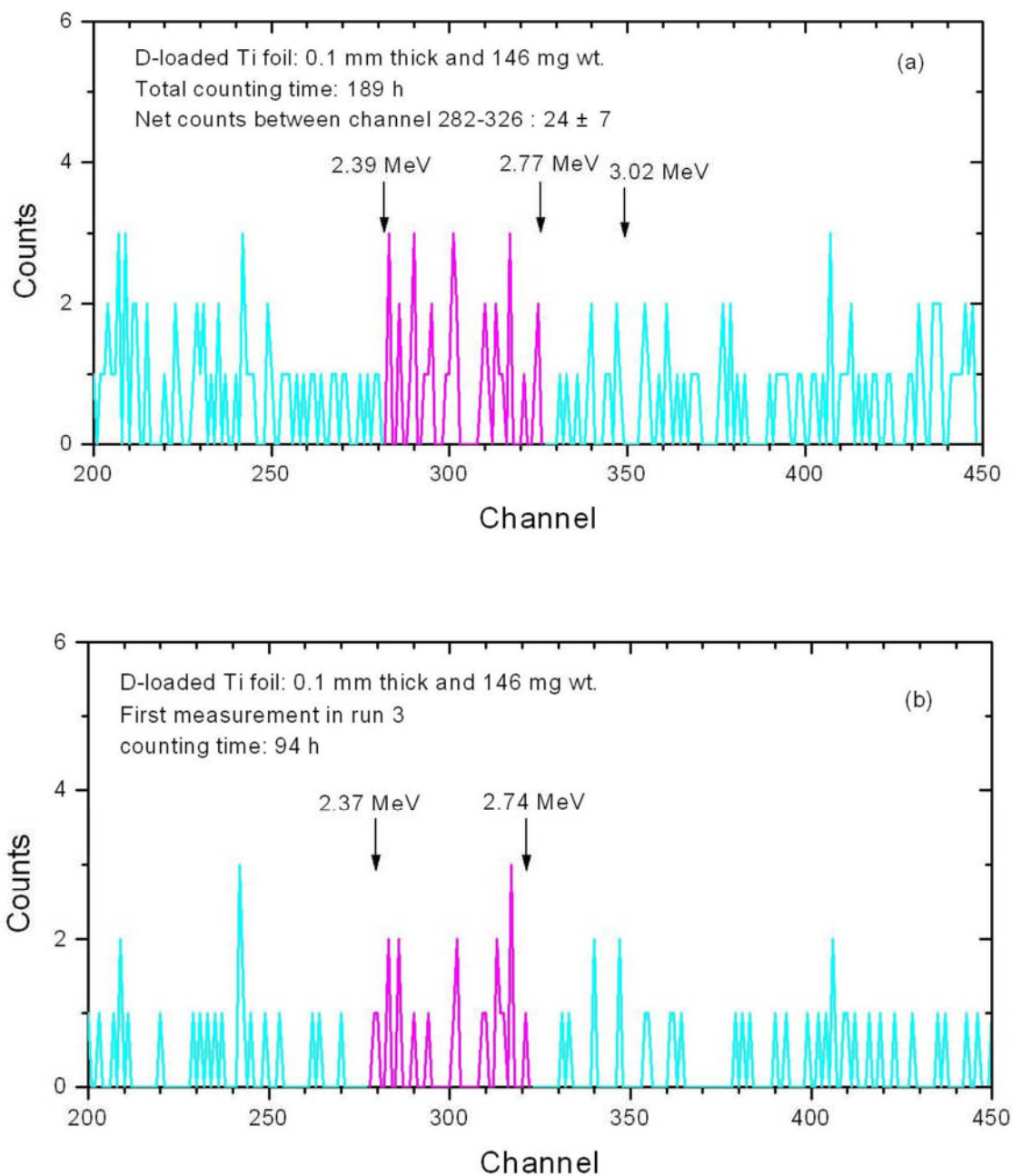


Figure 5. Spectrum of the deuterium-loaded titanium foil sample in run 3, for overall measurement time of 189 hours (Fig. 5a) and for the first 94 hours of run 3 (Fig. 5b).

The fourth run is made with blank sample: a titanium foil with no deuterium, 0.1 thick, 200 mg. No counts are observed above the background level in the energy range of interest (2.39-2.80 MeV, or channel 280-340) (Fig. 6). Therefore, the deuterium in the titanium foil is apparently the source of the charged particles emitted from the sample in the previous runs.

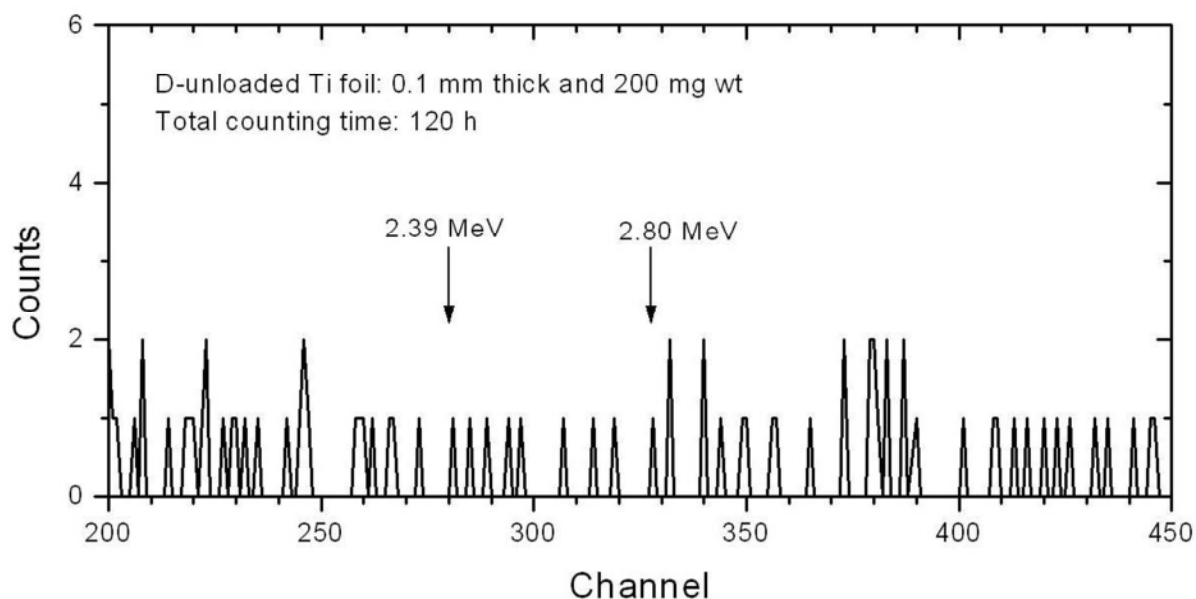


Figure 6. Spectrum of the blank sample, a titanium foil sample ($20 \times 20 \times 0.1$ mm) with no deuterium, in run 4.

We believe that the net counts in all three broad peaks in run 1-3 are induced by energetic protons released from the sample. The total net counts in the broad peaks for run 1, 2 and 3 are 102 ± 18 , at standard deviation ($1 \square \sigma$), and the value is greater than 3σ . The average counting rate is 0.138 ± 0.030 counts/h. Using the detection efficiency of 30%, the average proton yield for the 3 runs is deduced to be 0.46 ± 0.11 protons/h, or $1.28 \pm 0.31 \times 10^{-4}$ protons/sec.

The energy width in run 1 and 3 is about 0.34 and 0.38 MeV respectively, which indicates that the proton may come from a layer of about $10 \mu\text{m}$ thickness near the titanium surface, less than the range of 3-MeV proton in Ti, $57 \mu\text{m}$. The result indicates that most of the deuterium can only be loaded in the layer within about $10 \mu\text{m}$ of the titanium foil surface, in thick samples.

Assuming a d-d reaction is occurring within $10 \mu\text{m}$ of the titanium surface, and the atomic ratio of D/Ti to be 1, the reaction rate is estimated to be 1.4×10^{-24} fusion/d-d·sec.

The maximum energy of broad peak is about 2.8 MeV after exiting the sample, which is less than 3.02 MeV, the proton energy in a d-d reaction. It is not clear why the measured energy and proton energy in a d-d reaction are different. The same question was raised by other work.⁵ The energy scale of multi-channel analyzer is calibrated by a standard ^{241}Am α -source, thus a calibration with a proton source might be needed to answer this question.

The fluctuation of counts within the broad peaks is clearly observed. It can be explained as a statistic variation, a result of the very low counts. Background variations with the detectors are also observed.

3.2. Deuterium-loaded powder sample

The deuterium-loaded titanium powder sample was prepared by pressing the powder into a stainless steel disk (inner diameter 20 mm, depth of 2 mm) at 6 MPa. The thickness of deuterium-loaded titanium powder sample is 163 mg/cm^2 , and the D/Ti ratio is 1.6. The density of deuterium-loaded powder sample is 0.815 g/cm^3 , less than the Ti metal (4.52 g/cm^3).

The spectrum of deuterium-loaded powder sample is given in Fig. 7. The measurement was taken for 3 times for checking the reproducibility. The total measurement time was 508 hour. The result shows that no effect can be observed above the background level for the long-duration measurements in three runs.

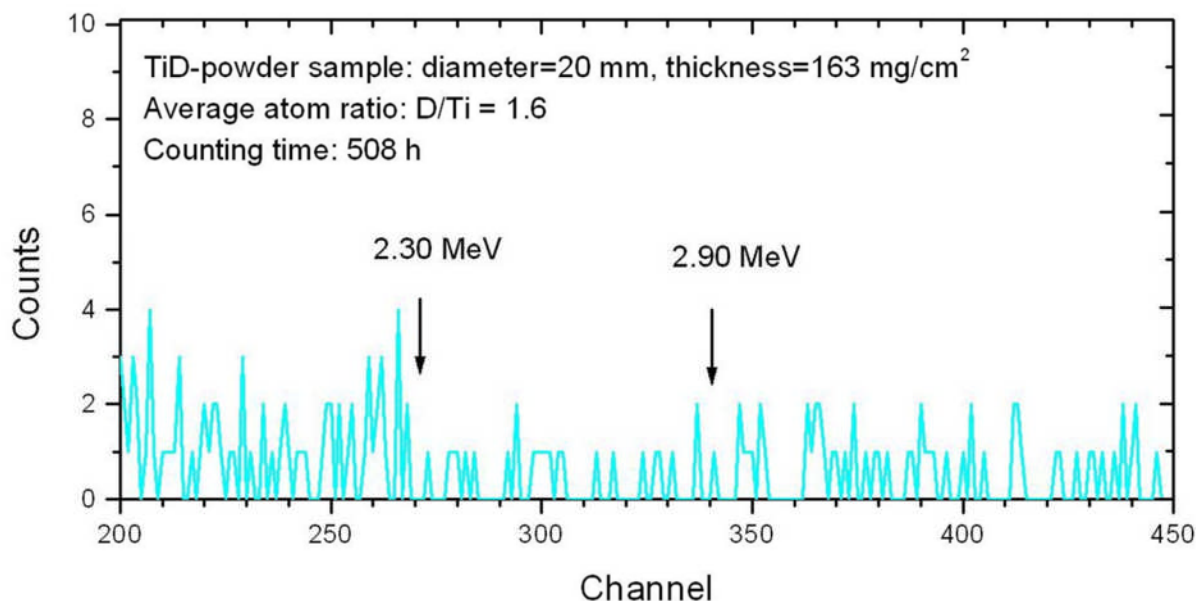


Figure 7. Spectrum of deuterium-loaded titanium powder sample.

3.3. TiD-Mo sample

The TiD-Mo sample was prepared by vaporizing $1.5 \text{ }\mu\text{m}$ titanium onto the surface of the molybdenum disk (20 mm diameter, 0.5 mm thick). The deuterium was loaded into the Ti layer with the technique described in section 2 and shown in Fig. 1. The atomic ratio of D/Ti is 1.4.

The spectrum of TiD-Mo sample is given in Fig. 8. A small narrow peak is observed clearly at the energy level of around 2.7-2.8 MeV. The net counts at the peak is calculated to be $0.058 \pm 0.18 \text{ counts/h}$. The ΔE (energy loss) of a 3-MeV proton in $1.5 \text{ }\mu\text{m}$ titanium is calculated to be about 0.05 MeV, covering 6 channels or so. The observed peak width is consistent with the calculated one. This result gives a further evidence for charged particle emitted from deuterium-loaded titanium metal at low temperature.

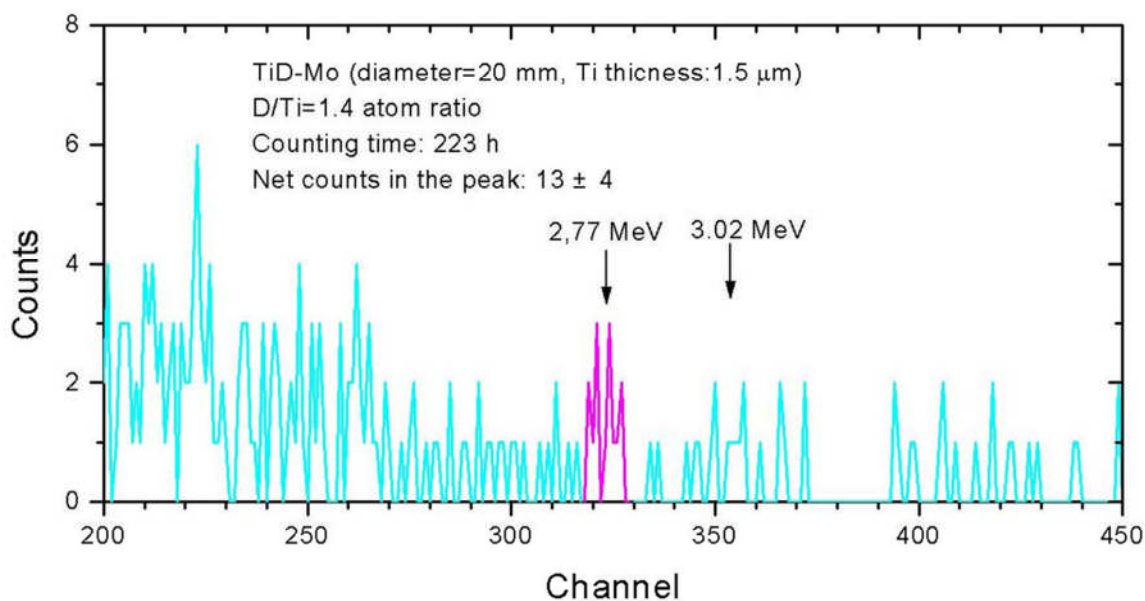


Figure 8. Spectrum of TiD-Mo foil sample, with titanium thickness of 1.5 μm and diameter of 20 mm, D/Ti atomic ratio =1.4.

4. Conclusions

From the experiment described above we can see that: (1) The reaction yields (counts) in this experiment are very low (~ 1 net count in 7.5 hours). (2) The energy range between 2 MeV and 3 MeV having low background plays a key role in this successful measurement. (3) The negative result of deuterium-loaded powder sample (Fig. 7) suggests that the reaction yield might be correlated to the density or microscopic variables of deuterium-loaded titanium materials, for the density of the powder sample much less than the titanium metal as mentioned above. (4) The results indicate that the characteristic of peaks correlate well with the loaded deuterium in the titanium, Al absorber and the thickness of the deuterium-loaded titanium samples.

The results show that the charged particles emitted from deuterium-loaded titanium metal have been detected at low temperature, and the charged particle is identified as proton having energy about 2.8 MeV after exiting the sample. The energetic proton might originate from the nuclear fusion, d-d reaction, and the d-d reaction rate is calculated to be 1.4×10^{-24} fusion/d-d-sec for the deuterium-loaded titanium foil sample. No data is observed above background level for the deuterium-loaded titanium powder sample. The negative result suggests that the reaction yield might be correlated with the density or microscopic variables of deuterium-loaded titanium materials, and also indicates that d-d reaction catalyzed by μ -meson from cosmic rays¹² can be excluded in the experiment.

This work provides a positive result of nuclear fusion at low temperature. Besides the d-d reaction, other types of nuclear fusion reactions might also be involved. This work may be helpful to the further study of the physical mechanism of nuclear reaction in the deuterium

(hydrogen)-loaded metals. The present work also suggests that it is worth doing further investigation on the origin of ^3He nuclear reactions in the deep Earth.

Acknowledgments

We thank Professor Li X Z for valuable comments. We also thank Professors Qi Bujia, Zhu Jiazheng and Dr. Diao Lijun for helpful discussion, and Dr. Wang Zhiqiang and Mr. Luo Hailong for providing the TiD-Mo samples.

This work supported by President Foundation of China, Institute of Atomic Energy, No. YZ0714.

References

1. Jiang S S and He M, Evidence for tritium production in the earth interior, *Chinese Sci. Bulletin* 53(2008)540-547.
2. Jiang S S, He M, Yue W H and Liu J, Tritium released from mantle source: implication for natural nuclear fusion in the earth interior, 2008, *J. Fusion Energy* DOI: 10.1007/s10894-008-9149-y,.
3. Fleischmann M, Pons S and Hawkins M 1989 Electrochemical induced nuclear fusion of deuterium, *J. Electroanal. Chem.* 261(1989) 301-308.
4. Jones S E, Palmer E P, Czirr J B, Decker D L, Jensen G. L, Thorne J M, Taylor S F and Rafelski J, Observation of cold nuclear fusion in condensed mater, *Nature* 338 (1989) 737-740.
5. Jones S E, Keeney F W, Johnson A C, Buehler D B, Cecil F E, Hubler G., Hagelstein P L, Ellsworth J E and Scott M R, Charged-particle emissions from metal deuterides, in *10th National conference on cold fusion*. Cambridge, MA: LENR-CANR.org, 2003.
6. Cecil F E, Lui H, Beddingfield D and Galovich C S, Observation of charged particle bursts from thin-titanium foil, *American Institute of Physics Conference Proceedings* 228, NY, p. 375-383, 1991.
7. Chamber G. P, Hubler G. K and Crabowski K S, Search for Energetic Charged-Particle-Reaction Products During Deuterium Charging of Metal Lattices, *American Institute of Physics Conference Proceedings* 228, NY, p. 383-395, 1991.
8. Koonin F E and Nauenberg M, Calculated fusion rates in isotopic hydrogen molecules *Nature* 339 (1989) 690-691.
9. Li X Z, Tian J, Mei M Y and Li C X, Sub-barrier fusion and selective resonant tunneling Penetration of deuteron into Coulomb potential barrier of neighbouring deuteron under several restriction condition *Phys. Rev.* 2000, **C** 61:024610-6.
10. Zhang Y M and Li J Q *Acta Physica Sinica* 51(2002)1244-1247, (in Chinese, with English abstract).
11. Ziegler J F SRIM-2006, <http://www.srim.org>.
12. Jackson J D Catalysis of nuclear reaction between hydrogen isotopes by μ^- mesons, *Physics Review* 106(1957) 330-339.

Development of New Detector System for Charged Particle Emission

Yu Toriyabe and Jirohta Kasagi

Laboratory of Nuclear Science, Tohoku University

1-2-1, Mikamine, Sendai 982-0826, Japan

Abstract

A charged particle detector system for high temperature gas permeation experiments was developed. We employed a phoswich scintillation counter which consists of a thin YAP(Ce) scintillator and a thicker plastic scintillator, BC-444. Scintillation pulse signals were recorded by a digital storage oscilloscope to realize careful off-line analyses by using the pulse shape discrimination (PSD) technique. Moreover, the system has large plastic scintillators surrounding the reaction chamber: they serve as veto counters and reject cosmic-ray events. Consequently, the system can identify energetic charged particles for emission rate as low as 3 counts/day. In a long period measurement of gas permeation through a Pd/CaO/Pd complex foil, a slight difference of counting rate between D₂ and H₂ gas was observed in the high energy region. It is suggested that high energy charged particles, most probably α particles, are emitted during D₂ gas permeation.

1. Introduction

Charged particle detection is the most sensitive method to verify the occurrence of nuclear reactions in condensed matter. A CR-39 track detector has generally been used in electrolysis and desorption experiments.¹⁻⁴ However, the detector cannot provide a time profile of the reaction rate, and it is difficult to get a good energy calibration as well as particle identification. Furthermore, background events caused by cosmic rays and natural radioisotopes cannot be easily suppressed. In order to overcome the disadvantages, we have developed a new charged particle detector system which is suitable for the type of gas permeation experiment originally reported by Iwamura et al.⁵

2. Detector system

The kernel of the new detector is Ce doped YAlO₃ scintillator (YAP(Ce)), which is chemically and mechanically stable even in high temperature hydrogen atmosphere⁶⁻⁸ where a Si semiconductor detector does not work normally. A variation of light yield of the YAP(Ce) is within +2 and -8% below 200°C: the temperature dependence is negligible below 100°C (i.e., in the present gas permeation experiment). The decay time of scintillation light of the YAP(Ce) is about 30 ns.

In our detector system, the YAP(Ce) crystal ($\phi 20 \times 0.5$ mm) is coupled to a BC-444 plastic scintillator (20×5 mm) which emits scintillation light with slower decay time (~ 280 ns) to

form a phoswich detector. As is shown in Fig. 1, a photomultiplier tube (PMT), which is placed outside of the chamber and kept at room temperature, is connected with the phoswich by a quartz light guide. An energy calibration curve of the YAP(Ce) was obtained with a 5.5 MeV α particle from ^{241}Am source, together with the reported values.⁹

Electric pulses from the PMT are recorded by digital storage oscilloscope and analyzed to identify energy and particles. Figure 2 shows schematically a function of the phoswich detector to distinguish necessary events from those of background originating mainly from cosmic rays. Charged particles (~ 50 MeV α and 12 MeV proton) emitted from a sample stop within the YAP(Ce) crystal due to large energy loss of them and make a fast electric pulse (YAP(Ce) component) whose shape is shown at a left part in Fig. 2. On the other hand, cosmic rays or high energy charged particles from another direction can pass through both the YAP(Ce) and the BC-444 scintillators, and therefore, make a pulse with a longer tail (BC-444 component) as shown in the right side pulse shape in Fig. 2, where the time 0 in Fig. 2 corresponds to the trigger time of the digital oscilloscope.

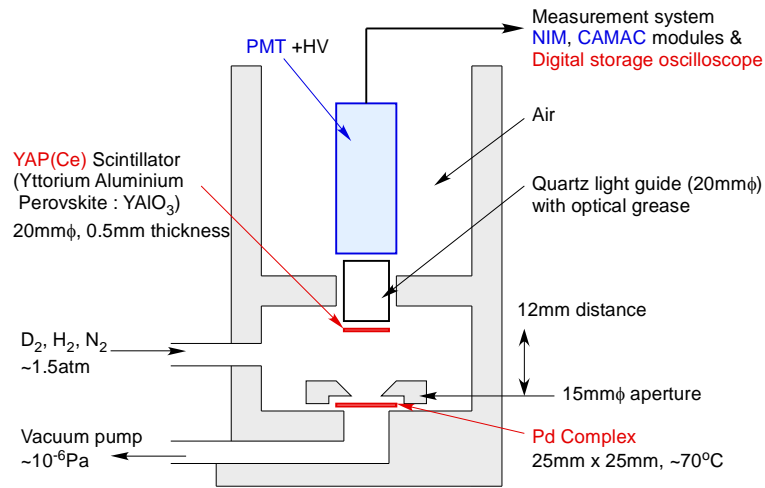


Figure 1. Schematic view of an experimental setup. A phoswich detector is placed 12 mm above a sample and covers a solid angle of 18 %. One side of the sample is pressurized by D_2 or H_2 gas and the opposite side is evacuated by a vacuum pump. The gas is absorbed into the sample and permeates through in it due to density divergence.

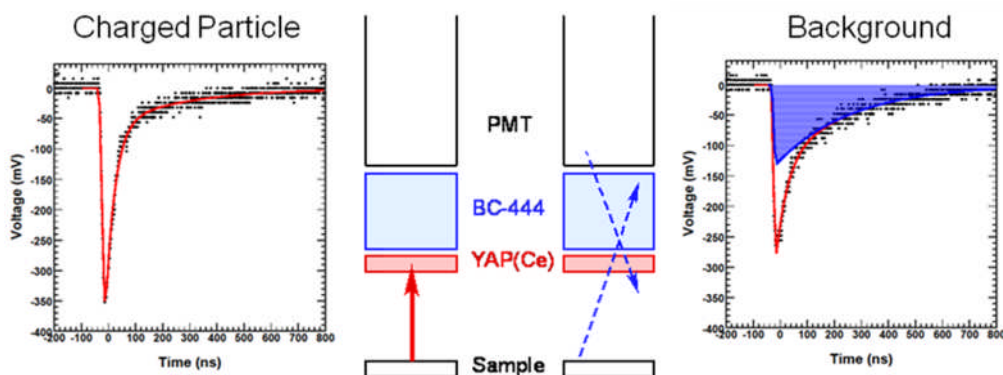


Figure 2. Function of YAP(Ce)/BC-444 phoswich detector and pulse shape discrimination technique. Heavier charged particles such as α particles or protons stop within the YAP(Ce) (left plot). On the other hand, energetic particles can pass through the YAP(Ce) and enter the BC-444, so that a pulse shape has a slower decay component caused by the BC-444 indicated by the blue area, in addition to a fast component indicated by the red curve (right plot).

Discrimination of the events was made by two steps. First, two time windows are set for the pulse shape spectrum, and light yield in each window was deduced: a short window covers between -25 and 75 ns while a long one between -50 and 800 ns. We excluded events with a sufficiently long tail in accordance with the ratio of the two yields. Next, a decay constant of each pulse shape was examined carefully, and events having an α -like pulse shape were finally selected: they are designated pulse shape discriminated (PSD) events. We can assume that the PSD events are heavier charged particles than proton (p, d, α etc.).

In addition to the phoswich detector, the system includes large plastic scintillators which surround the gas permeation chamber and serve as veto counters. These detectors reject 60% of counts as cosmic ray events. Consequently, the new detector system can identify charged particles emitted from the sample during gas permeation for quite low counting rate such as ~ 3 counts/day at several MeV region, because the background level is below 1 count/day.

3. Gas permeation

We have used the detector system to observe charged particles during the gas permeation experiment. Samples of Pd/CaO/Pd complex foil (the gas permeable area is circular shape with 15 mm diam.) were provided by groups at Iwate University and Mitsubishi Heavy Industries (MHI). Those from Iwate Univ. were prepared fully based on the original recipe of the MHI. In the present work, 4 samples were examined: 2 from Iwate (I-1 and I-2) and 2 from MHI (M-1 and M-2). Foils of I-1, M-1 and M-2 have a Cs deposited layer on the surface as described in Ref. 5.

As shown in Fig. 1, the sample was placed at a position 12 mm below the phoswich detector. Temperature of the sample was controlled by ohmic heaters to be about 70°C. Maximum pressure of D_2 and H_2 gas was 1.5 atm and a gas flow rate was typically about 0.1 \sim 0.5 ccm. It should be noted that the MHI group claims that a much higher flow rate, ~ 3 ccm, is important to achieve nuclear transmutations, but we have not been able to achieve such high rates in this

study. After the D₂ gas permeation continues for about 1 week we evacuated the chamber until the pressure falls below 10⁻⁴ Pa, promoting D₂ gas desorption. Measurement with the H₂ gas permeation, which can be regarded as a background run, was carried out with the same sample after the D₂ gas desorption. We ignored an effect of residual gas in the Pd complex sample, since its quantity was considered very small. Finally, we acquired data during 1 week for each gas and under a vacuum as well.

4. Results

In the offline analyses, energy spectra of the PSD events were made for D₂ gas (denoted D₂), H₂ gas (H₂) and vacuum (Vac.). Figure 3 shows such spectra for the I-1 foil: counting rate and total counts are plotted. In the lower energy region, the PSD becomes worse because the absolute pulse size is smaller due to lack of light intensity. However in the higher energy region we can clearly reject background events. The counting rate of the background for E > 7 MeV is less than 1 count/day. In order to discuss the observed events statistically, the events are summed up for three bins, 1, 2, and 3, as indicated in Fig. 3. In region 1 of the D₂ spectrum, total counts are clearly larger than the background (H₂ and Vac.).

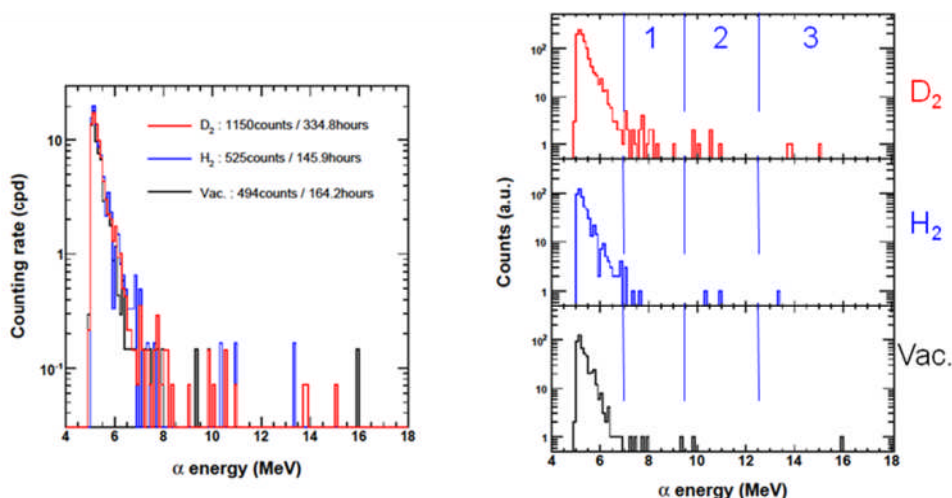


Figure 3. Energy spectra of the PSD events obtained with the I-1 foil. Duration of the D₂ run is 2 times longer than the other cases. Counting rate at lower energy region is not different each other, since background events cannot completely rejected because of smaller pulse shape.

In the present study, we performed the D₂ run first and obtained several counts in region 1. In the H₂ run carried out after the D₂ and Vac. runs, however, no significant count was observed. Then, we retried the D₂ run and observed several additional counts again, in region 1. A total of 22 event counts were observed in region 1, while 9 counts were observed during the background runs (with H₂ and Vac.).

Spectra for the M-1 foil are shown in Fig. 4. Significant events are seen in region 2.

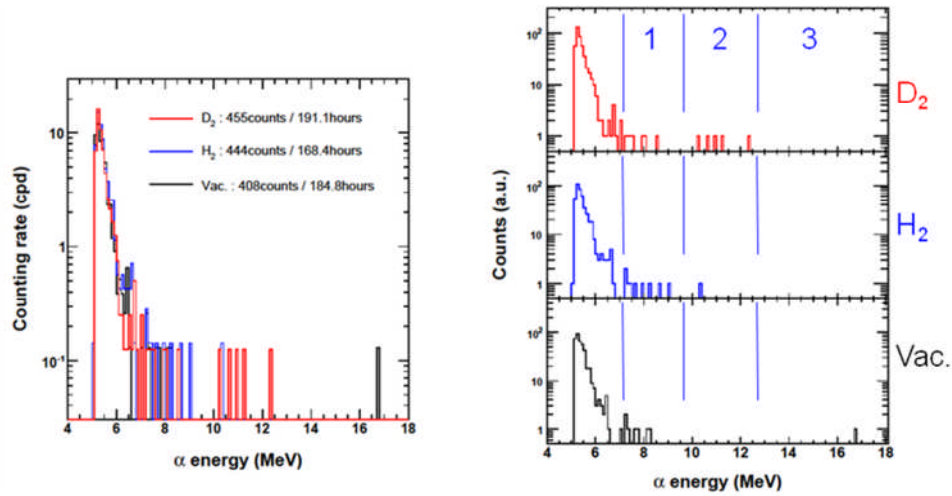


Figure 4. Same as Fig. 3 but for the M-1 foil.

Figure 5 summarizes the deduced counting rate for $E > 7$ MeV for I-1 and M-1 samples. Red points are data for D_2 runs and black points for background runs (H_2 and Vac.). Vertical error bars with dashed line show 90 % confidence level estimated from the Poisson distribution. As above mentioned, we have significant events in region 1 for the I-1 foil and in region-2 for the M-1 foil. In both cases the error bars of the foreground are not overlapped with those of the background, and the confidence levels are more than 99% in both cases.

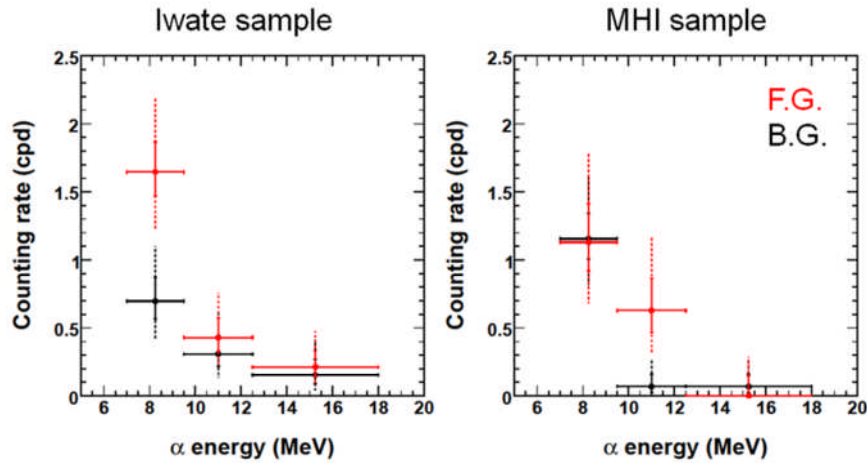


Figure 5. Counting rate for the I-1 (left) and M-1 (right) foils for $E > 7$ MeV. Data for the D_2 run and the background run (H_2 and Vac.) are plotted with red and black points, respectively. Vertical error bars indicate a confidence level of 68.3% (solid line) and 90% (dashed line) derived from the Poisson distribution.

Although we tried 4 samples, significant events of charged particle emission were observed only in the I-1 and M-1 cases. The I-2 foil which has no Cs deposition on the surface showed no emission within the same time period. Although the M-2 foil has a Cs layer, no clear difference was observed between foreground and background. We conjecture that this might be due to a low permeation rate of D_2 gas through the foil: the flow rate was less than 0.1 ccm.

It should be noted that we cannot completely eliminate high energy PSD events in the background runs with this detector system. In other words, there may be several MeV charged particles related to cosmic rays. We have confirmed that such events are not negligible. At present, we consider that these background events are due to elastic recoils of cosmic rays, such as the $p(\mu, \mu)p$ and $d(\mu, \mu)d$ reactions, that deposit large energy to the detector. The phoswich detector alone cannot identify these charged particle background events. Although use of the VETO detectors is the only way to eliminate these events, the phoswich detectors cannot be surrounded perfectly in the present work. Therefore an increase of foreground counts is required to improve the reliability with this setup.

5. Conclusion

We have developed the new detector system for charged particle detection in the gas permeation experiment. The YAP(Ce)/BC-444 phoswich detector provides particle identification and VETO detectors, and decrease background events to 1 count/day at several MeV region. This system can identify significant events with a counting rate as low as 3 counts/day for clear evidence of charged particle emission.

Candidate charged particles emitted from the Pd complex foils were observed for the D2 gas permeation with reliability of over 99% in 2 of 4 experiments. These are most likely to be α particles with kinetic energy between 7 and 12 MeV. It should be stressed that these events are caused neither by electronic noises nor by natural radio isotopes. Therefore, we infer that deuteron related nuclear reactions occurring in the sample emit these charged particles. At present, the number of the observed events is so small that the reaction mechanism can hardly be inferred. We conjecture that high permeation rate could induce high reaction rate and, thereby, material improvement are strongly required for the next step.

Acknowledgement

The authors thank Prof. Yamada, Iwate Univ. and Drs. Iwamura and Itoh, MHI, for providing us the Pd complex samples. This study is partially supported by JSPS grants and by Toyota Central R & D Labs., Inc.

References

1. K. Kamada, *Jpn. J. Appl. Phys.*, **31**, L1287 (1992).
2. R. A. Oriani and J. C. Fischer, *Jpn. J. Appl. Phys.*, **41**, 6180 (2002).
3. P. Moisie-Boss *et al.*, *Eur. Phys. J. Appl. Phys.*, **40**, 293 (2007).
4. G. Lipson *et al.*, Proc. ICCF12 (2005).
5. Y. Iwamura *et al.*, *Jpn. J. Appl. Phys.*, **41**, 4642 (2002).
6. M. V. Korzhik *et al.*, *Nucl. Inst. Meth. B*, **72**, 499 (1992).
7. S. Baccaro *et al.*, *Nucl. Inst. Meth. A*, **361**, 209 (1995).
8. M. Moszynski *et al.*, *Nucl. Inst. Meth. A*, **404**, 157 (1998).
9. E. Slunga *et al.*, *Nucl. Inst. Meth. A*, **469**, 70 (2001).

Introduction to Ion Beam Experiments

The previous section dealt with measurements of particles, namely neutrons and light ions, which are emitted from LENR experiments. It is also possible and instructive to use ion beams to impact materials to probe what is happening before, during or after a LENR experiment. In these experiments, the measured particles are either scattered incident ions or particles that have been ejected from the target by impacts. There are three motivations for such beam experiments, which generally use protons or deuterons as the energetic probing ions.

First, the interactions, scattering and effects stimulated by the impact of beams of low mass ions can reveal much about the character of the target. This is true independent of LENR. A wide variety of experimental methods employing ion beams is available for material analysis. The methods often yield information on the composition, that is, the distribution of elements, as a function of depth into the target. These methods can be used for measurements of the results of transmutations in LENR experiments. For example, the paper by Yamaguchi et al in the section of these proceedings on transmutations used four ion beam technologies for their study of transmutations.

The second reason to fire ions at a target is to determine the conditions and dynamics of deuterons (D) within the target material. A few studies have shown that impacting deuteron beams with energies of about 100 keV onto D rich targets (such as TiD_2) yields evidence of three body (D-D-D) reactions. The count rates are very low. It is possible that modeling of such experiments will give information on the probabilities of two deuterons in the target materials being very close to each other at the time of impact of the incident deuteron. The billiard ball metaphor that is used in these experiments has been very convenient analytically but it depends for its appropriateness on the existence of the strong binding force that holds nuclei together. This permits the treatment of the weaker electromagnetic force as a perturbation. LENR experiments may be probing a part of phase space where little is known. Astrophysical observations have prompted investigations in the “low energy” realms.

Finally and importantly, ion beams with relatively low energies have been used to measure interaction cross sections (probabilities) that are much greater than expected on the basis of the cross sections for ordinary two-body collisions at higher energies. In such experiments, the beam energies are relatively low (a few keV) by usual beam standards. As a result, the count rates are also low. But, the quantitative data show that the cross sections are as much as an order of magnitude greater than expected. The data are interpreted in terms of the screening potential energy that would be required in the normal two-body collision theory to yield such enhanced cross sections. It remains to be seen if such interesting experiments are directly relevant to LENR. On one hand, they may be the high energy beginning (as the beam energy is decreased) of the greatly enhanced nuclear reaction probabilities seen in ordinary LENR experiments. On the other hand, energies near 1 keV are still over 10,000 times greater than the energy equivalent of room temperature (1/40 eV), where most LENR experiments are run.

The number of papers at ICCF-14 on beam experiments was small. They all had to do with the third of the above reasons for incident-ion experiments.

Kasagi heads one of the three groups that have measured enhanced nuclear reaction cross sections at low beam energies during the past decade. He presented an invited overview of low energy D-D reactions, and new data on the effects of H and D ions collisions on both solid and liquid targets. It was found that the liquid Li has a screening potential substantially higher (by 300 eV) than the solid Li target. That difference was interpreted as due to differences in ion screening, which was said to be much stronger than ordinary electronic screening.

One of the two German groups measuring enhanced low energy cross sections presented two papers at the conference. However, the results were already available in the literature, so they were not provided for inclusion in these proceedings. Drs Huke and Czerski presented the experimental and theoretical work they and their collaborators have been doing. Reports of what they did and found are available in three publications:

F. Raiola et al., Eur. Phys. J. A13 (2002) 377.

K. Czerski et al., Eur. Phys. J. A 27 (2006) 83.

A. Huke et al., Phys Rev. C78 (2008) 015803

Screening Potential for Nuclear Reactions in Condensed Matter

J. Kasagi

*Laboratory of Nuclear Science, Tohoku University
Mikamine 1, Taihaku-ku, Sendai 982-0826, Japan*

Abstract

Screening for nuclear reactions in metal plays an important role in enhancing reaction cross sections in the ultra-low energy region. A simple extrapolation of the screening potential down to the thermal energy region from the keV beam experiment predicts the occurrence of “cold fusion” D+D reactions. In the present work, results so far obtained in low-energy beam experiments will be overviewed and the origin of the screening potential will be discussed: both electronic screening and ionic screening. For ionic screening we have studied nuclear reactions in liquid metal which can be regarded as a low-temperature dense plasma. In such a condition, the classical ions contribute to the screening more strongly than the quantum electrons do. Results on the $^7\text{Li}+p$ and $^6\text{Li}+d$ reactions with liquid Li target will be shown. The effects of the solid-liquid phase transition are clearly seen in these reactions. It can be concluded that the ionic Debye screening is much stronger than the electronic screening in low-temperature dense plasmas.

1. Introduction

It is well known that two miracles are necessary to explain the cold fusion experiments. They are a huge reduction of the Coulomb barrier between two deuterons in metals, and an anomalously large branching ratio of the D+D reaction leading to the $\gamma+X$ channel (X: energy transfer to the lattice). Such conditions are never realized for the free d+d fusion reaction. The study of nuclear reactions in metals using low-energy deuteron beams gives important information to understand the miracles of cold fusion, especially for the Coulomb barrier between deuterons in metals.

We have been investigating the effects of metal environments acting on nuclear reactions. In the present work, results so far obtained in low-energy beam experiments on the DD fusion reaction will be overviewed. The reaction rates are enhanced much larger than expected in metals. Furthermore, our recent work on nuclear reactions in the liquid phase will be discussed in detail; the reaction rate in the liquid phase is larger than the solid. In the liquid phase both the electronic and ionic screenings enhance the reaction rate very strongly.

Finally, the importance of the large-screen potential for low-energy nuclear reactions in condensed matter will be discussed.

2. Overview of DD reactions in metal

The D+D reaction during implantation of deuterium was measured by detecting neutrons already 30 years ago, but the aim of this research was to determine the distribution, trapping and diffusion of the deuterium implanted in the target. After the “cold fusion” claim in 1989, however, the enhancement of the reaction rates of the D+D reaction in metal has been intentionally searched for in the deuteron implantation by several authors. Roth et al. [1] first reported the reaction rate of the $D(d,p)T$ reaction in Ti as a function of the bombarding energy down to 3 keV and showed that the deduced excitation function is consistent with no enhancement in the cross section. Kasagi et al. [2] measured the thick target yields for the $D(d,p)T$ and $D(d,n)^3\text{He}$ reaction in Ti for $4.5 < E_d < 18$ keV, and concluded that the excitation function for both channels was explained well with the cross section of the compiled data by Bosch and Hale[3]. Yuki et al.[4] succeeded in measuring the reaction rates at lower bombarding energies down to 2.5 keV, and first deduced the screening energy of the DD reaction in metal, which is a quantitative scale of the enhancement at very low energies, as discussed in the next section. Although the screening energy for the DD reaction in Ti (27 eV) was turned out to be similar to the value deduced for a D_2 gas target (25 eV), that in Yb (80 eV) was clearly larger as seen in the enhanced reaction rate of about 1.5 times at 3 keV. This is the first clear evidence that the fusion reaction rate can be enhanced in the metal environment during keV deuteron bombardment.

In subsequent experiments, anomalously large values of screening energy was found for PdO (600 eV), Pd (310 eV) and Fe (200 eV).[5] In this case, the reaction rate for PdO at $E_d = 2.5$ keV became about 100 times of the normal rate. Such large screening energies of the DD reaction were found also in other materials by another group. Czersky et al.[6] has reported enhanced screening energy of the DD reactions in Ta; it was about 300 eV, and was confirmed by Raiola et al.[7] Raiola et al. have carried out a systematic measurement of the screening potentials of the DD reaction for a wide range of host materials including metals, semiconductors and insulators,[8] and claimed that the large screening in metals can be interpreted by the Debye screening based on their measurement of the temperature dependence of the screening potential.[9] However, this interpretation contradicts the fact that the conduction electrons are degenerated Fermi particles which obey the Thomas-Fermi distribution. Thus, there might be some problems to be overcome experimentally, such as how to fix the deuterium density in metal during the bombardment, as pointed out by Huke et al.[10].

The screening energy for the deuteron in metal was also theoretically studied. Ichimaru et al.[11] suggested that hydrogen nuclei in metal are strongly screened, since the electrons both in metallic d-band and hydrogen induced s-band can contribute to the screening effect. They calculated the effective static potential for hydrogen in Ti and Pd, and proposed that the screening distance between two hydrogen nuclei in metal is much shorter than that of atomic hydrogen. The calculated screening energy is 51 eV for Ti and 75 eV for Pd and cannot explain the large enhanced reaction rate at all. Czersky et al.[12] calculated the screening energy for the DD reactions in metal by applying a dielectric functional method which allows to treat the electron screening as a static polarization of the metallic medium induced by the positively

charged deuteron. Their results including the cohesion effects give clearly larger values of the screening energy in the metal environment, for example, about 130 eV for Pd, but less than half of the observed values.

Thus, one can summarize the present situation as follows: The low-energy DD reactions are enhanced very much when the reaction occurs in a metal environment. The mechanism of the enhancement is not fully understood, especially for the environment which provides screening energy of a DD reaction of more than 200 eV. All these arguments motivate further studies of screening due to positive charge ions which can move almost freely.

3. Liquid Li + p,d reactions

Liquid Li may be regarded as a plasma consisting of classical Li^+ ions and quantum electrons, and it has a much higher density ($\rho \sim 5 \cdot 10^{22}/\text{cm}^3$) than can be realized in laboratory gas plasmas. In a low-temperature dense plasma, the classical ions contribute to the screening more strongly than the quantum electrons do, because of a difference of the mean kinetic energy of the particles under equilibrium conditions. Since the mass of ions is much larger than that of electrons, the positive ions cannot respond quickly. For this reason, it is claimed that the ionic screening is reduced in stellar plasmas [13], while there is a strong assertion that the ionic screening is applicable to stellar plasmas [14]. Therefore, one of the interesting questions is whether or not the screening due to positive ions can work effectively. The present study of nuclear reactions in liquid Li may provide a good testing ground for the screening effect due to the positive ions in dense plasmas.

The experiments were performed using proton and deuteron beams obtained from a low-energy ion generator at the Laboratory of Nuclear Science at Tohoku University. Natural Li (92.4% ^7Li , 7.6% ^6Li) and enriched ^6Li were used for $^7\text{Li}+\text{p}$ and $^6\text{Li}+\text{d}$ reactions, respectively. A technique to generate the liquid Li metal target has been developed. A lump of natural Li or enriched ^6Li metal was placed horizontally on a small saucer which can be heated up to 500°C in a vacuum chamber. The temperature of the surface of the Li target was monitored directly by a radiation thermometer. The melting point of the Li metal is about 180°C ; a phase change was easily confirmed by watching the temperature. A beam was injected from the upper part of the chamber, with its angle of 30° with respect to the vertical line. Alpha particles emitted in the $^6\text{Li}(\text{d},\alpha)^4\text{He}$ and $^7\text{Li}(\text{p},\alpha)^4\text{He}$ reactions were measured with a Si detector of $300\text{ }\mu\text{m}$ in thickness. A $5\text{-}\mu\text{m}$ thick Al foil covered the detector surface to prevent electrons and scattered beam particles from hitting the detector directly.

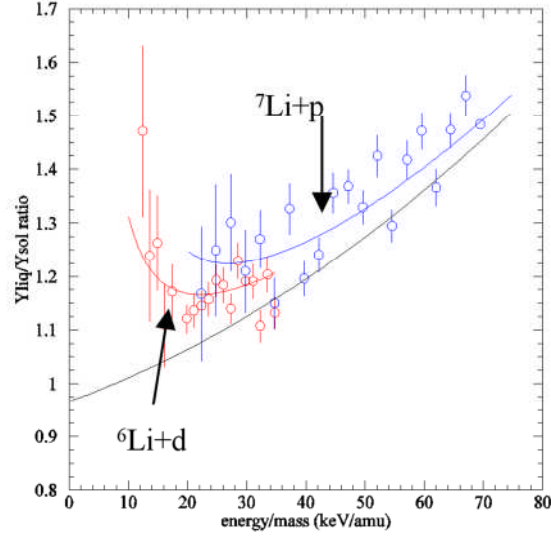


Figure 1. Ratio of α particle yield for the liquid target to that for the solid, plotted as a function of bombarding energy per nucleon. Red squares show the data of the ${}^6\text{Li}(\text{d},\alpha){}^4\text{He}$ reaction and blue circles show those of the ${}^7\text{Li}(\text{p},\alpha){}^4\text{He}$ reaction.

Thick-target yields of α particles from the ${}^6\text{Li}(\text{d},\alpha){}^4\text{He}$ and ${}^7\text{Li}(\text{p},\alpha){}^4\text{He}$ reactions were measured for solid ($T \sim 330$ K) and liquid ($T \sim 520$ K) Li targets as a function of bombarding energy between 22.5 and 70 keV in 2.5 keV steps. We measured the beam current on the target, around which a permanent dipole magnet was placed to suppress secondary electron emission. The beam intensity was varied for each bombarding energy level so as to keep the input beam power constant. Since Li combines easily with hydrogen (deuterium) to become LiH (LiD), the target surface was cleaned every 2 hours during the bombardment by a wiper attached to the chamber. Furthermore, the α particle yield at $E_p = 70$ keV ($E_d = 60$ keV) was measured at frequent intervals to check on any change in the target condition.

Observed excitation functions show a clear difference for the liquid and the solid target. In Fig. 1, we show ratios of the reaction rates in the liquid target to the solid as a function of E/mass (keV/AMU); red circles are for the ${}^6\text{Li}(\text{d},\alpha){}^4\text{He}$ reaction and blue circles for ${}^7\text{Li}(\text{p},\alpha){}^4\text{He}$. As seen, the reaction rates for the liquid Li are always larger than those for the solid in both the ${}^7\text{Li}(\text{p},\alpha){}^4\text{He}$ and ${}^6\text{Li}(\text{d},\alpha){}^4\text{He}$ reactions. Except for the very low energy region, two sets of data are connected smoothly, and one may say that the ratios are well scaled by E/M , that is, by velocity. This suggests that stopping power is a significant part of phenomena seen in Fig. 1. Stopping power is different in the liquid and solid phases; it is smaller in liquid Li than in solid Li. This smaller stopping increases the projectile path length and, therefore, the effective target thickness.

For the following analyses, we define and approximate the reduced yield and yield ratio for the thick target method as follows. This approximation works here to better than 2% accuracy.

$$Y_{red}(E_b) \equiv Y_{exp}(E_b) / \int_0^{E_b} \frac{d\Omega_{cm}}{d\Omega_{lab}} \sigma_{bare}(E) dE \cong (const) \exp\left(B\sqrt{\mu} \frac{U_s}{E_{cm}^{3/2}}\right) \cdot S^{sol(liq)}(E_b) \quad (1)$$

$$\frac{Y_{liq}}{Y_{sol}} = \frac{N^{liq}}{N^{sol}} \exp\left(B\sqrt{\mu} \frac{\Delta U_s}{(E_{cm})^{3/2}}\right) \frac{S^{sol}}{S^{liq}} \cong \frac{N^{liq}}{N^{sol}} \exp\left(B\sqrt{\mu} \frac{\Delta U_s}{(E_{cm})^{3/2}}\right) \cdot (0.98 + b_1 \left(\frac{E_b}{m}\right) + b_2 \left(\frac{E_b}{m}\right)^2) \quad (2)$$

Here, $d\Omega_{cm}/d\Omega_{lab}$ is the solid angle ratio of the cm to the laboratory (lab) system, $\sigma_{bare}(E)$ is the reaction cross section for bare nuclei, $E_{b(cm)}$ is the bombarding (cm) energy, S is the stopping power for the incident beam, m is the reduced mass of target and projectile nuclei, and ΔU_s is the difference of the screening potential ($U_{liq} - U_{sol}$). For the stopping power of the liquid Li we made a correction based on the stopping power of the solid. In eq. 2, the ratio of the stopping power for the solid to the liquid is simply assumed as a quadratic function of E/m , and b_1 and b_2 are parameters to be determined so as to give a best fit to the experimental ratios. For $\sigma_{bare}(E)$, the astrophysical S -factors are taken from ref. [15], because they agree with the values obtained recently by the so-called Trojan horse method [16] which may give the S -factor free from the Coulomb effect in the initial channel.

In Fig. 2, we show the reduced yield of the ${}^6\text{Li}(d,\alpha){}^4\text{He}$ as a function of the bombarding energy for the solid and liquid Li target, respectively, in the upper and lower graph. In order to obtain the screening potential together with the stopping cross section from the data in both phases, the values of the parameters in eqs. 1 and 2, U_{sol} , U_{liq} , b_1 and b_2 , are searched for so as to give the best fit to the data in Figs. 1 and 2. The resulting values (preliminary) of the screening potential were $\Delta U_s = 300 \pm 30$ eV, and $U_{sol} = 400 \pm 50$ eV and $U_{liq} = 700 \pm 60$ eV. The solid curves through the red and blue circles in Figs. 1 and 2 are the fits. The black solid curve in Fig. 1 shows the liquid/solid yield ratio due to the difference of the stopping power in both phases.

Thus, one may say that it is established experimentally that the screening potential for the liquid phase is very large: larger than for the solid phase by about 300 eV or about 1.75 times the solid value. Thus, a stronger screening from the ionic fluid is clearly shown in the present work.

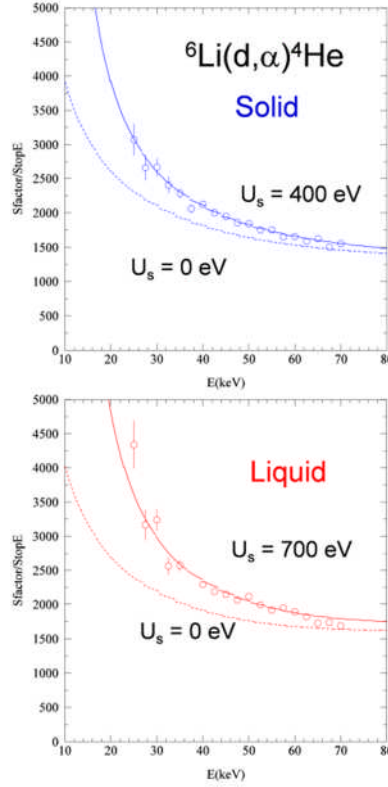


Figure 2. Reduced yield for the ${}^6\text{Li}(\text{d},\alpha){}^4\text{He}$ reaction in the solid phase (upper graph) and the liquid (lower).

For the solid Li, the screening originates only from the electrons, i.e., the bound and conduction electrons. The electronic screening from both may be described by $U_e = 3e^2 \times (1/\lambda_{be}^2 + 1/\lambda_{ce}^2)^{1/2}$, where $\lambda_{be(ce)}$ is a screening length due to the bound (conduction) electrons. The screening potential due to the bound electrons is estimated to be 186 eV as the adiabatic limit value [15], which gives $\lambda_{be} = 23.2$ pm. The Thomas-Fermi screening approximation [17] applied to the conduction electrons gives $\lambda_{ce} \sim (E_F/(6\pi e^2 n_e))^{1/2} = 61$ pm (E_F is the electron Fermi energy and n_e is the electron number density). Thus, the screening potential of the solid Li is expected to be $U_{sol} = U_e = 194$ eV, a value which is about 200 eV smaller than the present result. The discrepancy has already been pointed out for the bound electrons, i.e., for the screening potential measured with a LiF target (~ 340 eV) [15]. The larger value of U_{sol} found here might mean that the screening energy of the bound electrons is not explained well, since the estimated contribution from the conduction electrons is only 1/8 that of the bound electrons.

For liquid Li, the ionic screening should be included. Since the mobile Li^+ ion can be treated as a classical particle, the screening length is estimated with the Debye screening model, which gives $\lambda_{ion} \sim (kT/(4\pi e^2 n_{Li}))^{1/2} = 6.7$ pm at $T = 520$ K; much shorter than lengths originating from the degenerate quantum electrons. The screening potential due to the Li^+ ion alone is, then,

estimated as $U_{\text{ion}} = 3e^2/\lambda_{\text{ion}} = 645$ eV. As a consequence, the screening potential of the liquid Li, again using $U_e = 194$ eV, should be $U_{\text{liq}} = (U_e^2 + U_{\text{ion}}^2)^{1/2} = 673$ eV. Although the prediction is quite close to the experimental value (700 eV), the experimentally deduced value of U_{ion} is 580 eV, slightly larger than the prediction.

Summary

In the past ten years, the strong enhancement of the reaction rate for D+D reactions in metals has been independently observed in low-energy beam experiments by three groups. Although the values of the screening potentials of the D+D reaction obtained for the various host metals do not completely agreed with each data set, we can conclude that the large screening mechanism exists for the D+D reaction in metals. The origin of the large screening potential, for example, 300 eV or more deduced for the Pd host, is not yet understood. Probably, electronic screening due to the conduction electrons can contribute to 200 eV together with the cohesion effects. It should be noted here that one of the miracles of cold fusion is no longer miraculous from an experimental point of view, although the mechanism has not been revealed.

In order to study the effects of positive ions on the screening, we have investigated the ${}^7\text{Li}+p$ and ${}^6\text{Li}+d$ reactions with a liquid Li target, for the first time. The effects of the solid-liquid phase transition are clearly seen in the reaction rates. The reaction yield in the liquid phase is always larger than in the solid phase. This observation suggests that not only the screening potential but also the stopping power in the liquid Li is different from those in the solid. Using the data of the yield ratio between the liquid and the solid we have deduced an empirical correction factor for the stopping power between the liquid and solid Li.

Screening potentials for the Li+p,d reaction are successfully obtained for the liquid Li as well as the solid. It turns out that the liquid Li provides much larger screening potential than the solid: the difference is about 300 eV in the present preliminary analysis. This difference is very well explained by a simple plasma picture of the solid and the liquid Li metal. It can be concluded that the ionic screening is much stronger than the electronic screening in low-temperature dense plasmas. The present observation of the screening in the liquid phase is very important to understand the mechanism of the large screening of the D+D reaction in metals. For example, if deuterons in Pd metal behave like liquid, then the screening effect of D^+ ions should be considered; the screening potential would be much larger than the electronic screening alone.

Acknowledgements

The author thanks H. Yonemura, Y. Toriyabe, A. Nakagawa and T. Sugawara, with whom the experiments of the liquid Li target have been performed. This work was partly supported by the Grant-in-Aid for Scientific Research (No. 19340051) of the Ministry of Education, Japan.

References

1. J. Roth et al., Nucl. Fusion 30 (1990) 441.
2. J. Kasagi et al., J. Phys. Soc. Jpn. 64 (1995) 3718.
3. H.S. Bosch and G.M. Hale, Nucl. Fusion 32 (1994) 611.

4. H. Yuki et al., J. Phys. Soc. Jpn. 66 (1997) 73, H. Yuki et al., J. Phys. G23 (1997) 1459.
5. H. Yuki et al., JETP Lett. 68 (1998) 765, J. Kasagi et al., J. Phys. Soc. Jpn. 71 (2002) 277, J. Kasagi, Prog. Theo. Phys. Suppl.
6. K. Czersky et al., Europhys. Lett. 54 (2001) 449.
7. F. Raiola et al., Eur. Phys. J. A13 (2002) 377.
8. F. Raiola et al., Phys. Lett. B547, (2002) 193.
9. F. Raiola et al., J. Phys. G 31 (2005) 1141.
10. A. Huke et al., Phys Rev. C78 (2008) 015803.
11. S. Ichimaru, Rev. Mod. Phys. 65 (1993) 255.
12. K. Czerski et al., Eur. Phys. J. A 27 (2006) 83.
13. C. Carraoro, A. Shafer and S.E. Koonin, Astrophys. J. 331, 565 (1998); G. Shaviv and N.J. Shaviv, Astrophys. J. 529, 1054 (2000).
14. J.N. Bahcall, L.S. Brown, A. Gruzinov and R. F. Sawyer, Astron. Astrophys. 383, 291 (2002).
15. S. Engstler et al., Phys. Lett. B 279, 20 (1992).
16. C. Spitareli et al., Phys. Rev. C63, 055801 (2001); M. Aliotta et al., Eur. Phys. J. A 9, 435 (2000).
17. C. Kittel, Introduction to Solid State Physics (sixth edition), (John Wiley and Sons, Inc. 1986) pp. 264.

Introduction to Photon Measurements

As with energetic particles, there are two kinds of LENR experiments involving photons. The first are emission experiments, in which the LENR cause electromagnetic radiation of some wavelengths to be generated. The second category of experiments involves irradiating part or all of a LENR experiment with photons for some purpose. The reasons for such illumination include (a) diagnosing what is happening in an experiment or else (b) controlling the output of an experiment.

It should be noted that most of the electromagnetic spectrum has been employed, one way or the other, in LENR experiments. That is, measurements and stimulation have ranged from gamma ray spectroscopy to the use of tera-Hz (THz) radiation to the employment of radio frequency radiation. X-ray measurements and probes have been used. The emission of light and infrared radiation has been measured. Scattering of optical radiation is a useful *in situ* probe of kinetics within an operating experiment. Laser light has been used to turn on and turn up the production of excess power in electrochemical cells. Two laser beams with difference frequencies of 1-25 THz have also been used to stimulate and control excess power production.

At ICCF-14, there were several papers on optical and x-ray measurements. Two of them involved the use of lasers to control experiments. One of those papers and another involved interactions of light with optical phonons in Pd. Another paper reported soft-x-ray emission during and after the operation of a glow discharge LENR experiment.

Tian and his collaborators used a 532 nm laser to trigger a D and Pd gas loading experiment. Even though they did not have high loading (D/Pd ratio), the authors report 2.6 kJ within half an hour, that is about 1.5 W average power. Remarkably, the wire used in the experiment, when irradiated with a 25 mW laser over 1 cm length spot, achieved a power density exceeding 10^4 W per cm^3 of Pd.

Letts and Hagelstein employed dual lasers to produce tunable difference frequencies in the THz range. It was used to irradiate the Pd cathode in an electrochemical experiment. It is not known if the illuminated Pd is acting as a non-linear material and mixing the laser beams or some other phenomenon is occurring. Sharp peaks in excess power were found at laser frequency differences of 8, 15 and 20 THz. The first two frequencies are consistent with optical phonon frequencies in PdD. This indicates that such phonon modes are relevant to the mechanism for LENR in Pd.

Tsuchiya and his colleagues observed optical phonons in PdH and PdD using Raman spectroscopy. Raman peaks were found at 56 meV in PdH and both 57 meV and 59 meV in PdD. Note that 56 meV corresponds to 13.5 THz. Large effects, indicative of nuclear reactions, were not found in these experiments.

Swartz and his colleagues measured the spatial distributions and time histories of near infrared emissions from operating electrochemical cells. The observed infrared radiation was judged to be non-thermal because it appeared to be linked to an active cell's excess heat production and not its physical temperature. It was asserted that the observations might confirm the Bremsstrahlung-shift hypothesis. The idea is that a temperature-controlled shift from

penetrating ionizing radiation to infrared radiation from the surface of a cathode (within the skin depth) might accompany low-temperature nuclear reactions.

X-ray emissions from LENR experiments are frequently measured. Three papers found in other sections of these Proceedings include measured x-ray data. They are the paper by Karabut and Karabut in the section on Heat Measurements, the paper by Storms and Scanlon in the section on Particle Measurements and the paper by Kornilova in the section on Cavitation Experiments.

In this section, we include a paper reporting remarkable x-ray results. Karabut and Karabut measured x-ray emission in the photon energy range of 0.6 to 10.0 keV in glow discharge experiments. A wide variety of gases and cathode materials was used. The authors report the measurement of laser microbeams with 10^{-4} radian beam divergence, sub-picosecond emission times and x-ray powers of 10^7 to 10^8 W. Further, they state such emissions occurred within about 100 msec after turning off the discharge current.

More LENR electromagnetic emission and probe experiments are needed. There are many interesting reports that will influence (constrain) theories for the mechanism(s) active in these experiments. However, most of the experiments have not been adequately reproduced by other investigators, and many of them would benefit from the use of available modern apparatus for more sophisticated measurements.

Excess Heat Triggering by 532 nm Laser in a D/Pd Gas-Loading System

J. Tian, L. H. Jin, B. J. Shen, Z. K. Weng and X. Lu

*New Hydrogen Laboratory, Changchun University of Science and Technology
7989 Weixing Road, Changchun, Jilin 130022, PR China*

Abstract

A laser ($\lambda=532$ nm) operated in three modes (continuous, static pulsed and dynamic pulsed) was used to irradiate a series of palladium deuterides with different deuteron loading ratios in a D/Pd gas-loading system. (The loading ratios were D/Pd=0, 0.08, 0.10, 0.17 and 0.27.) The results showed that static pulsed triggering produces a maximum excess heat effect of about 2.6 kJ within a half hour when the loading ratio of Pd was about 0.1 and input power was 25 mW. This corresponds to 4.9×10^{-15} J/atom D or 1.8×10^4 W/cm³ Pd. The reason the static pulsed triggering produced more excess heat than other two modes needs to be further studied. The proper ratio in the Pd lattice matching a suitable triggering power may be a key point for heat production.

Key words: D/Pd gas-loading system, heat triggering, static pulsed laser, loading ratio, excess heat.

1. Introduction

Laser stimulation is one of the most potentially useful methods of triggering excess heat in cold fusion (or Condensed Matter Nuclear Science). Letts and Cravens^[1] presented this method for the first time in 2003, reporting that it generates highly reproducible significant excess heat from deuterated palladium electrodes in a heavy water cell. V. Violante^[2] and K. Sinha^[3] repeated and modified the Letts experiment in 2005 and 2006. In 2007, we^[4] found transmutation effects on the surface of Pd after exposure to a H₂ gas-loading system and was irradiated with a YAG frequency doubling laser. A gas-loading system can reach a relatively higher temperature with the same amount of input energy or excess heat than an electrolysis system can, due to the lower heat capacity of gas. But we did not find clear evidence for an anomalous exothermic effect. To improve the situation, a D/Pd gas-loading system was chosen and a new kind of triggering laser was applied. The laser has the same wavelength as before ($\lambda=532$ nm) but three different working modes were used: continuous, static pulsed and dynamic pulsed.

2. Experimental

2.1 Materials and equipments

A schematic of the experimental system was shown in reference^[4]. Both the reaction chamber and Pd material were the same as the previous study, but the Pd wire length ($l=50$ cm) was shorter. The spot length irradiated by the laser was about 1 cm, with a volume of about

$7.8 \times 10^{-5} \text{ cm}^3$ and contained 5.3×10^{18} Pd atoms. The deuterium gas was produced by an Ultra-Pure Gas Generator (Model DCH-IV, Beijing Tianwuyuan Company, China), which can produce D_2 gas with more than 99.999% purity. Pt-100 resistance thermometers monitored four temperatures: inside and outside the chamber; the whole Pd body; and the laser spot on the Pd wire. The loading ratio (x) of Pd wire was calculated by current and voltage with the four-wire resistance measurement method. A data acquisition system (Keithley 2700) was used for record the voltage and current in the Pd circuit and all temperatures. The laser (Changchun Zhongji Optical Electronic Company) wavelength was 532 nm after doubling frequency; pulse frequency was 1 s^{-1} ; pulse width was 50 μs for the static mode and 20 ns for the dynamic mode. The working voltage was 850 V, and maximum output power was 2.0 W. Another new feature of this gas-loading apparatus was the precision of its water circulation system. By adding isothermal material outside the flask the temperature fluctuating due to ambient temperature change decreased to $\pm 0.1^\circ\text{C}$.

2.2 Experiment process and results

2.2.1 Heat triggering of Pd wire with continuous laser

At the beginning of the experimental run, the pure palladium wire was irradiated with the laser as control. Then the wire was charged with deuterium in different ratios: 0.08, 0.10, 0.17 and 0.27. A spot on the wire was continuously irradiated with the laser for 1800 s. The temperature responses for different loading ratio were recorded by the data acquisition system. The results are shown in Figure 1.

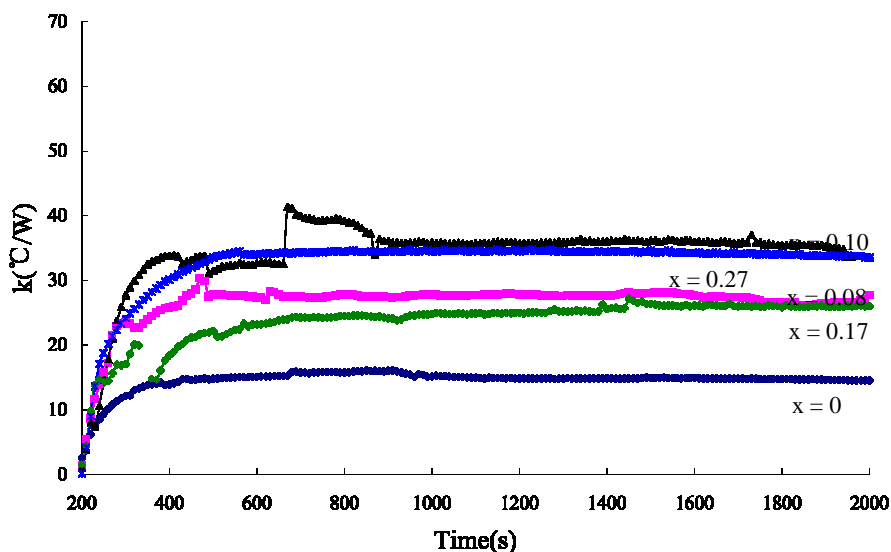


Figure 1. Heat responses of Pd wire with different D_2 loading ratios, triggered by a continuous laser. “ x ” represents the loading ratio.

2.2.2. Heat triggering of Pd wire with dynamic and static pulsed laser

The same Pd wire with the same deuterium loadings was triggered with dynamic pulsed laser (pulse width 20 ns) and static pulsed laser (pulse width 50 μ s) for 1800 s. The temperature responses for each triggering mode are shown in Figures 2 and 3.

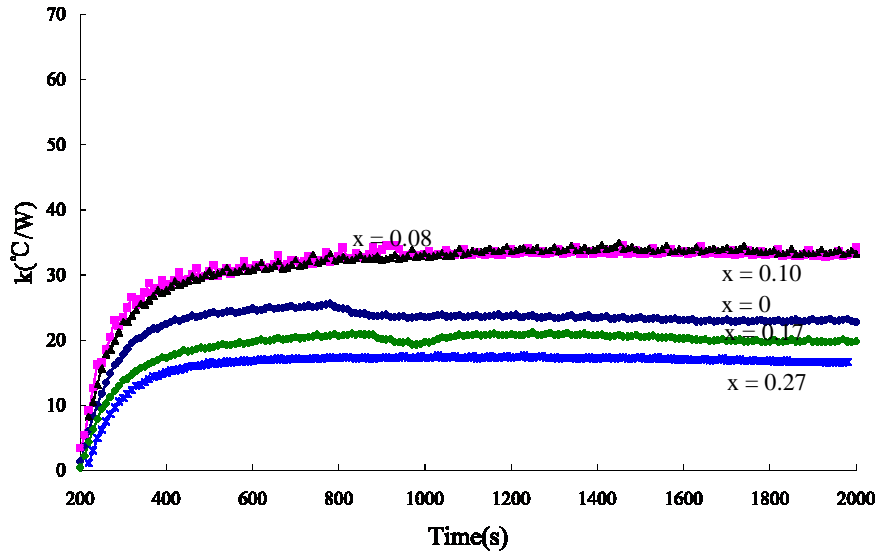


Figure 2. Heat responses of Pd wire with different D₂ loading ratios triggered by dynamic pulsed laser

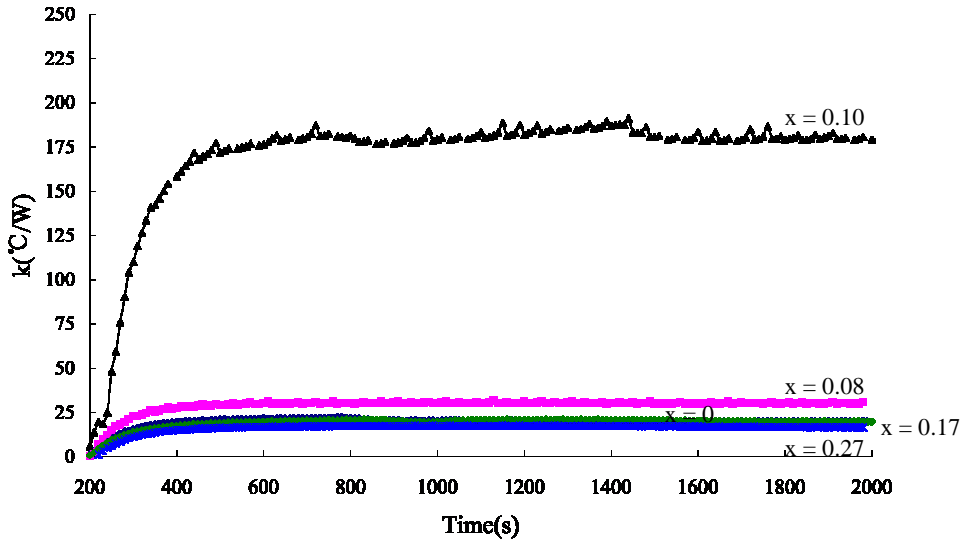


Figure 3. Heat responses of Pd wire with different D₂ loading ratios triggered by static pulsed laser

3. Analysis and discussion

3.1 The excess heat and excess power estimation

The excess heat and excess power were roughly estimated based on the following equations:

$$Excess\ heat = [(k - k_0) / k_0] \times E_{in} \text{ (Joule)}$$

$$Excess\ heat\ power = [(k - k_0) / k_0] \times P_{in} \text{ (Watt)}$$

where k is the System Constant. $k = \Delta T / \Delta P$ ($^{\circ}\text{C} / \text{W}$), in which ΔP was the difference of input power (W), ΔT was the difference of output temperature ($^{\circ}\text{C}$).

3.2. Excess heat and excess power calculation

For each triggering mode, a set of data was collected and calculations were made. Results are listed in Tables 1 to 3.

Table 1. Data and calculations for continuous laser triggering

x (D/Pd)	k ($^{\circ}\text{C} / \text{W}$)	P_{input} (mW)	Q_{input} (J)	Q_{eh} (J)	$Q_{eh} /$ Q_{input}	Q_{eh} / atom Pd (J)	Q_{eh} / atom D (J)
0	14.8	117	200	—	—	—	—
0.08	26.8	57.2	103.0	162	1.6	3.0×10^{-17}	3.8×10^{-16}
0.10	35.3	42.8	77.2	277	3.6	5.2×10^{-17}	5.2×10^{-16}
0.17	24.4	48.4	96.8	130	1.3	2.4×10^{-17}	1.4×10^{-16}
0.27	33.3	35	62.4	250	4.0	4.7×10^{-17}	1.7×10^{-16}

Table 2. Data and calculations for dynamic pulsed laser triggering

x (D/Pd)	k ($^{\circ}\text{C} / \text{W}$)	P_{input} (mW)	Q_{input} (J)	Q_{eh} (J)	$Q_{eh} /$ Q_{input}	Q_{eh} / atom Pd (J)	Q_{eh} / atom D (J)
0	23.7	166.3	299.3	—	—	—	—
0.08	32.9	45.5	82.0	116.8	1.4	2.2×10^{-17}	2.7×10^{-16}
0.10	32.8	93.9	168.1	114.9	0.7	2.1×10^{-17}	2.1×10^{-16}
0.17	20.1	89	161.1	—	—	—	—
0.27	17.1	83.9	151.1	—	—	—	—

Table 3. Data and calculations for static pulsed laser triggering

x (D/Pd)	k ($^{\circ}\text{C} / \text{W}$)	P_{input} (mW)	Q_{input} (J)	Q_{eh} (J)	$Q_{eh} /$ Q_{input}	Q_{eh} / atom Pd(J)	Q_{eh} / atom D(J)
0	20.6	191.2	344.2	—	—	—	—
0.08	32.1	71.8	128.5	192.9	1.5	3.6×10^{-17}	4.5×10^{-16}
0.10	177.5	25	45.7	2623.3	57.4	4.9×10^{-16}	4.9×10^{-15}
0.17	20.2	176.7	319.3	—	—	—	—
0.27	16.9	159	278.0	—	—	—	—

3.3 Description and discussion

From Figure 1 and Table 1 it can be seen that when the laser was continuously output, the largest heat responses and exothermic behavior was observed, no matter what the loading ratio was. The amount of heat was relatively small. For pulsed triggering, the dynamic mode produced better results when the loading ratio was less than 0.1, which can be seen in Figure 2 and Table 2. The most anomalous phenomena appeared with pulsed triggering with a static mode. When loading 0.1 and input power was 25 mW, the heat response from the Pd wire increased up to $k = 177^{\circ}\text{C}/\text{W}$ (see Figure 3 and Table 3), an astounding result. That meant each deuteron released 4.9×10^{-15} J, and the excess heat power density reached 1.8×10^4 W/cm³ Pd. The reason for this anomalous phenomenon needs to be further discussed. There might have been some resonant tunneling mechanism between deuterons with the help of palladium lattice, which was described by Dr. Li ^[5] in 2000.

4. Conclusions

Three conclusions could be drawn from the experiment:

1. D/Pd gas loading system has higher sensitivity to detect anomalous heat than the electrolysis method.
2. For excess heat by laser triggering, not only the wavelength but also a working model is important. Pulsed laser light might be more effective than continuous light.
3. It seems that palladium deuteride with high loading ratios need stronger triggering power to release more excess heat.

References

1. D. Letts and D. Cravens. Laser Stimulation of Deuterated Palladium: Past and Present. Infinite Energy, Vol. 50, 2003, p10
2. V. Violante, , M. Bertolotti, E. Castagna, I. Dardik, M. McKubre, S. Moretti, S. Lesin, C. Sarto, F. Tanzella, T. Zilov. Progress in Excess Power Production by Laser Triggering, Proceedings of 12th International Conference on Condensed Matter Nuclear Science. Yokohama, Japan, Nov. 27- Dec. 2, 2005, p. 55
3. K. P. Sinha and A. Meulenberg. Laser stimulation of low-energy nuclear reactions in deuterated palladium. Current Science, Vol. 91, No. 7, Oct. 10, 2006, p. 907
4. J. Tian and L. H. Jin *et al.*, Heat Measurements and Surface Studies of Pd Wires after Being Exposed to a H₂ Gas-Loading System Irradiated with a YAG Frequency Doubling Laser. The 13th International Conference on Condensed Matter Nuclear Science. Sochi, Russia, 2007. <http://lenr-canr.org/acrobat/TianJheatmeasur.pdf>
5. X.Z. Li, J.Tian, M.Y. Mei, and C.X. Li. Sub-Barrier Fusion and Selective Resonant Tunneling. Physical Review C, Vol. 61, 2000, p. 4610

Stimulation of Optical Phonons in Deuterated Palladium

Dennis Letts¹ and Peter Hagelstein²

¹ 12015 Ladrido Lane

Austin, Texas 78727

²Research Laboratory of Electronics,

Massachusetts Institute of Technology, Cambridge, MA

Progress made since 2007 in the triggering of excess power by terahertz stimulation of deuterated palladium is reported. The stimulation was provided by tuning dual lasers to one of three specific beat frequencies corresponding to the known optical phonon frequencies of deuterated palladium (8, 15, 20 THz). Results so far imply that optical phonons may be involved in the Fleischmann-Pons effect, giving preliminary support to Hagelstein's phonon theory.

1. Introduction

As is well known by now, Fleischmann, Pons and Hawkins first proposed the idea that nuclear reactions might be induced in deuterated palladium on March 23, 1989 [1]. The idea was controversial from its inception and was based on experimental results, not established nuclear theory. Due to the absence of energetic particles commensurate with the energy produced, whatever process is responsible must involve new physics.

In 1993 Miles and his collaborators reported the presence of ⁴He in roughly the amount expected from the mass energy different from two deuterons, suggesting that it was produced in amounts commensurate with the excess energy observed [2]. There is now enough diverse experimental evidence to suggest that a new nuclear process is occurring in the solid state at room temperature.

1.1. Hagelstein's Phonon Theory

From the beginning, one of the authors (Hagelstein) pondered the role of phonons in the solid state fusion of deuterium. His early work proposed a coherent fusion mechanism in which nuclear energy is coupled into phonon modes (reference [3], presented at the ASME meeting December, 1989). In his conjecture 4, page 847 of reference [4], one finds: "Anomalies in metal deuterides are stimulated by strong phonon excitation." Hagelstein suggests that the optical phonon modes are the most likely candidates, especially the modes with low group velocity typically located at the edge of an optical phonon mode [5]. In palladium deuteride, the band edges occur near 8 and 15-16 THz [6,7].

2. Experiment Meets Theory

The work discussed in this paper began in March 2007 as a series of experiments conducted by Letts and Cravens in collaboration with Hagelstein. Our goal was to see if an experimental connection could be made with the phonon aspects of Hagelstein's theory. Before experiments were run, Hagelstein predicted that the edges of the optical phonon band would be the best candidates for stimulation to produce excess power. This region is where low group-velocity

compressional phonon modes exist. This is consistent with our observations near 8 and 15 THz but the response near 20 THz requires an alternate explanation. Perhaps the simplest conjecture for this higher frequency response is due to proton contamination, which might be expected to produce a zero-group velocity band edge near 20 THz.

2.1. Instrumentation and Calorimetry

This work covers 19 tests from 3 cells; two time periods are involved – March 2007 to May 2007 and then April 2008 to the present. The goal of this work is the creation of a beat frequency versus excess power graph to determine if stimulation of the three optical phonon modes of palladium deuteride leads to the observation of excess power.

All experiments were conducted in Austin, Texas. Isoperibolic calorimetry was used on all tests. The standard deviation of power output from the calorimeter was approximately 20 mW and was very stable over a typical 10 hour experimental run (Figure 1).

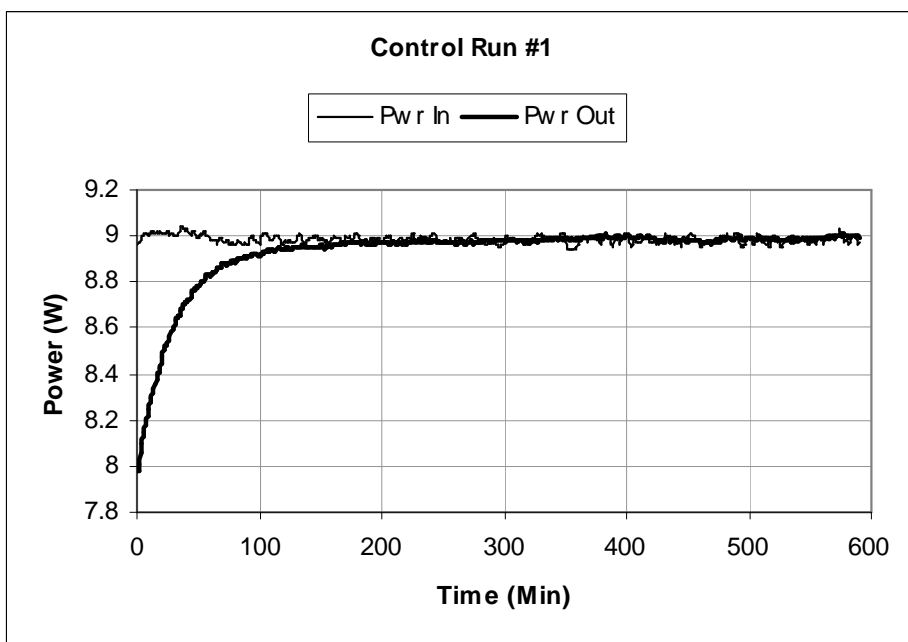


Figure 1. The isoperibolic calorimeter demonstrates good long-term stability when the cell is not producing excess power.

2.2 Experimental

Our cells were closed and consisted of a rectangular billet of palladium as the cathode and a coiled platinum wire as anode. The electrolyte was typically 100 mL of LIOD at 0.5 M concentration. This work consists of 49 data points from 19 runs and 3 electrolysis cells. The data points are listed table 1 (see the Appendix). We plotted the data in table 1 and a clear pattern emerged showing three frequencies capable of triggering excess power from deuterated palladium.

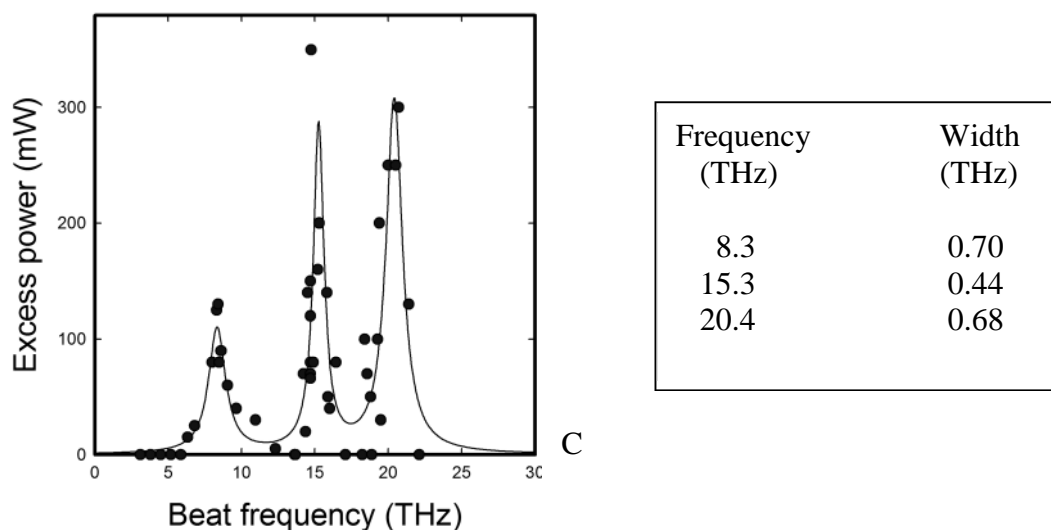


Figure 2. Three specific triggering beat frequencies. Vertical scale is XP in mW. Also shown is a curve from a least squares fit to a sum of three Lorentzians $\sum c_j/[(\omega-\omega_j)^2+\gamma^2]$, where the center frequencies $(\omega_j/2\pi)$ and broadening (width= $\gamma_j/2\pi$) parameters are indicated.

3. Discussion

Can these experiments connect with any known physics? On the face of it, the observation of a thermal response at the specific beat frequencies 8, 15 and 20 THz [Figure 2] combined with the observed dependence on polarization implicates compressional optical phonon modes in PdD as participating in the physical process responsible for excess heat production in the Fleischmann-Pons excess heat effect. The lower two specific beat frequencies observed (8 and 15 THz) are consistent with the interpretation of optical phonon modes with low group velocity in PdD. The higher frequency response (20 THz) represents a conundrum for a PdD explanation, since it lies above the LO band edge. One possible resolution of this is to assume that H is present as a significant impurity, and that 20 THz is due to an LO band edge associated with hydrogen in mixed PdD_xH_y . Whether this is the case or not can be determined in future experiments where the hydrogen content of the heavy water is better controlled. Additionally, our results motivate theoretical studies with mixed hydrogen and deuterium loading to verify under what conditions, if any, a splitting of the LO band near the band edge occurs.

Acknowledgements

Thanks to Christy Frazier and the New Energy Foundation for support of this research. Thanks also to Edmund Storms, Michael McKubre and Francis Tanzella for corrections and suggestions.

Appendix Table 1. 49 data points from 3 cells tested in 2007 and 2008 at 50-60°C.

No.	Experiment	Date	Freq. (THz)	XP(mW)
1	662n	3/25/2007	3.12	0
2	662n	3/25/2007	3.81	0
3	662n	3/25/2007	4.50	0
4	662n	3/25/2007	5.18	0
5	662n	3/25/2007	5.86	0
6	662n	3/25/2007	6.33	15
7	662n	3/25/2007	6.80	25
8	662i	3/21/2007	8.00	80
9	662g	3/20/2007	8.30	125
10	662k	3/22/2007	8.40	130
11	662i(2)	3/21/2007	8.48	80
12	662i(2)	3/21/2007	8.61	90
13	662i(2)	3/21/2007	9.06	60
14	662i(2)	3/21/2007	9.65	40
15	662i(2)	3/21/2007	10.95	30
16	662i(2)	3/21/2007	12.31	40
17	662i	3/21/2007	13.62	0
18	662i(2)	3/21/2007	13.68	20
19	662i	3/21/2007	14.23	70
20	662i(2)	3/21/2007	14.36	20
21	662f1	4/13/2007	14.50	140
22	662j1	4/15/2007	14.70	70
23	662w	3/31/2007	14.70	70
24	662y	4/2/2007	14.70	120
25	662a1	4/4/2007	14.70	80
26	662j1	4/15/2007	14.70	150
27	662s1	4/23/2007	14.70	66
28	669a1	5/8/2008	14.75*	350
29	662i(2)	3/21/2007	14.88	80
30	662f1	4/13/2007	15.20	160
31	662a1	4/4/2007	15.30	200
32	662f1	4/13/2007	15.82	140
33	662b2	5/5/2007	15.90	50
34	662w	3/31/2007	16.02	40
35	662f1	4/13/2007	16.45	80
36	662f1	4/13/2007	17.09	0
37	662i2	3/21/2007	18.23	0
38	662c2	5/5/2007	18.40	100
39	662w	3/31/2007	18.56	70
40	662t1	4/25/2007	18.80	50
41	662i2	3/21/2007	18.87	0
42	670a	6/6/2008	19.28	100
43	662o	3/25/2007	19.40	200
44	662i2	3/21/2007	19.50	30
45	669u	4/30/2008	20.00	250
46	662x1	4/29/2007	20.50	250
47	662o2	5/17/2007	20.70	300
48	662i2	3/21/2007	21.40	130
49	669a1	5/8/2008	22.11	0

References

1. Pons, Fleischmann and Hawkins, Electrochemically Induced Nuclear Fusion of Deuterium. *Journal of Electroanalytical Chemistry*, 261 (March, 1989) 301-308.
2. Miles et al., Correlation of Excess Power and Helium Production during D₂O and H₂O Electrolysis using Palladium Cathodes, *Journal of Electroanalytical Chemistry*, 346 (1993) 99-117.
3. Hagelstein, P. L., "Coherent Fusion Theory," 1989 ASME Winter Annual Meeting, paper 89-WA/TS4, San Francisco, CA, December 1989; *J. Fusion Energy*, **9**, 451-464 1990.
4. Hagelstein, Peter L., Unified Phonon Coupling SU(N) Models for Anomalies in Metal Deuterides, Tenth International Conference on Cold Fusion, Cambridge, MA 2003.
5. Hagelstein, Peter L., Progress Toward a Theory for Excess Heat in Metal Deuterides, Current Trends in International Fusion Research, the seventh symposium, National Research Council of Canada, 2007.
6. Rowe, J. M., J.J. Rush, H. G. Smith, M. Mostoller, H.E. Flotow, *Phys. Rev. Lett.* **33**, 1297 1974.
7. Glinka, C.J. J.M Rowe, J. J. Rush, A. Rahman, S.K. Sinha and H.E. Flotow, *Physical Review B* vol. **17**, p 488, 1978.

Observation of Optical Phonon in Palladium Hydrides Using Raman Spectroscopy

Ken-ichi Tsuchiya¹, Aya Watanabe¹, Masao Ozaki² and Shigeru Sasabe³

¹ Tokyo National College of Technology, 1220-2 Kunugida, Hachioji, Tokyo 193-0997

² Tokyo University of Agriculture, 1-1-1 Sakuragaoka, Setagaya, Tokyo, 156-8502

³ Tokyo Metropolitan University, 1-1 Minami-Ohsawa, Hachioji, Tokyo 192-0397

Abstract

The techniques of hydrogen loading in Pd are developed by many workers. And the states of hydrogen in Pd attract many interests because they might be related to the nuclear reactions. In this study, we have tried to observe optical phonon induced by hydrogen-hydrogen interactions in Pd using Raman spectroscopy. This measurement can be done for the sample completely sealed in a glass tube cutting off the influence of the external air, because glass materials are Raman inactive. In the measurement chamber of spectroscopy device, scattered waves of the incident laser beam from the hydrogen storage Pd are detected and Raman shifts including the information about the optical phonon in the sample are derived.

If the large changes in Raman spectra are found, they will help explain the nuclear effects in condensed states of palladium hydride. So far, we have not found large changes, but the peaks of Raman shift at 56 meV both for PdH_x and PdD_x are detected. The peaks for PdH_x are consistent with the data of Sherman *et al.* at 58.5 meV. However, the peaks for PdD_x are inconsistent with Sharman's result at 39.7 meV.

1. Introduction

In order to detect nuclear reactions in solids, calorimetry to measure the heat from the nuclear reaction has been used in many cases. However, it is not easy to measure heat only from nuclear reactions, because heat of formation of the hydrogen storage process is also generated in these systems. Mass spectroscopy also has been used for analyzing the nuclear products. However, it is not easy to do in-situ measurement. In this study, we have tried to develop the third way to detect the nuclear reaction in palladium hydrides, using Raman spectroscopy.

Raman spectroscopy is the method used to observe optical phonon in the molecular vibration or lattice vibration. When laser light is scattered from lattice vibration, most photons are elastically scattered. This is called Rayleigh scattering. However, a small fraction of scattered wave has different frequency from incident waves. In this case, the frequency shift $\Delta\nu$ is called Raman shift, which is created by the interaction between incident laser light and optical phonon. If the frequency of the scattered wave is increased, it is called anti-Stokes scattering. If it is decreased, it is called Stokes scattering. For example in Stokes scattering, the ground state phonon is excited to the virtual state by the incident laser wave, and then return to the first

exited state. So, it is inelastic scattering and Raman shift $\Delta\nu$ includes the information about the lattice vibration.

In usual Raman spectroscopy, only the optical phonon is Raman active, while the acoustical phonon is inactive. This means that Raman spectroscopy is not appropriate for analyzing the lattice vibration of pure Pd, because a face centered cubic lattice with one atom per primitive cell only has acoustical lattice vibrations [1]. Fortunately, H-H (D-D) interactions in Pd induce optical vibrations [2], and we can use Raman spectroscopy for hydrogen storage Pd. In this case, Raman shift $\Delta\nu$ directly includes the information about H-H (D-D) interactions. This was pointed out by R. Sherman *et al.* [3]. In this study, we observed the Raman shifts of PdH_x and PdD_x , and discussed the H-H (D-D) interactions.

2. Experimental

We used two types of samples. One is plate and the other is powder. The size of plate Pd is $5 \times 5 \times 0.5$ mm, and the average radius of powder Pd is 0.5 mm. A sketch of the device for gas loading is shown in Fig. 1.

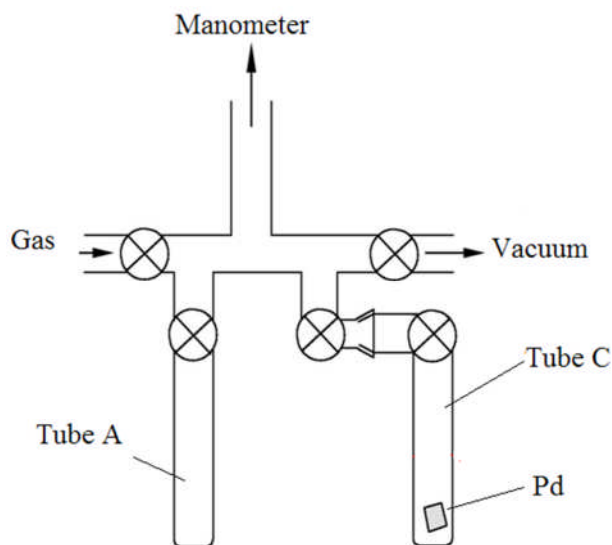


Figure 1. Sketch of the hydrogen storage apparatus.

We used 99.9% H_2 , 99.6% D_2 and 99.9% Pd. The atomic ratios of H/Pd and D/Pd were determined by constant volume method with the equation of states.

After loading, the tube C in Fig. 1 was removed by closing the cock, and put into the detection chamber of the Raman spectroscopy (NRS3100, JASCO). The excitation wavelength of the Raman spectroscopy is 532.25 nm.

3. Results and Discussion

The Raman spectra of plate PdH_x are shown in Fig. 2. In all cases, the peak position is 56 meV, which is consistent with the Sherman's results [3]. The peak at 210 meV corresponds to Ne, which was used as a reference signal. The peak at 80 meV corresponds to PdO. The surface of the pure Pd plates we used was slightly oxidized and PdO peak was detected. In order to compare the results for each hydrogen concentration, the arbitrary unit is adopted for vertical axis.

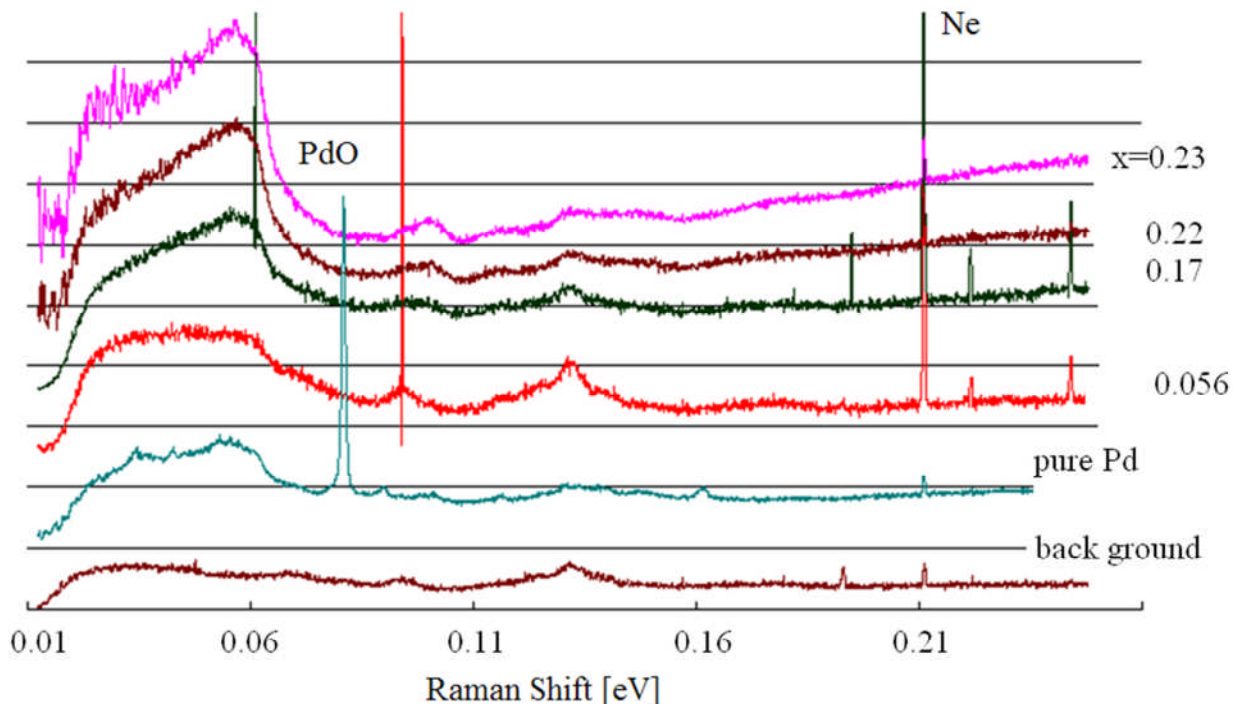


Figure 2. Raman spectra of plate PdH_x .

Raman spectra of PdD_x for powder and plate samples are shown in Fig. 3. The equivalent D/Pd ratios for powder and plate samples are 0.90 and 0.14, respectively. A broad peak exists at 59 meV for powder sample, and a sharp peak exists at 57 meV for plate sample. The differences between two spectra in Fig. 3 depend on the shape of the samples and D/Pd ratio. In the Sherman's result for PdD_x , a peak exists at 40 meV [3], which is smaller than our results. These differences depend on the temperature. Our experiments were done at room temperature, while Sherman's were done at 84 K.

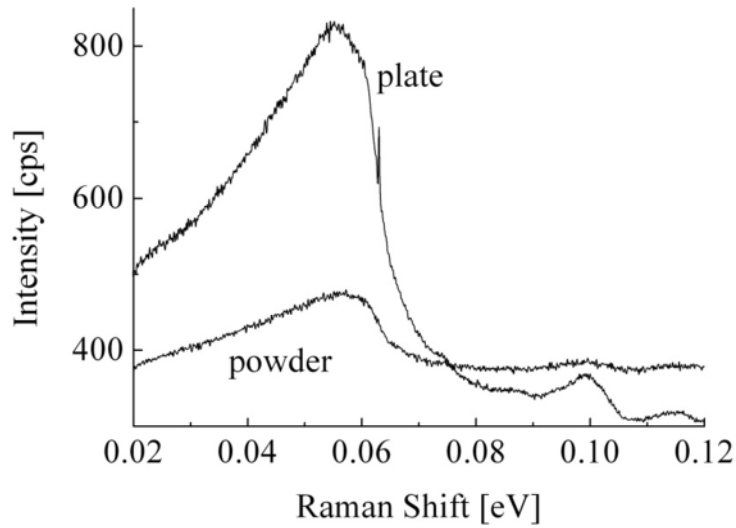


Figure 3. Raman shift for powder $\text{PdD}_{0.90}$ and plate $\text{PdD}_{0.14}$.

Twenty-four hours after the first measurement, we tried to measure the Raman spectra of the same samples. In all cases, results were nearly the same as first spectra (Figs. 2 and 3). If nuclear reactions had occurred in the sample during the 24-hour period, large changes between the spectra should have been observed. However, we did not find them. In near future, we will try to stimulate the hydrogen (deuterium) storage Pd by laser light with a wavelength different from the incident wave in Raman spectroscopy. If reactions are induced by this stimulation, large changes in spectra should be seen.

4. Conclusions

- (1) In this study, we have demonstrated a method of getting information about optical phonon in palladium hydrides (and deuterides) using Raman spectroscopy. The elementary results for the Raman spectra of hydrogen storage Pd were obtained.
- (2) In Raman spectra of PdH_x , a peak exists at about 56 meV for all concentrations. It is consistent with Sherman's results [3].
- (3) In Raman spectra of plate PdD_x , a peak exists at 57 meV. With powder PdD_x , a peak exists at 59 meV. They are not consistent with Sherman's results at 40 meV [3]. These differences depend on the temperature. Our experiments were done at room temperature, while Sherman's were done at 84 K.
- (4) The optical phonon in palladium hydrides (and deuterides) is induced by H-H (D-D) interactions. So, large changes of the spectra should indicate the effects of nuclear reactions. However, such large changes were not observed.
- (5) In near future, we will try stimulation by laser light with palladium hydrides (and deuterides), and we will measure the Raman spectra. If the large changes in Raman spectra are found, this may help explain nuclear reaction effects in condensed states of hydrogen in Pd.

Acknowledgements

The authors wish to thank Professor Hideo Kojima for the helpful discussions and encouragements during our trip to Washington. We also wish to thank Professor Noboru Akuzawa of TNCT for the advices on the hydrogen storage techniques.

References

1. C. Kittel, *Introduction to Solid State Physics*, John Wiley and Sons, Section 5.
2. J. M. Rowe, J. J. Rush, H. G. Smith, M. Mostoller and H. E. Flotow, "Lattice Dynamics of a Single Crystal of $\text{PdD}_{0.63}$ ", *Phys. Rev. Letts.*, **33**,1297(1974)
3. R. Sherman, H. K. Birnbaum, J. A. Holy and M. V. Klein, "Raman studies of hydrogen vibrational modes in palladium", *Phys. Lett.*, **62A**(1977)353

Non-Thermal Near-IR Emission from High Impedance and Codeposition LANR Devices

Mitchell Swartz, Gayle Verner and Alan Weinberg
JET Energy, Inc. Wellesley, MA (USA)

Dr. Mitchell Swartz does not wish to have his papers uploaded to LENR-CANR.org. A copy of this paper can be found here:

<http://www.iscmns.org/iccf14/ProcICCF14a.pdf>

This page intentionally left blank

This page intentionally left blank

This page intentionally left blank

This page intentionally left blank

This page intentionally left blank

This page intentionally left blank

This page intentionally left blank

This page intentionally left blank

This page intentionally left blank

This page intentionally left blank

This page intentionally left blank

This page intentionally left blank

This page intentionally left blank

This page intentionally left blank

This page intentionally left blank

This page intentionally left blank

This page intentionally left blank

This page intentionally left blank

Research into Spectra of X-ray Emission from Solid Cathode Medium During and After High Current Glow Discharge Operation

A. B. Karabut¹ and E. A. Karabut²

¹*FSUE "LUCH" 24 Zheleznodorozhnaya St, Podolsk, Moscow Region, 142100, Russia.*

Tel. (095) 5508129; Fax (095) 5508129

²*Moscow Power Engineering Institute (Technical University)*

Abstract

X-ray emissions ranging from 0.6 to 10.0 keV with a dose rate up to 0.1 J/s have been detected in experiments with high-current glow discharge. The experiments were carried out on the high-current glow discharge device using H₂, D₂, He, Kr, Ar and Xe at pressure up to 10 Torr, as well as cathode samples made from Al, Sc, V, Ti, Ni, Nb, Zr, Mo, Pd, Ta, W, Pt, at current up to 500 mA and discharge voltage of 1500 – 4500 V. Two emission modes were revealed under the experiments: 1. Diffusion X-rays was observed as separate X-ray bursts (up to 10⁵ bursts a second and up to 10⁶ X-ray quanta in a burst); 2. X-rays in the form of laser microbeams (with up to 10⁴ beams a second and up to 10¹⁰ X-ray of quanta in a beam; angular divergence up to 10⁻⁴; duration of the separate laser beams $\tau = 3 \cdot 10^{-13}$ - $3 \cdot 10^{-14}$ s; and individual beam power 10⁷ to 10⁸ W). The emission of the X-ray laser beams occurred when discharge occurred and within ~100 ms after turning off the current. The X-ray spectra were recorded on film with the curved mica crystal X-ray spectrometer. The X-ray emission spectrum from the Pd and other cathode material consists of spectral bands with energies ranging from 0.6 keV up to 10.0 keV.

1. Introduction

Experimental results detecting excess heat nuclear reaction products in the high-current glow discharge cathodes prove that there exist certain conditions and mechanisms that lead to the initiation of Low Energy Nuclear Reactions (LENR) in the condensed medium of the solid cathode. The formation of excited levels with energies ranging from 1.0 to 3.0 keV and lifetimes up to several milliseconds is assumed to be a necessary condition for LENR to proceed in the cathode solid medium (with the density up to 10²⁷ atom/m³). This may be achieved by devising a mechanism for conversion of 0.5 – 3.0 keV plasma ions flux initial energy into 0.5 to 10.0 keV high-energetic excitation of a solid nuclear electron system. Presumably such a conversion takes place in the cathode solid exposed to bombardment by the discharge plasma ions. This process is evidenced by intensive X-ray emission during glow discharge and after glow discharge current switch off. The energetic and temporal characteristics of the X-rays are determined by the energy and lifetime of the excited energetic levels in the cathode solid medium.

2. Experimental device

The measurements were carried out using a glow discharge device consisting of a water-cooled vacuum chamber and the cathode and the anode assemblies (Fig. 1). The cathode design allowed the placement of cathode samples made of various materials on a water-cooled surface. The experiments were carried out using a high-current glow discharge in D_2 , H_2 , He, Kr and Xe and the cathode samples are made of Al, Sc, Ti, Ni, Nb, Zr, Mo, Pd, Ta, W.

The X-ray emission detection was carried out by X-ray pinhole, thermo-luminescent detectors, and a scintillation detector with a photomultiplier. The energy spectrum of the X-ray emission was recorded with a curved mica crystal spectrometer. The cathode samples made of Pd and other metals were placed on a cathode-holder above which there is a window for the penetrating radiation output from the cell. The window was shielded by 15 μm -thick Be foil to protect the detectors from visual and ultraviolet radiation. Various detectors were installed by the window to measure the output penetrating radiation (Fig. 1).

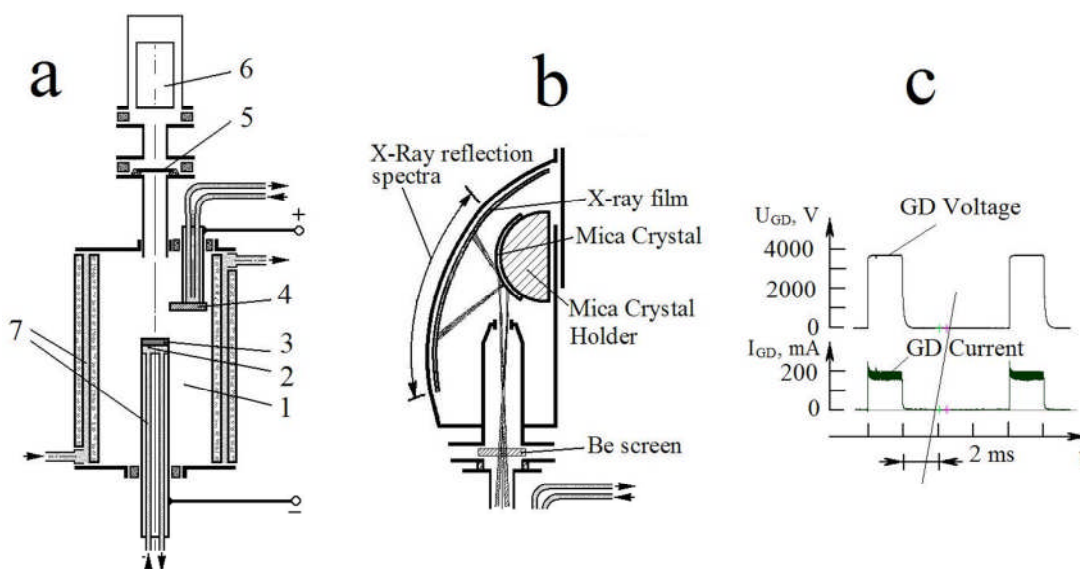


Figure 1. Schematic representation of the experiment. a. Glow discharge device, 1 – discharge chamber, 2 – cathode holder, 3 – cathode sample, 4 – anode, 5 – Be foil screens, 6 – X-ray detectors different kind (pinhole, TLD detectors, scintillator- photomultiplier, spectrometer), objective, 7 –cooling water; b. X-ray spectrometer, c. Glow discharge voltage and current oscillograms.

The glow discharge device power supply is designed to feed the glow discharge with a pulse-periodic direct current and permits the generation of the desired current forms of various pulse lengths and pulse periods, and to obtain the required current voltage. The power supply produced direct pulse-periodic current with a rectangular pulse shape (Fig. 1c). In different experiments the pulses duration varied from 0.1 ms up to 2.0 ms, and the period was from 0.3 ms up to 100 ms. The glow discharge conditions were following: current (amplitude) was from 30 mA up to 300 mA, voltage 1500 – 4300 V.

3. Experimental method and results

3.1. Pinhole method and results

The high intensity of the X-rays made it possible to obtain an optical image of the X-ray emission area with an X-ray pinhole. The X-ray measurements were confirmed by experiments with a transverse 0.3 T magnetic field induced upon the emission X-ray flux.

3.2. TLD detector method and results

To estimate the intensity and evaluate the mean energy of the soft X-ray emission in the glow discharge, thermo-luminescent detectors (TLD) based on crystalline Al_2O_3 and covered by Be foils of varying thickness were used. TLD measurements revealed that X-ray radiant intensity from the cathode increase exponentially with the increase in the glow discharge voltage (Fig. 2).

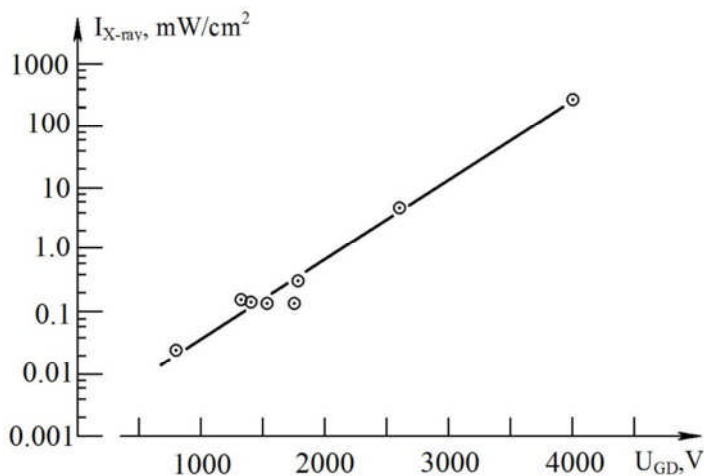


Figure 2. X-ray radiant intensity in relation to the glow discharge voltage.

3.3. Scintillation photomultiplier method and results

The temporal characteristics of the penetrating radiation were determined with scintillation detectors with photomultipliers (PM). Two modes of radiation emission were observed in the experiments: 1. Diffusion X-ray emission (Fig. 3a) and 2. X-ray emission in the form of laser beams (Fig. 3b). The diffusion X-ray emission occurs mainly during the current running in the form of flashes and conforming to the law $1/r^2$.

The generation of X-ray emission in the form of laser beams begins when glow discharge parameters increase (including current impulse duration time, current density and discharge voltage). The laser beams are observed as powerful flashes (Fig. 3b). The X-ray laser beams consist of the separate beams of a small size (up to 10^9 - 10^{10} photons, assuming that the system scintillator-PEM is operating in the linear field). The emission of X-ray laser beams occurs during discharge and up to 100 ms and more after turning off the current. Under certain discharge parameters the generation of X-ray laser beams lasts only milliseconds after turning off the discharge current (up to 20-30 beams after each current pulse).

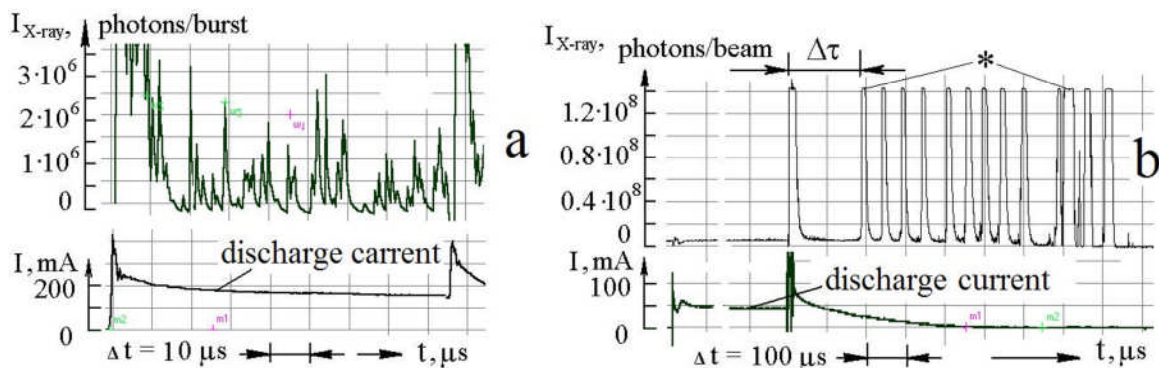


Figure 3. The typical oscillograms of the X-ray emission signal from the system scintillator – PM. The cathode sample is Pd, D₂ discharge. a – diffusion mode, b – form of laser beams; * - the pulse peak was cut a discriminator of amplifier.

3.4. The X-ray emission temporal characteristics

X-ray emission as a function of time was studied with scintillator photomultiplier detectors.

X-ray laser beam emissions were detected after passing the trailing edge of the glow discharge current pulses (Fig. 4). The different values of the time delay were recorded in experiments. The temporal characteristic of X-ray beam emissions was made for the following conditions: time zero corresponds to the trailing edge time of the discharge current pulse; and the number of X-ray beams was counted for each value of the time delay. The temporal characteristic of X-ray beam emissions show that the time delay has fixed values with a $\pm 2 \mu\text{s}$ deviation.

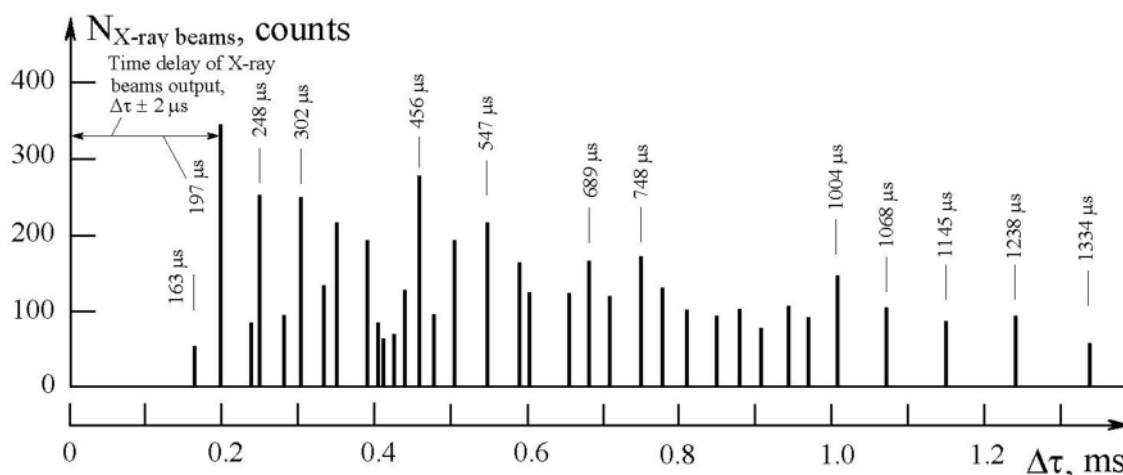


Figure 4. Temporal characteristic of X-ray beam emissions. The cathode sample is Pd, D₂ discharge, current 50 mA.

3.5. The X-ray emission spectra registration

The X-ray emission spectra were measured using the curved mica crystal X-ray spectrometer (the mica crystal holder is 50 mm diameter), with the spectrum being registered on X-ray film. The film includes the refraction spectra, the direct X-ray lighting, and reflection spectra, with

reflection spectra used for data processing. The direct X-ray lighting limits the reflection spectra in the high energy area. The wavelength and the energy of the X-ray were determined according to the expression:

$$m\lambda = 2d \sin\theta; E_{\text{X-ray}} = 1.235/\lambda.$$

Where m is the spectrum order; λ stands for the X-ray emission wave length in nm; $2d$ is the constant of the mica crystal lattice ($2d = 2.0$ nm); and θ represents the reflection angle. The spectra were repeatedly recorded during the glow discharge operation and after the glow discharge current switch off (for up to 20 hours afterwards). The spectra pattern includes bands, dark and light spots (consisting of multiple tiny dark and light dots) and separate dark and light small spots. The bands and spots were located in spectral areas specific for a given cathode material used. The registered energy of the X-ray emission bands and spots (the energetic position of the bands and spots within the spectrum) was dependent upon the cathode material used. The registered X-ray spectra in experiments was similar to characteristic X-ray spectra.

It was assumed that the diffusion component of the X-ray emission was registered on the spectrum as a series of bands.

The laser beams were recorded as dark spots and in case of the emission beam high density they turned white (solarization of the photoemulsion). The “solarization” is produced by a photographic negative in response to high energy density irradiation.

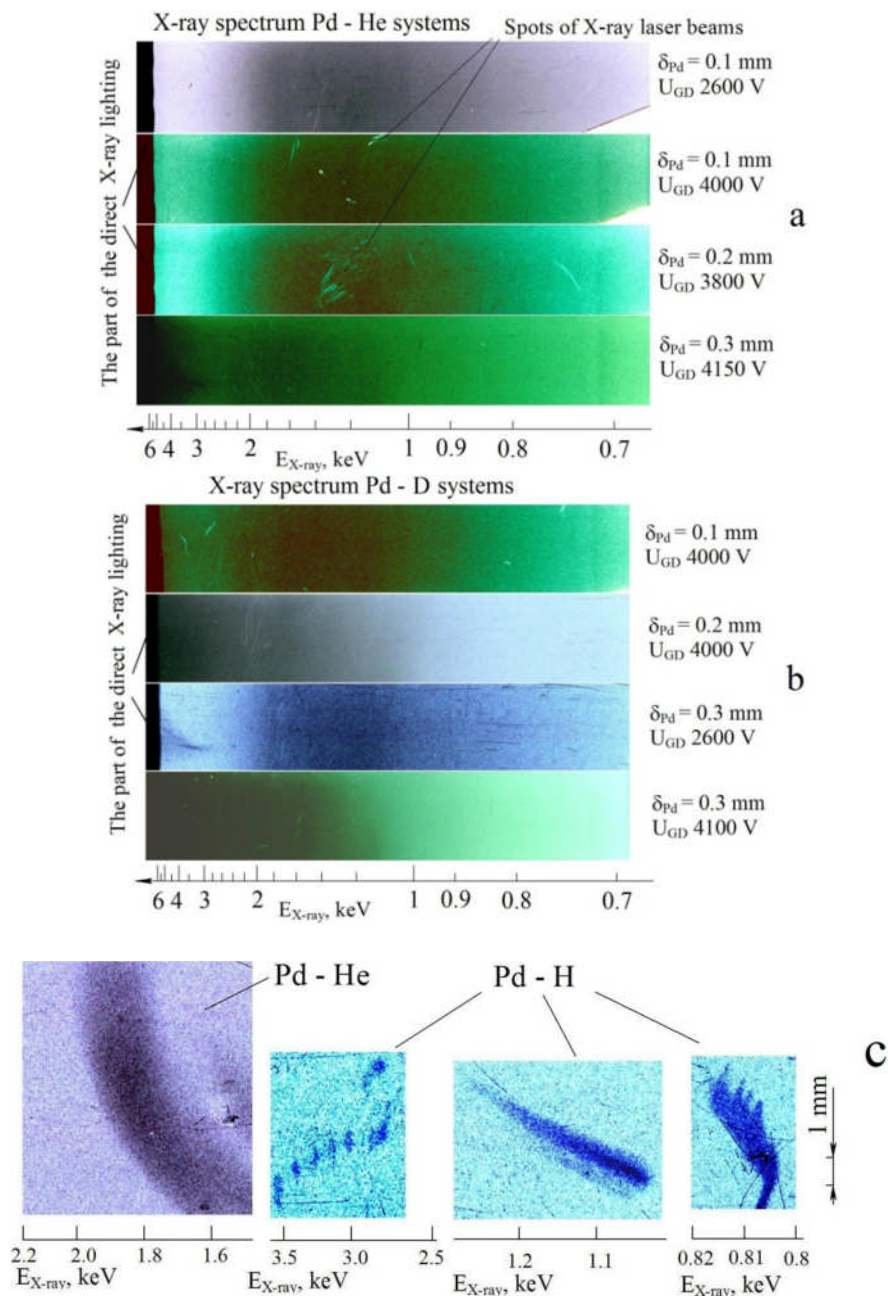


Figure 5. X-ray energy spectra. a, b – during the glow discharge operation, c – after the glow discharge in the spot modes.

4. Conclusion

Apparently, some long-lived excited levels with energies up to several keV are formed in the cathode solid-state medium when its surface is exposed to bombardment by the discharge plasma ions. These levels are characterized by fixed discrete values of energy and lifetime. The X-ray emission results from re-excitation of these levels.

Introduction to Gas Loading

The introduction of protons or deuterons into solids can be done from the gas phase, as an alternative to electrochemical loading from a liquid phase. This approach to loading has been pursued since the early days of the experimental study of low energy nuclear reactions. The characteristics and results of gas loading are the subjects of this section.

The energetics of gas loading can be favorable. With electrochemical loading, power has to be continuously applied to a cell, often for long periods (days and weeks) to initiate and, in general, to sustain LENR. In the case of gas loading, the only power that might have to be applied is to pressurize the hydrogen or deuterium gas that is in contact with the solid to be loaded. If the solid consists of small particles, loading happens rapidly without necessarily having to provide additional electrical power. If high temperatures are needed, power must be applied, at least to start continuing and self-heating reactions. By contrast, the production and maintenance of either plasmas or beams for loading by use of energetic particles is energy intensive. The production of plasmas requires both ionization and relatively high particle kinetic energies. Similarly, the generation of ions for beams takes energy, as does their acceleration for implantation into solids.

Practical systems that might emerge would be relatively simple if they are based on gas loading. Electrochemical systems have complexity similar to fuel cells, which are actually electrochemical systems. In such systems, there has to be a tightly integrated assembly of chemical, electrical, thermal and fluidic capabilities. The engineering of LENR electrochemical systems for consumer use is certainly possible. Batteries provide a paradigm for such systems. In fact, rechargeable nickel metal and hydrogen batteries are essentially the reverse of LENR electrochemical cells. In the batteries, a current is produced by deloading of hydrogen from the nickel, the reverse of what happens in an LENR experiment. However, commercial LENR energy sources are likely to be more complex than batteries, more like fuel cells, at least in the early stages of commercialization.

There are three papers in this section. The first is a commissioned review of gas loading by Biberian. It provides comparisons of the strengths and weaknesses of both electrochemical and gas loading. The following two lists from Biberian are useful –

There are definite advantages to gas loading:

- Pressures are easily controlled.
- It is possible to maintain clean environments.
- Operational temperatures can be high.
- It is easier to measure helium and charged particles.
- There is more potential for practical applications.

There are also some disadvantages:

- It is difficult to achieve very high pressures.

- To do good calorimetry requires more expensive equipment with this technique than with electrolysis.

A comprehensive set of 158 references on gas loading is provided by Biberian.

The last two papers in this section involve the use of nanoparticles, both inspired by the results reported by Arata and both conducted in deuterium atmospheres. Celani and his colleagues used electromigration in a long and thin wire of Pd coated with Pd nanoparticles. The wire was in deuterium gas at pressures of 1.2 to 5.2 atmospheres. One amp direct current was used to drive the deuterons in the Pd wire to the cathodic end of the wire. Excess power of 5.2 W was reported, which corresponds to 370 W/ gm Pd.

Nohmi and his colleagues reported the first results from a new university-industry collaboration in Japan. They did preliminary gas phase experiments with both deuterium and hydrogen in very similar chambers operated in parallel. Powders of Si, Pd and Pd black were placed in the two chambers. With the Pd black, the deuterium cell produced 8.3 +/-4.5 kJ, about a factor of two greater than the blank run of 4.0 kJ.

It is expected that interest in gas loading experiments will continue to grow as LENR near commercialization. It is likely that the first LENR-based products will employ gas loading. Small cartridges, such as those used for containment of carbon dioxide, might be used to provide either hydrogen or deuterium gas at elevated pressures. If initiation of LENR requires elevated temperatures, batteries might be used. In principle, they could be recharged by use of thermoelectric devices that capture energy from waste heat in LENR power systems. In short, both the engineering and operation of LENR energy sources based on gas loading might be simpler compared to electrochemical systems.

Cold Fusion by Gas Loading: A Review

Jean-Paul Biberian

Université d'Aix-Marseille, 163 Avenue de Luminy, 13288 Marseille cedex 9, France

Abstract

Since the announcement of the discovery of Cold Fusion by Fleischmann and Pons in 1989, scientists developed techniques other than electrolysis in order to achieve the Cold Fusion effect. A lot of effort has been made to develop gas loading. This approach has been followed by a large number of scientists all over the world and has proven to be productive. Excess heat has been demonstrated, as well as production of helium, tritium, neutrons, gamma rays and transmutation. Not only the palladium-deuterium system has been explored, but also titanium-deuterium and nickel-hydrogen, as well as several other systems. In this paper we review the large body of work that has been accomplished so far.

1 - Introduction

At the public announcement of Cold Fusion on March 23, 1989 by Pons and Fleischmann (1), the world discovered that there was a possibility of an endless energy source. Using an electrochemical method, they showed that it is very likely that nuclear reactions can occur at low energy. Interestingly, as early as 1986, Kluev et al. (2) had shown the production of neutrons when perovskite type compounds loaded with deuterium passed through the ferroelectric transition temperature. They also showed neutron production when heavy ice was crushed (3). These early experiments indicated that nuclear reactions could occur at low energy. Following the press conference most of the experimental work involved electrolysis. However, a large number of scientists started experimenting with gas phase materials. It is the purpose of this paper to review the large quantity of data available in this field.

In this paper we do not cover interesting works done with solid-state electrolytes and plasma discharges. Even though these experiments are performed in gas phase and not in liquid phase, there are many papers about it, which deserve review papers of their own.

2 – Why electrochemistry?

Fleischman and Pons (1) decided to perform their experiments in an electrolytic cell. The main reason being that according to thermodynamics, using Nernst law it is possible to achieve very high-pressures in the cathode of an electrochemical cell. At low pressure, in the case of hydrogen loading, the relation between the over-voltage and the pressure or fugacity inside the cathode is given in equation (1).

$$V = -\frac{RT}{nF} \log \frac{P}{P_0} \quad (1)$$

Where V , is the over-voltage, R , the perfect gas constant, T , the absolute temperature, n , the number of electrons involved in the water dissociation, F , the Faraday constant, P , the pressure or fugacity inside the palladium cathode and P_0 , the atmospheric pressure.

This formula indicates that if one can generate large over-voltages on the cathode, this will correspond to loading of the cathode with a very high pressure of deuterium gas. However, the challenge is to generate these over-voltages. There are several ways of doing so, one of them being an increase of the electrical current density. It is clear that achieving such high pressures in gas phase is impossible with our current technologies. That is one of the reasons the electrochemical method was selected. Another one is the simplicity of it, and the relative ease of doing calorimetry with high precision. It is also easy to change the current and therefore the conditions of the electrolysis.

3 – Why gas loading?

Even though electrochemistry has many advantages as explained above, it also has several limitations:

- It is difficult to achieve large over-voltages, because either it is necessary to have high current densities or to deposit a specific material at the surface of the cathode that helps produce them.
- It is difficult to maintain very clean experiments because many impurities in the electrolyte will end up on the cathode surface by cathodic deposition. Even if the concentration of impurities is low, very small amounts will produce atomic level layers of deposits at the cathode surface capable of greatly modifying the surface reactivity.
- Analysis of by-products of the reaction such as helium, alpha particles, transmutation is easier in gas phase.
- As pointed out by Fleischmann and Pons (4), there is a positive feedback, and excess heat increases with temperature. With water electrolysis, we are limited to 100°C at atmospheric pressure. It is possible to work at higher temperatures, but this calls for the use of pressurized cells or molten salts, which are much more difficult to operate.
- Finally it seems that future technological applications will be difficult to develop with electrochemical cells.

There are definite advantages to gas loading:

- Pressures are easily controlled.
- It is possible to maintain clean environments.
- Operational temperatures can be high.
- It is easier to measure helium and charged particles.
- There is more potential for practical applications.

There are also some disadvantages:

- It is difficult to achieve very high pressures.
- To do good calorimetry requires more expensive equipment with this technique than with electrolysis.

4- Excess heat production

Excess heat is certainly the goal of many scientists in the field of Condensed Matter Nuclear Science, because it would result in a practically infinite source of energy. (At present energy consumption rates, deuterium fuel will last for billions of years.) Therefore many different ways have been developed to reach that goal. In the following sections it is shown a number of different ways to succeed.

4.1 Palladium tubes and membranes

As early as 1989, Fralick et al. (5) at NASA loaded deuterium in a hydrogen purifier at 370°C and a pressure of deuterium gas of 1.4 MPa on both sides of the purifier palladium tube. Their primary goal was to detect neutrons. When the deuterium was pumped out, a temperature rise was observed. When filled with hydrogen no temperature variation was detected. However no neutrons were observed above background. This was a very simple and convincing experiment showing anomalous excess heat in the palladium deuterium gas system.

Many other experiments have been performed since then with many variations: solid metals, thin wires, and powders. Romodanov et al. (6) have shown the production of excess heat when deuterium flows through palladium foils. Similar results have been observed by Li et al. (7-14). In a similar type of experiments, Tian et al. (15) detected heat after death. Manduchi et al. (16) observed anomalous effects when palladium is cooled from 900°C to room temperature.

4.2 Palladium powders

Palladium powder loads deuterium better than solid palladium. This is why several groups have used such substrates to detect excess heat. Kirkinskii et al. (17,18) have measured one Watt of excess heat per gram of palladium in gas-loaded experiments. However, when palladium powder is heated, sintering occurs, and the original particle size is destroyed. Therefore it is better to use dispersed palladium in a medium. Case (19,20) tried various palladium catalysts and finally found one that was effective in producing excess heat. McKubre et al. (21) successfully replicated this experiment. The work by Arata and Zhang (22-38) is of particular interest. They started with a unique design using a Double Structure cathode consisting of a hollow palladium tube filled with palladium black. Even though their first set of experiments used electrochemistry, this was only used to dissociate heavy water and purify the deuterium gas at the outside wall of a solid palladium tube. Only deuterium reached the nano-particles in active portion of the experiment, on the inside of the cell. The deuterium diffuses through the walls of the tube and finally enters the center of the tube as atomic/molecular. Therefore this can be considered a method of performing gas loading of palladium black. Later, Arata and Zhang (39-42) used another approach. They loaded palladium nano-powder embedded in a ZrO₂ matrix by high deuterium pressure. They obtained very high loadings, and excess heat even at room temperature (40). Marmigi et al. (43) showed anomalous excess heat

using an oxidized palladium wire. Celani et al. (44) showed high loading and large excess heat when thin palladium wires are coated with nano-particles.

4.3 Excitation

The reaction has been triggered by various means of excitation. Li et al. (45) have measured excess heat when RF heating was used. Nassisi et al. (46-48) observed transmutations when irradiating etched palladium samples with an excimer laser.

4.4 Out-diffusion

One of the major goals of research in Condensed Matter Nuclear Science is to determine the mechanism responsible for the anomalous observations. It has been assumed that the reactions are not located in the bulk of the material, but at the surface of the metal. Early on Yamaguchi et al (49,50) have observed excess heat when deuterium flows out of a palladium foil covered on one side with gold. Similarly Liu et al. (51) show that excess heat occurs when deuterium flows out of the palladium. The amount of excess heat increases with the deuterium flow. Narita et al. (52) have also shown heat production when hydrogen is pumped out of a palladium foil covered on one side with MnOx or gold. Lipson et al. (53) showed excess heat while de-loading a palladium foil oxidized on one side and covered with gold on the other. Biberian and Armanet (101,102) showed excess heat production when deuterium flows out of a palladium tube.

4.4 Palladium wires

Li et al. (54) observed excess heat from palladium wires in deuterium gas. Marmigi et al. (43) have shown anomalous excess heat production when a previously oxidized palladium wire is heated in a hydrogen atmosphere. Celani et al. (44) showed that extremely large excess heat were detected when long (60 cm in the experiment shown) and thin (50 μm) Pd wires, coated with nano-materials, underwent the phase transition from beta to alpha phases and large current densities (10-50 kA/cm^2) were applied along the length of the wire. This effect was stable over time. The power density was up to 400 W/g of palladium. The operating temperatures were as large as 300-500°C. The effect happened mainly in pressurized deuterium atmosphere, however an effect was also observed at much lower levels using hydrogen.

5 – Neutron production

As early as 1986, Kluev et al. (2,3) discovered the production of neutrons when a strong mechanical action is exerted against heavy ice or LiD. Later, Derjaguin et al. (55) showed that neutrons were produced when titanium deuteride chips were subject to mechanical vibrations. Jin et al. (56) observed neutrons in a $\text{YBa}_2\text{Cu}_3\text{O}_7$ sample loaded with deuterium. Shioe et al. (57) and Shirakawa et al. (58) similarly observed neutrons in LiNbO_3 fractured in a deuterium atmosphere. Aiello et al. (59) have also observed neutrons in palladium loaded with deuterium. De Nino et al. (60-62) detected neutrons while varying the temperature of titanium foils loaded with deuterium. Menlove et al. (63-66) showed similar results. Fabrizio et al. (67) also found neutrons the same way. At the same time, Claytor et al. (68-70) and Tuggle et al. (71) at the Los Alamos National Laboratory detected neutrons by pulsing currents with palladium electrodes in deuterium gas. Since then many other scientists have tried to detect neutrons in gas loading experiments. Bressani et al. (72-74) have measured neutrons emission when

titanium foils are loaded with deuterium. Yamaguchi et al. (49,75) have demonstrated production of neutrons when deuterium de-loads from a palladium foil loaded with deuterium with one face of the palladium covered with gold. Shirakawa et al. (76) showed production of neutrons when LiNbO_3 is fractured in a deuterium atmosphere. Iwamura et al. (77) showed production of neutrons when a palladium foil loaded with deuterium is heated up. However Garg et al. (78) in a similar experiment with a palladium wire loaded with deuterium or hydrogen did not detect any neutrons. Aoki et al. (79) could not detect any neutrons above background in a tungsten sodium bronze loaded with deuterium when loading or de-loading the material. Shinojima et al. (80) did not detect neutrons when flowing deuterium through a palladium foil. However Lipson et al. (53,81) and Roussetski (82) did detect neutrons during exothermic desorption using a Au/Pd/PdO:D sample. Also, Dougar-Jabon et al. (83) detected neutrons during alpha/beta phase transition in palladium deuteride. Chicea et al. (84) detected neutrons in titanium deuteride when the metal was loaded at high temperature then the temperature was lowered. Itoh et al. (85) observed neutron emission when out-gazing a highly loaded palladium foil.

6 – Tritium detection

As early as 1990, Iyengar et al. (86), Srinivasan et al. (87) Iyengar et al. (88), Kauskik et al. (89) and Rout et al. (90,91) have shown production of tritium in palladium and titanium samples loaded with deuterium. Lamza et al. (93) measured tritium in various metals loaded with deuterium. De Nino et al. (62) detected tritium in titanium loaded with deuterium. Yamada et al. (94) have shown the production of tritium when deuterium is pumped out of a palladium foil covered on one side with MnOx . Narita et al. (52) have observed mass three corresponding either to tritium or helium-3 when hydrogen is pumped out of a palladium foil covered on one side with MnOx or gold. Similarly Wei et al. (95) have also observed mass three when deuterium flows through a palladium foil. Claytor et al. (70,97) measured tritium with Pd-Si electrodes in deuterium gas. Clarke et al. (96) detected tritium in titanium loaded with deuterium and later (98) observed production of tritium in a cell similar to the one of Arata. Romodanov et al. (6,99) have also detected tritium. Lipson et al. (100) detected significant amounts of tritium when cooling $\text{YBa}_2\text{Cu}_3\text{O}_{7-x}\text{D}_x$ to its Curie temperature (88-93K) in deuterium gas. Heating a palladium foil loaded with deuterium by Iwamura et al. (77) showed production of neutrons.

7 – Helium measurements

Detection of helium-4 is important in Condensed Matter Nuclear Science. Its measurement is another proof of the nuclear origin of the phenomenon. However few experiments have been performed so far. Botta et al. (103,104) have detected helium-4 using palladium foils covered on one side with gold and loaded with deuterium. Clarke et al. (96) measured helium-3 and helium-4 in titanium loaded with deuterium. Qiao et al. (105,106) showed production of helium from palladium in deuterium gas. McKubre et al. (21) have detected helium-4 in a Case type experiment, and showed a correlation between helium-4 production and excess heat. Arata and Zhang (32,107-109) showed, production of helium-3 and helium-4. Clarke et al. (98) showed

the presence of helium-4 and very large quantities of helium-3 in a cell similar to the one developed by Arata.

8 – Charged particles

Mo et al. (110,111), Wang et al. (112), Jin et al. (113), Li et al. (114) and Dong et al. (115) showed evidence of charged particles emission from deuterated palladium. Cecil et al. (116) have observed charged particles in deuterated titanium. By a coincidence method Jones et al. (117,118) showed that energetic protons and tritons are produced in non-equilibrium conditions in titanium deuteride samples. Roussetski et al. (119) have also detected charged particles from titanium hydrides and deuterides triggered by a pico-second powerful laser beam. Cecil et al. (120) have also measured charged particles from palladium deuterides. Lipson et al. (121) observed beta emission from deuterated titanium.

9 – Loading experiments

We have shown above that Nernst law explains why it is possible to load hydrogen or deuterium at high levels by electrolysis in palladium or other metals. In gas phase experiments, it seems that the limitation comes from the difficulty in reaching high pressures of gas. However, several researchers have tried to load palladium and other metals by various ways. Huang et al. (122) have shown that it is easier to load hydrogen than deuterium in palladium. They also showed that pulse heating a palladium wire did not help loading. They claim a maximum loading ratio of 0.84. Shikano et al. (123) have loaded palladium foils covered on one side with gold or silver. They showed that the electrical resistance increases with loading, then decreases, as predicted by the resistance ratio versus loading curve (124). Li et al. (125) have shown that they could load deuterium in palladium wires up to a ratio of 0.78. They measured the palladium grain size, which were 100 to 200 μm . Huang et al. (126) showed that the resistivity anomaly observed on the resistance ratio to loading curve was due to the alpha-beta phase transition. Del Giudice et al. (127) have developed a technique capable of operating at low temperature. They used a wire one meter long with a cross section $2 \times 50 \mu\text{m}^2$, made by sputtering palladium. Scaramuzzi (128) has shown with a system similar to the previous one that he could observe a resistance ratio between pure palladium and palladium loaded with deuterium of 2.64 at 30K. This value is much larger than the one usually measured at room temperature: 2.0 for a loading ratio of 0.74. Celani et al. (44) have shown that by depositing nano-particles of palladium and other elements of nanometric size on the surface of a palladium wire, they obtained ultra short loading times (of the order of 10 s with a Pd wire of 50 μm in diameter. Most of the work on gas loading has been performed with palladium. However, Shrikhande et al. (129) have tried to measure the resistivity of titanium versus loading, but the results were irreproducible. Arata and Zhang (130) showed that in palladium loadings up to three deuterium atoms per palladium could be obtained in nano-particles of palladium embedded in ZrO_2 .

10 – Transmutations

Transmutations are a by-product of Cold Fusion, they have been observed on electrodes after electrolysis, but they remain doubtful because of potential contaminations by impurities always

present in the electrolyte. In gas phase, there is not such a danger, and the results are more reliable. Kong et al. (131) and Qiao et al. (132) have detected several new metals on palladium in a deuterium atmosphere. Iwamura et al. (133-135) have pioneered this field. In their first paper (133), they use a palladium foil as a substrate on which multi-layers of thin films of palladium and low work function materials such as CaO, TiC, Y₂O₃ ... are deposited. They flow deuterium gas through the sample by placing a pressure of deuterium gas on one side, and pumping on the other side. They analyze in situ, without bringing the sample to atmosphere by Photo-Electron Spectroscopy the surface composition, and by Secondary Ion Mass Spectroscopy their isotopic distribution. In their first experiments they show production of sulfur with an anomalous isotopic distribution: S-33/S-32 is an order of magnitude larger than the natural distribution. They also observed the presence of silicon and magnesium. In another experiment, they doped the surface of the multilayer with lithium. They observed a decrease in lithium with time, and an increase of aluminum. Iwamura et al. (134) added Cs and Sr on the surface of their sample and observed the transmutation of Cs into Pr and Sr into Mo. The interesting aspect here is that the isotopic distribution of the molybdenum is not natural. This is a direct proof of the non-natural origin of the molybdenum. These transmutations correspond to adding four deuterons to the initial nuclei. Later Iwamura et al. (135) have shown that in other cases (Ba deposit), the transmutation consists in the addition of six deuterons to the initial nucleus. Several groups have reproduced Iwamura's work. In a similar experiment, Higashiyama et al. (136) have shown that the praseodymium formation is a function of the flow rate of deuterium through the sample. Minari et al. (137), Yamada et al. (138,139) and Kitamura et al. (140) have also observed transmutation. Castellano et al. (141) have shown that new elements are found on a deuterated palladium foil irradiated with a laser beam. Di Giulio et al. (142) have deposited thin films of palladium on silicon wafers. After laser irradiation they observe several transmutations products. Wei et al. (143) observed new elements (Gd, Tb, Nd) after diffusion of deuterium through a palladium foil.

11 – Nickel-Hydrogen system

Most of the work in gas loading has been made with the palladium-deuterium system. However, the nickel-hydrogen system is also of great interest. Sankaranarayanan et al. (92) reported tritium production with hydrogen in nickel wires. A team at the Siena University in Italy has performed some very promising work. Focardi et al. (144-150) have studied the nickel-hydrogen system. They have repeatedly produced excess heat. Battaglia et al. (151) have shown the production of neutrons, and Campari et al. (152,153) have shown the production of heat, gamma rays and neutrons. Focardi et al. (154) show the production of heat, particle emission and gamma rays. Campari et al. (155) have observed anomalous distribution of elements on a nickel alloy during experiments with hydrogen. All the work mentioned above is the product of a single team. It is interesting to know that Cammarota et al. (156) have reproduced the excess heat measurements. However, E. Cerron-Zeballos et al. (157) could not succeed. A different approach has been developed by Mastromatteo (158). He used a silicon based hydrogen source to load a nickel film in a small device. He observed anomalous melting of the nickel film.

12 - Conclusion

Gas loading is a very promising technique. During the past twenty years, it has been shown that all the ingredients of Cold Fusion have been found with this method: excess heat, neutrons, tritium, gamma rays and helium. However most of the work has been done with palladium and deuterium. It is interesting to note that for future applications the nickel-hydrogen system is very promising, and deserve a lot more attention.

References

1. M. Fleischmann and S. Pons, "Electrochemical Induced Nuclear Fusion of Deuterium", J. Electroanal. Chem., **261**(1989)301.
2. V. A. Kluev, A. G. Lipson, Yu. P. Toporov, B. V. Deryagin, V. I. Lushchikov, A. V. Strelkov and E. P. Shabalin: Sov. Tech. Phys. Lett. **12**(1986) 551.
3. V. A. Kluev, A. G. Lipson, Yu. P. Topornov, B. Derjaguin, V. I. Lushikov, A.V Strelkov and E.P. Shabalin in J. Sov Tech Physics Lett **12**(1986) 1333
4. M. Fleischmann and S. Pons, Physics Letters A **176**(1993)118
5. G. C. Fralick, A. J. Decker and J. W. Blue, NASA Technical Memorandum 102430, 1989.
6. V. A. Romodanov, N. I. Khokhlov and A. K. Pokrovsky in Eighth International Conference on Cold Fusion, Lerici, Italia, 2000, pp. 259.
7. X. Z. Li , B. Liu , J. Tian , Q. M. Wei , R. Zhou and Z. W. Yu, J. Phys. D: Appl. Phys. **36**(2003) 3095.
8. X. Z. Li, B. Liu, N. N. Cai, Q. M. Wei, J. Tian and D. X. Cao in Tenth International Conference on Cold Fusion. 2003. Cambridge USA, pp. 113.
9. X. - Z. Li, B. Liu, X. Z. Ren, J. Tian, D. X. Cao, S. Chen, G. H. Pan, D. L. Ho, Y. Deng in The 9th International Conference on Cold Fusion, Beijing, China, 2002, pp. 202.
10. X- Z. Li, B Liu, X. Z. Ren, J. Tian, W. Z. Yu, D. X. Cao, S. Chen G. H. Pan, S. X. Zheng in The Seventh International Conference on Cold Fusion, Vancouver, Canada, 1998, pp. 197.
11. W. Wu, X. Z. Li, J. H. Du, J. Tian, J. Z. Hao, B. Ma, J. P. Chen, B. Liu and S. Y. Lei in Ninth International Conference on Cold Fusion, Beijing, China, 2002, pp. 412
12. B. Liu, X. – Z. Li, Q. M. Wei, N. Mueller, P. Schoch and H. Oehre in Twelfth International Conference on Condensed Matter Nuclear Science, Yokahama, Japan, 2005, pp. 75.
13. J. Tian, X. Z. Li, W. Z. Liu, D. X. Cao, R. Zhou, Z. W. Yu, Z. F. Jiang, Y. Liu, J. T. He and R. X. Zhou, in Ninth international conference on Cold Fusion, Beijing, China, 2002, pp. 353.
14. X.Z. Li, W.Z. Yue, G.S. Huang, H. Shi, L. Gao, M.L. Liu and F.S. Bu, J. New Energy **1**(4) (1996)34.
15. J. Tian, X. Z. Li, W. Z. Yu, M. Y. Mei, D. X. Cao, A. L. Li, J. Li, Y. G. Zhao and C. Zhang, in Ninth International Conference on Cold Fusion, Beijing, China, 2002, pp. 360.

16. C. Manduchi, G. Zannoni, E. Milli, L. Riccardi, G. Mengoli, M. Fabrizio and A. Buffa, *Nuovo Cimento A* **107**(2)(1994)171.
17. V. A. Kirkinskii, V. A. Drebuschak and A. I. Khmelnikov, in Ninth International Conference on Cold Fusion, Beijing, China, 2002, pp. 170
18. V. A. Kirkinskii, V. A. Drebuschak and A. I. Khmelnikov *Europhys. Lett.*, **58**(3)(2002)462.
19. L. C. Case, *Fusion Technol.*, **20**(1991)478.
20. L. C. Case, in Seventh International Conference on Cold Fusion, Vancouver, Canada 1998, pp. 48.
21. M. McKubre, F. Tanzella¹, P. Tripodi and P. Hagelstein, in Eighth International Conference on Cold Fusion, Lerici, Italy, 2000, pp. 3.
22. Y. Arata and Y.C. Zhang, in Third International Conference on Cold Fusion, Nagoya, Japan, 1992.
23. Y. Arata and Y.C. Zhang, *Proc. Jpn. Acad., Ser. B*, **66**(1992)33.
24. Y. Arata and Y.C. Zhang, *Fusion Technol.*, **22**(1992)287.
25. Y. Arata and Y.C. Zhang, *Proc. Jpn. Acad., Ser. B*, **70**(1994)106.
26. Y. Arata and Y.C. Zhang. *Proc. Jpn. Acad., Ser. B*, **71**(1995)98
27. Y. Arata and Y.C. Zhang, in Fifth International Conference on Cold Fusion, Monaco, 1995, pp. 483.
28. Y. Arata and Y.C. Zhang, in Sixth International Conference on Cold Fusion, Lake Toya, Hokkaido, Japan, 1996, pp. 129.
29. Y. Arata and Y.C. Zhang, *Proc. Jpn. Acad., Ser. B*, **72**(1996)179.
30. Y. Arata and Y.C. Zhang, *J. High Temp. Soc.*, **23**(1997)1.
31. Y. Arata and Y.C. Zhang. *Proc. Jpn. Acad., Ser. B*, **74**(1998)155.
32. Y. Arata and Y.C. Zhang, *Jpn. J. Appl. Phys.* **38**(1999) L774.
33. Y. Arata and Y.C. Zhang, *Jpn. J. Appl. Phys. Part 2*, **37**(1998)L1274.
34. Y. Arata and Y.C. Zhang, *Proc. Jpn. Acad., Ser. B*, **75**(1999)76.
35. Y. Arata and Y.C. Zhang, *Proc. Jpn. Acad., Ser. B*, **75**(1999)71.
36. Y. Arata and Y.C. Zhang, in Eighth International Conference on Cold Fusion, Lerici, Italy, 2000, pp. 11.
37. Y. Arata and Y.C. Zhang, in Ninth International Conference on Cold Fusion, Beijing, China, 2002, pp. 5.
38. Y. Arata and Y. Zhang. in Tenth International Conference on Cold Fusion, Cambridge, USA, 2003, pp. 139.
39. Y. Arata and Y. C. Zhang in Twelfth International Conference on Condensed Matter Nuclear Science, Yokohama, Japan, 2005, pp. 44.
40. Y. Arata and Y. C. Zhang in Fourteen International Conference on Condensed Matter Nuclear Science, Washington, USA, 2008, in this volume.
41. Y. Arata and Y. Zhang, *J. High Temp. Soc.*, **34**(2)(2008)85.
42. Y. Arata and Y. Zhang, *High Temp.Soc. Japan*, **29**(2003)1.
43. A. Marmingi, A. Spallone, F. Celani, P. Marini and V. Di Stefano, in Eighth International Workshop on Anomalies in Hydrogen/Deuterated Loaded Metals, Sicily, Italy, 2007, pp. 224.

44. F. Celani, A. Spallone, E. Righi, G. Trenta, V. Andreasi, A. Marmigi, G. Cappuccio, D. Hampi, P. Marini, V. Di Stefano, M. Nakamura, F. Todarello, E. Purchi, U. Mastromatteo, A. Mancini, F. Falcioni, M. Marchesini, P. Di Biagio, U. Martini, P.G. Sona, F. Fontana, L. Gamberale and D. Garbelli, in Fourteenth International Conference on Condensed Matter Nuclear Science, Washington DC, USA, 2008, in this volume.
45. X. Z. Li, W. Z. Yue, G. S. Huang, H. Shi, L. Gao, M. L. Liu and F. S. Bu, in Sixth International Conference on Cold Fusion, Hokkaido, Japan. 1996, pp. 455.
46. V. Nassisi and M. L. Longo, *Fusion Technol.* 37(2000)247.
47. V. Nassisi, *J. New Energy*, **2(3/4)**(1997)14.
48. V. Nassisi, *Fusion Technol.*, **33**(1998)468.
49. E. Yamaguchi and T. Nishioka, *Jpn. J. Appl. Phys. Part 2*, **29**(1990)L666.
50. E. Yamaguchi, and H. Sugiura. in Seventh International Conference on Cold Fusion, Vancouver, Canada, 1998.
51. B. Liu, X. Z. Li, Q. M. Wei and S. X. Zheng in in Eighth International Workshop on Anomalies in Hydrogen/Deuterium Loaded Metals, Sicily, Italy, 2007, pp. 204.
52. S. Narita, H. Yamada, H. Monma, H. Onodera, N. Tanaka, T. Tateishi, M. Baba and E. Yamaguchi, in Ninth international Conference on Cold Fusion, Beijing, China, 2002, pp. 280.
53. A. G. Lipson, B. F. Lyakhov, A. S. Rousstesky and N. Asami, in Eighth International Conference on Cold Fusion, Lerici, Italia, 2000, pp. 231.
54. X. Z. Li, W. Z. Yue, G. S. Huang, H. Shi, L. Gao, M. L. Liu and F. S. Bu, in Sixth International Conference on Cold Fusion, Lake Toya, Hokkaido, Japan, 1996, pp. 455.
55. B. V. Derjaguin, A. G. Lipson, V. A. Kluev, D. M. Sakov and Y. P. Topporov, *Nature* **342**(1989)492.
56. S.-X. Jin, F.-X. Zhan and Y.-Z. Liu, in Fourth International Conference on Cold Fusion, Maui, USA, 1994, vol 3, pp. 4-1.
57. Y. Shioe, N. N. Mondal, M. Chiba, T. Hirose, M. Fujii, H. Nakahara, K. Sueki, T. Shirakawa and M. Utsumi, *Nuovo Cimento A*, **112**(1999)1059.
58. T. Shirakawa, M. Chiba, M. Fujii, K. Sueki, S. Miyamoto, Y. Nakamitsu, H. Toriumi, T. Uehara, H. Miura, T. Watanabe, K. Fukushima, T. Hirose, T. Seimiya and H. A. Nakahara *Chem. Lett.*, **22**(1993)897.
59. S. Aiello, E. De Filippo, G. Lanzano, S. Lo Nigro, and A. Pagano, *Fusion Technol.*, **18**(1990)115.
60. A. De Ninno, A. Frattolillo, G. Lollobattista, L. Martinis, M. Martone, L. Mori, S. Podda and F. Scaramuzzi, *Nuovo Cimento, note brevi*, **101**(1989)841.
61. A. De Ninno, A. Frattolillo, G. Lollobattista, L. Martinis, M. Martone, L. Mori, S. Podda and F. Scaramuzzi, *Europhysics Letters*, **9**(3)(1989)221.
62. A. De Ninno, F. Scaramuzzi, A. Frattolillo, S. Migliori, F. Lanza, S. Scaglione, P. Zeppa and C. Pontorieri, in Second Annual Conference on Cold Fusion, Como, Italy, 1991, pp. 129.
63. H. O. Menlove, M.M Fowler, E. Garcia, A. Mayer, M. C. Miller and R. R. Ryan, in Workshop on Cold Fusion Phenomena, Santa Fe, USA, 1989.

64. H. O. Menlove, M. A. Paciotti, T. N. Claytor, H. R. Maltrud, O. M. Rivera, and D. G. Tuggle and S. E. Jones, in Anomalous Nuclear Effects in Deuterium/Solid Systems, "AIP Conference Proceedings 228", 1990, pp. 467.
65. H. O. Menlove, M.M.. Fowler, E. Garcia, M.C.. Miller, M.A. Paciotti, R. R Ryan and S. E. Jones, *J. Fusion Energy*, **9**(4)(1990)495.
66. H. O. Menlove, M. A. Paciotti, T. N. Claytor, and D. G. Tuggle, in Second Annual Conference on Cold Fusion, Cuomo, Italy. 1991, pp. 395.
67. M. Fabrizio, C. Manduchi, G. Mengoli, E. Milli, G. Zannoni, in Rome Workshop on the Status of Cold Fusion in Italy, University of Rome III, 1993, pp. 74.
68. T. N. Claytor, P. Seeger, R. K. Rohwer, D. G. Tuggle, and W. R. Doty, in NSF/EPRI Workshop on Anomalous Effects in Deuterated Materials, Washington, DC, 1989.
69. T. N. Claytor, D. D. Jackson and D. G. Truggles, *Infinite Energy*, **2**(7)(1996)39.
70. T. N. Claytor, D. G. Tuggle, and H. O. Menlove, in Second Annual Conference on Cold Fusion, Como, Italy 1991, pp. 395.
71. D. G. Tuggle, T. N. Claytor, and S. F. Taylor, *Trans. Fusion Technol.* **26**(4T)(1994)221.
72. T. Bressani, D. Calvo, A. Feliciello, C. Lamberti, F. Iazzi, B. Minetti, R. Cherubini, Z. M. I. Haque and R. A. Ricci, in Second Annual Conference on Cold Fusion, Como, Italy, 1991, pp. 373.
73. T. Bressani, D. Calvo, A. Feliciello, C. Lamberti, F. Iazzi, B. Minetti, R. Cherubini, Z. M. I. Haque and R. A. Ricci in *Nuovo Cimento Soc. Ital. Fis. A*, **104**(1991)1413.
74. E. Botta, T. Bressani, D. Calvo, A. Feliciello, P. Gianotti, c; Lamberti, M. Agnello, F. Iazzi, B. Minetti, and A. Zecchina, in *Nuovo Cimento A*, **105**(1992)1663.
75. E. Yamaguchi and T. Nishioka in Third International Conference on Cold Fusion, Nagoya, Japan, 1992.
76. T. Shirakawa, M. Fujii, M. Chiba, K. Sueki, T. Ikebe, S. Yamaoka, H. Miura, T. Watanabe, T. Hirose, H. Nakahara and M. Utsumi, in Fourth International Conference on Cold Fusion, Maui, USA, 1994, vol 3, pp. 6-1.
77. Y. Iwamura, T. Itoh and I. Toyoda, in Fourth International Conference on Cold Fusion, Maui, USA, 1994, vol 3, pp. 12-1.
78. A. B. Garg, R. K. Rout, M. Srinivasan, T. K. Sankarnarayanan, A. Shyam and L. V. Kulkarni, in Fifth International Conference on Cold Fusion, Monaco, 1995, pp. 461.
79. T. Aoki, Y. Kurata and H. Ebihara, in Sixth International Conference on Cold Fusion, Hokkaido, Japan. 1996, pp. 291.
80. H. Shinojima, N. Takahashi, S. Koji and K. Hiroshi, in Sixth International Conference on Cold Fusion, Hokkaido, Japan, 1996, pp. 351.
81. A. G. Lipson, B. F. Lyakhov, A. S. Roussetski, T. Akimoto, T. Mizuno, N. Asami, R. Shimada, S. Miyashita, and A. Takahashi, *Fusion Technol.* **38**(2000) 238.
82. A. S. Roussetski, in Sixth International Conference on Cold Fusion, Lake Toya, Hokkaido, Japan, 1996, pp. 345.
83. V. D. Dougar-Jabon, V. I. Kariaka and N. V. Samsonenko, in Eighth International Conference on Cold Fusion, Lerici, Italia, 2000, pp. 219.
84. D. Chicea and D. Stoicescu, in Eighth International Conference on Cold Fusion, Lerici, Italia, 2000, pp. 247.

85. T. Itoh, Y. Iwamura, N. Gotoh and I. Toyoda in Fifth International Conference on Cold Fusion, Monte-Carlo, Monaco, 1995, pp. 189.
86. P. K. Iyengar and M. Srinivasan in First Annual Conference on Cold Fusion, Salt Lake City, USA, 1990, pp. 62.
87. M. Srinivasan, A. Shyam, T. C. Kaushik, R. K. Rout, L. V. Kulkarni, M. S. Krishnan, S. K. Malhotra, V. G. Nagvenkar, and P. K. Iyengar, AIP Conference Proceedings 228, 1990, pp. 514.
88. P. K. Iyengar, M. Srinivasan, S. K. Sikka, A. Shyam, V. Chitra, L. V. Kulkarni, R. K. Rout, M. S. Krishnan, S. K. Malhotra, D. G. Gaonkar, H. K. Sadhukhan, V. B. Nagvenkar, M. G. Nayar, S. K. Mitra, P. Raghunathan, S. B. Degwekar, T. P. Radhakrishnan, R. Sundaresan, J. Arunachalam, V. S. Raju, R. Kalyanaraman, S. Gangadharan, G. Venkateswaran, P. N. Moorthy, K. S. Venkateswarlu, B. Yuvaraju, K. Kishore, S. N. Guha, M. S. Panajkar, K. A. Rao, P. Raj, P. Suryanarayana, A. Sathyamoorthy, T. Datta, H. Bose, L. H. Prabhu, S. Sankaranarayanan, R. S. Shetiya, N. Veeraraghavan, T. S. Murthy, B. K. Sen, P. V. Joshi, K. G. B. Sharma, T. B. Joseph, T. S. Iyengar, V. K. Shrikhande, K. C. Mittal, S. C. Misra, M. Lal, and P. S. Rao, Fusion Technol. 18(1990)32.
89. T. C. Kaushik, A. Shyam, M. Srinivasan, R. K. Rout, L. V. Kulkarni, M. S. Krishnan and V. B. Indian J. Technol. 28(1990)667.
90. R. K. Rout, A. Shyam, M. Srinivasan, A. B. Garg and V. K. Shrikhande, Fusion Technol., 30(1996)273.
91. R. K. Rout, A. Shyam, M. Srinivasan, and A. B. Garg, in Third International Conference on Cold Fusion, Nagoya, Japan, 1992, pp. 547.
92. T. K. Sankaranarayanan, M. Srinivasan, M. B. Bajpai and D. S. Gupta in Fift International Conference on Cold Fusion, Monaco, 1995, pp. 173.
93. F. Lanza, G. Bertolini, V. Vocino, E. Parnisari, and C. Ronsecco, in Second Annual Conference on Cold Fusion, Como, Italy, 1991, pp. 151.
94. H. Yamada, S. Narita, I. Inamura, M. Nakai, K. Iwasaki and M. Baba, in Eighth International Conference on Cold Fusion, Lerici, Italy, 2000, pp. 241.
95. Q. M. Wei, X. Z. Li, B. Liu, N. Mueller, P. Schochi and H. Oehre, in Twelfth International Conference on Condensed Matter Nuclear Science, Yokohama, Japan, 2005, pp. 278.
96. B. W. Clarke and R. M. Clarke, Fusion Technol. 21(1992)170.
97. T. N. Claytor, D. D. Jackson, and D. G. Tuggle, J. New Energy 1(1)(1996)111.
98. B. W. Clarke, B. Oliver, M. McKubre, F. Tanzella and P. Tripodi in Fusion Sci. and Technol., 40(2001)152.
99. V. A. Romodanov, V. Savin, Y. Skuratnik and M. Yuriev, in Seventh International Conference on Cold Fusion, Vancouver, Canada, 1998, pp. 330.
100. A. G. Lipson, D. M. Sakov, B. F. Lyakhov, E. I. Saunin, and B. V. Deryagin, Tech. Phys., 40(1995)839.
101. J. P. Biberian and N. Armanet, in Thirteen International Conference on Condensed Matter Nuclear Science, Russia, 2006.
102. J. P. Biberian and N. Armanet, in Eighth International Workshop on Anomalies in Hydrogen/Deuterium Loaded Metals, Sicily, Italy, 2007, pp. 19.

103. E. Botta, R. Bracco, T. Breassani, D. Calvo, V. Cela, C. Fanara, U. Ferracin and F. Iazzi, in Fifth International Conference on Cold Fusion, Monaco, 1995, pp. 233.
104. E. Botta, T. Bressani, D. Calvo, C. Fanara and F. Iazzi, in Sixth International Conference on Cold Fusion, Lake Toya, Hokkaido, Japan, 1996, pp. 29.
105. G. S. Qiao, X. L. Han, L. C. Kong, S. X. Zheng, H. F. Huang, Y. J. Yan, Q. L. Wu, Y. Deng, S. L. Lei and X. Z. Li, in Seventh International Conference on Cold Fusion, Vancouver, Canada, 1998, pp. 314.
106. G. S. Qiao, X. M. Han, L. C. Kong and X. Z. Li *J. New Energy* **2**(2)(1997)48.
107. Y. Arata and Y.C. Zhang, *Proc. Jpn. Acad., Ser. B*, **73**(1997)1.
108. Y. Arata and C. Zhang, *Proc. Jpn. Acad., Ser. B*, **73**(1997)62.
109. Y. Arata and Y.C. Zhang, *Proc. Jpn. Acad., Ser. B*, **75**(1999)281.
110. D. W. Mo, L. Zhang, B. X. Chen, Y. S. Liu, S. Y. Dong, M. Y. Yao, L. Y. Zhou, H. G. Huang, X. Z. Li, X. D. Shen, S. C. Wang, T. S. Kang and N. Z. Huang, in Third International Conference on Cold Fusion, Nagoya Japan, 1992, pp. 535.
111. W. Mo, Y. S. Liu, L. Y. Zhou, S. Y. Dong, K. L. Wang, S. C. Wang, and X. Z. Li, in Second Annual Conference on Cold Fusion, Como, Italy, 1991, pp. 123.
112. C. Wang, T. S. Kang, K. L. Wang, S. Y. Dong, Y. Y. Feng, D. W. Mo and X. Z. Li, in Second Annual Conference on Cold Fusion, Como, Italy, 1991, pp. 169.
113. S. Jin, F. Zhang, D. Yao and B. Wu, in Second Annual Conference on Cold Fusion, Como, Italy, 1991, pp. 145.
114. X. Z. Li, S. Y. Dong, K. L. Wang, Y. Y. Feng, C. Luo, R. Hu, P. Zhou, D. Mo, Y. Zhu, C. Song, Y. Chen, M. Yao, C. Ren and Q. Chen, in Anomalous Nuclear Effects in Deuterium/Solid Systems, "AIP Conference Proceedings 228", 1990, pp. 419.
115. S. Y. Dong, K. L. Wang, Y. Y. Feng, L. Chang, C. M. Luo, R. Y. Hu, P. L. Zhou, D. W. Mo, Y. F. Zhu, C. L. Song, Y. T. Chen, M. Y. Yao, C. Ren, Q. K. Chen and X. Z. Li, *Fusion Technol.*, **20**(1991)330.
116. F. E. Cecil, H. Liu, D. H. Beddingfield, and C. S. Galovich, "AIP Conference Proceedings 228", 1990, pp. 375.
117. S. E. Jones, T. K. Bartlett, D. B. Buehler, J. B. Czirr, G. L. Jensen and J. C. Wang in "AIP Conference Proceedings 228", 1990, pp. 397.
118. S. E. Jones, F. W. Keeney, A. C. Johnson, D. B. Buehler, F. E. Cecil, G. Hubler, P. L. Hagelstein, J. E. Ellsworth and M. R. Scott, in Tenth International Conference on Cold Fusion, Cambridge, USA, 2003, pp. 509.
119. A. S. Roussetski, A. G. Lipson and V. P. Andreanov, in Tenth International Conference on Cold Fusion, Cambridge, USA, 2003, pp. 559.
120. F. E. Cecil, H. Liu, D. Beddingfield, and C. S. Galovich, in Tenth International Conference on Cold Fusion, Cambridge, USA, 2003, pp. 535.
121. A. G. Lipson, V. A. Klyuev, B. V. Deryagin, Y. P. Toporov, and D. M. Sakov, *Sov. Tech. Phys. Lett.* **15**(10)(1989)783.
122. G. S. Huang, D. W. Mo, W. Z. Yu, M. Y. Yao, X. Z. Li, and B. Y. Liaw, in Fourth International Conference on Cold Fusion, Maui, USA, 1994, vol 1, pp. 20-1.
123. K. Shikano, H. Shinojima, and H. Kanbe, in Fifth International Conference on Cold Fusion, Monaco, 1995, pp. 251.

124. M. McKubre, R. C. Rocha-Filho, S. Smedley, F. Tanzella J. Chao, B. Chexal, T. Passell, and J. Santucci, in First Annual Conference on Cold Fusion, Salt Lake City, Ut, USA, 1990, pp. 20.
125. F. S. Bu, X. Z. Li, L. Gao, H. Shi and G. S. Huang, in Sixth International Conference on Cold Fusion, Hokkaido, Japan. 1996, pp. 187.
126. G. S. Huang and X. Z. Li in Sixth International Conference on Cold Fusion, Hokkaido, Japan. 1996, pp. 198.
127. E. Del Giudice, A. De Ninno, A. Fratolillo, G. Preparata, F. Scaramuzzi and P. Tripodi, in Eighth International Conference on Cold Fusion, Lericce, Italy, 2000, pp. 211.
128. F. Scaramuzzi, J. Alloys and Compounds, **385**(2004)19.
129. V. K. Shrikhande, T. C. Kaushik, S. K. H. Auluck, A. Shyam and M. Srinivasan, in Fifth International Conference on Cold Fusion, Monaco, 1995, pp. 465.
130. Y. Arata and Y.C. Zhang, Proc. Jpn. Acad., Ser. B, **78**(2002)57.
131. L. C. Kong, X. L. Han, S. X. Zheng, H. F. Huang, Y. J. Yan, Q. L. Wu, Y. Deng, S. L. Lei, C. X. Li and X. Z. Li, J. New Energy, (1)(1998)20.
132. G. S. Qiao, X. L. Han, L. C. Kong, S. X. Zheng, H. F. Huang, Y. J. Yan, Q. L. Wu, Y. Deng, S. L. Lei and X. Z. Li, Seventh International Conference on Cold Fusion, Vancouver, Canada, 1998, pp. 314.
133. Y. Iwamura, T. Itoh and M. Sakano, in Eighth International Conference on Cold Fusion, Lericci, Italy, 2000, pp. 141
134. Y. Iwamura, T. Itoh, M. Sakano, S. Sakai and S. Kuribayashi, in Tenth International Conference on Cold Fusion, Cambridge, USA, 2003, pp. 435.
135. Y. Iwamura, T. Itoh, M. Sakano, N. Yamazaki, S. Kuribayashi, Y. Terada and T. Ishikawa, in Twelfth International Conference on Condensed Matter Nuclear Science, Yokohama, Japan, 2005, pp. 178.
136. T. Higashiyama, M. Sakano, H. Miyamaru and A. Takahashi, in Tenth International Conference on Cold Fusion, Cambridge, USA, 2003, pp. 447.
137. T. Minari, R. Nishio, A. Taniike, Y. Furuyama, and A. Kitamura, in Tenth International Conference on Cold Fusion, Cambridge, USA, 2003, pp. 218.
138. H. Yamada, S. Narita, S. Taniguchi, T. Ushirozawa, S. Kurihara, M. Higashizawa, H. Sawada, M. Itagaki and T. Odashima, in Twelfth International Conference on Condensed Matter Nuclear Science, Yokohama, Japan, 2005, pp. 196.
139. H. Yamada, S. Narita, H. Onodera, H. Suzuki, N. Tanaka, T. Nyui and T. Ushi, in Tenth International Conference on Cold Fusion, Cambridge, USA, 2003, pp. 455.
140. A. Kitamura, R. Nishio, H. Iwai, R. Satoh, A. Tanike and Y. Furuyama, in Twelfth International Conference on Condensed Matter Nuclear Science, Yokohama, Japan, 2005, pp. 272.
141. M. Castellano, M. Di Giulio, M. Dinescu, V. Nassisi, A. Conte and P. P. Pompa, in Eighth International Conference on Cold Fusion, Lericci, Italia, 2000, pp. 287.
142. M. Di Giulio, E. Filippo, D. Manno and V. Nassisi, J. Hydrogen Eng. **27**(2002)527.
143. Q. M. Wei, Y. C. Rao, S. T. Tao, D.-L. Luo and X. Z. Li, in Eighth International Workshop on Anomalies in Hydrogen/Deuterium Loaded Metals, Sicily, Italy, 2007, pp. 351.
144. S. Focardi, R. Habel, and F. Piantelli, Nuovo Cimento A **107**(1994)163.

145. S. Focardi, V. Gabbani, V. Montalbano, F. Piantelli, and S. Veronesi, *Atti Accad. Fisioc.*, Serie XV, XV **109**(1996).
146. S. Focardi, V. Gabbani, V. Montalbano, F. Piantelli and S. Veronese, *Il Nuovo Cimento*, **111**(1998)1233.
147. S. Focardi, V. Gabbani, V. Montalbano, F. Piantelli, and S. Veronesi, *Proceedings Asti Workshop on Hydrogen/Deuterium loaded metals*, **64**(1999)35.
148. S. Focardi, V. Gabbani, V. Montalbano, F. Piantelli, and S. Veronesi, *Atti Accad. Fisioc.*, Serie XV, XVIII **109**(1999).
149. S. Focardi, V. Gabbani, V. Montalbano, F. Piantelli and S. Veronesi, in *Anomalies in Hydrogen / Deuterium Loaded Metals*, Bologna Italy, **64**(1999)35.
150. S. Focardi, V. Gabbani, V. Montalbano, F. Piantelli and S. Veronesi, *Asti Workshop on Anomalies in Hydrogen/Deuterium Loaded Metals*, Villa Riccardi, Italy, 1997, pp. 35.
151. A. Battaglia, L. Daddi, S. Focardi, V. Gabbani, V. Montalbano, F. Piantelli, P. G. Sona, and S. Veronesi, *Nuovo Cimento A*, **112**(1999)92.1
152. E.G. Campari, S. Focardi, V. Gabbani, V. Montalbano, F. Piantelli, E. Porcu, E. Tosti, and S. Veronesi, in *Eight Internatinal Conference on Cold Fusion*, Lerice, Italy, 2000, pp. 69.
153. E. Campari, G. Fasano, S. Focardi, G. Lorusso, V. Gabbani, V. Montalbano, F. Piantelli, C. Stanghini, AND S. Veronesi , in *The Eleventh International Conference on Cold Fusion*, Marseilles, France, 2004, pp. 405.
154. S. Focardi, V. Gabbani, V. Montalbano, F. Piantelli and S. Veronesi, in *Eleventh International Conference on Cold Fusion*, Marseilles, France, 2004, pp. 70.
155. E. Campari, S. Focardi, V. Gabbani, V. Montalbano, F. Piantelli and S. Veronesi, in *Eleventh International Conference on Cold Fusion*, Marseilles, France, 2004, pp. 414.
156. G. Cammarota, W. Collis, A. Rizzo and C. Stremmenos, in *Conference on Anomalies in Hydrogen / Deuterium Loaded Metals*, Bologna, Italy 1999.
157. E. Cerron-Zeballos, I. Crotty, D. Hatzifotiadou, J. Lamas Valverde, M.C.S. Williams and A. Zibichi, *Nuovo Cimento A*, **109**(1996)1645.
158. U. Mastromatteo, *Eighth International Conference on Cold Fusion*, Vancouver, Canada, 2000, pp. 81.

Deuteron Electromigration in Thin Pd Wires Coated With Nano-Particles: Evidence for Ultra-Fast Deuterium Loading and Anomalous, Large Thermal Effects

Francesco Celani¹, P. Marini², V. Di Stefano², A. Spallone¹, M. Nakamura², E. Purchi², O. M. Calamai², V. Andreassi¹, E. Righi¹, G. Trenta¹, A. Marmigi¹, G. Cappuccio¹, D. Hampai¹, F. Todarello², U. Mastromatteo³, A. Mancini⁴, F. Falcioni⁵, M. Marchesini⁵, P. Di Biagio⁵, U. Martini⁵, P. G. Sona⁶, F. Fontana⁷, L. Gamberale⁷ and D. Garbelli⁷

¹ INFN-LNF Via E. Fermi 40, 00044 Frascati, Rome, Italy E-mail: francesco.celani@lnf.infn.it

² ISCMNS, Rome Group#1, Via Lero 30, 00129 Rome, Italy

³ STMicroelectronics SpA, Via Tolomeo 1, 20010 Cornaredo, Milan, Italy

⁴ ORIM SpA, Via Concordia 65, 62100 Piediripa, Macerata, Italy

⁵ CSM SpA, Via di Castel Romano 100, 00129 Rome, Italy

⁶ Via S. Carlo 12, 20090 Segrate, Milan, Italy

⁷ Pirelli Labs SpA, Viale Sarca 222, 20126 Milan, Italy

Abstract

Large excess heat is measured in a Pd wire coated with nano-particles. A long (65 cm) and thin (50 μm) Pd wire is coated with thin layers of Pd nano-particles, stabilized against self-sintering by the addition of selected chemical elements: the coating is adhered to the wire surface by heating it in air up to over 800°C. The wire is then heated with up to 1 A of direct current in a pressurized D₂ gas atmosphere. The D⁺ deuterons in the Pd lattice are forced to move toward the cathodic end of the wire because of the voltage drop along the wire (the Cöhn effect). Large excess power density (about over 400 W/g of Pd), at high temperatures (up to 400-500°C), is then measured using isoperibolic calorimetry. The reference experiment is made, in situ and without opening the cell, using a Pt wire of same dimensions as the Pd wire, to which was applied the same electrical power. The onset of excess heat occurs in during a phase change from an $\alpha + \beta$ combined phase of the Pd-D to the α phase, and is proportional to the current density, and to the corresponding voltage drop or input power applied, i.e. the Pd temperature. In the range of temperatures explored up to now, the excess power has exhibited “*positive feedback*” behaviour versus temperature. This may prove useful to developing future *self-sustaining* devices for *practical applications*. No anomalous effects were found using ⁴He (or Ar, or dry-air) gases.

1. INTRODUCTION

1.1. Nano-particles in Cold Fusion

The use of nano-materials in cold fusion studies started with the systematic studies of Yoshiaki Arata (Osaka University, Japan), and his Collaborators, which have been conducted

since 1993 [1]. They first used Pd-black, with particle sizes varying from several micrometers down to a fraction of a micrometer. Later, in 2002, they developed an innovative material by embedding Pd particles with a diameter of about 10 nm in a matrix of ZrO_2 [2].

In May 2008, Arata measured excess heat in the presence of pressurized (60 bar) D_2 , using the ZrO_2 -nano_Pd material without applying any input power. The excess heat lasted over 50 hours. The chemical heat of formation for this system was observed in a control run using H_2 with the same material: it did not produce persistent, long lasting heat. Large amounts of ^4He , as ashes from the D+D reaction, were also found. The ^4He gas, a known product of cold fusion reactions, was detected on line using a High Resolution Quadrupole Mass Spectrometer [3].

Another procedure to produce nano-materials was developed by Yasuhiro Iwamura and Co-workers (Mitsubishi Heavy Industries, Yokohama, Japan, 2000). The procedure is similar, in some ways, to the fabrication of silicon semiconductors. In the Iwamura experiment, a Pd wafer is fabricated which contains several thin Pd-CaO nano-layers, with a small amount of Sr, Cs or Ba on the surface. When a flux of slightly pressurized D_2 at a temperature of about 80°C is forced to pass through the wafer, the surface materials are transmuted into Mo, Pr and Sm respectively [4, 5].

Most of the other experiments in this field, using gas loading and/or nano-materials (even surface-oxidized Pd tubes), were summarized by Jean-Paul Biberian at this Conference [6].

1.2. Main results of our previous experiments with Pd nano-particles

The maximum excess power achieved in our previous experiments with Pd nano-particles was only about 0.5 W/g of Pd at 300°C and 60 bar of D_2 [7, 8]. These particles were tightly packed together, not coated onto a metal substrate as they are in the experiments described in the present paper. They were produced by filling nano-porous ($\Phi=5.8$ nm) materials (such as γ Alumina) with soluble salts of Pd and Sr. They were then decomposed to oxides through high temperatures cycles of calcination and controlled sintering under a controlled atmosphere in a quartz furnace.

The methodology of “incipient wetting impregnation” was adopted for the preparation of the nano-porous material. This standard procedure was modified in order to maximize the amount of Pd in the nano-porous material (up to 10-15% w/w).

A twin-chamber differential reactor (Fig. 1) was developed at INFN-LNF to evaluate the behaviour of the Pd nano-particles under a deuterium or hydrogen atmosphere.

The Pd nano-particles were placed in the stainless steel crucible inside the working chamber. Combinations of inert materials and gas such as Ag- γ Alumina and D_2 , or supposedly inert gas such as H_2 with active Pd-Sr- γ Alumina, were placed into the crucible of the reference chamber for calibration purposes.



Figure 1. The twin chamber differential reactor developed at INFN-LNF. Pressure: up to 100 bar. Temperature: up to 320°C. Useful volume of the crucibles: 15 cm³.

1.3. Electromigration and the main result of our previous experiments

Since 1994, a series of experiments using the so-called HPPE technique (“High Power Pulsed Electrolysis”) was performed by our research team at Frascati National Laboratory of the National Institute of Nuclear Physics. The geometric set-up of the cell was similar to that previously employed by Akito Takahashi (Osaka University, Japan) in 1992 [9]. From 1992 to 1993, we followed Takahashi’s procedure using up to 5 A of direct current to electrolytically load a Pd plate cathode (25×25×1 mm). Starting in 1994, we moved from DC to pulsed power: 300 V maximum, 150 A maximum, typical pulse duration 1-2 μs, repetition rate up to 30 kHz.

The HPPE procedure was later applied to long (50-300 cm) and thin (Φ=100-250 μm) Pd wires. In this case, in contrast to the Pd plate, we employed both electrolysis and strong electromigration, at the same time. The D⁺ deuterons in the Pd lattice are forced to move along the Pd wire (the Cöhn effect) because of the voltage drop between the most cathodic and less cathodic ends of the wire. We decided to adopt this technique after profitable discussions with Giuliano Preparata (Milan University, Italy) and his collaborators. The electromigration effect applied to cold fusion experiments was pioneered by Martin Fleischman and his collaborators since 1993 [10].

During electromigration, the equilibrium state for the deuterium concentration at a fixed point x of the Pd wire is given by:

$$C_x = C_o \exp \left[\frac{-eZ^* V(x)}{K_B T} \right] \quad (1)$$

Where:

e = electron charge ($1.602 \cdot 10^{-19} \text{C}$);

K_B = Boltzmann constant ($1.38 \cdot 10^{-23} \text{J/K}$);

T = temperature (K);

Z^* = effective charge number of H (or D) in Pd. The charge number is equal to 1 at low concentrations ($H/Pd \ll 0.6$). It decreases down to 0.1 at higher concentrations ($H/Pd > 0.8$). According to some authors (G. Preparata, 1996, unpublished), it increases again ($Z^* \rightarrow 1$) at very high loading ratios ($H/Pd > 1$).

The performance of pulsed electrolysis (current density along the wire up to $300,000 \text{ A/cm}^2$), in a specific experiment is described in one of our paper published by Physics Letters A [11].

In that series of experiments we found that the surface of the Pd wire was progressively covered with thin, uncontrolled layers made of different materials. The materials came from: impurities present in the electrolyte; the main chemical elements of the electrolyte itself; and partial anode dissolution (Ni in this experiment). We also found that such layers played an important role in the loading rate ($\delta D / \delta t$) and ratio (D/Pd) of the Pd cathode, which are key points for anomalous heat production.

In the present work we decided to perform the Pd loading in a D_2 atmosphere, by using (as in the HPPE technique) both electromigration and, in a substantial improvement over our previous studies, a *controlled coating* on the surface of the Pd wires, which is made without electrolysis.

Unlike the electrolytic technique, the gas loading technique allows us to easily explore the effect of temperatures well above 100°C . The Pd consists of a complex mixture of soluble Pd salts and other elements deposited on the surface of thin Pd wires. The wires are then heat treated by Joule heating in air, up to over 800°C . This temperature is high enough to decompose the PdO, which forms during heating the Pd in air at $500\text{--}750^\circ\text{C}$. Specific chemical compounds were added to the Pd soluble salts in order to improve both the thermal stability of the resulting Pd nano-layer and the mechanical strength of the Pd wire itself. Moreover, the other specific elements added to the Pd surface have the property of largely reducing the nano-Pd self-sintering caused by high temperatures and reduced dimensionality.

The method of preparation described above is also known as “Nanoscale Surface Modification” and is based on the “Atomic Layer Deposition” process.

2. Experimental Reactor

We modified an experimental reactor previously used by us, in 2004, for Pd experiments in hydrogen without fibre-glass sheaths. We tested D_2 loading of Pd wires (and inert gases for comparison). The reactor acts as a differential isoperibolic calorimeter. Inside it are three wires braided together: a Pd wire coated with nanoparticles (that can produces excess heat), and two Pt wires, designated Pt_{cal} and Pt_{mon} . Pt_{cal} serves as a calibration Joule heater and Pt_{mon} serves as

a distributed thermometer; that is, an RTD (resistance temperature detector) that is placed alongside the full length of the Pd and Pt_{cal} wires.

All three wires are of the same diameter (50 μm) and length (usually 65 cm). They are put inside thin, flexible fiberglass sleeves, which withstand a maximum temperature of 550°C, to ensure that they are electrically insulated from one another. The three fiberglass-covered wires are braided together, to insure that the positions of the three wires are symmetrically exposed to the gas and to the other two wires (Fig. 2).

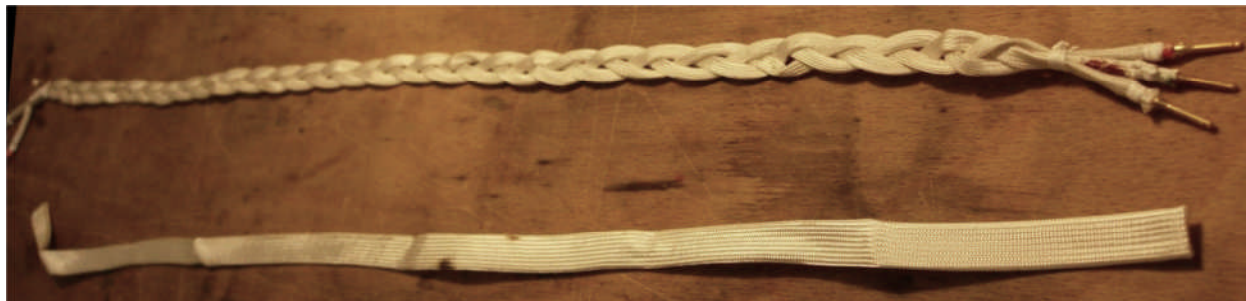


Figure 2. Three wires braided together: 1 coated Pd wire and 2 Pt wires (Pt_{cal}, Pt_{mon}). Each wire is 50 μm in diameter. The diameter of the fibre-glass sheaths is 2 mm. The braid is completely covered inside a larger sheath (6 mm) shown below. Ultra-pure (>99.99%) Pt was used for Pt_{cal} and Pt_{mon}. Pt_{cal} serves as a calibration Joule heater and Pt_{mon} serves as a distributed thermometer.

The braid is thermally insulated as shown in Fig. 3. Each wire can be individually supplied with constant direct current, on a rotating basis (one wire at a time). The electrical resistance of each wire is continuously computed by the V/I ratio. The braid covered by thermal insulation is put into stainless steel tube (36 cm length, 10 cm OD, 9.5 cm ID) (Fig. 4) capable of bearing pressurized D₂ (10 bar maximum). The tube is evacuated, and then D₂ gas is admitted into it.



Figure 3. The braid placed inside thermal insulation.



Figure 4. The pressurized experimental cell surrounded by a large water bath.

Typical operating pressure is 6 bar absolute. The stainless steel tube is placed inside a large water bath in order to make the temperature homogeneous; to dampen the effects of room temperature variations; and to dissipate the heat produced inside the tube. The large, thick flange covering the cell is made of an Al alloy to increase thermal conductivity. The internal wall of the cell is fully covered by a 1 mm thick Cu foil to improve thermal homogeneity. The water bath temperature is continuously measured.

The loading rate and loading ratio of the Pd wire is monitored by measuring its resistance ratio (R/R_0), with R_0 normalized at 20°C (details below). All gas is removed from the Pd by long-time vacuum degassing at high temperatures (about 450°C).

Once equilibrium is reached – meaning that the loading ratio is stable, the selected D_2 pressure is reached, and the cell is at room temperature – constant direct current power is fed to the Pd wire, which causes electromigration and Joule heating of the wire. Power is typically 5 W at the beginning of the experiment. The temperature of the system rises up until the electrical resistances of the three wires becomes constant (but different for each of the three wires). At this point thermal equilibrium is reached (isoperibolic condition) characterized by the temperature reached by the thermoresistance Pt_{mon} . The power supply is then turned off and the temperature of the system is allowed to fall to room temperature, or – to save time – the temperature is allowed to fall to a fixed value of Pt_{mon} above room temperature (usually 50°C).

The same power level (5 W) that was previously fed to the Pd wire is now fed to the Pt_{cal} wire. The new thermal equilibrium is again characterized through the measurement of the Pt_{mon} temperature. This is differential isoperibolic calorimetry.

Obviously, if the equilibrium temperatures of Pt_{mon} are the same in both cases, no excess heat is being produced. If, on the contrary, a temperature difference is measured, the excess power generated by the Pd wire can be estimated by simple means: e.g. by the extra power which has to be fed to the Pt_{cal} to close the gap between the two Pt_{mon} measured temperatures. Another simple and fast procedure adopted was graphic interpolation; e.g., Fig 5 with 4He gas shows no excess heat, whereas Fig. 8, with D_2 , shows large excess heat.

Further values of direct current power (e.g. 10, 15, 20, 25...50, 55 W) are then applied first to the Pd wire and then to the Pt_{cal} wire to measure excess heat as a function of the Pd temperature. This is evaluated by comparing the effects of the power fed to the Pt_{cal} wire on the temperature reached by Pt_{mon} .

The braid arrangement of the three wires should assure good symmetry, so that heat is distributed in the cell the same way regardless of which wire is heated. Thus, in the absence of excess heat, the temperature of Pt_{mon} should be the same when the same level of direct current power is fed to either the Pd wire or to the Pt_{cal} wire.

To verify the symmetry of the system, we begin the experiment by performing several blank tests in a helium atmosphere. The thermal conductivity of He is quite close to that of D_2 [12, 13].

To better understand the performance of the system and confirm the results as a whole, some tests were made in a vacuum (typically 10^{-5} to 10^{-6} bar), and in dry-air, and argon at different pressures and power levels.

3. Experimental Results

3.1. Blank test.

Before each experiment in a D_2 atmosphere, a preliminary blank test is always performed in a helium atmosphere to assess the geometrical and thermal symmetry of the braid. The helium test is repeated, if possible, at the end of each series of experiments.

The results of a blank experiment, with helium absolute pressure at 6.2 bar, are shown in Fig. 5. When the same power is applied to either the Pd wire (red line) or to the Pt_{cal} wire (dark blue line), the Pt_{mon} temperatures are practically the same. The two lines almost completely overlap. At the applied power of 42 W the measured temperature difference is less than 1%, a level of uncertainty of less than 0.4 W.

As far as the R/Ro ratio of the Pd wire is concerned: when the power is applied to the Pd wire (direct heating), the R/Ro ratio values are obviously higher than those observed when the Pd wire is indirectly heated by the Pt_{cal} . For example, at a pressure of 6 bar, direct heating of the Pd at 42 W produces a R/Ro ratio (with Ro measured at 20°C) of 2.03 (orange line) equivalent to a temperature of about 340°C. The indirect heat of the Pd with 42 W through the Pt_{cal} wire produces an R/Ro ratio of 1.45 (light blue line) equivalent to a temperature of about 140°C. In the latter case the Pd wire only reaches the temperature of Pt_{mon} .

The difference in temperatures between the direct and indirect heat depends on the geometry of the pressurized chamber and the specific configuration of the wires, together with the performance of thermal insulation. In this case, we designed chamber geometry to make the temperature changes large in order to easily study the effect of temperature. In a chamber designed to optimize the efficiency, i.e. to reduce input power and get at the maximum amount of anomalous excess heat, the geometry will be drastically changed. We have built a new cell that should reduce the amount of input energy needed to sustain the reaction. Not only is it more efficient, it is equipped with additional thermometers outside the stainless steel chamber in order to eliminate any possible influence due to slight differences in the thermal conductivity of deuterium and helium.

As noted the Pt_{mon} wire acts as an RTD (resistance temperature detector); temperature evaluations are made by a fourth order fit of resistivity data for Pd and Pt, according to CRC data-book (84th edition, 2004), in the temperature range of 273-900 K.

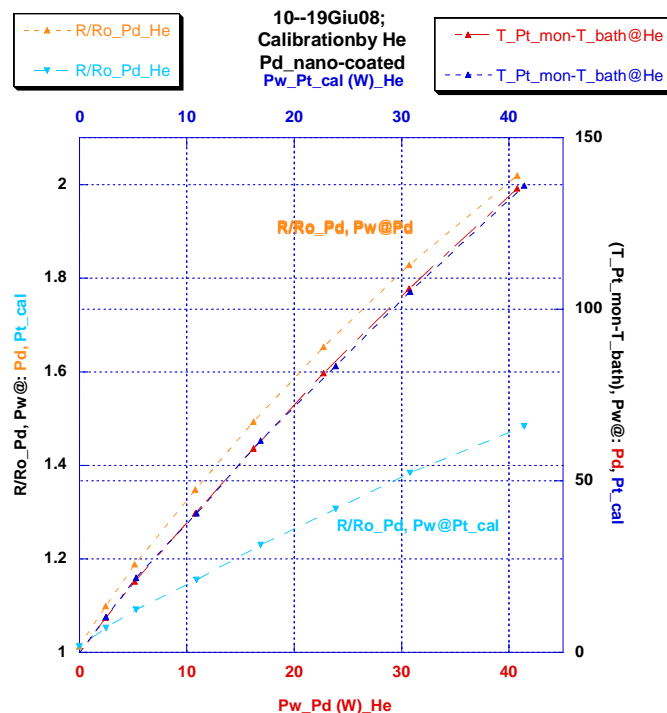


Figure 5. Calibration of the system with helium at 6.2 bar absolute.

3.2. Deuterium atmosphere

Once the blank test/experiments finished, the reactor temperature is allowed to drop down to room temperature for a final cross-check. The helium is then completely removed with a rotary pump equipped with a liquid nitrogen trap. The trap ensures that hydrocarbons from the oil pump vapor are not absorbed by the highly reactive nano-particles. To fully remove the helium from the Pd and Pt wires, the degassing is usually performed at high temperatures (about 450°C) under vacuum conditions. After final cooling to room temperature, a pressure valve is opened, allowing D₂ to rapidly enter the cell. In a few seconds the working D₂ pressure (6.2 bar absolute) is reached and the D loading of the coated Pd wire begins.

A loading rate up to $R/R_o = 1.9$ is achieved astonishingly quickly: typically in 10 seconds (Fig. 6, blue line). This is probably because of the chemical heat released by the absorption process, which increases the temperature of the wire (Fig. 6, red line). The higher temperature, in turn, increases the loading rate. The net importance of the nano-particles coating with respect to the Pd loading rate is highlighted in Fig. 7. This shows that with long treatments of the Pd wire without any coating, heated up to over 800°C in air, the required loading time is as long as 1000 seconds.

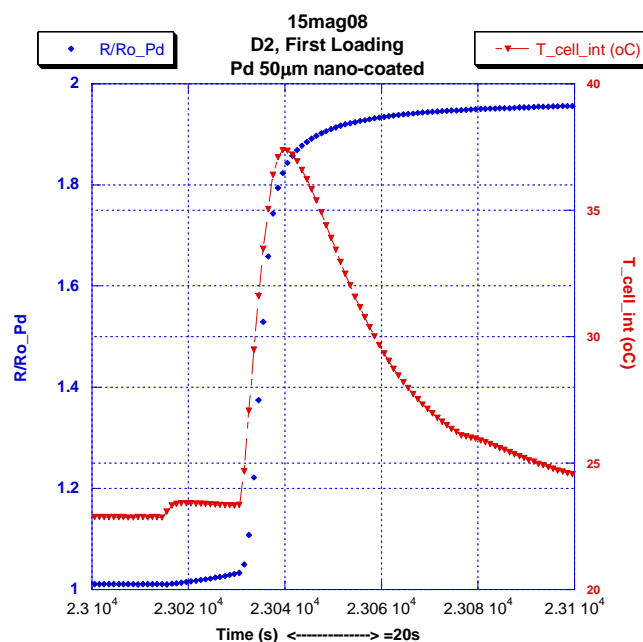


Figure 6. 50 μ m nano-coated Pd exposed to deuterium gas at 6.2 bar loads quickly, in 10 – 30 s. In the plot shown in Fig. 6 the “T_{cell int}” label means the temperature measured at the top of the three fibre-glass sheaths, thermally insulated (as shown in Fig. 3) The temperature is measured by a K type thermocouple installed in the stainless steel tube (Φ =1.5mm).

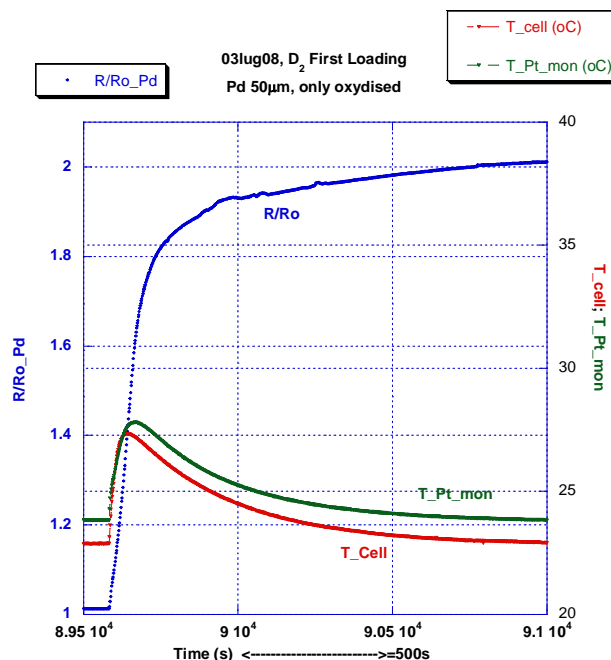


Figure 7. 50 μ m Pd without nanoparticles. It has been treated only by being oxidized at temperatures between 600 and 700°C, reduced at over 800°C, in several cycles for a total time of 30 minutes. Final cooling from the high temperatures was slow (two minutes) to avoid quenching, which causes an apparent increase in Pd resistivity because of thermal stress.

Once equilibrium is reached, with $D/Pd = 0.75$; $R/R_o = 2.0$; D_2 pressure 6.2 bar; and room temperature, the Pd wire and Pt_{cal} are alternatively fed with nearly equal direct current power. The power is then stepped up and again fed to each wire, until it reaches the maximum value of 52 W in the experiment shown at Fig. 8.

The evolution of the Pd wire loading ratio with temperature (R/R_o values), when directly heating (rather than being heated by Pt_{cal}), exhibits peculiar behaviour:

Region A - low power ($0 \rightarrow 13$ W): the Pd-D system is in the $\alpha + \beta$ phase; the R/R_o ratio increases almost exponentially from 2 up to a maximum of about 2.35 (orange line, Fig. 8, 9). This is in spite of the concomitant decrease of the D/Pd ratio, due to the degassing process, which naturally accompanies the temperature increase of the Pd wire. This phenomenon is not observed when the Pd wire is indirectly heated to the same temperature with the Pt_{cal} wire instead of with current in the Pd wire itself (light blue line, Fig. 8).

At present, we cannot fully explain the exponential increase of the R/R_o value when direct current is flowing. We do have some candidate hypotheses, such as the “*Preparata effect*” (2000) that predicts a sort of confinement of Deuterium inside the Pd wires due to large voltage drops along it.

In region A, no detectable excess power is observed.

Region B - power $13 \rightarrow 20$ W: massive degassing of the Pd wire suddenly occurs and the R/R_o value abruptly drops; the wire is now almost completely in the Pd-D α phase. In concomitance with the phase transition the excess power starts (Figs. 8, 9). Even though reliable values of the D diffusivity in the Pd-D α and β phases are not available, there is nearly general agreement on assigning to the α phase the higher value of deuterium diffusivity. Moreover, the effective Z^* charge in the electromigration formula (1) is higher in the α phase. Accordingly, the intensity of electromigration should be significantly enhanced in this phase.

Region C - power $20 \rightarrow 52$ W: the wire is fully in the α phase; the R/R_o ratio increases because of the increase of the Pd wire temperature. Excess power is observed, increasing with the direct current power fed to the Pd wire. Excess power reaches ≥ 5 W when the current is highest, at 52 W (Figs. 8, 9).

The results shown in Figs 8 and 9 are typical of this series of experiments. A short summary of the main experiments carried out with 50 μm Pd wire is shown in Table A.

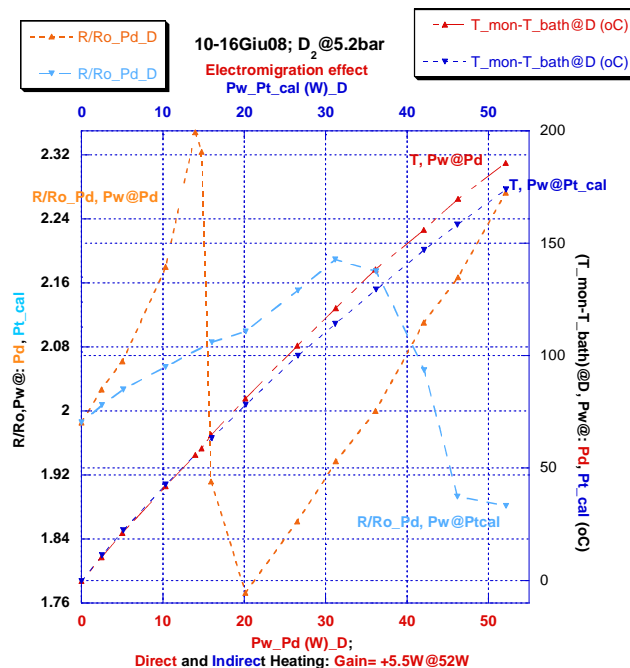


Figure 8. Pd wire nano-coated: deuterium at 6.2 bar abs. Temperature of (Pt_{mon} -bath) and Pd R/Ro, versus power applied to Pd and to Pt_{cal} .

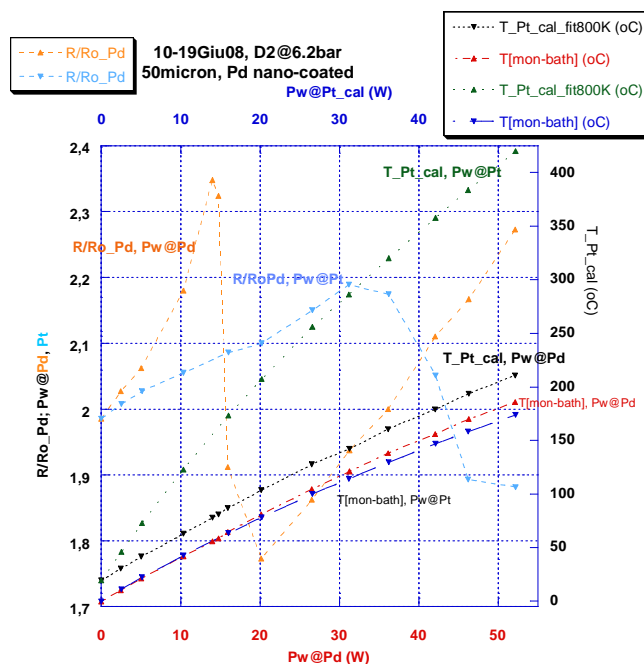


Figure 9. Pd nano-coated, deuterium at 6.2 bar abs. The curve of the Pt_{cal} temperature against power (green line) is also shown. While the massive degassing (Pd wire Joule heated - orange line) happens at 170°C , determined by the relationship to the Pt_{cal} green curve, the degassing of the indirectly heated Pd wire (sky-blue line) is computed based on the relationship to Pt_{mon} (black line).

Table A

Summary of the main 3-wire braid experiments
Pd (99.9% purity) by J/M, $\Phi=50\text{ }\mu\text{m}$, $l=60\text{--}65\text{ cm}$, $S=0.94\text{--}1.02\text{ cm}^2$, weight=14-15.3 mg;
coating weight ~1 mg.

Date	Pd wire treatments	Gas type, Pressure (bar)	Input Power (W)	Excess power (W)	Notes
10 Jun 08	nano-coated Air 800°C	He, 5.2	–	No excess power (blank test)	Wire prepared on 5 May 08 and used in previous experiments.
12 Jun 08	nano-coated Air 800°C	He, 1.2	–	No excess power (blank test)	Same wire
13 Jun 08	nano-coated Air 800°C	D ₂ , 5.2	52	5.2 (370 W/g Pd)	Same wire
19 Jun 08	nano-coated Air 800°C	D ₂ , 1.5	48	3.1	Wire operative for 50 days. Wire broken after 2 hours of experiments with H ₂ .
30 Jun 08	nano-coated Air 800°C	H ₂ , 5.2	41.6	1.4	New wire. Wire broken after 1 day with H ₂
02 Jul 08	Virgin	D ₂ , 5.2	–		Broken at loading
03 Jul 08	Air 800°C no nano-coating	D ₂ , 5.2	50	3.3	Broken after 4 days
			55	4.0	

4. Conclusions

A subtle, well-hidden systematic error is always possible but, up to now, no error has been found, by either our group or by several researchers who carefully examined our experiments and preprint. Moreover, during the ICCF-14 Conference we engaged in long discussions with several attendees: the aim was to find a mistake in the experiment. No such mistake was found.

We have shown that large excess power (about 400 W/g of Pd), at high temperatures (400-500°C), is produced when direct current is flowing in a long (60 – 65 cm) and thin (50 μm) Pd wire immersed in a pressurized deuterium atmosphere. The excess heat occurs when, because of the Joule heating of the Pd wire, a phase transition seems to happen from $\alpha+\beta$ to α phase of the Pd-D system and the interrelated diffusion coefficient of deuterium increases due to the

combined effect of both high temperature and low-deuterium concentration inside the Pd lattice.

When a thin layer of Pd nano-particles, mixed with other elements, is applied to a Pd wire surface, the wire is stabilized, preventing self-sintering (due to high temperatures) and/or self-destruction (due to localized hot-spot, anomalous thermal effects). The amount of the excess heat increases, and overall stability and reliability significantly improve.

We would welcome the opportunity to do studies of ^4He production as ashes of the D+D reactions, such as the measurements performed by Y. Arata [1, 3]. Unfortunately, we have not been able to do this so far, because we do not have access to the HR-QMS at the Frascati Research Center. The people operating this instrument report that it cannot be made available because of complex maintenance issues.

No anomalous thermal effects were detected in several long duration blank experiments with helium gas.

Moreover, there are indications in our other experiments (not described in this paper and only briefly discussed during the Conference) that the absolute temperature of Pd wire, by itself, has a significant effect on anomalous temperature generation. The next experimental apparatus will be optimized to detect also such effect.

Finally, the effects of the *fluxes* of active gas (e.g. deuterium or even hydrogen), through the nano-coated Pd surface and/or along the Pd bulk itself, has to be quantified by specific experiments.

Further work, especially at the engineering level, is needed to apply this new effect to a practical reactor for energy generation. The aim is to transfer the anomalous excess heat from *inside* the reactor (like in the experiment described), to *outside* for a practical use.

5. Acknowledgements

We deeply thank Prof. Yoshiaki Arata (holder of the Emperor's Order of Cultural Merit; Osaka University, Japan) who introduced us to the "special" world of nano-palladium.

We are indebted to Jed Rothwell (LENR-CANR.org, USA) for useful critical reading and editing of our manuscript.

We would like to thank Prof. Brian Josephson (Nobel laureate; Cambridge University, England) for very useful suggestions and comments on our manuscript.

6. References

1. Arata Y, Zhang Y-C; Koon Gakkaishi (J. of High Temp. Society), 20 (4) 1994 148 (in Japanese, Abstract in English): *A new energy generated in DS Cathode with Pd-black*.
2. Yamamaura S., Sasamori K., Kimura H., Zhang Y-C and Arata Y. Journal of Material Research, 2002; 17:1329-1334. *Hydrogen absorption of nanoscale Pd nanoparticles embedded in ZrO₂ matrix prepared from Zr-Pd amorphous alloys*.
3. Arata Y, Zhang Y-C; *Establishment of the "Solid Fusion" Reactor*. Journal of High Temperature Society, 2008; 34:85-93.

4. Y. Iwamura, M. Sakano and T. Itoh. Jpn J. Applied Physics 41, 4642-4648 (2002). *Elemental analysis of Pd complexes: effects of D₂ gas permeation.*
5. Y. Iwamura et al. Proceedings of ICCF12. (2005). pp. 178-187. *Observation of surface distribution of products by X-ray fluorescence spectrometry during D₂ gas permeation through Pd complexes.* World Scientific. ISBN: 981-256-901-4.
6. J. P. Biberian. *Cold Fusion by Gas Loading: A review in ICCF-14 International Conference on Condensed Matter Nuclear Science.* 2008. Washington, DC. Publishing by World Scientific.
7. F. Celani et al. Proceedings of ICCF13. June 24-July 2 2007. (2007) Sochi (Russia). *High Temperature Deuterium Absorption in Palladium Nano-Particles.* Publishing by World Scientific. Also report INFN-LNF 07-18(p).
8. F. Celani et al. *High temperature experiments, by differential reactor, on deuterium absorbed by HSA Pd_black or γ -Al₂O₃-Pd-Sr(NO₃)₂ nanopowder.* Presented at VIII International Workshop on Anomalies in Hydrogen/Deuterium-Loaded Metals. 13-18 October 2007 Catania (Italy). Also LNF-LNF08-11(P).
9. A. Takahashi et al., ICCF3, Nagoya October 1992. *Anomalous excess heat by D₂O/Pd cell under L-H mode electrolysis.* pp. 79-92, Universal Academic Press ISBN 4-946443-12-6.
10. M. Fleischmann et al., ICCF4, Maui (USA). December 5-9, 1993. Also at: Transactions of Fusion Technology, Vol. 26, pp 23-43, (1994). *Alfred Coehn and after: the α , β , γ , of the Palladium –Hydrogen system.*
11. F. Celani et al. Physics Letters A, Vol. 214, pp. 1-13, 1996. *Deuterium overloading of palladium wires by means of high power μ s pulsed electrolysis and electromigration: suggestions of a “phase transition” and related excess heat.*
12. Helge Petersen, Danish Atomic Energy Commission, Research Establishment RISO. Report No 224 (1970). *The properties of Helium: Density, Specific Heat, Viscosity and Thermal Conductivity at pressures from 1 to 100bar and from Room Temperature to about 1800K.*
13. S. C. Saxena. *Thermal conductivity data for hydrogen and deuterium in the range 100-1100°C.* J. Phys. A: Gen. Phys. 3-309-320, (1970).

Basic Research on Condensed Matter Nuclear Reaction Using Pd Powders Charged With High Density Deuterium

T. Nohmi¹, Y. Sasaki¹, T. Yamaguchi¹, A. Taniike¹, A. Kitamura¹, A. Takahashi², R. Seto² and Y. Fujita²

¹ *Division of Marine Engineering, Graduate School of Maritime Sciences, Kobe University
5-1-1 Fukaeminami-machi, Higashinada-ku, Kobe 6580022, Japan*

² *Technova Inc.*

*The Imperial Hotel Tower, 13F, 1-1 Uchisaiwaicho 1-chome, Chiyoda-ku, Tokyo 1000011,
Japan*

Abstract

We have constructed an experimental system to replicate the phenomenon of heat and ^4He generation by D_2 gas absorption in nano-sized Pd powders reported by Arata,¹ and to investigate the underlying physics. We performed calorimetry during D_2 or H_2 absorption with micronized powders of Si, Pd and Pd-black. With Pd-black and D_2 , after the palladium deuteride formed, the cell produced 8.3 ± 4.5 kJ (or 2.6 ± 1.4 kJ/g), which is somewhat larger than the systematic error of 4.0 kJ estimated from a D_2 blank.

1. Introduction

Arata recently reported¹ that high purity D_2 gas charging of Pd nano-powders in the form of Pd/ZrO₂ nano-composite induced significantly higher temperatures inside the reactor vessel than on the outside wall, while blank runs using H_2 gas showed almost no temperature difference. The temperature difference lasted for more than 50 hours. To verify that the excess heat came from a nuclear reaction, QMAS was employed to show the existence of ^4He as nuclear ash in the vessel. The phenomenon seemed to be highly reproducible as long as the same test equipment was used.

In the present work we constructed an experimental system to replicate the phenomenon of heat and ^4He generation and to investigate the underlying physics. We report preliminary results.

2. D_2/H_2 absorption system

The system is composed of two identical chambers (a twin system): one for a D_2 gas foreground run, and the other for H_2 gas blank run. Each system has an inner reaction chamber containing Pd powder and an outer chamber that is evacuated to provide thermal insulation. Inside the reaction chamber is located a sample cup, around which a heater is wound for baking. In addition to thermocouples located on the sample cup and the outer surface of the reaction chamber for temperature measurement, a pair of thermocouples is provided for flow calorimetry to estimate the heat production rate by measuring the temperature difference between the inlet and the outlet of a cooling water pipe. The D_2 gas is nominally 99.5% pure

and the H_2 is 99.998% pure. Flow rate control of D_2/H_2 gas purified with a liquid-nitrogen cold trap is made with a Pd membrane filter which also serves as an additional purifier.

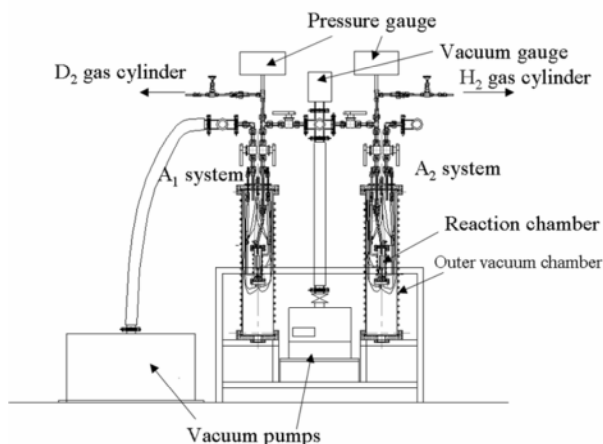


Figure 1. Simplified view of the system

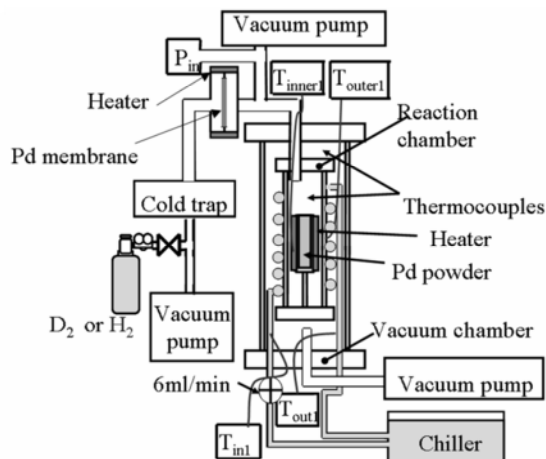


Figure 2. Functional view of the system

The reaction chamber is thermally isolated by evacuating the outer vacuum chamber. We measured the heat recovery rate with flow calorimetry under a variety of conditions: with input power of 1 W, 3 W, 6 W and 10 W; and reaction chamber D_2 gas pressure of 0 MPa, 0.1 MPa, 0.3 MPa and 1.0 MPa. The coolant flow rate was 6 ml/min in all cases.

We observed a temperature variation after changing the input power. Figure 3 shows the temperature difference during the power change from 10 W to 6 W. The variation is expressed by a sum of two exponential functions; one ($0 \sim 700$ s) with a time constant of τ_1 , and the other ($700 \text{ s} \sim$) with τ_2 . The values of τ_1 and τ_2 obtained from the fitting are listed in Table 1. The former we consider to be determined mainly by heat transfer from the cup to the reaction chamber due to convection and conduction through D_2/H_2 gas, while the latter is determined by conduction losses from the reaction chamber to the outer chamber.

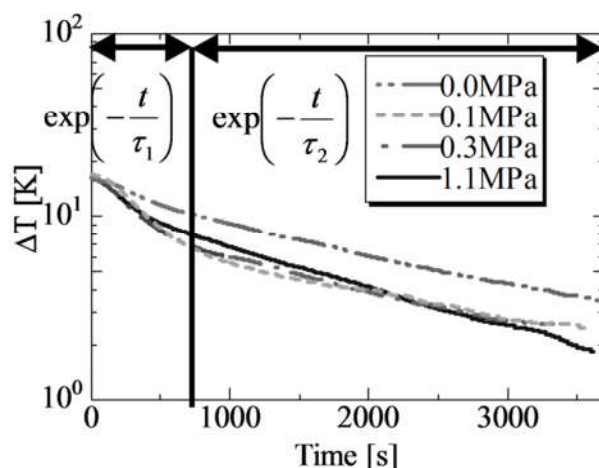


Figure 3. Calibration of flow calorimetry

Table 1. Thermal time constant deduced from the decay curves in Fig. 3.

MPa	τ_1 [s]	τ_2 [s]
0	1500	2700
0.1	690	3000
0.3	750	2600
1	930	2000

The heat recovery rate is summarized in Table 2. It is $66\% \pm 7\%$; and it is only marginally dependent on pressure and the input power.

Table 2. Heat recovery rate.

Pressure[MPa]	Input power [W]	Output power [W]	Heat recovery rate
0	10.0	5.9	59.3%
0	6.1	4.1	68.2%
0	3.0	2.2	72.5%
0	1.0	0.7	67.5%
3	10.0	7.0	70.2%
3	6.1	4.3	69.7%
3	3.0	2.2	71.8%
3	1.0	0.5	51.9%
1	10.0	6.8	68.1%
1	6.1	4.3	70.7%
1	3.0	2.0	68.3%
1	1.1	0.6	53.4%

4. Performance test of the Pd membrane filter

The Pd membrane (0.2 mm-t, 99.95%) separates the evacuated reaction chamber (1.6 ℓ) and the gas reservoir filled with D_2 at 1 MPa. The permeation rate of D_2 gas into the reaction chamber was derived as a function of membrane temperature by measuring the rate of pressure increase after stopping evacuation. Results are shown in Fig. 4. The D_2 gas flow rate is shown to be controllable between 0.1 and 25 sccm by varying the temperature from the room temperature to 900 K for membrane 2.

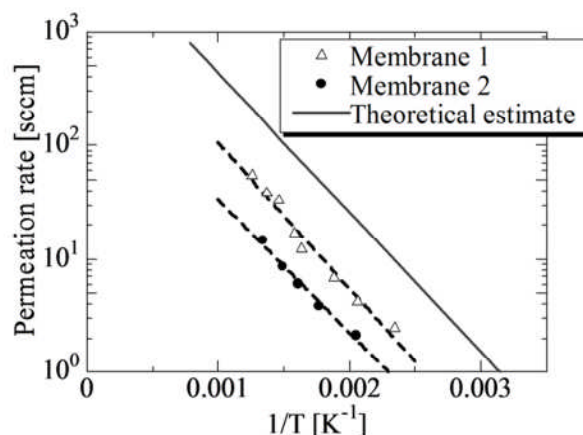


Figure 4. Permeation characteristics of the Pd membrane filter.

5. Blank run using a Si powder

We examined the temperature drift, or uncertainty, in the measurement of temperature using an 8-g, 150-mesh powder of Si with a purity of 99.999%. After evacuating the reaction chamber, the Si powder was baked at 470 K to outgas the Si powder. Next, highly pure D₂ gas was introduced into the reaction chamber through the Pd membrane filter. Figure 5 shows the variation of pressure in the system after introducing the D₂ gas, the inlet-outlet temperature difference ΔT of the coolant water, and the output power calculated from ΔT .

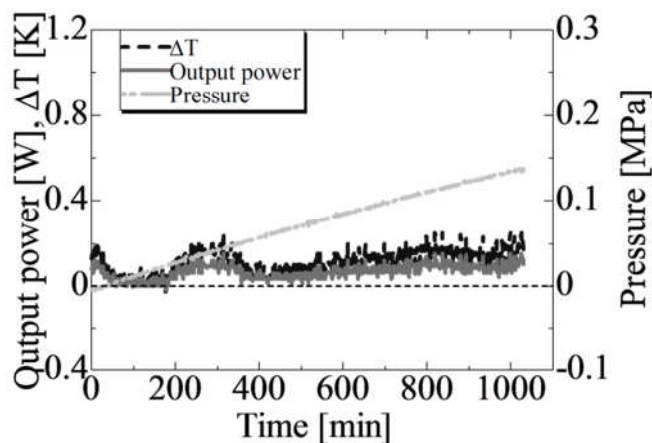


Figure 5. Evolution of temperature, heat and pressure in the vessel after exposure of the 150 mesh Si powder to D₂ gas.

The D₂ pressure in the system rises immediately after D₂ gas is introduced. The rate of pressure rise indicates a gas flow rate of 0.27 sccm. The observed variations in the temperature; *i.e.*, a short-term oscillation (with a period of few minutes) of about 0.1 K and a long-term drift (over a few hours) of about 0.2 K, should be considered inherent in the measurement system, and taken into account also in the foreground runs with Pd powders. The error in energy due to

the temperature drift amounts to 4.0 kJ for the 1000-minute run. This value is considered the error bound in output heat for the foreground runs in Tables 3 through 6.

6. 0.1- μm -diam. Pd powders with a purity of 99.5%

The sample cup was filled with 5 g of Pd powder with particle diameter size of 0.1 μm and a purity of 99.5%. The reaction chamber was evacuated, and the Pd powder was baked at 430 K. Then high purity D_2 or H_2 gas was introduced into the reaction chamber through the Pd membrane filter. The results are shown in Fig. 6 and 7 for two cases of D_2 absorption, and in Fig. 8 for H_2 absorption.

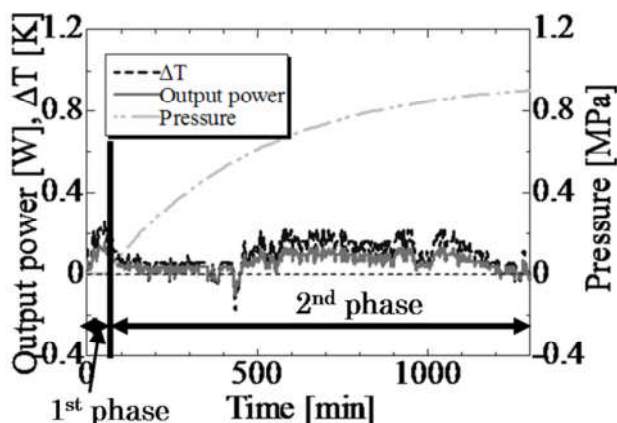


Figure 6. Absorption run for the 0.1- μm -diam. Pd powder. The D_2 gas flux is 4.3 sccm.

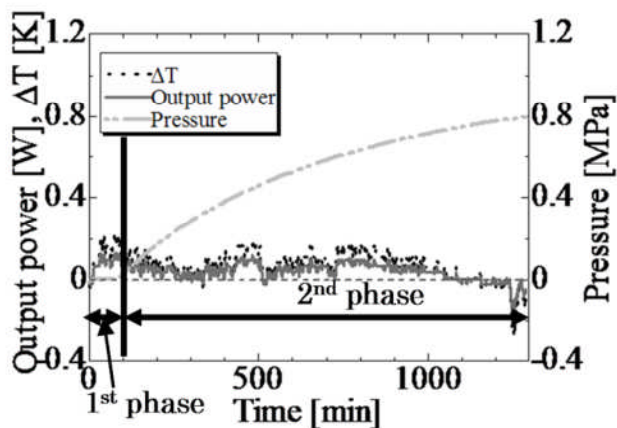


Figure 7. Absorption run for the 0.1- μm -diam. Pd powder. The D_2 gas flux is 3.5 sccm.

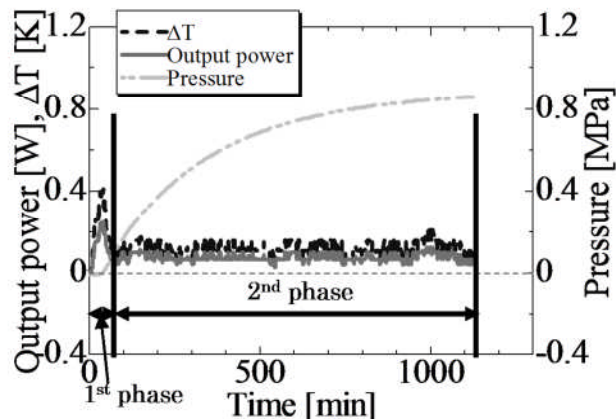


Figure 8. Absorption run for the 0.1- μm -diam. Pd powder. The H_2 gas flow rate is 6.8 sccm.

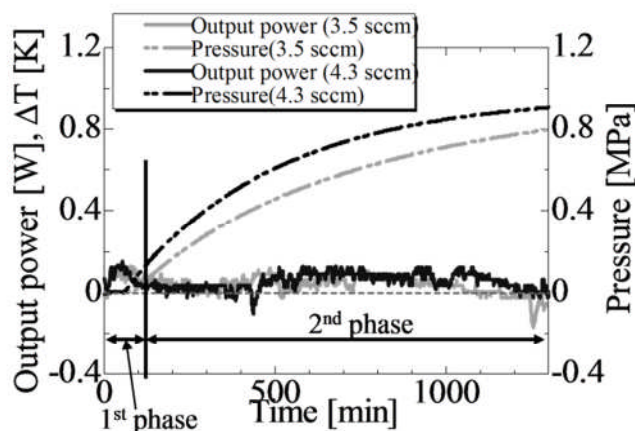


Figure 9. Absorption run for the 0.1- μm -diam. Pd powder; effect of flow rate.

After the gas is introduced, pressure does not begin to rise for a while. During this 1st phase the Pd powder absorbs almost all of the D_2 or H_2 gas as it flows in, and heat is released from the formation of the deuteride or hydride. Loading is estimated to reach $\text{PdD}_{0.43}$ or $\text{PdH}_{0.45}$. After about 30 minutes, the powder seems to stop absorbing gas; gas pressure begins to rise; and the heat release from deuteride or hydride formation subsides.

The performance with H_2 and D_2 gas was compared. The output energy in the 1st phase with H_2 (Fig. 8) is almost the same as that of D_2 , and is consistent with the nominal value of 100 to 405 J/g for the heat of hydride formation. The output energy in the 2nd phase appears to be larger for H_2 than D_2 . However, the difference is smaller than the error mentioned above, and is not meaningful in this case.

7. 300-mesh, 99.9% pure Pd black

The performance of Pd black absorption of D₂ (flow rate 4.5 sccm) was compared with H₂ (flow rate 5.6 sccm). Results are shown in Fig. 10 and summarized in Table 5. Much higher loading to PdD_{0.85} or PdH_{0.78} is realized compared to that in the case of 0.1- μ m-diam. Pd powder. The output energy in the 1st phase is almost the same for D₂ and H₂. It seems to be somewhat larger than the nominal values of 80 - 330 J/g (D₂) and 100 - 405 J/g (H₂). On the other hand, the output energy of 8.3 ± 4.5 kJ and 2.6 ± 1.4 kJ/g in the 2nd phase of D₂ absorption appears to be larger than that in the case of H₂. The difference is appreciably greater than the error due to the temperature drift of 5.5 kJ mentioned above for the Si blank run.

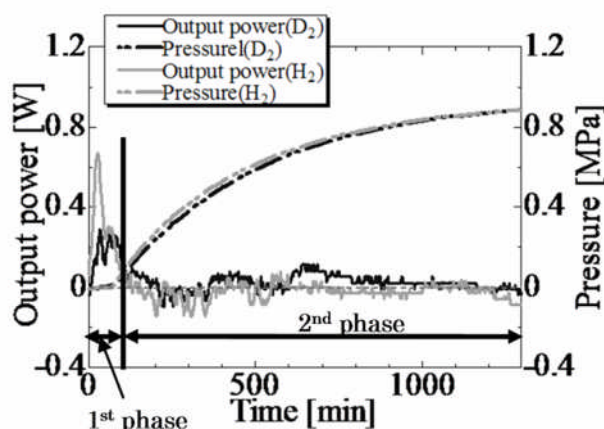


Figure 10. Absorption runs for 300-mesh Pd black; effect of gas species.

Table 3. Integrated output power for the 0.1- μ m-diam. Pd powder; effect of flow rate.

	3.5 sccm	4.3 sccm
1st phase	$(1.0 \pm 0.7) \times 10^2$ J/g	$(1.0 \pm 0.5) \times 10^2$ J/g
2nd phase	$(5.2 \pm 8.3) \times 10^2$ J/g	$(7.9 \pm 8.8) \times 10^2$ J/g

Table 4. Integrated output power for the 0.1- μ m-diam. Pd powder; effect gas species

	D ₂	H ₂
1st phase	$(1.0 \pm 0.5) \times 10^2$ J/g	$(1.2 \pm 0.3) \times 10^2$ J/g
2nd phase	$(7.9 \pm 8.8) \times 10^2$ J/g	$(1.1 \pm 0.8) \times 10^3$ J/g

Table 5. Results of absorption runs for 300-mesh Pd black; effect of gas species

	D ₂	H ₂
1st phase	$(5.4 \pm 1.0) \times 10^2$ J/g	$(4.5 \pm 0.8) \times 10^2$ J/g
2nd phase	$(2.6 \pm 1.4) \times 10^3$ J/g	$(-6.2 \pm 13) \times 10^2$ J/g

Table 6. Summary of the results of absorption runs.

Sample	weight [g]	Gas	Nominal flow rate [sccm]	Measured flow rate [sccm]	1st phase [J]	2nd phase [J]	1st phase [J/g]	2nd phase [J/g]	D/Pd or H/Pd
0.1 μ φ-Pd	5	D ₂	10	3.5	$(5.1\pm3.5)\times10^2$	$(2.5\pm4.1)\times10^3$	$(1.0\pm0.7)\times10^2$	$(5.2\pm8.3)\times10^2$	0.46
0.1 μ φ-Pd	5	D ₂	25	4.3	$(4.8\pm2.4)\times10^2$	$(4.0\pm4.4)\times10^3$	$(1.0\pm0.5)\times10^2$	$(7.9\pm8.8)\times10^2$	0.43
0.1 μ φ-Pd	5	H ₂	25	6.8	$(5.8\pm1.7)\times10^2$	$(5.6\pm3.9)\times10^3$	$(1.2\pm0.3)\times10^2$	$(1.1\pm0.8)\times10^3$	0.45
Pd black	3.2	D ₂	25	4.5	$(1.7\pm0.3)\times10^3$	$(8.3\pm4.5)\times10^3$	$(5.4\pm1.0)\times10^2$	$(2.6\pm1.4)\times10^3$	0.85
Pd black	3.6	H ₂	25	5.6	$(1.6\pm0.3)\times10^3$	$(-2.2\pm4.6)\times10^3$	$(4.5\pm0.8)\times10^2$	$(-6.2\pm13)\times10^2$	0.78

8. Concluding remarks

A Pd-H₂ / D₂ gas absorption system using commercial Pd powders has been constructed, with flow calorimetry and nuclear diagnosis. Calibration of the system and preliminary experimental results have been described. The results of the present work are summarized in Table 6.

When D₂ gas was used with Pd-black, apparent excess heat production was observed. However, temperature oscillations and drift were relatively large, so the accuracy of the system must be improved to confirm the result. For example, the time constant of the calorimeter has to be decreased by decreasing the heat capacity of the reaction chamber. Increasing the mass of the test sample should also help obtain clearer heat evolution. Nano-sized powders of Pd as well as a variety of alloy powders also deserve examination.

Reference

1. Y. Arata, et al.; The special report on research project for creation of new energy, J. High Temperature Society, No. 1. 2008.

These proceedings continue in Volume 2